PREPRINTS 4TH INTERNATIONAL WORKSHOP ON WAVE HINDCASTING AND FORECASTING

BANFF, ALBERTA
OCTOBER 16–20,1995

This workshop was supported by the Federal Panel on Energy R&D

Published by:

Environment Canada
Atmospheric Environment Service
4905 Dufferin Street
Downsview, Ontario
M3H 5T4

ACKNOWLEDGEMENTS

The organizers are indebted to many people who provided valuable assistance in the planning and conduct of the workshop. We would especially like to thank the sponsors, the federal Panel on Energy Research and Development and the Atmospheric Environment Service of Environment Canada, who provided the financial assistance for the workshop. The committee would also like to thank all those who submitted papers for the workshop program, and those who served as chairmen and rapporteurs for the various sessions. Special thanks are due to Krystyna Cutja who assisted in the assembly and production of this preprint, and to Andrew Cox of Oceanweather, Inc., who produced the cover photograph.

Cover: Photograph of the menu screen of a graphical interactive objective kinematic system for the north Atlantic Ocean. The system is described in paper P-3 in this volume (courtesy Oceanweather, Inc., Cos Cob CT).

VR, Swail, Chairman, Workshop Organizing Committee

4th International Workshop on Wave Hindcasting & Forecasting

AUTHOR INDEX

4th International Workshop on Wave Hindcasting & Forecasting

TABLE OF CONTENTS

Session P: Poster Session

Session C: Wave Modelling

Session D: Marine Boundary Layer

Session E: Wind Measurement and Remote Sensing

Session F: Wave Measurement and Interpretation

Session G: Operational Wave Forecasting

4th International Workshop on Wave Hindcasting & Forecasting

UNCERTAINTY IN PREDICTION OF EXTREME STORM SEAS (ESS)

V. J. Cardon[1] and V. R. Swail[2]

[1] Oceanweather, Inc.
Cos Cob, CT

[2] Environment Canada
Downsview, Ontario

1. INTRODUCTION

This paper addresses the uncertainty in predictions of Extreme Storm Seas (ESS), defined as occurrences of significant wave height (HS) greater than about 12 m. ESS should not be confused with extreme individual crest and crest-trough heights (Extreme Storm Waves or ESW) which often occur within ESS and which are often referred to as "rogue" or "freak" waves. ESS (and ESW) are of great importance in the specification of design wave climates for use in calculation of loads on offshore and coastal structures and study of ship responses. ESS are also, of course, of operational interest to the shipping and offshore industries.

This study is stimulated in part by the somewhat surprising frequency of measurements of ESS in recent years from buoys moored off the east and west coasts of North America and from offshore oil production platforms in the northern North Sea, and in part by recent hindcast studies which suggest a tendency for otherwise well validated wave models to under specify storm peak ESS even when forced by carefully hindcasted wind fields. The apparent increasing incidence of ESS has also been argued to be a signal for climate change. The issues addressed in this paper should be resolved before wave measurements or model derived series of storm maxima may be used to assess climate change or variability. Therefore, we strive in this study to identify the sources of uncertainty in the wind/wave hindcast process and attempt to estimate the uncertainty associated with each source.

The sources of uncertainty considered include: errors in wave height measurements themselves under ESS conditions (Section 2); errors in wind fields used to drive wave models (Section 3); effects associated with wave model physics or numerics (Section 4). We conclude (Section 5) with an overall estimate of the uncertainty in specification of ESS under even the b-st wave prediction circumstances and recommend research needed to reduce this uncertainty.

2. MEASUREMENTS OF EXTREME WAVES

2.1 Occurrences

Until the proliferation of moored data buoys off the east and west coasts of North America, instrumental measurements of ESS were quite rare. One notable earlier occurrence is the highest sea state sampled by an array of platform mounted capacitance wave gages operated in the northern Gulf of Mexico between 1969/1971 during the ODGP-OCMP programs (Ward, 1974, Forristall et al., 1980). In hurricane Camille (1969), a category 5 hurricane, one platform in deep water off the Mississippi Delta measured a HS of 13.4 m and a maximum wave height of 21.9 m in the core of the storm. Since the ODGP-OCMP programs, many measurements of waves have been acquired in tropical cyclones from buoys moored in the Gulf of Mexico and off the cast coast of the U. S. The maximum HS in a hurricane recorded to date was 14.3 m at NOAA buoy 41002 in hurricane Gloria (1985).

Significantly greater ESS have been measured just within the past five years in severe extratropical cyclones (ETC). Table 1 gives a by no mean; exhaustive list of measurements of ESS in recent years. These are unsmoothed highest single estimates and are likely to overestimate the true storm peak ESS, as discussed below. Two highly publicized occurrence,,; are the "Halloween Storm" (HOS) of October 26 - 1 November, 1991 (HOS) (Wang and Mettlach 1992) and the "Storm of the Century" (SOC) of March 12-15, 1993 (Wang, 1995). At Environment Canada (EC) buoy 44137, moored in deep water south of Nova Scotia, the measured peak HS exceeded 15 meters in both storms, with maximum HS of 17.4 m and crest-trough amplitudes exceeding 30 meters in HOS. At EC buoy 44141, the maximum HS was 15.2 m. These heights exceed current estimates of 100-year return period wave height extremes in deep water south of Nova Scotia (Eid et A, 1992) by up to 50%. At NOAA buoy 41002, moored in deep water east of South Carolina, the peak measured HS in the SOC was 15.7 meters, an all time record high for NOAA buoys and again exceeding current estimates of design wave heights in that area by a wide margin (e.g. the WIS estimate (Corson et al., 1981) for this site is about 12 meters for the 100-year condition). Even more recently, several events with peak HS greater than 14 m were observed in the EC buoy array, most recently 14.0 m at 44141 in the storm of 6 April, 1995.

In the eastern North Pacific Ocean, NOAA buoy 46001 measured HS of 14.8 m on 28 November, 1979 the highest ever reported by a NOAA buoy up to that time (Hamilton, 1982). Between 1986 and 1993 at least 15 occurrences of ESS are contained in the reports from the NOAA-EC array of buoys, with the highest of 15.7 m at EC buoy 46208 on 12 November, 1990. In the eastern North Atlantic Ocean and North Sea, ESS have been measured mainly within the last 5 years in association with an apparent increase in storminess there (WASA Group, 1995). Off the coast of Iceland, where 4 waveriders have been monitoring offshore since 1988, (Viggoson et al., 1993) a peak HS of 16.7 m was measured on 9 January, 1990 at one of the buoys and 16.3 m at another as the center of an intense ETC (minimum pressure < 940 mb) passed just north of Iceland. Some notable ESS measured recently in the northern North Sea/Norwegian Sea include a peak HS of 15.7 m in the ferocious storm of 1 January, 1992 and 13.6 m in the storm of 31 January, 1995 both measured at Magnus platform located at 61.6N, 1.30E.

2.2 Measurement Errors

The U. S. array of meteorological and oceanographic data buoys off the East, Gulf and West coasts of the U. S. were deployed mainly during the 1980's and now number more than 60 with exposures ranging from very near the coast (within 10 km) to moorings in very deep water up to 500 km offshore. An array of similar buoys but with slightly different measurement payload systems was deployed by EC offshore beginning in 1987 off the West Coast and expanded to off the East Coast beginning in 1991.

The most important characteristics of the buoy wave measurements in relation to this study are:

(i) Canadian and U.S. non-directional wave measurements use a "strapped down" accelerometer aligned with the buoy's mast, with the exception of buoy 44139, which employs a gimbaled Datawell heave sensor; the directional buoys (44014, 44025) use a gimbaled Hippy 40 sensor;

(ii) Canadian buoys sample waves at 1 Hz for 35 minutes; the NOAA buoys sample at 2.56 Hz (DACT payload) or 1.5 HZ (GSBP payload) for 20 minutes;

(iii) significant wave height in tenths of meters and peak period in tenths of seconds computed from the sample is recorded, along with the 1-D (or 2-D) spectra;

The detailed specifications for the NOAA and EC buoy payloads in operation during these events is given in NDBC (1993) and Axys Environmental Systems Ltd., (1992), respectively. For waves, the total measurement system accuracy is usually quoted as ± 0.2 m or 5% for HS and ± 1 sec for TP. These estimates however, are derived from calibrations carried out in low to moderate sea states (Gilhousen, 1987). In a recent field program, undertaken in the winter of 1994-1995 from a NOMAD buoy moored off the west coast of Canada, two different heave accelerometers were recorded twice per second when the HS exceeded 8 in. The preliminary analysis of the data (Skey et al.,

1995) shows generally good agreement between the two sensors. However this experiment does not indicate how faithfully the buoy itself is tracking the sea surface in ESS conditions. Thus, while ESS have been measured from buoys (North Atlantic, North Pacific) and fixed sensors on platforms (e.g. Gulf of Mexico, North Sea) we are not aware of measurements from both systems in the same sea state which might allow an assessment of the errors associated with buoy motions and/or mooring effects. We strongly recommend that such a comparison be made in areas where ESS are possible (e.g. near platforms in the North Sea or Norwegian Sea, and perhaps near the future Hibernia platform east of Newfoundland). Until such an experiment is carried out it is prudent to consider measurement errors in ESS conditions to be at least 5% and possibly up to 10%.

2.3 <u>Sampling Effects</u>

In addition to possible measurement errors, one must consider the effect of sampling variability, which for typical buoy sample lengths imparts an uncertainty of ± 10-15% in estimates of HS and ± 5% in estimates of peak spectral period (Donelan and Pierson, 1983). Sampling variability also imparts a bias in measurements of storm peak HS. Typically, a buoy or platform obtains an estimate of HS once each one, two or three hours, each estimate based upon a sample length of 18-35 minutes. If the duration of the storm peak at a measurement site is at least 6-12 hours, which is a reasonable assumption for typical extratropical storms, the buoy provides several measurements around the storm peak, and the maximum of those samples is therefore a biased overestimate of the true storm peak HS. For example, Table 2 shows a part of the record of hourly reports from 44137 in the HOS around the storm peak. Storm peak conditions evidently occurred between about 0355 UT and 0855 UT 30 October. The average HS over this period is 16.2 m. The absolute maximum estimate of HS is 17.4 in. The positive bias of the highest HS is therefore about 7.4%. Forristall. et al. (submitted) used accepted distribution functions for spectral estimates and for HS and computed the expected value of the maximum HS in a storm as a function of the spectral shape, the sample length, number of measurements and the storm peak duration. For typical sample lengths and storm durations in ETC, they find a positive bias in peak HS of 5-10%, increasing with the number of measurement samples made during peak conditions. In the validation of hindcasts of the HOC and SOC made by different models (Cardone et al, 1995a) the highest average of three consecutive estimates was used to represent the storm peak in order to minimize this source of bias.

3. WIND FIELD SOURCES

Errors in wind fields used to drive wave prediction models in a hindcast mode may be attributed to basically two sources: errors in measured winds which may contaminate analyses into which they are assimilated, and deficiencies in wind field analysis methods themselves, including the assimilation method and spatial and temporal resolution. In addition, when wave models are used in a forecast mode, additional wind errors arise in the inevitable growth of forecast error with time of synoptic scale systems to the chaotic limit of skill (typically 7-10 days). In this section these sources are discussed with particular regard to high wind regimes typically associated with ESS.

3.1 Wind Measurement Errors

Uncertainties in measured winds arc discussed for each source: ship reports; buoy winds, platform winds, satellite winds.

Ship Reports. Ship reports of wind come in two flavors: Beaufort estimates and anemometer estimates, and it is not always known which type a given report falls into. A great deal of new research is currently underway to improve the conversion of Beaufort Force or Number into equivalent wind speed (e.g. Cardone et al., 1990; see also COADS (1995)). That research has been stimulated by interest in historical marine winds for studies of climate variability and change. However, the upper limit of the Beaufort Scale, namely Beaufort 12, is equivalent to wind speeds which vary according to which scale is adopted from 56 knots for the Cardone et al. (1990) scale to ">563 knots" for the official WMO scale. Thus, even if the estimation of Beaufort number was unequivocal and the perfect equivalency scale was known, this system simply runs out of dynamic range at wind speeds associated with the generation of ESS.

An increasing percentage of ship wind reports are anemometer estimates taken at some (often unknown) location on the ship. There are numerous sources of error or uncertainty associated with wind measurement from ships, including the height of the anemometer above sea level, corrections (or lack of) for ship motion, averaging interval of the measurement, and distortion of the true marine wind field by the superstructure of the ship itself. A detailed review of the accuracy of ship measurements is given by Taylor et al. (1995). The flow distortion errors are almost always non-negligible, and may be the dominant factor at high wind speeds depending on the location of the anemometer and relative direction of the wind to the ship. The errors may also be of either sign. For this reason, Dobson (1983) recommended that corrections to measured winds from ships for anemometer height not be done unless corrections were also done for flow distortion. The latter is very difficult since there are many different, usually unknown, effects which contribute to the flow distortion problem.

A joint study has been undertaken between Environment Canada, Bedford Institute of Oceanography and the James Rennell Centre for Ocean

Circulation (U.K.) using a Computational Fluid Dynamics (CFD) approach to investigate flow distortion for various combinations of ship type, loading, wind speed and direction. The CFD study shows that the flow around the main anemometer site is very complex. The effect of the ship is detectable up to 100 in upstream of the bow and for tens of meters above the ship itself. There is no site on the ship which is unaffected by the ship's distortion of the air flow. From the results of this study it may be possible to produce a more homogeneous set of marine wind measurements from ships, corrected for the effects of shipboard flow distortion, on which climate variability analysis can be carried out and for use in assimilation of ship reports of wind into storm wind field analyses. Until such effects are better understood, ship reports should be considered unsuitable for very refined analyses of wind fields in extreme storms.

Buoy Winds. Meteorological buoys are widely considered to be the best possible source of data for marine winds. In addition to their direct use in climate analysis, buoy winds are widely used for a number of different applications: operational numerical weather prediction analysis schemes; validation of wind fields; use as "truth" for the validation and calibration of satellite and radar remote sensing systems. Buoy winds by no means form a homogeneous data type. For example considering only the U.S. and Canadian arrays we find the following differences:

(i) winds from the NOAA buoys are 8.5 minute scalar average speeds; directions are unit vector averages;

(ii) winds from the Canadian buoys are 10 minute vector average speeds and directions;

(iii) winds from the NOAA buoys may be at either 5, 10 or 13.8 m level; wind observations from the Canadian NOMAD buoys are at 4.6 to 5.4 in;

(iv) Canadian buoys also report the highest 8 second running scalar mean peak wind speed in the 10-minute sample; NOAA buoys report the highest 5 second window average obtained in the 8.5 minute sample.

It is therefore essential that the characteristics of these observing platforms be well understood, in a wide range of environmental conditions. Considerable work has been devoted to the demonstration of buoy capability in low to moderate sea states (e.g. Gilhousen, 1987). However, there has been little or no investigation of buoy winds in ESS conditions. It is commonly believed by operational meteorologists in Canada and the U.S. that the buoy average wind speeds are significantly underestimated in these conditions and that the reported gust speed is a more reasonable measure of the true sustained wind speed.

The field program noted above, undertaken during the winter of 1994-95 off the west coast of Canada, measured winds and waves from a NOMAD buoy twice per second when significant wave heights exceeded 8 m. Air temperature, magnetometer, buoy heading and vertical wind speed were also recorded at 2 H_z; sea surface temperature was recorded every 10 minutes. Preliminary results show that wind speeds vary considerably over a very short time frame, e.g. a factor of 2 over less than 10 seconds (see Figure 1). The wind direction may vary by more than 100 degrees over 10 minutes, with a standard deviation of 16 degrees (Figure 2). This variability will have a significant impact on the vector mean wind speed computed for the hourly wind report. Detailed analysis is presently being carried out to assess the magnitude of errors introduced by this vector averaging, as well as potential effects due to sheltering of the anemometers by the high waves (individual waves up to 22 m were sampled), and errors due to buoy motions (Skey et al., 1995).

Platform Winds. Winds measured from offshore platforms are potentially the most accurate source of marine winds in extreme storms. Instrument error can be very low provided the sensor is calibrated and checked periodically, there is no appreciable sensor motion, and flow distortion is minimal for sensors mounted well above the platform superstructure. These conditions are increasingly being satisfied for the newer platforms in the Gulf of Mexico, North Sea, Norwegian Sea and in other frontier areas of offshore exploration and production. Typically, the anemometer is a modem design, is calibrated, electronically recorded and averaged, and mounted at the top of the drilling derrick at heights of 40 in to as much as 100 meters off the sea surface. The only adjustments typically needed for such measurements are for sensor height and adjustment to neutral stratification. Interesting data sets have been acquired in the recent North Sea extreme storms noted above in ESS conditions which indicate that sustained winds in the marine boundary layer in ESS conditions, reduced to equivalent 20 in neutral stratification, can range as high as 40 m/s with gusts to as high as 50 m/s. Interestingly, in the HOS and SOC no buoy recorded average winds greater than 30 m/s during ESS conditions.

Satellite Winds. Remote sensing of the ocean is clearly an essential component of any future climate observing system due to the immense area to be covered and the difficulties and expense of using conventional in situ systems. However, these remote systems do not measure the desired geophysical parameters directly, but instead measure other parameters such as radar backscatter. Algorithms to convert to winds and waves must be developed and verified using high-quality in situ measurements from ships and buoys - this reinforces the importance of understanding the characteristics of such measurements.

Several types of satellite sensors capable of producing information on ocean waves and marine winds have been developed in recent years, including scatterometers, passive microwave radiometers, altimeters and synthetic aperture radars (SAR).

The scatterometer produces estimates of both wind speed and direction from the measured radar backscatter from the ocean surface. Wind speed accuracy may reach ± 1 m/s in low to moderate wind speed conditions and the uncertainty in wind direction is at least ± 10 degrees after a 180 degree ambiguity is removed by using neighbouring data or a good first guess field. Spatial sampling is of the order of about 25-50 km. Further algorithm development in conjunction with reliable ground truth is needed to improve accuracy.

The altimeter and microwave radiometers provide information on wind speed only. The radiometer provides wind speed data over a wide swath; the altimeter provides information only on the sub-satellite track. Accuracy is about ± 1-2 m/s for the altimeter, and about ± 2 m/s for the radiometer for most cases. Little or no calibration has been done for high wind speed cases.

The SAR provides detailed information over a wide swath with errors in wind speed of about ± 1 m/s for low to moderate wind speeds in comparison with accurate in situ measurements (Vachon and Dobson, 1995). The wind direction may be deduced from SAR imagery under some circumstances or may be taken from a wind analysis chart. The SAR data may be used to study kilometer-scale wind speed variations and is therefore useful in conjunction with mesoscale wind models.

With regard to ESS, one key question which remains unanswered is the upper limit of sensitivity to wind speed for remote sensors. Empirical evidence to date does not support sensitivity above equivalent 10 meter wind speeds of about 25 m/s which, if true as well for future systems (e.g NSCAT) would seriously limit the usefulness of satellite winds to prediction of ESS. Another limitation of remote sensing systems which needs to be appreciated is temporal resolution. Several recent hindcast studies suggest that the wind field features responsible for the generation of ESS are relatively small scale and evolve and propagate rapidly. Ideally, a three-hourly sampling is needed to resolve such features. For even a wide-swath remote sensor to satisfy this requirement, it must be mounted on at lust three operational polar orbiting satellites.

3.2 Wind Modeling Error Sources

SWADE (Weller et al., 1991) provided the first opportunity to develop surface wind fields in a large ocean area during several storms, from a data base which included not only high-quality surface wind measurements from buoys but also a sufficient number of them to avert the data gaps typical of open ocean areas. Initially, it was thought that this data base (available in real time over the GTS) would automatically lead to high-quality surface wind fields derived by objective analysis schemes as applied in real time within the operational systems of major centers such as NMC, ECMWF, FNOC and UKMO or in post-analyses produced by NASA. Unfortunately, when these wind fields for SWADE IOP-1 (centered on the development of an intense east coast cyclone of October 23-31, 1990 which deepened at about 1 Bergeron) were used to drive the WAM-4 wave model adapted to the SWADE area at high-resolution, errors in modeled sea states were found to be intolerably large (Graber et al., 1991). However, when the same data base was subjected to an intensive manual analysis using classical kinematic analysis, and the resulting wind fields were used to drive the WAM-4 wave model, wave hindcasts of unprecedented skill were found (Cardone et al., 1995b), Figure 3 (from Cardone et al., 1995b) compares the hindcast and buoy measurements of wave height at NOAA buoy 41001 from WAM-4 hindcasts driven by the alternative objectively analyzed wind and the kinematically derived winds.

The maximum HS observed in the SWADE array during IOP-1 was about 9 m. Therefore, at least for this sub-ESS event, the SWADE study of Cardone et al. (1995b) strongly suggests that the dominant error in specification of sea state in moderately intense marine cyclones arises in wind field errors. This in itself is not particularly new. However, the study further shows: (1) that these errors can be brought down to an acceptable level though an available tough tedious analysis method, provided accurate surface wind measurements are available at a data density roughly comparable to that achieved in the buoy array off the East Coast; (2) given high-quality winds, 3G models provide essentially perfect specification of the storm peak sea states about developing marine storms, at least in deep water.

The most significant wind field features found in the storms modeled in SWADE as well as in the hindcast studies of the HOS and SOC, in terms of generation of storm peak sea states, were relatively small scale, rapidly propagating surface wind maxima or ”jet streaks” which by virtue of their spatial and temporal coherency provide a dynamic fetch to couple very effectively to the surface wave field. The propagation speeds of these jet streaks, typically 15-20 m/s, do not necessarily match the speed of the parent cyclone center. The most extreme sea states in the SWADE IOP-1, HOS and SOC were measured at buoys directly in the path of the core of jet streaks. Figure 4 , for example shows the evolution of the surface wind jet streaks in HOS which are believed responsible for the generation of areas of ESS north of center of the storm.

Unfortunately, the SWADE hindcast study also shows that the objective analysis systems used at major operational centers do not yet fully realize the potential of the enhanced buoy array for surface wind analysis, and do not accurately resolve the small scale rapidly evolving features.

The deficiency of the operational systems is not simply attributable to grid spacing or time step, as shown by Graber et al., (1995) who used the SWADE kinematic winds in IOP-1 to systematically investigate the effect of degrading the spatial and temporal resolution of the reference SWADE wind fields on the accuracy of the hindcasts. Figure 5 is taken from their study. Figure 5a shows the reference wind field and the jet maximum with 25 m/s peak winds at its core, which was responsible for the generation of the storm peak sea states at buoy 41001 (see Figure 3). The time is just prior to the occurrence of peak HS at 41001. Figure 5b shows the field of hindcast HS hindcast, from the reference winds, at the same time. The effect of degrading the temporal and spatial resolution is shown in Figure 5c in terms of the distribution of peak HS at each buoy as a function of spatial and temporal resolution. The reference winds were specified on a 0.5 degree grid at hourly intervals.

Figure 5c shows a variety of responses at different buoys, which represent different locations within the evolving storm. At 41001, the buoy directly in the path of the jet streak, the maximum sensitivity is seen, and winds with 0.5 degree spatial resolution and no more than 3-hourly temporal resolution are required before the HS peak is reduced. At buoys such as 44001 and 44008, which were moored north of the storm track in a nearly linear slowly evolving wind field, even 12 hour sampling and 1.5 degree spacing did not degrade specification of the local HS storm peaks. Well outside the SWADE array, at buoy 4401 1, where even the reference winds were not very accurate, the storm peak HS was uniformly underestimated for all resolutions simulated. Within the SWADE array, however, it was found that the errors in the hindcasts of storm peaks resulting from the operational wind fields were always significantly greater than the errors for the particular cases simulated which matched the spatial and temporal resolution of the operational center winds.

Given the difficulties of hindcasting accurate wind fields even in data rich areas, one might expect even greater errors in forecasted surface wind fields in intense storms. While this is in general true, there is increasing evidence that primitive equation mesoscale NWP models when initialized from and nested within hemisphere or global NWP models, can provide realistic mesoscale wind field features such as those seen in storms which have generated ESS. For example, Ohm (1993) (see also Gronas, 1994) modeled the North Sea/Norwegian Sea storm of 1 January, 1992 and found quite accurate depiction of intensification of the parent cyclone and of the main wind field feature responsible for the generation of ESS which invaded the northern North Sea and Norwegian Seas in this storm. In a related study DesJardins (1995) used the EC MC2 mesoscale model, a fully elastic nonhydrostatic model, to forecast the SOC and specifically to examine how mesoscale features in the pressure field and sea surface temperature patterns affect the boundary layer winds. These new studies suggest that mesoscale NWP models include the essential physics and dynamics to model many of the small scale wind field features such as rapidly propagating jet streaks, mesoscale features associated with the Gulf Stream and its meanders, mesocyclones propagating along the bent-back warm front and sharp discontinuities in the wind field. While mesoscale NWP models are typically designed to be used in the forecast mode, they may also add value and accuracy in wind fields if used as a dynamic assimilation tool to produce accurate hindcasts of historical storm scenarios associated with ESS.

4. WAVE MODEL SOURCES

Numerical ocean wave models have advanced significantly within the past decade, particularly with the introduction of the so-called third generation (3G) class of models. First (1G) and second generation (2G) models have also been improved and remain in widespread use for climate assessment, engineering studies and operational forecasting. For example, a number of comprehensive extreme wave climate assessment studies using wave hindcasts made by the ODGP 1G model have been carried out since 1988 for the east and west coasts of Canada. Detailed verification studies have been carried out on these hindcasts, using all available measured data for Canadian waters. The results are summarized in a recent report (Atmospheric Environment Service, 1995). The east coast study was recently updated using a 3G model (Khandekar et al. (1994) and the old and new results are compared by Swad et al. (1995). The 3G approach has also been used to define the extreme wave climate in a basin (South China Sea) dominated by typhoons (Cardone et al. 1994) and we would expect the 3G model to be used increasingly in studies of this type over the coming years. The WAM-4 cycle of the official WAM 3G model (WAMDI, 1988) is used for operational global wave forecasting at several major NWP centers.

The three wave model classes are differentiated mainly by the simulation of the physics of deep water wave growth and decay. Due to remaining uncertainties in the underlying physics, however, all models rely to some degree on empirical tuning, based mainly on observations of wave growth in stationary fetch-limited wind fields of moderate strength. Most models are also tuned to allow the growth under constant winds to saturate at or at least approach asymptotically the wind speed dependent form for fully developed sea states proposed by Pierson and Moskowtiz (1964) over thirty years ago, which was based upon measured data over the wind speed range of 40 knots and HS up to about 9 meters.

The extensive suite of wave measurements made in HOS and SOC provides a rare opportunity to validate contemporary models in wave regimes far removed from those used for model tuning, but comparable to those encountered in the model applications cited above. Cardone et al. (1995a) applied four widely applied spectral wave models, namely Oceanweather's 1G and 3G models (Khandekar et al., 1994), a 213 wave model (Resio and Perrie, 1989) and WAM-4 (WAMDI, 1988) to these events using identical grids, and driven by a common wind field derived for each storm. The wind field was developed using kinematic analysis which used all conventional data, including ship and buoy observations received too late for use in real-time.

The alternative wave hindcasts were evaluated against time series of measured HS, dominant wave period, TP, and one-dimensional (frequency) wave spectra obtained at nine US and Canadian buoys moored in deep water between offshore Georgia and Newfoundland. Extensive statistical evaluation against time series and storm peaks were reported by Cardone et al (1995a) and in general indicates that all models are very skillful over a wide dynamic range of sea states up to the ESS threshold. Above the ESS threshold, however, it was found that despite the use of high-quality wind fields, the hindcast waves underestimated the peak HS at those buoys which measured ESS conditions, as shown in Figure 6 . Investigation of the earlier hindcast results cited above off the east and west coasts of North America showed a similar tendency - when the measured HS exceeded 12 in, the hindcast results were biased increasingly low (Figure 7). Similar results have been reported in other ocean basins and hindcast studies.

At the present time it does not appear possible to implicate any single cause for this under specification of ESS. Speculation with respect to causes for this tendency includes: (1) wind speeds are still underspecified, due to measurement uncertainties in ship and buoy winds, which feed into the kinematic analysis; (2) wave model growth reaches saturation prematurely; that is the P-M form can not be simply extrapolated into ESS conditions; (3) the tuned mechanisms for atmospheric input and dissipation source terms are extrapolated beyond the limits of applicability; (4) mesoscale and gust-scale features embedded in the synoptic scale flow contribute additional energy; (5) at these wave heights wind-wave coupling considerations become important; (6) spatial and temporal resolution were insufficient. While the temporal and spatial resolution of the wave hindcast models applied in the SWADE and HOS/SOC studies are very high compared to operational models, the relatively small scale of low-level jet streaks and the Lagrangian nature of the generation process of very extreme sea states may require even greater resolution.

5. CONCLUSIONS AND RECOMMENDATIONS

Numerous occurrences of significant wave heights greater than about 12 in (ESS) have been detected in recent years in routine wave measurements from data buoys moored off the east and west coasts of North America and from Northern North Sea and Norwegian Sea platforms. ESS have been measured by a variety of instruments including strapped-down and gimballed heave accelerometers mounted in a variety of buoys, and capacitance wave gages, radar and laser profilometers mounted from offshore platforms. These occurrences present a new and extreme challenge to modem wave prediction technology.

We have discussed the sources of uncertainty in predictions of ESS in terms of uncertainties arising in wave and wind measurements in ESS generation regimes, in wind fields used to drive the wave prediction models and in the wave models themselves, and offer the following assessments and recommendations for further investigation.

Wave measurements. Instrument and/or buoy induced wave measurement errors in ESS are unknown but are probably less than 10%. ESS measured from fixed gages mounted on platforms are comparable to buoy measured ESS, though the two types of measurements have not been acquired in the same location in the same event. We strongly recommend a field program be carried out to obtain such comparative data sets. Such a program may be carried out now at any of several platforms in the northern North Sea or within a few years at the Hibernia platform. Absolute highest estimates of individual storm peak HS are biased typically 5-10% high due to sampling variability, but averaging over all measurement samples acquired during a storm peak duration can reduce this bias to negligible levels.

Wind measurements. Ship reports of wind should be considered unsuitable for very refined analyses of wind fields in extreme stores because of the upper limit in the Beaufort Scale for such estimates and contamination of anemometer estimates due to flow distortion, instalment error and averaging uncertainties.

Winds from the buoy networks off the east and west coasts have greatly increased the accuracy of wind fields carefully hindcast there from resulting in wave predictions of unprecedented accuracy in sub-ESS regimes. However, operational meteorologists suspect buoys winds are too low in ESS conditions and this is supported somewhat by the difference between buoy wind speeds and platforms winds (as adjusted to 10 in equivalent neutral) in ESS conditions. A field program conducted off the west coast has sampled winds at high frequency in high sea states. Those data may provide insight into the effects of vector averaging and trough sheltering on operational buoy wind reports in ESS. In addition we recommend a field program to obtain both buoy winds and winds measured from a fixed platform at the same location in ESS conditions. Satellite active and passive microwave remote sensors promise routine global estimates of marine surface wind, but for ESS prediction, two limitations need to be addressed. First, there is no compelling field evidence to date that backscatter or emissivity remain responsive to wind speed at wind speeds (at 10 m) above 25 m/s. Second, unless such sensors are mounted on several operational satellites, the spatial and temporal sampling required to resolve the fast moving smaller scale wind field features apparently responsible for ESS in many storms will not be achieved.

Wind Fields. Recent hindcast studies of extratropical storm scenarios off the east coast of North America and over the North Sea indicate that assimilation of the enhanced surface wind data provided by the buoy and/or platform arrays through manual kinematic analysis provides surface wind fields which are considerably more accurate than real-time products of operational NWP centers. The same studies suggest that such analyses may also successfully resolve and track smaller scale rapidly propagating jet features which appear to be critical to the generation of ESS within extratropical cyclones. The recent implementation of kinematic analysis of marine surface winds on an interactive graphical workstation (Cox et al., 1995) greatly decreases the level of effort required to produce accurate wind fields in data rich areas. However, if the wind data (e.g. buoy winds) are biased in ESS conditions, so will the resulting wind fields in critical generation areas. This emphasizes the need for a better understanding of buoy winds in ESS conditions.

Real time forecasts of ESS conditions tend to be biased low because small scale high wind speed areas are not well resolved by synoptic scale NWP models. However, several recent and ongoing studies with mesoscale NWP models nested within synoptic scale NWP models suggest that such features may be resolved in cyclogenetic situations even in the absence of initialization of small scale features within the nested grid domain.

Wave Models. In sub-ESS wave regimes, contemporary wave models, including the WAM model, and highly tuned 1G, 2G and alternative 3G models, may provide outstanding skill in specification of the principal shape (total wave variance and HS) and scale (peak spectral period) properties of evolving sea states about developing marine storms when they are driven by high-quality winds, at least in deep water. However, in ESS in extratropical settings, these same models tend to underpredict the most extreme sea states by about 10%. This tendency has not been observed in hindcasts of extreme tropical cyclones (e.g. Cardone et al. 1994). This may be attributable to the fact that wave models adapted to tropical cyclone problems typically use much finer grids and time steps than when adapted to extratropical problems. In addition, such models are driven by winds determined not by in-situ surface wind but by primitive equation boundary layer models which have been previously tuned against high-quality data sets (e.g. Thompson and Cardone, 1995). Finally, in terms of stage of wave development, tropical cyclone peak sea states are quite immature, and therefore represent a wave regime within the tuning range of wave models.

Our overall assessment of uncertainty is that the bias in ESS using the most carefully hindcast wind fields in data rich marine environments and a well validated spectral wave model is negligible in tropical cyclone regimes and up to about 10% (low) in extratropical regimes. It does not yet appear to be possible to separate the contributions to this bias between buoy wind errors in ESS conditions to this bias between buoy wind errors in ESS conditions and model physics or tuning, though recent experimental and analytical work may soon resolve the bias in buoy winds at ESS due to buoy motion or trough sheltering, thereby allowing assessment of the pure wave model contributions.

6. REFERENCES

Axys Environmental Systems, 1992: Operations/maintenance/reference manual for NOMAD ZENO payloads. Available from AXYS Environmental Systems, Sidney, B. C.

Cardone, V. J. , J. G. Greenwood and M. A. Cane, 1990: On trends in historical marine wind data. J. of Climate, 3, 113-127.

Cardone, V. J., H. C. Graber, R. E. Jensen, S. Hasselmann and M. J. Caruso, 1995 a: In search of the true surface wind field during SWADE IOP-1: ocean wave modelling perspective. Accepted in: The Global Atmosphere and Ocean System

Cardone, V. L R. E. Jensen, D. T. Resio, V. R. Swail and A. T. Cox, 1995 b: Evaluation of contemporary oceanwave models in rare extreme events: "Halloween Storm" of October, 1991; "Storm of the Century" of March, 1993. Accepted in: J. Atmos. and Ocean. Tech.

Cardone, V. J. and C. K. Grant, 1994: Southeast Asia Meteorological and Oceanographic Hindcast Study. Offshore Southeast Asia 10th Conference and Exhibition, 6-9 December, Singapore.

COADS, 1994: Proceedings of the COADS Wind Workshop. May 30 - June 1, 1994, Kiel, Germany.

Corson, W. D., D. T. Resio, R. M. Brooks, B. A. Ebersole, R. E. Jensen, D. S. Ragsdale, and B. A. Tracy, 1981: Atlantic coast hindcast deepwater significant wave information. WIS Report 2, US Army Engineer Waterways Experiment Station, Vicksburg Ms.

Cox, A. T., J. A. Greenwood, V. J. Cardone and V. R. Swail, 1995: An interactive objective kinematic analysis system. Fourth International Workshop on Wave Hindcasting and Forecasting. October 16-20, 1995. Banff, Alberta, Canada.

Desjardins, S., 1995: The influence of the Gulf Stream and its meanders on the marine boundary layer winds. Fourth International Workshop on Wave Hindcasting and Forecasting. October 16-20, 1995. Banff, Alberta, Canada.

Dobson, F. W., 1983. Review of reference height for and averaging time of surface wind measurements at sea. Report No. 3, Marine Meteorology and Related Oceanographic Activities. World Meteorological Organization, Switzerland, 56 p.

Donelan, M. A. and W. J. Pierson, 1983: The sampling variability of estimates of spectra of wind-generated waves. J. of Geophys. Res., 88, C7, 4381-4392.

Eid, B. M., C. Morton, E. Dunlop and T. Pierce, 1992: Development of wind and wave climate atlas for the east coast of Canada and the Great Lakes. Preprints of the Third International Workshop on Wave Hindcasting and Forecasting, May 19-22, 1992, Montreal, Quebec, 362-372.

Forristall, G. Z., E. G. Ward and V. J. Cardone, 1980: Directional wave spectra and wave kinematics in hurricanes Carmen. In Proceedings of the 17th International Coastal Engineering Conference, March 23-28, ASCE, Sydney, Australia.

Forristall, G. Z., J. C. Heideman, J. de Ronde and L. Vanderschuren, 1995: The effect of sampling variability on the comparison of hindcast and measured wave heights. Submitted to J. of Waterway, Port and Coastal Engineering.

Graber, H. C., M. J. Caruso and R. E. Jensen, 1991: Surface wave simulations during the October storm in SWADE. Proc. MTS '91 Conf.,

Marine Technology Society, November 11-13, 1991, New Orleans, La., 159-164.
Graber, H. C., R. A. Jensen and V. J. Cardone, 1995: Sensitivity of wave model predictions on spatial and temporal resolution of the wind field. Fourth International Workshop on Wave Hindcasting and Forecasting. October 16-20, 1995. Banff, Alberta, Canada.

Gilhousen, D. B., 1987: A field evaluation of NDBC moored buoy winds. J. Atmos. Ocean. Tech., 4, 94104.

Gronas, S., 1994: The seclusion intensification of the New Year Day storm of 1992. International Symposium on the Life Cycles of Extratropical Cyclones. 27 June - 1 July, 1994. Bergen, Norway. p. 432 - 437.

Hamilton, G. D. 1982. Severe buoy wave heights. Mariner's Weather Log, 26, (3), 122-126.

Khandekar, M. L., R- Lalbeharry and V. J. Cardone, 1994: The performance of the Canadian spectral ocean wave model (CSOWM) during the Grand Banks ERSI SAR wave spectra validation experiment. Atmosphere-Ocean, 32, 31-60.

NCDC, 1993: NOAA Marine Environmental Data on CD-ROM. 14-disc set available from National Climatic Data Center, Asheville, NC

Ohm, C., 1993. Numerical simulations of the New Year's Day Storm 1992: Master Degree Thesis in Meteorology. Geophysical Institute of Bergen. 101 pp.

Pierson. W. J. and L. Moskowitz, 1964: A proposed spectral form for fully developed wind seas based on the similarity theory of S. A. Kitaigorodskii. J. Geophys. Res., 69, 5181.

Resio, D. T. and W. Perrie, 1989: Implications of an P 4 equilibrium range for wind-generated waves, J. of Phys. Oceanog., 19, 193-204.

Skey, S. G. P., K. Berger-North and V. R. Swail. 1995. Detailed measurements of winds and waves in high sea states from a moored NOMAD weather buoy. Fourth International Workshop on Wave Hindcasting and Forecasting. October 16-20, 1995. Banff, Alberta, Canada.

Swail, V. R., M. J. Parsons, B. T. Callahan and V. J. Cardone. 1995. A revised extreme wave climatology for the east coast of Canada. Fourth International Workshop on Wave Hindcasting and Forecasting. October 16-20, 1995. Banff, Alberta, Canada.

Taylor, P. K., E. Kent M. Yelland amd B. Moat 1995: The accuracy of wind observations from ships. Proceedings of International COADS WIOnds Workshop, Kiel, Germany, 31 May-2 June, 1994.

Thompson, E. F. and V J. Cardone. 1995. Practical modeling of hurricane surface wind fields. Accepted in J. of Waterway, Port and Coastal Engineering.

Vachon, P. and F. Dobson. 1995. Validation of wind speed retrieval from ERS-1 SAR images. Fourth International Workshop on Wave Hindcasting and Forecasting. October 16-20, 1995. Banff, Alberta, Canada.

Viggosson. G., S. Sigurdarson and L Jonsdottir. 1993. Wave measurements in Iceland. Workshop on climate Trends and Future Design and Operation Criteria. Reykjavik, Iceland 29-30 March 1993. Available from Norwegian Meteorological Institute, Bergen.

Weller, R. A., M. A. Donelan, M. G. Briscoe and N. E. Huang. 1991. Riding the crest: A tale of two experiments. Bull. Amer. Met. Soc.. 72, 2, 163 -183.

WAMDI Group. 1988. The WAM model - a third generation ocean wave prediction model. J. Phys. Oceanogr., 8, 1775-1810.

Wang, D. 1995. Extreme waves during the storm of the century, Fourth International Workshop on Wave Hindcasting and Forecasting. October 16-20, 1995. Banff, Alberta, Canada.

Wang, D. and T. Mettlach. 1992. The Halloween storm: data observations from NDBC stations. Preprints of the Third International Workshop on Wave Hindcasting and Forecasting, May 19-22, Montreal, Quebec, 383400.

Ward, E. G., 1974. Ocean Data Gathering Program An Overview. Paper OTC 2108-B. Sixth Annual Offshore Technology Conference. Houston, TX, May 6-8, 1974. 771-780.

WASA Group. 1995. Wave and Storm Climate in the North Atlantic - WASA Project. Fourth International Workshop on Wave Hindcasting and Forecasting. October 16-20, 1995. Banff, Alberta, Canada.

TABLE 1

Instrumental measurements of Extreme Storm Seas
(ESS, HS > 12 m) through 1993

Date (YMD)	Site	Location	ESS (m)	Remarks
690817	Platform	Gulf of Mexico	13.4	Hurricane Camille
791128	46001	Gulf of Alaska	14.8	Hamilton (1982)
810304	46003	S. Aleutians	14.0	
811112	Platform	North Sea	12.8	
820114	Platform	Norwegian Sea	14.8	
820214	MEDS 140	Grand Banks	12.7	Ocean Ranger Storm
830219	46006	E. Pac SE PAPA	13.0	
831110	46002	E. Pac Oregon	12.0	
831222	MEDS 134	Grand Banks	12.5	
831222	MEDS 168	Grand Banks	13.3	
840224	46002	E. Pac. Oregon	13.5	
840225	46022	E. Pac. Eel River	12.0	
850417	46003	S. Aleutians	12.0	
850926	41002	S. Hatteras	14.5	Hurricane Gloria
861123	46004	E. Pac. Brit. Col.	14.0	
871201	46005	E. Pac. Washington	13.5	
871215	46003	S. Aleutians	12.0	
880216	46003	S. Aleutians	12.0	
880305	46036	E. Pac. Brit. Col.	12.0	
881127	46004	E. Pac. Brit. Col.	14.8	
881127	46205	E. Pac. Dixon Ent.	12.8	
881221	46002	E. Pac. Oregon	12.5	
881130	46205	E. Pac. Dixon Ent.	12.2	
890105	44138	S. Cape Race	14.2	
891010	46035	Bering Sea	12.9	
900109	Buoy	S. Iceland	16.7	
901027	46004	E. Pac. Brit. Col.	12.6	
901027	46205	E. Pac. Dixon Ent.	15.0	
901112	46004	E. Pac. Brit. Col.	14.0	
901112	46208	E. Pac. Q. Char. Is.	15.7	
901112	46205	E. Pac. Dixon Ent.	14.7	
901212	Platform	North Sea	14.0	
910923	46003	S. Aleutians	13.2	
911030	44011	Georges Bank	12.0	Halloween Storm
911030	44137	SE Sable Is.	17.4	Halloween Storm
911030	44141	SE Sable Is.	15.2	Halloween Storm
911220	46185	Hecate Strait	14.3	
920101	Platform	North Sea	15.4	New Year's Day Storm
921204	44137	SE Sable Is.	13.4	
921213	46184	W. Dixon Entr.	14.1	
921214	46004	E. Pac. Brit. Col.	13.8	
921225	44138	S. Cape Race	12.3	
930118	44141	SE Sable Is.	12.7	
930119	46185	Hecate Strait	13.1	
930314	41002	S. Hatteras	15.7	Storm of the Century
930314	44137	SE Sable Is.	15.0	Storm of the Century
931227	44138	S. Cape Race	14.2	
931231	44138	S. Cape Race	14.3	

Table 2.

Hourly observations at AES buoy 44137 (41.2N, 61.1W) in Halloween Storm. Hour is UT. Dir1/D2 is wind direction, SPD1/SPD2 is wind speed (m/s), SWH is significant wave height (M), PER is peak wave period (sec), HMAX is maximum wave height (m), PRESS 1/2 is sea level pressure, TAIR is air temperature, TSEA is sea temperature, both in deg. C.

YEAR	MON	DY	HOUR	DIR1	SPD1	DR2	SPD2	SWH	PER	S1MX	S2MX	HMAX	PRESS1	PRESS2	TAIR	TSEA	BUOY#	WATER
1991	Oct	29	2355	359	10.3	30	10.4	2.7	32.0	12.4	12.3	6.3	1003.5	1003.4	15.9	20.2	44137	0
1991	Oct	29	055	355	12.4	24	12.3	3.1	32.0	14.5	14.4	6.0	1002.8	1002.8	15.7	20.2	44137	0
1991	Oct	29	155	358	14.0	26	13.9	3.3	7.4	16.5	16.3	5.7	1002.7	1002.7	14.9	20.2	44137	0
1991	Oct	29	255	2	13.5	30	13.4	3.8	7.4	16.8	16.8	6.7	1002.8	1002.8	14.5	20.2	44137	0
1991	Oct	29	355	3	16.1	31	16.0	4.5	9.5	20.4	20.2	9.5	1002.4	1002.3	13.4	20.3	44137	0
1991	Oct	29	455	10	17.7	38	17.5	5.9	10.7	21.7	20.6	12.0	1002.6	1002.6	12.7	20.3	44137	0
1991	Oct	29	555	4	18.4	32	18.4	6.1	11.1	22.6	21.9	10.9	1003.3	1003.3	11.9	20.4	44137	0
1991	Oct	29	655	6	18.0	36	18.4	7.2	12.2	22.3	21.4	16.4	1003.6	1003.6	11.5	20.4	44137	0
1991	Oct	29	755	11	18.2	43	18.3	7.9	11.6	22.7	22.5	14.9	1003.1	1003.1	11.7	20.5	44137	0
1991	Oct	29	855	9	20.3	43	20.3	8.5	12.8	25.4	24.8	15.6	1003.3	1003.3	11.3	20.7	44137	0
1991	Oct	29	955	17	20.6	50	20.8	8.5	13.5	25.5	24.8	13.4	1003.3	1003.3	11.0	20.7	44137	0
1991	Oct	29	1055	15	20.5	51	20.4	9.7	13.5	25.8	25.9	18.9	1004.0	1004.0	11.0	20.7	44137	0
1991	Oct	29	1155	14	19.7	53	19.5	9.2	13.5	24.9	24.3	21.5	1004.1	1003.9	11.1	20.8	44137	0
1991	Oct	29	1255	17	20.0	58	19.4	9.9	12.8	23.9	24.1	17.7	1004.6	1004.5	10.9	20.8	44137	0
1991	Oct	29	1355	19	18.6	59	18.3	9.4	12.8	24.5	23.5	14.2	1004.2	1004.2	11.6	20.8	44137	0
1991	Oct	29	1555	25	18.9	62	19.0	11.6	15.1	24.1	23.9	20.1	1004.3	1004.3	11.7	20.6	44137	0
1991	Oct	29	1655	31	19.0	65	18.8	10.3	15.1	25.1	24.9	18.1	1003.0	1003.0	12.4	20.5	44137	0
1991	Oct	29	1755	26	19.4	59	19.3	11.5	15.1	26.2	25.3	21.2	1003.1	1003.1	11.9	20.4	44137	0
1991	Oct	29	1855	29	20.7	58	20.5	12.3	16.0	26.8	25.9	17.6	1003.0	1002.9	12.0	20.3	44137	0
1991	Oct	29	1955	30	20.7	59	20.5	12.0	16.0	26.2	25.9	24.6	1002.4	1002.4	12.2	20.2	44137	0
1991	Oct	29	2055	27	21.6	57	21.3	11.8	17.1	28.4	27.7	18.4	1001.9	1001.8	12.5	20.2	44137	0
1991	Oct	29	2155	32	20.6	64	20.7	12.5	17.1	27.4	26.5	22.9	1001.3	1001.3	13.1	20.2	44137	0
1991	Oct	29	2255	44	21.7	76	21.5	13.6	17.1	27.5	27.2	24.2	1000.9	1000.9	13.7	20.2	44137	0
1991	Oct	30	2355	43	21.7	77	21.8	14.5	15.1	29.6	29.2	29.8	1000.8	1000.7	14.2	20.2	44137	0
1991	Oct	30	055	39	22.6	75	22.8	13.3	15.1	29.0	29.0	23.9	999.3	999.3	14.3	20.2	44137	0
1991	Oct	30	155	41	24.3	79	23.8	14.3	17.1	32.7	32.0	26.3	997.1	997.1	14.5	20.2	44137	0
1991	Oct	30	255	41	24.8	80	24.7	15.2	17.1	35.1	33.9	22.4	998.2	998.1	14.6	20.1	44137	0
1991	Oct	30	355	40	23.7	80	23.5	17.4	18.3	32.3	32.0	30.7	996.9	996.9	14.8	20.1	44137	0
1991	Oct	30	455	41	24.3	81	24.0	16.3	16.0	31.4	31.3	29.4	996.3	996.4	14.5	20.0	44137	0
1991	Oct	30	555	41	23.7	82	23.3	17.2	18.3	31.7	31.5	30.6	995.1	995.2	14.4	19.9	44137	0
1991	Oct	30	655	55	24.4	95	23.9	14.7	18.3	34.0	33.8	24.0	994.0	994.0	15.7	19.9	44137	0
1991	Oct	30	755	57	21.6	98	20.9	15.8	16.0	29.3	28.6	24.1	994.2	994.2	16.9	19.9	44137	0
1991	Oct	30	855	77	15.6	121	15.4	15.8	18.3	19.5	19.9	26.4	994.5	994.5	19.2	20.0	44137	0
1991	Oct	30	955	95	13.0	145	12.4	15.2	18.3	16.3	15.9	22.4	995.8	995.9	19.4	20.1	44137	0
1991	Oct	30	1055	108	14.2	158	13.5	14.1	16.0	19.3	18.7	23.3	997.8	997.7	19.5	19.9	44137	0
1991	Oct	30	1155	110	14.1	158	13.4	13.1	18.3	19.8	19.2	24.1	999.0	999.0	19.0	20.1	44137	0
1991	Oct	30	1255	105	17.6	151	16.7	12.4	17.1	22.3	21.9	25.2	999.6	999.5	20.2	20.1	44137	0
1991	Oct	30	1355	119	17.0	164	16.3	12.2	17.1	22.8	22.0	19.6	1001.4	1001.4	21.3	20.3	44137	0
1991	Oct	30	1455	126	17.4	167	16.7	13.3	17.1	23.0	22.0	21.3	1003.3	1003.4	21.4	20.4	44137	0
1991	Oct	30	1555	128	16.5	167	15.8	11.1	17.1	21.2	20.5	18.0	1003.8	1003.8	21.3	20.4	44137	0
1991	Oct	30	1655	138	15.4	173	14.8	11.6	13.5	19.2	18.7	20.0	1005.1	1005.1	21.5	20.3	44137	0
1991	Oct	30	1755	146	13.5	177	13.0	11.4	16.0	17.6	16.4	19.9	1006.7	1006.6	21.6	20.3	44137	0
1991	Oct	30	1855	140	12.6	169	12.1	10.5	13.5	16.3	15.5	18.2	1008.0	1008.0	21.6	20.3	44137	0
1991	Oct	30	1955	139	12.2	168	11.9	10.3	11.6	17.8	17.2	18.9	1009.8	1009.6	21.6	20.2	44137	0
1991	Oct	30	2055	140	11.8	169	11.7	9.4	11.6	15.4	15.3	14.9	1011.2	1011.1	21.1	20.1	44137	0
1991	Oct	30	2155	127	9.1	156	8.8	8.7	13.5	12.1	11.7	15.5	1012.1	1012.0	21.0	19.8	44137	0
1991	Oct	30	2255	131	11.2	164	11.0	8.6	15.1	13.6	13.8	13.6	1013.3	1013.1	21.7	19.7	44137	0
1991	Oct	31	2355	135	11.0	175	10.9	8.0	13.5	14.1	14.2	11.9	1014.6	1014.5	21.6	19.6	44137	0

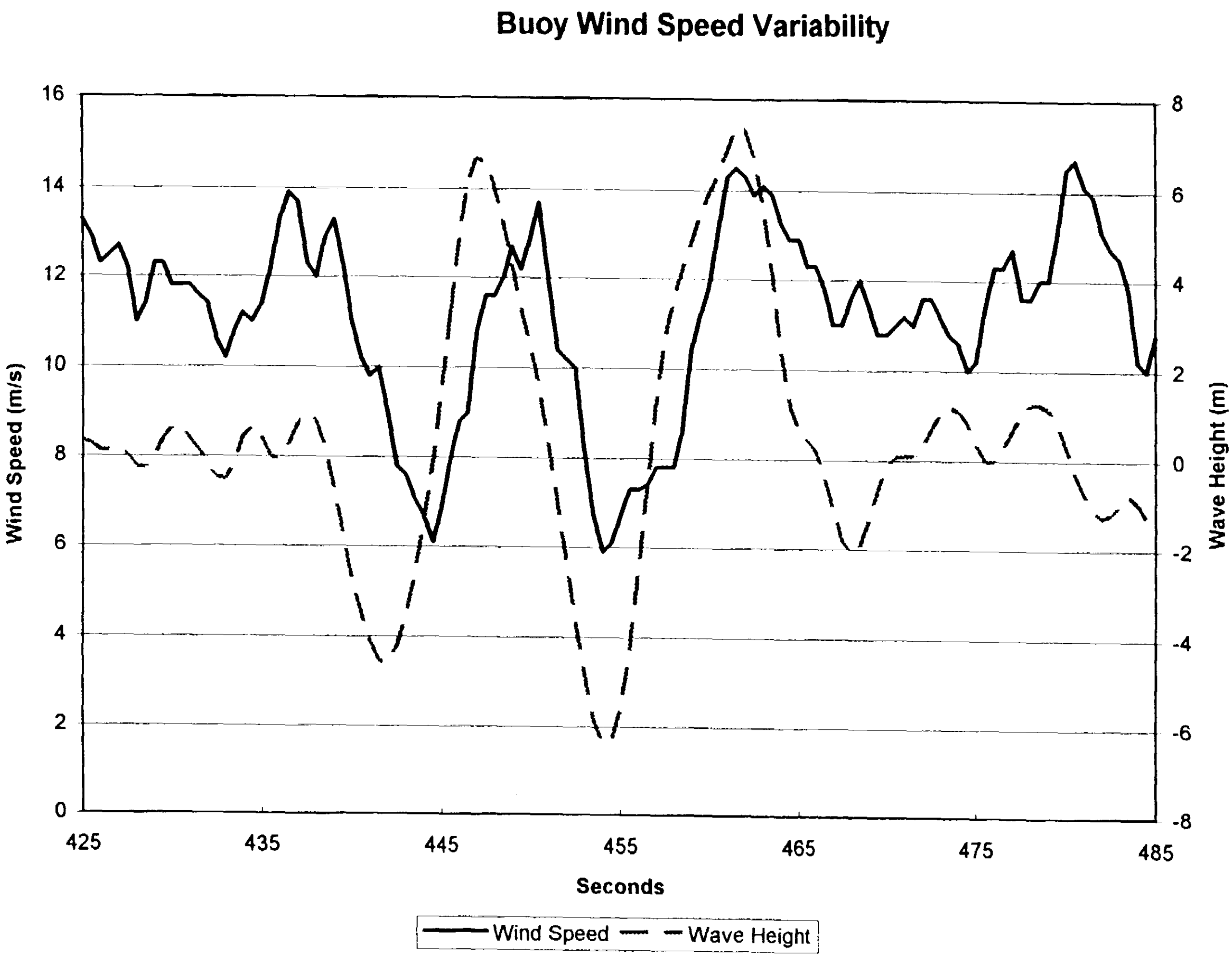

Figure 1. Sample of 2-Hz record of wind speed and surface elevation from a NOMAD buoy moored off the West Coast of Canada

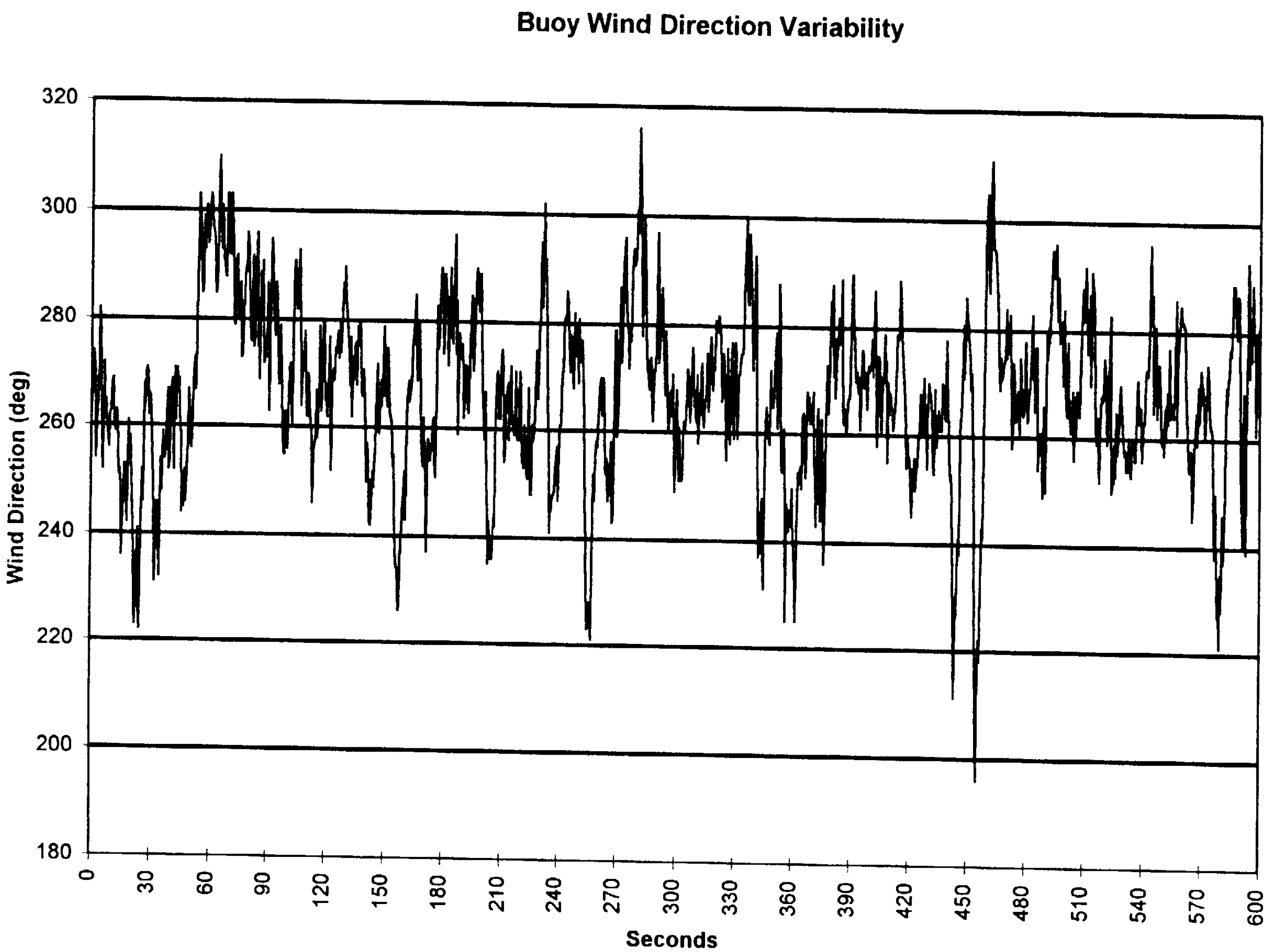

Figure 2. Sample of 2–Hz record of wind direction from a NOMAD buoy moored off the West Coast of Canada.

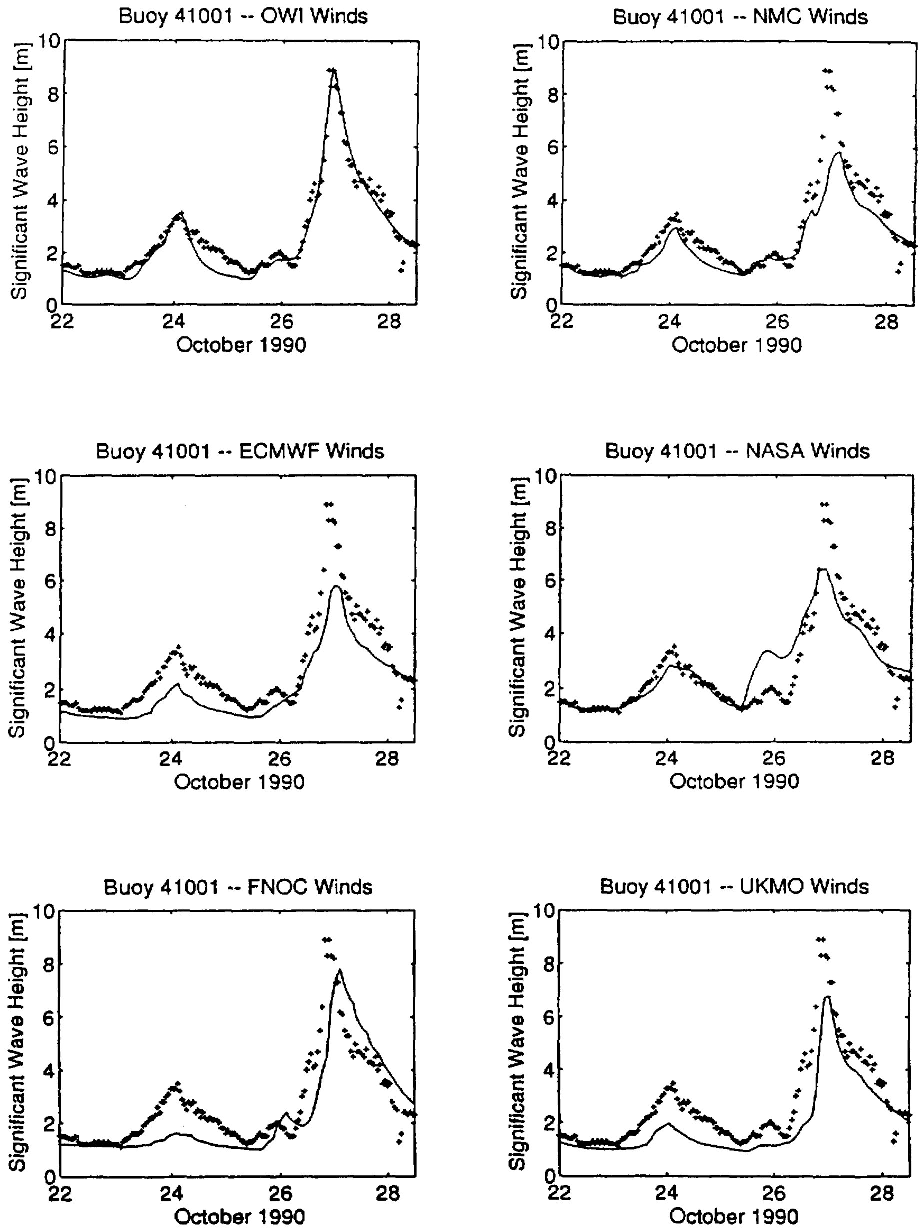

Figure 3. Comparison of hindcast (solid line) and hourly buoy measurements (+) of HS in SWADE IOP-1 with WAM-4 model driven alternatively by kinematically reanalyzed winds (OWI) and wind fields from indicated NWP centers (from Cardone et al.,1995b).

Halloween Storm
October 1991

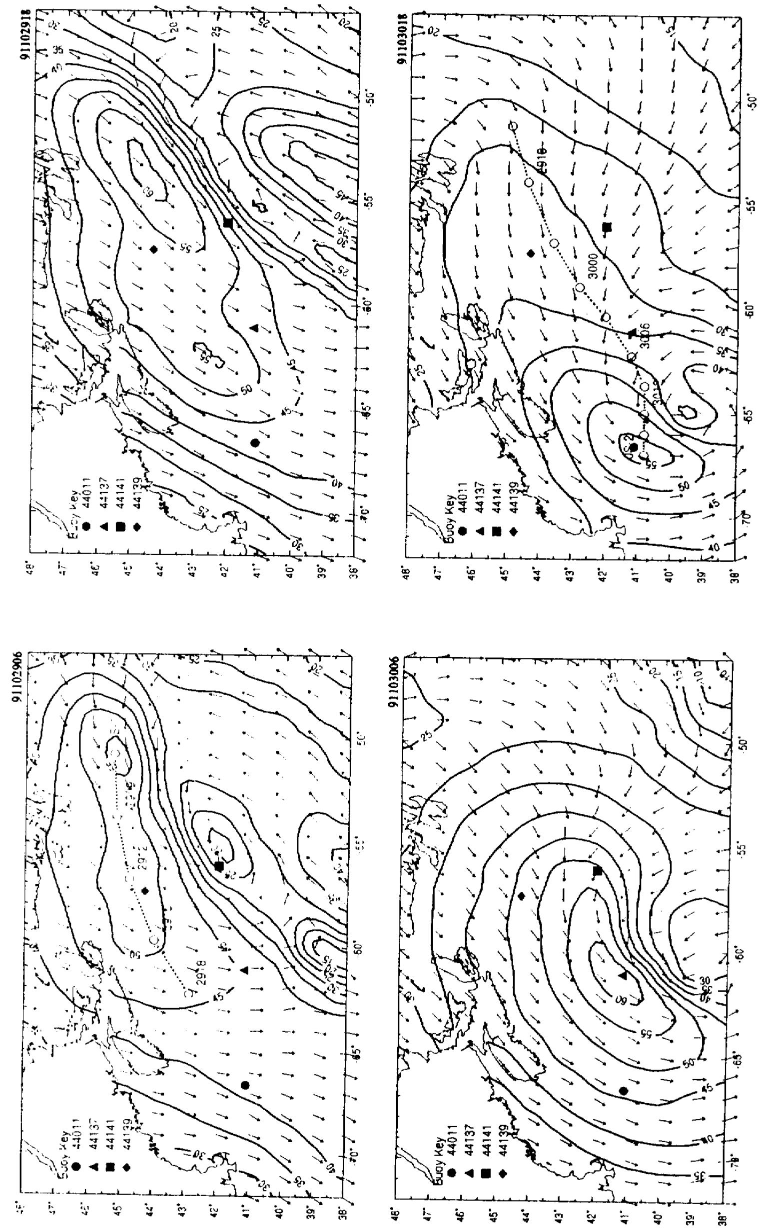

Figure 4. 12-hourly surface (20 m neutral) wind field analyses in Halloween Storm showing evolution of major circulation features including jet streaks (from Cardone et al., 1995a).

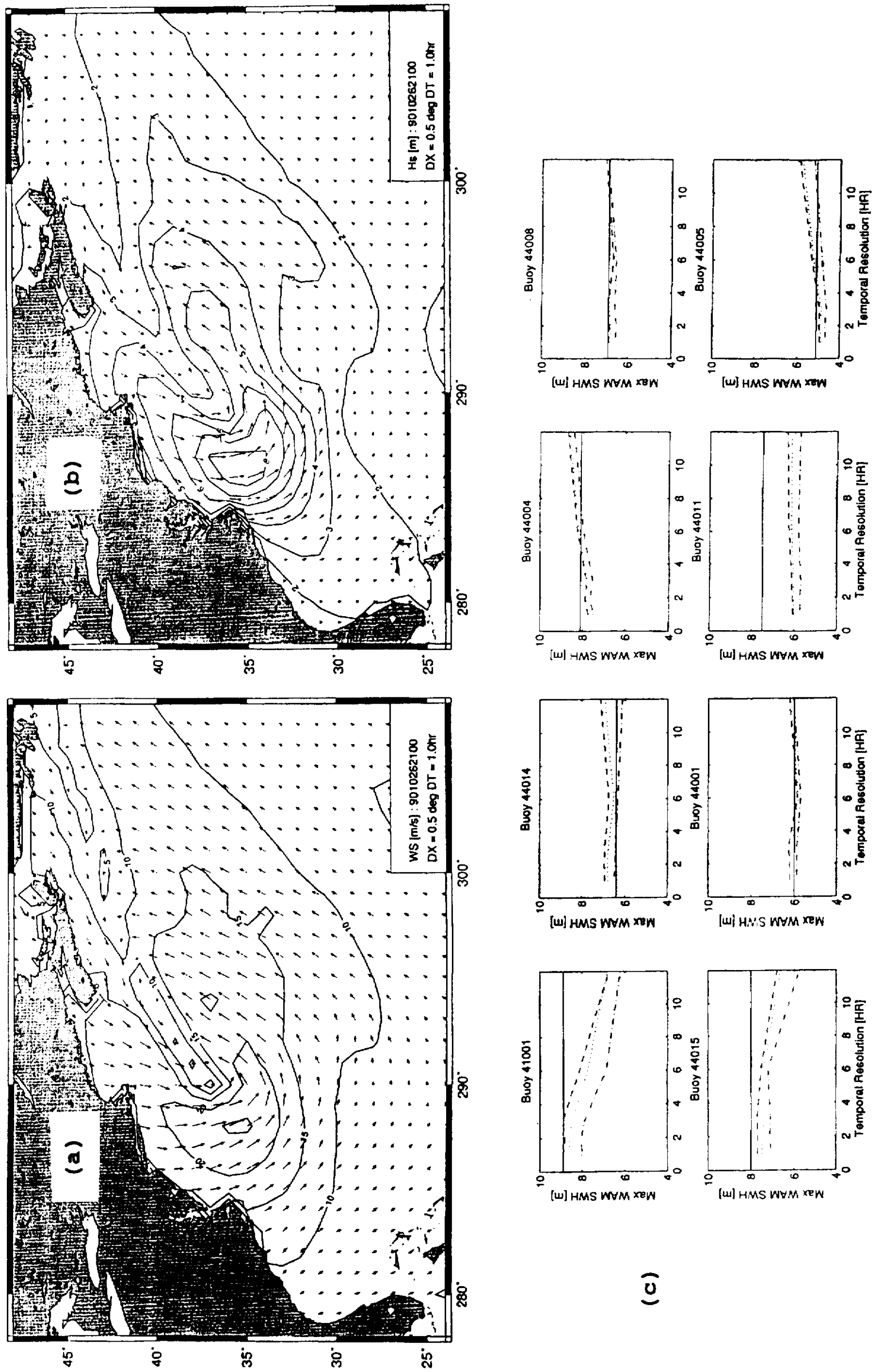

Figure 5. (a) surface wind field (OWI) in SWADE IOP-1 hindcast at 9010262100UT; (b) corresponding hindcast field of HS; (c) hindcast of peak event HS at indicated buoys relative to that measured (horizontal solid line) as a function of temporal resolution for three spatial resolutions: 0.5 degrees (OWI) (dashed line); 1.0 degrees (dotted line); 1.5 degrees (dot-dash line) (from Graber et al., 1995).

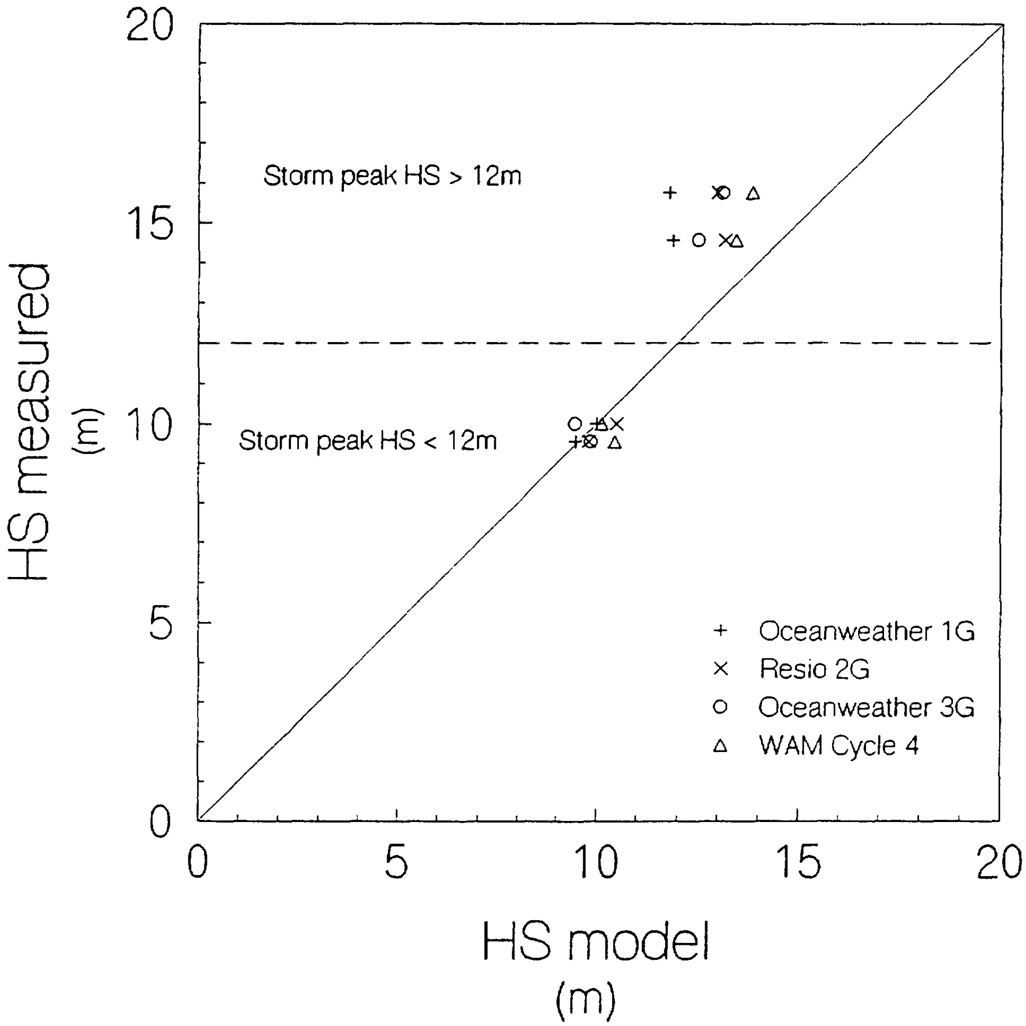

Figure 6. Average of measured and model hindcast of peak HS in HOS and SOC over groups of sites representing HS peaks above and below 12 m (from Cardone et al., 1995a).

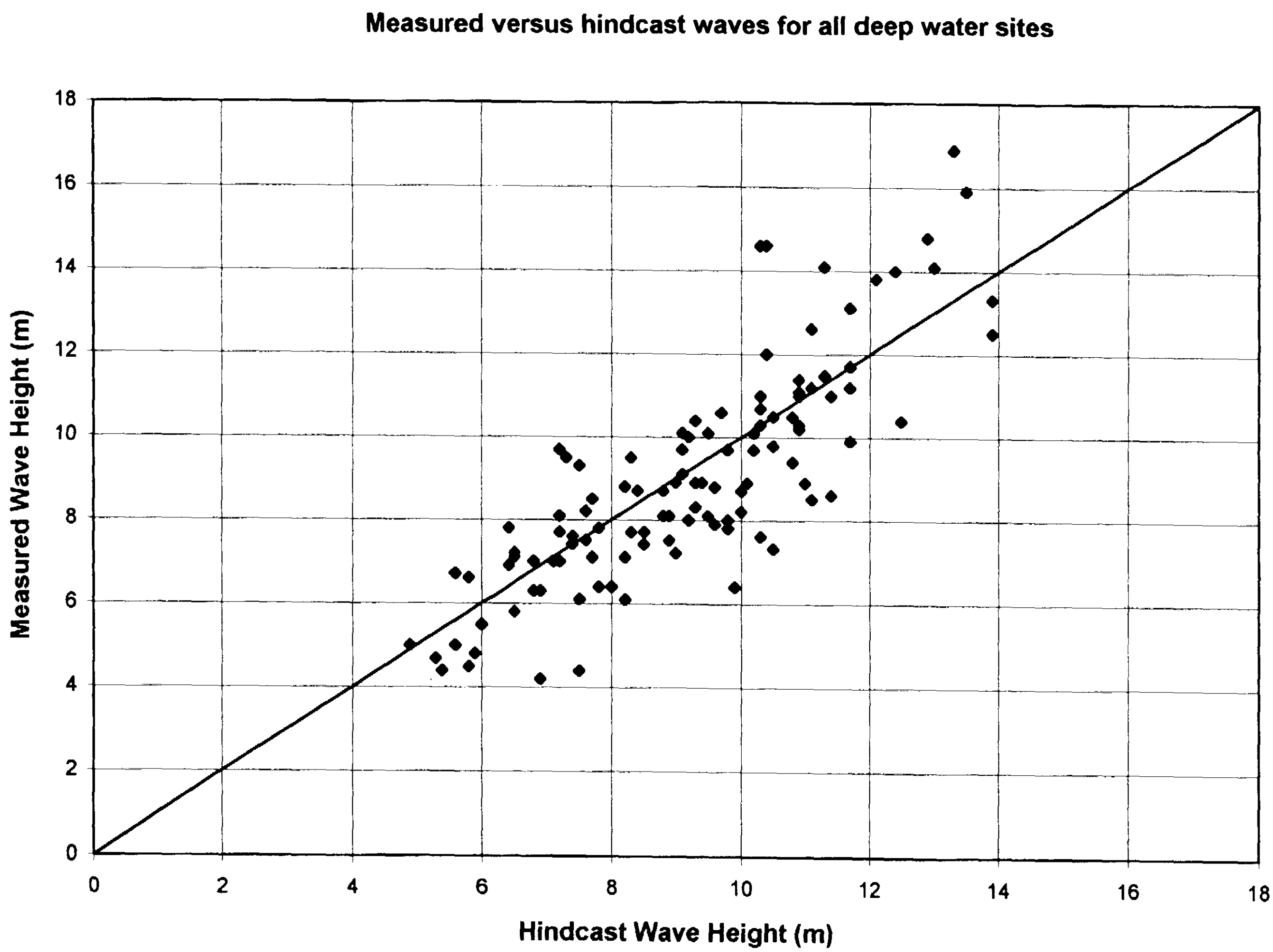

Figure 7. Measured versus hindcast peak HS for all available comparisons based on west coast and east coast PERD hindcasts (e.g. Eid et al., 1992)

POSSIBLE IMPACTS OF CLIMATE CHANGES REGARDING SAFETY AND OPERATION OF EXISTING OFFSHORE STRUCTURES

Sverre Haver
Statoil, Exploration & Production
Stavanger, Norway

1 INTRODUCTION

Over the last 10 years an increasing attention has been given to the possibility of future climate changes due to man-induced disturbances of the "green house" balance. Since the late eighties nearly all winters have include one or more rather extraordinary storm event. This is indicated by Table 1 showing the storms exceeding 10m significant wave height. Too much attention should not be given to this table. The measurements during the last few years have not all been carefully verified. In spite of this, it clearly suggests that most of the last 6 - 7 years have been much more severe than the previous 15 - 20 years. Not necessarily in terms of the average weather, but most of these years have included at least one storm well in the excess of what was typical for the seventies and eighties. Although the severity of the last few years may well be due to a natural cyclic variation, it has resulted in an increased focus on possible climate changes both among the public and in the mass media.

Offshore structures are typically planned to stay in operation for 20 - 30 years, or in some cases even longer. This means that offshore structures installed during the eighties and nineties are likely to be exposed to the consequences of possible climate changes. The consequences of a climate change which can affect existing offshore structures are:

- Changing air - and sea temperatures.
- Increasing water level.
- Increasing rate of occurrence of storms.
- Increasing severity of storms.

Two questions are of main interest concerning the long term operation of marine structures. i): Does a climate change result in larger environmental loads? ii): Does a climate change reduce the regularity of important marine operations, e.g. offshore loading of oil? The first question may be crucial concerning the safety of the platforms, while the latter mainly will effect the economics of an existing field concept.

Regarding offshore structures, small changes in the mean temperature are not expected to have any direct influence. It is reasonable to believe that the temperature changes will be small as far as the present pattern of ocean currents essentially are maintained. This will be assumed to be the case herein, and we will therefore focus on the possible impacts of increasing water level and changing wave climate. However, if the main current flows changes dramatically, it may well be that the temperature aspect will turn out to be the most important one, and, of course, important in a much broader sense than the safety of offshore platforms.

A proper consideration of the consequences of climate changes with respect to offshore installations would of course require that the climate changes themselves where reasonably well known. This is not the case. At present there seems to be a rather general agreement that the mean global temperature will increase with about 1°C during the next 50 years. However, when it comes to the consequences of this heating concerning the actual weather, no generally accepted scenario is known to this author. Herein we will not discuss the impact of climate changes on the actual weather pattern. We will rather carry out some sensitivity studies in order to at least identify, the most crucial environmental parameters. Their importance will be ranked in view of their possible consequences for design and operation of offshore structures. It is worthwhile to note that the Norwegian Petroleum Directorate presently requires the designers to add 0.3m to the present water level to account for future climate changes.

The impacts of possible climate changes will be indicated for the following offshore related cases:

- Annual largest base shear of a drag dominated jacket.
- Annual failure probability of a jacket exposed to wave - deck impacts.
- The annual failure probability of the tether of a tension leg platform.
- Estimated fatigue life for a structural member.
- Estimated down time of a marine operation.

2 DRAG DOMINATED JACKET

At first we will study the impact of possible climate changes on the estimated base shear of a steel jacket. For this purpose a parametric model for the base shear is adopted. Subsequently, the following generic load model is used, Haver and Gudmestad (1992):

$$Q_{max} = A\left\{\frac{\left[4\pi D + L\sinh\frac{4\pi D}{L}\right]}{T^2\sinh^2(\frac{2\pi D}{L})}C_{max}^2 + \frac{\left[4\pi D + L\sinh\frac{4\pi D}{L}\right]}{DT^2\sinh^2(\frac{2\pi D}{L})}C_{max}^3\right\} \quad (1)$$

Q_{max} is the maximum base shear, C_{max} is the maximum wave crest, D is the water depth, T is the wave period, L is the wave length, and A is a proper coefficient. For the example jacket A = 0.015 is found to be adequate. It should be noted that A is not a dimensionless coefficient. Its dimension is such that with C_{max} and L in m and T in s, the base shear is given in MN,

The original design parameters are assumed to be: $C_{max,100}$ = 15m, D = 70m, and T = 14s. ($C_{max,100}$ is the 100-year crest height). The 100-year load is then found to be about 19MN. If the water level is increased with one meter, the load is more or less the same. On the other hand, if the crest height is increased with 1m, the load is increased to 21.8MN, an increase of 15%. Increases the 100-year crest height with 2m, the corresponding load is found to be 24.9MN, i.e. an increase of about 30%. If the overturning moment had been considered, the effects of increasing the crest height would have been even stronger. The sensitivity to the water level, however, would also for the overturning moment have been rather small.

The design load is obtained by multiplying the 100-year load with a load factor of 1.3 - 1.35. It is seen from this exercise that if a climate change results in an increase of 10-15% of the 100-year crest height, all the safety margin provided by the use of the safety factor is lost.

The 100-year crest height is effected by the *number* of severe storms, the *severity* of the storms, the *duration* of the peak of the storms, and the *distribution* of the crest heights of a given storm. However, in terms of the climate type of parameters, the crest height level is completely governed by the severity of the storms. This means that if the 100-year storm is increased by 10-15% due to climate changes, the safety margin is in principle lost.

In practise, the structure is not likely to fail even if the design loads are exceeded. Safety margins are also introduced for the capacity of the structure. Furthermore, as the post-yielding strength of the structure is utilized, it is found that the resulting safety margin for jackets regarding collapse rather is in the order of 2-4. In order to obtain such large forces, the waves have to become very large and their crest will for many structures reach the deck level.

As wave-deck impacts take place, the failure mode of the structure will usually be very different from the most likely failure mode without wave-deck impacts. As a consequence of this, the capacity of the structure will typically be significantly reduced. The probability of a severe wave-deck impact load will therefore be the leading contribution to the failure probability of the jacket. In order to assess the impacts of climate changes with respect to jacket failure, it is assumed that the jacket will fail as the crest height reaches 2m above the lowest deck level. The deck height of the example structure is taken to be h_D = 18m above storm sea level.

Concerning ultimate load calculations, one may consider the joint distribution of the annual largest significant wave height, $H_{m0,1}$, and the corresponding spectral peak period, $T_{p,(1)}$. Herein $H_{m0,1}$ is described by the following distribution, Haver(1992):

$$F_{H_{m0,1}}(h_{m0}) = \exp\left\{-\phi \exp\left[-\left(\frac{h_{m0}}{\theta}\right)^{\gamma} + \left(\frac{\alpha}{\theta}\right)^{\gamma}\right]\right\}; \quad h_{m0} > \alpha \qquad (2)$$

ϕ is the expected number of storms exceeding the level α, and θ and γ are parameters that are estimated by fitting the distribution to observations. Herein we will adopt ϕ=7.6, α = 7.5m, γ=2.0 and $\theta_{(\gamma)} = (8.79^{\gamma} - 7.5^{\gamma})^{1/\gamma}$ = 4.58. The corresponding spectral peak period is modelled by a log normal model with parameters being a function of the significant wave height. This distribution is not important for the present sensitivity study and it is therefore not given herein. Reference is made to e.g. Haver (1992).

For a jacket structure in moderate water depths, the annual largest loads are very well approximated by the loads occurring in connection with the annual largest wave height. Herein the annual largest wave is furthermore assumed to equal the largest wave within the peak part of the annual largest storm. The wave heights in a stationary sea state is modelled by a Weibull distribution with parameters, β=2.26 and λ=2.13, according to Forristall (1978). The distribution of the largest wave out of N waves, H_N, is then given by:

$$F_{H_N|H_{m0,1}}(h|h_{m0}) = \exp\left\{-N \exp\left[-\beta\left(\frac{h}{h_{m0}}\right)^{\lambda}\right]\right\}; \; h > 0 \qquad (3)$$

$N=\Delta/t_z$ is the expected no. of waves during the stationary peak of the storm. The duration of the storm peak is assumed to be Δ=21600s and

$t_z=0.75t_p$. The corresponding crest height is taken to be the crest of a Stokian 5th order wave, and for the actual depth the crest height, C, is approximately given by, Dalane and Haver (1995):

$$C=0.36H^{1.16} \tag{4}$$

Structural failure takes place when the wave crest reaches a level 2m above lowest deck level, i.e.:

$$g(C,\Delta D)=h_d+2-\Delta D-C<0 \tag{5}$$

where ΔD is the climate induced change in water level.

The failure probabilities are shown in Table 2 for various values of

- the annual no. of storms, ϕ
- the most probable largest significant wave height during one year, $\tilde{h}_{m0,1}$
- the climate change in water level, ΔD.

It is seen from the table that it is mainly the sea state severity that will affect the failure probability.

With respect to the safety of jackets against ultimate collapse, the only parameter that seems to be important is the sea state severity of the most extreme sea states. Accordingly, focus should be given to this parameter as possible consequences of climate changes are considered. A small or moderate increase in water level is much less important.

3 TETHERS OF A TENSION LEG PLATFORM

A crucial part of the tension leg platform (TLP) concept is the tether system. A tether failure may develop into a catastrophic event if the failure is due to overload. Subsequently, we will illustrate the effects of possible climate changes concerning the safety of a tether against yielding. The most unfavourable wave direction regarding tether loading will for most TLP's be waves propagating along the platform diagonal. For the actual area, the annual largest significant wave height corresponding to the diagonal direction is described by the following Gumbel model, Haver (1996):

$$F_{H_{m0,1}}(h_{m0}) = \exp\left\{-\exp\left[-\frac{h_{m0}-\varepsilon}{\kappa}\right]\right\} \tag{6}$$

The distribution parameters, ε and κ, are herein given by:

$$\varepsilon = \varepsilon_0(1+X_\varepsilon) \text{ and } \kappa = \kappa_0(1+X_\kappa) \qquad (7)$$

ε_0=7.88 and κ_0=1.44 are the base case parameter values, while X_ε and X_κ are parameters which are introduced in order to model possible changes concerning the storm climate. The effects of such changes are assessed in two ways. In the first approach, the consequences of climate changes are demonstrated for various fixed choices of the parameters, X_ε and X_κ. Secondly, both parameters are modelled as Gaussian variables with mean values equal to 0.1 and a coefficient of variation of 50%. In words, this means that we expect both distribution parameters to increase somewhat, but we are very uncertain about this so the actual values may be much larger or much less. By introducing the climate parameters as random variables, we will see how important our uncertainties related to the climate changes are when they are compared to other sources of uncertainties.

The variation of water level is due to tide, surge and, possibly, a variation due to climate changes. The resulting water level is given by:

$$W=W_{Tide}+W_{Surge}+W_{Climate} \qquad (8)$$

The various components are modelled by the following distributions:

$$F_{W_{Tide}}(w) = \frac{1}{2\pi}\left[2\pi - 2Arc\cos\left(\frac{w}{w_0}\right)\right]; \qquad (9)$$

$$w_0 = 1.2m$$

$$F_{W_{Surge}}(w) = N(\mu_{W_{Surge}}, \sigma_{W_{Surge}}); \qquad (10)$$

$$\mu_{W_{Surge}} = 0.025h_{m0}, \qquad \sigma_{W_{Surge}} = 0.2m,$$

The climate contribution is modelled in two ways. At first it is modelled as a deterministic parameter and the effect of an increase in water level is shown for different values. Thereafter $W_{Climate}$ is also modelled as a Gaussian variable with a mean value equal to 0.3m and a coefficient of variation of 50%.

Herein the mean wind speed, U, is modelled as a function of the significant wave height.

The force in the tether can be written as a sum of components of different origin. A simple model is given by:

$T=T_0+T_{Waterlevel}(W)+T_{Sustained}(U,H_{m0})+T_{Dynamic}(U,H_{m0})$ (11)

The meaning of these components are:

T_o: Tether force due to pretension at mean water level.

$T_{Waterlevel}$: Tether force variation due to the variation in the water level. Tide, surge, and a possible climate effect, contribute to this component.

$T_{Sustained}$: Tether load due to the mean motion induced set-down of the platform and the mean wind-induced overturning moment.

$T_{Dynamic}$: Tether load induced by the motions of the platform, this includes the loads caused by both the slowdrift motion, the wave frequency motion, and the springing/ ringing (high-frequency) motion.

We will not go into details regarding the modelling of the various load components. For that purpose reference is made to Haver(1996). The failure mode considered herein is yielding. The axial stress caused by the load discussed above is given by:

$$\sigma_x = -\frac{T}{A} \quad (12)$$

where A is the cross section area of the tether. Denoting the yield stress by σYeild, failure is defined as the limit state function given below becomes negative, i.e. the actual stress exceeds the yield stress.

$$g(\sigma_x,\sigma_{Yield}) = \sigma_{Yield} - \sigma_x(W,U,H_{m0}) \quad (13)$$

The probability of yielding in a tether for this particular wave direction is given in Table 3 for various choices concerning climate changes. It is clearly seen that a small change in the water level do not affect the safety of a TLP tether. It is more important to assess the possible effects of changes in the storm climate.

The relative importance of the various random parameters are compared in Table 4 . In this connection X_ε, X_κ, and $W_{Climate}$ are introduced as random variables with properties as given above. The probability of yielding is given in the table heading and it is seen that it is increased by a factor of 4 due to the assumed effects of climate changes. Furthermore, it is clearly seen that the failure probability is still completely dominated by the contributions which are due to the inherent randomness of the annual largest storm, and the inherent randomness of the largest dynamic tether load in the annual largest sea state. This means that only $H_{m0,1}$ and $T_{Dynamic}$ have to be described as random quantities. The remaining parameters may just as well be set equal to their respective mean values. Concerning climate changes, the most important quantities to address from a tether safety point of view is the expected effects regarding the statistical properties of the annual largest storm.

4 SIMPLIFIED FATIGUE ASSESSMENT

Assuming that the long term distribution of stress ranges can be modelled by a 2-parameter Weibull distribution, the expected annual fatigue damage is given by:

$$\bar{d}_1 = \frac{1}{a} \cdot n_1 \cdot \delta^m \cdot \Gamma\left(1 + \frac{m}{\eta}\right) \tag{14}$$

n_1 is the expected number of stress cycles in one year, δ and η are the Weibull-parameters, m is the slope of the S-N curve (fatigue capacity curve), and a is a location parameter for the S-N curve.

Denoting the 100-year stress range with $\sigma_{r,100}$, the scale parameter of the Weibull distribution can be written:

$$\delta = \frac{\sigma_{r,100}}{(\ln n_{100})^{1/\eta}} \tag{15}$$

where n_{100} is the number of stress cycles in 100 years. For the purpose of this discussion we will assume $n_{100}=5 \bullet 10^8$. Introducing Eq. (15) into Eq. (14) and using Sterlings formula, Abramowitz and Stegun (1965), for the Gamma function, Eq. (14) can be written:

$$\bar{d}_1 = k \frac{r^m}{(\ln n_{100})^{m/\eta}} \cdot \exp\left\{-\left(1 + \frac{m}{\eta}\right)\right\} \cdot \left(1 + \frac{m}{\eta}\right)^{\left(0.5 + \frac{m}{\eta}\right)} \tag{16}$$

r is a factor describing the effect of climate changes with respect to 100-year stress range, i.e. $\sigma_{100,\text{New climate}} = r \bullet \sigma_{100}$

Eq. (16) is convenient for assessing the impacts of climate changes. The effects will be indicated for two materials, steel with m = 3 , and aluminium with m = 7. The climate effects are indicated by showing the effects on the annual fatigue damage of varying values of r and η. If a climate change increases the 100-year sea state by 10%, the corresponding effect on the 100-year stress range will typically be in the order of 10 - 20%. We will therefore show the results for r = 1.1 and r = 1.2. A climate change may of course also effect the shape parameter of the Weibull distribution for the stress ranges. Results are therefore shown for shape parameters between 0.9 and 1.1. A reasonable base case value is taken to be η = 1. It should be noted that the 100-year stress range is kept the same for varying values of η by changing δ properly, see Eq. (15).

The results of this exercise are shown in Table 5 . It is seen that for steel the fatigue damage is increased by a factor between 1 and 3. For aluminium, however, the impact is stronger, and the damage is for the worst scenario increased by a factor of 7.

For critical structural intersections of steel structures, where inspection is hard to carry out, a safety factor of 10 is used for fatigue. In view of this, the impacts of the suggested climate change are not dramatic. However, for intersections which are not critical concerning structural safety, a safety factor of 2 is used, and for these cases the impacts of climate changes may be of concern - in particular when it comes to determine proper inspection intervals.

The present discussion concerning fatigue is obviously far from complete. In some cases a lower level for the stress range is introduced. The idea is that below this level, fatigue damage is not accumulated. If a climate change causes a great number of stress cycles to exceed this cut-off level, the effect may, of course, be much stronger than indicated above.

The main message from this fatigue discussion is that concerning this type of failure, the impacts of possible climate changes on the long term distribution of stress ranges are of main concern. In order to assess these impacts the effects of climate changes with respect to the long term distribution of the significant wave height should first of all be investigated.

5 CONSEQUENCES CONCERNING MARINE OPERATIONS

A climate change may have a significant effect on routine marine operations. Herein we will illustrate this by consider the down-time of a marine operation defined as follows. The operation has to be stopped as the significant wave height exceeds 6m, and it can not be started again before the significant wave height has decreased below 4m. One can think of this as a simplified model of an offshore oil-loading process.

A typical property of the oil-loading process is that the oil production can go on as usual as far as storage capacity is available for the produced oil. When this is no longer the case, the oil production has to stop until the weather improves. In the present example we will assume that production has to stop if the loading process has stopped for more than 5 days. If the production stop goes on for a long time, this will of course represent a significant loss of income. Subsequently, we will illustrate how a climate change may affect the estimated down-time, both with respect to the loading process itself, and its effect regarding the annual accumulated duration of the production stop. It should be stressed that the various thresholds selected above are chosen for illustrative purposes and do not represent any particular offshore loading system.

Hindcast data for the Statfjord area covering the years 1955 - 1986 are used for assessing the impacts of possible climate changes. At first down-time episodes of the loading process is identified by scanning through the hindcast data series. Thereafter a similar search is carried out after multiplying the significant wave height series with 1.1 and 1.2, respectively. In this way we can illustrate the effects of a constant increase in sea state severity of 10 and 20%, respectively.

The mean and standard deviation for the duration of the down-time episodes are given in Table 6 . It is seen that both the mean and the standard deviation of the duration increase as the sea state severity increases. The number of down time episodes are shown versus year in Fig. 1 . It is seen that the number of down-time events increases considerably as the significant wave height severity increases.

As far as the down-time duration is less than 120 hours, the production is not affected by the fact that loading does not take place. This means that most of the down-time events concerning the loading process do not affect production. The annual number of events with a duration larger than 120 hours are shown in Fig. 2 . The impact of the selected climate changes is now seen to be very strong.

The annual accumulated duration of weather induced production stop is shown in Fig. 3 . It is clear that a loading concept like the concept of this example will be rather sensitive to climate changes. With the present climate the expected annual duration of no production is found to be 35 hours. This number increases to 122 hours if the sea state severity increases with 10%, and to 226 hours if it increases with 20%.

It is hard to imagine that water level can have any effect on a marine operation, and again we will conclude that the most important parameter, for which the effects of climate changes should be further investigated, is the significant wave height.

7 CONCLUSION

The impacts of possible climate changes are discussed for some offshore related cases. Although this study is of an illustrative nature, the following can be concluded:

- The most important consequence concerning structural safety and marine operations is if and to which extent the storms grow worse due to climate changes. The most important parameter to ”monitor” is the significant wave height.
- A small to moderate increase in water level will not have any significant effect on the structural safety.

If a climate change result in a 10% increase of the significant wave heights of storms, it is likely to be rather important both concerning safety of existing structures and the regularity of marine operations.

In the future it is also important to investigate to which extent the main pattern of ocean currents may change due to climate changes.

8 ACKNOWLEDGMENT

Statoil is acknowledged for the permission to publish this paper. The opinions expressed herein are those of the author and they should not be construed as reflecting the views of Statoil.

9 REFERENCES

Abramowitz, M. and Stegun, I. A. (1970): ” Handbook of Mathematical Functions”, Dover Publications, Inc., New York, 1970.

Dalane, J.I. and Haver, S. (1995): ”Requalification of an Unmanned Jacket Structure Using Reliability Methods”, OTC 7756, Houston, May 1995.

Forristall, G.Z. (1978): ”On the Statistical Distribution of Wave Height in a Storm”, Journal of Geophysical Research, Vol. 83, No. C5, 1978.

Haver, S. (1992): "Effects of Uncertainties in Hindcast Data on the Estimated Fatigue Damage and Failure Probability of Marine Structures", 3rd International Workshop on Wave Hindcasting and Forcasting, Montreal, 1992.

Haver, S. (1996): " Reliability Assessment of Maximum Stress in the Heidrun TLP Tethers", To be presented at the 6th International Offshore and Polar Engineering Conference, Los Angeles, 1996.

Haver, S. and Gudmestad, O.T. (1992): "Uncertainties Related to the Kinematics of Ocean Waves and Their Effect on Structural Reliability", 2nd International Offshore and Polar Engineering Conference, San Francisco, 1992.

Table 1 Storm events exceeding 10m significant wave height in the Northern North Sea

Year	No.of Storms	Significant wave height (m)	Year	No.of Storms	Significant wave height (m)
July 73 - June 74	2	11.8, 12.1	July 84 - June 85	1	11.0
July 74 - June 75	0		July 85 - June 86	0	
July 75 - June 76	2	10.3, 10.1	July 86 - June 87	0	
July 76 - June 77	1	10.1	July 87 - June 88	1	10.0
July 77 - June 78	1	11.3	July 88 - June 89	3	13.0, 10.1, 10.3
July 78 - June 79	0		July 89 - June 90	1	10.0
July 79 - June 80	3	10.4, 10.2, 10.6	July 90 - June 1	2	13.6, 11, 6
July 80 - June 81	1	11.2	July 91 - June 92	5	11, 10, 10.5, 10.5, 13
July 81 - June 82	1	10.1	July 92 - June 93	3	10.5, 13.0, 10
July 82 - June 83	2	10.4, 10.5	July 93 - June 94	1	10
July 83 - June 84	1	10.2	July 94 - June 95	5	11, 11, 10, 10, 13

Table 2 Failure probabilities for various combinations of parameters that may be effected by climate changes.

ϕ	P(g()< 0)	$\tilde{h}_{m0,1}$	P(g()<0)	ΔD	P(g()<0)
7.6	$2.3 \cdot 10^{-4}$	10.0	$2.3 \cdot 10^{-4}$	0.0	$2.3 \cdot 10^{-4}$
8.8	$2.7 \cdot 10^{-4}$	10.5	$1.4 \cdot 10^{-3}$	0.5	$3.7 \cdot 10^{-4}$
10.0	$3.1 \cdot 10^{-4}$	11.0	$4.6 \cdot 10^{-3}$	1.0	$5.8 \cdot 10^{-4}$
15.0	$4.5 \cdot 10^{-4}$	12.0	$2.5 \cdot 10^{-2}$	2.0	$1.4 \cdot 10^{-3}$

Table 3 Effects of possible climate changes on the probability of yielding in a tether

X_ε	P(g() < 0)	X_K	P(g)()< 0)	$W_{Climate}$	P(g()< 0)
0.0	$4.1 \cdot 10^{-5}$	0.0	$4.1 \cdot 10^{-5}$	0.0	$4.1 \cdot 10^{-5}$
0.1	$7.0 \cdot 10^{-5}$	0.1	$8.7 \cdot 10^{-5}$	0.5	$4.6 \cdot 10^{-5}$
0.2	$1.2 \cdot 10^{-4}$	0.2	$1.7 \cdot 10^{-5}$	1.0	$5.2 \cdot 10^{-5}$

Table 4 Relative importance of the various sources of randomness concerning yielding in a tether.

($p_f = 1.6 \cdot 10^{-4}$)

Parameter	Relative importance (%)
$H_{m0,1}$	76.8
$T_{Dynamic}$	20.6
σ_{Yield}	0.9
X_K	0.7
W_{Tide}	0.6
X_ε	0.4
W_{Surge}	0.0
$W_{climate}$	0.0

Table 5 Factor reflecting the increase in fatigue damage due to possible climate changes. (Factor is equal to 1 for base case climate and γ = 1.)

m	3			7		
k	1.0	1.1	1.2	1.0	1.1	1.2
γ	Fatigue factor					
0.90	0.57	0.76	0.98	0.50	1.00	1.80
0.95	0.76	1.01	1.32	0.73	1.40	2.60
1.00	1.00	1.33	1.73	1.00	2.00	3.67
1.05	1.28	1.71	2.22	1.40	2.80	5.10
1.10	1.62	2.16	2.80	2.00	3.70	7.30

Table 6 Characteristics for the duration of down-time events for offshore loading.

Case	Mean (Hours)	Standard deviation (Hours)
Base case climate	55.0	39.8
10% increased severity	65.7	53.5
20% increased severity	74.5	64.4

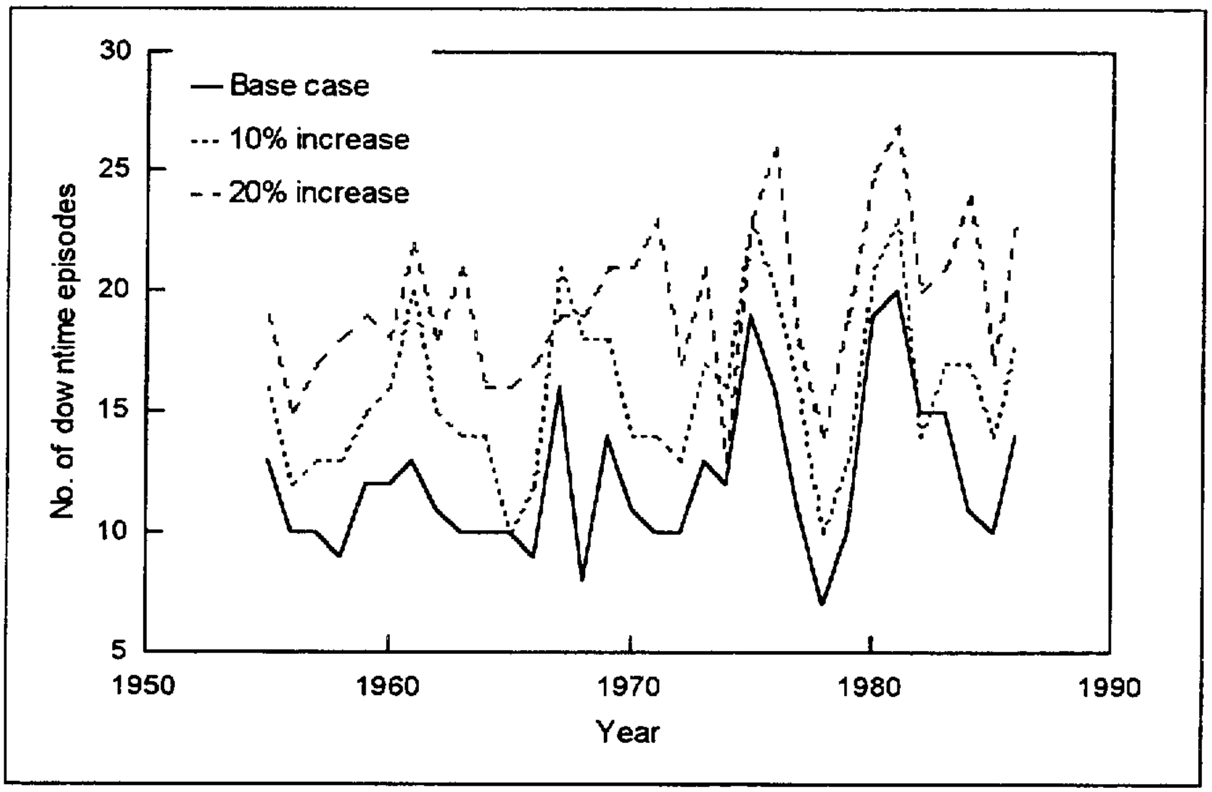

Figure 1 No. of down–time events concerning offshore loading

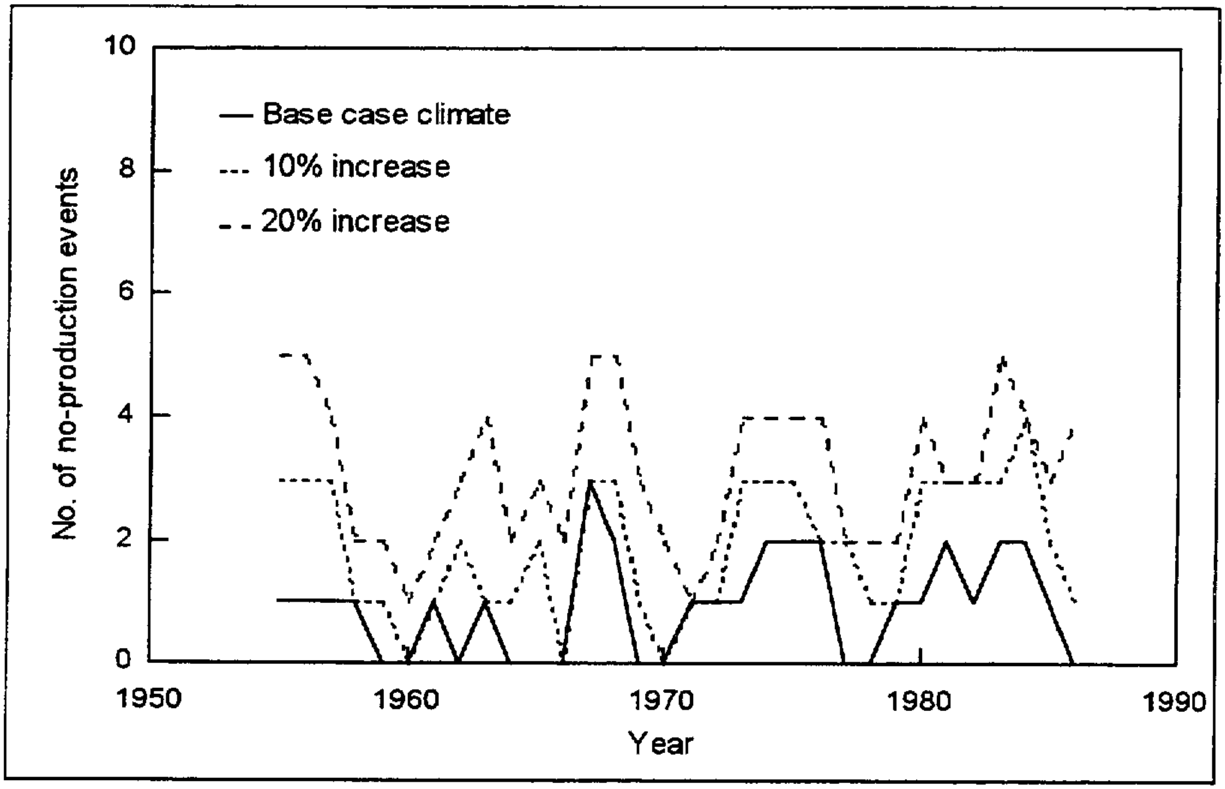

Figure 2 No. of events of production stop.

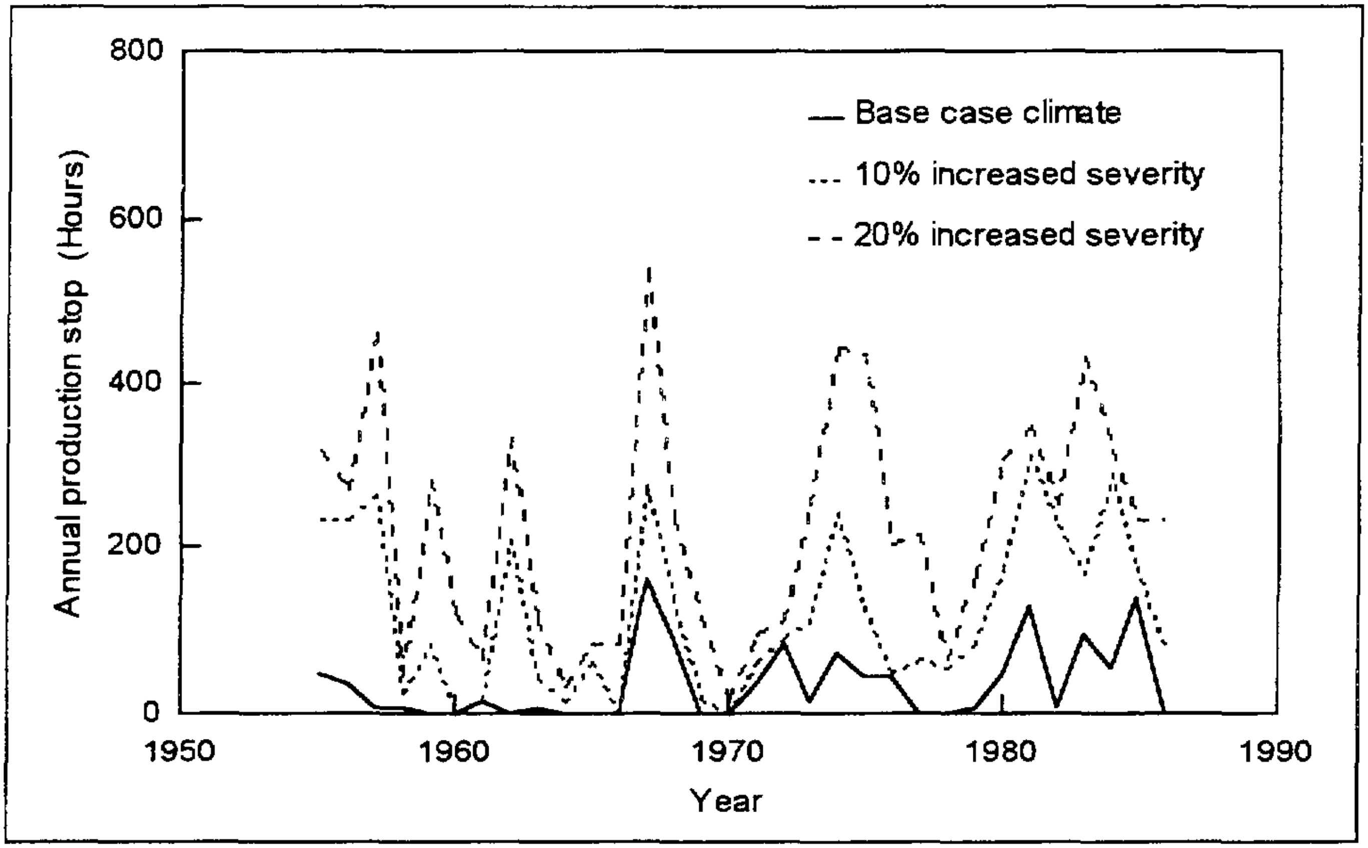

Figure 3 Annual Duration of production stop

The WASA project:

Changing Storm and Wave Climate in the Northeast Atlantic and adjacent seas?[1]

by the WASA[2] group[3]

Abstract

The European project WASA has been set up to verify hypotheses of a worsening storm and wave climate in the Northeast Atlantic and its adjacent seas. The observational record of the past hundred years is analysed and GCM based scenarios of possible future climate change due to increasing atmospheric greenhouse gas concentrations are examined.

In the present paper, the status of WASA is reviewed and a preliminary assessment of the storm climate in the past hundred years and of the wave climate in the past thirty is given. Also, an overview of the wave hindcast activities is given.

A major methodical obstacle for WASA are the inhomogeneities of the observational record, both in terms of local observations and of analysed products (such as weather maps), which usually produce an artificial increase of extreme winds and waves. To overcome these obstacles, WASA is relying on robust indicators, such as annual distributions of geostrophic wind speeds, and on state-of-the-art hindcast simulations with wave models.

The results obtained so far are:

- The storm climate in the near-coastal areas of Northwest Europe has not systematically worsened in the past century. There is, however, considerable natural variability on the decadal time scale.

- The statistics of the significant wave height in the Northeast Atlantic has undergone a steady increase of the wave height in the last 30 years. An upper bound estimate for this increase amounts to 2-3 cm/year for the 50% percentile of the annual wave height distribution and 3-4 cm/year for the annual 10% percentile.

---

[1] Paper presented at the Fourth International Workshop on Wave Hindcasting and Forecasting, Banff, Canada, October 16-20, 1995

[2] WASA is an abbreviations of Waves and Storms in the North Atlantic. The project is funded by the European Union's Environment program. Coordinator is Hans von Storch, Max-Planck-Institut fur Meteorologie, Bundesstrasse 55, 20146 Hamburg, Germany, e-mail: storch@dkrz.d400.de

[3] with contributions by Hans Alexandersson [6], Evert Bouws [7], Juan Carlos Carretero [1], Johannes Guddal [2], Ignacio Lozano Gonzalez [1], Heinz Günther [4], Dennis Jannink [7], Viacheslav V. Kharin [3], Gerbrand Komen [7], Hinrich Reichardt [3], Wolfgang Rosenthal [4], Antonio Ruiz de Elvira1, Torben Schmith [5], Mark Stawarz [4] and Hans von Storch [3].

([1] Clima Maritimo, Madrid, Spain; [2] Det Norske Meteorologisk Institut, Bergen, Norway; [3] Max-Planck-Institut für Meteorologie, Hamburg, Germany; [4] Institut fur Gewässerphysik, GKSS, Geesthacht, Germany; [5] Danmarks Meteorologiske Institut, Copenhagen, Denmark; [6] Sveriges Meteorologiska och Hydrologiska Institut, Norrköping, Sweden;[7] Koninklijk Nederlands Meteorologisch Instituut, De Bilt, The Netherlands)

1 Background

In the public debate concerning climate change due to increasing emissions of radiatively active gases into the atmosphere many people are concerned about the possibility of an intensification of extratropical storms. Even though the IPCC took a cautious stand in this matter because of lack of evidence, a mixture of indirect evidence (van Hoff, 1993; Hogben, 1994) and misleading scientific statements (Schinke, 1992) created a substantial uneasiness in the public. The offshore oil industry in the North Sea was confronted with reports about extreme waves higher than ever observed. The insurance industry organized meetings with scientists because of greatly increased storm-related damages. The Northern European newspapers were full of speculations about the enhanced threat of extratropical storms in the early part of 1993.

In this situation the Norwegian Weather Service organized two workshops ”Climate Trends and Future Offshore Design and Operation Criteria”, in Reykjavik and Bergen, and brought together people from the oil industry, certifying agencies and scientists to discuss the reality of a worsening of the wave and storm climate. The workshops did not create definite statements but the general impression that hard evidence for a worsening of the storm and wave climate was not available (for a summary see von Storch et al., 1994). A group of participants then agreed to establish the ”WASA project”. A research plan was worked out and funding by the European Union was obtained.

In this paper the present status of WASA is reviewed.

2. The Scope of the WASA project

WASA aims at the

- *Reconstruction* of the storm and wave climate in the Northeast Atlantic and adjacent seas in the 20th century, and at the

- *Construction of future perspectives* of the storm and wave climate in the 21st century.

Two central questions are raised

- Is the storm climate in the past 100 years consistent with the notion of intensifying or more frequently forming storms in the Northeast Atlantic and adjacent seas?

- How was / might be the response of the wave field and of the storm surge statistics to the past / possible future changes in the storm climate and other atmospheric features?

To address these questions, long homogeneous observational data are examined (Section 3), and extended hindcast experiments are run with wave models (Section 4). Also the output of climate change scenario experiments conducted with coupled ocean-atmosphere general circulation models is evaluated and will be used to prepare scenarios for possible future wave climates, but this aspect is not covered by the present progress report.

3 The Analysis of the Observational Record

3.1 The Storm Climate

When assessing the temporal evolution of the storm climate, two different types of data may in principle be considered. One source of information could be the archive of weather maps, which covers more than hundred years. Indeed, several attempt have been made to count the number of storms, stratified after the minimum core pressure, in the course of time (Schinke, 1992; Stein and Hense, 1994). These studies are useful in describing the year-to-year fluctuations in the past, say, 10 years. However, for the longer perspective this approach renders inconclusive simply since the quality of the weather maps has steadily improved. Thus any creeping worsening of the storm climate apparent in the observational record (as reported by Schinke, 1992) might reflect a real signal or a result of the ever increasing quality of the operational analyses due to more and better observations, more powerful diagnostic tools and other improvements in the monitoring of the state of the troposphere. A more detailed mapping of the pressure distribution, however, automatically yields deeper lows.[4]

[4] This problem is severe for instantaneous maps when dealing with monthly mean maps, the inhomogeneity becomes less significant.

The inhomogeneity problem is illustrated by Figure 1 in which the ratio of high-pass filtered standard deviations of air-pressure variations in winter in the decade 1984-93 and in the decade 1964-73, as derived from the DNMI analyses, is plotted. Obviously is the variability greatly enhanced since the 1960’s in areas where little or no in-situ observations are routinely available; this increase is likely spuriously. In the area marked in Figure 1 , between 70° N and 50°N and east of 20°W the bias seems less severe. For this area a storm count was made (Figure 2). There were slightly more storms in the 1984-93 decade than in the previous decades (348 as opposed to 339, 336 and 330). In particular the number of analysed severe storms per year in the area in the decade 1984-93 has increased. We do not know to what extent changes in the analysis scheme is responsible for the changing storm numbers in that area, therefore the result of this storm count should be taken as an upper bound of an increase of storm frequency and intensity. The results presented in the next sections indicate that the signal is indeed, at least in the eastern part of the area, spurious.

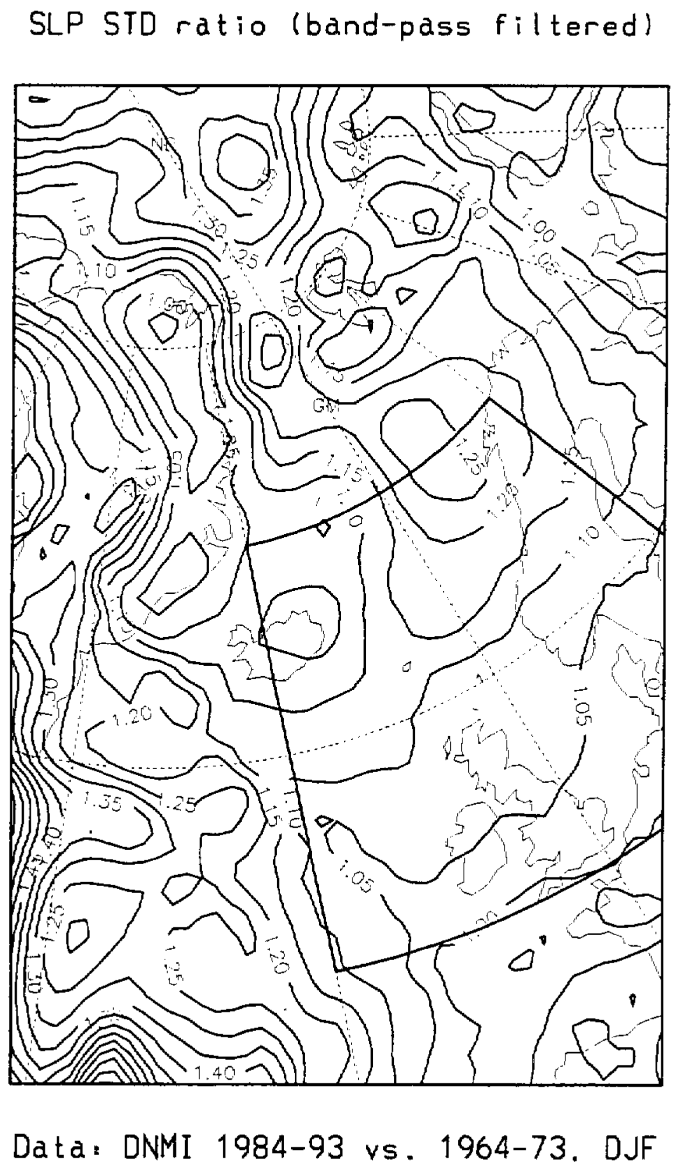

Figure 1:

Ratio of synoptic scale standard deviation of air pressure variations in winter (DJF) as derived from DNMI analysis in the decade 1984–1993 and in the decade 1964–1973. The area "A" south of 70°N and east of 20°W is marked

Therefore any analysis of changes of the storm climate should be supported by an analysis of local observations which are unaffected by improvements in the process of mapping the weather. A good parameter would be wind-speed, since it relates directly to damages and impact of waves and surges. However wind observations - either determined instrumentally or estimated - are usually of limited value due to inhomogeneities such as: change of scale, change of observer, change of surroundings etc. (cf. Peterson and Hasse, 1987).

Therefore one must look for other and more homogeneous proxies for storminess. An obvious choice is to base these on station air pressure, the time series of which are considered to be rather homogeneous because more or less the same instrument (mercury barometer) and procedures have been used throughout the entire observation period.

From air-pressure two proxies for storminess may be formed, namely the annual (seasonal, monthly) distribution of the geostrophic wind speed derived from three stations in a triangle (Schmidt and von Storch, 1993; see Section 3.1.1). An alternative is to consider the annual (seasonal, monthly) distribution of the pressure tendency, possibly after suppressing the non-synoptic variations by means of a digital filter (Schmith, 1995) (see Section 3.1.2).

Another homogenous proxy data time series is provided by high-frequency sea level variations at a tide gauge. The variance of such variations is controlled by the variance of the high-frequency atmospheric disturbances[5] (see Section 3.1.3).

[5] "High–frequency" refers here to the time scale of synoptic disturbances, i.e. a few days.

Figure 2: Storm count in the area 70°N to 50°N and east of 20°W (see Figure 1) in the DNMI data in DJF for different multi–year intervals. The storms are sorted after the core value *z* of the 1000 hPa level in meters. The pressure in mb is approximately *z*/8 + 1000

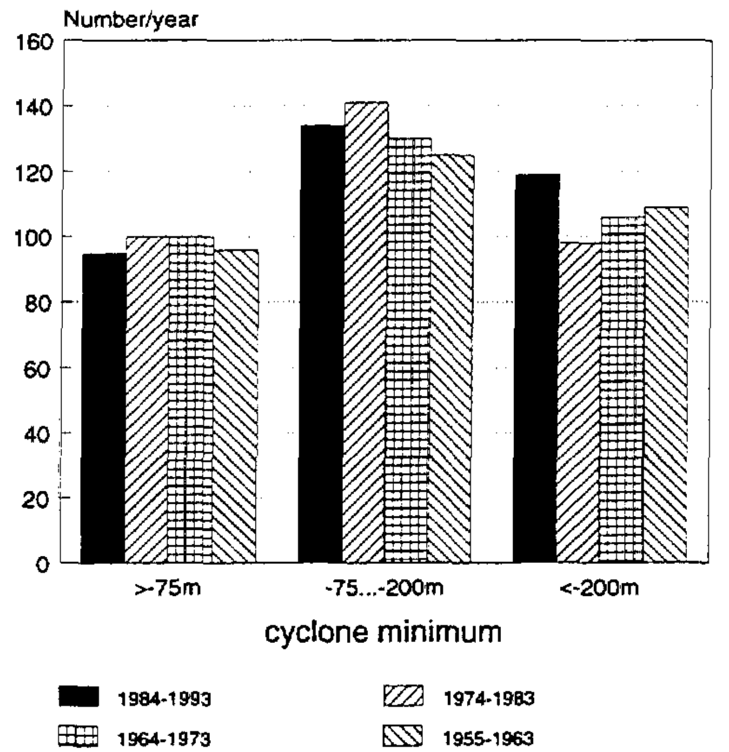

Figure 3: *Scatterdiagram of station-mea*
wind speed and geostrophic wind speed ove
Denmark.

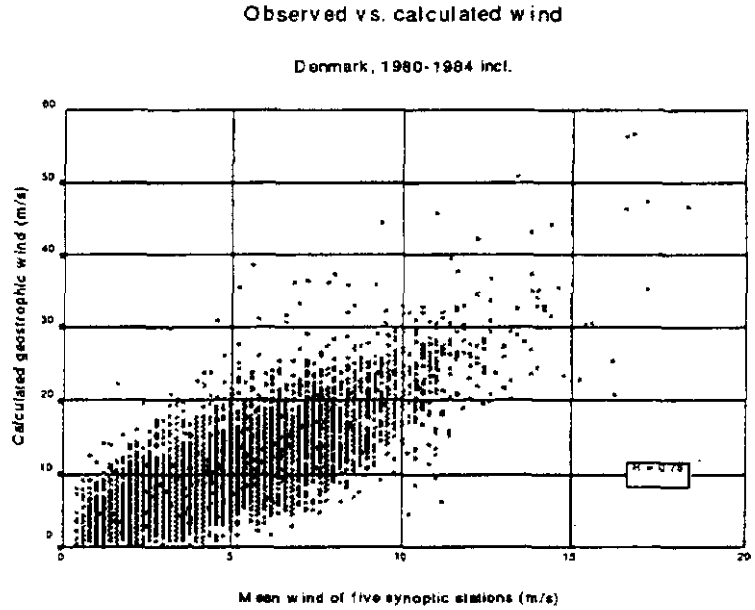

These proxy data geostrophic wind, high-frequency pressure tendency and sea level variations, can not be used to reliably estimate actual wind speeds; however, characteristic changes of the statistical moments of the annual (seasonal, monthly) distributions are connected with similar changes in the distributions of the wind speed. Figure 3 demonstrates the link between the winds speeds, averaged over 5 stations, from 1980 to 1984, and the geostrophic wind speed derived from a triangle of pressure observations. There is an overall good agreement except for high wind speeds. For example, an observed mean wind exceeding 15 m/s corresponds to geostrophic winds varying between 20 m/s and 60 m/s.

Even if the fit between simultaneous geostrophic wind speeds and anemometer wind speed exhibits a significant scatter, correspond the distributions of the two quantities well (Figure 4). Thus changes of statistical moments and percentiles of the wind speed distribution may be deduced from changes of the same statistical moments of geostrophic wind speed distribution.

Figure 4: *Percentile-percentile plot of station mean wind speed and geostrophic wind speed for the Danish triangle, derived from 5 years of daily data.*

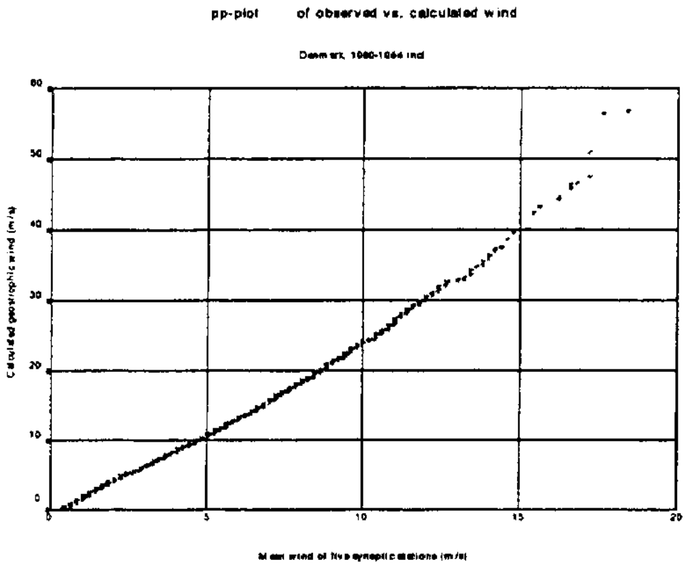

A further proxy data from storminess is the number of ”storm days” derived from local observations. This approach was pursued by Jónsson (1981), who found no systematic changes for Iceland (cf. von Storch et al., 1994). The Koninklijk Nederlands Meteorologisch Instituut published an official assessment on the state of climate and its change for the territory of the Netherlands (KNMI, 1993). According to that report the maximum wind speeds observed during severe storms have not been increased between 1910 and today.

3.1.1 Geostrophic Wind Analyses

Only 15 stations, situated in Northwestern Europe and the Northeast Atlantic, with a continuous pressure record for about the last 100 years of three or four daily observations are considered in the WASA project. For the time being only a subset of these stations are available for analysis. The distance between stations is non-uniform, ranging from approximately 100 km in Northwestern Europe up to 1000 km in the North Atlantic.

A homogeneity test similar to Alexandersson (1986) was performed on a subset of stations, where the distance to neighbouring stations was not too big. In some cases it was necessary to adjust biases, but these were less than 0.5 hPa in most cases. Subsequently, a (manual) quality check for single mis-readings etc. of the pressure was performed. It was found, that around 20% of these severe values were in error. These erroneous reading could in many cases be (also manually) corrected.

Geostrophic wind time series were generated from two triangles, namely one over Denmark and one over southern Sweden. Another time series was computed earlier by Schmidt for the German Bight (Schmidt and von Storch, 1993). All three analyses show a similar result - namely no systematic increase, or decrease, of the 50%, 90% and 99% percentiles of the annual distributions of geostrophic wind speeds. Time series of these annual percentiles are shown for the Danish triangle in Figure 5 . For the Swedish triangle Göteborg-Visby-Lund the number of geostrophic wind speeds exceeding 25 m/s per year is plotted in Figure 6 .

Figure 5: *Time series of percentiles of geostrophic wind speed over Denmark. Units: m/s.*

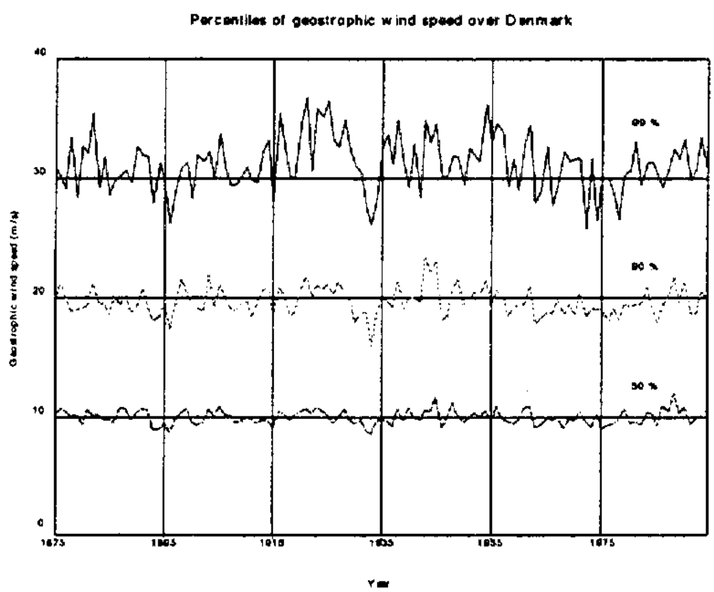

Figure 6: *Time series of number of daily geostrophic wind speeds exceeding 25 m/s, derived from the triangle Göteborg-Visby-Lund in Southern Sweden. The solid line represents a low-pass filter.*

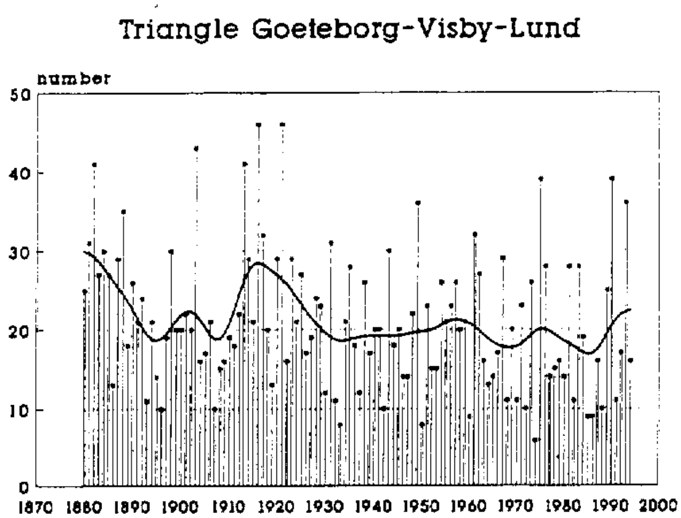

In a similar analysis of geostrophic winds in the Southern Baltic Sea area Mietus (1994) found an increase of the annual maximum geostrophic wind speed (derived from the triangle Hel-Swinoujscie-Visby) since 1960 of about 0.2 m s-1/year.

3.1.2 Pressure Tendency Analysis

Large air pressure tendencies are indicative for major baroclinic developments so that large wind speeds are likely to occur somewhere in the neighborhood. Therefore the use of 24-hourly pressure tendency as another possible proxy for storminess was investigated for two stations, namely Fanφ in Denmark and Thorshavn on the Faroe Islands in the North Atlantic. In both cases no systematic increase of the 50%, 90% and 99% percentiles of the annual distributions of the pressure tendencies were found, as is exemplified in Figure 7 for Fanφ.

[6] The 90% percentile of a distribution X is that number $\mathfrak{X}_{90\%}$ so that the probability to observe any realization of $X < \mathfrak{X}_{90\%}$ is 90%. In case of distributions formed from 365 daily geostrophic wind speeds during one year, the actual geostrophic wind is at 36 days equal or larger than the 90% percentile.
Percentiles are often called fractiles or quantiles.

Figure 7: *Time series of percentiles of 24-hour pressure tendencies over Denmark Units: 0.1 hPa/3 hrs.*

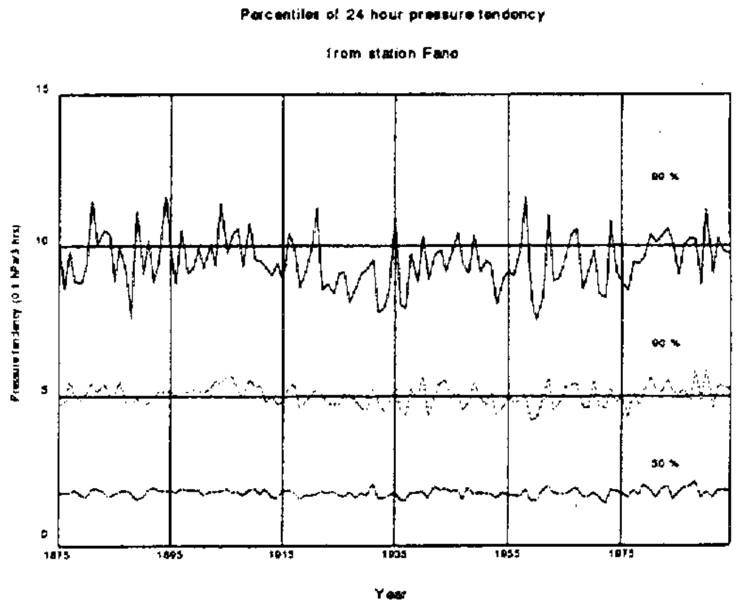

3.1.3 High Frequency Sea Level Variations

The idea to use high-frequency variations of sea level as a proxy for storm activity was suggested by de Ronde (cf. von Storch et al., 1994), who analysed data from Hoek van Holland. For this port in the Southern North Sea no trend towards more violent high-frequency events were found.

A similar analysis has been made for Cuxhaven (German Bight), where storm surge levels have increased continuously since the beginning of the record in the middle of the 19th century. A closer inspection of the data reveals however, that the increase of storm surge levels is due to an increase of the annual mean sea level and not due to changes in the intensity of high-frequency atmospheric events (Annutsch and Huber, pers. comm.). Figure 8 displays the temporal evolution of the annual mean sea level, with an increase of about 30 cm in 100 years, and the time series of various percentiles for the sea level variations *relative to the annual mean.*

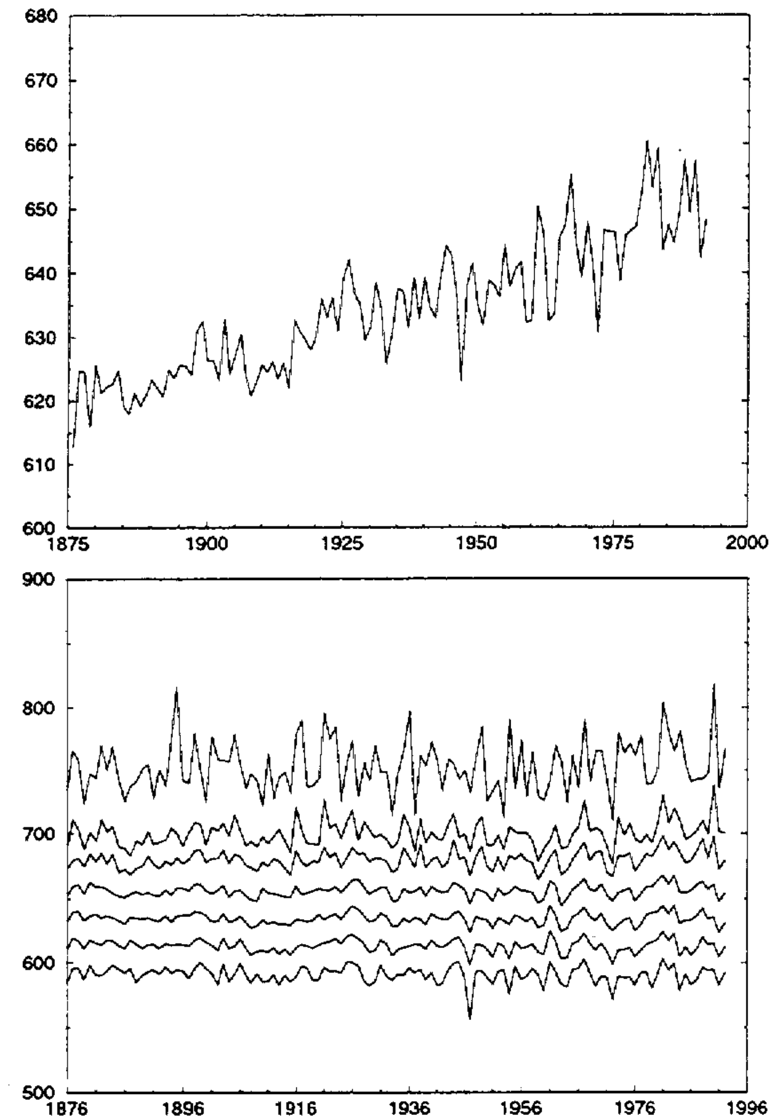

Figure 8: *Time series of the annual mean of the sea level reported by the Cuxhaven (German Bight) tide gauge (top), and the time series of various percentiles (1%,5%, 10%, 50%, 90%, 95%, 99% from bottom to top) of sea level relative to the annual mean (bottom). Units: cm*

3.2 The Wave Climate

The analysis of data on wave height, gathered from ships of opportunity or from ocean weather stations and light vessels, have revealed a in part substantial worsening of the wave climate in the North Atlantic (Carter and Draper (1988), Bacon and Carter (1991), Hogben (1994)). However, such local data must be considered with great care since they may exhibit upwards trends for various unphysical reasons (cf. WASA, 1994).

To further examine the hypothesis of increasing wave heights we have analysed the wave height reports from Ocean Weather Station M (66°N, 2°E) (Figure 9). One might be tempted to see a slight systematic increase in the data. However, these increases may well be artificial due to the inhomogeneities in the series: in the early 50ies the numbers seem to be systematically too low; before 1979 the reports were based on visual assessments and after 1979 on instrumental data. There is certainly an increase since the early 1980's, but this increase seems to be well within the "normal" range of variability when compared with the earlier part of the record.

Figure 9: *Time series of 1%, 5%, 10%, 25% and 50% percentiles of the annual wave height distribution at Ocean Weather Station M. Units: m. Updated from WASA (1994).*

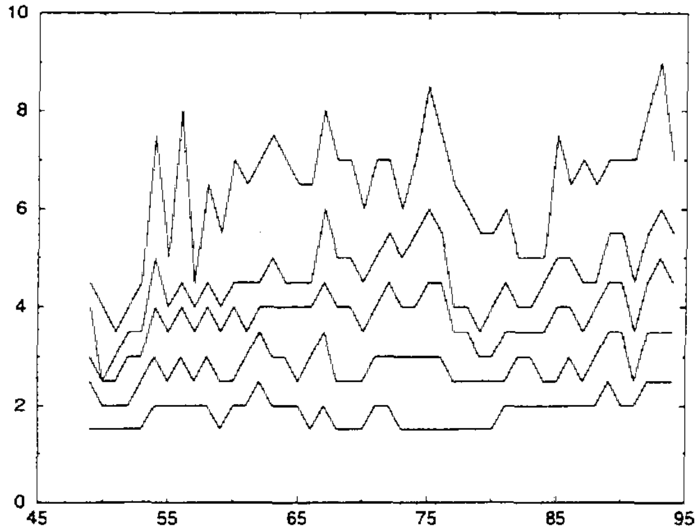

We have another data set at our disposal, namely the operational wave height maps prepared by Koninklijk Nederlands Meteorologisch Instituut for ship routing purposes. An example of such a map is shown in Figure 10 . When analysing these maps one has to keep in mind that they suffer from the same homogeneity problems as all analysed products such as weather maps (cf. Figure 1). Also, one should be aware of the fact that the local observations from ocean weather stations and the like are incorporated into the maps so that the two data sets - local information and analysed maps - are not independent evidence. Nevertheless any increase in wave statistics estimated from these maps represent an upper bound for any real signal.

Figure 10: *Example of a KNMI analysis of the wave height field prepared for shiprouting purposes.*

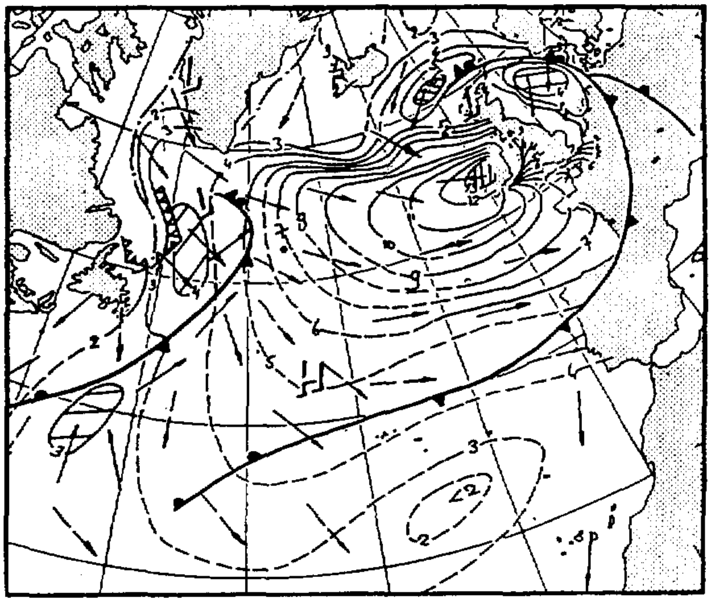

For two areas, 10° - 20°W x 50° - 55°N and 40° - 50°W x 50° - 55°N, from each map the minimum and maximum wave heights were derived. Maps are available every 12 hours from 1961 to 1987. A distribution of the 12 hourly box maximum wave height as well as the box mean (= 1/2(minimum. + maximum)) is derived for both boxes.

The percentiles for the resulting time series for one of the boxes is displayed in Figure 11 . The regression coefficients for the three curves are 2.7 cm/year for the 1% percentile, 3.4 cm/year for the 10% percentile and 2.7 cm/year for the 50% percentile. If we assume independence of the (annual) samples, the null hypothesis of zero correlation is rejected with little risk.

Similar results are obtained for the other box; the results are insensitive whether we use the box mean or the box maximum.

The rates of increase of the 50% percentile in Figure 11 fit remarkably well with the rates derived by Bacon and Carter (1991) for Light Vessel Sevenstones (2.4 cm/year) or Ocean Weather Station Juliett (2.8 cm/year) for the mean wave height. Similar estimates, derived from visual observations have been reported by Hogben (1994) (2.8 cm/year of Sevenstones and 3.3 cm/year for OWS J).

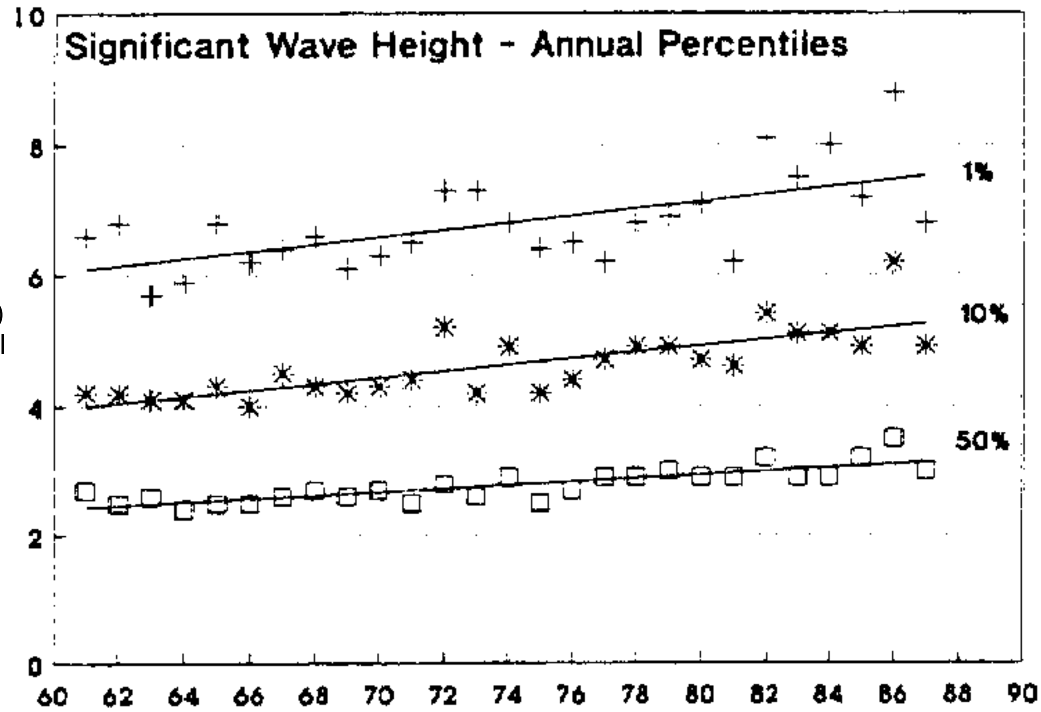

Figure 11:

Time series of 1%, 10% and 50% percentiles of the annual wave height distribution in an area west of Ireland (10°–20°W, 50°–55 °N) derived from operational shiprouting maps prepared by KNMI. Units: m

Kushnir's et al. (1995) analysis supports these estimates of the rise in annual mean wave height. They first integrated a wave model over 10 years using surface winds from the ECMWF analyses as forcing. Then a statistical model was built which describes the mean wave field as a function of the mean air pressure field. This statistical model was then used to estimate the mean wave field from the air pressure field from 1962 onward. This procedure resulted in an increase of 1.9 cm/year at Sevenstones.

An interesting aspect is whether the distribution of wave heights is merely displaced towards taller waves as a result of a shift of the mean or if the spread of the distribution has becoming wider as well, so that the extremes have grown disproportionately. The analysis of the wave maps in the area west of Ireland indicates that the spread has indeed become wider: The estimated rise from 1961 to 1987 is for the 50% percentile is 73 cm whereas the increase of the 10% is 1.30 cm in the area west of Ireland (Figure 11).

4 Hindcast Experiments with the Wave Model WAM

Because of the limited value of the observational record of the North Atlantic wave climate, a 40 years reconstruction (1954 to 1994) of the wave conditions in the North Atlantic Ocean and adjacent seas is be attempted by running the WAM wave model (Komen et al., 1994). Two versions of this model are used:

- a "coarse" resolution version (1.5° x 1.5° latitude x longitude; 2094 active grid points) covering the whole North Atlantic (80°N to 9.5°N, 78°W to 48°E)

- a "fine" resolution (0.5° x 0.75° latitude x longitude; 4105 active grid points) covering the Northeast Atlantic (77°N to 38°N, 30°W to 45°E)

For running the numerical simulations, two different wind data sets are used. For the fine resolution simulation. wind estimates from the air-pressure analyses prepared routinely by Det Norske Meteorologisk Institutt (DNMI) are readily available. For the coarse resolution model operational analyses of the Fleet Numerical Oceanography Centre (FNOC) are used. An example of a FNOC wind field is shown in Figure 12 .

Figure 12: *An example of a FNOC wind field.*

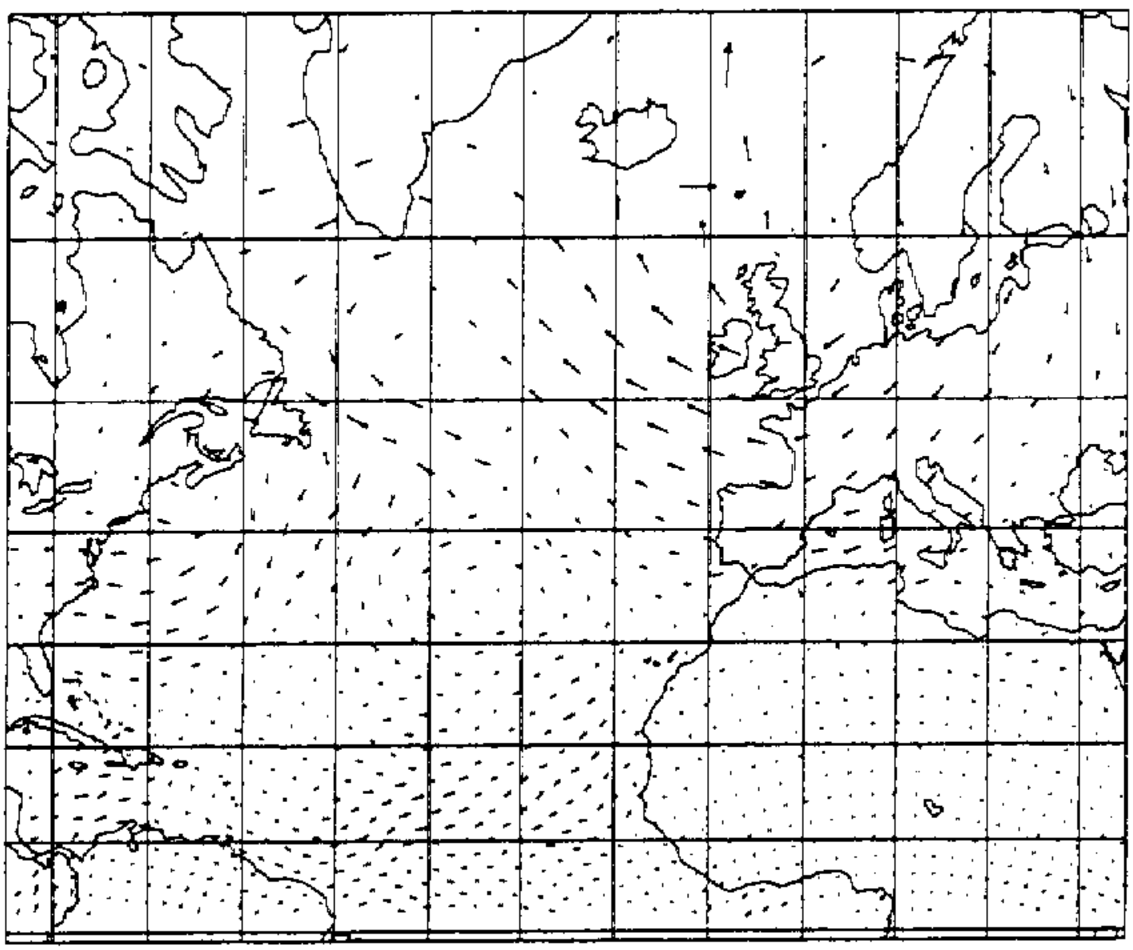

The FNOC data set suffers from a few gaps, in particular all 1994 is missing. These gaps are filled by temporal interpolation and by the use of ECMWF analyses. A polynomial method was used to interpolate the wind field on the WAM grid of 1.5° resolution. Furthermore several changes in the preparation of the analysis have taken place in the course of time: until 1971 the pressure maps were prepared by hand, and after that year dynamical analysis models were used. Until 1977 winds were geostrophically derived winds; the change from manual to computer analyses was connected with an abrupt change of about 1 m/s in the wind. Afterwards a "Planetary Boundary Layer Model" (PBLM) was used to specify the wind. During some time, the archived winds refer to the 19.5 m level and sometimes to the 10 rn level. This inconsistency was repaired by applying a standard logarithmic wind speed profile. As a consistency tests PBLM winds and geostrophically derived winds were compared in an overlapping period of 8 months (April to December 77) when both sets of data are available. The two sets of winds compared well in terms of directions, but the geostrophically derived wind speed was found to be systematically lower than the PBLM wind speed (see Figure 13). A statistical correction was applied to overcome the bias.

Figure 13: Analysis of paired observations of geostrophically derived wind speeds and PBLM-generated winds. The frequency distribution for the geostrophically derived wind speeds and for the PBLM derived winds are labelled "distribution of". The "bias" ist the difference between the man geostrophically derived wind speed, conditional upon a PBLM wind speed given at the horizontal axis, and the specified PBLM wind speed. "SI" is the (conditional) coefficient of variation (standard deviation devided by the mean).

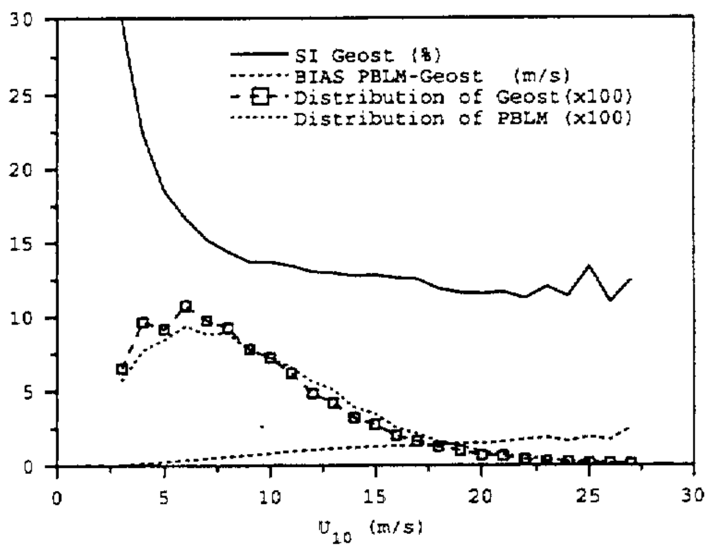

Apart from these "detectable" inhomogeneities there are also "non-detectable inhomogeneities" in the data, due to the changing observational record (withdrawal of ocean weather stations; advent of satellites etc), improved analysis techniques (such as computerized analysis schemes) and other nonstationary operational conditions (as a demonstration of this problem, see Figure 1). We use these data nevertheless since we do not have a better product available at this time. The wave climate response to the FNOC/DNMI winds will supply us with an upper bound of the worsening of the wave climate; at a later time we could redo the hindcast runs with the re-analysed wind fields presently prepared at the US NMC and at ECMWF.

Some storms from recent years were hindcasted at Clima Maritimo using the coarse resolution Atlantic version of WAM and the FNOC winds. The model data compared well in situ data gathered by buoys at the Cantabric Coast of Spain and at the Canary Islands. Also some multiyear hindcasts were already executed.

The skill of these hindcasts is demonstrated by a case study for 1992 for a position off the Spanish coast (Figure 14) and a statistic for the years 1980 to 1982 for the Northern North Sea (Figure 15). The hindcast for the 1992 case is almost perfect, for both wind analyses used, but the skill during the 3-year hindcast is somewhat mixed, with good results in the second half and a severe overestimation by the model in the first half.

Figure 14: *Hindcast of the significant wave height for the location of the buoy "Bilbao" for two weeks in February 1992. The heavy (upper) line represents the measurements made by the buoy and the light (lower) line the hindcast using the FNOC wind analyses.*

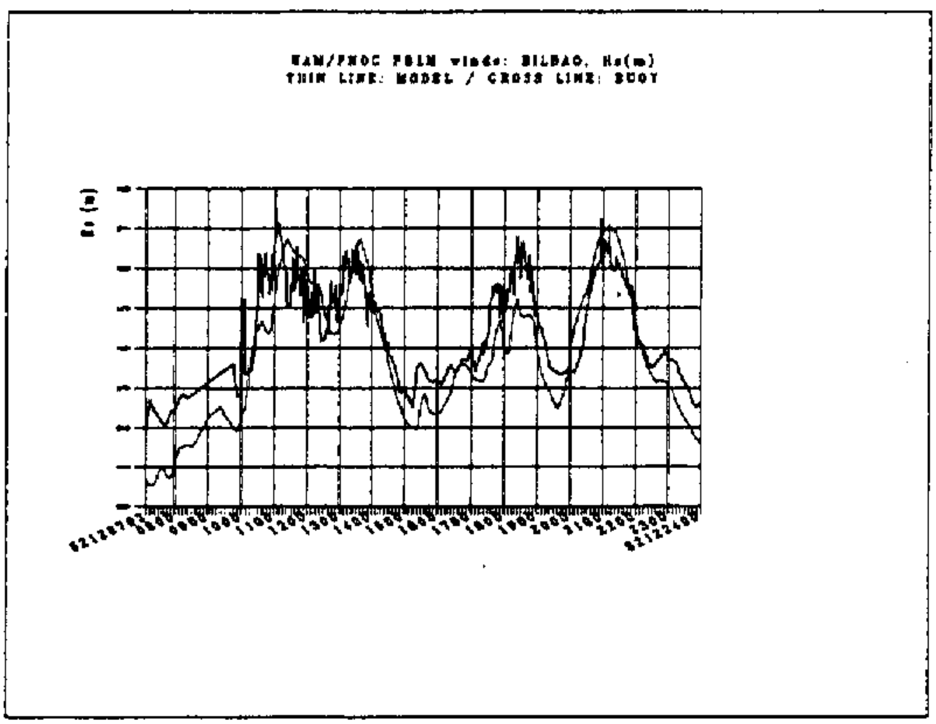

5 Conclusions

The results of our joint efforts for determining whether the storm and/or wave climate in the North Atlantic Ocean and adjacent seas has roughened are not unequivocal. Almost all local indicators, representative for storminess, indicate no worsening of the storm climate, with the possible exception of the Southern Baltic Sea (as reported by Mietus, 1994). For the wave climate, on the other hand, more evidence has shown up in favour of the hypothesis of a worsening wave climate, not only in the man wave height but also in the extremes.

There are a number of caveats. The analysis of geostrophic winds, pressure tendencies and high-frequency sea level variations covers only the near-coastal areas of Northern Europe, and no robust analysis is available for the en ocean regions. For the wave field, both the analysed maps and the local observations are prone to inhomogeneities which introduce an artificial increase of mean and extreme wave heights. Because of these caveats further wave hindcast experiments are presently underway to test the hypothesis of "taller waves without a worsening of the local storm climate".

An inconsistency in these statements concerning the storm and wave climate concerns the considered time scales. The storm climate is studied by time series of typically 100 years lengths, and seen in this perspective, the storm climate does not appear to have changed. The wave data, however, cover only the period since about 1960 - and it could be that the trends of the last 30 years appear as mere variations when compared with variations earlier this century. Indeed, a recent analysis by Hurrel (1995) on the North Atlantic Oscillation (NAO) has revealed that the NAO (in winter) which represents the strength of the winter mean zonal circulation over the Atlantic has steadily increased since about 1960. This intensification is remarkable but not really "un-normal" if compared to the full record of the NAO since 1864. Thus, the increase in wave heights, if it is real, might well be another swing in the never ending sequence of up's and down's of natural variability. Further close monitoring of the development is required to eventually evaluate whether the other possible explanation - systematic changes because of anthropogenic climate change - might be adequate (cf. von Storch and Hasselmann, 1995).

Figure 15: *Monthly percentiles of significant wave height at the location of Statfjord/Gullfaks for the years 1980 to 1982. The dotted line represents the observed wave heights, and the dashed line the hindcasted wave heights.*

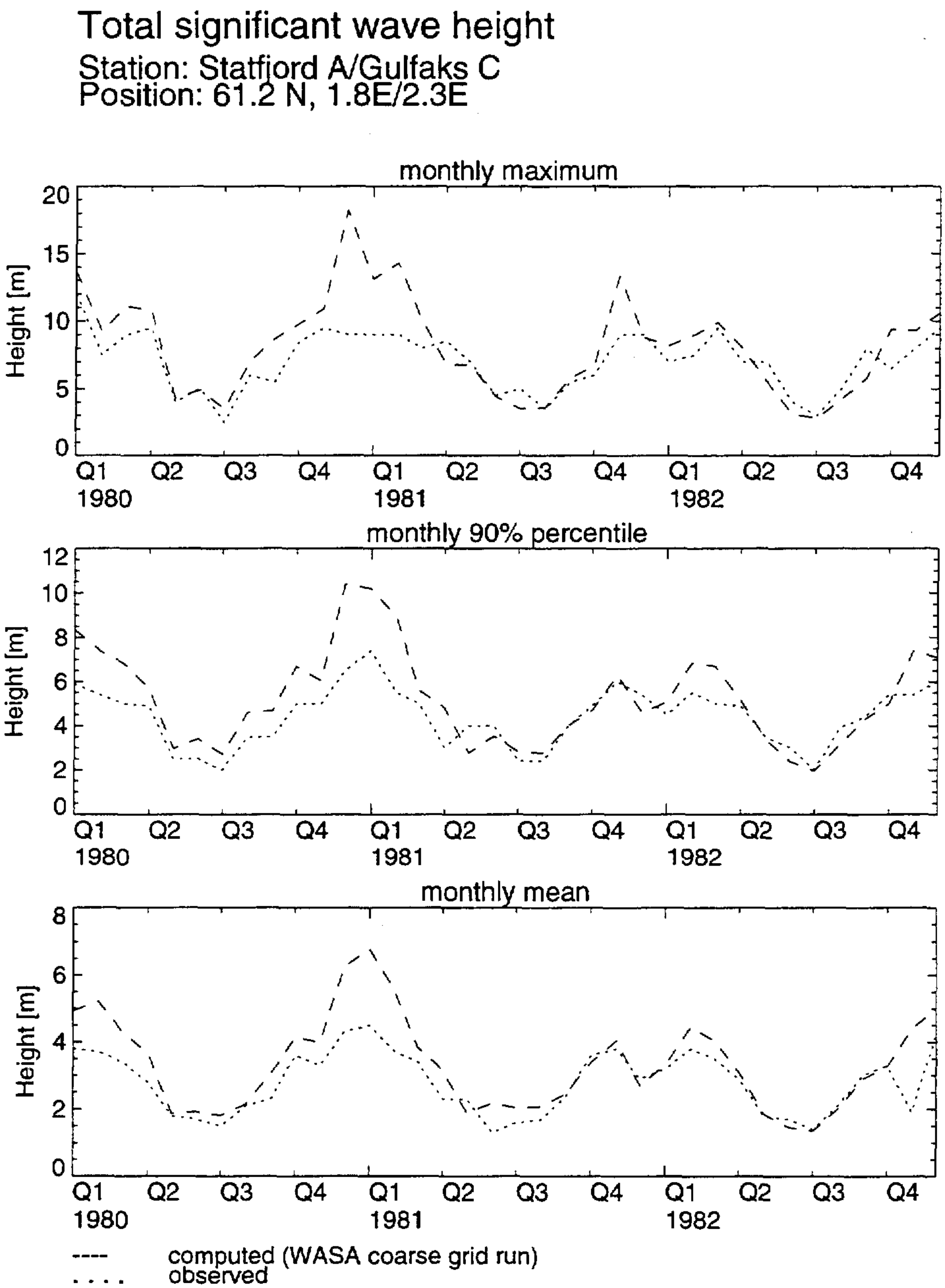

6 References

Alexandersson, H., 1986: A homogeneity test applied to precipitation data. J. Climatol. 6, 661-675

Bacon, S. and D.J.T.Carter, 1991: Wave climate changes in the North Atlantic and the North Sea. Int. J. Climat. 11, 545-558.

Carter, D.J.T. and L.Draper, 1988: Has the North-east Atlantic become rougher? Nature 332, 494.

Hogben, N. 1994: Increases in wave heights over the North Atlantic: A review of the evidence and some implications for the naval architect. Trans Roy. Inst. Naval Arch., 93-101

Hurrel, J.W., 1995: Decadal trends in the North Atlantic Oscillation regional temperatures and precipitation. Science 269, 676-679

Jónsson, T., 1981: Hitt og thetta um ofvidri (Odds and ends on storms). Vedrid (Soc. professional Icel. Meteorologists, Reykjavik) 21, 64-70 (in Icelandic).

KNMI, 1993: De toestand van het klimaat en van de ozonlaag in Nederland. Koninklijk Nederlands Meteorologisch Instituut, De Bilt, The Netherlands, 20 pp.

Komen, G.J., L. Cavaleri, M. Donelan, K. Hasselmann, S. Hasselmann and P.A.E.M. Janssen, 1994: Dynamics and Modelling of Ocean Waves. Cambridge University Press, 532 p.

Kushnir, Y, V.J. Cardone and M. Cane, 1995: Link between Atlantic climate variability of surface wave height and sea level pressure. Proc. Fourth International Workshop on Wave Hindcasting and Forecasting, Banff, Canada, October 16-20, 1995 (this volume)

Mietus M., 1994: Vector of geostrophic wind in the Baltic Sea region as an index Of local circulation and its relationship to hydro-meteorological characteristics along the Polish coast. Climate variations in Europe, SILMU 278-292 (Proceedings of the European Workshop on Climate Variations, Majvik, Finland, 15-18 May 1994).

Peterson, E.W. and L. Hasse, 1987: Did the Beaufort scale or the wind climate change? J. Phys. Oceano. 7, 1071-1074

Schinke, H., 1992: Zum Auftreten von Zyklonen mit niedrigen KerndrÜcken im atlantisch-europäischen Raum von 1930 bis 1991. Wiss. Zeitschrift der Humboldt Universität zu Berlin, R. Mathematik/Naturwiss. 41, 17-28

Schmidt, H. and H. von Storch, 1993: German Bight storms analysed. Nature 365, 791.

Schmith, T, 1995: Occurrence of severe winds in Denmark during the Past 100 Years. in: Proceedings of the Sixth International Meeting on Statistical Climatology, Galway, Ireland.

Stein, O. and A. Hense, 1994: A reconstructed time series of the number of extreme lows pressure events since 1880. Z. Meteor. (in press)

von Storch, H., J. Guddal, K. Iden, T. Jonsson, J. Perlwitz, M. Reistad, J. de Ronde, H. Schmidt and E. Zorita, 1994: Changing statistics of storms in the North Atlantic? Max-Planck-Institut fÜr Meteorologie-Report 116 (available from Max-Planck-Institut für Meteorologie, Bundesstrasse 55, 20146 Hamburg, Germany)

von Storch, H. and K. Hasselmann, 1995: Climate variability and change. MPI Report 152

WASA group (K. Iden, H. Reichardt, M. Reistad, W. Rosenthal, A. Ruiz de Elvira and H. von Storch), 1994: Comment on ”Increases in Wave Heights over the North Atlantic: A Review of the Evidence and some Implications for the Naval Architect” by N Hogben. Trans Roy. Inst. Naval Arch. 107110

VARIATION OF MEASURED METEOROLOGIC AND OCEANIC VARIABLES OFF THE U.S. ATLANTIC COAST, 1980-1994

J. M. Hubertz

U.S. Army Engineer Waterways Experiment Station
Coastal Engineering Research Center
Vicksburg, Mississippi 39180-6199

1. INTRODUCTION

The National Data Buoy Center, within the National Weather Service of the National Oceanic and Atmospheric Administration, operates buoys off the coasts of the United States from which atmospheric and oceanic measurements are made. This program began in the mid-1970's with only a few buoys in the Atlantic, Pacific, and Gulf of Mexico measuring meteorological variables. More buoys were gradually added in the 1980's and 1990's, and measurements became more sophisticated.

This study examines data from five buoys off the Atlantic Coast for the 15-year period from 1980 to 1994. These buoys are identified as 44011, 44004, 41001, 41002, and 41006. Their locations are shown in Figure 1 . The data from these buoys were chosen for study because of location along the coast in deep water and long period of record for both meteorological and oceanic data.

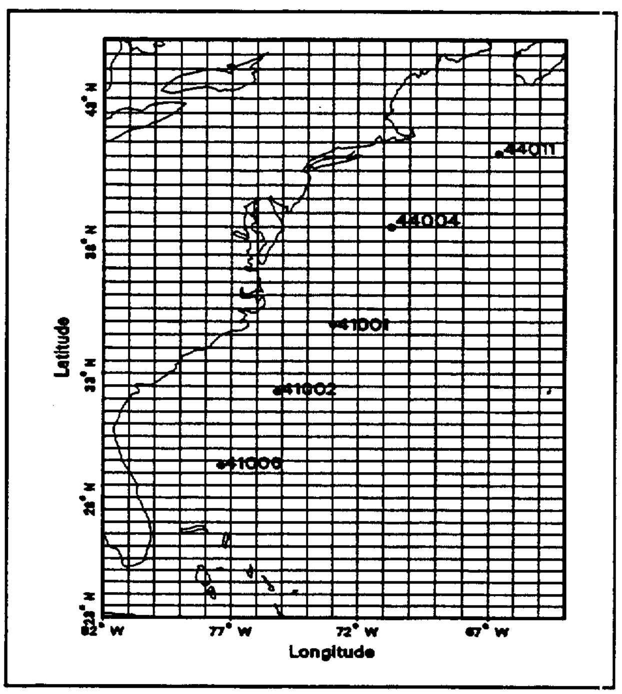

Figure 1. Location of Buoys (solid dots) with ID Numbers.

2. BUOY DATA

Data from all buoys, since inception of the program, are contained on compact disks. Data from the above buoys were copied to a personal computer hard drive. The "B" type records were extracted from all possible records for each hour data were measured. This "B" record contains information such as air and sea temperature, surface atmospheric pressure, wind speed and direction, and wave height and dominant period. This study emphasizes the long-term variation in wind speed and wave height at each of the five buoy locations. The long-term variation of air and sea temperature and surface atmospheric pressure is examined at Buoy 41001. Gilhousen (1990) lists the accuracy of the wind speed measurements as +/- 0.98 m/s or 10%, wave heights as +/- 0.2 m or 5%, wave periods as +/- 1 sec, air sea temperatures as +/- 1 deg C, and surface pressure as +/- 1 mb.

Early in the measurement program, data were recorded every 3 hours. Subsequently, at different times and at different locations, data were recorded at a 1-hour interval. For various reasons, there are gaps of varying length throughout the length of record. These gaps need to be filled with valid data in order to obtain a continuous time series so that averages over time are equally populated. In order to do this, a file was constructed from the information in the "B" records which consisted of records containing a date-time group and various parameters. Each of these time series files was compared to a standard set of dates and times every hour from 00 hours UT on Jan 1, 1980, to 2300 hours UT on Dec 31, 1994. When a gap in the buoy data was detected, it was filled with the appropriate date-time, and the parameter space was filled with zeros. This resulting time series was then subsampled to obtain a time series with a 3-hour interval. A 3-hour interval was chosen since that corresponds to the frequency of hindcast information from the Wave Information Study (WIS). Figures 2 and 3 illustrate the gaps in wind speed and wave height data at 41001. The longer gaps are presumably due to major overhauls and replacement of equipment.

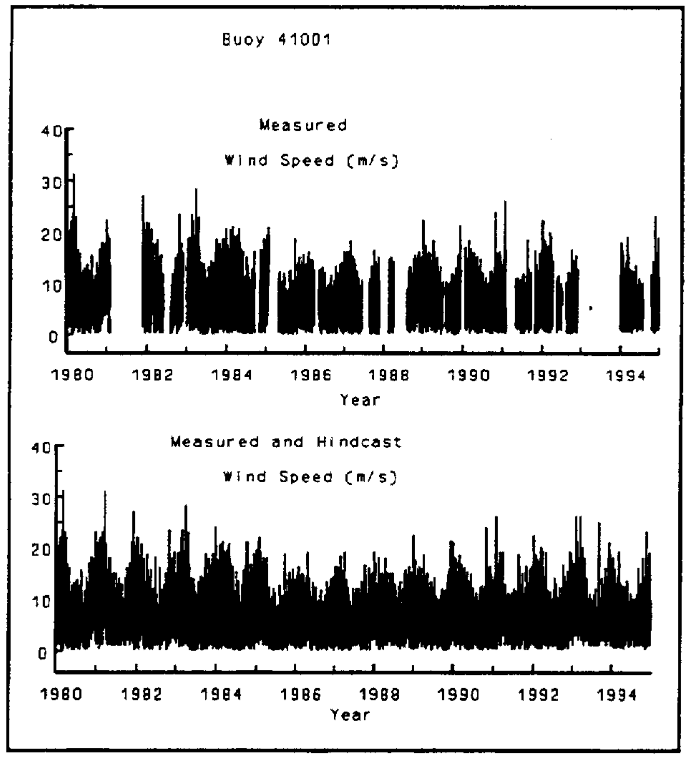

Figure 2. Time Series of Measured Wind Data with Gaps and Filled with Hindcast Data

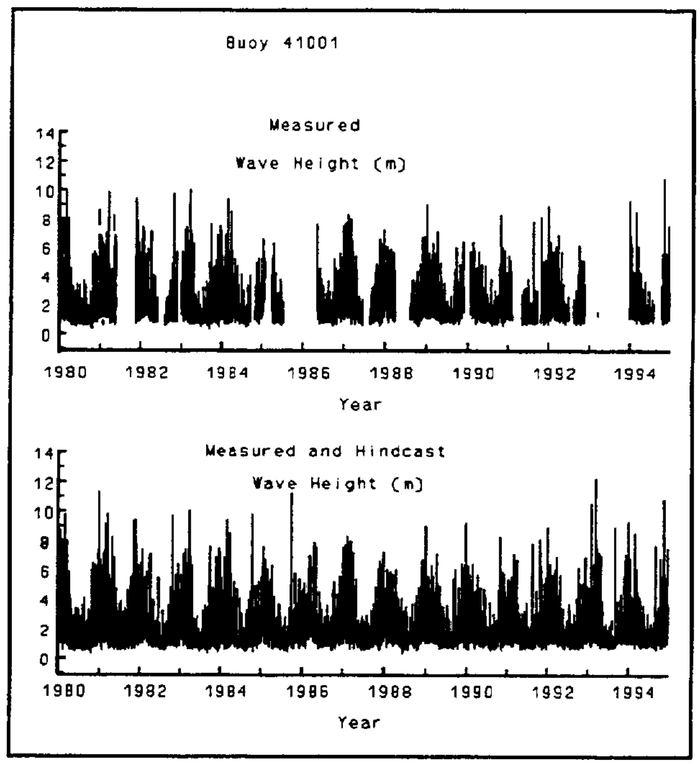

Figure 3. Time Series of Measured Wave Data with Gaps and Filled with Hindcast Data

3. HINDCAST DATA

A wave hindcast for the U.S. Atlantic Coast was recently completed, Brooks (1995), for the period 1976-1993. The Corps of Engineers' wave model WISWAVE 2.1 was used with global winds (2.5 deg at 19.5 m every 6 hours) produced by the U.S. Navy's Fleet Numerical Meteorological Oceanographic Center (FNMOC) to hindcast wave conditions on a 1-degree latitude longitude grid over the North Atlantic. Results from the 1-degree grid were linked to a quarter degree grid covering from 65 deg W to the Atlantic Coast. Hindcast results were saved every 3 hours at WIS stations along the coast and at locations of measurements from buoys. The latter were used to validate the hindcast results. The Corps' planetary boundary layer tropical cyclone wind model, Cardone et al. (1994), was used to model tropical storms and hurricanes passing through the finer grid since FNMOC wind fields do not accurately represent these small storms. Modeled cyclone winds were fused with far field FNMOC winds to produce a continuous history of winds over the region including tropical cyclones.

Hindcast results were compared to available measurements to validate the accuracy of the model results. Table 1 summarizes comparison statistics for wave height from the measurement sites in Figure 1 . The first row for each buoy is the bias (model-measured), the second row is root mean square difference, and the third row the correlation coefficient r. Complete tables for all 38 possible buoys are in Brooks (1995). The results in Table 1 indicate a negligible bias, with a mean absolute difference of about 0.6 m, and about 65-80% of the variance of the measured record reproduced by the model. The WIS group is continuing to keep hindcast wave information up to date by performing monthly hindcasts with the most accurate wind data available now. Work is underway to improve wind fields and wave hindcast results by assimilating measured data.

4. DATA ANALYSIS

The hindcast wind and wave information is considered an accurate representation of conditions during the 15-year period. The measured record is considered the most accurate, but it suffers from gaps in time. Thus, to obtain the most complete representation of climate, the gaps in the measured record were filled with hindcast values for every 3-hour interval which was missing data. Minimums, maximums, means, and standard deviations were calculated for each of these filled time series. Table 2 summarizes these basic statistics for wind speed, wave height, and peak period at the five locations listed in a north to south order.

Table 1. Comparison of Hindcast to Measured Wave Heights (m)

Buoy	Years													
	93	92	91	90	89	88	87	86	85	84	83	82	81	80
44011	0.4	0.0	0.0	0.1	0.0	–0.0	0.1	0.4	0.1	0.1				
	0.7	0.6	0.7	0.6	0.6	0.6	0.8	0.9	0.7	0.7				
	0.8	0.9	0.8	0.8	0.8	0.9	0.8	0.8	0.8	0.8				
	1420	2143	2233	2780	2601	2380	2802	2157	2629	1769	0	0	0	0
44004	0.1	–0.1	–0.2	–0.0	–0.1	–0.2	–0.0	0.1	0.0	0.1	–0.0	–0.1	0.9	0.6
	0.6	0.6	0.6	0.6	0.6	0.6	0.7	0.7	0.7	0.9	0.7	0.6	1.4	1.2
	0.9	0.9	0.9	0.8	0.9	0.9	0.9	0.8	0.8	0.8	0.8	0.9	0.8	0.9
	2897	2889	1771	2754	1949	2464	2207	2782	2050	1034	2794	1550	1074	2084
41001	0.1	–0.3	–0.1	–0.0	–0.1	–0.2	–0.2	0.0	–0.2	0.0	–0.0	–0.2	0.3	0.5
	0.6	0.6	0.6	0.5	0.6	0.6	0.7	0.7	0.7	0.8	0.7	0.7	1.1	1.1
	0.9	0.9	0.9	0.9	0.8	0.8	0.8	0.8	0.8	0.8	0.8	0.8	0.8	0.8
	2224	2327	2007	2721	2182	1925	2384	1859	1025	2618	2842	2177	1337	2598
41002	0.1	–0.1	–0.0	0.1	–0.0	–0.2	–0.1	–0.0	–0.1	–0.1	–0.2	–0.2	0.2	0.3
	0.6	0.5	0.5	0.5	0.6	0.6	0.6	0.6	0.6	0.9	0.8	0.6	0.8	0.7
	0.9	0.8	0.9	0.8	0.8	0.8	0.8	0.8	0.7	0.7	0.8	0.8	0.8	0.8
	2508	1538	2915	1536	1926	2229	2898	1933	669	1004	2318	2883	2489	2028
41006	0.1	–0.1	–0.2	0.1	0.0	–0.2	–0.1	0.0	–0.0	–0.1	–0.1	–0.2		
	0.4	0.5	0.5	0.4	0.4	0.5	0.5	0.5	0.5	0.6	0.6	0.6		
	0.9	0.8	0.9	0.8	0.9	0.7	0.8	0.8	0.8	0.8	0.8	0.8		
	2898	2686	422	2577	1956	1931	2028	2115	2835	2912	2666	1744	0	0

Table 2. Summary Statistics

Buoy ID	Parameter	Minimum	Maximum	Mean	Std. Dev.	No. of Observations
44011	Wind Speed (m/sec)	0.1	30.0	6.68	3.66	32144 @3hrs=11 yrs
44004		0.1	35.0	7.32	3.72	43832 @3hrs=15 yrs
41001		0.1	31.2	7.39	3.74	43832
41002		0.1	30.1	6.60	3.25	43832
41006		0.1	30.0	5.75	2.87	37984 @3hrs=13 yrs
44011	Wave Height (m)	0.3	11.6	2.11	1.27	
44004		0.3	13.9	2.02	1.26	
41001		0.3	12.2	2.04	1.20	
41002		0.3	15.7	1.85	1.04	
41006		0.3	9.6	1.68	0.85	
44011	Peak Period (sec)	2.6	20.0	8.29	2.24	
44004		2.6	22.0	8.03	2.31	
41001		2.7	24.0	8.15	2.25	
41002		2.9	24.0	8.25	2.38	
41006		2.6	24.0	8.54	2.35	

There is little difference in mean and maximum wind speed from north to south along the coast. Mean wave heights tend to be slightly higher for locations north of about 35 deg. Maximum wave heights are a function of storm passage with respect to buoy location. There is little difference in maximum and mean wave peak periods. Note that there may be some effect on periods due to the Gulf Stream which generally flows west of 41006, 41002, and 41001, but through the area where 44004 and 44011 are located. In general, there does not appear to be trends or large variability in wind speed, wave height, or peak period offshore along the U.S. East Coast, with the exception of lower wind speeds and wave heights south of about Cape Hatteras.

4.1 Monthly Means

Mean values of wind speed and wave height were calculated from the combined record for each month of the 15-year period at each of the five locations. In addition, a mean for all Januaries, Februaries, etc., over the 15 years was calculated. This latter mean is referred to as the long-term mean. Figures 4 -8 are plots of monthly mean wind speed and wave height at each buoy for the period of record. The long-term mean for each of the 12 months is also plotted, being repeated for each year of the period of record. This allows comparison of monthly means each year to the long-term mean.

4.2 Wind Speeds

There is a definite seasonal cycle for wind speed. Differences between winter and summer long-term means are 4.0 to 2.5 m/sec with larger ranges being at more northern locations. Monthly means in the summer months generally do not depart more than the accuracy of measurements (+/-1 m/sec) from the long-term means. The largest departures from the long-term mean are in the winter months where it is evident that some years are less and more "stormy" than others. There is no consistency, though, along the coast. No long-term trends over the 15 years are evident, i.e., a gradual increase or decrease in wind speeds, but there are periods when wind speeds are above and below the long-term mean. For example, at 41001 wind speeds during the winters of 19801983 are higher and for 1986-1988 lower than the long-term mean. There is less variability at 41002 and 41006, reflecting the lower incidence of winter storms.

4.3 Wave Heights

Wave heights reflect the seasonal nature of the winds. Departure of the monthly means from the long-term mean is small in the summer months, but from 0.5-1.0 m during the winter months. There are almost no cases when the maximums of the winter months are below the long-term mean. For example, at 41001 during the winters of 1986-1988 when monthly mean winds were below the long-term mean, wave heights were at or above the long-term mean. This probably is due to arrival of swell at the site in addition to local wind-generated waves. No long-term trends in wave height are apparent at any of the sites. This contrasts with the observation of Carter and Draper (1988) that wave heights have increased by 0.034 m/yr from 1962 to 1983 at a point off Land's End, England, at the western end of the English Channel.

4.4 Storm Occurrences

Histograms of wind speed and wave height were calculated from the data at each buoy for 1980-1994. Table 3 summarizes the number of occurrences by year at each location for wind speeds greater than or equal to 15 m/sec and wave heights greater than or equal to 5.0 m. These are arbitrary thresholds chosen to represent fully developed seas in at least gale conditions. The period 1984-1994 was chosen to equally represent each location, and thus describe conditions along the U.S. East Coast. There are no data for 1980-1983 at 44011 and no data for 1980-1981 at 41006.

Storminess, as defined by the thresholds above, varies year by year without any trend. The number of storms decreases south of 41001 as evidenced by wind speed, and there is a steady decrease in the number of high waves from north to south. Figure 9 shows the total number of occurrences from all buoys by year. The effect of the "Storm of the

Century” in March 1993 is evident in Figure 9 by the greater number of storm conditions. This is also true in 1989 when Hurricane Hugo occurred. The large number of high waves without corresponding high winds in 1987 is probably due to storms passing far from any of the buoys but propagating swell to them. An example is Hurricane Floyd.

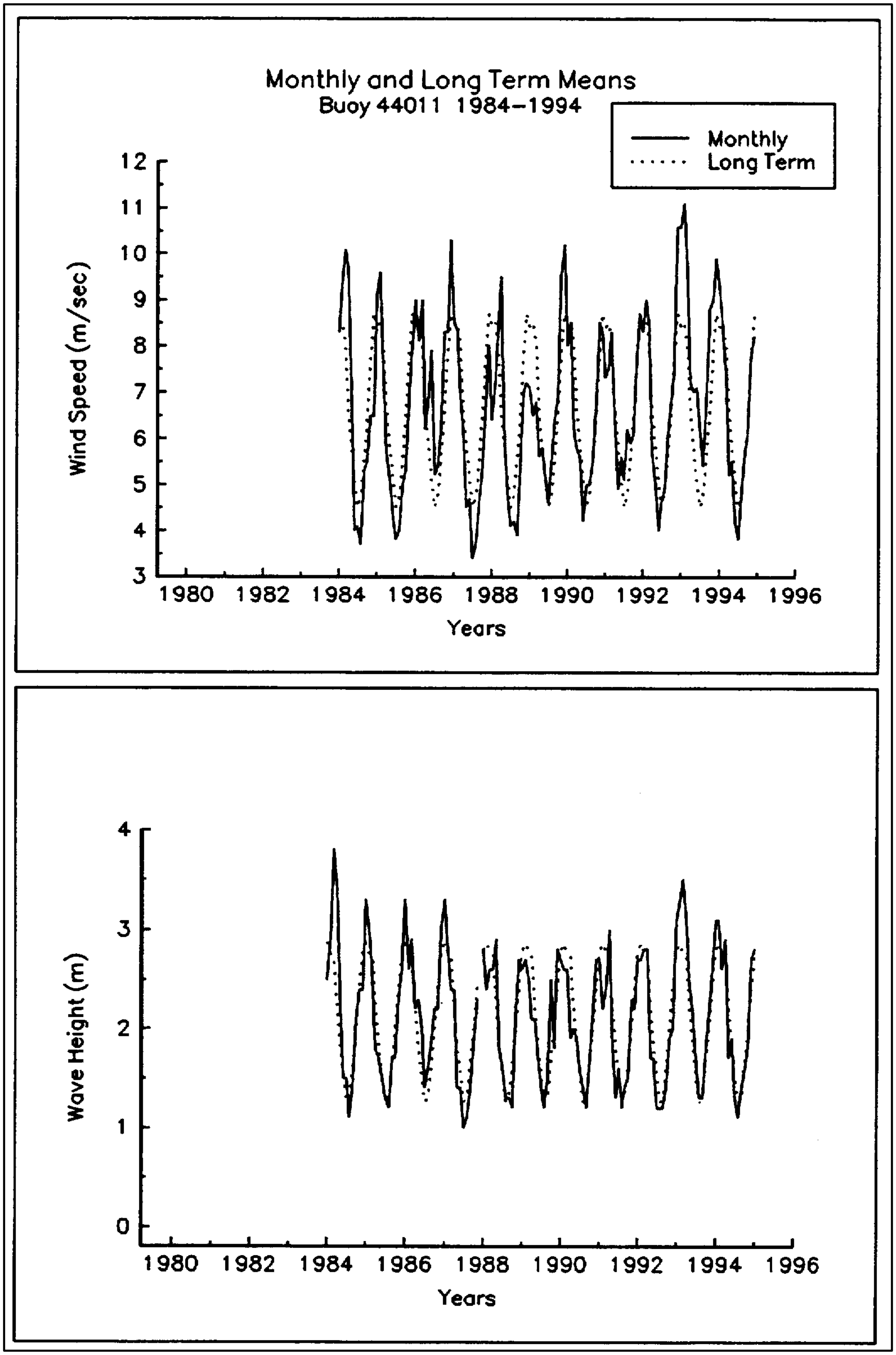

Figure 3. Mean Wind Speed and Wave Height at Buoy 44011

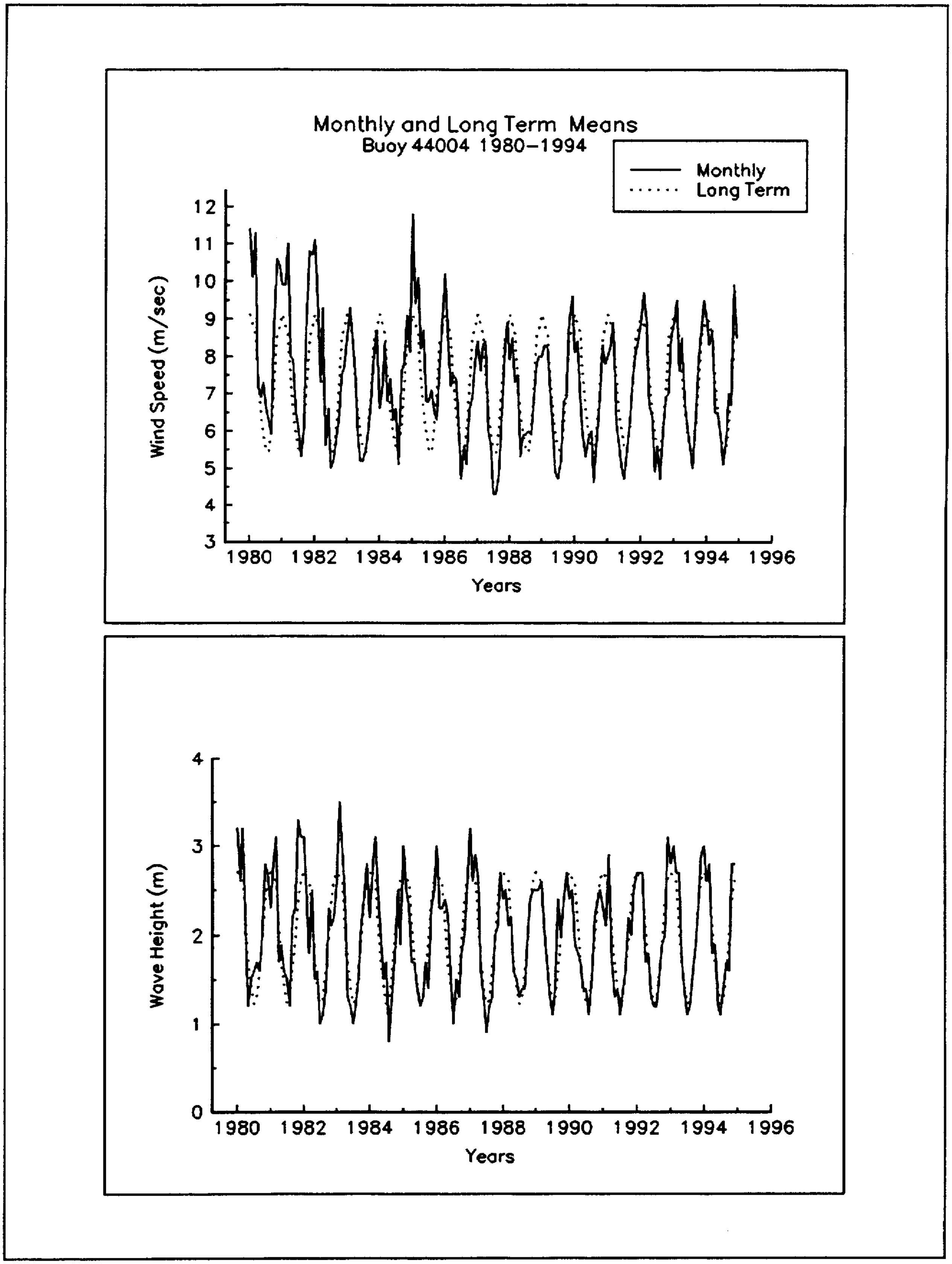

Figure 4. Mean Wind Speed and Wave Height at Buoy 44004

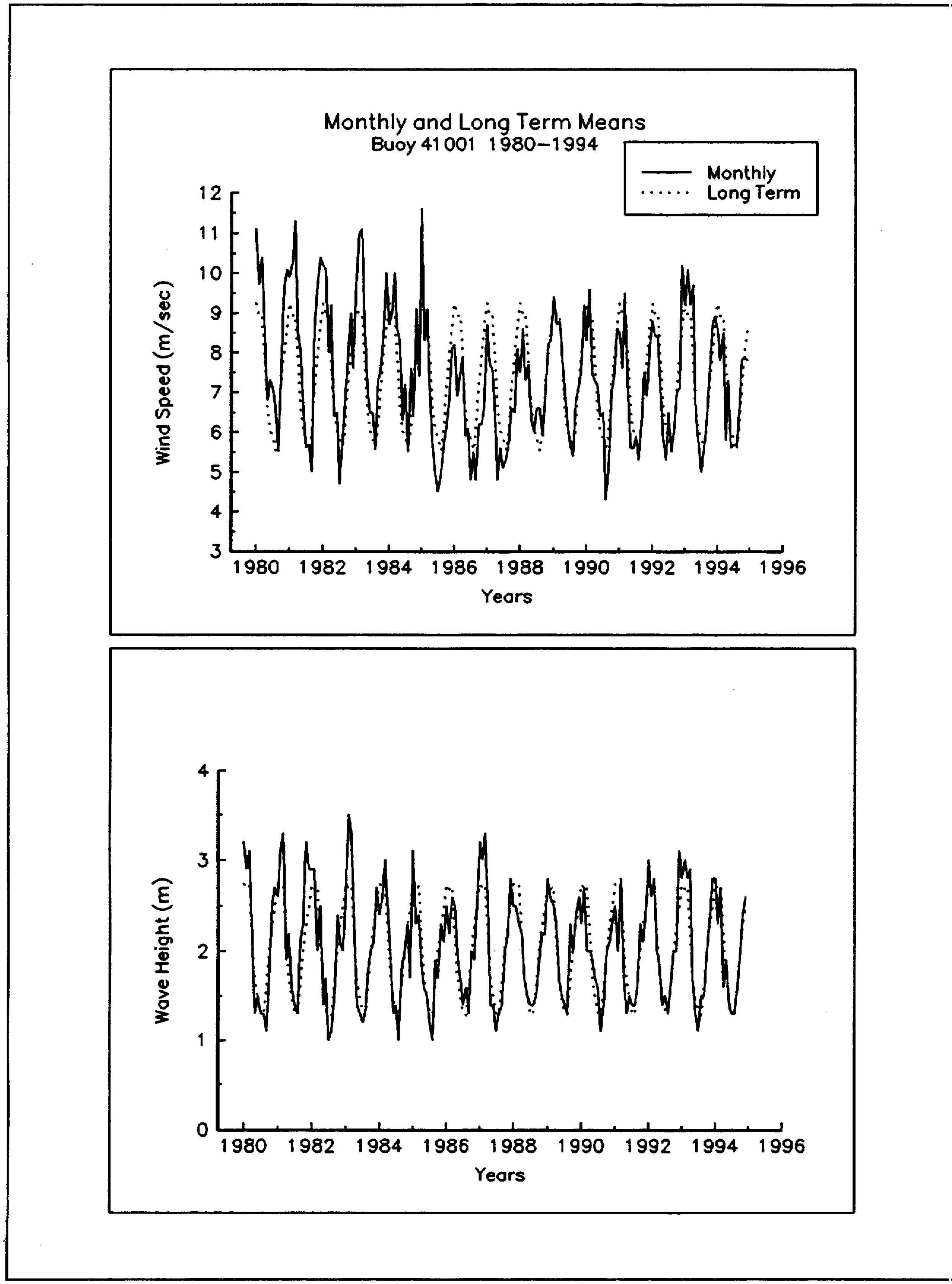

Figure 5. Mean Wind Speed and Wave Height at Buoy 41001

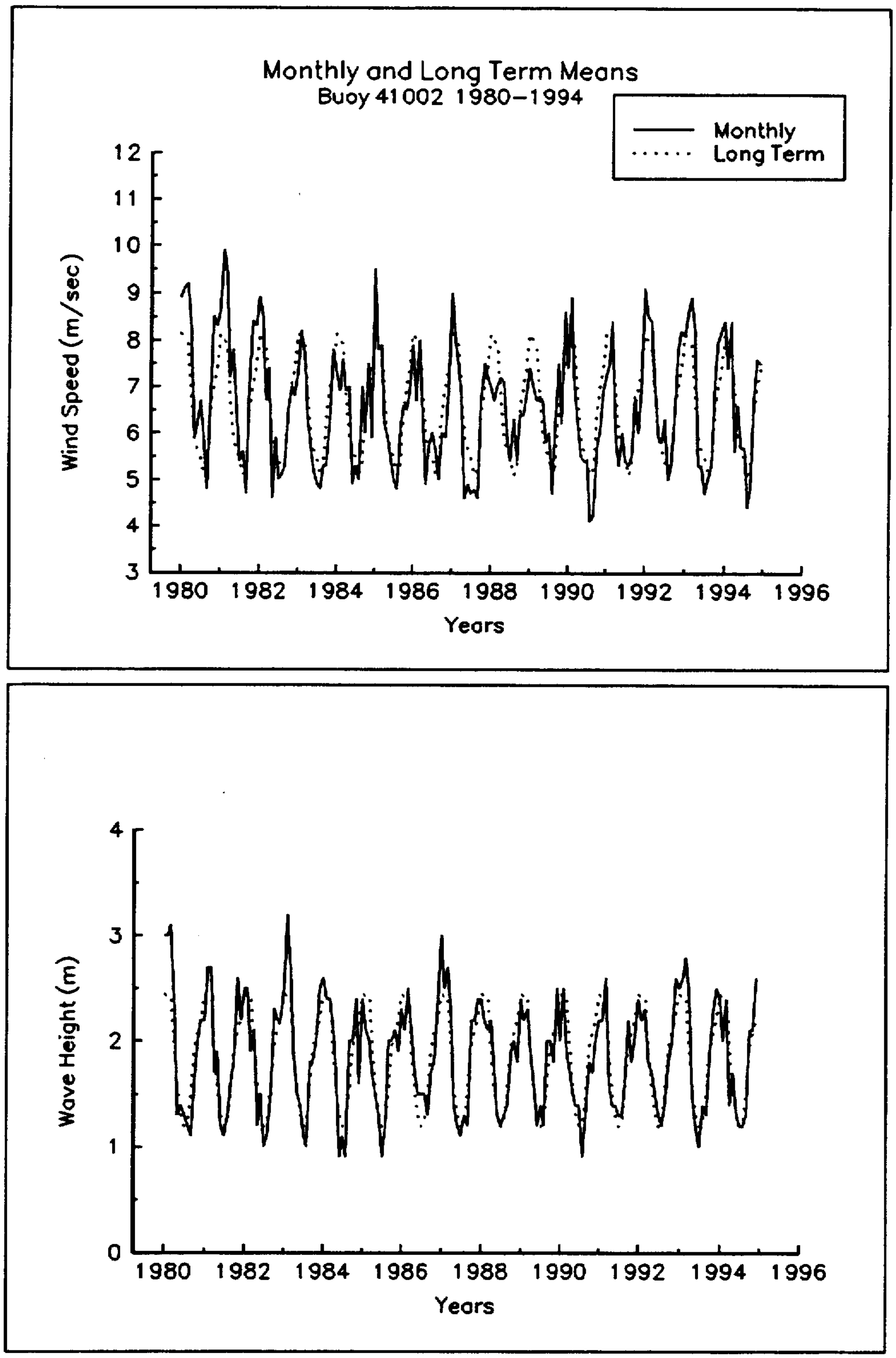

Figure 6. Mean Wind Speed and Wave Height at Buoy 41002

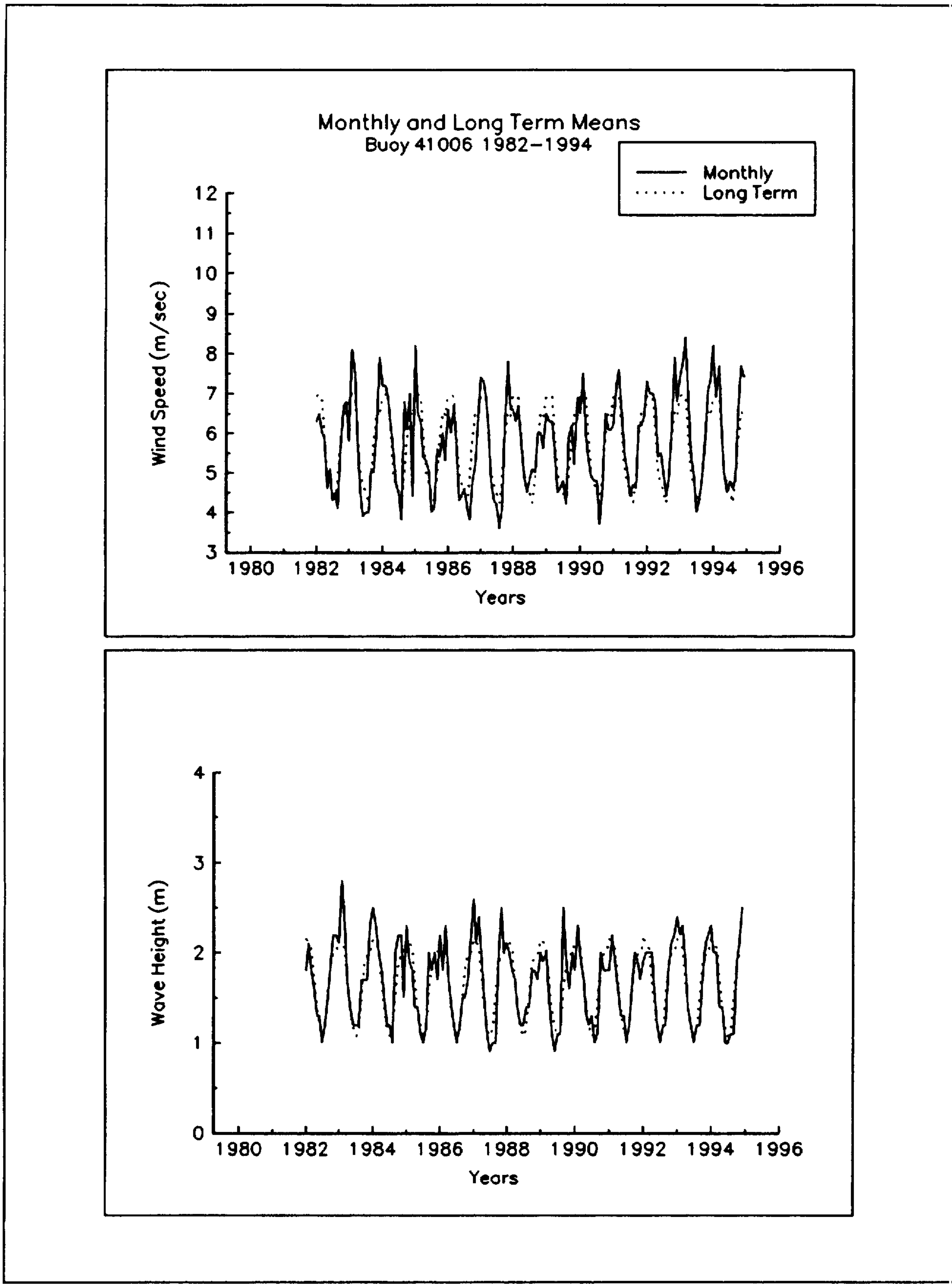

Figure 7. Mean Wind Speed and Wave Height at Buoy 41006

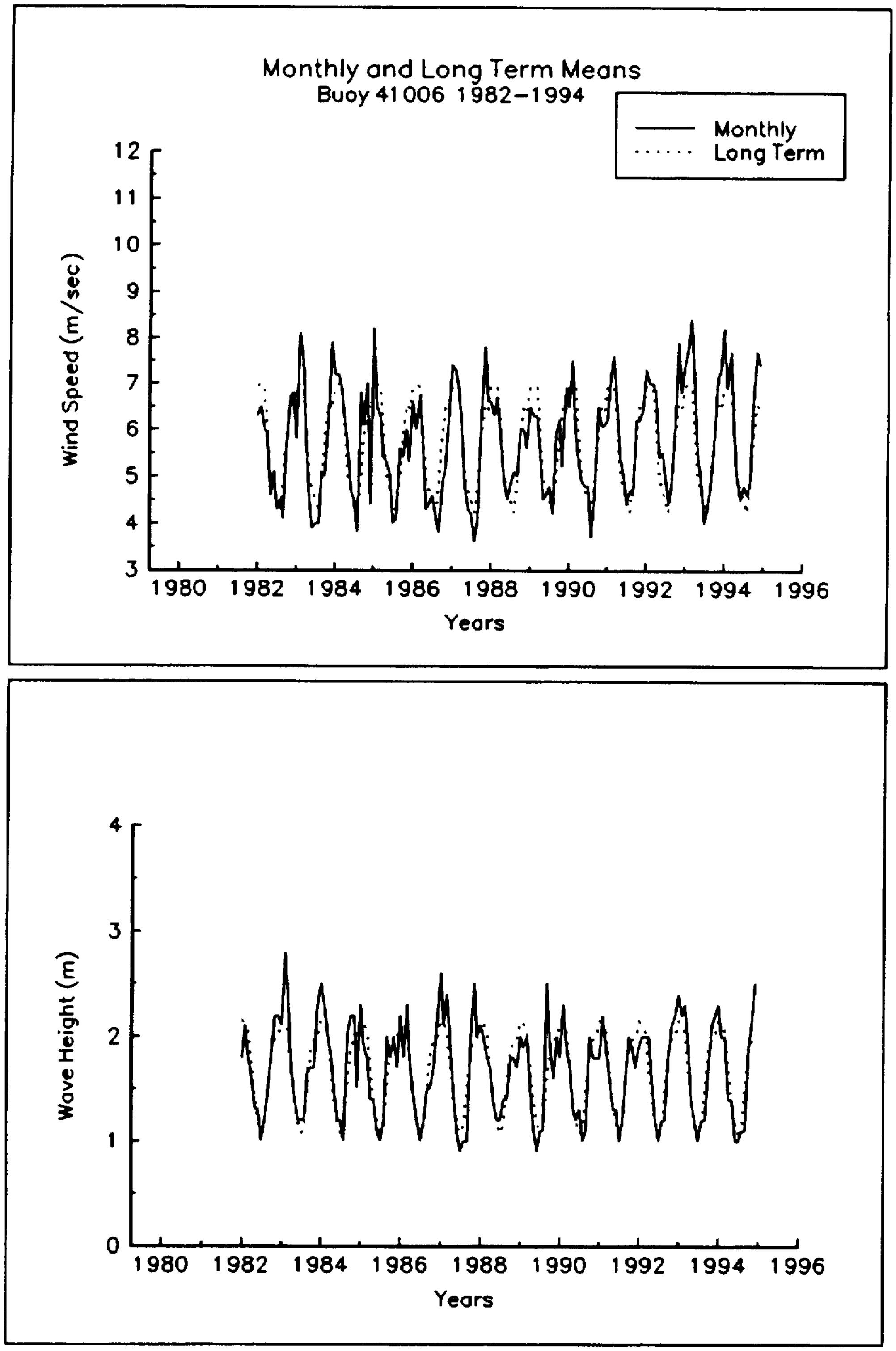

Figure 8. Mean Wind Speed and Wave Height at Buoy 41006

Table 3. Storm Wind and Wave Conditions

Year											
Buoy ID	84	85	86	87	88	89	90	91	92	93	94	Total
Number of Occurrences of Wind Speeds > = 15. 0 m/sec												
44011	87	43	115	20	50	34	49	50	75	156	45	724
44004	55	161	69	69	29	51	49	43	86	89	23	724
41001	130	129	12	31	36	63	56	61	93	187	54	852
41002	25	30	29	23	5	33	22	16	50	46	23	302
41006	28	8	2	10	5	20	1	17	6	20	277	144
Total	325	371	227	153	125	201	177	187	310	498	172	
Number of Occurrences of Wave Heights > = 5.0 m												
44011	168	118	156	129	119	77	84	78	99	162	122	1312
44004	87	95	96	158	55	82	62	53	106	128	34	956
41001	81	68	63	138	26	75	44	69	88	145	81	878
41002	60	20	40	77	25	64	13	55	43	50	64	511
41006	35	16	19	21	3	57	1	17	4	26	36	235
Total	431	317	374	523	228	355	204	272	340	511	337	

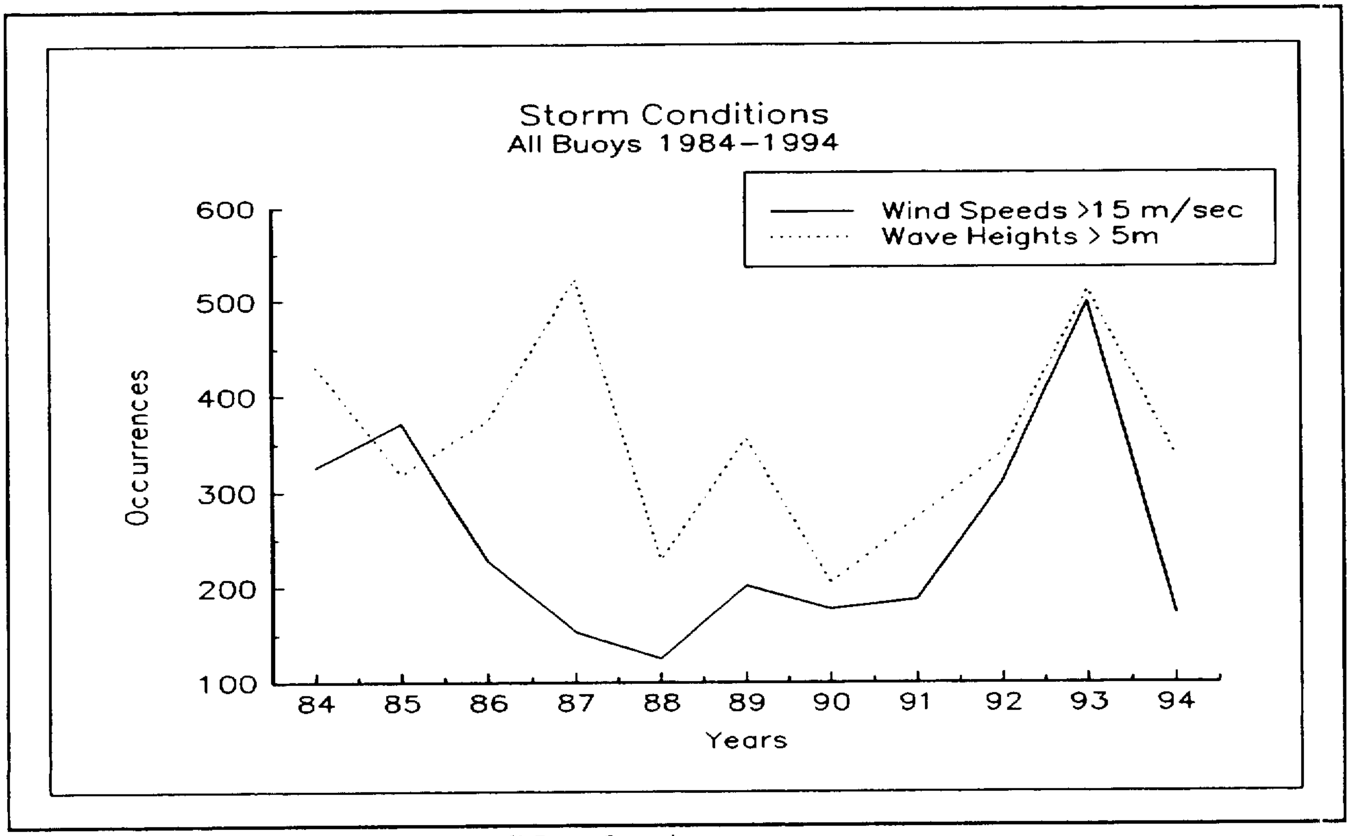

Figure 9. Storm Conditions by Year at All Buoy Locations

4.5 Other Parameters

Monthly mean values of air and sea surface temperature and surface atmospheric pressure were calculated from measurements at Buoy 41001. No data were available to fill in the gaps in the measured record. A monthly value was calculated if at least 8 days of data (sampled hourly, but not necessarily consecutively) were available in each month.

The variation of air, sea, and air-sea temperatures is shown in Figures 10 -12 , respectively. There is an apparent trend for increasing air and sea temperatures in the 1980's and more constant values for the first half of the 1990's. The range in seasonal air-sea temperature differences is about constant from 1980 to 1988 when it starts to decrease, being about 2 deg C less from that point through 1994.

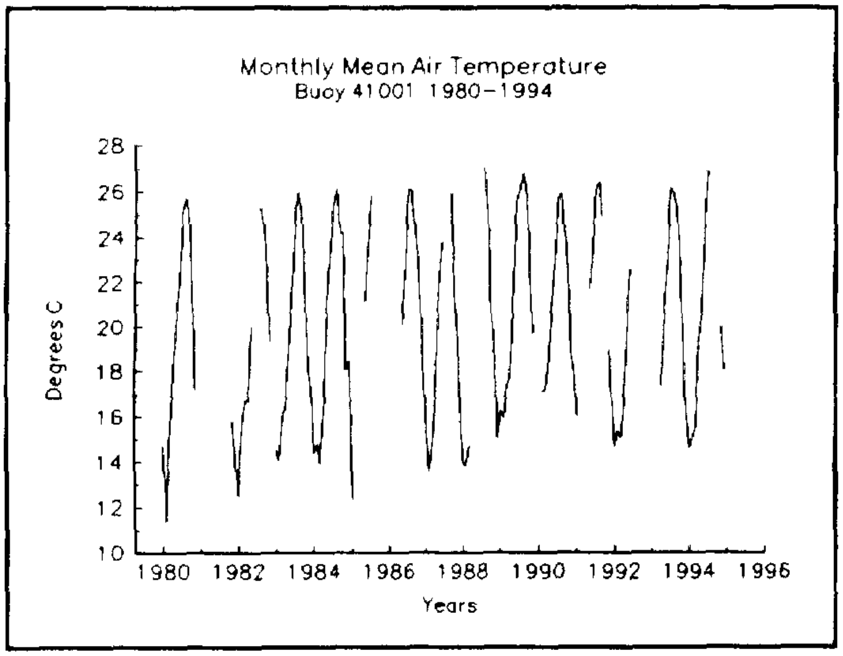

Figure 10. Mean Monthly Air Temperature at 41001 for 1980-1994

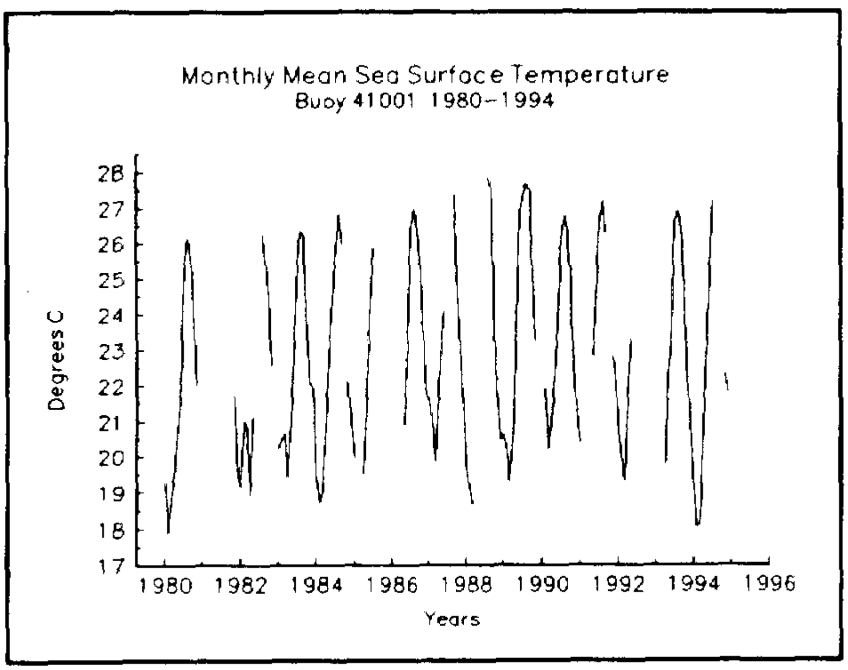

Figure 11. Mean Monthly Sea Surface Temperature at Buoy 41001 for 1980-1994

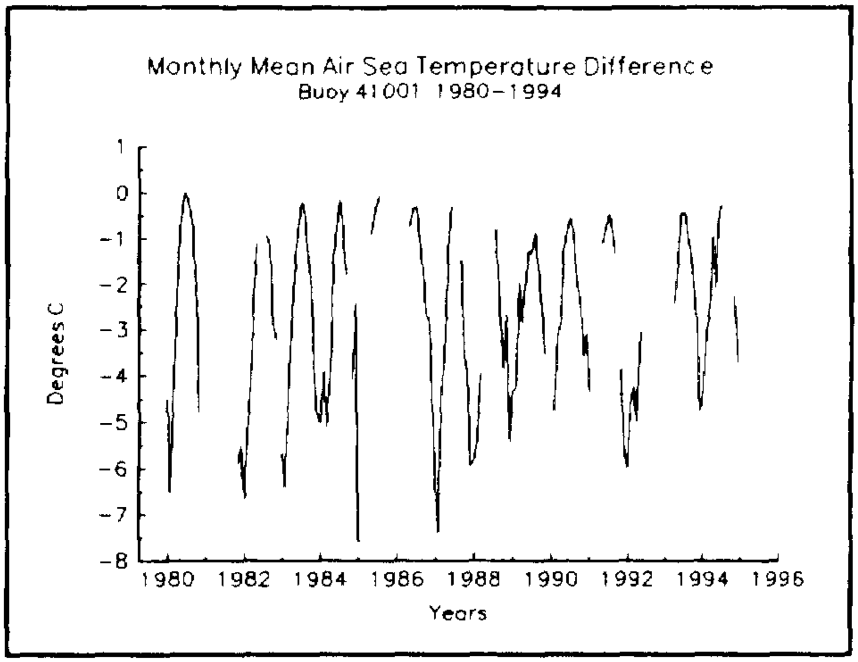

Figure 12. Mean Monthly Air Sea Temperature Difference at Buoy 41001 for 1980-1994

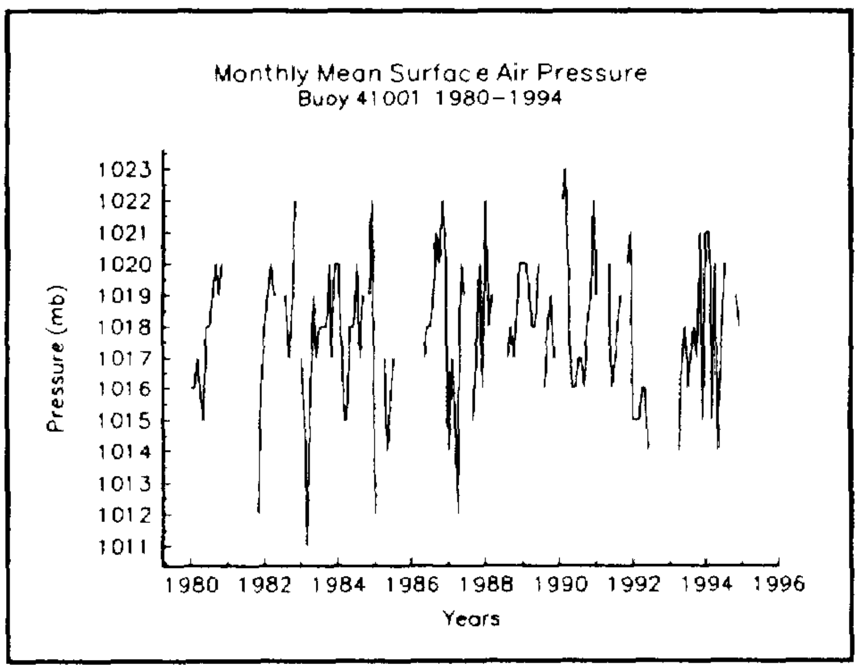

Figure 13. Mean Monthly Surface Air Pressure at Buoy 41001 for 1980-1994

The variation of surface atmospheric pressure is shown in Figure 13 . The range in seasonal variation of surface atmospheric pressure is larger in 1980 to 1988 than from that point through 1994. This is consistent with less wind and wave energy at this site, as shown in Figure 5 , where values are closer to the long-term mean from the late 1980's to 1994.

5. SUMMARY

Monthly mean values of wind speed and wave height derived from a combination of measured and hindcast values at five locations spread along the U.S. East Coast were examined to determine their variability over the 15-year period from 1980 to 1994. No long-term trends of increasing or decreasing wind speeds

or wave heights were apparent at any of the sites. The seasonal variation, especially in the winter months, did depart from the long-term mean as a function of year and location.

Storm wind speeds and wave heights, as determined by thresholds, did not show any trends in time but did indicate fewer storm conditions south of about 33 deg N.

Monthly means of air and sea temperature at the location off the coast of North Carolina (Buoy 41001) indicate an increasing trend in the 1980's which levels off in the 1990's. Seasonal variations in air-sea temperature difference and surface atmospheric pressure indicate a more energetic period from 1980 to about 1988 when variations become smaller. This is consistent with higher/lower wind speeds and wave energy at this location for these periods.

6. ACKNOWLEDGEMENTS

This work was carried out under the Coastal Field Data Collection Program, Coastal Engineering Functional Area of Civil Works Research and Development. The author acknowledges the Office of the Chief of Engineers, U.S. Army Corps of Engineers, for authorizing publication of this paper. I wish to thank Ms. Heather Samaitis and Mr. Chris Babin for assisting in analysis of the data and preparation of the figures and Ms. Dee Hubertz for preparing the manuscript in the required format.

7. REFERENCES

Brooks, R.M. and W.A. Brandon, 1995: Hindcast Wave Information for the U.S. Atlantic Coast: Update 1976-1993 with Hurricanes. WIS Report 33, U.S. Army Engineer Waterways Experiment Station, Vicksburg, MS 39180-6199.

Cardone, V.J., A.T. Cox, J.A. Greenwood, and E.T. Thompson, 1994: Upgrade of Tropical Cyclone Surface Wind Field Model. CERC MP 94-14, U.S. Army Engineer Waterways Experiment Station, Vicksburg, MS 39180-6199.

Carter, D.J.T. and L. Draper, 1988: Has the North-East Atlantic Become Rougher? Nature, 332, 494.

Gilhousen, D.B., E.A. Meindl, M.J. Changery, P.L. Franks, M.G. Burgin, and D.A McKittrick, 1990: Climatic Summaries for NDBC Buoys and Stations Update 1. National Weather Service, National Data Buoy Center, NSTL, MS 39529.

LINK BETWEEN NORTH ATLANTIC CLIMATE VARIABILITY OF SURFACE WAVE HEIGHT AND SEA LEVEL PRESSURE

Y. Kushnir[1], V.J. Cardone[2], J.G. Greenwood[2], and M.A. Cane[1]

[1]Lamont-Doberty Earth Observatory, Palisades, NY

and

[2]Oceanweather Inc., Cos Cob, CT

1. INTRODUCTION

With increased interest in climate variability the issue of changes in storminess, in particular over the oceans, has been raised. Carter and Draper (1988) and Bacon and Carter (1991) presented convincing evidence for a positive trend in surface wave heights at various North Atlantic sites, between the early 1960s and the late 1980s. Of particular interest is the long record of wave height measurements at the Seven Stones Light Vessel (SSLV) located off the southwestern tip of England. Significant wave heights appear to have increased there by an average rate of 2% per year between 1962 and 1986. A similar trend is displayed at Ocean Weather Station Lima (LIMA; 57°N, 20°W), between 1975 and 1988. The positive trend in these records occurs mainly in the months of December, January, and February. If real, these trends in wave heights should be related to changes in storminess over the North Atlantic basin, and may reflect significant changes in the intensity of individual storms. The consequences to marine activities should be studied, and the possibility of continued increase in storminess evaluated. It is important therefore that we try to substantiate the wave height observations by examining other climatic data directly associated with the sea state, such as winds or pressure.

So far it was not clearly demonstrated that the trend in wave heights is related to other climatic changes in the North Atlantic. However, Kushnir (1994) noted a large-scale, interdecadal sea level pressure (SLP) fluctuation in the North Atlantic. During the 1970s and early 1980s the pressure gradient between about 50°N and 60°N was stronger than during the 1950s and early 1960s. This variability is consistent with the strengthening of the westerlies in this latitude belt that could have lead to the trend in wave heights. Kushnir linked the SLP change to the basin wide cooling of North Atlantic sea surface temperature (SST). If the link between surface wave heights and SLP, on interannual and interdecadal time scales, can be more clearly demonstrated, one can substantiate and explain the surface wave observation, and help understand the change in storminess in the context of hemispheric and global climate variability.

The goal of our study is to hindcast the surface wave field from meteorological data, and compare the results with the observed wave data. Since the meteorological data are independent from the observed wave data, the hindcast can be used to verify the findings of the observational studies described above. Because of the non-local nature of the surface wave field, we need data from the entire North Atlantic to hindcast the two decades of wave observations al SSLV and LIMA. The ideal situation would be to use a basin-wide analysis of observed surface winds, sampled several times per day, for a time interval equivalent to the length of the observed wave records. Such data are however not readily available. The approach taken in this study is to combine a numerical wave hindcast based on a decade of detailed wind analysis with a statistical hindcast based on the sea level pressure - wave relationship found from the numerical hindcast, thus extending the hindcast further into the past to the early 1960s.

Section 2 below describes the numerical hindcast. Section 3 explains the statistical hindcast and its results, and is followed by the conclusions.

2. NUMERICAL WAVE HINDCAST

The numerical daily significant wave height (HS) hindcast from observed wind information was derived using a highly developed and widely applied first-generation discrete spectral model known as ODGP. This model has been found to be skilful in the specification of integrated properties of the wave spectrum, such as HS, as more recently proposed second and third-generation models (Khandekar et al., 1994). Vector winds from the 1980-1989, 12-hourly, 1000 hPa ECMWF analysis, were used to force the wave model. The hindcast was performed on a 2.5 by 2.5 degree, latitude-longitude grid covering the entire North Atlantic from the equator to 70°N. The ECMWF 1000 hPa winds are not necessarily representative of the surface winds at a reference height (10 or 20 m) required to drive the ocean response model. Therefore the 12-hourly winds were compared to reported synoptic winds at weather stations LIMA and MIKE for all available reports between 1983 and 1989. Systematic differences were expressed as the mean ratio of 1000 hPa wind speed to weather ship wind speed, and mean difference of 1000 hPa wind direction to weather ship wind direction, in regular bins of 1000 hPa speed and direction. These means were then applied to adjust the 12-hourly 1000 hPa winds at all grid points. At LIMA (MIKE) the mean ship/gridpoint adjusted wind speed difference over 3535 (3856) comparisons is -0.04 m Sec-1 (-.39 m Sec-1) and the rms error is 3.41 (2.77) m Sec-1. These differences can be attributed to systematic differences between reporting vessels in such parameters as ship structure, anemometer height and location, and instrument calibration. The adjusted 12-hourly wind fields were interpolated in time to obtain a 3-hourly time series used to force the wave model.

The 3-hourly numerical wave hindcast provides a 10-year time series of wave spectra and integrated properties at each grid point, between 1 January 1980, and 31 December 1989. The time series of mean monthly HS at the grid points nearest LIMA and SSLV are in excellent agreement with the monthly means derived from measurements tabulated in Bacon and Carter (1991). The year-around correlation between monthly averaged hindcast and observed HS is 0.91 at LIMA and 0.95 at SSLV, with better agreement in winter than in summer.

3. MONTHLY SLP AND HS VARIABILITY

To extend the wave hindcast back to the early 1960s we sought to find the link between HS and a meteorological variable for which data from this time period are available. Such variable is SLP, linked to 1000 hPa height by a simple conversion (to a reasonable accuracy 8 geopotential height meters correspond to a pressure change of 1 mb at the sea level). We first established the statistical relationship between monthly averaged ECMWF 1000 hPa height fields, and monthly averaged hindcast HS fields using a canonical correlation analysis (CCA, Barnett and Preisendorfer 1987; Bretherton et al., 1992). Since the trend in annual mean wave height reported in Bacon and Carter (1991) was largely due to changes in winter, we used 1000 hPa heights and HS data for the cold-season months (November-March) only. A CCA analysis resolves pairs of patterns that describe the covariability of two samples. In the present analysis two pairs of such patterns were found to dominate the covariability of the 1000 hPa height and HS fields. The first pair of patterns (Fig. 1) explains 38% of the 1000 hPa height variance and 37% of the HS variance, with a correlation coefficient of 0.97 between the corresponding time series. The second pair of patterns (Fig. 2) captures 12% of the geopotential height variance and 27% of the HS variance and the temporal correlation coefficient is 0.83. Thus there exists a coherent relationship between monthly perturbations in 1000 hPa heights and HS. One such relationship (Fig. 1) is in the form of a geopotential height dipole resembling the North Atlantic Oscillation (NAO, e.g., Lamb and Peppler, 1987) and a corresponding wave height dipole between the ocean area northwest of the British Isles and the middle of the subtropical North Atlantic. A weaker than normal geopotential height gradient along 50-60°N (hence weaker than normal westerlies there) generally corresponds to stronger then normal gradient along 25-35°N (hence a westerly wind anomaly). Other studies show that these changes in monthly mean conditions also imply changes in the path and intensity of individual synoptic disturbances in the sense that areas of strong monthly westerlies experience more frequent passes of storms

(Lau, 1988; Rogers, 1990). This relationship is found in our analysis to bring along a reduction in wave heights in the eastern North Atlantic and an increase in wave heights in the middle subtropical North Atlantic. The second relationship between 1000 hPa height and HS (Fig. 2) is between a pattern reminiscent of the eastern Atlantic teleconnection pattern (Wallace and Gutzler, 1981), and wave heights in the southeastern North Atlantic.

Normalized time series describing the evolution of the two CCA modes of 1000 hPa height, for the period of HS record at SSLV, were reconstructed from historical monthly mean SLP data. These SLP data were taken from the COADS, summaries of ship observations (Woodruff et al., 1987). The normalized SLP difference between the centers of action in Fig la (65°N 15°W and 40°N 35°W) was used as a proxy for the temporal evolution of the first CCA pattern, and the normalized SLP at the single center of Fig. 2a (50°N 25°W) as proxy for the second pattern. The wintertime average of the first sea level pressure index (Fig. 3) displays a negative trend between 1950 and 1992, consistent with the findings of Kushnir (1994) and Hurrell (1995). This trend in sea level pressure implies the deepening of the Icelandic low and intensification of the Azores high between the early 1960s and the present. The SLP index corresponding to the second CCA pattern displays no consistent trend over the period of interest. Using the two SLP indices and the relationship implied derived from the CCA analysis we calculated the winter months' anomalies of HS between 1962 and 1986 (the period of wave observations at SSLV). At SSLV the correlation coefficient between the statistical hindcast HS and the observed values is 0.72.

The trend in winter average HS due to the interdecadal trend in North Atlantic SLP, as calculated from the statistical wave hindcast, is shown in Fig. 4a for the entire ocean basin. A positive HS trend of up to 0.3 m/decade is found north of 40°N, and a negative trend of up to 0.2 m/decade is found to the south of that latitude circle. At SSLV itself (Fig. 4b) our wintertime hindcast displays a 0.185 m/decade trend compared to the observed trend of 0.255 m/decade calculated from the data in Bacon and Carter (1991). Since the statistical hindcast explains only part of the of the observed variability, a difference between the observed and hindcast data is expected.

4. CONCLUSIONS

A combination of a numerical significant wave height hindcast based on twice daily wind analysis from observations, and a CCA analysis of the corresponding geopotential height data, enabled us to determine the relationship between wave height and SLP since the early 1960s. These SLP data confirm the existence of a trend in wave heights (and storminess) in the eastern North Atlantic. The basin-wide character of the wave height trend is uncovered by the analysis. The trend is found to be linked to changes in SLP consistent with those documented in Kushnir (1994) and Hurrell (1995). The reasons for these climatic changes are not revealed by the present analysis. The SLP indices in Kushnir (1994) and Hurrell (1995) indicate that trends of the opposite sense occurred in the past. Thus the more recent fluctuation may be part of a multidecadal signal, linked to a long term interaction between the Atlantic Ocean and the atmosphere.

REFERENCES

Bacon, S. and D. J. Carter, 1991: Wave climate changes in the North Atlantic and North Sea. Int. J. Climatol., **11**, 545-558.
Barnett, T. P. and R. W. Preisendorfer, 1987: Origin and levels of monthly and seasonal forecast skill for United States surface air temperatures determined by canonical correlation analysis. Mon. Wea. Rev., **115**, 1825-1850.
Bretherton, C. S., C. Smith and J. M. Wallace, 1992: An intercomparison of methods for finding coupled patterns in climate data. J. Climate, **5**, 541-560.
Carter, D. J. T. and L. Draper, 1988: Has the northeast Atlantic become rougher? Nature, **332**, 494.
Hurrell, J. W., 1995: Decadal trends in the North Atlantic Oscillation: Regional temperatures and precipitation. Science, **269**, 676-679.
Khandekar, M. L., R. Lalbeharry and V. J. Cardone, 1994: The performance of the Canadian ocean wave model (CSOWM) during the Grand Banks ERS-1 SAR Wave Spectra Validation Experiment. Atmos.-Ocean, **32**, 31-60.
Kushnir, Y., 1994: Interdecadal variations in North Atlantic seasurface temperature and associated atmospheric conditions. J. Climate, **7**, 141-157.
Lamb, P. J. and R. A. Peppler, 1987: North Atlantic oscillation: Concept and an application. Bull. Amer. Meteor. Soc., **68**, 1218-1225.
Lau, N. C., 1988: Variability of observed midlatitude storm tracks in relation to low-frequency changes in the circulation pattern. J. Atmos. Sci., **45**, 2718-2743.
Rogers, J. C., 1990: Patterns of low-frequency monthly sea level pressure variability (18991986) and associated wave cyclone frequencies. J Climate, **3**, 1364-1379.
Wallace, J. M. and D. S. Gutzler, 1981: Teleconnections, in the geopotential height field during the Northern Hemisphere winter. Mon. Wea. Rev., **109**, 784-812.

Woodruff, S. D., R. J. Slutz, R. L. Jenne and P. M. Steurer, 1987: A comprehensive ocean-atmosphere data set. Bull. Amer. Meteor. Soc., **68**, 521-527.

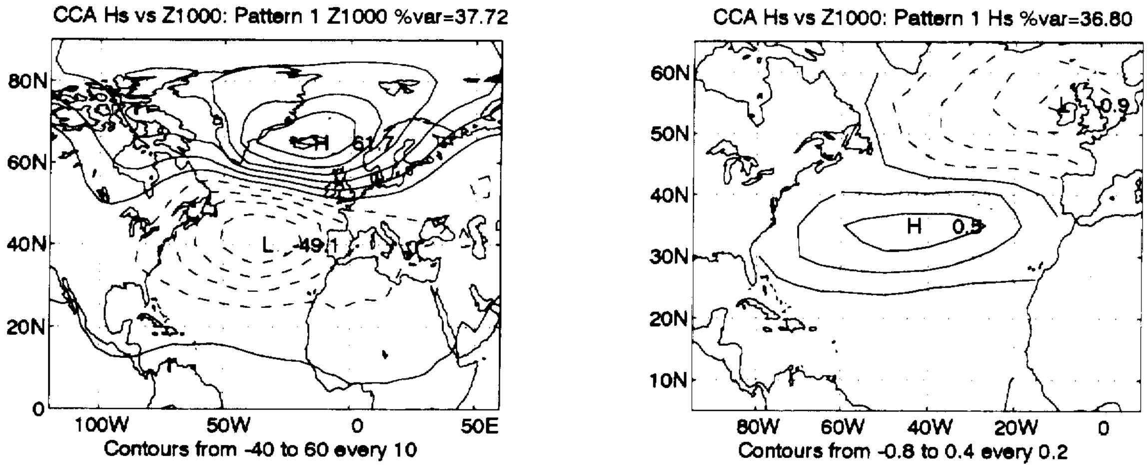

Figure 1: The leading mode of a CCA analysis between wintertime (Oct.-Mar.) monthly mean 1000 mb height and significant wave height (HS) in the North Atlantic Ocean, for the period Nov.-Mar. 1980-1989. Left panels (a) displays the pattern of 1000 mb heights (in m) and right panel (b) is the pattern of HS (in m). Negative contours are shaded.

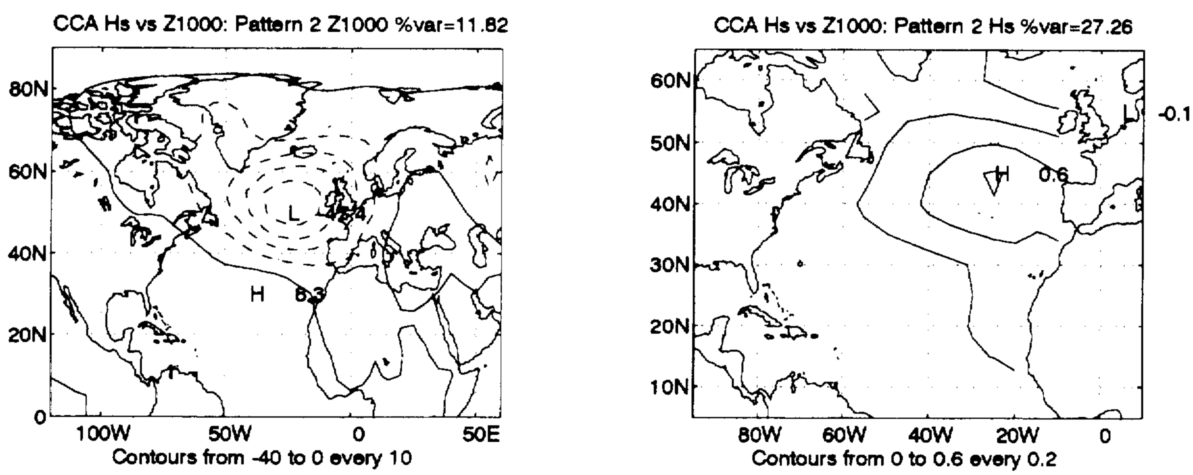

Figure 2: The second mode of a CCA analysis between wintertime (Oct.-Mar.) monthly mean 1000 mb height and significant wave height (HS) in the North Atlantic Ocean, for the period Nov.-Mar. 1980-1989. Left panels (a) displays the pattern of 1000 mb heights (in m) and right panel (b) is the pattern of HS (in m). Negative contours are shaded.

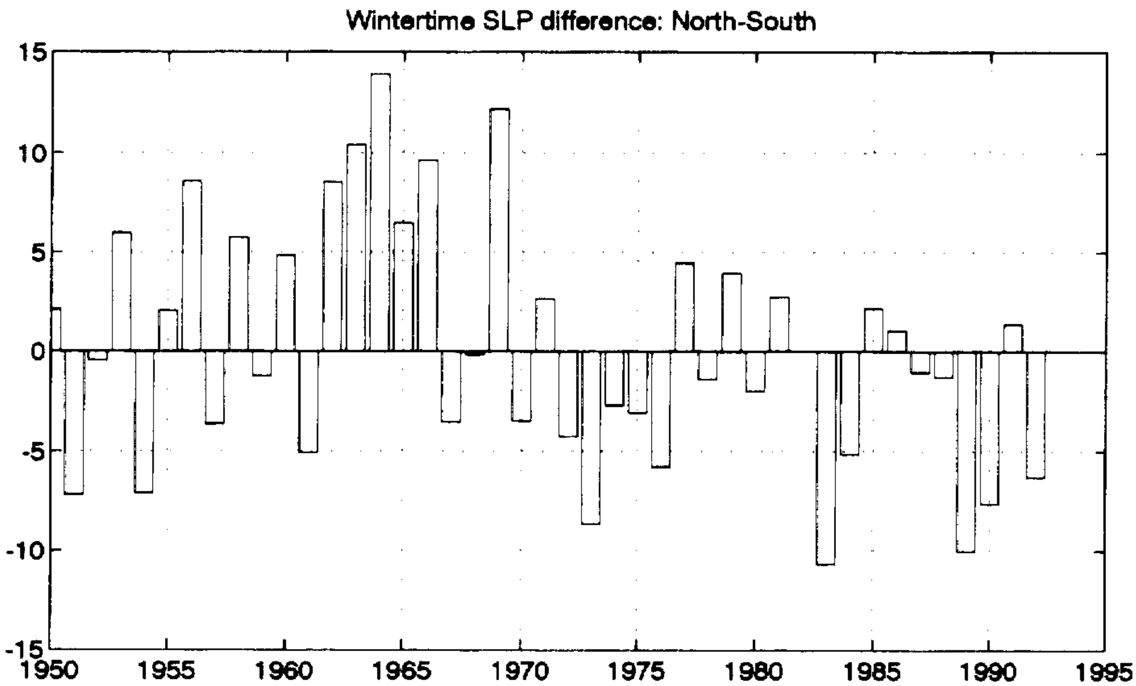

Figure 3: The wintertime time series of sea level pressure difference (in mb) between the ocean areas near Iceland and near the Azores.

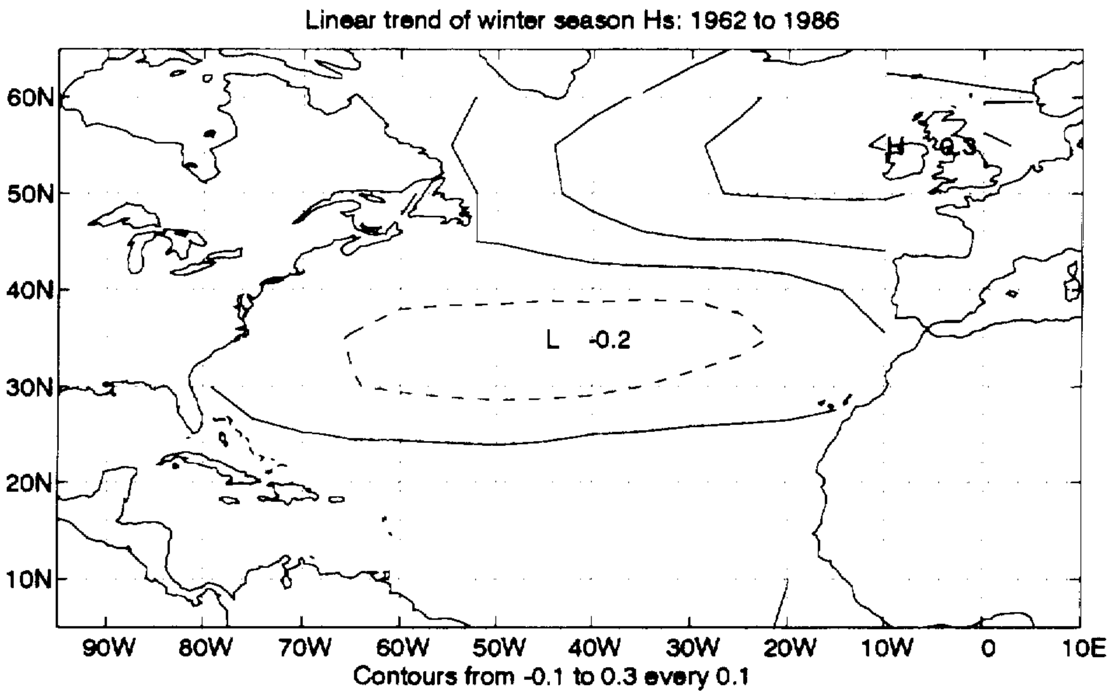

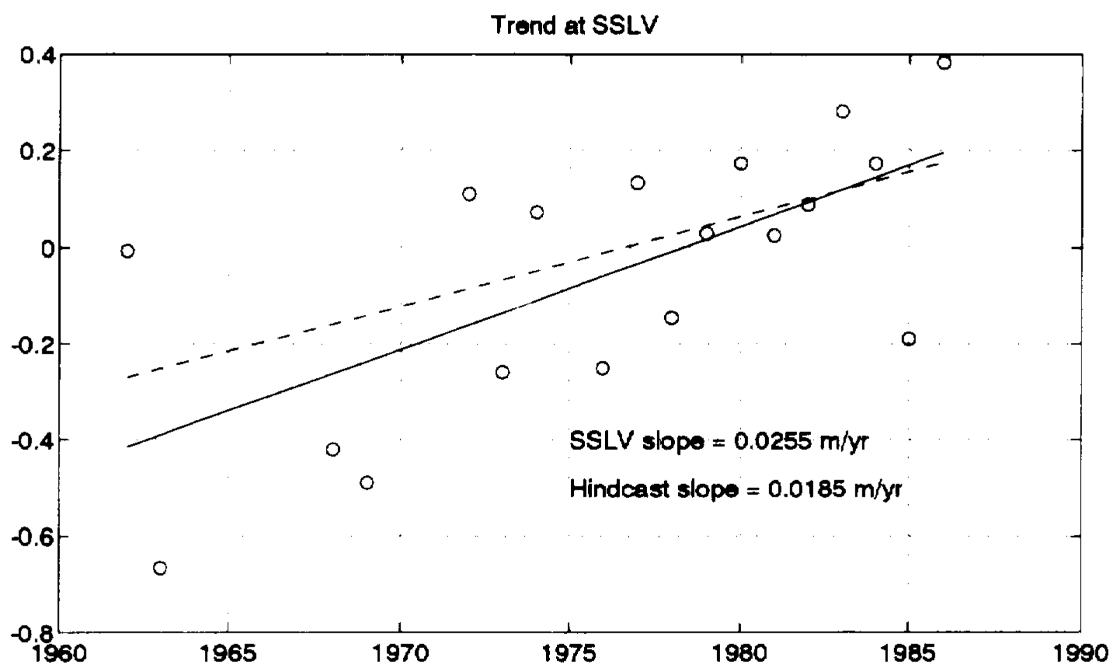

Figure 4: Upper panel (a): The projected trend of significant wave height (HS) between 1962 and 1986 based on the combined dynamical hindcast and CCA projection, in m/decade. Lower panel (b): Observed seasonal (Nov.-Mar. average) wave heights (m) at SSLV (data from Bacon and Carter, 1991). A comparison of the linear trend fitted to the observations (solid line) and the hindcast trend (dashed) in HS is also shown.

A STUDY OF RELATIONSHIPS BETWEEN LARGE-SCALE CIRCULATION AND EXTREME STORMS IN THE NORTH ATLANTIC OCEAN

Donald T. Resio

U.S. Army Waterways Experiment Station
Vicksburg, Mississippi

Val R. Swail

Environment Canada
Downsview, Ontario

Rita L. Atkins

Florida Institute of Technology
Melbourne, Florida

1. INTRODUCTION

In the 1980's, the spectre of global warming created a renewed interest in climate research. At that time, a direct link between increases in atmospheric carbon dioxide (CO_2) and mean global temperature was hypothesized. Furthermore, extensive measurements such as the data set from Mauna Loa Observatory in Hawaii indicated that CO^2 was increasing at a rate such that global temperatures would rise by 3° or more by the middle of the next century. Implicit in this theory was the premise that a single dominant factor, CO_2 levels in the atmosphere, controlled global climate and that climatic variations tended to follow large secular patterns in time. Although little or no empirical evidence existed to support a strong link between global temperatures and CO^2 levels, mathematical simulations using a variety of climate models (Schlesinger and Mitchell, 1987; Hansen et al., 1988; and Bryan et al., 1988) suggested that such a link was plausible.

In the early 1990's it began to be evident that the large secular trends in temperature predicted in the 1980's were not occurring, at least not in the simple fashion originally, envisioned. Instead of continuous global warming, a lowering of mean global temperatures occurred approximately from 1990 through 1993. Part of this could have been explained via the volcanic eruption of Mt. Pinatubo; however, given the predicted magnitude of the effects of increased CO^2, the concept of a pronounced climate change dominated by long-term variations in CO^2 seemed to be vastly overstated.

Today, there remains considerable debate concerning the fundamental nature of climatic variability. On one hand, the concept of large secular variability does not seem consistent with recent observations. On the other hand, the idea that climatic variability occurs on such a slow time scale that it is of little practical concern appears equally unfounded. Thus, we are now in the midst of studies which are attempting to establish a new paradigm for interpreting and understanding observed variations in global circulation. In this new paradigm, we must reconcile the apparent observed importance of climatic variations within this century with the lack of a strong, secular signal in contemporary measurements.

One tool for exploring complex climatic interrelationships is termed "downscaling." Downscaling attempts to establish links among climatic-scale variability and synoptic-scale phenomena. The present study represents an initial effort to examine possible coupling between long-term measures of atmospheric circulation and extreme extratropical storms in the region of the North AtlantiC between latitudes 30° and 55° North, longitudes 45° and 75° East. As discussed by Resio (1978) such a coupling could play an important role in the accurate estimation of extreme wave conditions of the type used in designs of offshore structures. Given that recent storms such as the Halloween Storm and the Storm of the Century (Cardone et al., 1995) have far exceeded design wave conditions established in western Atlantic areas, this, in turn, could have an important bearing or future offshore developments in Canadian and U.S. offshore areas.

2. THE DATA SETS

Two fundamental data sets, covering the period from 1899 to the present, are used in this study for examining climatic-scale variations. These are 1) digital pressure fields and 2) synoptic weather charts. Each of these data sets will be described below, along with various data processing and analytical operations used to convert these data into appropriate forms for analysis in this study.

2.1 Northern Hemisphere Pressure Fields (1899 present)

At the time of this study, daily pressure fields were available from the U.S. National Center for Atmospheric Research (NCAR) for the interval January 1, 1899 through the end of November 1993. Although the nominal spatial coverage of the pressure data is from 80° South latitude to 80° North latitude for all longitudes on a 5° spacing, the actual geographic coverage of valid data varies considerably through time. Since this project is focused on extreme waves in the Atlantic Ocean near the coast of Canada, a subset of data covering 20° N to 70° N and from 0° E to 180° E was selected to minimize situations with extensive missing data. Such situations would have been very difficult to accommodate within the framework of subsequent analyses and, potentially, could have biased the final results.

Weather maps used as the basis for the digital pressure fields contain information on synoptic-scale features. Since we are seeking here more of a large-scale circulation index, incremental five-day averages were formed from the daily values. There are 72 such increments in a typical year and 72 increments and one extra day in leap years. In order to not have a sequence of 5-day intervals that varied from year to year, February 29 was always included with the 5-day interval containing February 28 on leap years.

2.2 Synoptic Weather Charts

For this study, data were collected by hand measurements from projected microfilm charts. Measurements were taken for each day that an intense storm existed within the study area. Although there may have been some subjectivity in the cutoff used to decide whether or not to include a particular storm, a very large number of storms were sampled in this study. Consequently, it is likely that all very intense storms are included within the final sample. After January 1 1955, six-hourly charts became available. Measurements were taken every twelve hours for intense storms on these charts. In this study, information on 368 intense storms was taken by hand measurements from weather maps. This information included the following parameters:

1. location of storm center,
2. central pressure
3. peripheral pressure
4. storm shape; and
5. storm pressure profiles.

An investigation of storm track characteristics over various intervals of time indicated that significant variations occurred both in terms of areas of cyclogenesis and in storm track locations and orientations. Figure 1 shows storm tracks for the time intervals 1963-1966 and 1973-1985. Storms in the interval 1963 through 1966 tended to form quite far to the south off the U.S. east coast and move essentially shore parallel up the coast past Nova Scotia. Storms in the 1973-1985 interval tended to form farther to the north and farther offshore and moved more zonally away from the coast. Visual examination of these storm track patterns suggests that storm waves generated in different coastal areas in the U.S. and Canada should be very different in these two time intervals in response to these shifting storm track patterns.

Table 1 gives the frequency of storms per decade from the extreme storm sample. It is fairly evident in this table that the number of large storms per decade varies substantially over time. Some of the variability in these numbers may be due to the selection procedure used in this study and some might be due to the lack of resolution on the earlier weather charts; however, since we restricted our study to only large storms, it is unlikely that storms such as these would have been missed in the original analyses. Consequently, we feel that most of the variations contained in Table 1 represent actual variations in the number of severe storms per decade. It should be noted here that even though the frequency of large storms varies substantially, it is not necessarily true that this variation will directly affect the predicted extremes. For example, if fewer storms occur, but the intensities of these storms are more variable, it is possible that larger extrapolated extremes would be associated with the time intervals of fewer storms.

2.3 Potential Limitations in Data Sets

One problem with the data that should be pointed out at this point is the lack of temporal and spatial resolution in the pressure fields in the pre- 1955 data.

Plotted profiles indicated that many of the storm profiles have a flat section near their centers in this earlier time period; whereas, in the period after 1955 essentially all storms have a relatively well-defined minimum at their center. This suggests that the actual lowest pressures were not properly resolved on the weather maps before 1955. This difference, along with the difference in temporal resolution in the two time periods (24 hours vs. 12 hours), could have some bearing on the hindcast wave heights, but it is difficult to modify the pressure profiles objectively. Consequently, the data were retained as taken from the maps. Possibly a subsequent study could investigate alternative methods of specifying the pressures near the centers of these storms.

3. PRESSURE-FIELD ANALYSES

3.1 Description of EOF Methodology

Let us define a discretized scalar field to be represented by a set of n elements (in our analyses, n different pressure grid points), each with m samples taken through time. At each specific observation time, our data can be viewed as an n-dimensional random vector, $\underline{S}$. From m samples of these random vectors, we can construct a covariance matrix with elements, A_{ij} given by

$$A_{ij} = \frac{1}{m} \sum_{k=1}^{m} s_{ik} s_{jk} - \mu_i \mu_j \tag{1}$$

where s_{ik} and s_{jk} represent the k^{th} value at the i^{th} location and the k^{th} value at the j^{th} location, respectively, and μ_i, and μ_j are the means of the i^{th} and j^{th} variables, respectively.

The fundamental algebra of the eigenfunction problem is the solution of a set of values, $\lambda_1, \lambda_2, \ldots, \lambda_n$, for the set of homogeneous linear equations in n unknowns

$$\underline{Ax} = \underline{\lambda x} \tag{2}$$

where $\underline{A}$ is any matrix (the covariance matrix or correlation matrix for our purposes here), $\underline{x}$ is a set of orthogonal column vectors (x_1, x_2, ..., x_n) and $\underline{\lambda}$ is a diagonal matrix.

Rewriting equation 2 yields

$$\underline{A}-\underline{\lambda I})\underline{x} = 0 \tag{3}$$

where $\underline{I}$ is the identity matrix, which has a nontrivial solution if, and only if, the determinant is singular, that is

$$|\,\underline{A}-\underline{\lambda I}\,| = 0 \tag{4}$$

Equation 3 is invariant with respect to multiplication of both sides by a scalar constant. To remove this ambiguity, the eigenvectors are constrained by the relationship

$$|\,\underline{E}_p\,| = 1 \tag{5}$$

which means that the sum of the squares of all of the components of the vector must equal 1.

From the above description, we see that the EOF methodology represents a transform from a coordinate system of n mutually dependent variables into a coordinate system of n mutually independent variables (eigenfunctions). If we hypothesize that a natural system always contains a mixture of deterministic and random influences, the ordered eigenfunctions represent a set of optimal linear estimators of the structure of the covariance among all of the stations. It is then intuitive to select a subset of the first few eigenfunctions and consider them as possible deterministic descriptors of the spatial field of motions. The remaining unexplained variance can be treated as a random residual.

To accomplish this separation of deterministic and random field elements, we first form inner products between each n-dimensional eigenfunction and each n-dimensional random vector containing the observations for a particular time, i.e.

$$W_{ip} = \langle E_{kp} S_{ik} \rangle \tag{6}$$

where the subscript "i" denotes the observation time, the subscript "k" denotes the observation location (or station), and the subscript "p" denotes the eigenfunction number. This defines a sequence of weightings (a measure of similarity) on each eigenfunction. Since the eigenfunctions have been ordered via their eigenvalues, we can choose to form these weightings for only a subset of all of the eigenfunctions, say, sufficient to explain some desired percentage of the total variance i.e.

$$S'_{ik} = \mu_k + \sum_{1}^{n'} W_{ip} E_{kp} \tag{7}$$

where μ_k, is the mean value of the observations at station k, n' is an integer less than n and S'_{ik} is the $(i\text{-}k)^{th}$ element of the partial sum (restricted to only n' eigenfunctions). The form of equation 7 emphasizes the fact that the origin of the eigenfunction coordinate system is at the mean value of all variates, not at zero (ie. for our study the mean pressure fields must be added to the vector sum in equation 7).

3.2 Results of EOF Analysis

Figure 2 shows the mean pressure field for the entire period from January 1, 1899 through November 1993. As can be seen there, the dominant mean circulation features appear to be low pressure centers near the southern tip of Greenland and along the Aleutians, along with high pressure areas centered in the Atlantic and Pacific Oceans at about 30° N.

Table 2 gives the percent of the total variance contained in each eigenfunction axis. As can be seen there, the first five eigenfunctions contain over 88 percent of the total variance; consequently, these functions will be treated in detail, while the remaining eigenfunctions will be neglected in subsequent analyses. The purpose of this reduction is only to simplify subsequent analyses and discussions. Identical procedures based on a larger number of eigenfunctions could be adopted in later studies if this appeared fruitful.

Figure 3a shows that the first eigenfunction represents a pattern of pressures in the Atlantic and Pacific Oceans that co-oscillate in the same sense (i.e. when one is higher than the mean the other will also be higher than the mean and when one is lower than the mean the other will also be lower than the mean). The center of the Atlantic system is at about 65°N; and the center of the Pacific system is at about 50°N. The fact that the Atlantic center has larger values than the Pacific center indicates that the Atlantic Ocean has more variance represented in this eigenfunction. When circulation patterns are weighted positively on this eigenfunction, pressures will tend to be higher than average near these centers of action. When circulation patterns are weighted negatively on this eigenfunction, pressures will tend to be lower than average in these areas. Figure 3b shows a pattern with two major centers (again co-oscillating); however, in contrast to eigenfunction 1, the location of these centers is shifted southward to about 48°N in the Atlantic and 40°N in the Pacific. When the circulation is weighted negatively, on this eigenfunction, a large trough of low pressure exists along the middle of the North American continent; and the pressures are higher than average in the mid-latitudes in the Atlantic and Pacific Oceans. When the circulation is weighted positively, pressures will tend to be lower in the middle part of the continent, and pressures will tend to be higher in the oceanic areas. It appears that a negative weighting on this pattern seems to be indicative of a meridional flow rather than a zonal flow. Figure 3c shows a pattern with oppositely oscillating regions in the Atlantic and Pacific. When the circulation is positively weighted on this eigenfunction, the Aleutian low is stronger than average and the Icelandic low is weaker. When the circulation Is negatively weighted on this eigenfunction, the Aleutian low is weaker and the Icelandic low is stronger than the mean. Figure 3d also shows a pattern with oppositely oscillating regions in the Atlantic and Pacific Oceans; however, in this case, the systems are shifted farther south. Figure 3e shows a pattern with a very strong signature over northern Europe and an elongated trough/ridge running northwest to southeast from northern Canada through the Atlantic Ocean.

When unsmoothed weightings on eigenfunctions 1-5 were plotted it became apparent that the resulting time series contained large seasonal components within them. This high-frequency variability made it difficult to recognize any long-term characteristics in these time series. In order to emphasize the longer-term characteristics, a running 73-increment average was used to filter the eigenfunction weightings. Figure 4 shows that this smoothing results in a time series that retains a great deal of information for short time intervals yet still shows a signal that is rich in terms of multi-year variability. Since we are interested here in climatic-scale variability more than in large-scale variability, the smoothed weightings will be used in all subsequent analyses.

In Figure 4 , we see that variations in the eigenfunction weightings contain some very abrupt transitions along with quasi-cyclical departures from the means that can persist for several years. There also appear to be intervals in which the weightings on different eigenfunctions are relatively in phase with each other (for example, weightings on eigenfunctions 2 and 3 up to about 1915) and periods in which the eigenfunctions are completely out of phase (for example, weightings on eigenfunctions 2 and 3 in the early 1940’s). Since the eigenfunctions are constrained to be uncorrelated, this is not surprising; however, this behavior strongly suggests that climate Variability is not well described by a simple scalar function, such as mean global temperature.

Of all of the series shown in Figure 4 , only weightings on eigenfunction 1 appear to contain a very long-term scale of variability. Weightings on this eigenfunction rise from a minimum value around 1925 to a maximum value around 1970 and then fall from 1970 to the end of the record in 1993. This indicates that the mean pressures over this period varied in a fashion such that annual mean pressures in the centers of the low pressure systems at northern latitudes increased by about 6 millibars from 1925 to 1970 (from about 1003 mb to 1009 mb) and have since been intensifying back to about the 1920’s values (to about 1004 mb by the end of 1993). This finding is quite interesting, since analyses of northern hemisphere mean temperatures indicate a maximum value around the late 1930’s followed by a small minimum in the 1960’s and another maximum in the 1980’s. Hence, the pressure fields analyzed here do not seem to contain the same signal as found in mean temperatures.

4. A SIMPLE WAVE MODEL DRIVEN BY STORM PARAMETERS

4.1 Description of the Model

Storm size, intensity, and track are all known to affect wave generation during the passage of an extratropical storm. Unlike the case for tropical storms, however, extratropical wind fields cannot in general be accurately determined by a small number of parameters. Thus, hindcasts driven by such a set of parameters should be regarded as providing a measure of wave generation potential and should probably not be regarded as providing actual wave values for these storms. In this study, it is assumed that a simple duration-limited prediction method will suffice to estimate wave-generation potential. This should be reasonable since most waves in oceanic areas are duration-limited rather than fetch-limited.

The simple model used here consists of two components, a wind estimator and a wave estimator. The wind estimator used a simple geostrophic estimate of wind speed, driven by the total pressure difference across the storm modified by some shape functions. This wind speed is reduced to sea level via a simple constant of proportionality (0.53) and limited to no more than (33 m/sec) to reduce the impact of individual extreme gradients on the predicted wave field. This would be particularly catastrophic in the pre-1955 data in which the storms are sampled only once per day. The wave height estimator is a simple algorithm which is equivalent to the duration-growth in 2nd generation wave model.

4.2 Application of the Model to the Synoptic Data Set

The simple wave prediction model was exercised for all storms in our data set. A single maximum value was retained for each storm from these hindcasts; and the recorded maximum values from the Halloween Storm and the Storm of the Century were added to this data set. The largest predicted wave heights are in the 16 to 17 meter range, which is roughly consistent with expected values for very large storms, but is possibly a bit high, given the number of storms that attain this magnitude in our data series. The wind-wave model could be tuned to reduce all of the values; but since the values are only used here as a i indicator of relative wave conditions, and not as an actual hindcast value, this was not done for this study.

Table 3 gives the distributions of the wave height as a function of month and three-metre wave height categories. As expected, a very strong seasonal pattern is observed. In this pattern, there are no large (extratropical) waves occurring in the summer and an apparent double-peaked distribution of very large waves in the rest of the year, with maxima in storm wave heights occurring in Autumn and Spring.

5. RELATIONSHIPS BETWEEN EXTREME WAVE CONDITIONS AND CIRCULATION STATES (DETERMINED BY EOF WEIGHTINGS)

In order to explore relationships between extreme wave conditions and circulation patterns, the set of wave height maxima were plotted against the smoothed weightings on eigenfunctions 1-4 (Figure 4). As seen in this Figure, most of the relationships appear to show no clear pattern; however, the relationship between weightings on eigenfunction 2 and the wave heights seems to indicate a fairly persistent relationship across the entire range weightings, It appears that a weighting of less than - 10 on this eigenfunction significantly reduces the magnitudes of the expected extreme wave heights, In order to test this hypothesis, a contingency table was formed with the following categories in terms of weightings on eigenfunction 2 and wave heights, respectively:

1) W_{2-1}: W2 < -10
2) $W_{2-2:}$ -10 < W2 < 0
3) W_{2-3}: 0 < W2

and

1) H_1: 10 < H < 12
2) H_2: 12 < H < 14
3) H_3: 14 < H

where the units for the wave height stratification are meters. Table 4 constitutes a 3 by 3 contingency, table in which each entry represents the number of occurrences within a particular joint W_2-H category. A Chi-Squared test can be used to examine whether or not the two variables are independently distributed. Using the distribution of values shown in Table 4 a Chi-squared value of 10.38 was calculated. Since this table has 2 degrees of freedom, it can be found to be i significant at the 0.01 confidence level.

In order to investigate the effect of the relationship between circulation states and waves on extrapolated wave height probabilities, the hindcast wave heights were stratified into the three categories of weightings on eigenfunction 2 as used in Table 5 . Each sub-population was analyzed separately using a generalized extreme value (GEV) analysis, with a maximum likelihood fitting method. Best-fit Gumbel-distribution estimates for each sub-population are given in Table 5 . These results show that the 100-year wave heights from these sub-populations vary considerably. In light of Figure 4 , it is evident that long-term fluctuations in weightings on eigenfunction 2 do occur, and, from the results shown in Figures 5a-e , it seems likely that these variations will affect the frequencies of extreme wave heights. The next section will develop a methodology to treat the estimation of expected variations in extreme wave conditions due to this effect.

6. VARIATIONS IN EXTREMES RELATED TO VARIATIONS IN CIRCULATION PATTERNS

The estimation of expected variations in extreme wave frequencies can be approached via a compound distribution perspective. Each of the three populations of storms (stratified by W, category) can be analysed to determine expected wave probabilities for storms within that population. Using the Fisher-Tippett Type I distribution from extremal theory, the cumulative distribution within a single population can be expressed as

$$F_i(H) = e^{-e^{-y}} \qquad (8)$$

where $F_i(H)$ is the cumulative distribution for category i and y is given by

$$Y = \frac{(H - a_1)}{a_2} \qquad (9)$$

with a_1 and a_2 representing the two parameters of the distributions,

To convert this to an expected exceedance of a given wave height, we define an exceedance probability as

$$P(H) = 1 - F(H) \qquad (10)$$

Given that each storm category has a probability of exceeding a particular wave height, it is clear that the total probability of exceedance may be obtained by summing these three independent probabilities. i.e.

$$P(H) = \sum_{i=1}^{n} P(H|W_i)\, p(w_i) \qquad (11)$$

where P(H/wi) is the conditional exceedance probability, given that some discretized circulation indicator is in "state i", and p(wi) is the probability of circulation state "i." The effect of including additional populations can be see by noting that a 25.1-metre wave height is the largest 500-year wave height of all three populations in Table 5 whereas from the summation estimate, a 25.1-metre wave height is expected to occur every 326 years.

7. EXPECTED VARIABILITY IN EXTREME WAVES DUE TO CLIMATIC FLUCTUATIONS

Figure 4 , which shows the smoothed weightings of pressure fields on the first five eigenfunctions, seems to contain little support for the existence of dominant secular variations in circulation patterns this century. Instead, the patterns in these weightings seem to emphasis a combination relatively short-term variations (2-5 years) superposed on longer-term (decadal and longer) variations. In order to use equation 11 to estimate the effect of climatic variations on expected frequencies of extreme waves, it is necessary to recognize that the stratified analyses essentially treated each population as though it occurred with its mean probability over the entire length of record. From Table 6 we see that the mean probabilities of each category are . 1694 for category W_{2-1}, .3306 for category W_{2-2}, and .5000 for category $W,_{2-3}$. Departures from these mean values will lead to a change in the expected return periods. The magnitudes of these departures can be obtained by inserting a multiplier inside the summation sign in equation 11, with the value of the multiplier taken as the ratio from some subset of years to the mean value over the entire interval.

Table 6 gives normalized decadal probabilities of occurrence for each category of eigenvector 2 defined in Table 4 (considering only the months October through April). The normalization factors in this table are the mean probabilities of occurrence for the entire length of record as discussed at the end of the last section. As can be seen there, substantial trends exist in these probabilities, with fluctuations of up to 300% in the probabilities of occurrence for various categories. Inputting this type of variation into equation 11, we find that decadal variations in the value of the 100-year wave height can be over 30%.

Since the occurrence of the W_{2-1} category of circulation pattern is quite high and the occurrence of the W3 category is quite low near the beginning of this century, we would expect only moderate storms during this time. This is consistent with the data collected from the weather maps, which indicate that large storms were relatively infrequent and not as intense as those occurring later in the century. Variations in circulation probabilities after 1920 have not been as large as those before 1920. During the 1930-1940 period the circulation pattern produced more large storms due to the large probability of occurrence of category W_{2-3}. This same increase in the occurrence of category W_{2-3}, is evident in the 1970-1980 data. The 1950's and 1960's, although producing a large number of storms, did not appear to produce as many, very intense storms as those intervals with higher probabilities of W_{2-3}, circulation patterns.

An interesting point to note here is that the circulation pattern produced by a positive weighting on the second eigenfunction tends toward higher pressures off the east coast of North America. This, at first, might seem somewhat contradictory, since one might expect the pressures off of the coast to be lower when intense storms are located there. The reason that this is not strictly true is that the pressures reflected by the smoothed eigenfunction weightings are averaged over a one-year interval; thus, the effect of a single storm, even if very intense, will be relatively small. It is only when a large number of storms occur (such as in the 1960's) that the long-term average is substantially affected. In a previous analyses of extreme storms, it has been noted that some of the most intense storms appear to occur following dramatic reductions in the zonal index. It is possible that during periods of more zonal flows, the energy fluxes of smaller storms preclude instabilities from generating extreme storms; whereas, during periods of more meridional flows, the atmosphere is more unstable in terms of large-scale oscillations which can produce extreme storms. This is quite speculative, but does seem to be an interpretation that is consistent with the data.

8. CONCLUSIONS

The analyses performed here provide information on a number of topics of interest to researchers in areas related to climate variability and potential consequences of climate variations. One clear advantage of the downscaling methodology over analyses of global means is that results can be related directly to synoptic-scale phenomena which are of some recognizable significance.

The results of this study support the following conclusions:

1. Variations in large-scale circulation patterns do not exhibit large secular variations. Furthermore, temporal variations in the weightings of eigenfunctions, used to index circulation patterns, do not appear to have a simple relationship to mean global temperatures. Since several dimensions are required to represent the pressure field, our results suggest that scalar estimates of climate variability (such as El Nino vs. non El Nino years or mean global temperature) cannot be used very effectively to categorize climatic variability.

2. The index of wave height generation potential used in this study suggests that periods of more meridional flows may produce more

extreme storms in terms of wave conditions. These variations can be about 30% in the 100-year wave height; or, to put it in a slightly different perspective, this variability can amount to a plus or minus 4.3 metres for a 100-year wave height of 13-metres.

3. The inhomogeneities in the surface pressure data, especially from pre- 1955 to the present are a source of unknown error in the present study. Some effort in the future should be directed toward addressing this problem.

4. Calculated error bands in extremal statistics may have little relationship to the actual uncertainty extremal estimates of long term waves. The role of climatic variability, in this area appears to be very significant. Consequently, it may not be possible to define a "sufficient" number of years to perform a hindcast such that once that number of years is achieved, there is no need to add additional years to the record. Updating of hindcast data bases at regular intervals is strongly recommended.

9. ACKNOWLEDGEMENTS

This work was funded by the Atmospheric Environment Service of Environment Canada. The authors acknowledge the Office of the Chief of Engineers, U.S. Army Corps of Engineers, for authorizing publication of this paper.

10. REFERENCES

Bryan, K. S. et al., 1988: Interhemispheric asymmetry in the transient response of a coupled ocean-atmosphere model to CO^2, forcing. J Phys. Res., **18**, 851-867

Cardone, V.J., R.E. Jensen, D.T. Resio, V.R. Swail and A.T. Cox., 1995: Evaluation of contemporary ocean wave models in rare extreme events: Halloween Storm of October 1991; Storm of the Century March 1993. Accepted for Publication in J. of Atmos. and Oceanic Technology.

Hansen, J.D. et al., 1988:Global climate changes as forecast by Goddard Institute for Space Studies three-dimensional model. J. Geophys., **93**, 9341-9364.

Resio, D.T., 1978: Some aspects of extreme wave prediction related to climatic variations. Offshore Tech. Conf., Houston, TX, Vol 3, 1967-1980,

Schlesinger, M.E. and Mitchell, J.F.B., 1987: Climate model simulations of the equilibrium climatic response to increased carbon dioxide. Rev. Geophys.,**25**, 760-798.

Table 1
Number of Storms Per Decade

Decade	Number of Storms
1900 – 1909	28
1910 – 1919	24
1920 – 1929	32
1930 – 1939	20
1940 – 1949	28
1950 – 1959	37
1960 – 1969	99
1970 – 1979	63
1980 – 1989	53

Table 2
Cumulative Percentage Variance Explained

Eigenfunction	Cumulative Percent Variance
1	38.1
2	56.4
3	71.2
4	81.8
5	88.7
6	92.2
7	93.7
8	95.5
9	96.4

Table 3
Monthly Distributions of Hindcast Wave Height Maxima

Month	Upper Limit of H_s Category					
	3	6	9	12	15	18
Jan	1	8	32	24	11	0
Feb	1	17	28	28	10	2
Mar	1	13	19	24	19	5
Apr	0	12	11	9	7	2
Sep	0	0	0	0	1	0
Oct	1	2	5	5	4	0
Nov	0	7	11	13	8	4
Dec	1	6	17	10	10	1

Table 4
Contigency Table of Wave Heights And Eigenfunction Weightings

	H_1	H_2	H_3
W2-1	42	18	2
W2-2	82	30	9
W2-3	94	66	23

Table 5
Estimated Gumbel Wave Heights For Storms in Each of the Three E2 Weighting Categories

Return Period (yrs)	W_{2-1}	W_{2-2}	W_{2-3}
	(wave heights in metres)		
10	11.2	13.5	16.2
50	13.2	15.7	17.9
100	14.7	17.4	21.3
250	16.2	19.0	23.4
500	18.2	21.1	25.1

Table 6
Decadal Averages of the normalized Multiplier, λ

Decade Starting Year	λ_1	λ_2	λ_3
1900	3.10	0.95	0.34
1910	1.40	1.54	0.54
1920	0.32	1.28	1.04
1930	0.78	0.29	1.49
1940	0.84	0.58	1.30
1950	1.09	1.00	0.96
1960	1.31	1.57	0.55
1970	0.11	0.81	1.39
1980	0.00	0.93	1.35

Figure 1. Comparison of storm tracks in 1963-1966 and 1973-1985 periods.

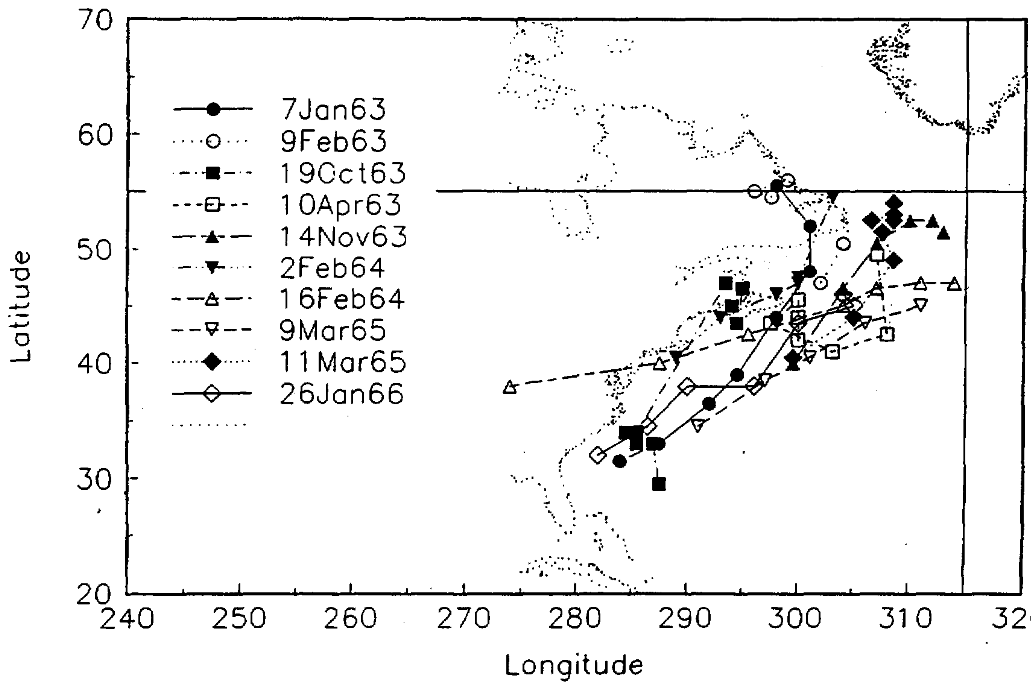

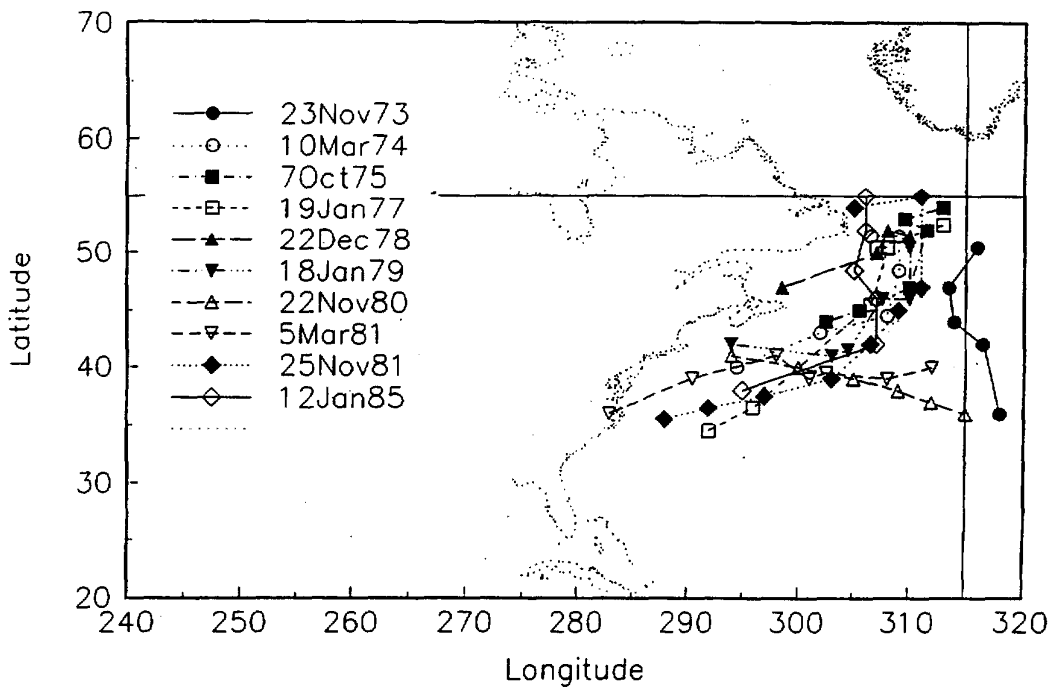

Figure 2. Mean pressure field for study area for the period 1899-1993.

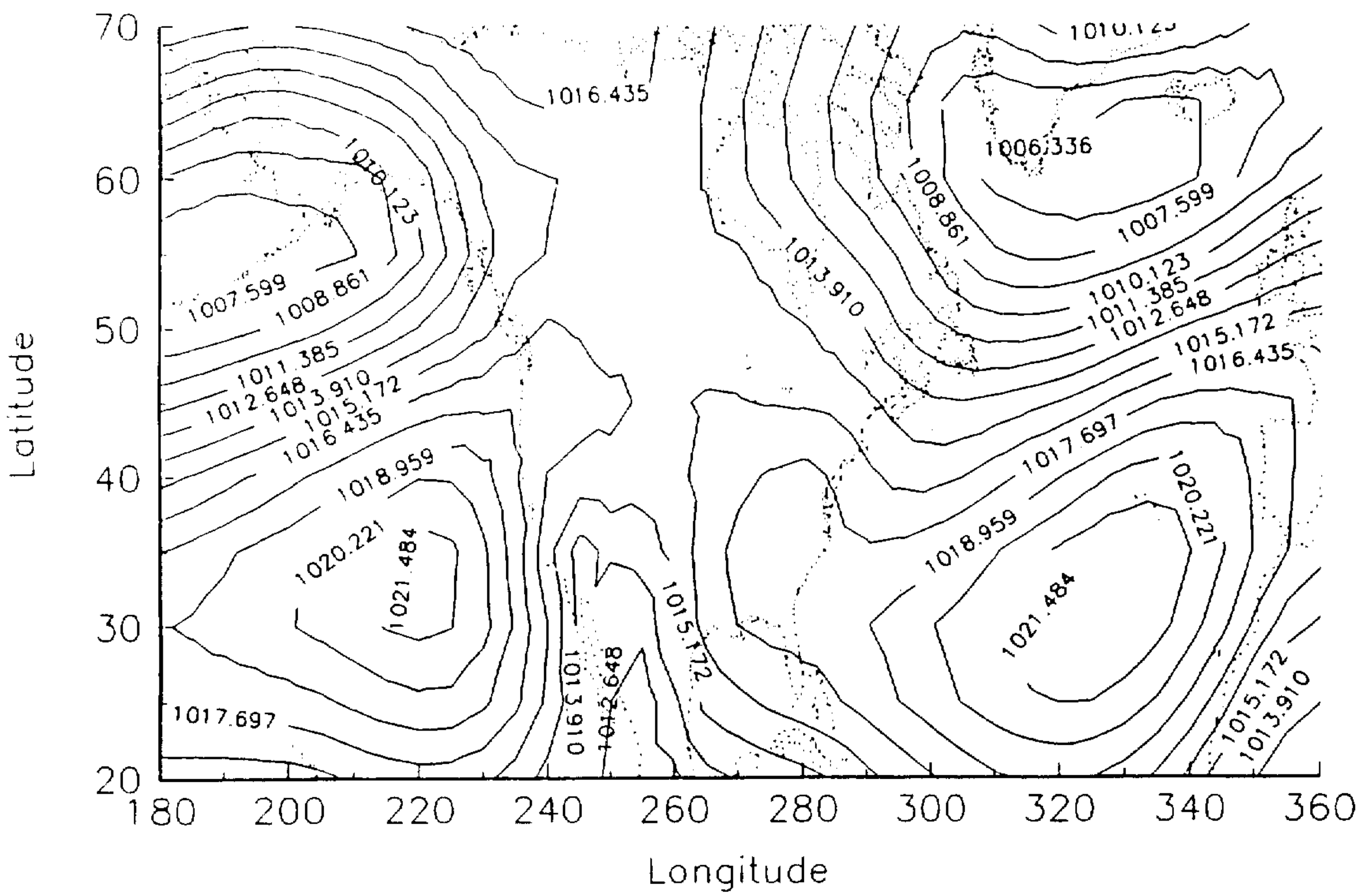

Figure 3a. Eigenvector 1

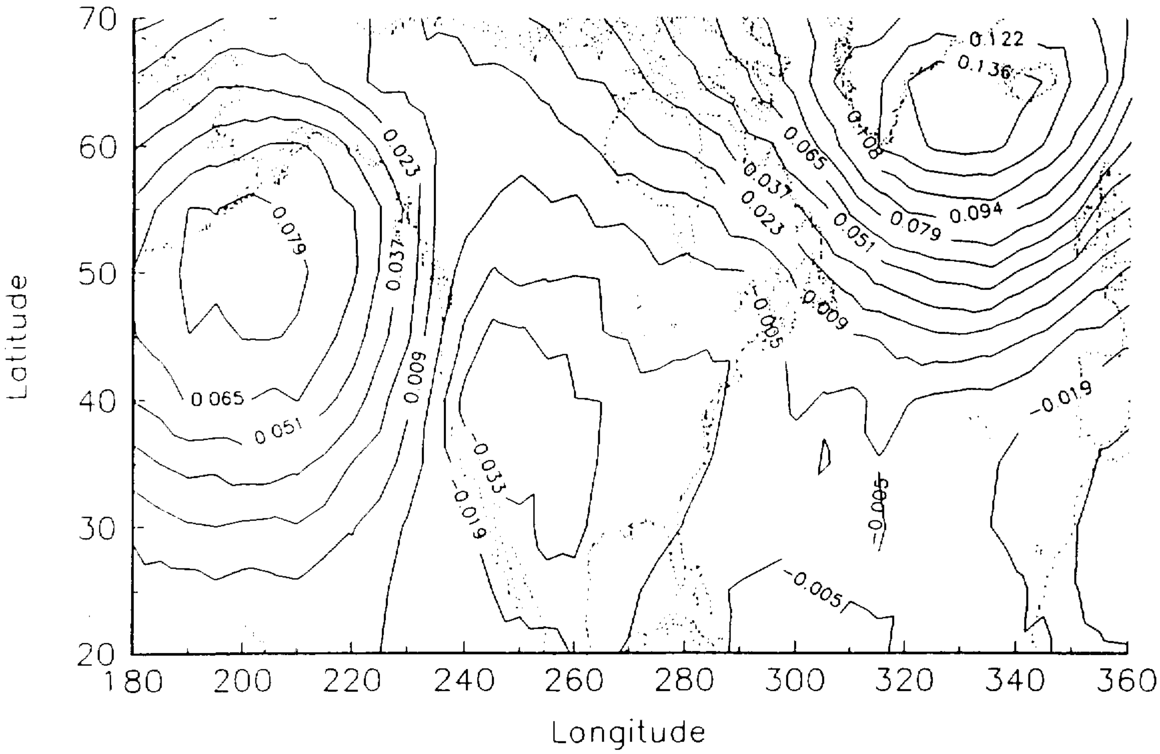

Figure 3b. Eigenvector 2

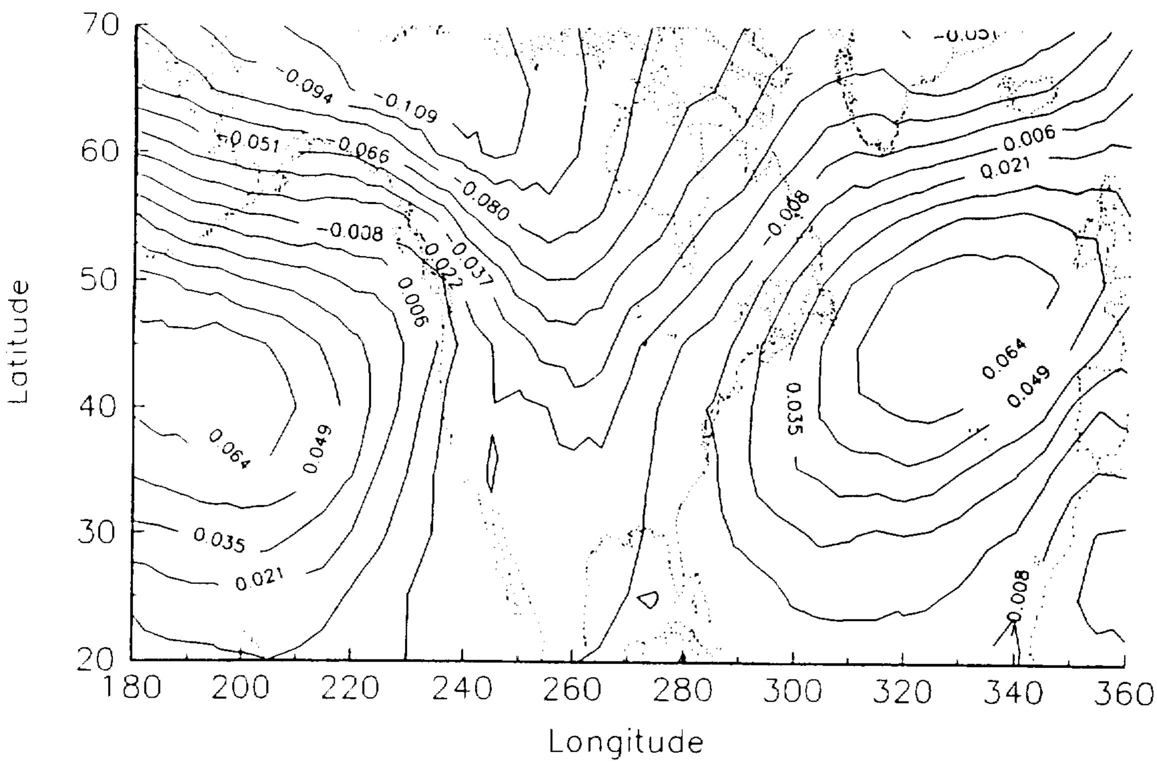

Figure 3c. Eigenvector 3

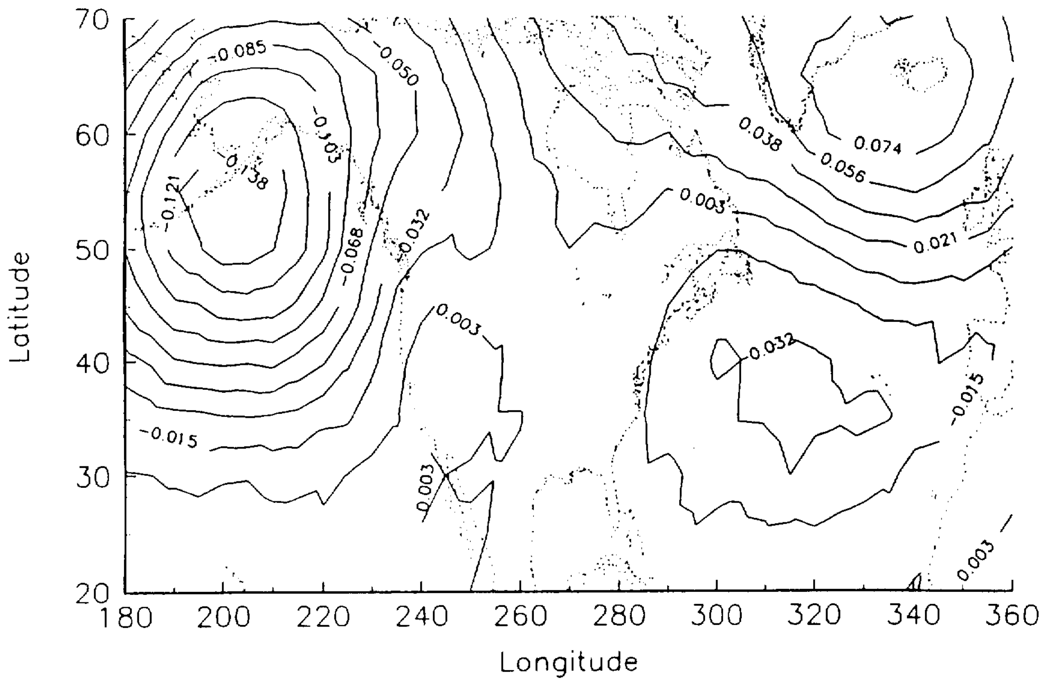

Figure 3d. Eigenvector 4

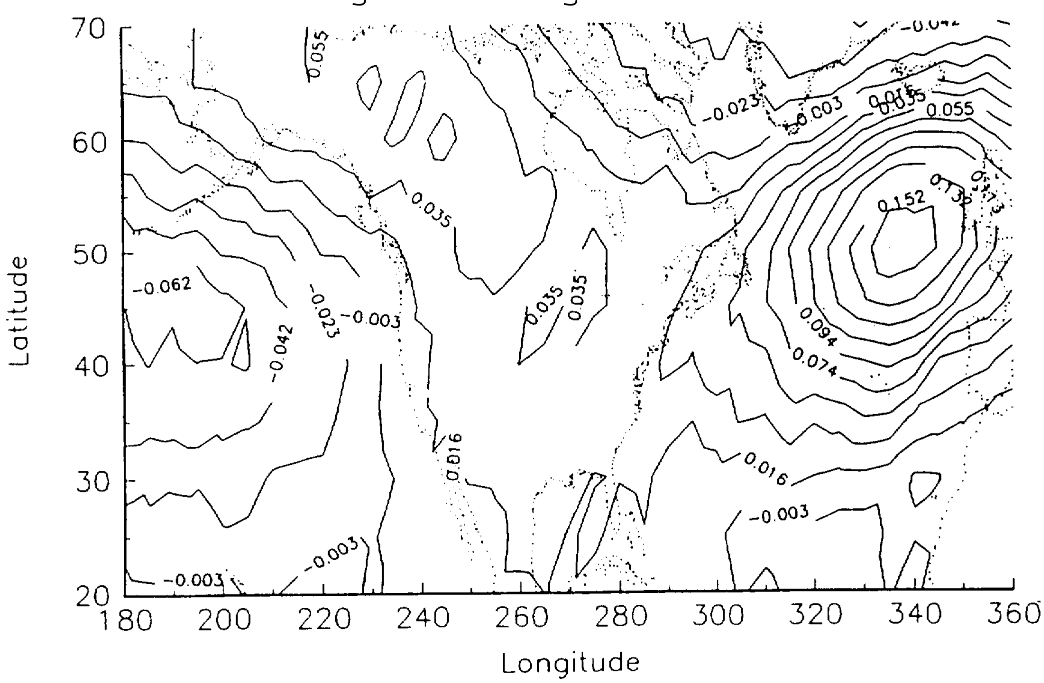

Figure 3e. Eigenvector 5

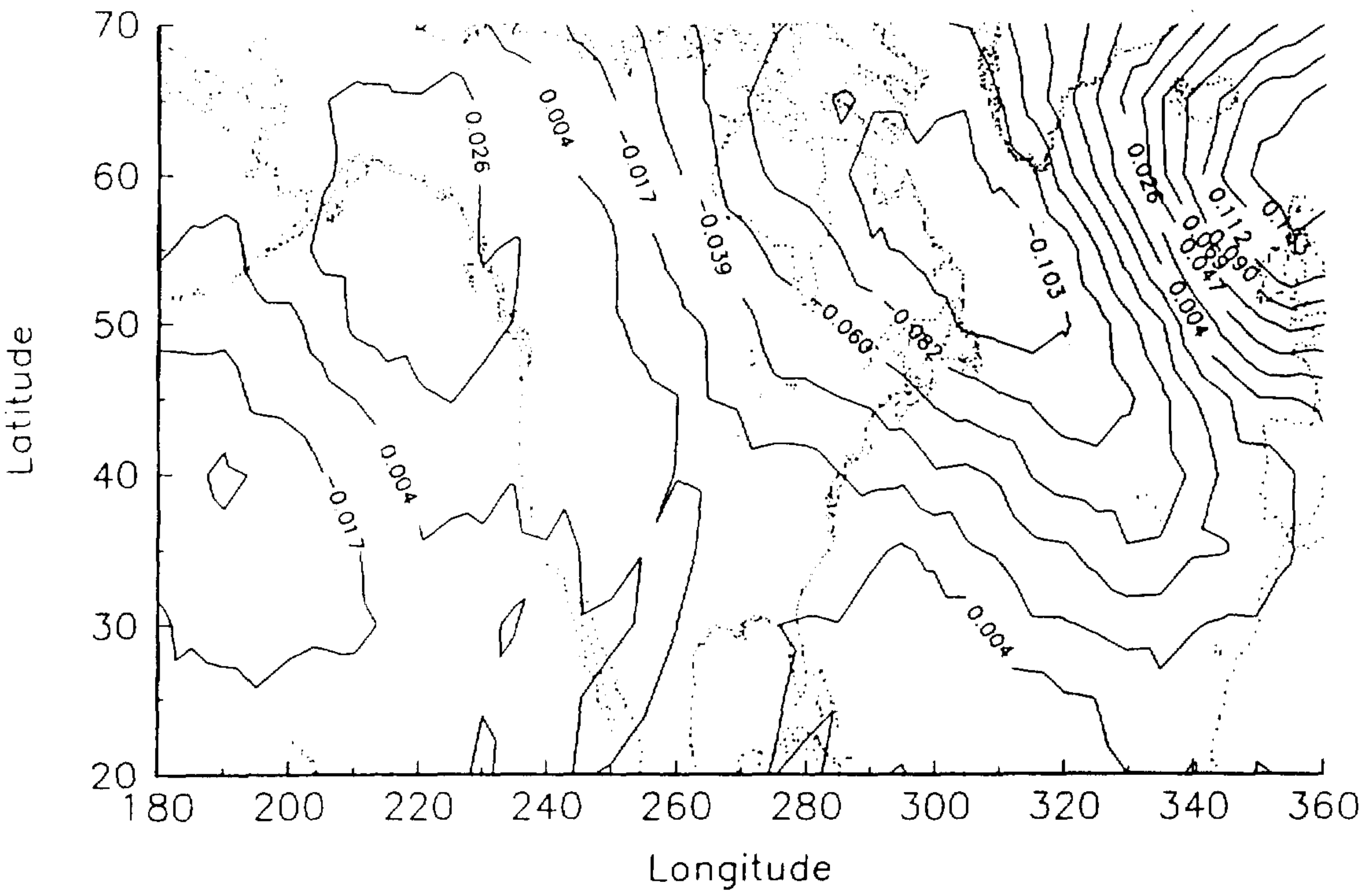

Figure 4. Smoothed weightings on eigenfuctions 1-5.

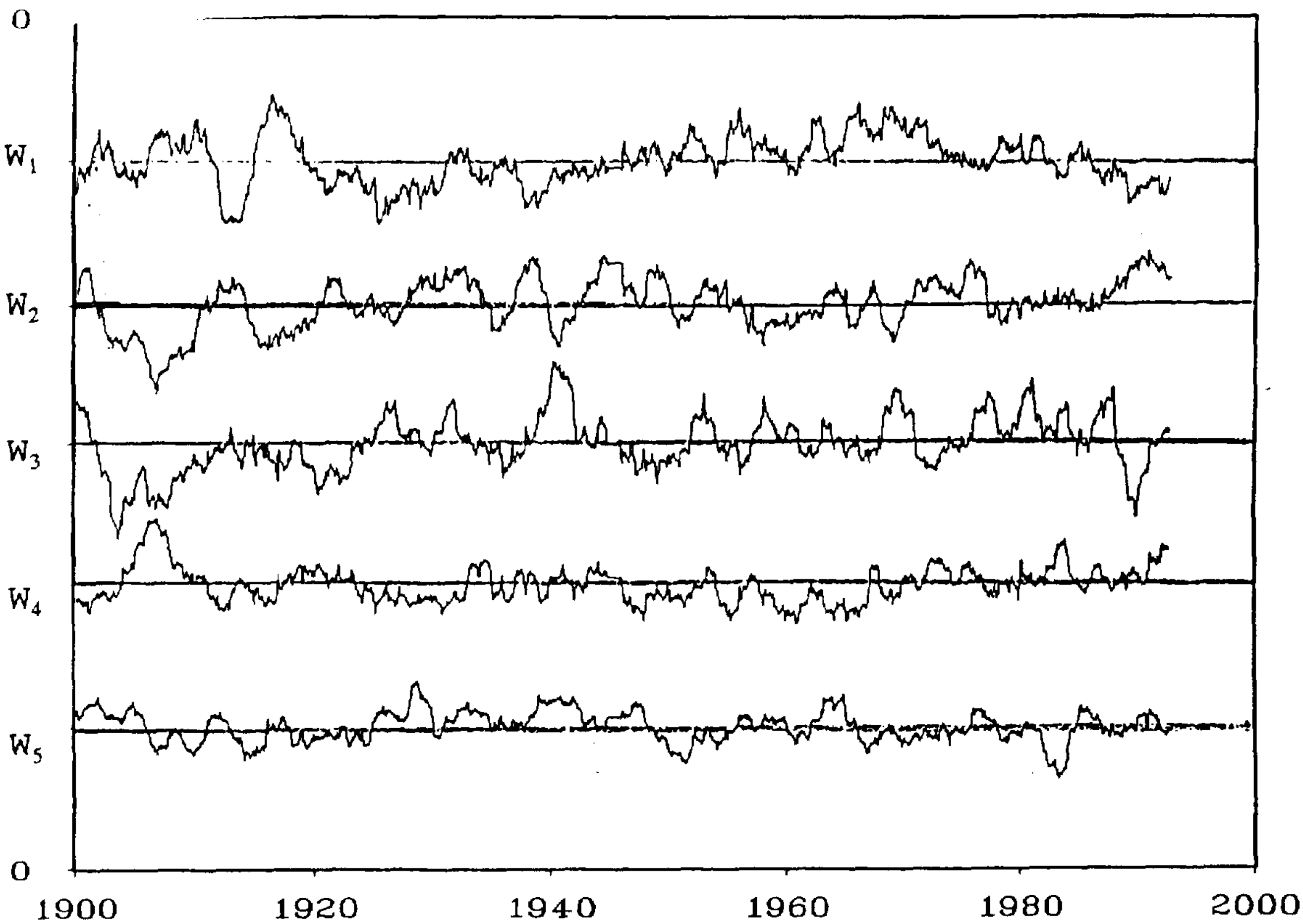

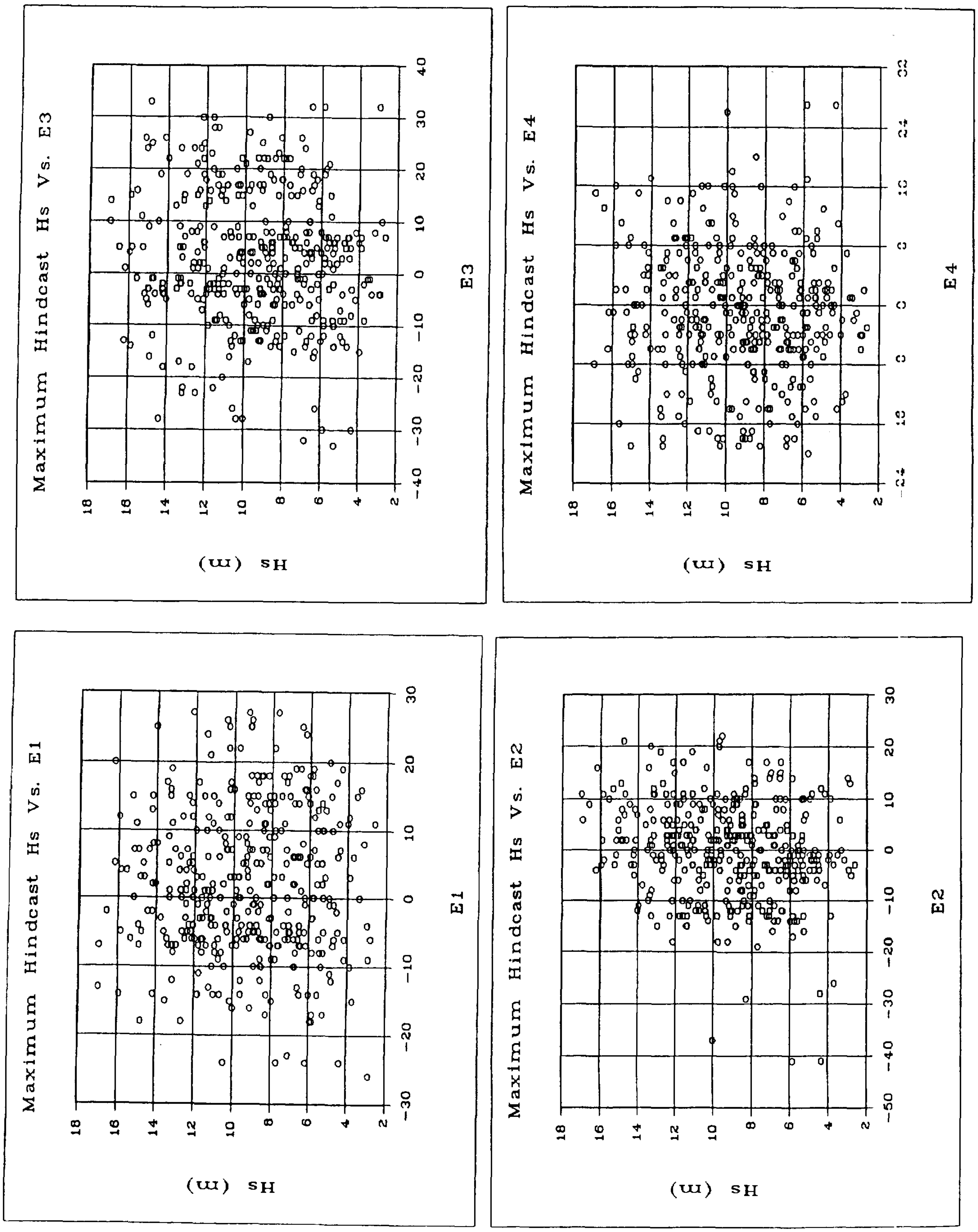

Figure 5. Plots of maximum hindcast wave heights as a function of eigenfunction weighting for eigenfunctions 1-4.

A REVISED EXTREME WAVE CLIMATOLOGY FOR THE EAST COAST OF CANADA

V.R Swail[1], M Parsons[2], B.T. Callahan[2] and V.J. Cardone[2]

[1]Environment Canada
Downsview, Ontario

[2]Oceanweather, Inc.
Cos Cob, CT

1. INTRODUCTION

Present design criteria for the northwest Atlantic Ocean off the east coast of Canada are based on a wave hindcast of 68 severe storms covering the period 1957-1987 (Canadian Climate Centre, 1991, Swail et al., 1989). That hindcast employed a 1-G deep water wave model, which was expected to yield conservative results since water depths in many areas of the Scotian shelf are 50 m or less, and on the Grand Banks there arc areas of 40 m depth; the Hibernia area itself is characterized by 80 m water depths. In the verification stages of that hindcast study it became apparent that for the large waves which characterized the extreme storm data set, i.e. significant wave heights greater than 12 m, that even the 80 m depths at Hibernia were showing effects of shallow water. A subsequent more extensive verification study of all wave hindcasts for Canadian waters (Atmospheric Environment Service, 1995) confirmed this finding, revealing a positive bias in the hindcasts for all cast coast areas, including the Grand Banks at sites in about 80 m depth.

As a result of this finding, and with the advent of new 3-G shallow water wave models, it was decided to re-hindcast the 68 storms to produce a revised wave climatology. At the same time the hindcast was updated to 1995, to incorporate several more recent new storms detected by the introduction of the Canadian moored buoy network in 1990, including the two largest wave events ever recorded, the Halloween storm of 1991, and the "Storm of the Century" of March 15, 1993. These two storms have been extensively documented by Cardone et al. (1995).

Sections 2 -4 of this report describe the wave model used in the revised hindcast, the parameters of the production hindcast, including the wind fields, bathymetry and ice edge, and the comparison of the various 3-G model results with the original 1-G hindcast at selected gridpoints. Section 5 describes the update of the storm population to 1995, while Section 6 shows the results of the revised extremal analysis based on the 3-G model.

2. WAVE MODEL

The wave model used for the revised hindcast was the Canadian Spectral Ocean Wave Model (CSOWM) described by Khandekar et al. (1994). This wave model can be used to produce either 1-G or 3-G hindcasts, in deep-water or shallow-water mode. It can also be used either with a coarse grid alone, or with a coarse grid and a nested fine mesh grid. In this study, all possible physics variations (1-G/3-G, deep/shallow) were carried out; however, only the grid incorporating the nested fine mesh was used. The CSOWM grid is laid out on a transverse Mercator projection with an assumed equator at 51° W and a coarse grid spacing of 1.084° of longitude on the assumed equator, The nested fine grid has a grid spacing of about 0.3610 of longitude. The model grid is shown in Figure 1 . The model has 24 direction bands and 23 frequency bands ranging from 0.039 to 0.32 Hz increasing in geometric progression with a constant ratio of 1. 10064 for both the coarse and fine grids. Winds corresponding to 19.5 m above mean sea level are input to the wave model at 3-hour time steps. Further model details are provided in Khandekar et al. (1994).

3. PRODUCTION HINDCAST

3.1 Wind Fields

The wind fields used in the hindcast of the previous 68 storms were adapted for use in the present hindcast. These winds represent the "effective neutral" 20 m winds. For use in this study the winds were interpolated from the original latitude-longitude grid (1.25° latitude by 2.5° longitude in the coarse mesh; half that in the fine mesh) to the CSOWM grid. The winds were also interpolated in time, from the original 2 hour timestep, to the 3 hour timestep used in tire CSOWM hindcast.

3.2 Bathymetry

The bathymetry used in the study was the digital bathymetry file produced in ETOPO5, which gives depths on a 5 minute grid. The depth at each model grid point is simply the average of the depths of all ETOPO depths which lie within the box represented by that point.

3.3 Ice Edge

The ice edge information was derived from the Walsh and Johnson (1979) data set of monthly ice concentrations, updated to 1992 and interpolated to the dates of the storms. The 5/10 ice concentration contour was used as the definition of the ice edge - points with ice concentrations greater than 5110 were considered as land by the model, those with concentrations 5/10 or less were considered as open water. Figure 2 shows an example of the determination of the ice edge at the time of a storm, as interpolated to the storm date from the end-of-month ice edges.

The production hindcast of the original 68 storms was carried out using the CSOWM wave model in 3 different modes - 1-G deep, 3-G deep, 3-G shallow using the wind fields, bathymetry and ice edge as described above. From each model run the following elements were archived for all grid points in the fine mesh area south of 54°N:

Hs - significant wave height
Tp - spectral peak period
VMD - vector mean direction

In addition, the full 2-D wave spectra were archived at 129 grid points uniformly distributed within the fine mesh area.

4. COMPARISON OF MODEL RESULTS

The following paragraphs describe various intercomparisons of the 3 runs made with the CSOWM model in its various configurations, and the original 1-G hindcast. In particular, the CSOWM 1-G deep results were compared with those from the CSOWM 3-G deep model; the CSOWM 3-G deep hindcast was compared to the 3-G shallow; and the 3-G shallow values were compared to the results from the original 1-G hindcast.

In Figure 3 , the results of the hindcast time series for the "Ocean Ranger storm" of February 14-15, 1982 are shown. These results are typical of time series from large storms on the Grand Banks. It is clear that using the 3-G model in deep-water mode increases the hindcast wave heights compared to the 1-G deep-water run. There is, for this grid point at about 80 in depth, a corresponding reduction in the 3-G shallow water hindcast, so that at the peak of the storm the 3-G shallow results are virtually identical to the 1-G deep. While not all time series showed such exact correspondence of the 3-G shallow hindcast and the 1-G deep, this tendency was predominant. Spectral peak period was less variable among the model runs, although there was a distinct tendency for the periods to be reduced in the 3-G models at the peak of the storm.

Figures 4 -6 show scatter plots for significant wave height and spectral peak period for three pairs of comparisons: 1-G deep versus 3-G deep (Figures 4 a, b); 3-G deep versus 3-G shallow (Figures 5 a, b); and 3-G shallow versus original 1-G (Figures 6 a, b). The following conclusions can be drawn from these figures.

(1) **In the most severe storms the 3-G deep model provides greater storm peak HS than the 1-G model.** This can be seen in Figure 4 which

compares peak HS at the Grand Banks grid point for 3-G deep versus 1-G deep. At the Scotian Shelf and Georges Bank locations this tendency was seen over the whole range of storms hindcast, The average increase in HS is 0.38 in for large storms (> 10 m) on the Grand Banks, and 0.29 in for all storms on the Scotian Shelf (not shown). Despite the increase in HS, the 3-G model provides consistently lower peak periods than the 1-G model (Figure 4b), with an overall bias of 0.49 s for peak period in the range of 13.5 s. For the Scotian shelf the bias was 0.21 s for a mean peak period of about 11.7 s.

(2) **The 3-G shallow water processes in the model result in lower storm peak HS than the 3-G deep model.** The effect of shallow water processes on the Grand Banks is shown in Figures 5 a, b . The mean difference in HS is 0.30 m (shallow lower than deep) over all 66 storms (in 2 storms sea ice covered the grid point selected). The effect is greater, as expected, in the most extreme events. For example, in the Ocean Ranger storm, which produced significant wave heights around 14 in, the difference was 1.18 in. For TP, the period is reduced by 0.61 s over the whole range of storms (Figure 5b).

(3) **The combined effects of 3-G physics and shallow water processes, coupled with differences in spatial and temporal resolution between the original CCC and new CSOWM hindcasts results in increased wave heights at deep water sites, and reduced values in shallow areas.** This can be seen in Figures 6 a, b , which compare the 3-G shallow versus the original 1-G. This then compares the runs on which the new, revised wave climatology will be based, with the runs from the original east coast hindcast (Canadian Climate Centre, 1991). It is clearly seen in these figures that the combined effects of 3-G physics, shallow water processes, higher spatial resolution and lower temporal resolution produces an average decrease of 0.69m in storm peak HS (3-G shallow lower than original 1-G), and 1.10 s in spectral peak period for the grid point nearest Hibernia.

The question immediately arises as to which of these runs agrees better with measurements, Table 1 compares the storm hindcast peak HS and associated TP with measurements, for those storms where measured data were available near this location (10 storms). The bias for this subset of 10 comparisons of measured data versus the original CCC hindcast is identical (0.84 in) to that in the full verification study over 34 comparison points. It is clearly seen that the new 3-G shallow water hindcast gives by far the best agreement with measurements, for both HS and TP (bias 0.11 m and 0.6 s respectively). Correlation coefficients and rms errors were both slightly better as well.

5. UPDATE OF STORM POPULATION

When the original hindcast was completed in 1991, it included storms occurring up until December 1987. Subsequently, several large storms have occurred, including December 1989, January 1990, April 1995, and the two largest wave events ever recorded by an instrument anywhere in the world, the Halloween storm of October 31, 1991, and the "Storm of the Century" of March 15, 1993. The significant wave heights measured by the Canadian network of moored buoys were 17.3 m and 16.3 m respectively, with estimated maximum waves of 30.7 m and 30.4 m. Four of these recent storms were hindcast because of impacts associated with the wave conditions. In addition, the Halloween storm and the Storm of the Century were the focus of the most intensive wave hindcast ever carried out for Canadian waters, as befitting their status as record-breaking storms. The results of those two hindcasts are described by Cardone et al. (1995).

As part of a separate study to develop interactive graphical approaches to kinematic wind field analysis (Cox et al., 1995), a set of the most recent storm event s occurring off the cast coast covering the period 1988-1995 was identified and hindcast as a verification of the new hindcast procedures. Those results were also added to the updated storm population for the revised climatology.

The new storms were identified and selected through the following stages:

1. scan U.S. National Data Buoy Center and Canadian buoys for high wave events

2. scan microfilm synoptic charts from National Meteorological Center for potential storms

These scans produced a Master Candidate List (MCL) of 71 storm events with waves greater than 7 in between October 1988 - April 1995 in study area. This list of storms was then reduced to the most severe 18 events, the top 10 of which were hindcast for inclusion in the revised climatology. Table 2 lists the dates of the 18 events, showing peak height observed and mean wave height of available buoys, and an indication as to whether the storms were added to the final list for hindcast.

6. EXTREMAL ANALYSIS

Hindcast fields of significant wave height and peak period from the 3-G shallow water and 1-G (old) runs were assembled for the original 68 storms. Extremal analysis was carried out on the results using a Gumbel distribution fitted by method of moments at 3 points for significant wave height; associated peak period was also computed as in the original study, by regression c n the significant wave heights, For the extremal analysis two thresholds were adopted. One admitted storm peak heights above half the maximum value of the top-ranked storm HS at each point. The second threshold was determined by the top 30 ranked storms. The latter method is the one used in the original CCC study.

It can be seen from Table 3 that the 100-year values from the half-maximum technique gave larger extremes than the top-30 method. This is certainly due to the larger number of storms admitted by this technique, which increase the standard deviation of the extreme sample, and hence the slope of the Gumbel distribution function. It should also be noted that the differences between the threshold techniques exceeds those between the different wave models. It is also clear that, in cases of shallow water, that the 3-G shallow water model gave lower 100-year values than the original hindcast; however, for deep water sites the 3-G physics resulted in a higher 100-year value, since there was no compensating effect from the shallow water processes.

7. SUMMARY AND FUTURE WORK

A revised hindcast has been produced for the northwest Atlantic Ocean off the east coast of Canada, using a state-of-the-art 3-G wave model incorporating shallow water effects. The hindcast data sets produced replace those created in the earlier hindcast using a 1-G wave model assuming deep water everywhere. Intercomparison of the time series and scatter plots of the original hindcast and the various new CSOWM hindcasts shows an increase in significant wave height due to the 3-G wave model, and a corresponding decrease in shallow water areas due to the shallow water effects in the model. The extremal analysis of the significant wave heights and associated peak periods replace those produced with the earlier hindcast. The differences are mostly small, but some increase is noted in deep water areas due to the 3-G model, and some decrease is noted in shallow water regions due to the shallow water effects in the model.

Work which remains to be done is to hindcast the remaining 10 of the new 14 storms after 1988, and incorporate the results into a final extremal analysis of the whole domain for all grid points in the fine mesh area south of 54° N.

Finally, the variability in storm climate from 1899-1993 shown by Resio et al. (1995) illustrates the uncertainty associated with extrapolating 100-year return period wave heights from limited subsets of data. Reliable design should therefore be based on the longest possible data period. Also, the occurrence of several large wave-producing storms in the period immediately following the original hindcast highlights the need to update such hindcasts on a periodic basis, especially given the hypothesis that the wave climate may be changing due to global warming.

8. REFERENCES

Atmospheric Environment Service, 1995: Verification of wave models for Canadian waters. Prepared under contract no. KM 170-2-8930101-XSE by MacLaren Plansearch Ltd., Halifax, N.S., and Oceanweather, Inc., Cos Cob CT, 123 p.

Canadian Climate Centre, 1991; Wind wave hindcast extremes for the east coast of Canada, Volume 1. Prepared under contract no. KM169-6-6678 by MacLaren Plansearch Ltd., Halifax, N.S., and Oceanweather, Inc., Cos Cob CT, 109 p. plus appendices.

Cardone, V.J., D.T. Resio, R.E. Jensen, V.R. Swail and A.T. Cox, 1995: Evaluation of contemporary ocean wave models in rare extreme events: Halloween storm of October, 1991; Storm of the Century of March. 1993. Accepted in J. Atmos. Ocean. Technology

Cox. AT., A. Greenwood, V.J. Cardone and V.R. Swail, 1995: An interactive objective kinematic analysis system. Proc. 4th Int'l Workshop on Wave Hindcasting and Forecasting, Banff, Alta.

Khandekar, M.L., R. Lalbeharry and V.J. Cardone, 1994: The performance of the Canadian spectral ocean wave model (CSOWM) during the Grand Banks ERS-1 SAR wave spectra validation experiment. Atmosphere-Ocean 32(1), 31-60.

Resio, D.T., V.R. Swail and R.L. Atkins, 1995. A study of relationships between large-scale circulation and extreme storms in the north Atlantic Ocean. Proc. 4th International Workshop on Wave Hindcasting and Forecasting. October 16-20, 1995, Banff, Alta.

Swail, V.R., V.J. Cardone and B. Eid, 1989. An extremes wind and wave hindcast off the east coast of Canada. Proc, 2nd Int'l Workshop on Wave Hindcasting and Forecasting, Vancouver, B.C.: 151-160.

Walsh, J.E., and C.M. Johnson, 1979. An analysis of Arctic sea ice fluctuations, 1953-1977. J. Phys. Ocean., 9, 580-591.

Table 1. Verification statistics for CSOWM hindcast runs versus measurements for Hibernia site.

	1-G DEEP	3-G DEEP	3-G SHALL	1-G ORIG
HS:				
BIAS (hind-meas)	0.18	0.53	0.11	0.84
ST. DEV. (m)	1.31	1.23	1.18	1.21
CORR. COEFF.	0.77	0.86	0.81	0.79
TP:				
BIAS (hind-meas)	1.71	1.23	0.65	1.87
ST. DEV. (m)	2.35	1.83	1.64	1.91
CORR. COEFF.	0.45	0.53	0.63	0.56

Table 2. List of most severe wave-producing storms 1988-95 (new)

STORM DATE	PEAK WAVE HEIGHT (m)	MEAN WAVE HEIGHT (m)	HINDCAST
881122	9.5	9.5	N
890105	14.2	10.6	Y
901111	10.7	9.1	N
920301	11.2	10.2	Y
920322	11.3	10.1	N
921204	13.4	11.6	Y
921213	10.8	9.7	N
921225	12.3	10.7	Y
930117	12.7	10.4	Y
930228	11.7	10.0	N
931227	14.3	11.2	Y
931230	14.3	11.2	Y
940304	10.1	8.9	N
941108	10.9	9.5	N
941209	11.5	11.3	Y
950205	9.1	8.7	N
950213	10.6	10.6	Y
950406	14.0	12.0	Y

Table 3. Extremal analysis for 3 points for HS and associated TP for the original CCC 1-G hindcast (1-GO) and the revised 3-G shallow water hindcast (3-GS) based on the original 68 storms for 2 threshold techniques.

	Grand Banks	Scotian Shelf	Georges Bank
Depth (m)	88	65	131
Top-30 Threshold			
HS (m):3-GS	14.53	11.21	11.49
1-GO	15.12	11.72	11.32
TP (s):3-GS	16.29	14.24	14.19
1-GO	18.00	16.77	14.43
1/2 Max Threshold			
HS (m):3-GS	15.39	12.57	12.09
1-GO	16.20	12.83	11.85

ATLANTIC GRID FOR CSOWM

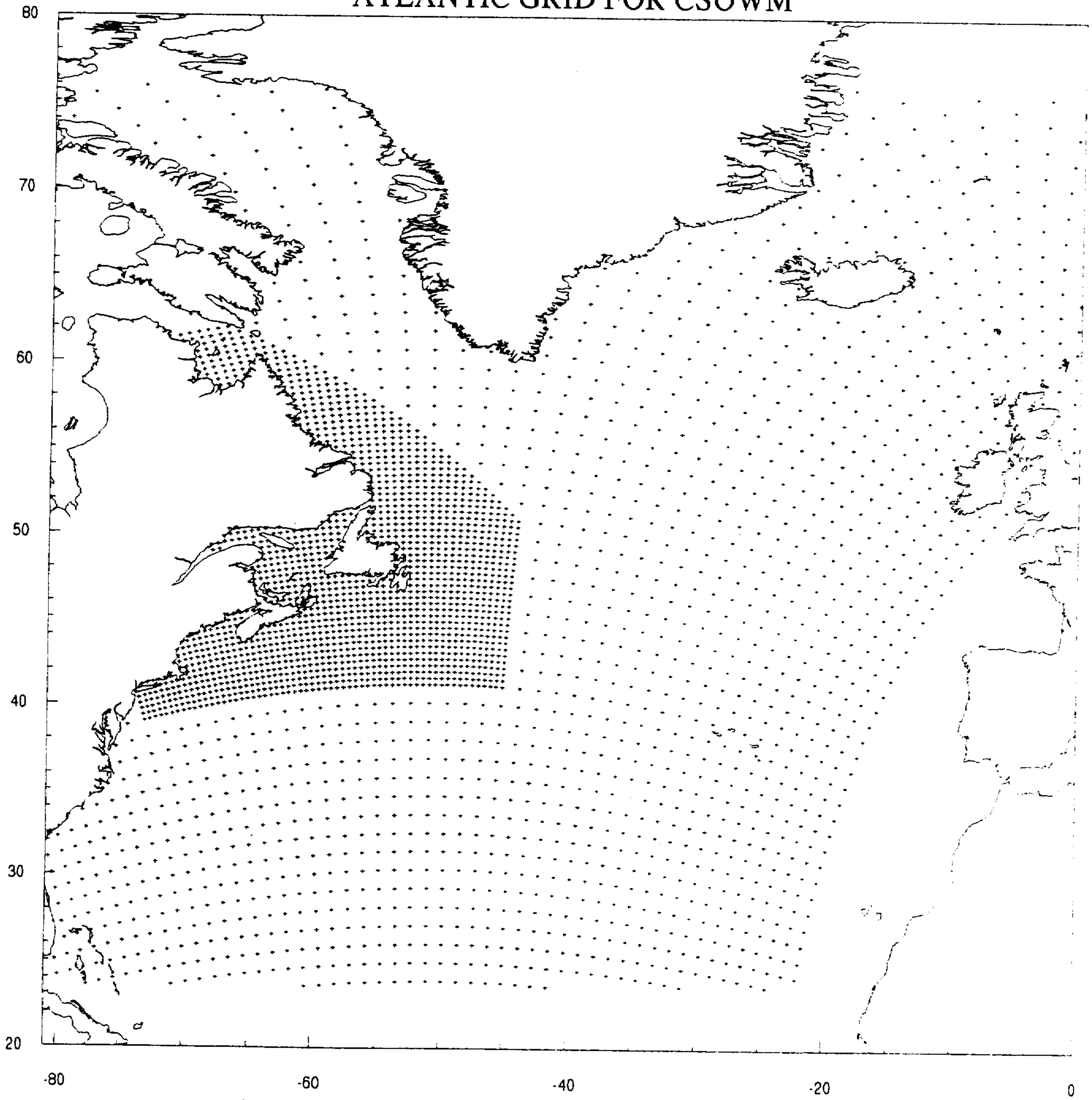

Figure 1. Canadian Spectral Ocean Wave Model (CSOWM) North Atlantic Grid (after Khandekar et al., 1994)

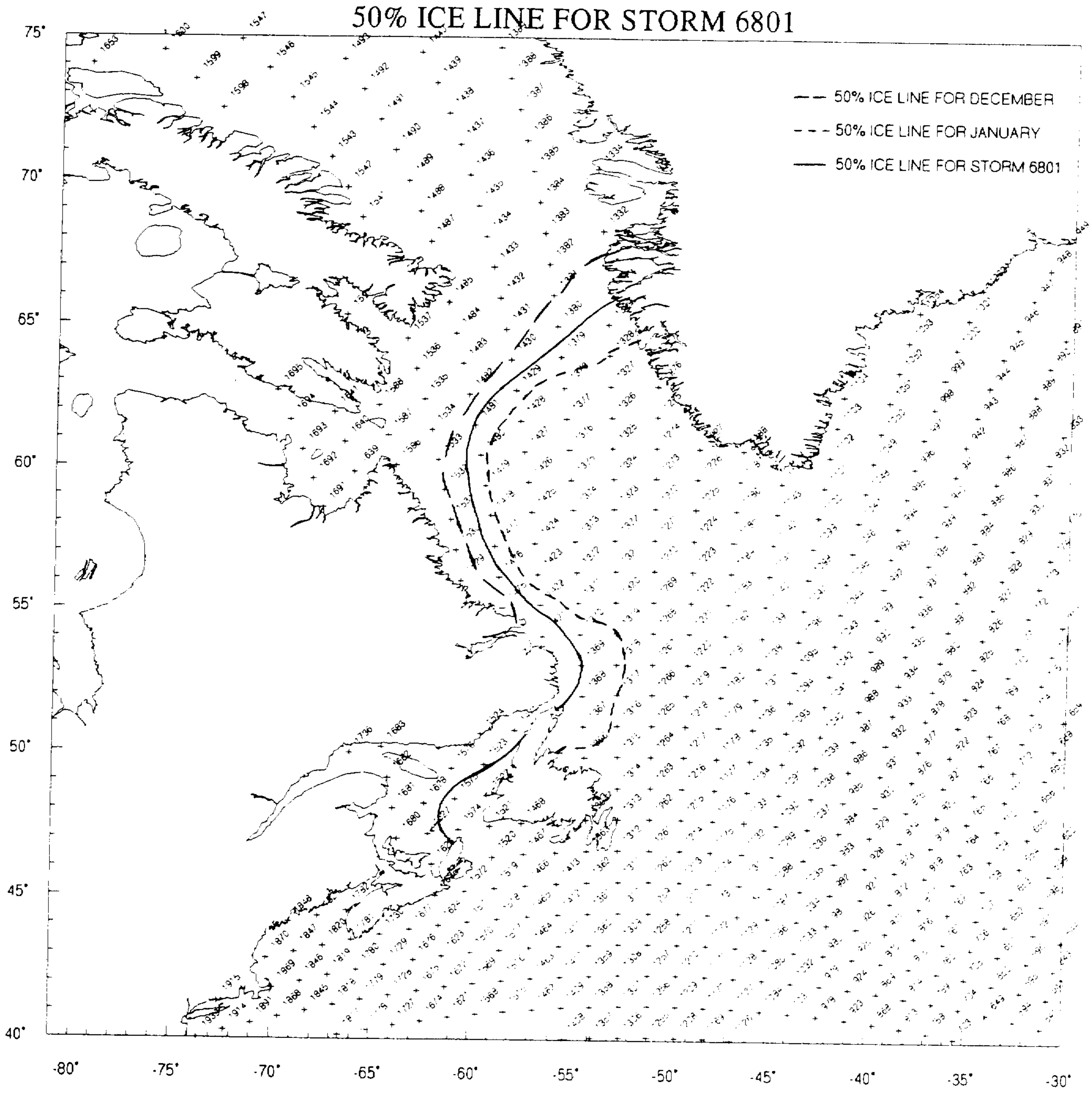

Figure 2. Interpolation of 5-10ths ice cover contour line to storm date from end-of-month concentrations

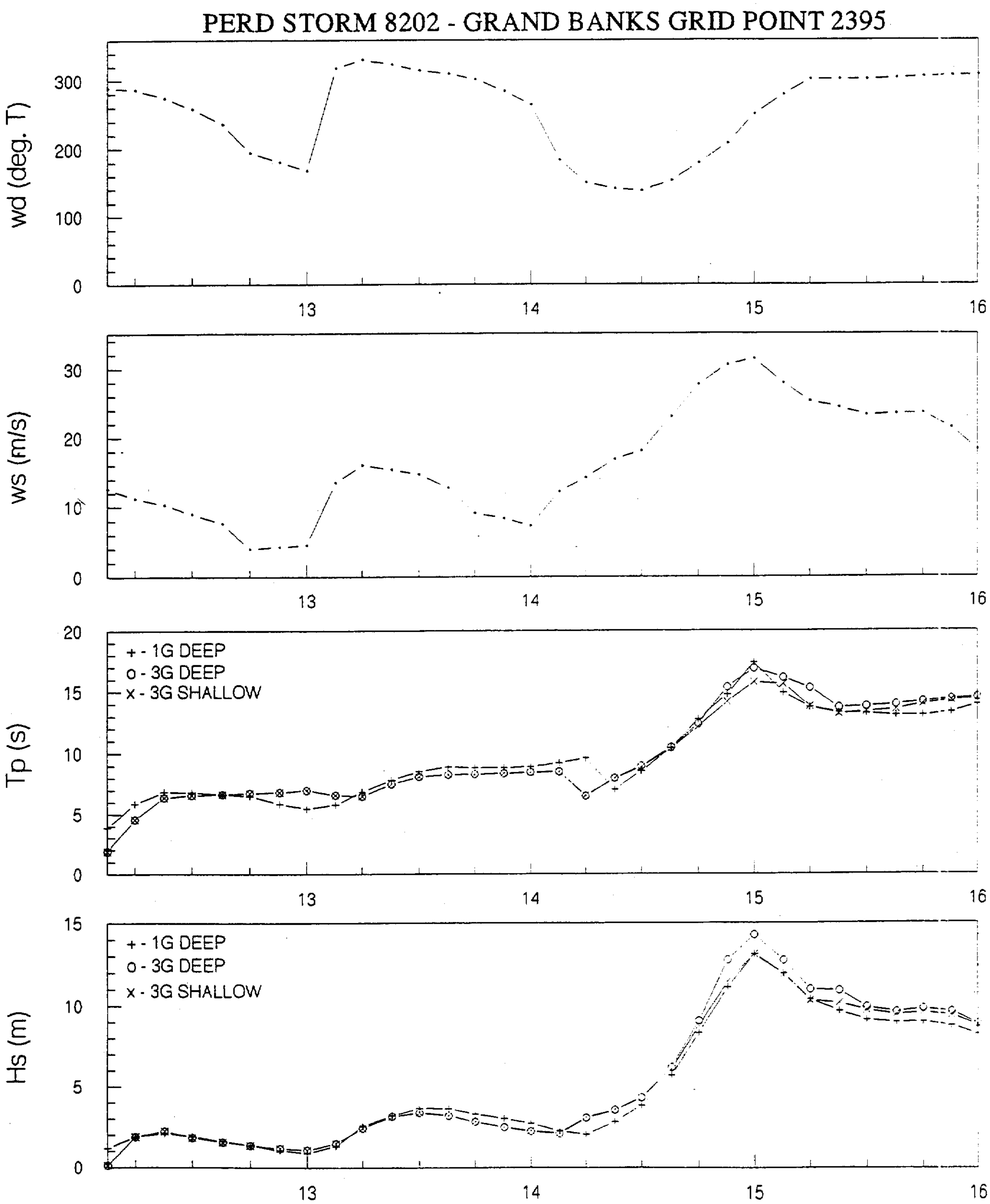

Figure 3. Comparison of various CSOWM configurations at grid point 2395 on the Grand Banks for the "Ocean Ranger" storm of February 15, 1982

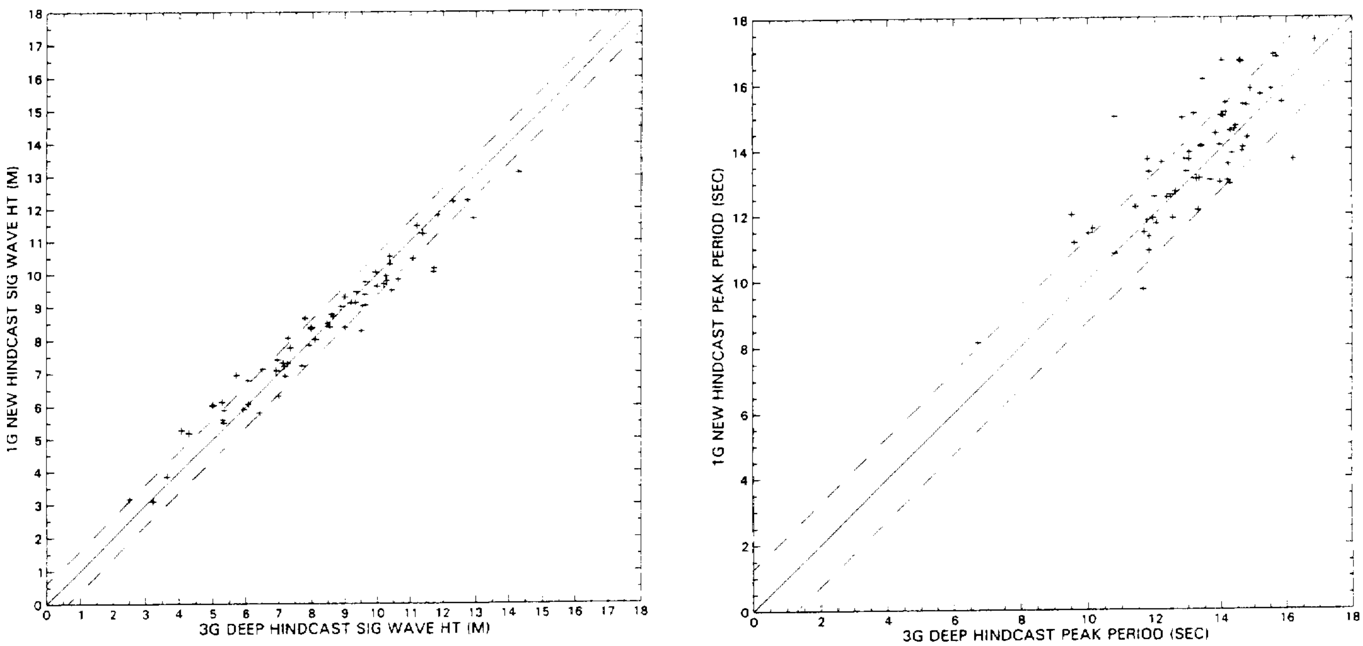

Figure 4. Comparison of CSOWM 1-G deep water wave model with 3-G deep water model at grid point 2395 on the Grand Banks for (a) significant wave height , and (b) spectral peak period

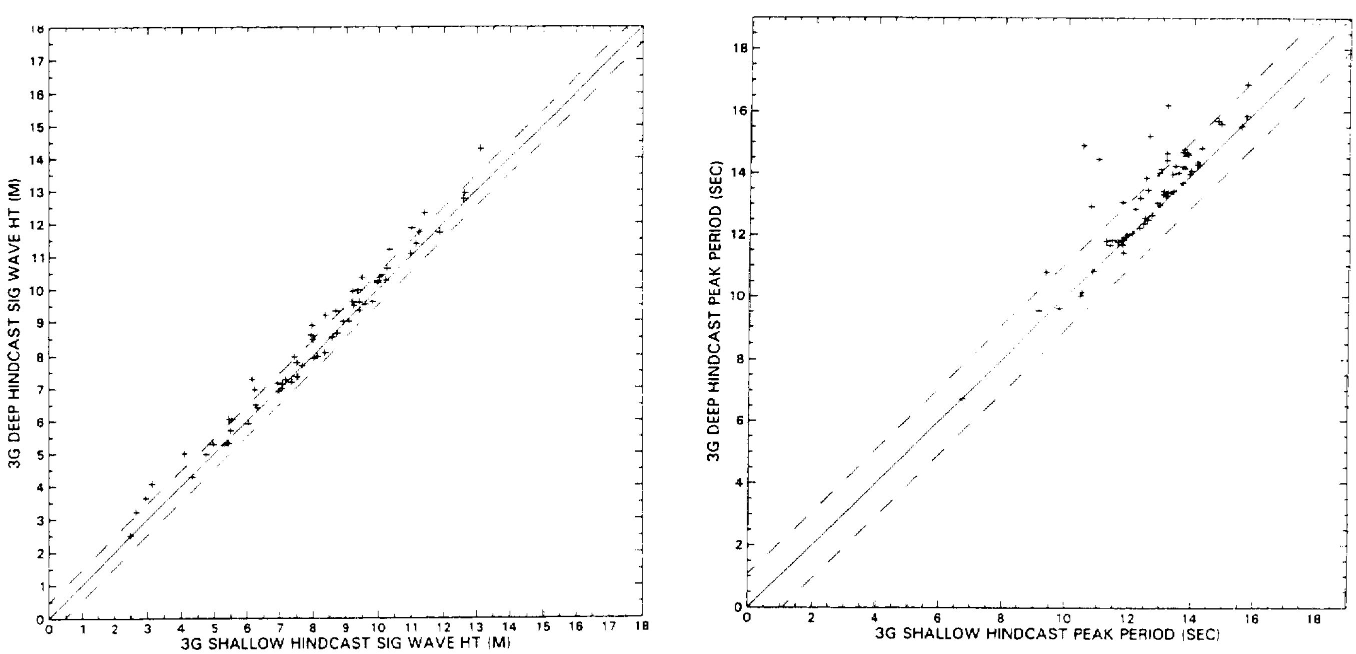

Figure 5. Comparison of CSOWM 3-G deep water wave model with 3-G shallow water model at grid point 2395 on the Grand Banks for (a) significant wave height , and (b) spectral peak period

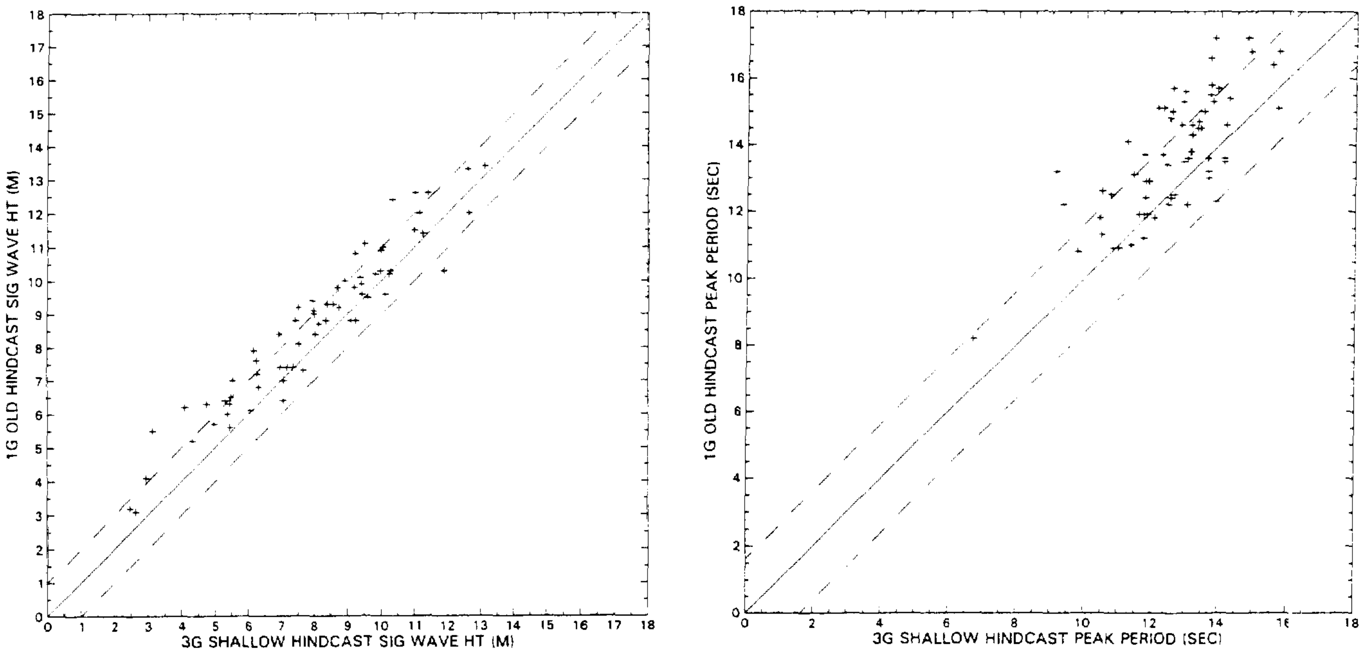

Figure 6. Comparison of CCC (original) 1-G deep water wave model with CSOWM 3-G shallow water model at grid point 2395 on the Grand Banks for (a) significant wave height , and (b) spectral peak period

Use of an Interactive Graphical Analysis System to Hindcast the Storm of the Century, March 12-15, 1993

by B. Thomas

Atmospheric Environment Service
Bedford, Nova Scotia

1. INTRODUCTION

The Storm of the Century (SOC), March 12 to 15, 1993, deepened explosively over the Gulf of Mexico then tracked northeastward across the eastern US and Canada. Storm to hurricane force winds over the western Atlantic built up extremely high waves. Buoy 44137, off the Scotian Shelf southeast of Halifax, Nova Scotia, reported a significant wave height of 16.3 in, and buoy 41002, off the South Carolina coast, reported 14.7 in. The heavy seas caused the sinking of the bulk carrier Gold Bond Conveyor early on March 15, about 100 km southeast of Yarmouth, NS, with the loss of the entire crew.

Estimates of the 100 year return period significant wave heights for the Scotian Shelf region of Canada's east coast are 10 to 12 m (Canadian Climate Centre, 1991). The significant wave height of 16.3 m at buoy 44137, in deep water off the edge of the continental shelf, south of Nova Scotia, exceeded the estimate of the 100 year return period wave height at that location by 40%. Questions were raised as to whether the unusual severity of the storm and the exceptionally high waves were a consequence of climate change.

This study investigates the severe winds and waves that occurred along the east coast of U.S. and Canada during the storm during the period from March 13 to 15. An interactive graphical system called FPA (Forecast Production Assistant) was used to hindcast the wind and waves. FPA was developed by Environment Canada (de Lorenzis, 1988, Paterson, et. al, 1992), and its use as a wind and wave hindcast system was described by Swail, et. al. (1992). Latest versions of the FPA workstation software incorporate the wind and wave models developed by Cardone (1969, 1976) as optional "black box" components.

2. DATA

Buoy, ship, and drill platform data were used to edit and verify the analysed fields in FPA and the hindcast wind and wave data. The station locations are shown in Figure 1 ; with details in Table 1 . The buoys were all 6 in NOMADs, with the exception of 44014, a 3 m Discus. Buoy anemometers are near 5 m whereas the anemometer of the Cohasset Panuke rig 44144 was at about 80 m. The Canadian buoys report a 10 minute mean and an 8 second peak wind speed, whereas the U. S. buoys report an 8 minute mean and an 8 second peak wind speed. The wind speeds were converted to effective 19.5 m winds using the MPBL model, described in Section 4 , for comparison with the modelled winds (times series of data, Figs 5 -11).

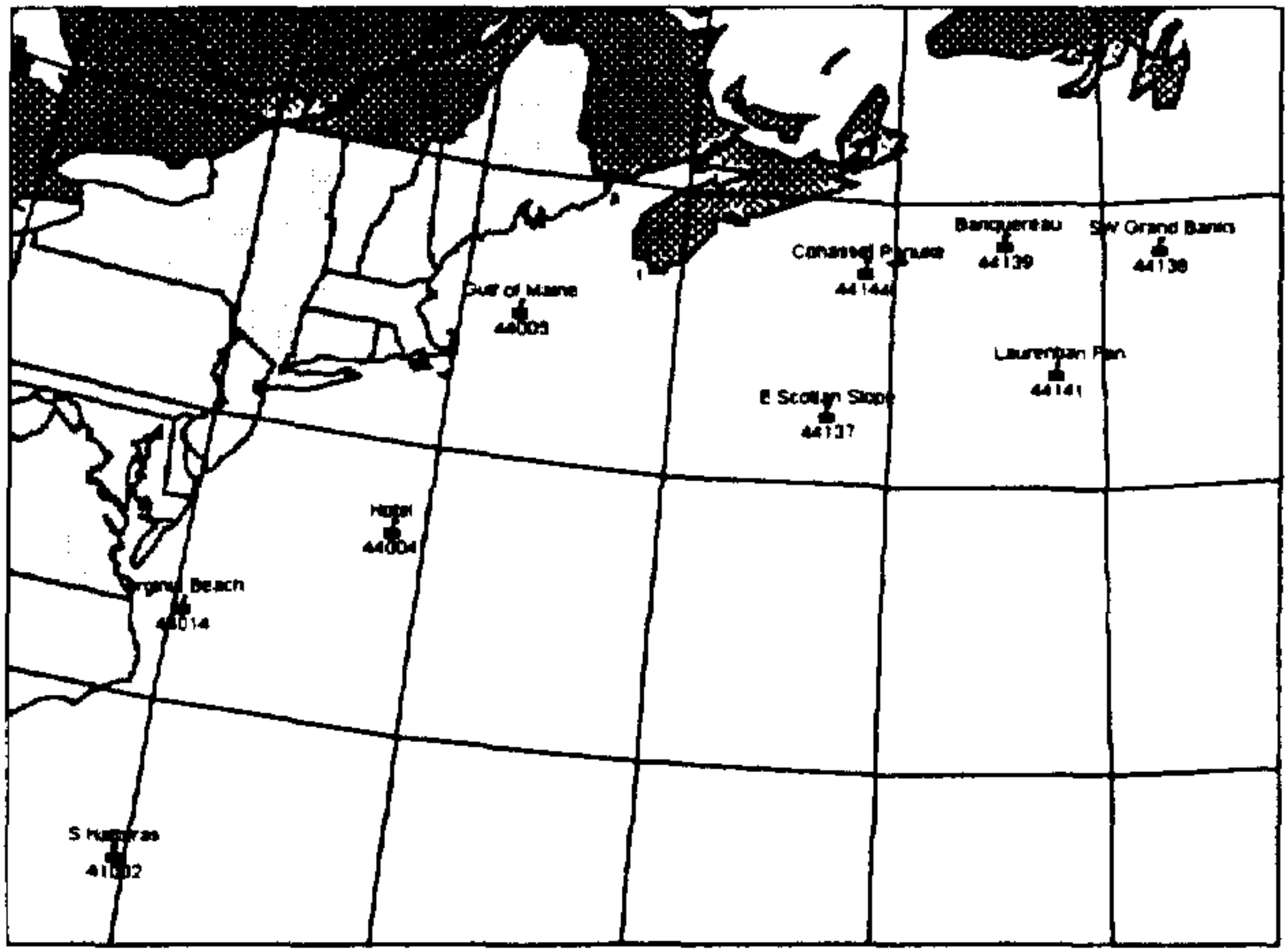

Figure 1. Station locations

Table 1. Station information

Station	Name	Depth (m)	Lat/Long
44137	E. Scotian Slope	4500	41.2/61.1
41002	S. Cape Hatteras	3658	32.3/75.2
44004	Hotel	3231	38.5/70.7
44139	Banquereau	1100	44.3/57.3
44141	Laurentian Fan	4500	42.0/56.1
44138	SW Grand Banks	1500	44.2/53.6
44005	Gulf of Maine	202	42.6/68.6
44014	Virginia Beach	48	36.6/74.8
44144	Cohasset Panuke	30	43.8/60.7

3. SYNOPTIC OVERVIEW

The low that would become known as the Storm of the Century (SOC) developed over unusually warm waters in the northwestern Gulf of Mexico on Friday March 12, 1993 (Walker, 1993). Over the 24 hours from 12 UTC 12 March to 12 UTC 13 March, the low deepened explosively from 1000 hPa to 972 hPa, as it moved east northeastward over the Gulf, across northern Florida, to Georgia. Huo et. al. (1995) document the synoptic evolution of the low and discuss the deepening mechanisms that contributed to its explosive development. These included tropopause depression latent heat release, weak static stability, jet streak-induced ageostrophic circulation, and surface sensible and latent heat fluxes. They describe the intensification of the warm front and cold front with a well developed squall line ahead of the cold front which was evident on satellite imagery by 00 UTC 13 March. A low-level jet developed ahead of the prefrontal squall line. By 12 UTC 13 March the cold front had moved east of Florida and the prefrontal squall line had spawned about 25 tornadoes as it swept across Florida.

At 00 UTC 14 March the low reached its lowest pressure of 963 hPa near Washington, DC while moving northeastward at 40 knots (Fig. 2). (Note, the FPA analysis shows 962 hPa as a result of final editing of the pressure gradient). Pronounced troughing extended northeastward from the low, and pressure falls of 18 hPa in 3 hours were observed north of the trough, out ahead of the low. A well defined warm front lay in the trough, extending northeast from the low out over the Atlantic. The cold front had advanced to the east and northeast at about 50 knots, and a line of thunderstorm cells was evident along the squall line from satellite imagery, moving northeast over the waters south of Cape Cod. Satellite imagery and upper air soundings indicate that the squall line was associated with an upper cold front, a feature related to tropopause depressions. A cut-off low had formed at 500 hPa and the jet at 250 hPa had strengthened to 163 knots and rotated around the base of the long wave trough, to lie downstream of it. Note that the boundary layer over the western Atlantic prior to the approach of the Storm of the Century had been destabilized by a cold outbreak behind another low centre that deepened to 984 hPa on March 12 as it tracked northeastward past Nova Scotia.

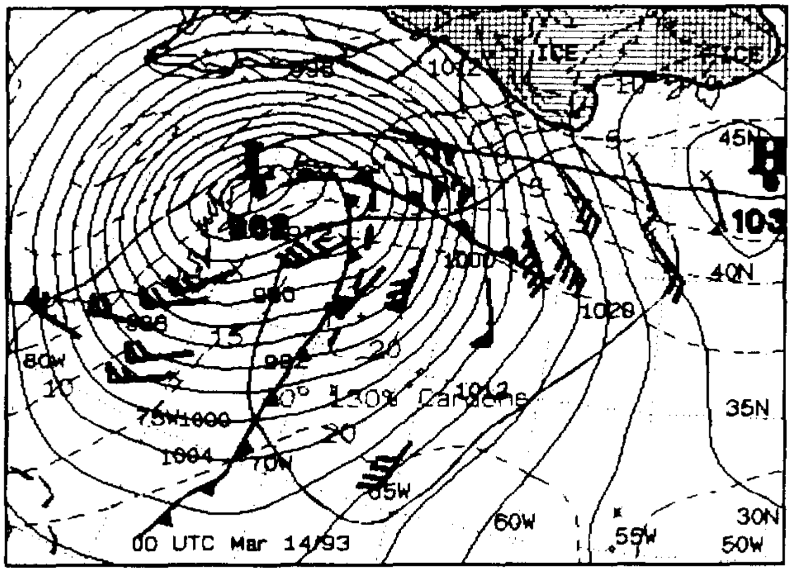

Figure 2. Edited analysis at 00 UTC 14 March 1993. Mean sea level pressure at intervals of 4 hPa, air temperature (dashed) at intervals of 5°C, and subjectively analyzed fronts. Edited modelled winds sampled at buoy/ship locations and wind edit areas superimposed.

The SOC low centre began filling slowly after 06 UTC 14 March. It continued to track rapidly northeastward, reaching the New Brunswick coast near 12 UTC 14 March (Fig. 3) and crossing the Gulf of St Lawrence by 00 UTC 15 March (Fig. 4). During this time the 250 hPa southwesterly jet strengthened further, to 175 knots. The cold front and squall line crossed the waters south of Nova Scotia and Newfoundland on March 14. Convection had weakened along the squall line, although the low level jet ahead of the squall line maintained its strength.

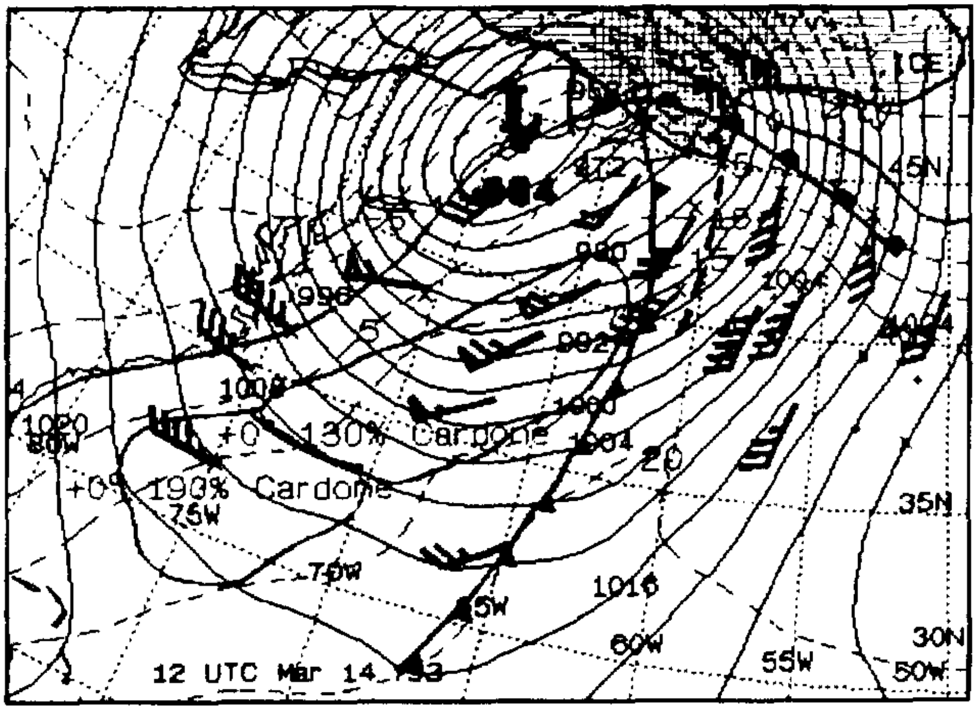

Figure 3. As in Fig. 2 but for 12 UTC 14 March 1993.

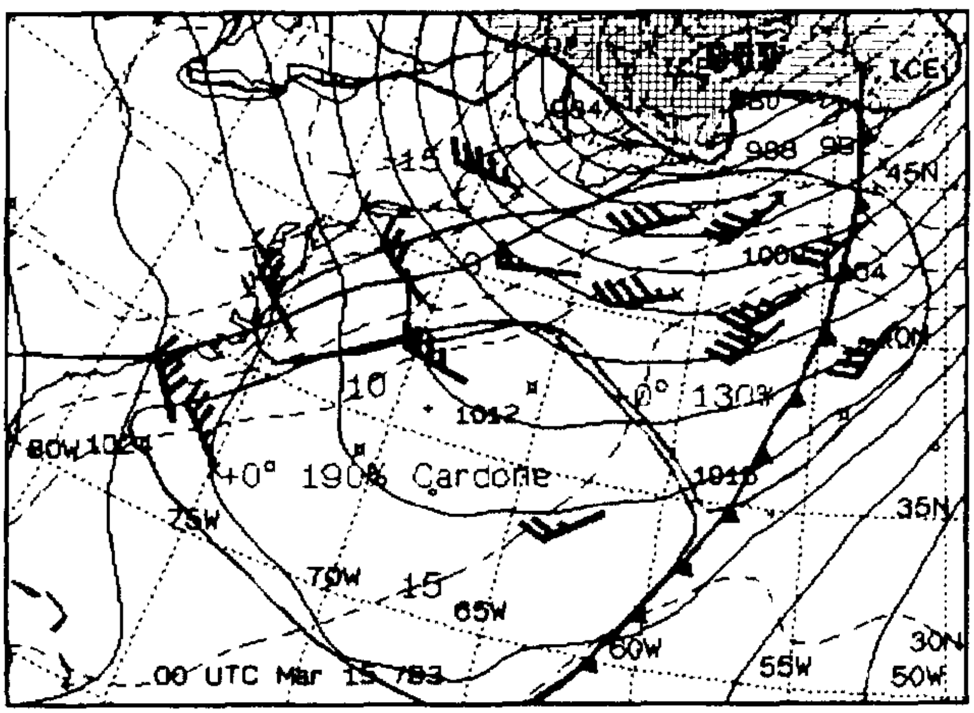

Figure 4. As in Fig. 2 but for 00 UTC 15 March 1993.

The approach of the squall line was evident at the buoys (see Figs 5 -11) by increasing temperatures and strong southeast winds, and rapidly failing pressures. The winds shifted to the south and diminished slightly with the passage of the squall line, and pressure levelled off. The cold front followed a few hours later, with rising pressures, winds veering to southwest and increasing, and rapidly falling air temperatures. Satellite imagery of the cold airmass over the warm waters off the U.S. coast showed streamers and deep open and closed cell convection, indicating a large degree of vertical mixing in the cold air behind the front.

On March 15 the cut off low at 500 hPa became absorbed into the general flow over southern Quebec, and the surface low pressure centre moved into Labrador, leaving a slowly weakening broad trough of low pressure back over the Maritimes and southward.

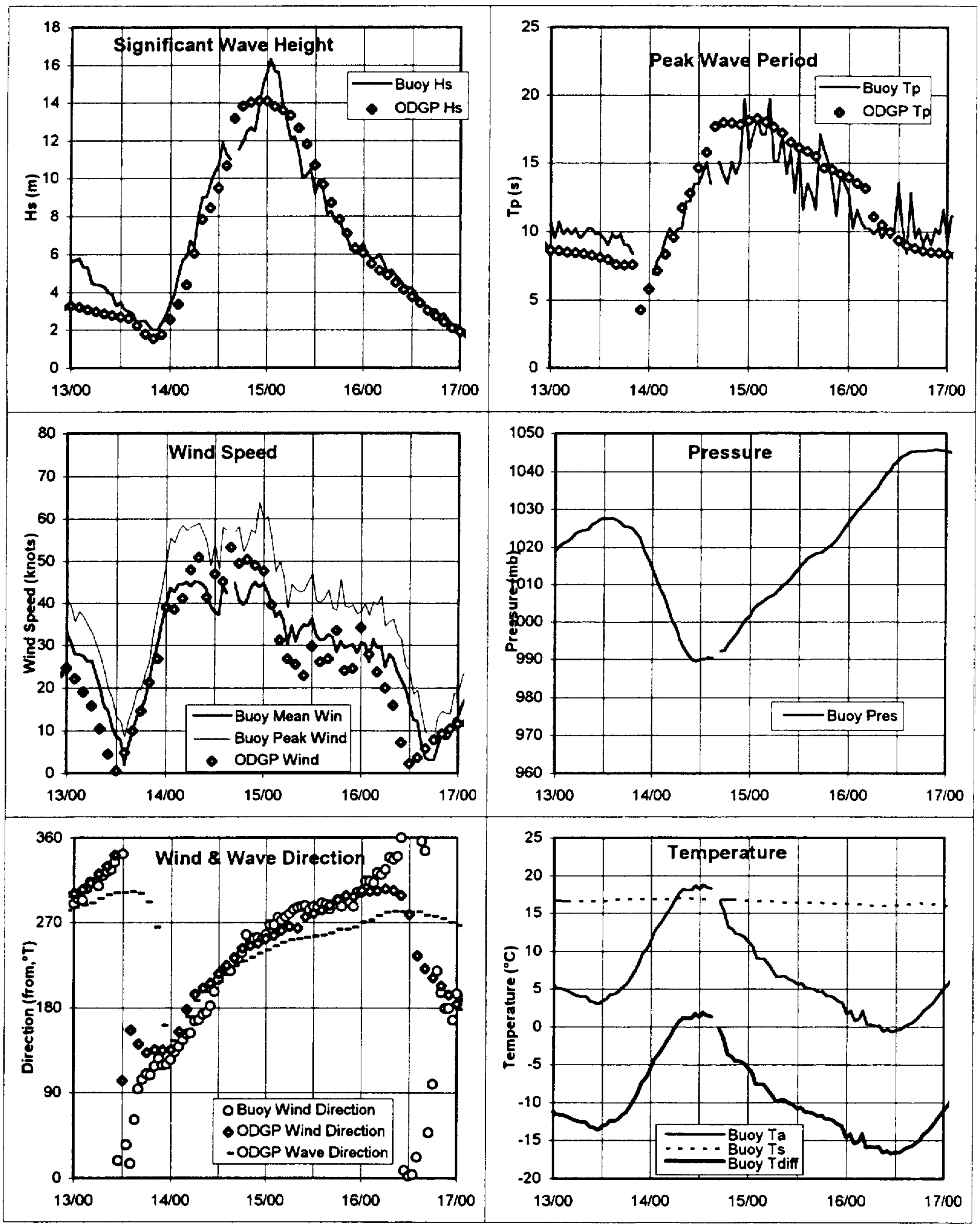

Figure 5. Buoy 44137 (E. Scotian Slope) measured and modelled (ODGP) data for 13-15 March 1993.

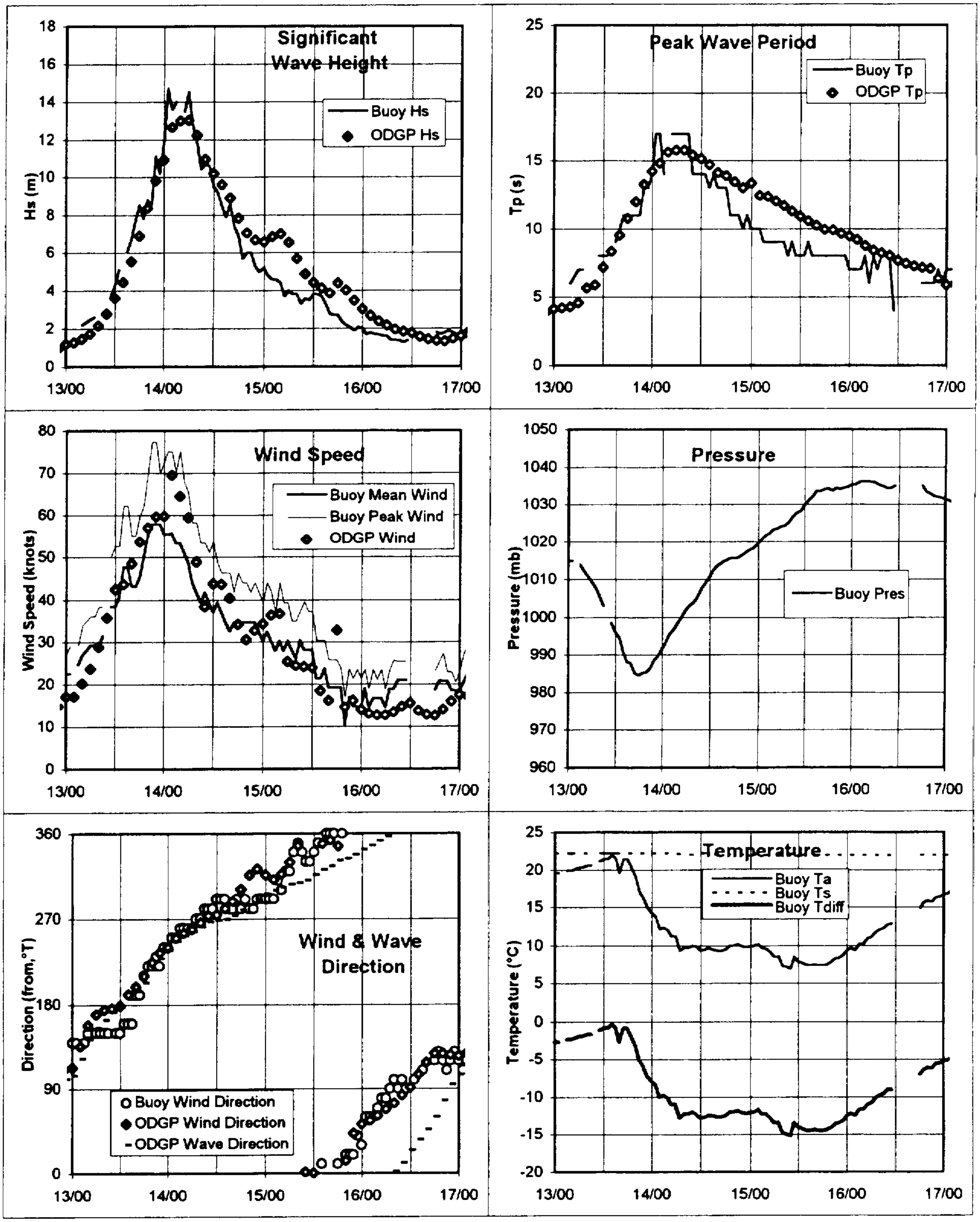

Figure 6. Buoy 41002 (S. Cape Hatteras) measured and modelled data for 13-17 March 1993.

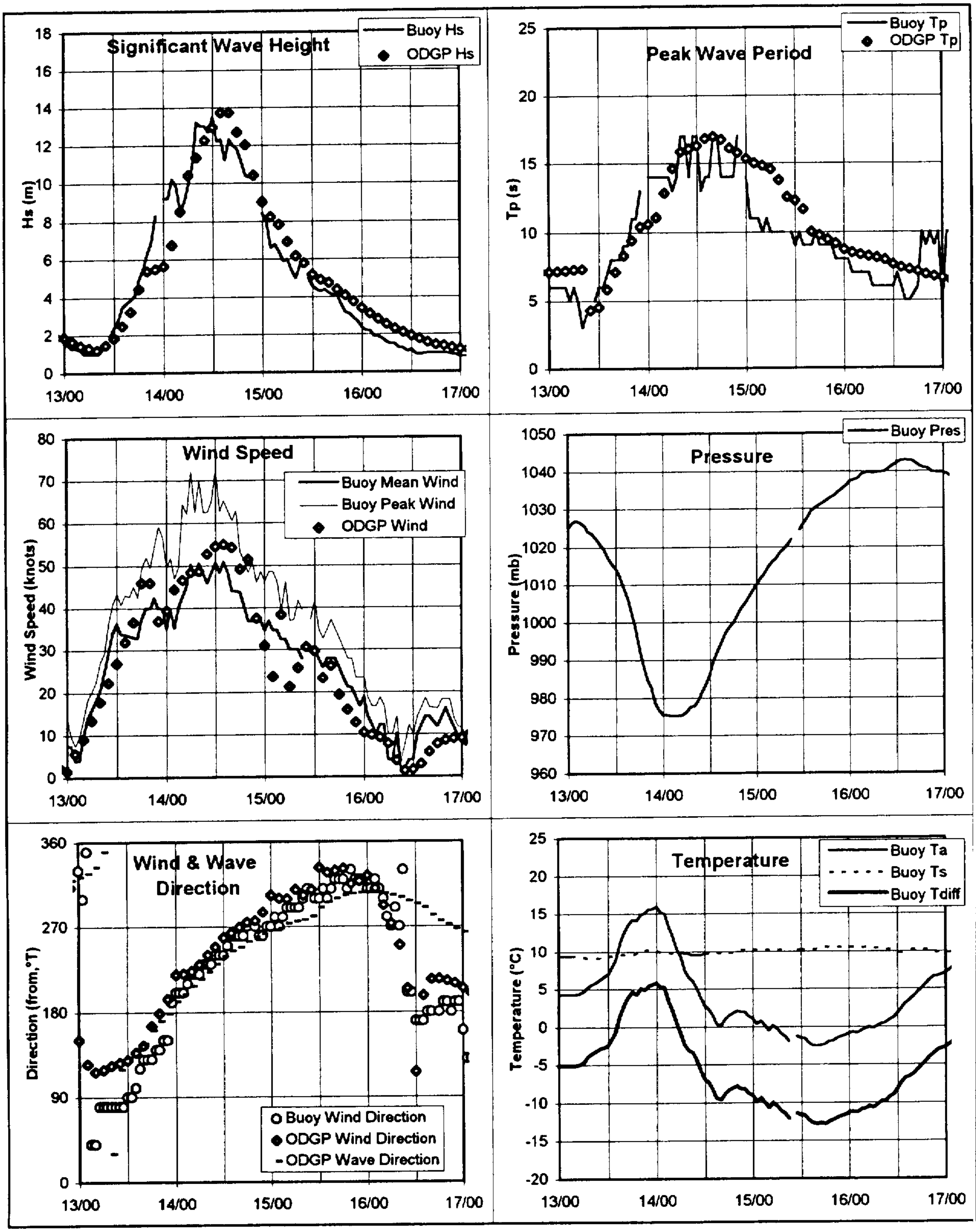

Figure 7. Buoy 44004 (Hotel) measured and modelled (ODGP) data for 13-17 March 1993.

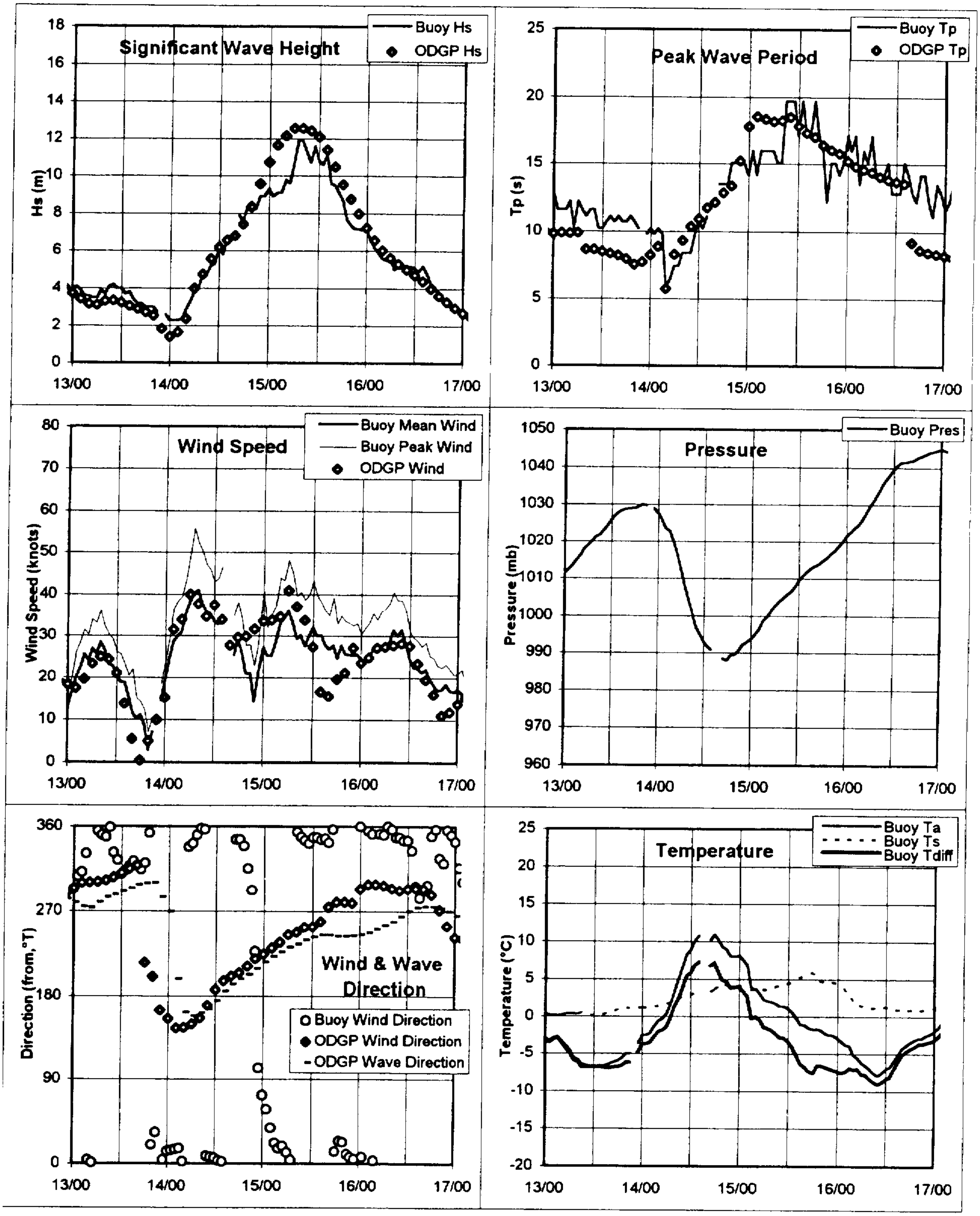

Figure 8. Buoy 44139 (Banquereau) measured and modelled (ODGP) data for 13-17 March 1993. Buoy wind direction bad.

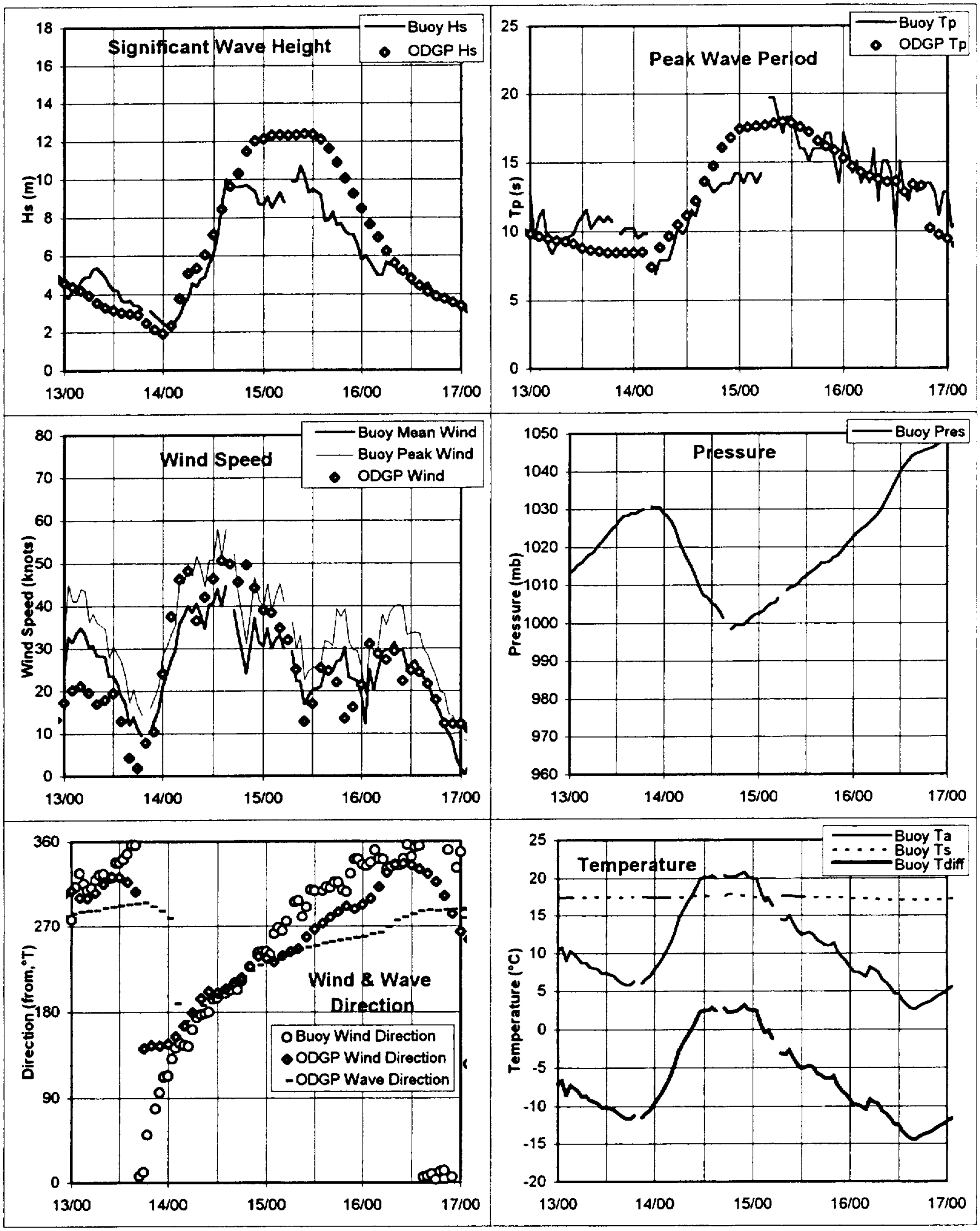

Figure 9. Buoy 44141(Laurentian Fan) measured and modelled (ODGP) data for 13-17 March 1993.

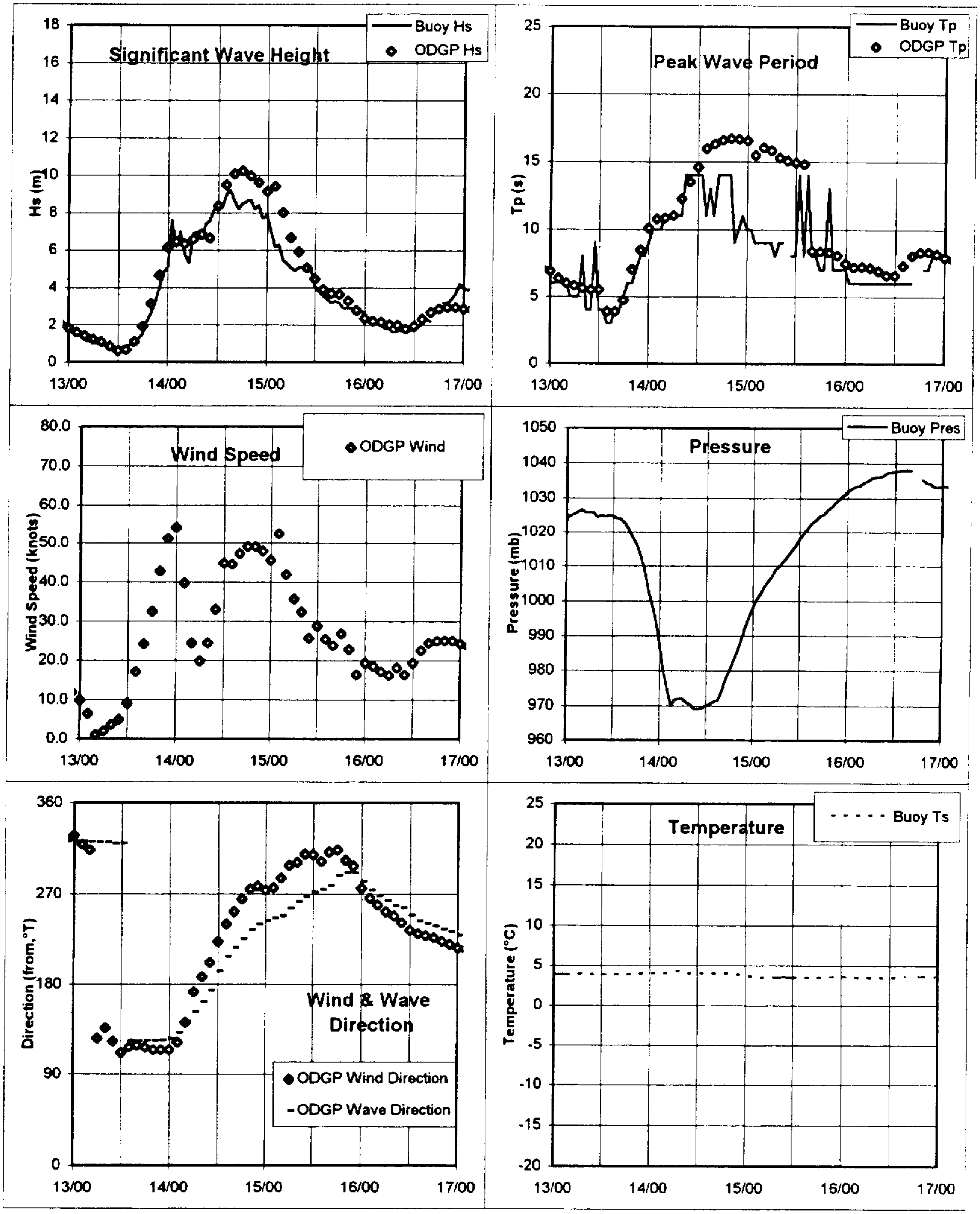

Figure 10. Buoy 44005 (Gulf of Maine) measured and modelled (ODGP) data for 13-17 March 1993. Buoy wind speed and direction and air temperature missing.

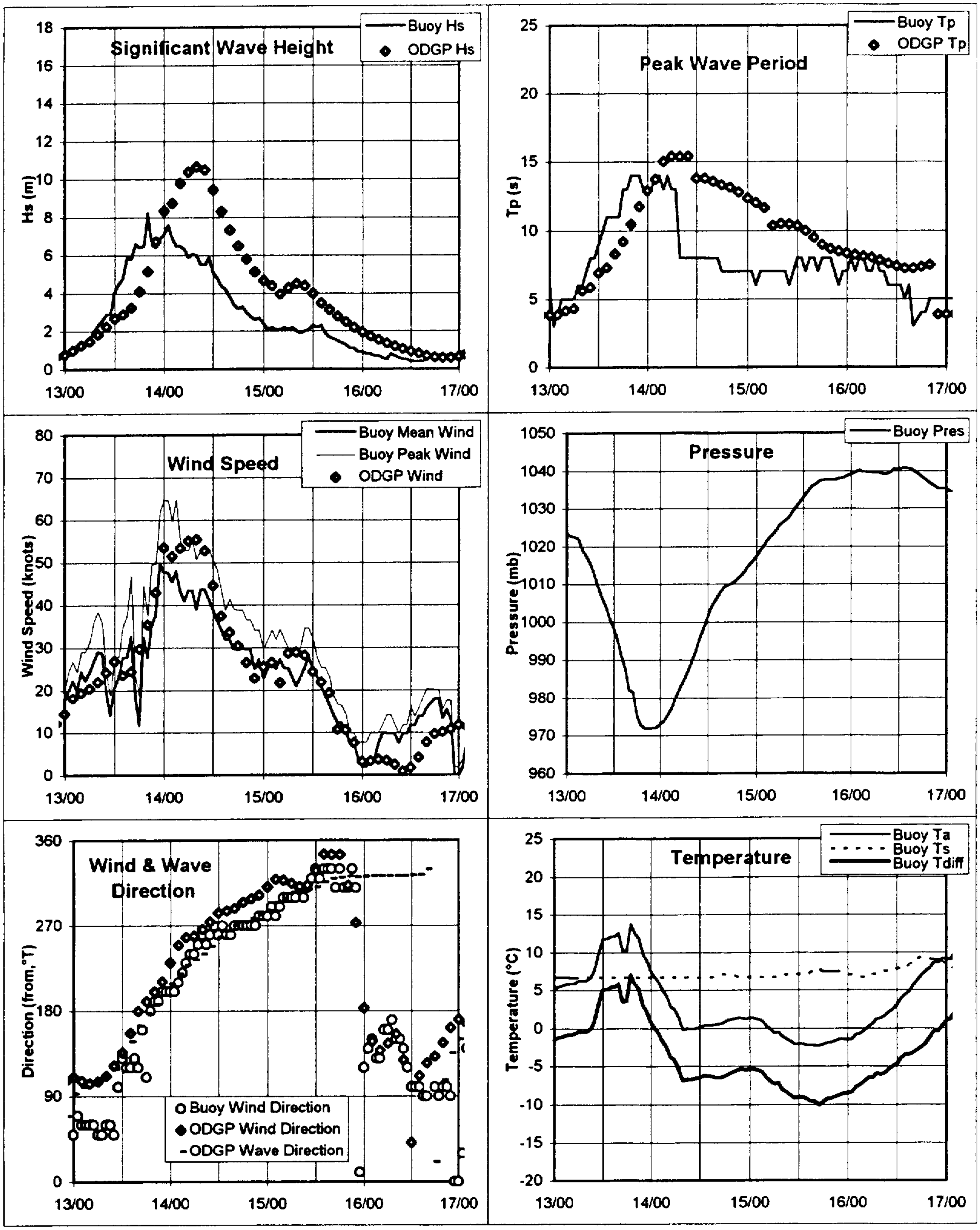

Figure 11. Buoy 44014 (Virginia Beach) measured and modelled (ODGP) data for 13-17 March 1993.

3.1 Winds north of the warm front

Easterly winds strengthened extremely quickly ahead of the advancing warm front. At 00 UTC 14 March, in the Gulf of Maine, ships reported 50 to 65 knot east winds, about 80% of the surface pressure gradient, with air temperatures colder than the water.. There was a low level jet of northeast to east winds located north of the low and warm front. Upper air soundings and the CMC chart of maximum winds in the low level indicate the jet increased in strength from about 45 knots at 5000 feet at 12 UTC 13 March, to about 85 knots at 4000 feet at 00 UTC 14 March, over the Gulf of Maine.

As the warm front continued northward over the Maritimes, early on March 14, gale to storm force easterlies developed over the Gulf of St. Lawrence. A downslope wind storm occurred on the west side of Cape Breton Island, where the station Grand Etang reported a gust of 114 knots.

3.2 Winds in the warm sector

Southeasterly gales south of the warm front, and ahead of the cold front, increased to storm force on March 13, over a large area of the western Atlantic. A narrow (about 100 km wide) band of 55 to 65 knot south to southeast winds were reported along the squall line. Most of these reports were estimates, from ships just north of the Gulf Stream or south of it, in neutral to unstable boundary layer conditions.

Upper air soundings and the CMC chart of maximum winds in the low level showed that an intense low level jet was associated with the squall line. At 12 UTC 13 March, the CMC chart showed a southerly jet of 80 knots southwest of Cape Hatteras, which verified well with the sounding. At 00 UTC 14 March, the jet was analysed with a 95 knot maximum, southeast of Cape Cod. A ship near the squall line, just south of Cape Cod at this time, reported gusts to 80 knots (measured) in the past three hours. At 12Z 14 March satellite imagery and surface observations indicate the squall line was just west of Sable Island. The upper air sounding from Sable Island showed a phenomenally strong low level jet of 104 knots, from the south southwest, at 3000 feet. On the CMC chart (Fig. 12) the jet was analysed in a north-south line just cast of Sable Island with a maximum of 95 knots.

The strongest wind reports from Sable Island prior to passage of the squall line were at 11 UTC, with south southeast 35 to 40 knots with gusts to 56. The boundary layer became more stable as the warm air moved further to the north, over the colder shelf waters off Nova Scotia and Newfoundland. By 00 UTC March 15 the jet had moved east of Newfoundland.

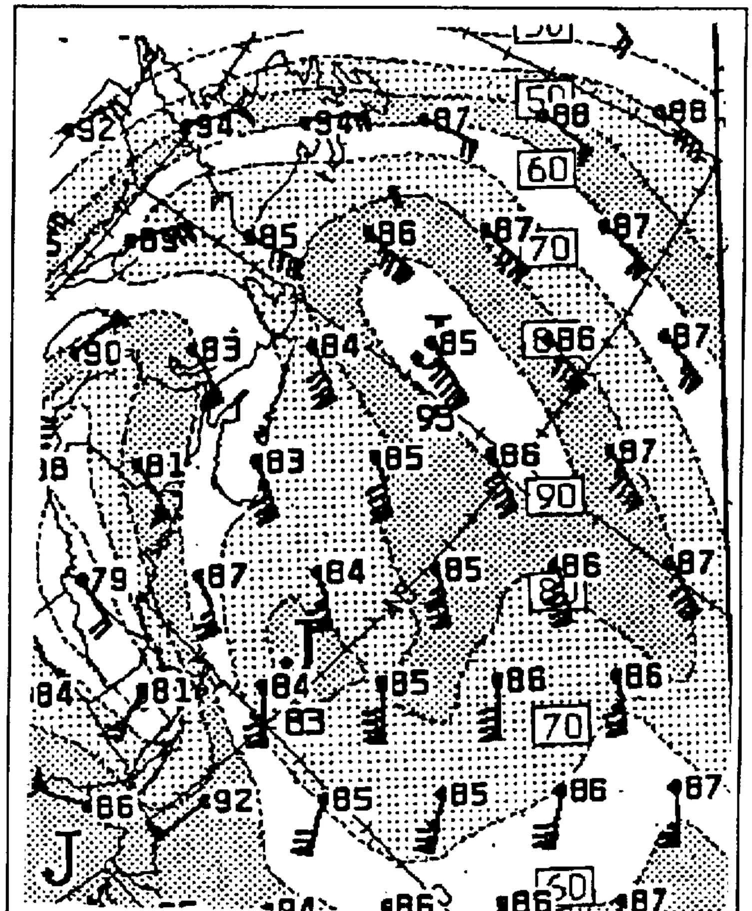

Fig. 12. CMC Max.winds in low level, 12 UTC 14 March 1993.

3.3 Winds behind the surface cold front

An intense southwesterly pressure gradient developed over a large area of Atlantic coastal waters behind the cold front on March 13 and 14. The boundary layer in the cold airmass became increasingly unstable, as air temperatures plummeted behind the cold front, dropping 15°C in 12 hours, and quickly became 5° C to 10°C colder than the water temperature. The band of strongest southwest winds was south of Cape Hatteras at 00 UTC 14 March, with ship reports of 55 to 60 knots, and one report of 70 knots (estimated) from the ship Providence Bay (GCSW), just south of Cape Hatteras, on the edge of the Gulf Stream. The air temperatures had dropped 8° prior to the observation to 10°C, and the water temperature was 19°C. Between 06 UTC 14 March and 18 UTC 14 March there were several ship reports of hurricane force winds (mostly estimates), in a band roughly 600 km long, aligned southwest to northeast, about 300 km wide, in the general vicinity of the Gulf Stream. Buoys 41002, 44014, and 44004 were on one side or the other (southeast or southwest) of the band of strongest ship reports, but reported lighter winds.

The CMC charts of maximum winds in the low level showed an area of strong southwesterlies, to the west of the intense prefrontal southerly jet (Fig. 12). The axis of the southwesterly jet was less well defined, as it lay in a broad fairly uniform area of strong winds. There appears to have been one main jet core with a second analysed only at 12 UTC 14 March (Fig. 12). From 00Z 14 March to 00Z 15 March, the southwesterly low level jet moved from southwest of Cape Hatteras, to southeast of Cape Cod, to just south of Newfoundland, following behind the cold front. The CMC charts showed maximum winds of 84 to 91 knots in this area. The presence of this low level jet was verified by the sounding at Cape Hatteras at 00Z 14 March, which measured a low level jet of 80 knot southwesterlies at 4000 feet.

Momentum from this strong southwesterly jet would have been transferred downward to surface, since the airmass was increasingly unstable, and vertical mixing would have been enhanced by the low wind shear. Increasingly colder air moved out over the warm waters of the Atlantic and over the very warm Gulf Strewn, and the flow was aligned from the southwest, through a large depth in the atmosphere.

3.4 Winds in the weakening pressure gradient behind the storm

The southwesterly gradient over the water behind the low and the cold front began to weaken over the southeastern U.S. around 12 UTC 14 March, south of about 35°N latitude. By 00 UTC 15 March the gradient had weakened over a larger area, to as far north as the latitude of Cape Cod, roughly, and by 12 UTC 15 March the pressure gradient was very weak in a broad trough of low pressure extending back over the Maritimes and southward. The boundary layer was unstable, with a cold airmass over warmer water. Winds at the surface became supergeostrophic as the gradient aloft remained fairly strong. Strong to gale force (25 to 40 knot) westerlies were reported at the surface. These winds were 100 to 200% stronger than the geostrophic wind. The CMC charts of maximum winds in the low levels show strong to gale force winds at a few thousand feet. It appears that vertical mixing was able to bring these stronger winds to the surface, despite the slack surface pressure gradient.

4. WIND AND WAVE HINDCAST

4.1 Hindcast Method

The hindcast procedure had three main steps 1) obtain surface pressure, air temperature, and sea temperature analysed fields from an NWP model, and edit the fields to fit subjective analyses, 2) run a wind modal to calculate winds from these fields, for input to the wave model, then correct the winds to get a better fit with observations, and 3) run the wave model. FPA (Forecast Production Assistant) version

3.8, installed on an HP 9000 755 series workstation, was used to perform the hindcast. The hindcast procedure was performed several times, with successive levels of editing of the pressure and wind fields, in order to improve the fit of hindcast pressure fields and winds to observations, and in that way to improve the hindcast wave results. The hindcast period was from 00 UTC March 11 to 12 UTC March 17.

The surface pressure, surface air temperature and sea surface temperature fields were obtained from the twice daily analysis fields from CMC's global model, on a grid of 2° latitude x 2° longitude, over an area covering the entire North Atlantic, in GRIB (GRIdded Binary) files. FPA uses a GRIB to spline conversion routine to extract the data then represent the data internally as a surface using cubic splines, An internal resolution ("knot spacing"), of 200 km was used. The fields are displayed as contoured analyses. The term "depiction" is used to refer to the display of data fields at each time.

The 12 hourly fields were interpolated to 2 hourly fields, to provide the information at the interval required by the wave model. In order to interpolate the fields, the user must provide trajectory information on important features, such as low pressure centres. This process is called "linking", where the user marks the position of the important features at each depiction time. The analysed fields at every main synoptic time (each 6 hours) were subjectively edited using graphical techniques to make the data fit better with observed data. Pressure fields were edited, but temperature fields were not.

The winds which were used to drive the wave model were calculated according to marine planetary boundary layer (MPBL) theory developed by Cardone (1969, 1978). FPA contained a graphical feature that allowed these winds to be subjectively editing prior to input to the wave model. The MPBL model uses surface pressure, air, and sea temperature to calculate the wind and adjust for stability. The winds are "effective neutral" winds, calculated at 19.5 m. These are winds that would produce the same surface stress on the sea surface in a neutrally stratified boundary layer as the wind speed in a boundary layer of a given stratification.

The wave model used was the first generation ODGP deep water spectral ocean wave model (Cardone et. al, 1976), configured for the north Atlantic. It runs with a two hour time step and a spectral resolution of 15 frequencies by 24 directions. The coarse grid spacing is 1.25° latitude x 2.5° longitude; the fine grid spacing is .625° latitude x 1.25° longitude. The fine grid covers Canadian waters and extends south to latitude 38.75°N. In the model, energy is transferred to and from the wave spectrum from energy input by the wind, and energy dissipation. The non-linear transfer of energy by wave-wave interaction is not explicitly included. Shallow water physical processes such as shoaling and refraction are not included in the version of ODGP used. The model can output data at specified grid points, corresponding to locations nearest the marine stations. This data was exported to a spreadsheet and plotted as time series for comparison with observations. The modelled wave data can also be used by FPA to prepare analyses of the hindcast wave height fields.

4.2 Pressure Fields in FPA

It was discovered that using many links on each depiction in FPA produced errors in some of the interpolated pressure fields. Without actually looking at each 2 hourly interpolated depiction, the errors only showed up as spurious low or high wind speeds on the time series of modelled winds, which were compared to buoy observations. In order to eliminate these problems, which usually appeared as spurious deep lows somewhere on the interpolated depiction, only minimal linking was done. The position of the storm's centre was the only link for most of the hindcast period.

FPA analysed pressure fields were edited by comparing the depictions to the subjective analyses from the Maritimes Weather Centre (MWC), Bedford, NS, and deepening centres and tightening gradients, etc., as necessary. The pressure fields were edited successively with more detail each time, and the model run each time to see how the results (hindcast winds and waves) improved. Most of the editing was quite minor. Comparing the results at buoy 44137 showed that the pressure fields editing produced relatively small improvements to the modelled winds and waves at that location.

The first wave model run was based on the original, unedited depictions. For the second m only pressure centres were edited. The low centre was deepened 1 hPa each at 00 UTC and 12 UTC 13 March and 3 hPa at 00 UTC 14 March. The position was shifted northeastward about 250 km at 00 UTC 14 March. Otherwise, changes to the low and high pressure centres were fairly minimal or were not needed. (Slightly larger changes were needed with a preliminary hindcast, which was using an internal grid spacing of 400 km: the low centre was deepened 3 hPa at 12 UTC 13 March and 6 hPa at 00 UTC 14 March.) Detailed editing of the pressure gradients was done on the next run, for each 12 hourly depiction, to improve location and sharpness of troughs, tightness of gradients, etc. For a third man additional editing of the pressure field was done to some of the 12 hourly depictions, to make small improvements to the gradient. Finally, the 6 hourly interpolated depictions were chocked and some small improvements to the gradient were made to some of those. The feature that needed the most editing was the troughing northeast of the low, on March 14.

4.3 Wind Fields in FPA

Once the editing of the hindcast pressure fields was complete, the objective MPBL winds were edited. Editing the modelled winds produced the biggest improvements to the hindcast waves, compared to editing the pressure field. For each 6 hourly depiction from 00 UTC 14 March to 18 UTC 15 March, the modelled wind was sampled at the locations of buoy and ship observations, and compared to the adjusted observations. For each sampled wind, the amount of correction, as a percentage of the original modelled wind speed, was determined. The modelled wind was compared to the adjusted peak buoy wind, since the mean buoy wind appeared to be too low in the high seas. The percentages at each sampled point were generalized to areas, which were drawn on the depictions (Figs. 24). Only one value (percentage) could be applied to each area, and the same value was used for the given area throughout the series of depictions. Only one or two edit areas per depiction were applied, and wind speeds only, not directions, were corrected. FPA applied the corrections to the 2 hourly fields by interpolating the edit areas on the 6 hourly depictions. Although the method of applying the corrections did not allow much detail, it had the advantage of being fairly quick. After running the wave model to assess the results, the wind editing was redone once, to make slight improvements to the winds, and thus to the resultant waves.

Sampling the objective MPBL modelled winds and comparing them to ship and buoy observations showed that the objective MPBL winds were significantly too light in some sectors of the storm. Therefore, the wind speeds were increased subjectively. The wind speed percentage correction for one area was 130%, i.e. modelled wind speeds at wave model grid points within the area were increased to 130% of their original value (increased by 30%). This area was generally over the intense south to southwest gradient both ahead of and behind the surface cold front. It covered a fairly large area from 00 UTC to 18 UTC 14 March, including the location of buoy 44137.

In the second area the modelled winds were increased to 190% of their original value. This area corresponded to the weakening pressure gradient in the wake of the storm, where observed winds became supergeostrophic. The 190% correction covered a small area south of Cape Hatteras at 12 UTC 14 March then the correction was applied to an increasingly larger area as the pressure gradient slackened over more of the western Atlantic. The 190% correction probably did not have much effect on the modelled waves which might have propagated into the area near the buoy 44137, based on the location of the correction area and the winds in that area. The 190% correction area was not applied to the area near buoy 41002, south of Cape Hatteras, where the second highest significant wave height of the storm was reported, until after the highest waves had already occurred.

5. WAVE FIELDS

5.1 Observations

Table 2. Largest measured and modelled significant wave height at each station.

Buoy	Measured Hs (m)	Modelled Hs (m)	Difference in Hs (m)	Time of Observation (day/hour)
44137	16.3	14.1	-2.2	15/01
41002	14.7	13.0	-1.7	14/01
44004	13.5	13.7	.24	14/12
44139	11.9	12.6	.65	15/08
44141	10.7	12.4	1.7	15/09
44138	9.9	11.7	1.8	15/13
44005	9.2	10.3	1.1	14/15
44014	8.2	10.7	2.5	13/20
44144	7.8	13.7	5.9	15/06

Waves built rapidly in the strengthening winds north of the warm front. The waves at the Gulf of Maine buoy, 44005, built to 7 to 8 metres in the easterlies ahead of the warm front by 00 UTC 14 March. They built to about 4 metres at buoy 44137 before the passage of the warm front which occurred shortly after 00 UTC 14 March. Waves in the warm sector continued to build rapidly, reaching 8 to 12 in the south to southeast winds. The waves continued to grow, after the passage of the cold front, and the highest wave heights were measured by the buoys in the cold airmass southwesterlies. Table 2 shows the largest significant wave heights at each station. Buoys 44137, 41002, and 44004 (Figs. 5 -7) measured the largest significant wave heights, with 16.3 m, 14.7 m, and 13.5 m. respectively, about six to twelve hours after the passage of the cold front. These buoys were within 200 km or so of the ships with the strongest winds speeds.

Further north and east, at buoys 44141 (Fig. 9), 44139 (Fig. 8), and 44138, the waves peaked at about 8; to 10 m in the warm sector southerlies, then diminished as the winds weakened. Winds at 44141 and 44138 diminished to 20 knots or less in the southwesterlies behind the cold front, as the low was further away by this time, but the waves increased again as swell arrived at the sites. At 44139, closer to the tight gradient behind the low, the winds increased to gale force, and waves were correspondingly higher. The arrival of the swell can be seen by the jump in peak wave period.

The stations 44014, 44005, and 44144 reported largest significant wave heights of 8 to 9 m in the storm, the lowest values of all the stations. Energy dissipation due to bottom friction was a factor. Water depths were only about 30 m and 48 m at rig 44144 and buoy

44014, respectively. Buoy 44005 was in water of about 200 m depth, but the long period waves travelling from the south southwest would have moved over depths of less than 100 m before reaching the buoy. Bottom friction would have begun to affect the waves in depths of less 225 m (half the wavelength of the 17 second period waves). Wang anti Mettlach (1992) noted the effect of bottom friction on 20 second waves generated by the northeasterlies of the 1991 Hallowe'en Storm at most nearshore U.S. buoys. Also. at buoy 44014, the fetch became increasingly limited as the winds veered from south to southwest in the cold airmass.

5.2 Evaluation of wave hindcast

The largest hindcast wave heights at each station are compared to the largest measured values in Table 2 . The wave model produced quite good results at several buoys, with differences between highest modelled and measured significant wave heights of less than a metre. At buoys 44137 and 41002, with the two largest significant wave reports of the storm, the modelled wave heights were about 2 m too low. At buys 44138 and 44141, where the highest waves were swell waves, arriving at the buoys when the winds had decreased. the highest modelled heights were almost 2 m too high this may indicate the modelled winds were increased over too large an area ahead of the warm front).

The effect of editing the wind fields was significant. The modelled winds were increased 30% from the objective modelled winds, primarily in the cold airmass, but also in the warm airmass over the wanner waters of the Gulf Stream and Sargasso Sea. Wind editing increased the largest modelled wave height at buoy 44137 from 10 m to 14 m. Prior to the correction to the winds, modelled winds at buoy 44137 were 5 to 10 knots lower than the mean wind for most of the 24 hours prior to the occurrence of the largest significant wave height. This is consistent with results from Thomas (1993) where large corrections to the objectively modelled winds were necessary in cold outbreaks over warm ocean waters. At buoy 44137, beginning about 6 hours before the 16.3 m wave was reported, the modelled winds were diminishing too quickly. This may explain why the hindcast was 2 m too low.

The error statistics for wave height (Table 3) show that when all the data are compared, the errors at buoy 44137 are not as pronounced as when just the highest significant wave is examined. The model results had a negative bias of about half a metre at buoy 44137. The bias at the other buoys was positive, ranging from fairly small values to about a metre at buoy 44014. The worst error statistics were for buoy 44014, with a very large scatter index (77%), compared to 14 to 32% at the other buoys. The modelled winds at buoy 44014 (Fig. 11) appear to have been too high, and that may, have contributed to the hindcast waves being too high. Statistics for rig 44144 were not calculated since observations were only 3 hourly by day, and missing at night.

Table 3. Significant wave height (Hs) statistics, for coincident observed and modelled data. 00 UTC 13 March to 00 UTC 17 March 1993.

Stn	Mean Obs. Hs (m)	Mean Model Hs (m)	Bias (m)	RMSE (m)	S.I. (%)	r
44137	6.8	6.4	-.43	1.1	16	.97
41002	5.2	5.6	.44	1.2	23	.96
44004	5.2	5.4	.20	1.2	23	.96
44139	5.9	6.1	.18	.94	14	.99
44141	5.8	6.7	.90	1.8	30	.95
44138	5.4	6.3	.89	1.7	32	.96
44005	4.0	4.4	.42	.89	22	.97
44014	2.8	3.9	1.1	2.2	77	.80

Table 4 shows error statistics for the peak wave period comparison over the course of the storm. Wave period was fairly well modelled. The largest scatter indices were at buoys 44005 and 44014, where the peak wave period diminished more quickly than the hindcast periods.

Table 4. Peak wave period (Tp) statistics, for coincident observed and modelled data, 00 UTC 13 March to 00 UTC 17 March 1993.

Stn	Mean Obsvd Tp(s)	Mean Model Tp(s)	Bias (s)	RMSE (s)	S.I. %	r
44137	11.9	12.0	.16	1.7	15	.91
41002	9.8	10.7	.93	1.8	19	.88
44004	9.7	10.6	.92	2.2	23	.85
44139	13.3	12.3	-.96	2.4	18	.82
44141	12.7	12.8	.07	1.9	15	.83
44138	12.3	12.8	.46	2.4	19	.76
44005	8.1	9.9	1.8	3.2	40	.77
44014	7.8	9.5	1.8	3.5	45	.52

The biggest difference between the observed and modelled wave height was at the rig 44144, where the modelled height was nearly 6 m higher than what was observed. Bottom friction as the long period waves travelled over the continental shelf probably reduced the waves at the site. This effect is not included in the wave model.

5.3 Comparison of largest wave heights with the estimated 100 year return wave heights

The largest significant wave height measured at buoy 44137 exceeded the estimated 100 year return value (Canadian Climate Centre, 1991) by 40%. However, at other Stations the wave heights were less than, or near to the 100 year climate extremes (Table 5).

Table 5. Largest observed significant wave heights compared to estimated 100 year return period sig. wave heights.

Station	Observed	Est. 100 yr.
44137	16.3	11.7
44139	11.9	11.3
44138	9.9	12.4
44005	9.2	10.1
44144	7.8	11.5

The estimated 100 year return period wave heights were based on hindcasts of the winds and waves of top ranked severe storms from 1957 to 1988. The extremal analysis was prepared for the wave model grid points on the Georges Bank, Scotian Shelf, and Grand Banks. The value for buoy 44137, outside the study area, was taken from the contour representation of the data. The same ODGP wave model as in the SOC hindcast was used. The winds were produced using the same objective MPBL model from pressure fields, then subjectively edited at each wave model grid point using available observations (from ships and drilling platforms) and streamline analyses. The values correspond to wave heights with a probability of occurrence in any one year of .01. For long period waves it was shown in the previous section that bottom friction on the continental shelf may play a role in diminishing the heights. Also, generally cooler water over the shelf would result in relatively lighter winds than over the Gulf Stream and waters southeast of it. Thus one would expect a higher extreme wave climate off the edge of the continental shelf, compared to over the shelf. The extreme wave climate results may be less applicable where buoy 44137 was located, as a result of these effects.

5.4 Hindcast wave height analyses

The hindcast wave height analyses are produced by FPA by fitting the gridded modelled waves to a 3-D surface over the entire map area (see Fig. 13 –15). At the coast, the wave contours spread inland because the surface must fit smoothly from the wave heights over the ocean to ”zero” heights over the land. A note of caution: when the long period high waves reach the shallower waters of the continental shelf, the hindcast analysed wave heights may be too high, as discussed in the previous section.

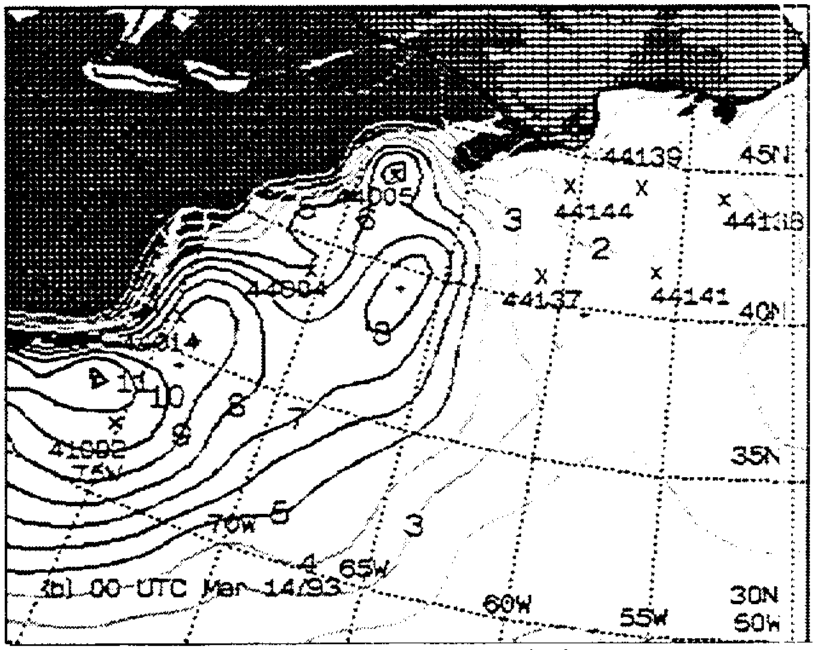

Figure 13. Hindcast wave height analysis for 00 UTC 14 March 1993. Ice covered water hatched. Buoy locations indicated by x.

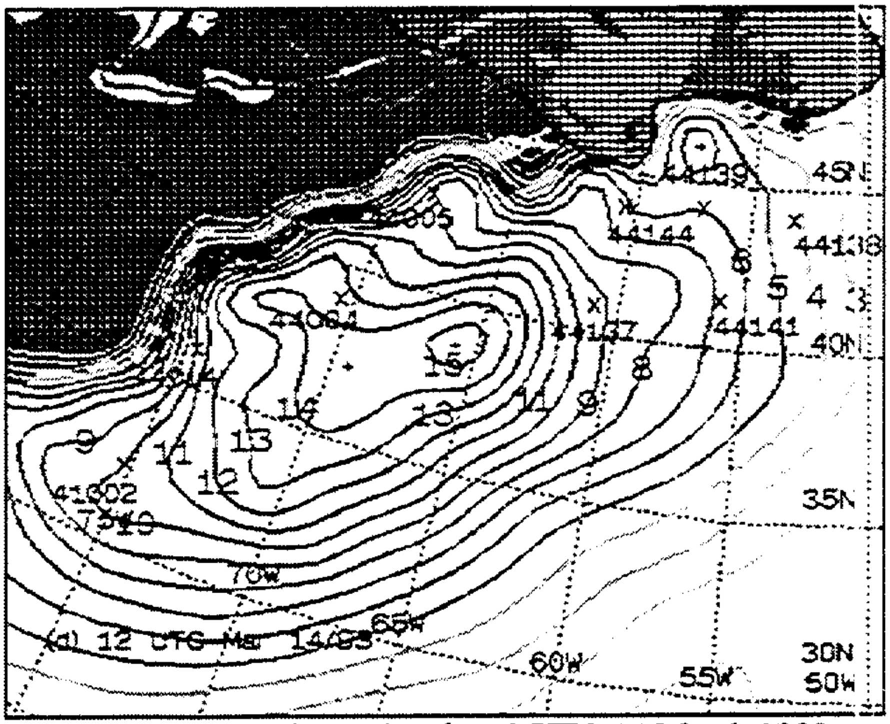

Figure 14. As in Fig. 13 but for 12 UTC 14 March 1993.

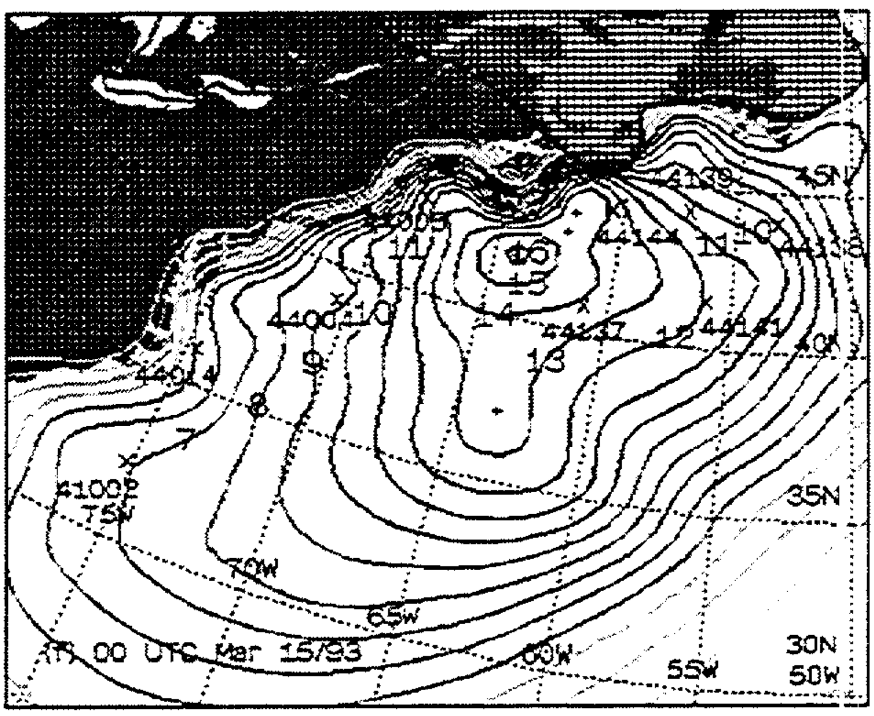

Figure 15. As in Fig. 13 but for 00 UTC 15 March 1993.

The analyses show waves building rapidly south of Cape Hatteras on March 13, reaching 11 to 12 m by 00 UTC 14 March. In another 6 hours there were at least 12 rn seas in an area roughly 1100 km long and 300 km wide.. The largest analysed wave heights of the storm occurred between 12 UTC 14 March and 00 UTC 15 March, with a large area of 14 m seas and a smaller area of 15 to 16 m seas. The analysed wave maximum is over the shallower waters of the continental shelf by 00 UTC 15 March, however, so the maximum height may be too high. Throughout the period from March 13 to 15, the wave maximum was located in the cold air behind the surface cold front. The wave maximum moved along an axis oriented southwest to northeast, in the general vicinity of the Gulf Stream and passing near but not over the buoys 41002, 44004, and 44137. After about 00 UTC 15 March, the analyses show the wave heights decreasing, as the area of high waves continues to propagate eastward. The swell actually decreased more rapidly after 00 UTC 15 March than shown (from the results at buoys 44141 and 44138).

The general pattern and values of the hindcast analysed wave heights agreed fairly well with the METOC analyses, particularly at 12 and 18 UTC 14 March with analysed maximum of 15 m. There are differences by 00 UTC 15 March, with the METOC analyses showing the wave maximum moving eastward, passing south of buoy 44137 rather than northwest, and remaining too high in the diminishing swell at the eastern buoys of 44141 and 44138.

The 00 hour analyses of the operational CSOWM showed waves considerably lower at 12 UTC 14 March than the hindcast waves and the METOC analysis, with waves of only 7 to 9 m, compared to 14 to 15 m. The winds used to drive the operational model were only about 45 knots in the area of the wave maximum, which would explain the lower wave heights. The operational model does move the maximum toward the northeast close to the Nova Scotia coast, at 00 UTC 15 March, as does the FPA hindcast, as opposed to the METOC analysis which shows the maximum much further east. However the CSOWM analysed wave height near the buoy 44137 was only about 8 m at 00 UTC 15 March, compared to the 15 to 16 m measured. Over the continental shelf measured wave heights were lower than offshore and the difference between measurements and the operations CSOWM was not as marked. For example at the Gulf of Maine buoy at 12 UTC 14 March and 00 UTC 15 March the measured wave heights and the CSOWM analysed wave heights were both about 8 m.

6. SUMMARY AND CONCLUSIONS

Winds and waves over the western Atlantic increased dramatically on March 13 and 14, 1993, during the Storm of the Century. There were hurricane force winds reported from all sectors of the low. The intense well defined southerly jet in low levels was associated with a squall line ahead of the cold front. The area of strong southwesterlies behind the cold front was quite broad, with the jet axis at low levels less well defined. The winds in all quadrants were very strong due to an intense pressure gradient around the low Centre, and unstable conditions near the surface, particularly near the Gulf

Stream, in the warm sector, and over all waters in the cold airmass. The southwesterly winds in the very cold airmass would have been enhanced by vertical mixing and downward momentum transport through a particularly deep layer, as the flow at all levels in the troposphere was very strong and aligned from the southwest.

Waves increased rapidly ahead of the warm front and in the warm sector, and continued to increase behind the cold front reaching the highest reported values, of 14 to 16 m at buoys near the Gulf Stream, in deep water off the edge of the continental shelf. The hindcast wave height analysis indicate that the exceptionally high waves covered a large area of the western Atlantic, with the maximum behind the cold front.

A wind and wave hindcast of the storm performed using the ODGP wave model and FPA software for display and editing of the fields, produced good results that verified well with the measurements from the buoys in most cases. At buoy 44137 the hindcast wave of 14.1 m compared fairly well with the measured 16.3 m. However the hindcast was very sensitive to editing of the input winds, which were increased by 30% over a large area, in order to improve the agreement with buoy and ship wind observations.

Measured wave heights during the most intense period of the storm were several metres lower at stations located on the continental shelf, compared to stations further offshore. The observations and model results suggest that bottom friction over the continental shelf, and limited fetch very near shore, in the southwesterlies, reduced the heights of the long period waves. Also, the offshore stations were located in or near warmer water, where increased instability would result in stronger winds.

The waves measured at buoy 44137, located in deep water off the edge of the continental shelf, just north of the Gulf Stream, exceeded the estimated 100 year return period wave height by 40%. However at other sites in or near Canadian waters the waves were less than, or in one case comparable to, the estimated climate extremes.

References

Canadian Climate Centre, 1991. Wind/wave hindcast extremes for the east coast of Canada, Volume I, Prepared under contract no. KM169-7-6678 by MacLaren Plansearch Ltd. and Oceanweather, Inc., 109 p. plus appendices.

Cardone, V.J., 1969. Specification of the wind field distribution in the marine boundary layer for wave forecasting. Report TR-69-1, Geophs. Sci. Lab., New York University.

Cardone, V.J., W. J. Pierson, E.G. Ward, 1976. Hindcasting the directional spectrum of hurricane generated waves. J of Petrol. Tech,, 28,385-394.

Cardone, V.J., 1978. Specification and prediction of the vector wind on the United States continental shelf for application to an oil slick trajectory forecast program. Final Report, Contract T-35430, NOAA, US. Dept. of Commerce, Silver Spring, Maryland.

de Lorenzis, B., 1988. Interactive graphics editor. Proc. of AMS 4th International Conference on Interactive Information and Processing Systems for Meteorology, Oceanography, and Hydrology, Feb. 1-5, 1988, Anaheim, CA. 143-145.

Desjardins, S., 1995. The Influence of sea surface temperature distribution on marine boundary layer winds. This publication.

Huo, Z., D-L. Zhang, J. Gyakum (1995). A diagnostic analysis of the superstorm of March 1993, Monthly Weather Review, 123, 1740-1761.

Paterson, R., B. de Loreratis, N. Driedger, E. Goldberg, B. Greaves, R. Trafford (1992). The Forecast Production Assistant, Fourth AES/CMOS Workshop on Operational Meteorology, Whistler, B.C., 15-18 Sept, 1992.

Swail, V.R., B. de Lorenzis, B., C. Doe, R. Bigio, C. Calnan, 1992. An inter-active graphics approach to wave analysis and forecasting, Proc. of 3rd International Workshop on Rave Hindcasting and Forecasting, May 19-22, 1992, Montreal, QB, 333-338.

Walker, N.D., 1993. A preliminary look at cyclogenesis in Gulf of Mexico during the March 1993 blizzard Mariners Weather Log, Spring 1993.

Wang, D. W-C., T. Mettlach, 1992.The Hallowe'en storm: data observations from NDBC stations. Supplement to Proc. of 3rd International Workshop on Wave Hindcasting and Forecasting, May 19-22, 1992, Montreal, QB, 71-88.

AN INTERACTIVE OBJECTIVE KINEMATIC ANALYSIS SYSTEM

A.T. Cox[1], J.A. Greenwood[1], V.J. Cardone[1] and V.R. Swail[2]

[1]Oceanweather Inc.
Cos Cob, CT

[2]Environment Canada
Downsview, Ontario

1. INTRODUCTION

The need for high-quality wind fields for ocean response models arises in hindcast studies of operational and extreme climate, in coastal and offshore structure design, and in forecasting for ocean platform operation and ships. Ocean response models such as the third generation (3G) wave model (WAM) and the Oceanweather's 3G wave model have shown great skill in producing nearly perfect hindcasts of significant wave height and peak period in severe tropical and extratropical systems when driven by high quality wind fields. The Surface Wave Dynamics (SWADE) study special Intense Observational Period (IOP) of the October 1990 US East coast event put several wind fields using both objectively derived and band-drawn man-intensive wind fields through a common wave model (WAM 3G). The results show (Cardone et.al., 1995) that the suite of hindcasts produced by very sophisticated purely objective analysis schemes was clearly beaten by hand-drawn kinematic analysis (Figure 1). Unfortunately, this man intensive, tediously produced analysis took approximately 100 man-hours to produce a 10 day hindcast, which is a time frame clearly inapplicable to long term hindcast studies and forecasting applications.

The Interactive Objective Analysis (IOKA) system was developed al Oceanweather to combine the advantages of manual analysis both shown during SWADE study and emphasized by Sanders (1990) and Uccellim et al. (1992), with the speed of a purely objective analysis scheme in deriving high quality marine surface winds, Using the SWADE winds as a control, Oceanweather first developed the objective analysis algorithm, Seidel, for the express purpose of analyzing wind fields. The interactive part of IOKA consisted of manual editing/deleting of wind inputs in ASCII format. This procedure worked well in SEAMOS (Southeast Asia Meteorological and Oceanographic Hindcast Study) where ships, typhoon model output winds and a background climatology wind fields were combined using Seidel to achieve high quality wind fields for some 200 typhoons and monsoons. While the procedure was considerably faster that manual-kinematic analysis and yielded better results than running pure typhoon winds by including observations, the system needed a final component: an interactive graphical workstation. The Wind WorkStation was developed to allow the user to display and manipulate the wind inputs to Seidel. This work station is already used operationally in Oceanweather's global 7-day wind/wave forecasting service and has been used in several hindcast studies, the most recent being the addition of 10 storms to the Canadian Climate Center (CCC) East Coast Storm Study (CCC, 1991; see also Swail et. al., 1995). This paper will present the steps involved in the IOKA process, and describe the development and use of a graphical Wind WorkStation.

2. INTERACTIVE OBJECTIVE KINEMATIC ANALYSIS

2.1 Overview

The heart of the IOKA system is the graphical interface known as the Wind WorkStation (WWS). The WWS is an analyst-friendly MS Windows based program (version 3.1, Windows 95 or Windows NT) which allows the analyst to view and manipulate wind inputs for the objective analysis algorithm. The display is very flexible and allows the user to both scroll and use a true zoom capability (the wind barbs are redrawn to the best possible resolution) to display any region of the basin. The analyst may also customize the wind inputs displayed by the WWS to plot optional information such as Significant Wave Height, Peak Period, Surface Pressure and Station/Call Sign Identification, and may display any or none of the wind inputs (useful for a final check of the analyzed wind field). A selectable latitude/longitude grid may be displayed with the data, and the final objective analysis wind field can be displayed from every barb to every 4th barb according to the user's preference. The program also supports printing on a true Mercator projection with a fine resolution digitized coastline,

The WWS can be set up very easily in any basin, and supports any latitude/longitude grid which is a sub-multiple of 2.5 degrees down to .25 degrees. The latitude and longitude grid spacing need not be identical. which is very useful in northern latitudes where less resolution in longitude is desirable for computational speed considerations. Currently, the objective analysis algorithm, Seidel, supports up to 200 by 200 parallel grid (a 30 by 30 degree latitude/longitude area with a .25 degree resolution, 300 by 300 degree area at 2.5 degree resolution) although this limit can be easily increased should the need ever arise. Typically, grids between 60 and 70 parallels square arc used as a trade-off between resolution and computational speed. The basic objective analysis method follows the approach of Ooyama (1987) ky fitting quadratic forms to the velocity components and wind speed separately, minimizing the differences between the analysis and the observations in the least-squared sense:

$$\sum_{k=1}^{n} \mathbf{wt}_k \sum (F_k - F_{int})^2 + \beta \left[\sum \left(\frac{\Delta F}{\Delta X}\right)^2 + \sum \left(\frac{\Delta F}{\Delta Y}\right)^2 \right]$$

where wt_k is the weight assigned to the inputs of class k; F_k is a measurement of class k, F_{int} is the analysis value at the location of the measurement, and ß is a scale factor which is used to achieve the desired level of smoothing. The fitted velocity components arc used to recover the wind direction only, the wind speed is directly analyzed (Cardone, et, al. 1993, see also Cardone and Grant, 1994).

The WWS uses a flexible storm database file to contain all wind inputs and output (objectively analyzed) winds. This provides a single source file for a particular storm/hindcast period and is very convenient for archiving purposes, The WWS makes no assumptions as to the length of a particular hindcast (though the storm database file can grow rather large) and more importantly imposes no restrictions on the time difference between maps. For instance. maps can be analyzed every 12 hours for a spin-up period, every 6 hours during the initial stages of a storm, then every 3 hours during the intense period. The resulting wind fields can then be time-interpolated to the desired time step for input into a wave model. This flexibility greatly decreases the time the analyst needs to spend on spin-up periods and greatly enhances his/her ability to do a fine time step analysis during the storm peaks. This is also very useful for long term operational climate studies where long periods of inactivity can be hindcast with a larger time step and important storm events can use a shorter time step.

2.2 Meteorological Inputs

The first stage in the IOKA system is the preprocessing of meteorological inputs. Typically wind observations from buoys, ships, off-shore platforms, coastal manned stations (CMANS), cloud track winds, well exposed land stations and satellite-derived scatterometer winds are used in the analysis of the marine wind field. The WWS places no restrictions on the number of types of data, or the inclusion of other types of data. Typically a pressure-derived background wind field is also used, although this is optional if the data density is significantly fine (grid spacing dependent). The inclusion of other wind fields such as typhoon model output for tropical locations is also commonly done. All data to be brought into the WWS is first adjusted for stability and brought to a common reference level, typically 20 meters, following the methodology developed by Cardone (1969; see also Cardone et. al., 1990). Standard buoy wind measurements (usually 5 to 10 minute averages) are temporally smoothed to effective hourly averages. Averaging is done on meridional and zonal wind components of the wind to calculate the wind direction, and on scalar wind speed to recover the average wind speed. Buoy wind speeds derived by the ”vector averaging” method are inflated to effective ”scalar-averaged” using the empirical relationship described by Gilhousen (1987). Asynoptic observations can be optionally repositioned to on-hour locations via moving centers relocation, which is essentially similar to the procedure that relocates aircraft flight level winds to a moving vortex. Asynoptic observations can also be included without moving centers by giving them a lower weight in the objective analysis scheme, and signifying to the analyst that it is an asynoptic observation and should be given extra scrutiny to determine its representativeness in the wind field. All wind inputs are put into the WWS input format, so-called ‘uvw’ file, and brought in the WorkStation storm database. Weights can be assigned to each type of wind input; common wind inputs such as buoys, ships, scatterometer winds, CMAN stations, typhoon model input and background pressure-derived winds can be assigned default weights in the objective analysis scheme which were determined by Oceanweather to be representative of the wind’s reliability. Typically, buoys get a very high weight, while ships get lower weight in the objective analysis scheme. The analyst can also over-ride these standard default weights, if they are deemed inappropriate for a certain data type. Types of winds are also assigned standard colors (although these can be customized for individual preference and display types), which is very useful for the analyst when all the data is plotted on the screen.

2.3 Interactivity with the Wind WorkStation

Once the wind data is incorporated into the WorkStation, it is displayed as color-coded wind barbs (by type) over a coastline map on an xy plot projection. The wind field can be viewed as a full basin, or zoomed and scrolled to display any section. The analyst can ‘point and click’ on any wind observation to bring up a text box which displays the latitude, longitude, wind speed, wind direction and station identification of the wind observation and its neighbors. The analyst has the ability to delete individual wind observations, deleted data, displayed in a light blue color, can be undeleted if the analyst changes his/her mind. Usually quality control of the wind inputs is done at this step, although automatic quality control can be performed in the preprocessing step before bringing the winds into the WWS. The analyst typically uses the background wind field, handdrawn pressure charts, continuity analysis and other sources to determine the quality and reliability of each piece of data.

The most important feature of the WWS is the ability to add highly weighted Kinematic Control Points (KCP) to the wind analysis. This is the analyst's most powerful tool in shaping the resulting wind field. With the KCP, the analyst can input and define the fine-scale frontal features, and add and maintain jet streaks and other features which have proven to be very important in extreme storm seas (ESS) and are often missed by purely objective methods. The analyst can use KCPs to define data-sparse areas using continuity analysis, satellite interpretation, climatology of developing systems and other analysis tools. Winds can be run (put through the objective analysis) on an individual map for instant feedback to the analyst, or run for the entire length of the storm. When the winds are run interactively (one map at a time) the analyst has the ability to add KCP points, run the winds, analyze the changes reflected in the final winds, and either make more changes or accept the winds as final. This interactivity greatly enhances the analyst's ability to make changes to the wind field and boosts his/her confidence in the final wind product.

2.4 Export and Interpolation of the Wind Field

Once the final wind field is run through the objective analysis scheme and accepted by the analyst, the final winds can then be exported from the storm file database. If the output of the WWS is not at a regular time step, or if a finer time step is required, a general time interpolation program, TIME_INTERP, is used. This program can produce time interpolated wind fields on any time step, and can be optionally used with a file of moving centers to help preserve features in the interpolated maps. Output of the time interpolator can be sent directly into a matching grid wave model, or put though a separate spatial interpolation program, WIND2WAVEGRID, which can place the winds onto any target wave model grid.

3. APPLICATION IN THE CCC EAST COAST STORM UPDATE STUDY

The IOKA system is currently being implemented in the addition of 10 recent storms to the CCC East Coast storm population. The previous 68 storms were hindcast using the same hand-drawn kinematic analysis technique that was proven to give high quality winds in the SWADE study. In this update study, the WWS was set up on a area from 22.5°N to 77.5°N and 82.5°W to 0°E. Grid spacing was selected to be 1.25° in longitude and .8333° in latitude, resulting in a 4489 grid point wind grid (Figure 4). A three-hour time step was selected to do the wind analysis this is also the time step of the wave model. Winds were spatially interpolated to the CSOWM (Canadian Spectral Ocean Wave Model) wave grid (Khandekar et. al., 1994) using the WIND2WAVEGRID utility.

Wind inputs for the 10 update storms include US and Canadian buoys, ships and CMAN stations. All data inputs are adjusted for height and stability to 20 meters neutral. The buoy observations are temporally smoothed to effective hourly averages. Asynoptic data are not currently being used in this study. The background field used for this study is the ECMWF wind analysis for storms through 1994, and Oceanweather's wind analysis from its real-time global forecast for the February and April 1995 storms. Both background wind fields are on 2.5 by 2.5 degree grids, and both have had real-time observations already blended into the wind fields. However, Oceanweather's global winds have gone through the IOKA process and have had some analyst interaction in a forecast mode.

Initial work on the April 1995 event has shown the WWS to be a time-saving tool in the analysis of the winds. The analyst was able to complete the analysis of the wind field in less time, due to the ability to view all the input and output winds together on one display, and the ability to run winds interactively to achieve a final wind product. Further significant time savings were also achieved by not having to manually grid and enter a kinematic winds fields by hand, which had been done in previous hindcasts. While some kinematic sketches were done on printouts of the wind field, most work was done directly on the WWS. Time histories (Figure 5) at two Canadian buoys (44138 and 44141) show good agreement between the measured significant wave height and the hindcast wave heights using the CSOWM 3G shallow wave model. These wave time histories are equivalent to those expected with hand-drawn kinematic analysis.

4. SUMMARY AND FUTURE DEVELOPMENT

IOKA system has proven to be an effective and time-saving tool for the analysis of marine surface winds. It successfully blends the man-intensive kinematic analysis with the speed of a purely objective analysis. The development of the graphical Wind WorkStation has increased both the efficiency with which an analyst can produce a final wind field, and the analyst's confidence in the final wind fields delivered to the wave model. Additional tools such as the general time interpolation and spatial interpolation routines have allowed the analyst to use flexible intervals between maps, and easily port the wind output to any target grid.

Development of and improvements to the Wind WorkStation continue almost on a daily basis, owing to the number of current hindcasting and forecasting studies the system is being used on. As the system is applied to different basins, both tropical and extratropical, the need for new tools arises and most users' requests have already been implemented into the current system. Areas of future development include: the addition of a manipulative moving-centers table in the WWS which can used for repositioning of asynoptic data as well as in the time interpolation of wind fields; addition of continuity tools which would better allow the user to track and smooth such weather features as fronts, troughs, ridges, and jet streaks; looping of final wind fields in a movie sequence for final check of the continuity of the wind fields; and contouring of the final wind fields.

5. REFERENCES

Canadian Climate Center, 1991. Wind wave hindcast extremes for the east coast of Canada, Volume 1. Prepared under contract no, KM169-6-6678 by MacLaren Plansearch Ltd., Halifax, N.S., and Oceanweather Inc., Cos Cob, CT 109p. plus appendices.

Cardone, V.J., 1969. Specification of the wind distribution in the marine boundary layer for wave forecasting, Report TR-69-01, Geophys. Sciences Lab., Neu, York University, 137pp. (Available from NTIS: Order AD 702 490).

Cardone, V.J., J.A. Greenwood, and M.A. Cane, 1990. On trends in historical marine wind data. J. of Climate, 3. 113-127.

Cardone, V.J., J.A. Greenwood, 1993. Final Report: Development and Initial Test Against SWADE of an Interactive Objective Kinematic Analysis Program for Marine Surface Wind Field Analysis. Submitted to U.S. Army Engineer Waterways Experiment Station.

Cardone, V.J, H.C. Graber, R.E. Jensen, S. Hasselmann, and M.J. Caruso, 1995, In Search of the True Surface Wind Field in SWADE 10P-I: Ocean Wave Modeling Perspective. Accepted July 10, 1995 to Global Atmo. and Ocean Sys.

Cardone, V.J., and C.K. Grant, 1994. Southeast Asia Meteorological and Oceanographic Hindcast Study. Offshore Southeast Asia 10th Conference and Exhibition. 6-9 December, Singapore.

Cardone, V. J., and V.R. Swail 1995. Uncertainty in Prediction of Extreme Storm Seas (ESS). Fourth International Workshop on Wave Hindcasting and Forecasting. October 16-20, 1995. Banff, Alberta, Canada,

Khandekar, M.L., R. Laftharry and V.J. Cardone, 1994. The performance of the Canadian spectral ocean wave model (CSOWM) during the Grand Banks ERS-I SAR wave spectra validation experiment. Atmosphere-Ocean, 32. 31-60.

Gilhousen, D. B., 1987 A field evaluation of NDBC moored buoy winds. J. Atmos. Ocean. Tech., 4, 94-104.

Sanders, F., 1990. Surface weather analysis over the oceans - Searching for the sea truth. Wea. Forecasting, 5, 596-612.

Swail, V.R., M.J. Parsons, B.T. Callahan and V.J. Cardone, 1995. A revised extreme wave climatology for the east coast of Canada. Fourth International Workshop on Wave Hindcasting and Forecasting. October 16-20, 1995. Banff, Alberta, Canada.

Uccellini, L.W., S.F. Corfidi, N.W. Junker, P.J. Kocin, and D.A. Olson, 1992. Report on the Surface Analysis Workshop held at the National Meteorological Center, 25-28 March, 1991. Bull. Amer. Meteor. Soc., 73, 495-472.

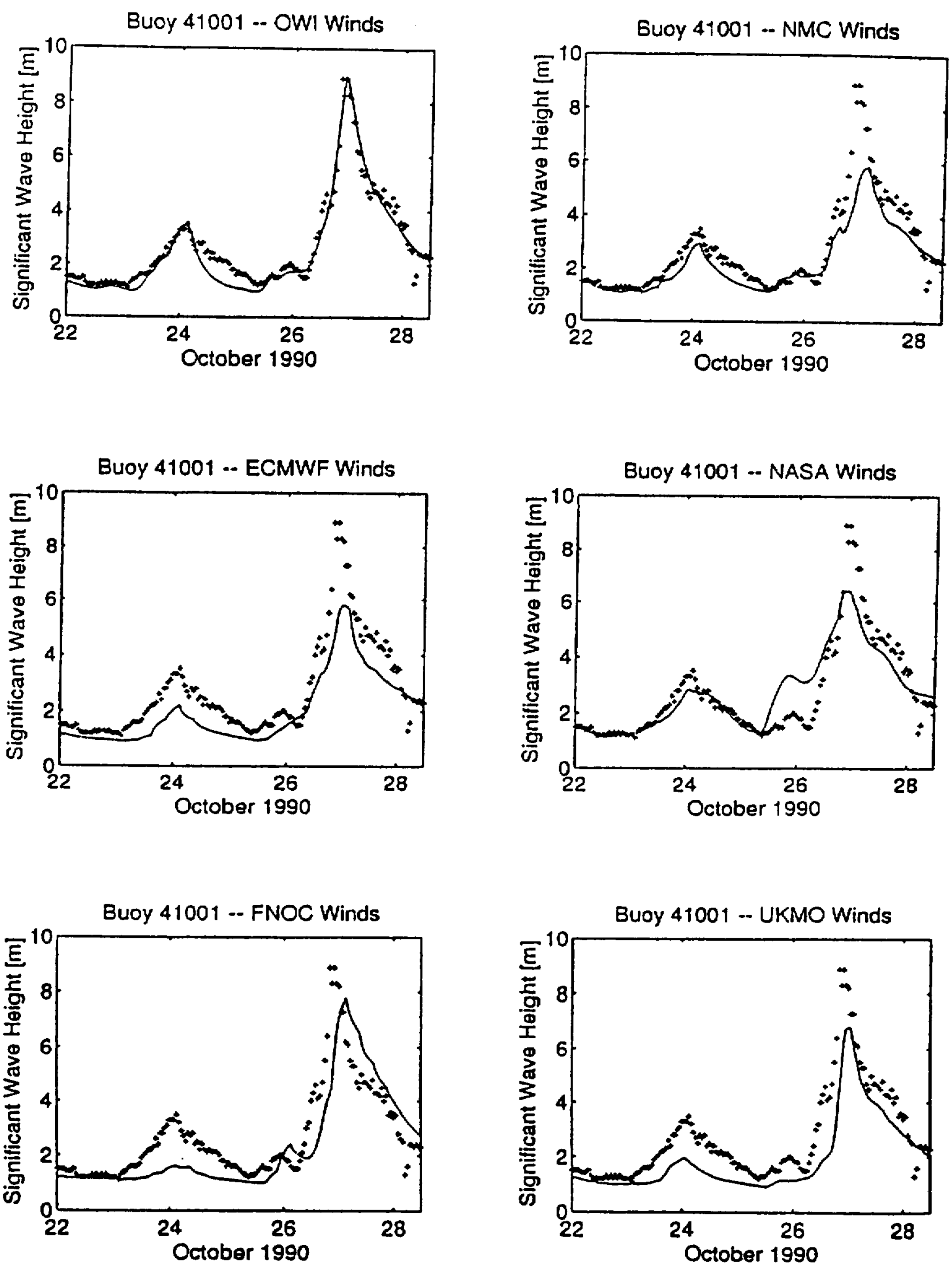

Figure 1. Comparison of Wave Heights derived from five objective analysis winds (NMC, ECMWF, NASA, FNOC, UKMO), and Oceanweather's (OWI) hand-drawn kinematic analysis winds during SWADE IOP2.

Interactive Kinematic Analysis Flow Chart

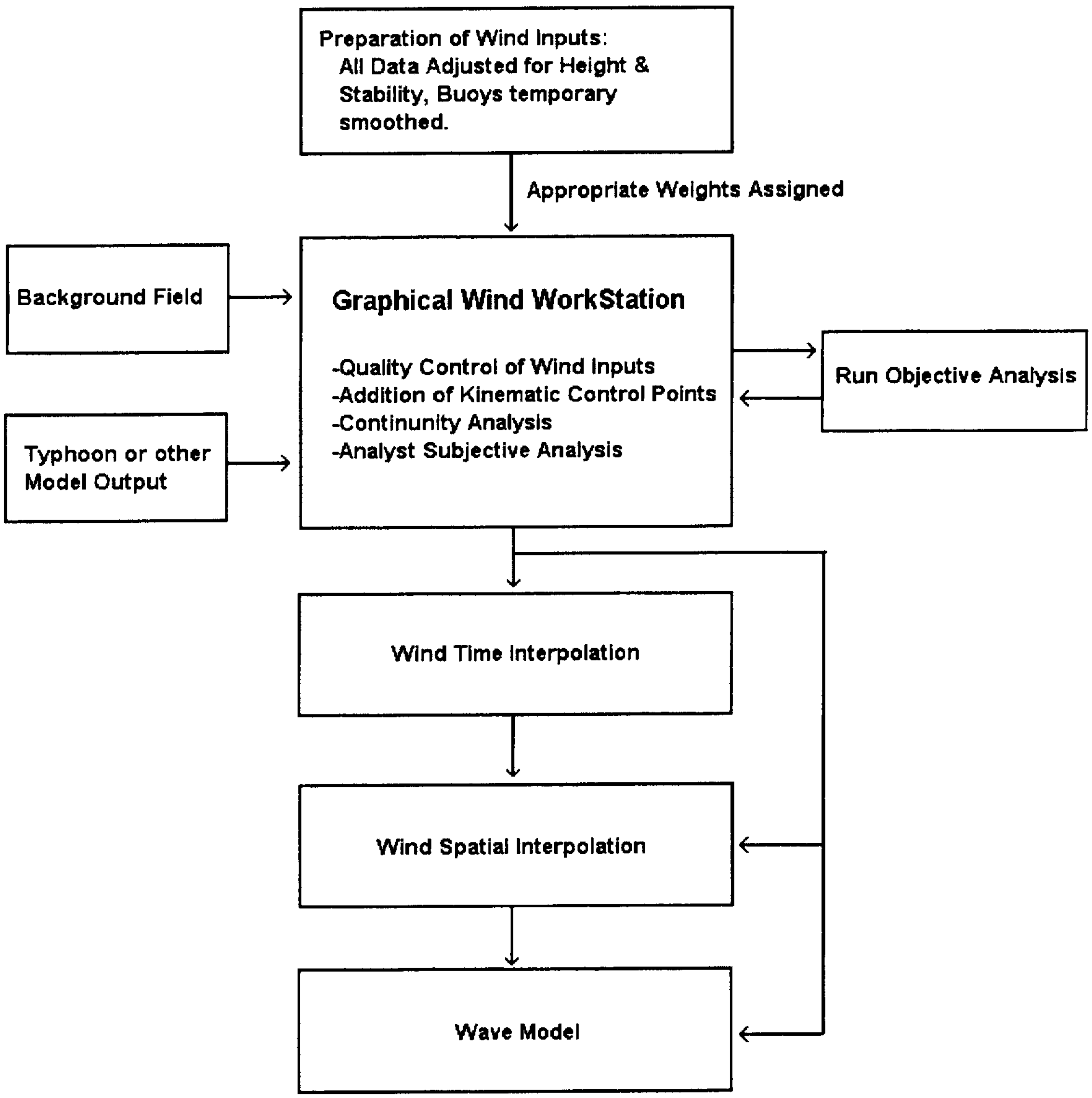

Figure 2.

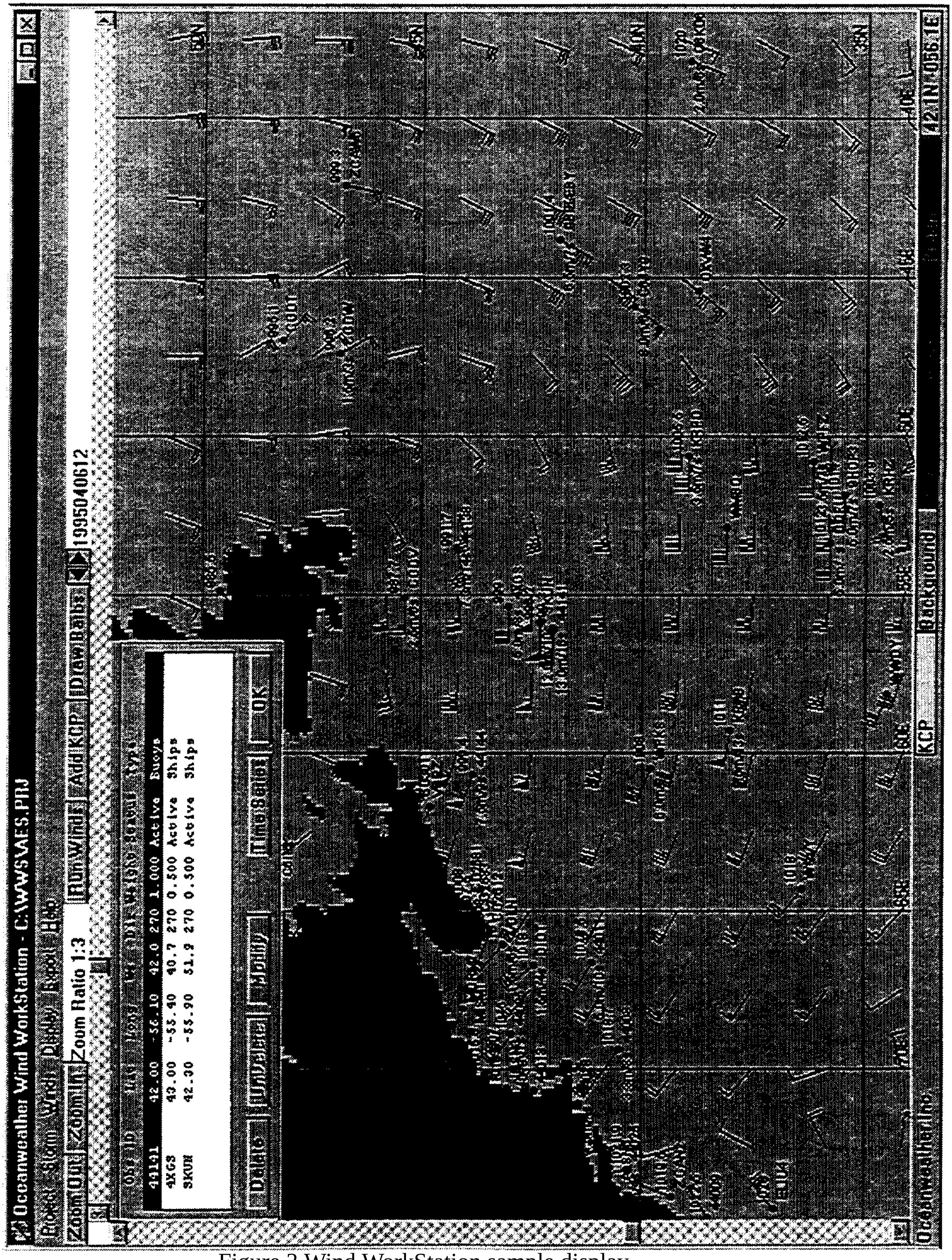

Figure 3 Wind WorkStation sample display

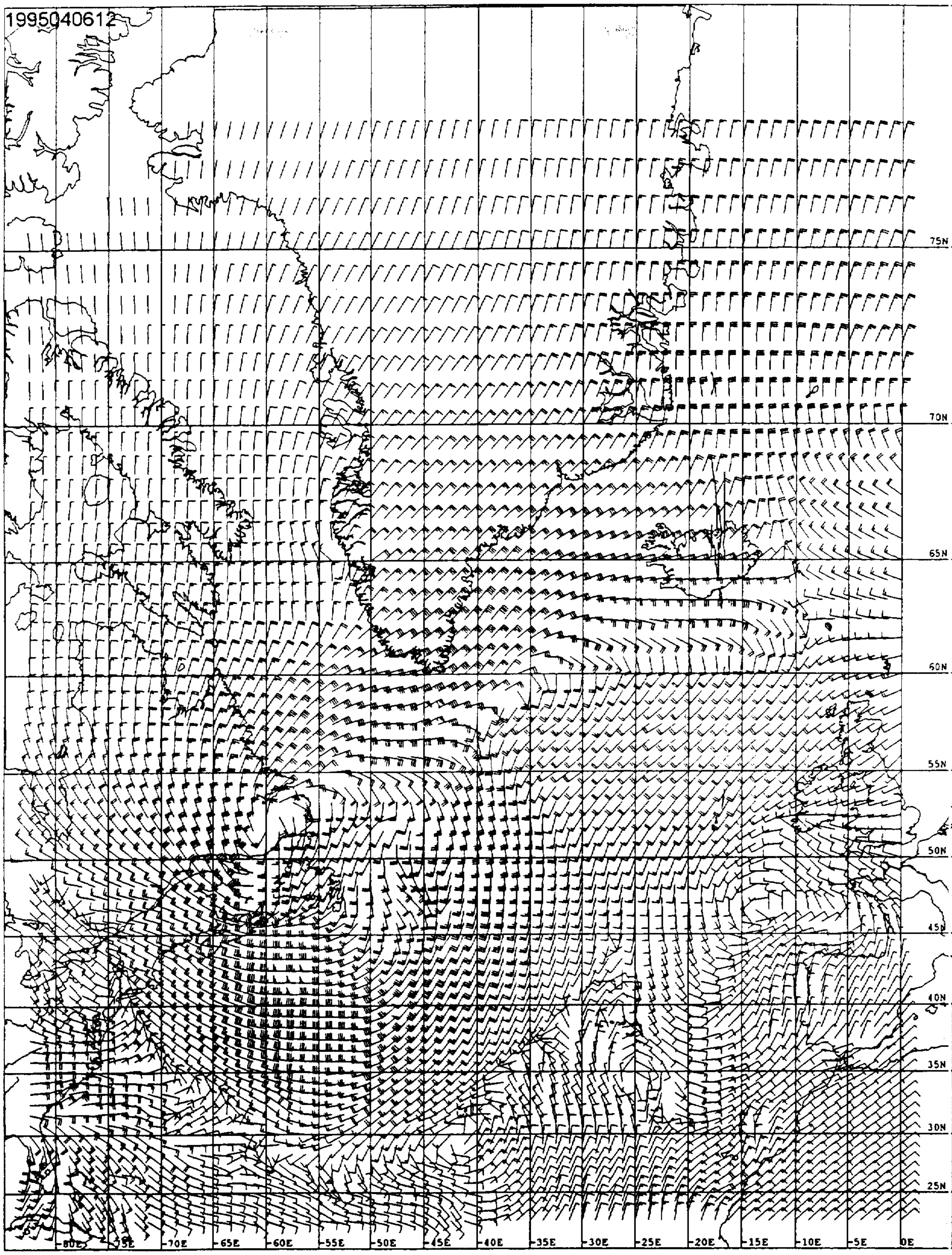

Figure 4. Final Wind Barbs in the April 1995 CCC Storm. (Note: Winds are allowed to fall off in the Baffin Bay since the basin is enclosed by ice.)

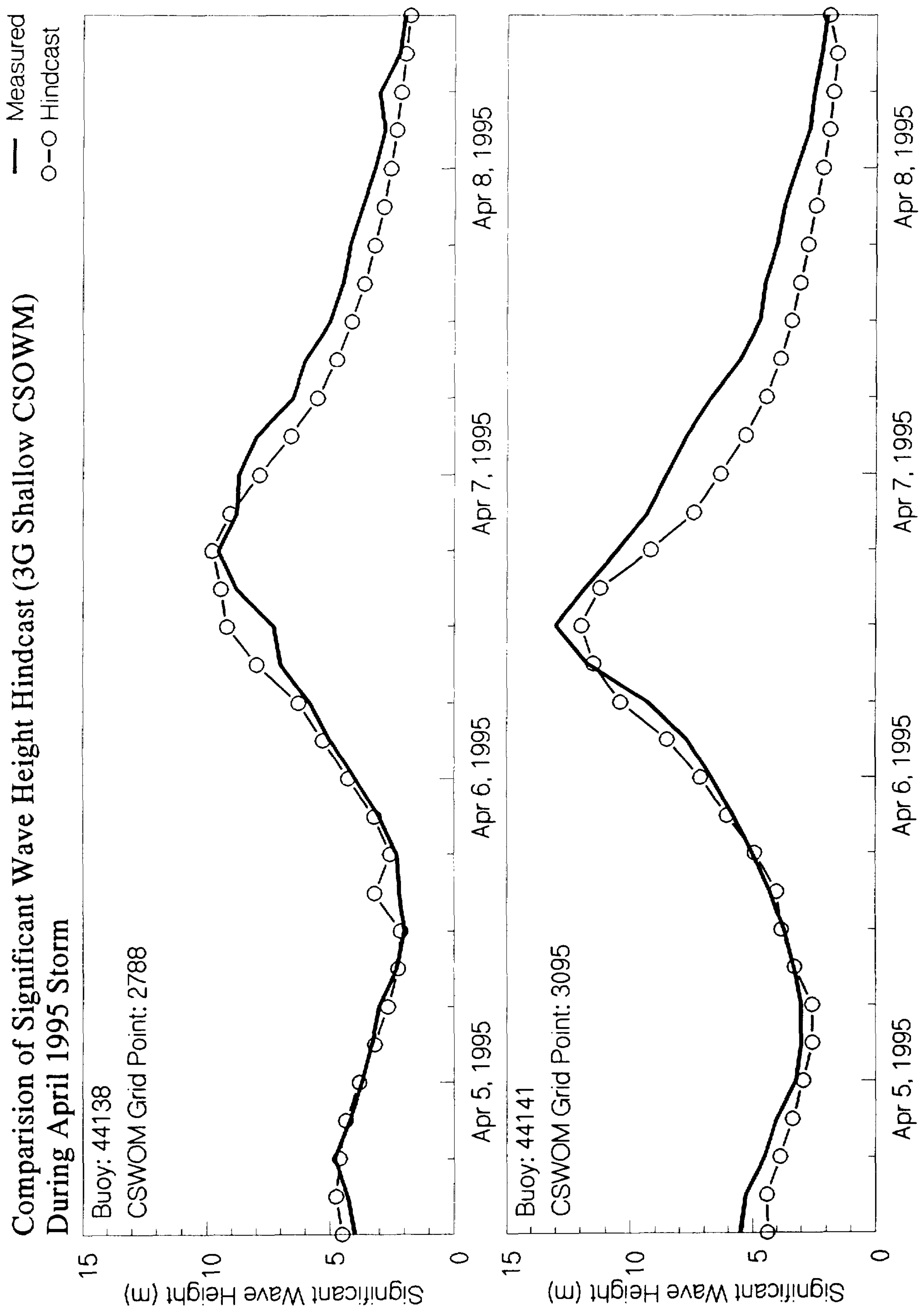

Figure 5. Wave Height Comparison During April 1995 Storm.

A CASE STUDY OF THE 09 AUGUST 1988 SOUTH ATLANTIC STORM: NUMERICAL SIMULATIONS OF THE WAVE ACTIVITY

Valdir Innocentini
Instituto Nacional de Pesquisas Espaciais
Sao José dos Campos, Brazil

Ernesto dos Santos Caetano Neto
Instituto de Pesquisas Meteorológicas
Bauru, Brazil

1. INTRODUCTION

Many cyclones develop or intensify in the 30° - 50° latitude belt in the region east of the Andes Cordillera. Using ECMWF 1000-hPa analyses during 1980-1986, Sinclair (1994) reported a high number of intense cyclones over the South Atlantic cast of Uruguay during the winter. Gan and Rao (1994) showed evidences that the Andes Cordillera plays a significant role on westerly transient disturbances originating frontogenesis on its lee side.

A typical example occurred in the period 9-11 August 1988. A severe storm developed over the ocean and was responsible for an unusual wave activity and flooding in some locations along the Brazilian shoreline from 22° to 32° S. The news media reported several instances of damages and the loss of lives. The Brazilian newspaper Jonial do Brasil from Rio de Janeiro wrote in its edition of 11 August 1988: *At 14h yesterday ... eight tubes of the drainage pipes at Leblon (a beach in Rio de Janeiro) were damaged by the water strength. One of them, with 8000 kg, disappeared carried out by the sea ... waves 3 m high caused several damages ... people walking on the streets were forced to run inside the buildings trying to find protection in higher points.* The editions of 12, 13, and 14 August are plenty of notices about deaths and damages.

The aim of this work is, utilizing numerical models, to hindcast this elusive event. We employ a hydrostatic mesoscale meteorological model (LAM) to simulate the storm, and a 2nd generation wave model (SWM) to hindcast the associated oceanic condition. The purpose is (i) to investigate the possibility of forecasting extreme ocean wave events due to lee cyclones developing over Uruguay and moving towards the ocean, and (ii) to examine the surface wind evolution responsible for the intense wave activity observed in Rio de Janeiro.

2. MODELS DESCRIPTION

The use of wind generated by a limited area atmospheric model is more suitable to study the ocean wave evolution because many atmospheric mesoscale systems can be explicitly simulated, and generally more realistic surface winds are obtained than in global models. Also, the analyses and forecasts provided by international centers operating global models are available only at each 6 or 12-h interval, reducing the frequency to update the wind forcing for ocean waves.

Just a brief description of the numerical models is given here. More detailed description can been found in Nagata et al. (1986) and Innocentini and Caetano Neto (1994) regarding LAM and SWM, respectively.

2.1 Limited area atmospheric model - LAM

The LAM is a flux-form primitive equation model developed by researchers of the Numerical Prediction Division, Japan Meteorological Agency (Yamagishi 1980; Tatsurni 1983), and modified by Nagata and Ogura (1991). The version used here has 14 layers vertically in sigma coordinate system

[$\sigma \equiv (P-P_{top})/(P_{surface}-P_{top})$)] with P_{top}=100 hPa. The layers are defined by the 15 σ-levels corresponding to the pressure 1000, 990, 970, 940, 900, 850, 790, 720, 640, 550, 450, 350, 250, 150, and 100 hPa for $P_{surface}$=1000 hPa. The prognostic variables $\Pi \equiv P_{surface}-P_{top}$, u,v,q, and specific humidity q are placed on the middle of each layer, and the diagnostic variable dp/dt on the levels. As usually assumed in numerical models with this kind of vertical coordinate, the surface pressure tendency equation is formulated so that ω=0 at surface and top. The geopotential height is calculated on the middle of each layer by the vertical integration of the hydrostatic equation.

The horizontal domain utilized by the atmospheric model to simulate the case study is represented in Fig. 2 . It consists of 73 and 55 grid points in the east and north directions, respectively, in a Mercator projection. The grid distance on this map is 104.125 km true at 30° latitude. This resolution is more appropriated to capture the broad-scale synoptic features of the event and not to simulate explicitly the mesoscale embedded on it. The horizontal resolution of the atmospheric model is fundamental in wave forecasting; Dell'Osso et it. (1992) simulated the wave activity during the Gorbursh Storm occurring in Mediterranean Sea with two ECMWF numerical models, one the global model with resolution T106 and the other the limited-area model with resolution T333, corresponding approximately to 125 and 40 km, respectively. They obtained realistic wave height forecasting only with the 10-m winds provided by the limited area model.

The ECMWF global model resolution in 1988 was T106, very similar to the resolution used in the present research. However, the 10-m winds obtained with the LAM model are stronger than that provided by ECMWF analysis (at least in this case study), and the ocean waves generated, as it will be shown, are due to a long-lived and very large fetch originated from the synoptic scale, and therefore the resolution used here seems to be satisfactory for the present purpose. In future research (his case study must be carried out with higher resolution and the results compared.

2.2 Ocean surface wave model - SWM

The SWM is a 2nd generation wave model incorporating advection, refraction, shoaling, dissipation due to the bottom, input of energy due to the horizontal wind 10 m above the surface, dissipation due to the wave-breaking, and conservative nonlinear interactions. It is based on the energy balance equation written for the wave spectral variance. It follows the model developed by Golding (1983) in many aspects. Concerning the parametrization of physical processes, the main distinctions between the two models are the following:

- the advective process is performed using a semiLagrangian scheme (Bates and Mcdonald 1982);
- the sources terms (generation, dissipation due to the wave-breaking, and nonlinear interactions) are tuned to fit the empirical Sanders' duration-limited growth curve (Sanders et al. 1981);
- the nonlinear interactions are performed so that the windsea is reshaped to resemble the Kruseman spectrum (Janssen et al. 1984).

The wave spectrum is represented at each grid-point in 13 frequencies corresponding to the periods 1, 2, 3, 4, 5, 6, 7, 8, 10, 13, 16, 20, and 25 s, and 36 directions with an angular interval of 10°.

The only physical process requiring boundary conditions is the advection. At the coast the spectral energy is imposed equal to zero. At the open ocean boundaries, since the semi-Lagrangian scheme requires the value of the advected variable in the point where "the parcel" was located in the previous time-step, when this point is outside of the domain (energy entering into the domain) the nearest boundary point value is used. If this point is inside, the semi-Lagrangian scheme is applied normally.

The SWM is integrated in the same domain and grid mesh utilized by the LAM, represented in Fig. 2 .

2.3 The validation of SWM

An intercomparison among several operational models for idealized experiments described in The SWAMP Group (1985) are presented in Innocentini and Caetano Neto (1994). This study shows that the wave model employed in this research is satisfactory as a 2nd generation wave model. However, the wave model is not considered in its final version. A formulation controlling how fast the windsea average direction aligns with the wind direction is currently being investigated. The results are being compared with the method adopted in the VAG 2nd generation model (Guillaume 1990) and with the EXACT-NL 3rd generation model (Hasselmann and Hasselmann 1985). This procedure will reduce the shortcoming detected in 2nd generation wave models submitted to situations of varying wind directions and wind velocities (Günther et al. 1981, van Vledder and Holthuijsen 1993).

Recently Innocentini (1995) studied the wave activity simulated by SWM in the Mediterranean Sea forced by the Gorbush storm (Dell'Osso et al. 1992). Fig. 1 depicts the significant wave height, mean direction, and mean period at Malta for the SWM (continuous line) and the third generation wave model employed by them (dotted line refers to the forcing given by the atmospheric model T106, and broken-dotted to the T333). The SWM results were obtained with the 10m wind provided by the ECMWF limited area with resolution T333. There is a general tendency for SWM presenting higher wave in the maximums and smaller wave in the minimums, but the difference always is less than 0.5 m. Greater discrepancies are expected in mean period and mean direction, since the third generation wave model utilizes 25 frequencies and a 300 angular interval, and aligns the directional spectrum with the wind direction slower. However, the difference in mean period and mean direction never exceeds 1.5 s and 30° during the most active period of the storm (from 2 to 3 December 1989).

3. SIMULATION OF THE 09 AUGUST 1988 STORM

The LAM is integrated for 48 hours initialized with the ECMWF global analysis 1200 UTC 9 August 1988, when the lee cyclone shown by the analysis is well defined. The analyses used are available at 1000, 850, 700, 500, 300, 200 and 100 hPa pressure levels with 2.5° of horizontal resolution, and the variables are interpolated to the σ-levels and model grid-points using a cubic spline.

The 1200 UTC 10 and 1200 UTC 11 ECMWF global analyses are used to update the LAM boundary values.

Fig. 1. Evolution of (a) significant wave height in meters, (b) mean period in seconds, and (c) mean direction in degrees for the Gorbush Storm at Malta. The SWM simulation (continuos line) is obtained with the wind from the limited-area atmospheric model, while the third generation wave simulations with the limited-area (broken-dotted) and global models (dotted).

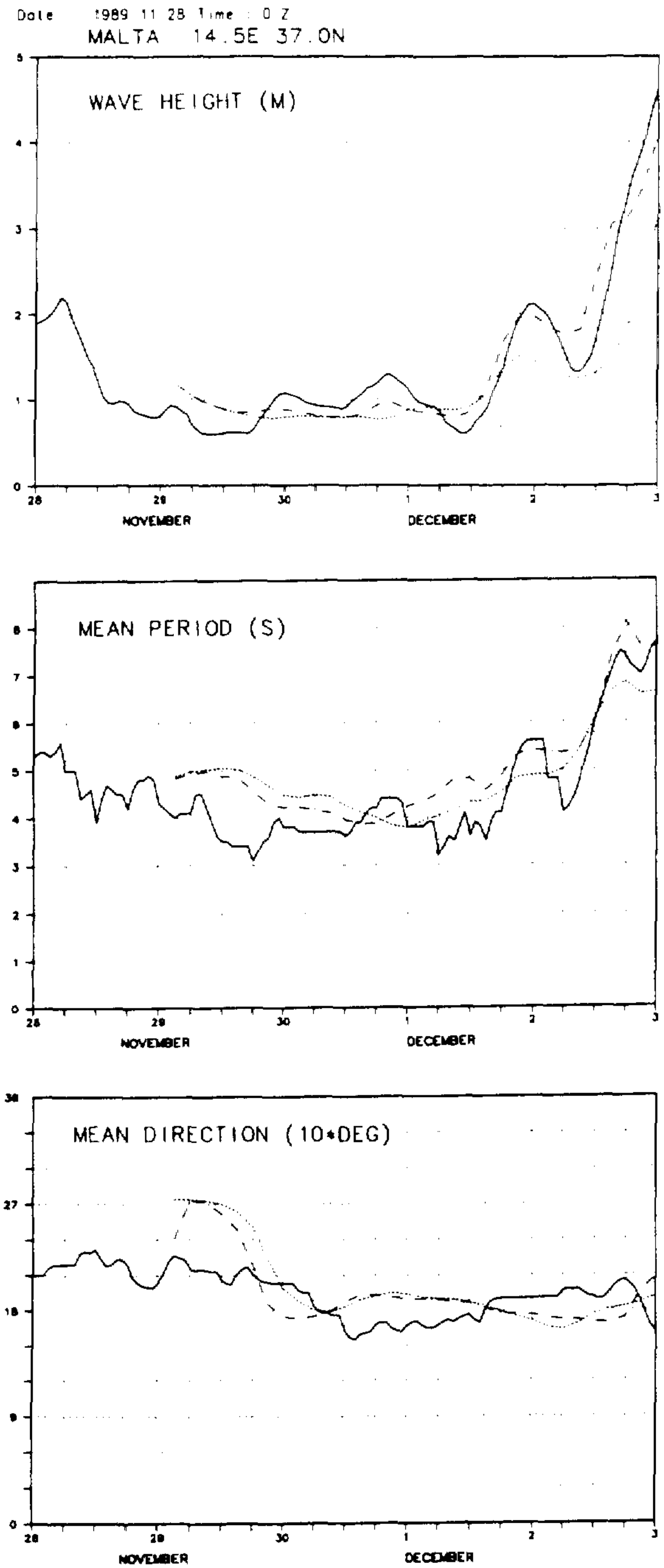

The water depth is assumed constant and equal to 1000 m in the SWM simulation, which means that refraction, shoaling, and bottom dissipation are neglected. This is a reasonable assumption, because the ocean depth in the region considered relevant for this study is smaller than 200 m only about 200 km from the coast. The 10-m wind data is used to update the wind forcing at each 3-h period during the SWM integration.

The coupling between the two models is performed in a one-way form. The LAM simulates the meteorological episode and provides a 10-m wind field at 3-h intervals to force the SWM. The initial wave field is obtained running the SWM for 9 hours from an ocean state at rest forced by the initial surface wind.

The 10-m wind is obtained by the relation

$$|u(z)| = \frac{u^*}{0.41} \ln\left(\frac{z}{z_o}\right)$$

where z_0=0.05m in and u* is the friction velocity. First, u* is calculated using |u| at the first LAM level imposing |u|=0 at $Z=z_0$. With u* computed, the same relation is evoked again to compute using |u| at z=10 m. The wind direction at the first model level above 10 m is assumed at z=10 m.

The 10-m wind obtained with LAM forecasting at T+0h, T+24h, and T+48h are depicted in Fig. 2 . Initially the maximum velocity center of 12 ms-1 is located around 45°W, 38°S (Fig. 2a). The next forecasts show this maximum enhancing to 20 ms-1 and moving northeastwards in the first 24 h and southeastwards in the next period (Figs. 2b and 2c). The most remarkable feature of these fields is the large region around the point 40°W, 35°S at T+24h (Fig. 2b) with velocity higher than 12 ms-1 directed towards the coast, except in its north flank and near the coast. At T+48h (Fig. 2c) the area around 42°W, 25°S (near the coast of Rio de Janeiro) embedded in this large region experiments a counterclockwise rotation of wind direction decreasing its eastward component in relation to T+24h. The remaining part of this large region displays nearly no change in wind direction. Then, one can expect a vigorous windsea built at the area with wind speed greater than 20 ms-1 being propagated towards the coast. The large fetch and counterclockwise wind rotation observed above shall favors the swell propagation along the shoreline 22°-26°, where Rio de Janeiro is located.

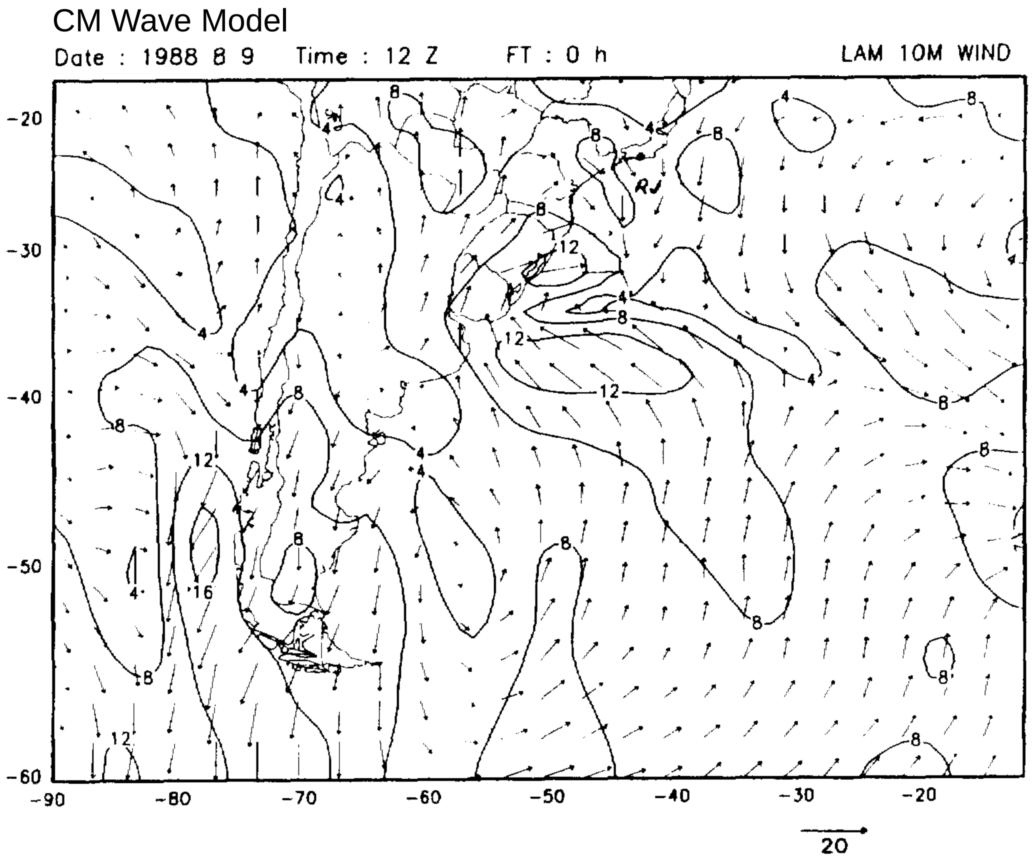

Fig. 2. Wind field in ms^{-1} at 10 m height provided by the atmospheric model for T=1200 UTC 09 August 1988 at (a) T+0h, (b) T+24h, and (c) T+48h. The isotachs are contoured every 4 ms^{-1} (2 ms^{-1}) for values below (above) 16 ms^{-1}. RJ refers to Rio de Janeiro location.

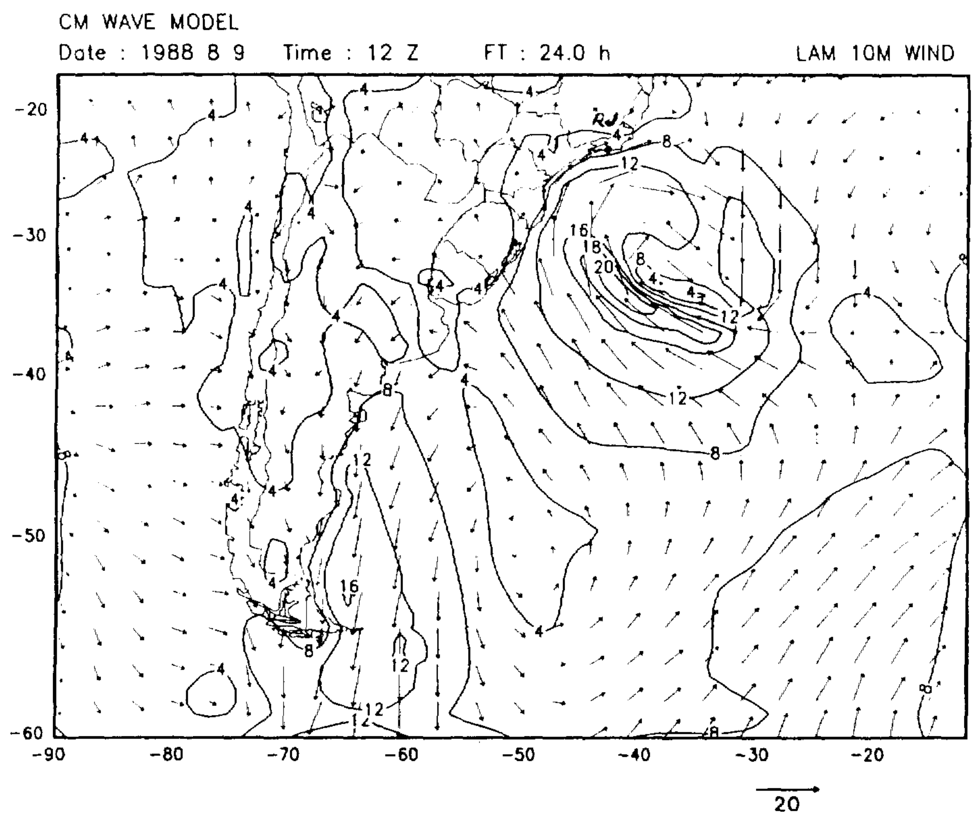

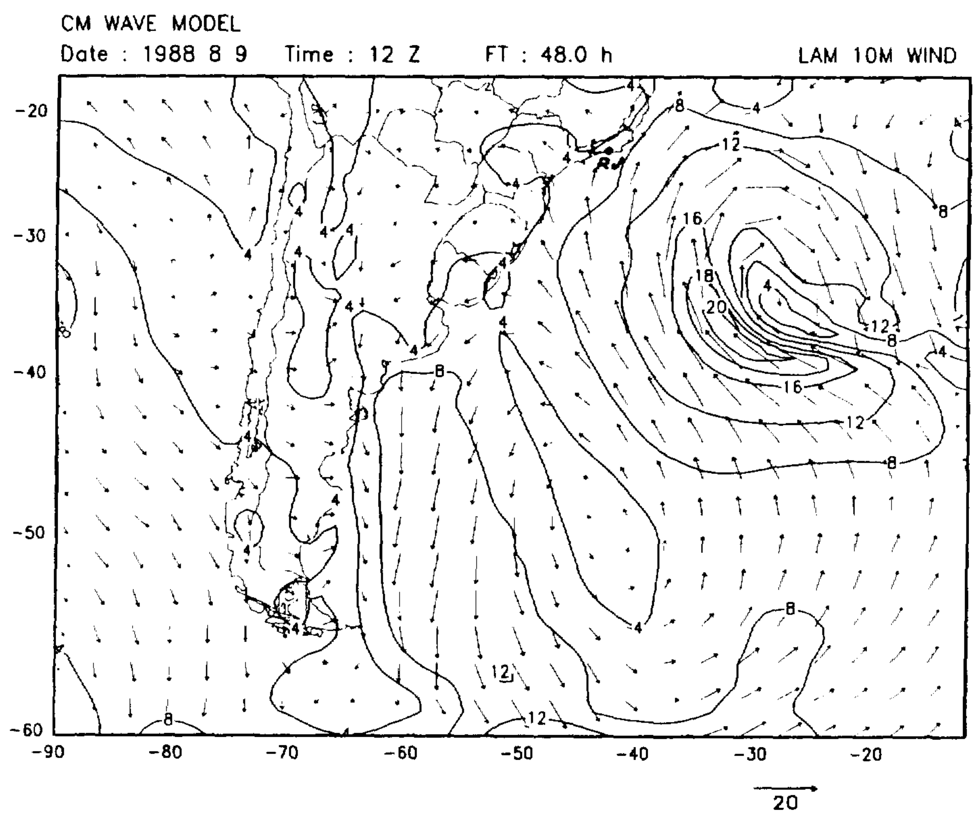

Fig.2 (*Continued*)

Once the 10-m wind is obtained in the LAM through a crude interpolation, a comparison with this field given by a global analysis is instructive. Fig. 3 shows the 10-m wind ECMWF analyses at 1200 UTC 09 and 10 August 1988. Comparing Figs. 2a and 3a at 09 one can note that the two maximum centers of 16 ms^{-1} north and south of the point 50°W, 35°S presented by the global analysis are not captured in the LAM initial field. Some smoothing should be expected, because the fields used initially to feed the LAM are obtained with a very coarse vertical resolution near the surface. However the maximum location and the direction agree reasonably. The next 24-h ECMWF analysis (Fig. 3b) shows a minimum of 8 ms^{-1} at 34°W, 34°S (the position of the cyclone center) surrounded by two maximums of 16 ms^{-1} and 18 ms^{-1}. At this time, this minimum simulated by the LAM is nearly in the same position (Fig. 3b), but with a value of 4 ms^{-1} and elongated in the direction northwest. The LAM is able to simulate a maximum of 20 ms^{-1}, 2 ms^{-1} greater than that provided by the ECMWF analysis. However the closed contour of 16 ms^{-1} around the point 32°W, 28°S reported by the analysis is not reproduced by the LAM. At 1200 UTC 11 August 1988 the discrepancies noted above are still present (the ECMWF analysis for this time is not shown): (i) the minimum is smaller in the LAM: (ii) the maximum southwest to the minimum is stronger in the LAM; and (iii) the maximum north to the minimum is not captured by the LAM. Although these differences must be investigated in future research, we conclude that the main feature of the fetch responsible by the intense wave activity propagating towards the south Brazilian coast is reproduced by the LAM, and satisfies the main purpose of this paper.

Figure 4 shows the significant wave height H_s and average wave direction D_{ave} at T+0h, T+24h, and T+48h. At T+0h the sea state is obtained by the 10-m wind at 1200 UTC 09 August 1988 frozen for a time period of 9 hours. The initial fields H_s and D_{ave} closely resemble the location of wind maximum and wind direction, but not exactly because the initial spin of SWM is obtained with the advection due to the wave group velocity switched on. The time period of 9 hours to spin wave models is an arbitrary practice usually adopted (Golding 1983) before the availability of altimeter wave height data obtained by satellite. Presently several operational wave models are initialized with the assimilation of satellite data (Breivik and Reistad 1994). The wave height of 3 m. built in the region with 10-m wind of 12 ms^{-1} (Fig. 4a) does not correspond to a fully developed spectrum, which requires this wind value blowing for about 15 hours without any variation (Innocentini and Caetano Neto 1994). However there is no reason to force the wave models starting with fully developed spectrum because the 10-m wind is a consequence of the developing and moving cyclone from the continent towards the coast. An inspection in the 10-m wind analysis 12 hours earlier (not shown) reverts that the maximum wind was 12 ms^{-1} concentrated in a smaller area around 52°W, 45°S directed towards the coast. Since at the initial time the wind is weaker than that simulated in the forthcoming hours and the fetch is still not well characterized, one can guess the time period chosen to spin the wave model does not affect significantly the main features of the wave simulation. An experiment was carried out with the initial 10-m wind field frozen for a time period of 48h. The results obtained (not shown) were very similar.

At T+24h, high waves are evident in many parts of the coast in south of Brazil; $H_s \approx$ 4-5 m are found at 50°W, 30°S (Fig. 4b). Qualitatively, stronger winds generate waves with smaller frequencies, which have greater group velocities and are propagated faster. When they reach a region with smaller wind speed than in its original region, part of this energy (that in the spectral bmd with higher frequencies) becomes windsea suffering an angular relaxation towards the wind direction and the spectrum is reshaped. The remainder energy says in lower frequencies with its original group velocity and direction. This situation seems to take place around Rio de Janeiro (nearly 23° S), as depicted at Fig. 4b , where the wind blows northeastwards, Conversely, around the point 48°W, 30°S the wind direction is almost the same of the incoming wave energy.

From T+24h to T+48h (Fig. 4c) the wind changes its direction around Rio de Janeiro allowing the swell and windsea propagation towards the coast. Hs>3 m contours extend northward reaching regions very close to the coast of Rio de Janeiro with direction towards the coast. Fig. 5 presents the spectrum at 43° W, 28°S (indicated by X in Fig. 2c) for T+45h. One can note the swell being build along the north direction (nearly the local wind direction), and energy in smaller frequencies in the northwest quadrant corresponding to the swell which have been propagated from the region with stronger wind southeast of this point.

The windsea generation in a location where waves are being propagated from a remote region with higher wind speed depicted above is a physical constrain which must be captured by wave models. However this effect is too rapidly reproduced by many 2nd generation wave models (as the one employed here), in contrast with 3rd generation models where the nonlinear interactions build explicitly the windsea spectrum (The SWAMP Group 1985). Probably a 3rd generation wave model could show greater waves along the coast of Rio de Janeiro even before T+24h.

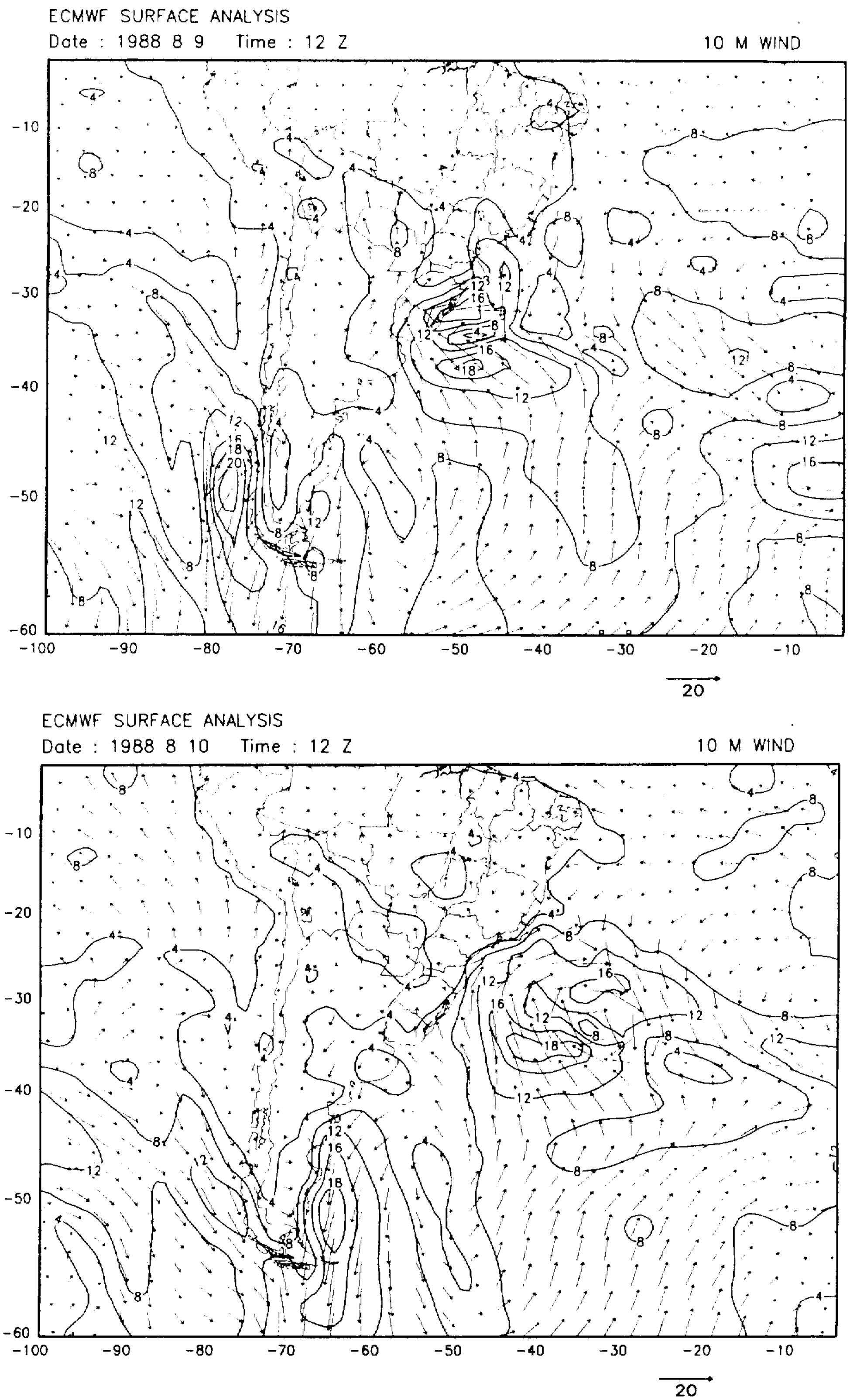

Fig. 3. ECMWF 10-m wind analyses for 1200 UTC August 1988 at (a) 09 and (b) 10. The isotachs are contoured every 4 ms^{-1} (2 ms^{-1}) for values below (above) 16 ms^{-1}.

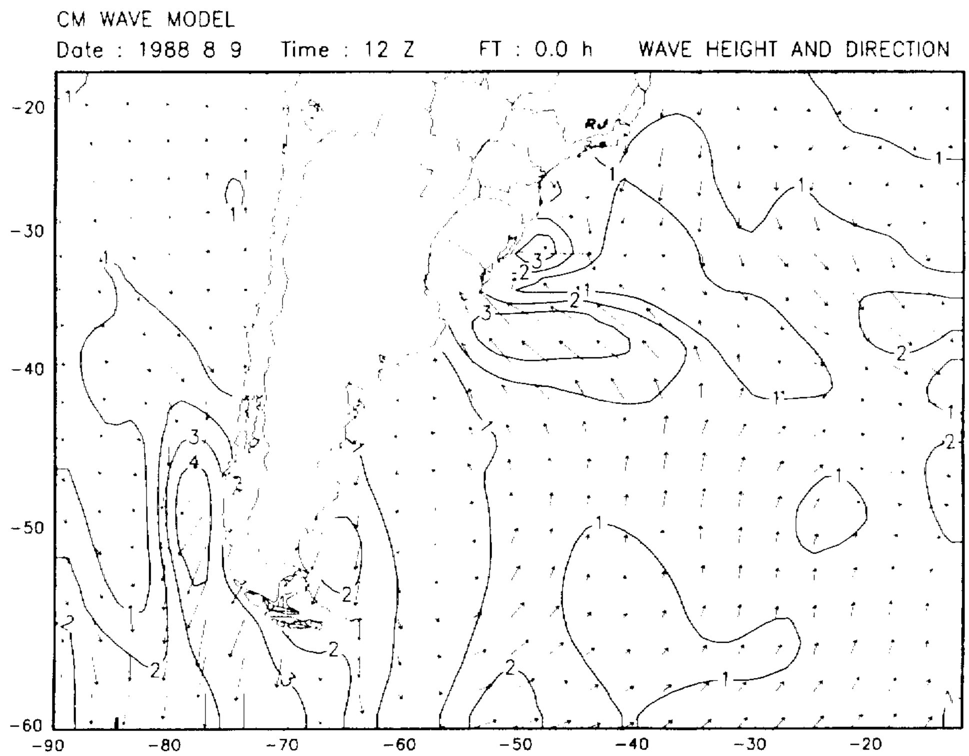

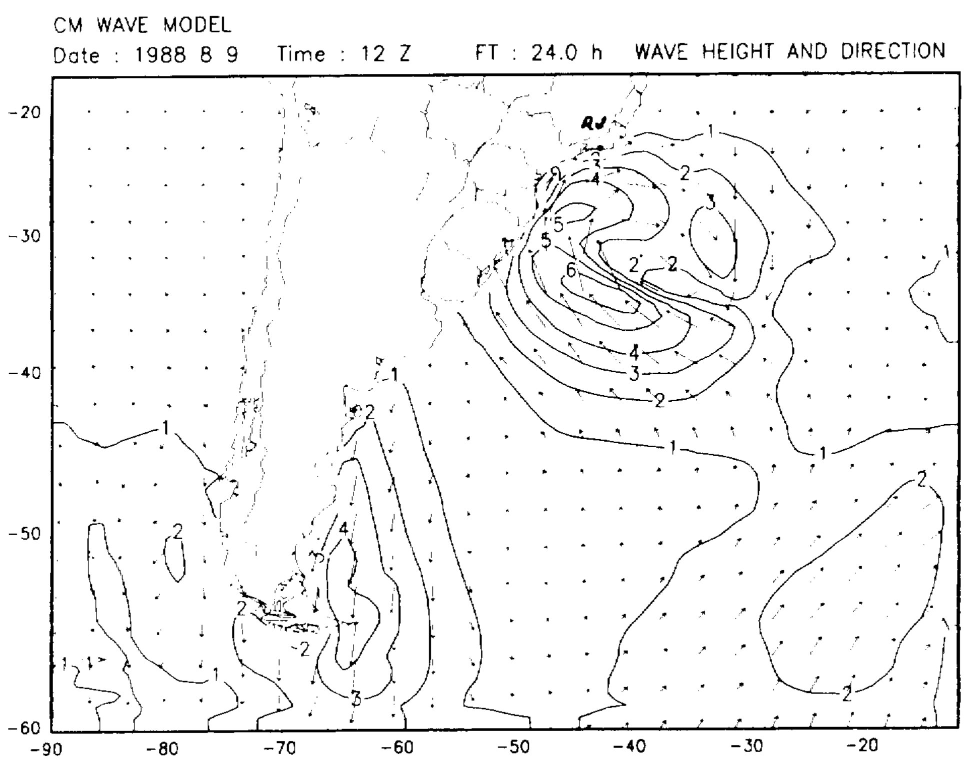

Fig. 4. Isolines of significant wave height (m) and average direction provided by the wave model for T=1200 UTC 09 August 1988 at forecasting time (a) T+0h, (b) T+24h, and (c) T+48h. Vectors are plotted at each 3 grid points.

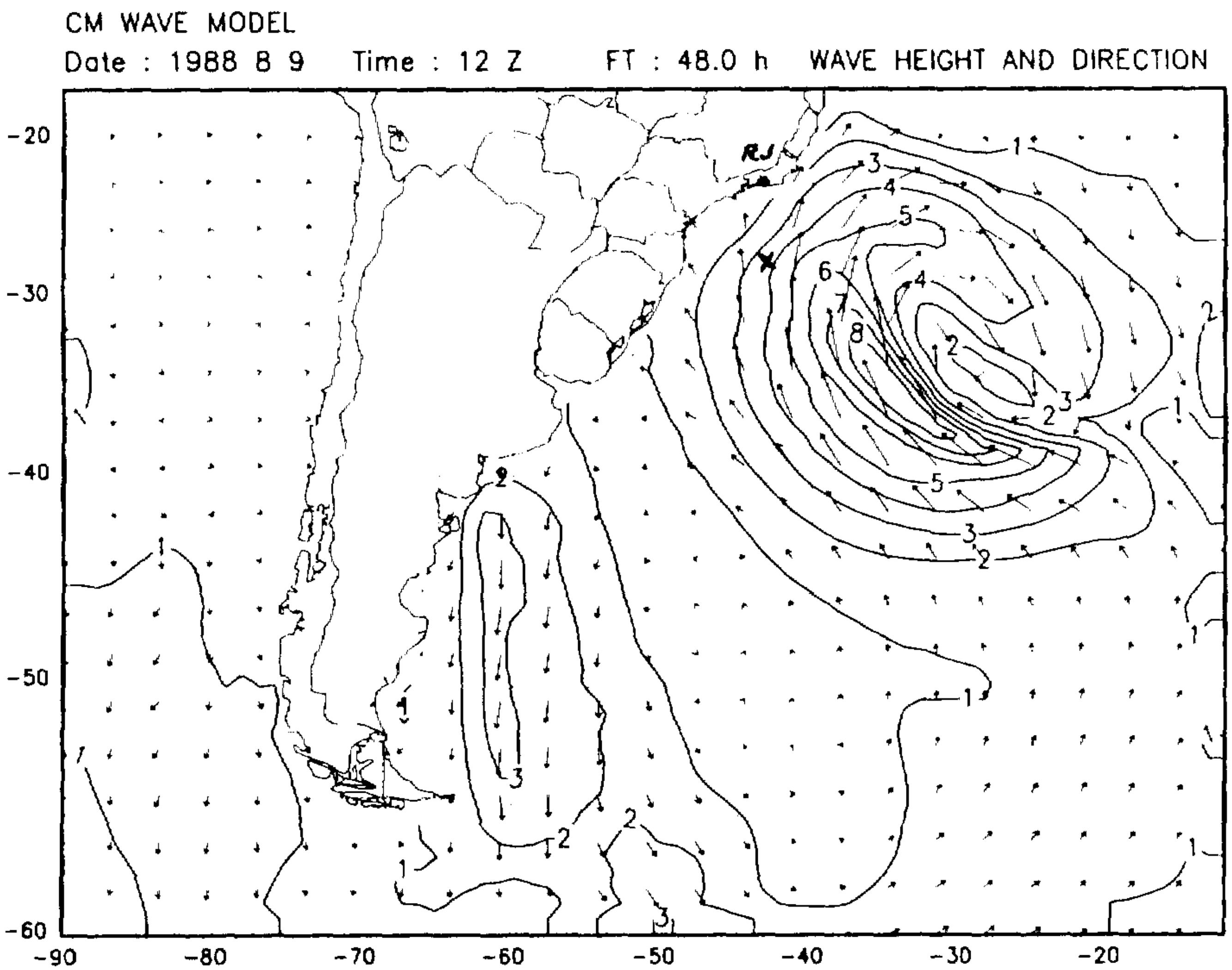

Fig.4 (*Continued*)

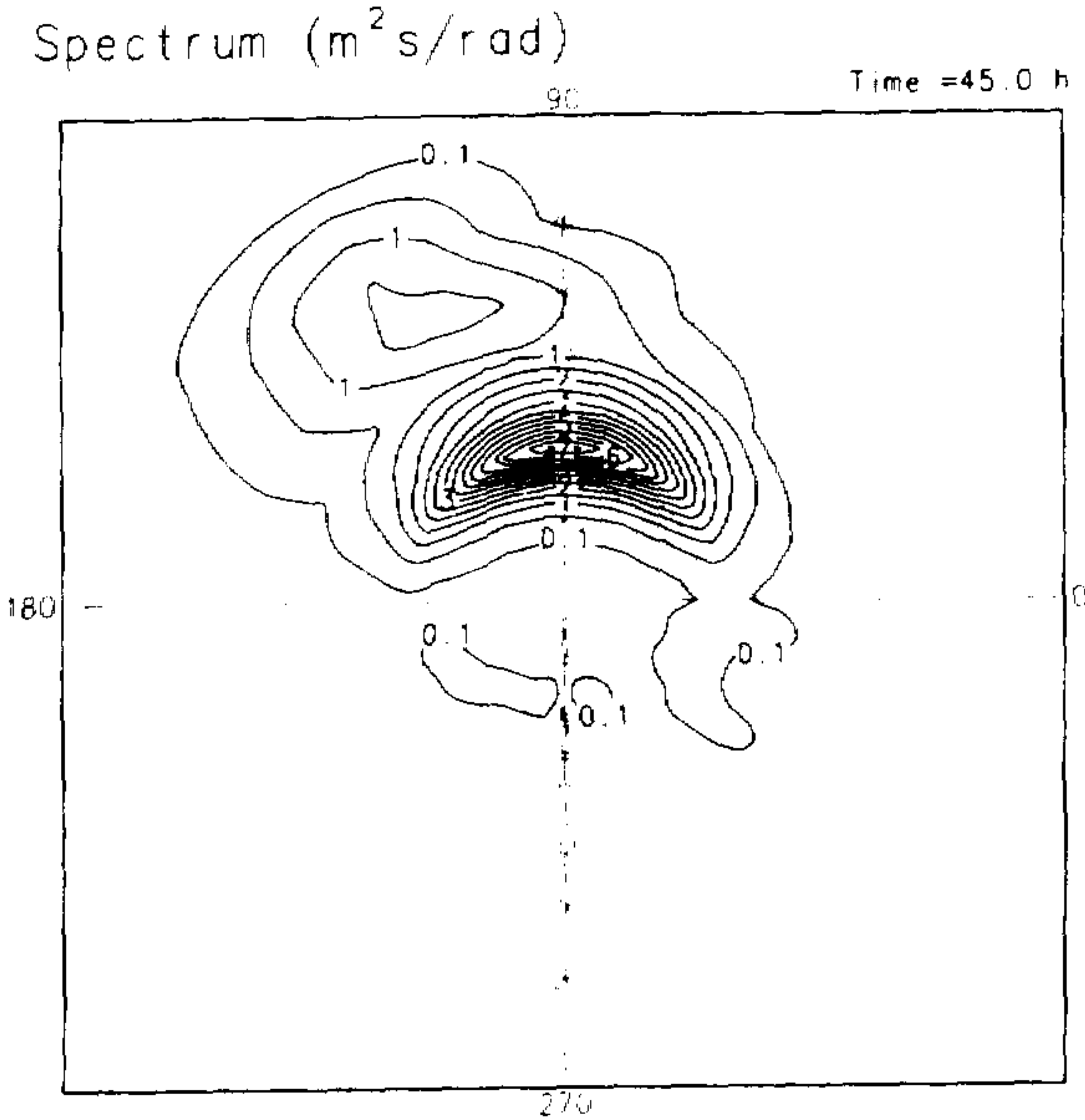

Fig. 5. Two-dimensional spectrum at 43°W, 28°S, indicated by X in Fig. 4c, for T+45h. The circles refers to the periods 1, 2, 4, 5, 6, 7, 8, 10, 13, 16, 10, and 25s. The directions are defined counterclockwise from eastwards which corresponds to 0. The interval chosen is 0.5 m^2 s(rad)$^{-1}$.

4. SUMMARY AND CONCLUSION

During the Southern Hemisphere winter a high frequency of cyclogenesis occurs over Uruguay generated by the effect of the Andes Cordillera on westerly atmospheric baroclinic waves. Many cases of intense ocean wave activity during this period are observed, probably due to this kind of cyclones moving towards the South Atlantic and evolving into intense storms. The 9 August 1988 storm was a typical example. The ocean waves reached the South Brazilian coast causing severe instances of damage and the loss of at least one life, as reported by the Brazilian news media. Waves 3 m high observed at Rio de Janeiro and the disappearance of a 8000 kg weight tube from a drainage pipe illustrated the strength of the waves.

This elusive phenomenon is studied in this paper through ECMWF analyses, a hydrostatic limited area meteorological model (LAM), and a 2nd generation wave model (SWM).
After the lee cyclone has been formed over the Atlantic Ocean at T= 1200 UTC 09 August 1988, the ECMWF analyses present a deepening rate of 8 hPa per day, which does not configure an explosive cyclogenesis in the sense suggested by Walsh el al. (1992). The atmospheric model simulate a deepening rate of 10 hPa in 12 hours, and in some instant 4 hPa per 3 hours (not shown). However, even the best operational numerical model fails in reproducing observed deepening rates in explosive cyclones (Kuo and Reed 1988).

The ECMWF 10-m wind agrees with this field simulated by the atmospheric model concerning the location of the maximum and minimum intensities. The discrepancies noted are: (i) the minimum wind in the cyclone center is smaller in the LAM: (ii) the maximum wind southwest to the cyclone center is stronger in the LAM; and (iii) a maximum wind north to the cyclone center shown by the analyses is not captured in the LAM simulation. Despite these differences and the coarse mesh-grid employed by the LAM, the long-lived and large fetch generating waves propagating towards the south Brazilian coast is reproduced.

The SWM simulates waves with significant height $H_s \approx$ 4-5 m in south of Brazil at T+24h. At this time a northeastwards 10-m wind around Rio de Janeiro seems to obstruct the swell propagation from the fetch. However, as the surface cyclone moves eastwards from T+24h through T+48h this obstruction is removed and high waves directed to the coast achieve regions close to Rio de Janeiro. Then the two-dimensional spectrum around this region presents two peaks in distinct directions and frequencies, revealing the simultaneous presence of swell and wind-sea.

Although the objectives of this research, concerning the elucidation of the cause related to the intense wave activity observed in Rio de

Janeiro at 10 August 1988 and the ability in its forecasting, were successfully achieved, further research must be addressed in order to enlighten several points. For example, higher waves were observed at Leblon (a beach of Rio de Janeiro) probably due to the bathymetry, not incorporated in the present SWM run. A more realistic parameterization of nonlinear interactions shall simulate higher incoming waves into Rio de Janeiro coast during the first 24-h period

of simulation. Also, further examination of how dynamics and thermodynamics interact to help the cyclogenesis over Uruguay and its displacement over the ocean must be investigated.

REFERENCES

Bates, J. R., and A. Mcdonald, 1982: Multiple up-stream, semi-Lagrangian advective schemes: analysis and application to a multilevel primitive equation model. Mon. Wea. Rev., **110**, 1831-1842.

Breivik, L.-A., and M. Reistad, 1994: Assimilation of ERS-1 altimeter wave heights in an operational numerical wave model. Wea. Forecasting, **9**, 440-451.

Dell'Osso, L., L. Berlotti,and L. Cavaleri, 1992: The Gorbush storm in the Mediterranean Sea: atmospheric and wave simulation. Mon. Wea. Rev., **120**, 77-90.

Golding, B., 1983: A wave prediction system for realtime sea state forecasting. Quart. J. Meteor. Soc., **109**, 393-416.

Gan, M. A., and V. B. Rao, 1994: The influence of the Andes Cordillera on transient disturbances. Mon. Wea. Rev., **122**, 1141-1157.

Guillaume, A., 1990: Statistical tests for the comparison of surface gravity wave spectra with application to model validation. J. Atmos. Ocean. Technol., **7**, 551-567.

Gunther, H.. W. Rosenthal, and M. Dunckel, 1981: The response of surface gravity waves to chugging wind directions. J. Phys. Oceanogr., **10**, 718-728.

Hasselmann, S., and K. Hasselmann, 1985: Computations and parameterizations of the nonlinear energy transfer in a gravity-wave spectrum. Part I: A now method for efficient computations of the exact nonlinear transfer integral. J. Phys. Oceanogr., **15**, 1369-1377.

Innocentini, V., 1995: The Gorbush storm wave activity simulated by SAWMO model., Technical Report no. 03-95. Instituto de Pesquisas Meteorologicas, Bauru, Brazil.

Innocentini, V., and E. S. Caetano Neto, 1994: The SAWMO model: A second generation wave model applied to the South Atlantic., Technical Report no. 01-94. Instituto de Pesquisas Meteorologicas, Bauru, Brazil.

Janssen, P. A. E., G. J. Komen, and W. J. P. de Voogt, 1984: An operational coupled hybrid wave prediction model. J. Geophys. Res., **89**, 3635-3654.

Kuo, Y.-H., R. J. Reed, 1988: Numerical simulation of and explosively deepening cyclone.. Mon. Wea. Rev., **116**, 2081-2105.

Nagata, M., M. Ikawa, S. Yoshizumi, and T. Yoshida, 1986: On the formation of a convergent cloud band over the Japan Sea in winter: numerical experiments. J. Meteor. Soc. Japan, **64**,841-855.

Nagata, M., and Y. Ogura, 1991: A modeling case of interaction between heavy precipitation and a low-level jet over Japan in the Baiu season. Mon. Wea. Rev., **119**, 1309-1336.

Sanders, J. W., W. J. de Voogt and J. Bruinsma, 1981: Fysisch Golfonderzoek Noordzee, Sei. Rep. MLTP-2, Raad Overleg Fys. Oceanogr. Onderz. Noordzee, De Bilt, The Netherlands.

Sinclair, M. R., 1994: An objective cyclone climatology for the Southern Hemisphere. Mon. Wea. Rev., **122**, 2239-2256.

The SWAMP Group, 1985: Ocean wave modeling. Plenum Press, 256 pp.

Tatsumi, Y., 1983: An economical explicit time integration scheme for primitive model. J. Meteor. Soc. Japan., **61**, 269-288.

Van Vledder, G. P., and L. H. Holthuijsen, 1993 :The directional response of ocean waves to turning winds. J. Phys Oceanogr., **23**, 177-192.

Yamagishi, Y., 1980: Simulation of the air mass transformation process using a numerical model with the detailed boundary layer parametrization. J. Meteor. Soc. Japan., **58**, 357-377.

Wash, C. H., R. A. Hale, P. H. Dobos, and E. J. Wright, 1992: Study of explosive and nonexplosive cyclogenesis during FGGE. Mon. Wea. Rev., **120**,40-51.

ERS-1 DATA ASSIMILATION IN A SECOND GENERATION WAVE MODEL FOR THE NORTH SEA

F. Ovidio[1], J.-R. Bidlot[1], D. Van den Eynde[1], W. Luo[2] and J. Monbaliu[2]

[1] Management Unit of the Mathematical Model of the North Sea (MUMM)
100 Gulledelle, B-1200 Brussels, Belgium

[2] Catholic University of Leuven (KUL)
de Croylaan 2, B-3001 Heverlee, Belgium

1. MODEL

The MU-WAVE model (Van den Eynde, 1992) is composed of different modules. The core of the system is formed by the second generation wave model HYPAS (Gunther and Rosenthal, 1985) which combines the traditional approach of independent calculation of swell energy for each frequency and direction through a ray technique, with a parametrical wind sea model, using the parameters of the JONSWAP spectrum (Hasselmann et al., 1973) and the mean wind sea direction as prognostic variables. Some shallow water effects, such as shoaling, are included in the model.

The model is implemented on two nested grids. The coarse grid (Figure 1) has a 50 km x 50 km resolution (stereographic projection) and covers the entire North Sea to intercept swell generated far away that may travel to the Belgian coast. In MU WAVE, the open boundaries are treated as walls where limited fetch laws ire applied. In front of the Belgian coast, a higher resolution is needed to account for the complex bathymetry of the Flemish Banks. A 10 km x 10 km fine grid is used (Figure 2), coupled to tile coarse grid through the open boundaries.

MU-WAVE uses the wind fields of the United Kingdom Meteorological Office (UKMO) as forcing. Analysed fields or forecasts are used depending oil their availability. They are interpolated to the stereographical coarse grid.

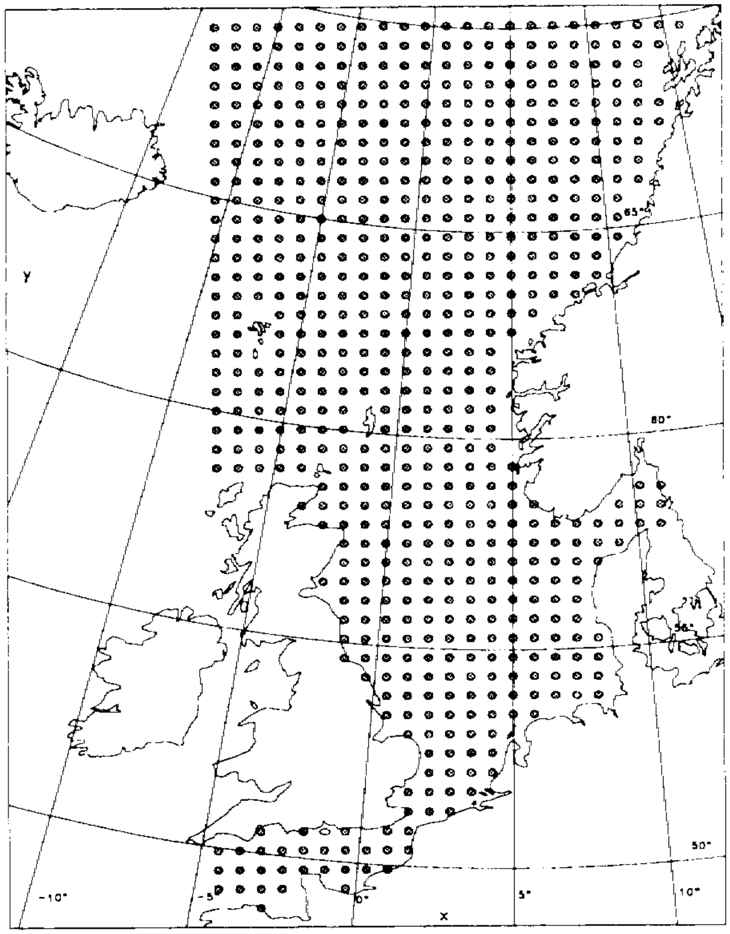

Figure 1. Coarse grid domain and active grid points.

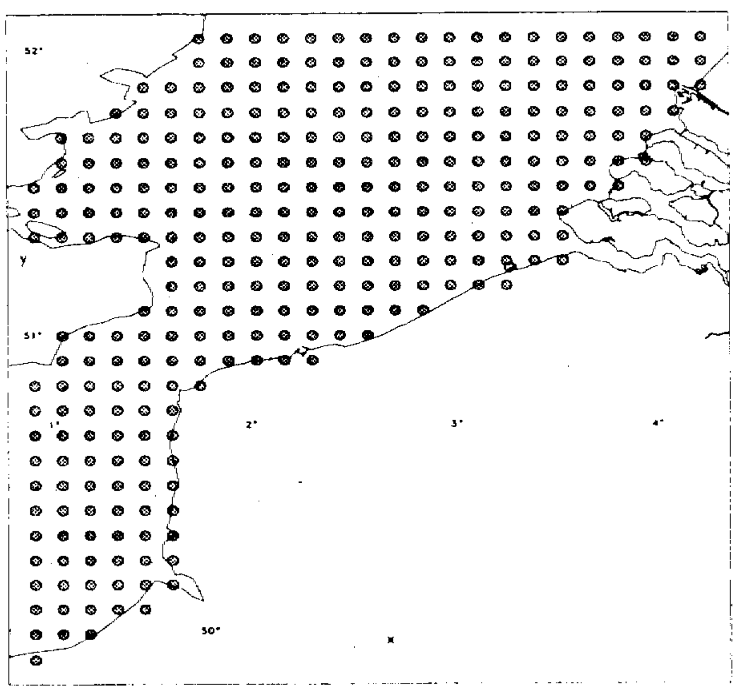

Figure 2. Fine grid model domain and active grid points.

2. DATA

2.1. Satellite data

We obtained ERS-1 fast delivery altimeter data from the European Space Agency as part of Pilot Project PP2-B9, from October 1992 to March 1993. Along tile altimeter track, groups of eight consecutive observations are constructed, out of which a mean is computed. This procedure smooths the raw data and leads to data points spacing from about 52 km, which is close to the resolution of the coarse grid. Then each data point is relocated to the nearest model grid point.

2.2. Buoy data

We have analysed data from various buoys. Their locations are displayed in Table 1 . Sources are the RijksInituut voor Kust en Zee (The Netherlands) and the Afdeling Waterwegen Kust (Belgium).

Table 1. Wave stations

Station	Code	Latitude	Longitude
Platform Auk	AUK	56°23’59”N	2°03’56”E
Platform k13	K13	53°12’03”N	4°35’18”E
Meetpost Noordwijk	MPN	52°16’26”N	4°17’46”E
Westhinder	WEH	51°55’05”N	2°26’30”E
Akkaert	AKK	51°24’49”N	2°46’18”E
A2-Buoy	A2B	51°21’58”N	3°07’47”E
Bol van Heist	BHE	51°22’46”N	3°12’32”E

AUK, K13 and MPN are located only in the coarse grid domain, while WEH, AKK, A2B and BHE lie in the find grid as well. Data at these last four buoys were only available for the months of October-November 1992 and February 1993. Statistics will only be presented for these three months in order to make a comparison between the impact of data assimilation on the coarse and fine grid results. AUK is located in deeper water (90m). The depth at the fine grid buoys ranges from 17m (WEH) to only 7.5m (BHE). We used a 3-hour smoothing on all buoy data before comparing them to the model results.

3. DATA ASSIMILATION METHOD

We opted for an optimal interpolation scheme, described in Mastenbroek et al. (1994), in which all observations available in a 6-hour time window are used to construct the most likely estimate of the field at the middle time of the window. By comparing those data with buoy measurements, it is possible to estimate the error that can be associated with these data. This estimate is indeed an important parameter of the data assimilation scheme. Table 2 summaries some of the available wave data comparisons including our own despite the limited number of correlations.

Table 2. Statistics for the ERS-1 fast delivery product wave data inferred from comparisons with buoy measurements as compiled by three authors. Negative bias means the satellite deduced parameter overestimates the buoy observations. The linear regression is defined by $Hs_{sat} = aHs_{buoy} + b$ and could be used to correct the systematic overprediction of the satellite SWH measurements, as done in Mastenbroek et al. (1994).

	Queffeulou et al. (1995)	Mastenbroek et al. (1994)	This study
Buoys location	N. Atl. & Pac. Ocean, NOAA	North Sea	North Sea
Nb. of correlated data points	279	85	42
standard deviation			
σ (m)	0.39	0.41	0.31
total bias (m)	0.04	0.02	-0.13
linear regr.	0.75	0.80	0.82
b	0.54	0.39	0.46

As discussed in Mastenbroek et al. (1994), there are different sources of error that cause the observe d buoy-altimeter discrepancy. An estimate of the maximum error of the averaged altimeter observation can nevertheless be obtained by assuming that all other error sources give a smaller contribution to the scatter than the systematic errors in the altimeter wave height:

$$\sigma^0=\max(0.4\mathrm{m}:0.08H_s) \qquad (1)$$

Following Queffeulou's discussion and our limited analysis, we choose for the altimeter wind speed error

$$\sigma^0=1.5 \text{ m s}^{-1} \qquad (2)$$

It is a simple matter to group the satellite data in time windows centred at t=0, 6, 12, ... hour. This procedure results in uneven groups of up to 40 data points as illustrated in figure 3 which shows that the assimilation procedure will only use a small number of data points (if any) at each assimilation step.

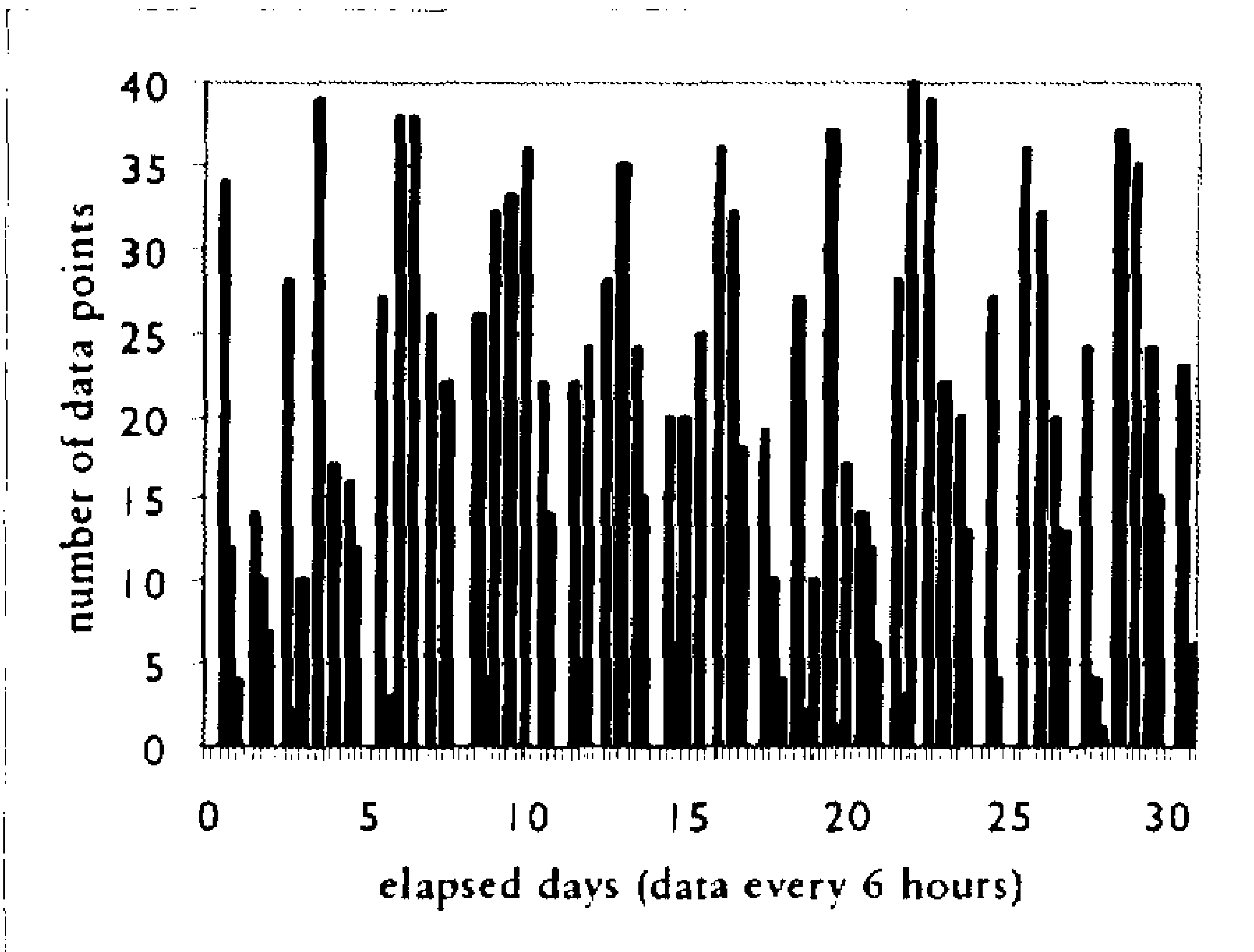

Figure 3. Number of data points per assimilation window in October 1992.

3.1. Analysed fields

One of the first steps in the assimilation procedure requires the computation of the analysed SWH and wind fields. These fields are obtained by combining the observations with the model first guess values at the model grid points by means of an optimal interpolation scheme which in matrix notation can be written as

$$\Psi^a = \Psi^f + MC^T(CMC^T + O)^{-1}(d^0 - C\Psi^f) \qquad (3)$$

where ψ^a, ψ^f and d^0 denote respectively the vectors of the analysed, model first guess and observed values. ψ^a and ψ^f correspond to the values at each active sea grid points (N^{mod}=649 points) and d^0 collects the N^{ob} satellite data points for the corresponding time window (t=0, 6, 12, 18, ...). Those observations do not usually correspond exactly to the model grid value; hence, C is a N^{mod} x N^{ob} matrix introduced to relate the model grid values to the observation points. The matrix M (N^{mod} x N^{mod}) is the error covariance matrix of the model first guesses, and O(N^{ob} x N^{ob}) is the error covariance matrix of the observations. For the sake of simplicity, the simplest possible form is chosen for C, namely protecting each observation onto the nearest active grid point.

The main problem of the optimal interpolation scheme lies in the selection of the standard deviations of the observations and the model as well as the error covariance matrices. We followed a relatively simple method similar to the approach of Mastenbroek et al. (1994) in which no account is made of the wind field on the SWH correlations or vice-versa. The actual values of the parameters in the equations below were obtained front the analysis of MU-WAVE model results and LRS-1 altimeter data. As all approximation, we can neglect the errors between different observations. Thus the matrix O is diagonal and the following expression is used:

$$O_{kl} = \delta_{kl}\left(\sigma_k^o\right)^2 \tag{4}$$

We have already discussed the expression of the standard deviation σ_k^o of observation k as given by (1) and (2) for the SWH and the wind observations.

For the model error covariance matrix M we took (see Mastenbroek et al. 1994)

$$M_{ij} = \begin{cases} \sigma_i^f \sigma_j^f \left(1 + \dfrac{d_{ij}}{d_{corr}}\right) \exp\left(-\dfrac{d_{ij}}{d_{corr}}\right) & d_{ij} \le d_{\max} \\ 0 & d_{ij} \ge d_{\max} \end{cases} \tag{5}$$

where σ_i^f is the model standard deviation at model grid point i, d_{ij} is the distance between grid points i and j (except in the SWH case where $d_{ij}=d_{max}$ if d_{ij} intersects land), $d_{corr}=1.8$ and $d_{max}=10$ grid units is a cut-off length. For the standard deviation σ_i^f of the first guess model wave height H_i^f grid point i we could use an expression that was obtained from a validation of the model at several buoys in the southern North Sea; however it was also found in the 6-month validation using the present satellite and buoy data (Ovidio et al., 1994) that the model error was significantly larger (up to a factor 2) in the northern part of the domain where limited fetch growth laws are used at the open sea boundary condition. To account for this, we introduced a multiplicative factor that varies from 1 in the South to 2 in the North with a rapid transition at the latitude of northern Scotland:

$$\sigma_i^f = \left[1.5 - 0.5\tanh\left(\frac{i-425}{25}\right)\right] \cdot \max\left(0.25\,; 0.15 + 0.15 H_i^f\right) \qquad (6)$$

since i=1 corresponds to the upper left corner grid point. A similar analysis of the wind field gave

$$\sigma_i^f = 1.7 m\, s^{-1} \qquad (7)$$

3.2. Splitting of the analysed wave field

MU-WAVE is a second generation wave model in which wind sea and swell components of the energy spectrum are represented rather differently. Unfortunately, the satellite altimeter data only measures the total energy, as the sum of the contribution of wind sea generated under the direct local influence of the wind, and the different swell components that have propagated from the areas where they were originally created is wind sea. If separate corrections are to be made to each of these wave energy spectrum components, then the proportion of the total analysed energy which is due to each must be estimated. This requires extra information in addition to the analysed SWH as well as a few assumptions that may prove to limit the assimilation efficiency.

We followed the same approach as Thomas (1988) in which the analysed wind is also used to determine the wind sea proportion of analysed energy. The method is based either oil the conservation of the wind sea age (the time during which a certain wind has blown over a region to produce a given wind sea energy state) or alternatively oil the conservation of the wind sea stage of development parameter γ. Both approaches yield an estimate for the analysed wind sea energy E^{a}_{ws} from the first guess wind sea energy E^{f}_{ws} and a given power of the ratio of analysed to first guess wind speed, respectively w^a and w^f:

$$E^{a}_{ws} = E^{f}_{ws}\left(\frac{w^a}{w^f}\right)^p \tag{8}$$

with p=2.57 in the first scheme and p=4 in the second one.

E^{f}_{ws} is a direct model output as MU-WAVE hybrid nature always results in the numerical splitting of the energy spectrum in wind sea and swell contribution. w^a is found by the optimal interpolation on the wind speed. At this point, we assume that the altimeter wind speed is reliable (in agreement with our validation) and that errors in the model wind have resulted in errors in the wind sea which can then he corrected using (8). There is however a limit on E^{a}_{ws}, as it cannot physically exceed the value of the total analysed energy. In cases where the analysed wind sea energy is less than the total measured energy, the remaining portion of the energy is assumed to be swell. Unfortunately, it is not possible to predefine a swell distribution (as is the case for wind sea) since each swell component is essentially non interacting and not related to the local wind. However, the total swell energy can be corrected by multiplying the model swell components along the characteristics by the ratio of estimated to first guess swell energy. This correction is rather arbitrary as it updates all components without any account of the possible propagation direction of the swell energy and will only update components if they were already present (i.e. non zero). This constitutes a major limitation.

3.3. Reconstruction of the wind sea spectrum

In MU-WAVE, prognostic parameters are used to define the wind sea spectral shape, modelled as the product of a directional distribution centred around a mean direction by a one-dimensional energy spectrum. This latter spectrum is determined at each time step by three prognostic parameters, respectively defined as the peak frequency, f_m Phillips' parameter α and the peak enhancement factor γ (Hermans, 1989). The reconstruction of the wind sea spectrum will therefore require the prescription of these three parameters, as no information is available in this study on the actual directional distribution of the wave spectrum; the first guess model directional distribution will be retained. These three parameters were empirically, found to mainly be function of the wind speed, the wind sea energy and the water depth (Bouws et al., 1987). These relations were first tried to reconstruct known MU-WAVE spectra, but discrepancies persisted without any apparent reason. It may well be that the model wind sea spectra do not entirely, satisfy these empirical formulas. Consequently, we designed an alternative approach by denying similar relations for f_m directly from the analysis of the model results. γ was approximated by a piecewise linear distribution that best fits the model correlations and α was tuned to satisfy the total energy constraint. Namely, MU-WAVE uses the following approximation to determine the wind sea energy E_{ws}

$$E_{ws} = E_{TAB} \frac{\alpha}{f_m^4} c(\gamma) \tag{9}$$

where E_{TAB} is a tabulated integral, only function of f_m and the water depth D, through $w_m = 2\pi f_m \sqrt{D/g}$:

$$E_{TAB} = \frac{g^2}{5(2\pi)^4} \int_0^\infty \frac{e^{-\frac{5}{4}\xi^{-4}}}{\xi^4 \chi^2 \left[1 + w_m^2 \xi^2 \left(\chi^2 - 1\right)\right]} \, d\xi \tag{10}$$

in which g is the acceleration due to gravity and with χ solution of

$$\chi \tanh\left(w_m^2 \xi^2 \chi\right) = 1 \tag{11}$$

Note that

$$E_{TAB} \rightarrow \frac{g^2}{5(2\pi)^4} \text{ as } D \rightarrow \infty$$

$c(\gamma)$ is introduced to account for the non fully developed sea state (γ>1):

$$c(\gamma) = \begin{cases} e_1 & \gamma \geq 3 \\ e_2 + \gamma(e_3 + e_4\gamma) & \gamma < 3 \end{cases} \qquad (12)$$

with e_1=1.541, e_2=0.1514, e_3=1.0413, and e_4= -0.1927

The empirical relations can be found if we define the non-dimensional wind sea energy ε and peak frequency ν_m using the wind speed w and g:

$$\varepsilon = \frac{E_{ws} g^2}{w^4} \quad ; \quad \nu_m = \frac{f_m w}{g} \qquad (13)$$

For the purpose of this study, we considered shallow (D<40m) and deep water (D≥40m) correlations determined from the analysis of a one-month run (October 1992):

$$\nu_m = \begin{cases} 0.0213\varepsilon^{-0.3322} & D < 40\text{m} \\ 0.0209\varepsilon^{-0.3376} & D \geq 40\text{m} \end{cases} \qquad (14)$$

hence f_m from (13)
γ is then approximated using

$$\gamma = \begin{cases} 1 & \nu_m \le 0.13 \\ 51.111\nu_m - 5.644 & 0.13 < \nu_m < 0.175 \\ 3.3 & \nu_m \ge 0.175 \end{cases} \quad (15)$$

if $D < 40$m or

$$\gamma = \begin{cases} 1 & \nu_m \le 0.13 \\ 46\nu_m - 4.98 & 0.13 < \nu_m < 0.18 \\ 3.3 & \nu_m \ge 0.18 \end{cases} \quad (16)$$

if D ≥ 40m. Finally, α determined from (9). In the actual reconstruction of the wind sea spectrum that follows the determination of the wind sea proportion to the total energy, we used the previous relations by substituting E_{ws} and w with the analysed wind sea energy E^{a}_{ws} and the corresponding analysed wind speed w_a .

3.4. Update of the wind speed

The effects of the assimilation will only last if the wind speed at later time steps is modified to account for the changes following the assimilation. Indeed, an abrupt return to the first guess wind speed in the following time steps will quickly relax the wind sea back to a state that would prevail if no assimilation had occurred. For that reason, the difference between the analysed and the first guess wind speed at each grid point is used it later time steps to correct the corresponding wind speed value by linearly decreasing the latter difference to zero at the next assimilation time.

4. RESULTS

4.1. Times series

In the following, the bias refers to the difference between the means of buoy data and model results. A positive bias then means an underestimation by the model. The scatter index (S.I.) is defined as in Zambresky (1989) and Romeiser (1993).

Tables 3 , 4 , 5 and 6 present respectively the computed significant wave height (SWH) and mean wave period (MWP) bias and S.I. for the reference and assimilation runs for the months of October 92, November 92 and February 93, i.e. months for which fine grid buoy data were available.

The results for the assimilation runs are still preliminary, and some necessary fine tuning will be made in the near future. We can nevertheless already highlight certain features. First, the effects of the assimilation procedure are clearly visible in the time series of both significant wave height and mean wave period at station AUK (figures 4 and 5). At K13 (figures 6 and 7), effects are already less pronounced.

At this point, following Mastenbroek et al. (1994), we call speculate that if the recalibrated altimeter observations, which result from applying the linear fit of the altimeter to buoy observations (Table 2) are used instead, the scatter will be reduced. However, it was also shown to only be valid at the time and place of the assimilation, and that the improvement apparently disappears quickly. In the limited time span of each improved update, the time series (figures 4 -7) already support this notion. It appears therefore that enough altimeter data leave been assimilated into the model to reduce its bias. Nevertheless, it may well be that this extra wave energy was incoherently supplied to the model as attested by the small reduction of the different scatter indicators. This shortfall suggests that the necessary spectrum reconstruction scheme is inappropriate. If the first guess frequency and angular spectrum differ too much from the actual one, the relatively simple spectrum reconstruction scheme may not produce analysed spectra that lead to a better wave field it later time. As shown below, from the comparison of observed energy spectra with first guess and analysed counterparts, the spectrum reconstruction scheme can fail even in cases where a net positive improvement of the model SWH is obtained.

4.2. Comparison of observed and modelled spectra

The location of station AUK is such that it will still be subject to intense low frequency wave systems propagating from different origins. These wave systems have distinctive spectral characteristics; to see how the assimilation procedure handles the reconstruction and update of these wave systems, we can compare the modelled and observed spectra.

Figure 8 illustrates how the spectrum reconstruction benefits from the satellite data assimilation at that time. This is in ideal case in which the wind sea spectrum is updated following the correction of the local SWH and wind speed. This spectrum update is maintained at later time steps (not shown) even though the effects of the assimilation are slowly vanishing (oil a time span of the order of twelve hours) until an unpredicted wave system appears in the region. For example, the agreement is already less satisfactory in figure 9 : the analysed spectrum keeps the first guess structure and totally misses the existence of a second higher frequency peak, more likely linked to a recent shift in the wind direction.

Satisfactory spectrum reconstruction is not limited to single peak spectra as illustrated in 10, but sometimes (as shown in figure 11) it fails to adequately shift the spectrum peak to lower frequencies. In both previous examples, the assimilation has lead to a satisfactory correction of the SWH (figure 4); however, from the analysis of the evolution of the wave field, it appears that the lack of spectral model wave components at lower frequency in figure 11 call be linked to the inability of the model to advect enough swell energy from an area to the north where the windsea was converted to swell following a change in wind. Therefore, the assimilation is unable to reconstruct the swell field as it was not present in the first guess solution.

Ultimately, to improve the quality of the analysed wave field, spectral observations should be taken into account in the assimilation procedure. In the future, these observations could be obtained from buoys or satellite SAR measurements. To assimilate such spectra, more elaborate assimilation schemes are needed.

Table 3. Significant wave height bias

	October 92		November 92		February 93	
	Ref.	Assim.	Ref.	Assim.	Ref.	Assim.
AUK	0.36	0.24	0.24	0.18	0.18	0.10
K13	0.16	0.10	0.17	0.13	-0.07	-0.11
MPN	0.17	0.11	0.18	0.14	-0.02	-0.03
WEH	-0.11	-0.11	-0.09	-0.11	-0.19	-0.19
AKK	0.15	0.14	N/A	N/A	-0.13	-0.10
A2B	0.05	0.09	-0.16	-0.17	-0.18	-0.19
BHE	0.09	-0.13	-0.19	-0.21	-0.21	-0.22

Table 4. Significant wave height scatter index

	October 92		November 92		February 93	
	Ref.	Assim.	Ref.	Assim.	Ref.	Assim.
AUK	0.34	0.30	0.21	0.20	0.29	0.24
K13	0.21	0.20	0.20	0.20	0.23	0.24
MPN	0.30	0.29	0.32	0.32	0.33	0.34
WEH	0.17	0.23	0.32	0.32	0.29	0.29
AKK	0.10	0.15	N/A	N/A	0.40	0.36
A2B	0.20	0.23	0.39	0.39	0.30	0.31
BHE	0.14	0.23	0.38	0.39	0.32	0.32

Table 5. Mean wave period bias

	October 92		November 92		February 93	
	Ref.	Assim.	Ref.	Assim.	Ref.	Assim.
AUK	0.69	0.43	0.17	0.07	0.39	0.30
K13	0.30	0.21	0.07	-0.02	0.35	0.26
MPN	0.46	0.36	0.51	0.46	0.37	0.34
WEH	-0.19	-0.21	0.07	0.00	-0.14	-0.19
AKK	-0.15	-0.19	N/A	N/A	-0.25	-0.17
A2B	-0.54	-0.73	-0.81	-0.87	-0.62	-0.69
BHE	-0.10	-0.28	-0.22	-0.29	-0.21	-0.28

Table 6. Mean wave period scatter index

	October 92		November 92		February 93	
	Ref.	Assim.	Ref.	Assim.	Ref.	Assim.
AUK	0.20	0.16	0.13	0.10	0.20	0.20
K13	0.15	0.14	0.12	0.11	0.18	0.17
MPN	0.17	0.15	0.18	0.17	0.17	0.17
WEH	0.16	0.15	0.15	0.15	0.16	0.14
AKK	0.10	0.10	N/A	N/A	0.19	0.18
A2B	0.20	0.23	0.29	0.30	0.22	0.22
BHE	0.14	0.16	0.19	0.20	0.15	0.15

Figure 4. Times series of SWH at AUK, Oct. 92

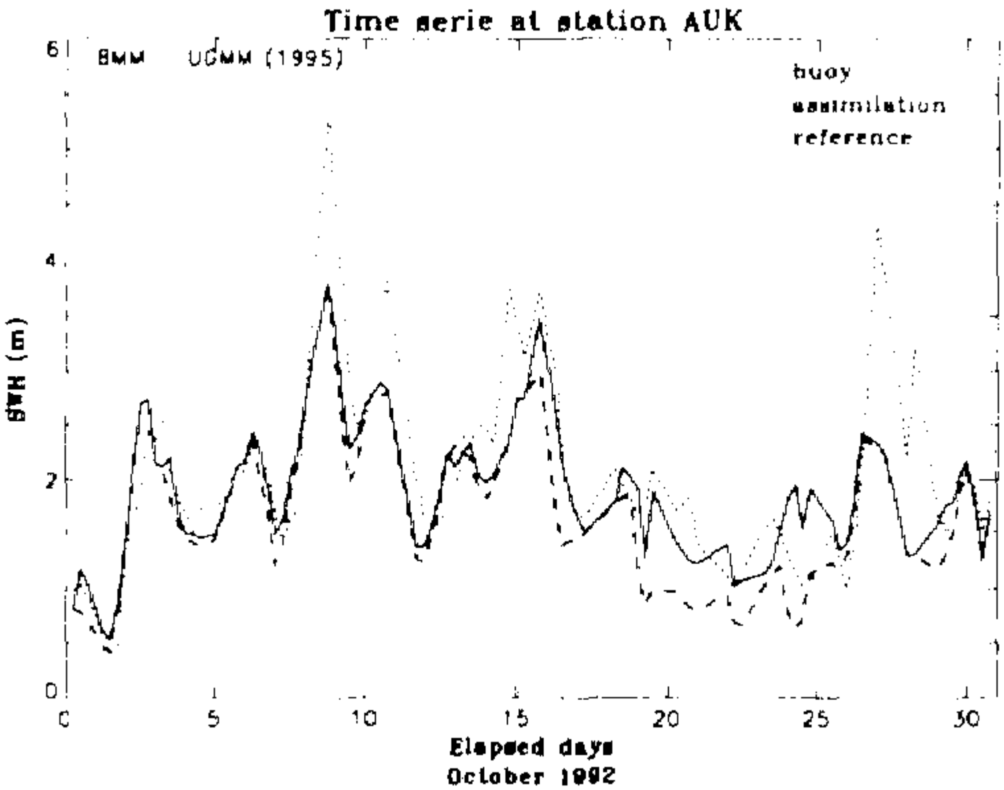

Figure 5. Times series of MWP at AUK, Oct. 92

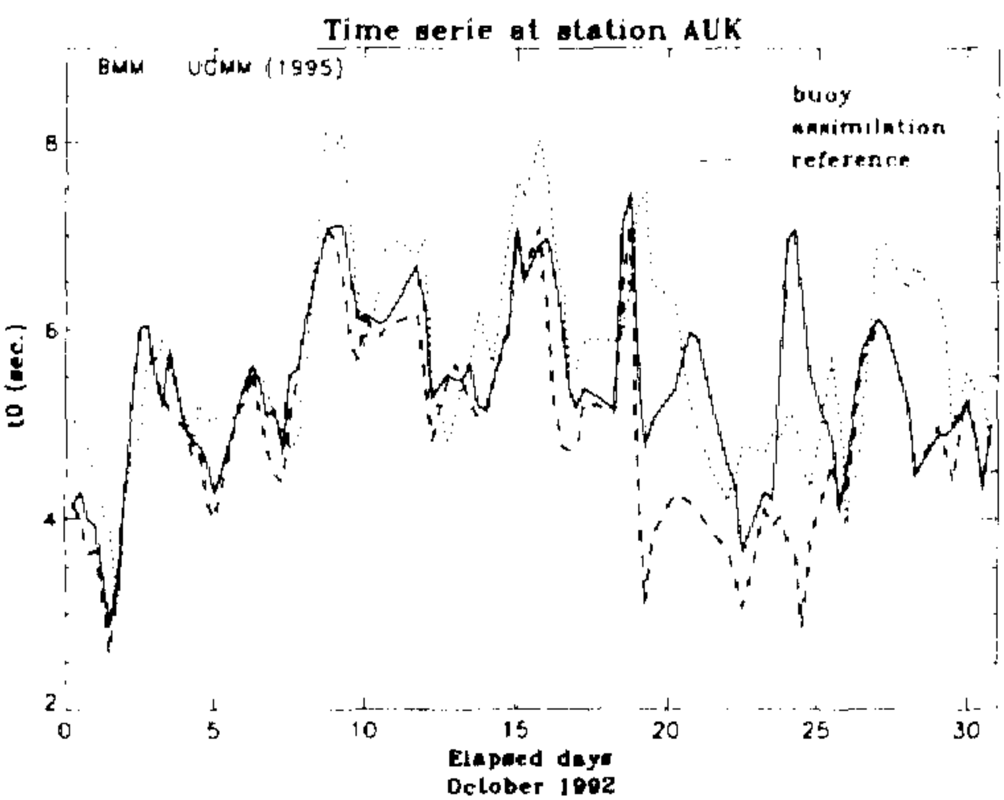

Figure 6. Times series of SWH at K13, Oct.92

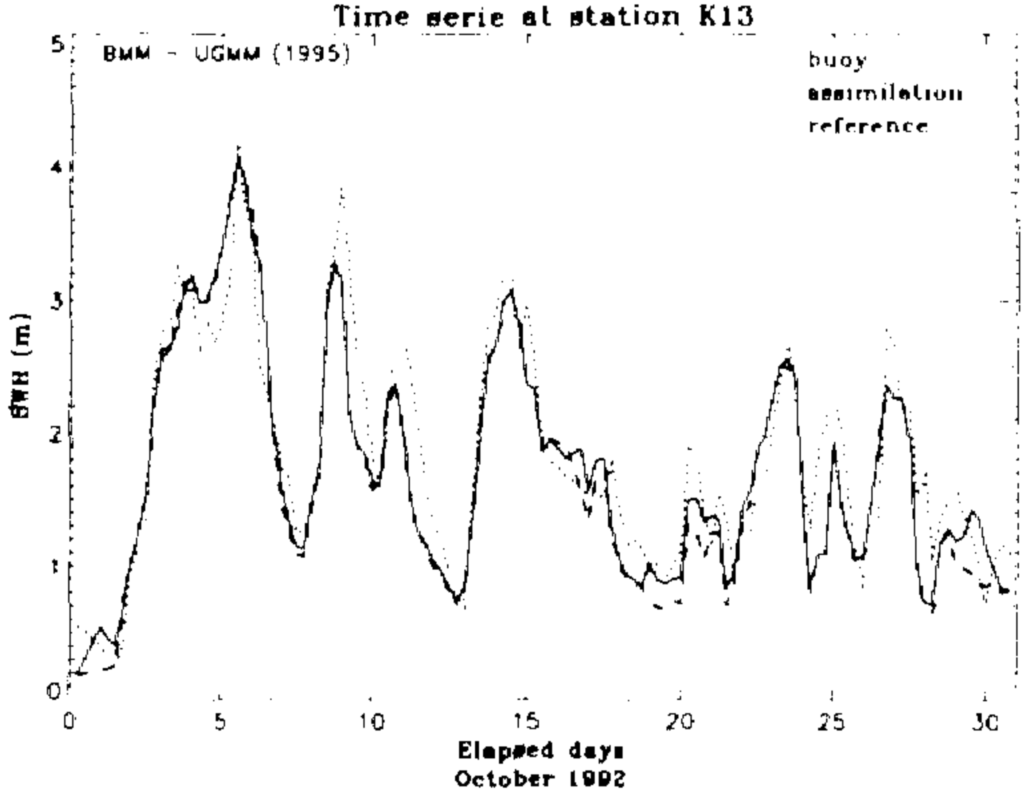

Figure 7. Times series of MWP at K13, Oct. 92

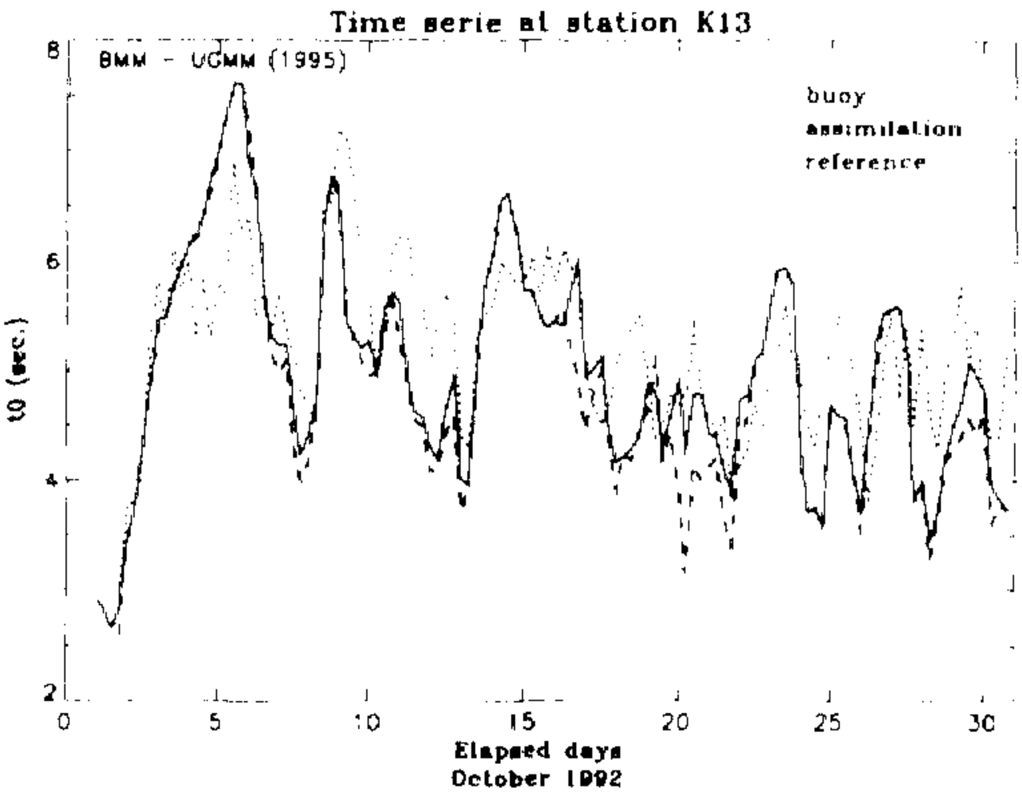

Figure 8. Energy spectrum at AUK, Oct. 7, 1992, 0h

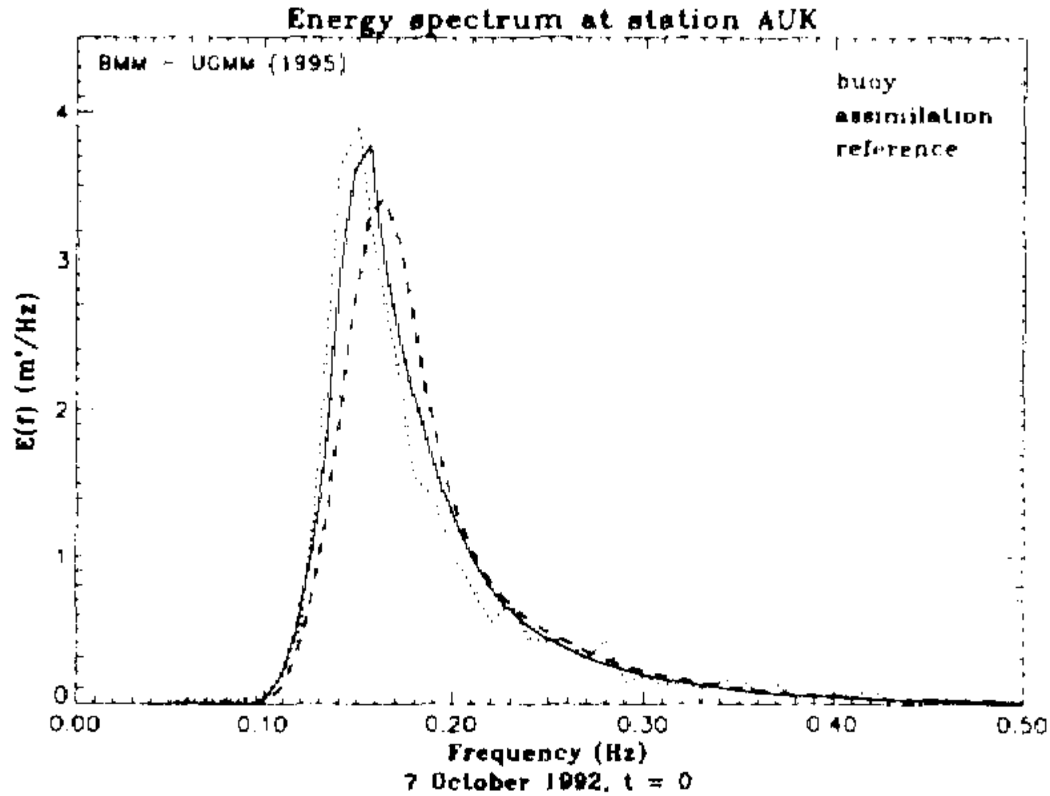

Figure 9. Energy spectrum at AUK, Oct. 7, 1992, 18h

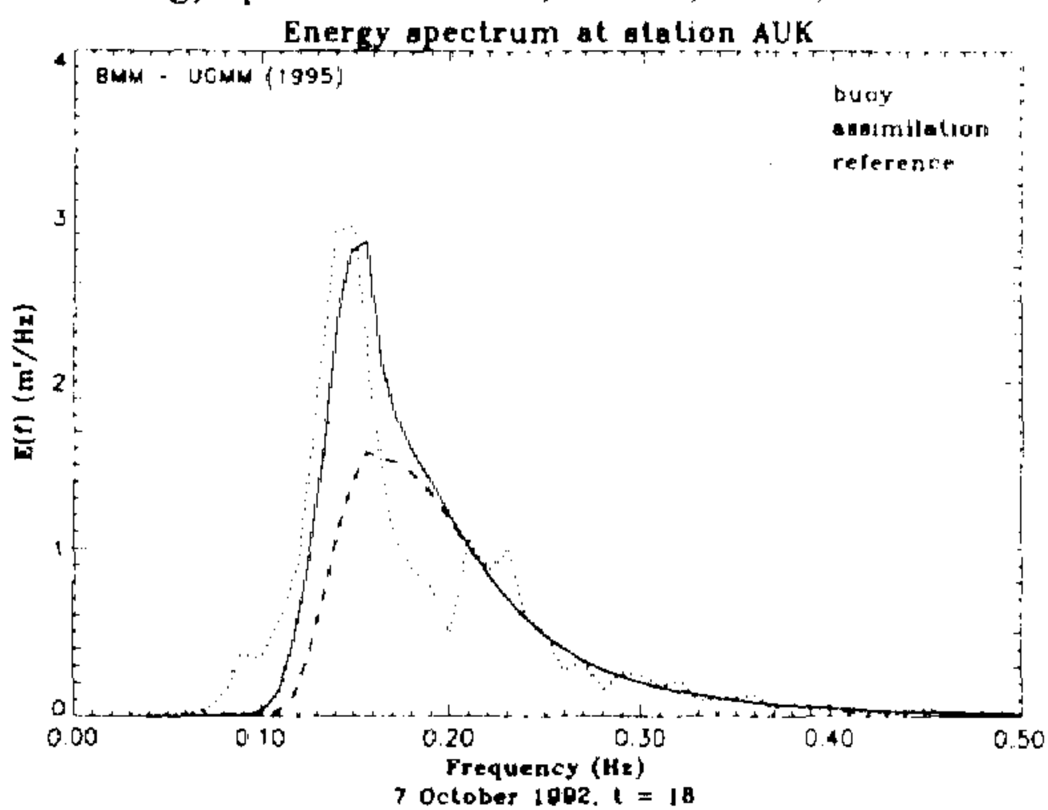

Figure 10. Energy spectrum at AUK, Oct. 17, 1992, 6h

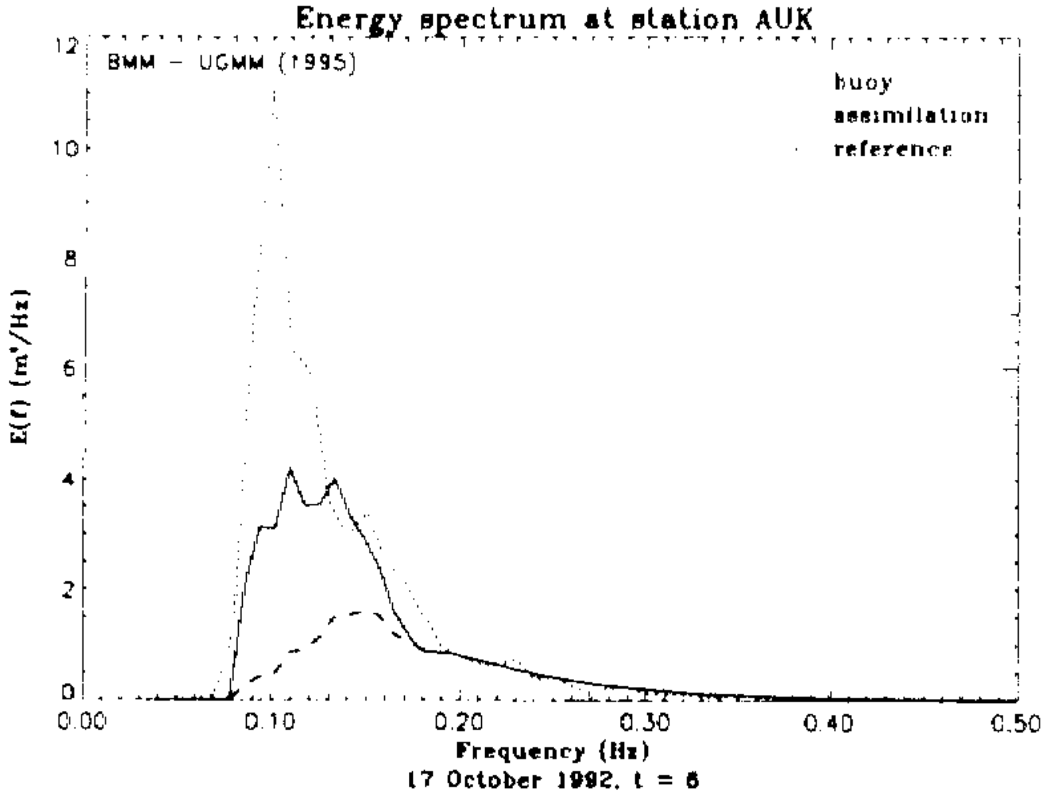

Figure 11. Energy spectrum at AUK, Oct. 20, 1992, 18h

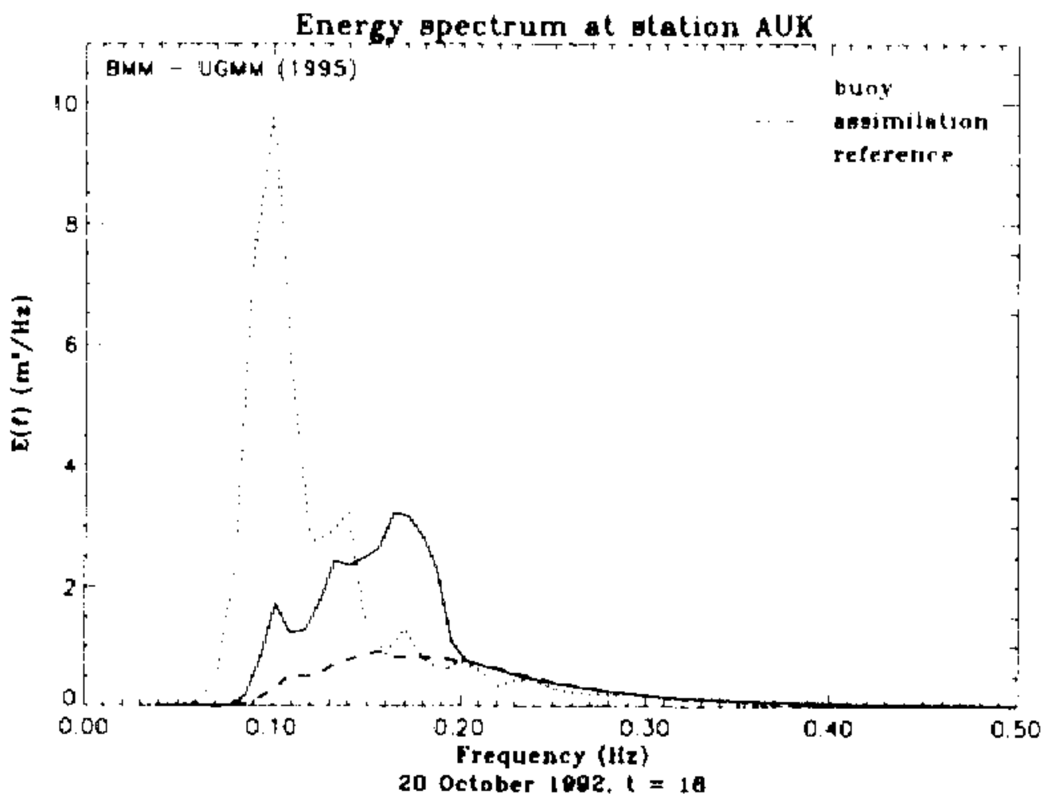

5. CONCLUSIONS

ERS-1 altimeter data has been assimilated in the second generation wave model MU-WAVE using a simple optimal interpolation scheme, and the resulting wave fields were compared to buoy measurement. The bias in the analysed field was significantly reduced. This was not the case for the scatter index of the swale and the mean wave period. These results are in agreement with those of Mastenbroek et al. (1994) obtained with a third generation wave model for the North Sea. A better selection of the different parameters used in the assimilation may slightly improve these preliminary results. However, as already stated supra, it may be necessary to include directional information in the assimilation scheme.

6. ACKNOWLEDGEMENTS

This work was carried out in the framework of the European Space Agency Pilot Project PP2-B9. The authors wish to think ESA for providing the altimeter and scatterometer data.

We also wish to thank the Rijkslnsituut voor Kust en Zee and the Afdeling Waterwegen Kust for providing the buoy data.

F. Ovidio and J.-R. Bidlot are funded by the Belgian Science Policy Office, Research Program on Remote Sensing (third phase, TELSAT/III) under convention T3/58/011.

7. REFERENCES

Bouws, E., H. Gunther, W. Rosenthal and C.L. Vincent, 1987. Similarity of the wind wave spectrum in finite depth water. Part 2: statistical relations between shape and growth stage. Dtscb Hydrogr. Z., 40, H. 1

Gunther, H., W. Rosenthal, 1985. The hybrid parametrical (HYPA) wave model, Ocean Wave Modelling, The SWAMP Group, Plenum Press, New York, 211-214.

Hasselmann, K., T.P. Barnett, E. Bouws, H. Carlson, D.E. Cartwright, K. Enke, J.I. Ewing, H. Gienapp, D.E. Hasselmann, P. Kruseman, A. Meerbrug, P. Muller, D.J. Olbers, K. Richter, W. Sell and H. Walden (1973). Measurements of wind-wave growth and swell decay during the Joint North Sea Wave Project (JONSWAP), Dtsch, Hydrogr. Z., A8(12), 95p.

Hermans, I., 1989. Wave modelling at the Belgian coast by means of the HYPAS model, Progress in Belgian Oceanographic Research, G. Pichot, Science Policy Office & Management Unit of the Mathematical Model of the North Sea and Scheldt Estuary, 75-110, Brussels.

Mastenbroek, D, V.K. Markin, A.C. Voorips & G.J. Komen, 1994. Validation of ERS-1 altimeter wave height measurements and assimilation in a North Sea wave model, Glob. Oc. Atm. Sys., 2, 143-161.

Ovidio, F.,J.-R. Bidlot, D. Van den Eynde, W. Luo and J. Monbaliu, 1994. Validation of the second generation operational wave forecasting model MU-WAVE: comparison with ERS-1, buoy data and WAM forecasts. Proceedings of the First ERS-1 Pilot Project Workshop, Toledo, Spain, ESA SP-365, 21-28.

Queffeulou, P., A. Bentamy, Y. Quilfen and J. Tournadre, 1995. Validation of ERS-1 and TOPEX POSEIDON altimeter wind and wave measurements. Submitted to J. Geophys res.

Romeiser, R. 1993. Global validation of the wave model WAM over a one-year period using geosat wave height data. J. Geophys. Res. 98, C3, 4713-4726.

Thomas J., 1988. Retrieval of energy spectra from measured data for assimilation into a wave model. Q.J. R. Meteorol. Soc., 114, 781-800.

Van den Eynde, D., 1992, MU-WAVE : an operational wave forecasting system for the Belgian coast, Proceedings of the third International Workshop on Wave Hindcasting and Forecasting, May 19-22, Montreal, Quebec, Canada 313-324.

Zambresky, L.F., 1989. A verification of the global WAM model : December 1987 - November 1988, Report GKSS 89/E/37, GKSS Forschungszentrum GmbH, Geesthacht, 86 pp.

4th International Workshop on Wave Hindcasting & Forecasting

A WAVE MODEL WITH A NON-LINEAR DISSIPATION SOURCE FUNCTION

H. Gunther and W. Rosenthal

GKSS Forschungszentrum Geesthacht
Geesthacht, Germany

1. INTRODUCTION

Substantial progress has been made in the recent years in predicting ocean surface gravity waves. The third generation WAM model (Komen et al., 1994) has demonstrated its excellent performance on global and regional scales, which are the deep ocean and shallow water shelf areas. However, difficulties have been found in the coastal zone. The space and time scales in these areas are normally too small to allow the non-linear interactions to control the energy balance. The growth and decay of waves is dominated by the input from the atmosphere and by enhanced dissipation of wave energy in the water column and at the sea floor.

In particular the dissipation in the water column is the most unknown process. In this paper we arc presenting a spectral wave model which uses the dissipation source function derived from turbulent diffusion in the hydrodynamic equations (Rosenthal, 1989). It is shown that this non-linear dissipation leads to a wave model that reproduces standard wave generation and explains self similar spectral shape without taking into account harmonic wave-wave-interaction.

2. STATE OF THE ART

Our present understanding of the physical processes of wave generation is shown in fig 1 . The atmospheric input S_{in}, the nonlinear interaction S_{nl}, and the dissipation S_{dis} balance each other with the propagation of energy to create a self similar spectral shape that resembles the energy density spectra found in deep water (Hasselmann et al 1973 or Toba 1973) and in shallow water (Bouws et al 1985). There is no doubt that all three processes are present and contribute to the development of the ocean waves. From the success of numerical wave models we conclude that the lump sum of the source functions seems to be quite accurate. But when it comes to discuss the error bars of our knowledge of the exact magnitude for any of the three components of the source function the situation is less satisfying. Burgers and Makin (1992) showed that in standard situations the change of S_{in} and S_{dis} by orders of magnitude do not change the results of the wave model as long as the sum of both S_{in} + S_{dis} is the same. The nonlinear interaction source function Snl is also modified in its high frequency tail to contribute to the correct balance of the source functions. That results in the additional dissipation of energy in todays third generation models, although from theory S_{nl} is energy conserving by definition.

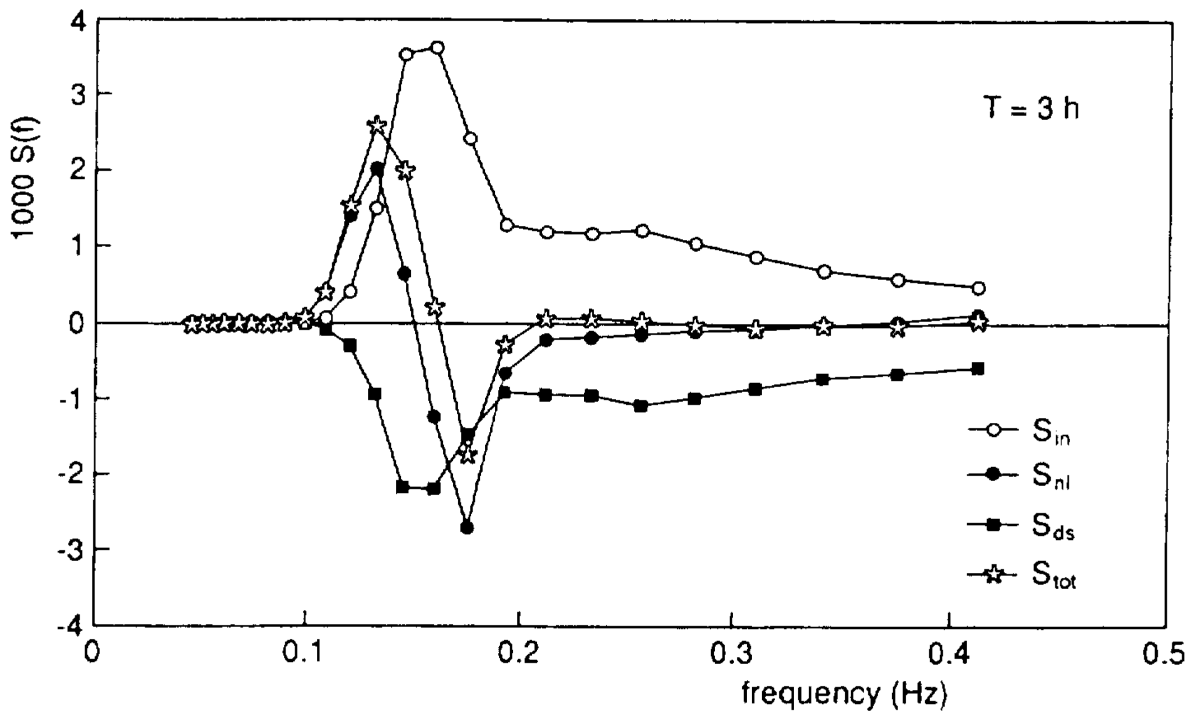

Fig. 1 The energy balance for young duration-limited windsea. (Fig.3.9 from Komen et al 1994).

It seems useful to research for a better link between actual physical processes and the algorithms that are used in todays wave models. The reported deficiencies of accurate knowledge of the individual parts S_{in}, S_{nl}, and S_{dis} of the source function have an effect in situations where the sea state is not in quasi equilibrium, e.g. in situations where the source functions are riot almost balancing each other, or the balance taking place in the open ocean is disturbed by variable bottom topography or by coastal boundaries.

3. THE TRANSPORT EQUATION

Since the pioneering work of Gelci et al (1957) all wave prediction models are based on the spectral transport equation for the action density N(t,x,k)

$$\frac{\partial N}{\partial t} + \nabla_x \bullet \dot{\mathbf{x}} N + \nabla_k \bullet \dot{\mathbf{k}} N = S \qquad (1)$$

where

S is the sum of different source functions which are discussed in the next chapter,
$x = (x_1, x_2)$ is the location vector,
$k = (k_1, k_2)$ is the wave number vector,
the velocities are defined by

$$\dot{\mathbf{x}} = +\nabla_k \Omega$$
$$\dot{\mathbf{k}} = -\nabla_x \Omega \tag{2}$$

The circular frequency Ω and the frequency f are defined by the dispersion relation

$$\Omega = 2\pi f = \sigma + \mathbf{k} \bullet \mathbf{v} \tag{3}$$
$$\sigma = \sqrt{gk \tanh(kd)} \tag{4}$$

which depends on the water depth d and the current vector v.

In most numerical models the action density equation is replaced by the transport equation of the energy density spectrum F as function of frequency f and direction Θ.

$$F(t,\mathbf{x},f,\theta) = \sigma N(t,\mathbf{x},\mathbf{k}) J \tag{5}$$

where J is the Jacobian

$$J = \left| \det\left(\frac{dk_1 dk_2}{df\, d\theta} \right) \right| \tag{6}$$

and the wave direction Θ is defined by

$$k_1 = k\sin\Theta$$
$$k_2 = k\cos\Theta \tag{7}$$

The advantage of choosing frequency as an independent coordinate is a simplification of the transport equation for fixed topography and current. But having in mind applications in the coastal zone where tides are changing depth and currents, this benefit is lost. Moreover, this coordinate transformation is only possible as long as the Jacobian J is not zero. A strong current flowing against the wave propagation direction therefore has to be excluded.

A more fundamental reason to avoid the replacement of action density by energy density is the fact, in the presence of non-uniform currents wave energy is not conserved (Tolman 1990).

Therefore a wave model for the coastal zone should be formulated in terms of action density and in wave number space. To achieve the same directional resolution for all wave lengths, a switch from vector components to polar coordinates in the wave number space seems to be appropriate.

4. SOURCE FUNCTIONS

The physical processes of growth and decay of ocean surface waves are described by the source function

$$S = S_{in} + S_{dis} + S_{nl} + S_{bot} \qquad (8)$$

which is the sum of the atmospheric input S_{in}, the dissipation S_{dis}, the nonlinear interaction S_{nl}, and the dissipation by bottom effects S_{bot}. Details of all processes and their actual implementation in the WAM model are presented in Komen et al 1994.

All functions besides S_{nl}, are proportional to the action density. Nevertheless, the common dissipation source terms contain non-linearities because mean quantities of the spectrum are used for scaling.

4.1 Non-linear dissipation

A non-linear dissipation source term was introduced by Rosenthal 1989. The process of vertical momentum exchange by turbulent eddy viscosity resulted in

$$S_{dis} = -\gamma\omega^2 k^4 N^2(\mathbf{k}) \qquad (9)$$

where γ is a constant.

4.2 Input and bottom dissipation

The standard source function of the input from the atmosphere and bottom dissipation are linear in the action density. We adopt here the common forms of a Snyder-Cox input function

$$S_{in} = \beta\omega \,\mathrm{Max}\left(28\frac{\mathbf{u_*k}}{\omega} - 1; 0\right) N(\mathbf{k}) \qquad (10)$$

$$\beta = 0.0003$$

where u_* is the friction velocity vector, and a bottom dissipation function originally developed in JONSWAP and widely used in numerical wave modelling.

$$S_{bot} = -\alpha\omega^{-2}k^2\left(1 - \tanh^2 kd\right)N(\mathbf{k}) \qquad (11)$$

$$\alpha = 0.04\mathrm{m}^2\mathrm{s}^{-3}$$

5. THE UNCOUPLED WAVE MODEL

The transport (1) together with the source functions (9 to 11) is a decoupled wave model. In the following we consider a homogeneous ocean of constant water depth without currents and a stationary homogeneous wind field. In this case the equation can be solved analytically and the solutions will be used to fix the remaining dissipation constantly and to tune the drag coefficient.

5.1 Analytical Solution

If $N_O=N_O(k)$ is the initial spectrum at $t=t_O$, the solution is

$$N(t,\mathbf{k}) = \frac{A}{B}\left[\frac{1}{1 - \left(1 - \frac{A}{BN_0}\right)e^{-A(t-t_0)}}\right] \qquad (12)$$

where

$$A = \beta\omega \,\mathrm{Max}\left(28\frac{\mathbf{u.k}}{\omega} - 1;0\right)$$

$$-\alpha\omega^{-2}k^2\left(1 - \tanh^2 kd\right) \qquad (13)$$

$$B = -\gamma\omega^2 k^4$$

The stationary state solution is

$$N(t = \infty, \mathbf{k}) = \mathrm{Max}\left(\frac{A}{B}, 0\right) \qquad (14)$$

which is basically the ratio of the linear and nonlinear source functions. In deep water the stationary solution (14) can be transformed analytically into the frequency direction space (cf. 5 and 6) and the one dimensional power spectrum E(f)

$$E(f) = \frac{4\beta g^2}{\gamma(2\pi)^4 f^{-5}} *$$

$$\left[\sqrt{\mathrm{D}^2 - 1} - \arccos\frac{1}{\mathrm{D}}\right] \qquad (15)$$

and the directional distribution R(f,Θ)

$$R(f,\theta) = \frac{\mathrm{Max}(D\cos(\theta - \varphi) - 1;0)}{2\left(\sqrt{D^2 - 1} - \arccos\frac{1}{D}\right)} \qquad (16)$$

can be calculated by integration, where φ is the wind direction and

$$D = 28\frac{2\pi u_* f}{g} \qquad (17)$$

5.2 The Peak Frequency

The peak frequency fp of the spectrum E(f) can be calculated from (15) as

$$f_p = 0.22\frac{g}{28u_*} \qquad (18)$$

It depends only on the friction velocity. A comparison of (18) with the Pierson Moskowitz frequency

$$f_{PM} = 0.13g/u_{10} \qquad (19)$$

for fully developed sea gives

$$u_*^2 = 3.6 * 10^{-3} u_{10}^2 \qquad (20)$$

This value for the drag coefficient is high, but the value of 28 included in the input source function (10) is originally obtained by tuning the WAM model.

5.3 The High Frequency Tail

In the high frequency tail of E(f), where D has large values, the I-d power spectrum is approximately

$$E(f) \approx \frac{4\beta}{\gamma} 28u_* g(2\pi)^{-3} f^{-4} \qquad (21)$$

This spectrum has the same form as the spectrum proposed by Toba (1973):

$$E_{Toba}(f) = \alpha_T u_* g (2\pi)^{-3} f^{-4} \tag{22}$$

Comparing both spectra and using Toba's α_T=0.062 determines 0.54 as a first approximation of the dissipation constant γ. Integrating (15) over frequency and comparing the total energy with the energy of the Pierson Moskowitz spectrum requires a γ = 0.14 to get the correct value. The differences are related to the rough approximation used to obtain (21) and in the use of different drag coefficients.

5.4 <u>The Time Evolution And Model Spectra</u>

The time evolution of the one-dimensional wave spectrum (Fig. 2) clearly shows the behaviour of a decoupled model. An overshoot of the spectral peak energy is not present. The computations have been done with a wind speed u_{10} = 10m/s and the initial spectrum N_O was fixed as 0.001 of the stationary solution (14). The model became stationary after about 120h. As it was expected the peak frequencies of the Pierson Moskowitz spectrum and of the stationary model spectrum are equal. The spectral forms are different but both spectra contain the same total energy. The model spectrum has less peak energy but a higher energy level in the higher frequencies.

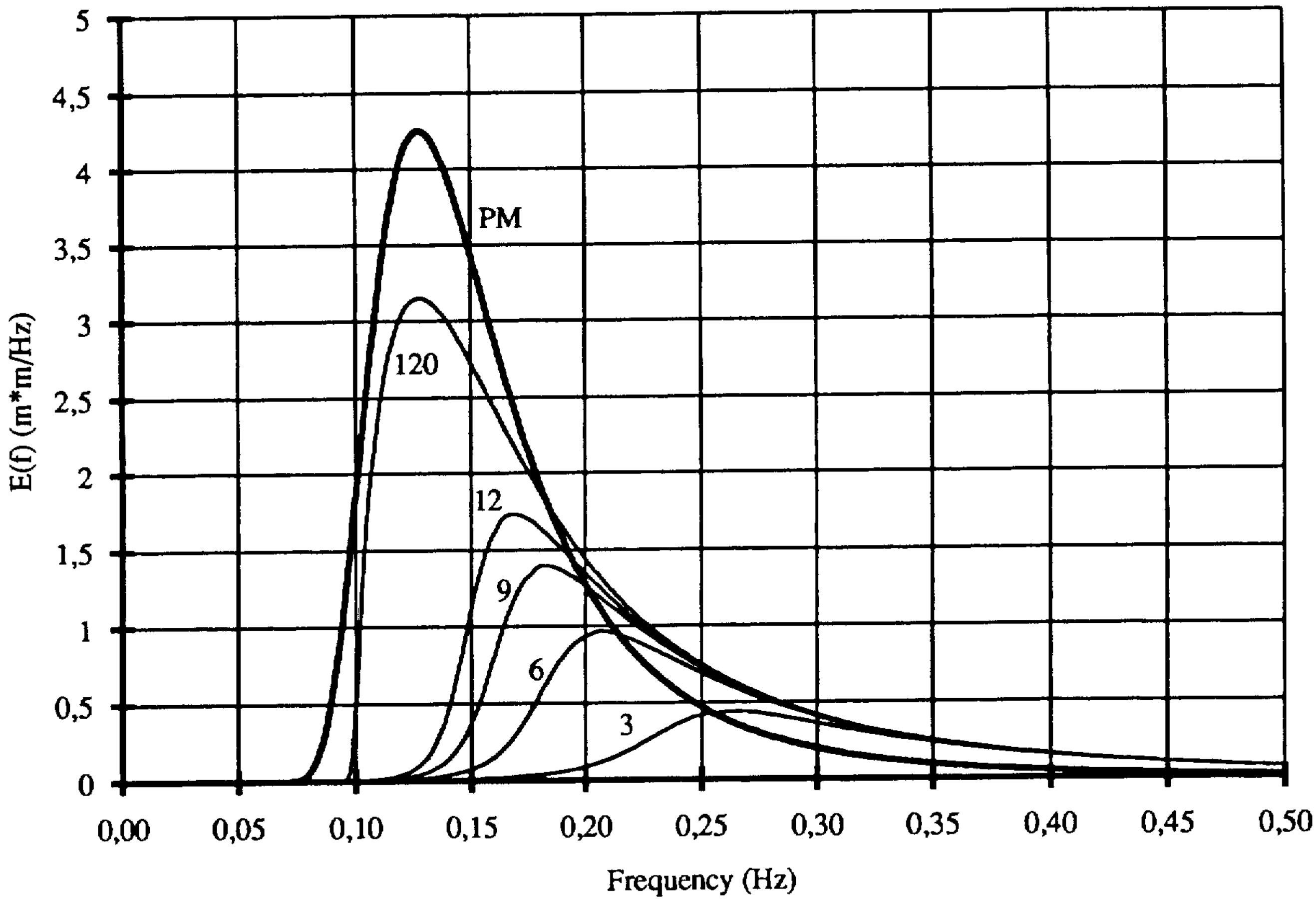

Fig.2 Evolution of the one-dimensional wave spectrum for duration limited growth for a wind speed of 10m/s in deep water. The spectra are marked by the duration in hours. The corresponding Pierson Moskowitz (PM) spectrum is shown for comparison.

The time development of the peak frequency (Fig. 3) compares quite well with the HYPA model (Gunther et al 1979), which was in the middle of the bulk in the SWAMP (1985) growth curve comparisons. The same behaviour is achieved for the total energy comparison.

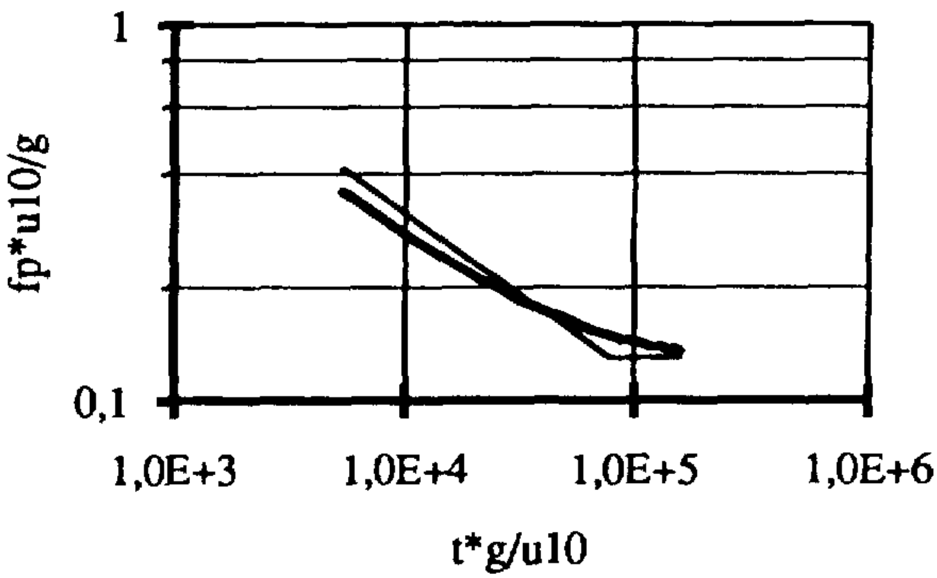

Fig. 3 Evolution of the dimensionless peak frequency with dimensionless time. The thin line corresponds to the HYPA growth curve.

The directional distribution (16) of the steady state spectrum (Fig.4) is narrow for low frequencies and spreads to a cosine square distribution at about twice the peak frequency.

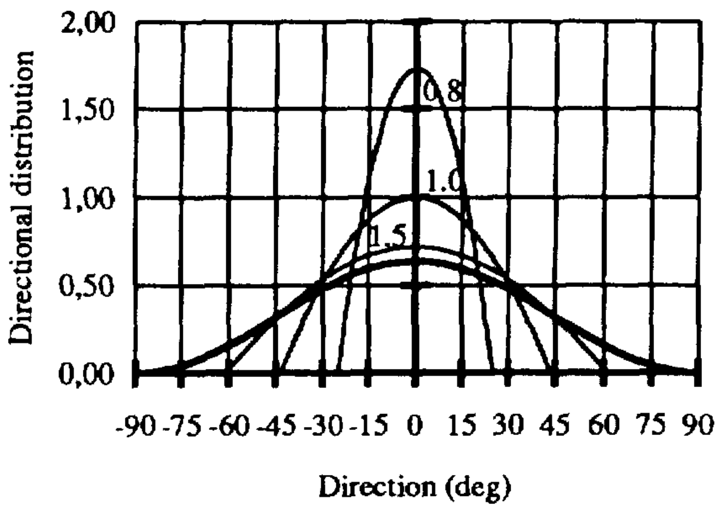

Fig. 4 Directional distribution of wave energy for 0.8, 1.0 and 1.5 times peak frequency (thin lines) and the cosine square distribution (thick line).

6. The Coupled Wave Model

From the previous section it is clear that the model spectra do not develop the observed overshoot at the spectral peak. This can be achieved either by introducing the non-linear interaction source term or by introducing an additional parameter in the dissipation source function, which reduces the dissipation at the forward front of the spectrum. In the WAM model both methods are applied. The most convenient parameter of a model formulated in wave number space is the mean wave number

$$\bar{k} = \frac{\iint kN(\mathbf{k})d\mathbf{k}}{\iint N(\mathbf{k})d\mathbf{k}} \qquad (23)$$

We replace the dissipation constant γ by

$$\gamma = \gamma_0 \frac{p_1 * (p_2 \frac{k}{\bar{k}})^q + 1}{(p_2 \frac{k}{\bar{k}})^q + 1} \qquad (24)$$

Choosing the constants γ_0=0.056, P_1=6.0, P_2=1.15 and q=8.0 the model correctly computes the Pierson Moskowitz energy. Fitting the spectra with the JONSWAP spectral form (Gunther 1981) produces overshoot factors between 2 and 3 at the peak (Fig. 5). Compared to the decoupled model (Fig.2) this result is satisfying in the growing phase but now the fully developed spectrum is clearly much too narrow.

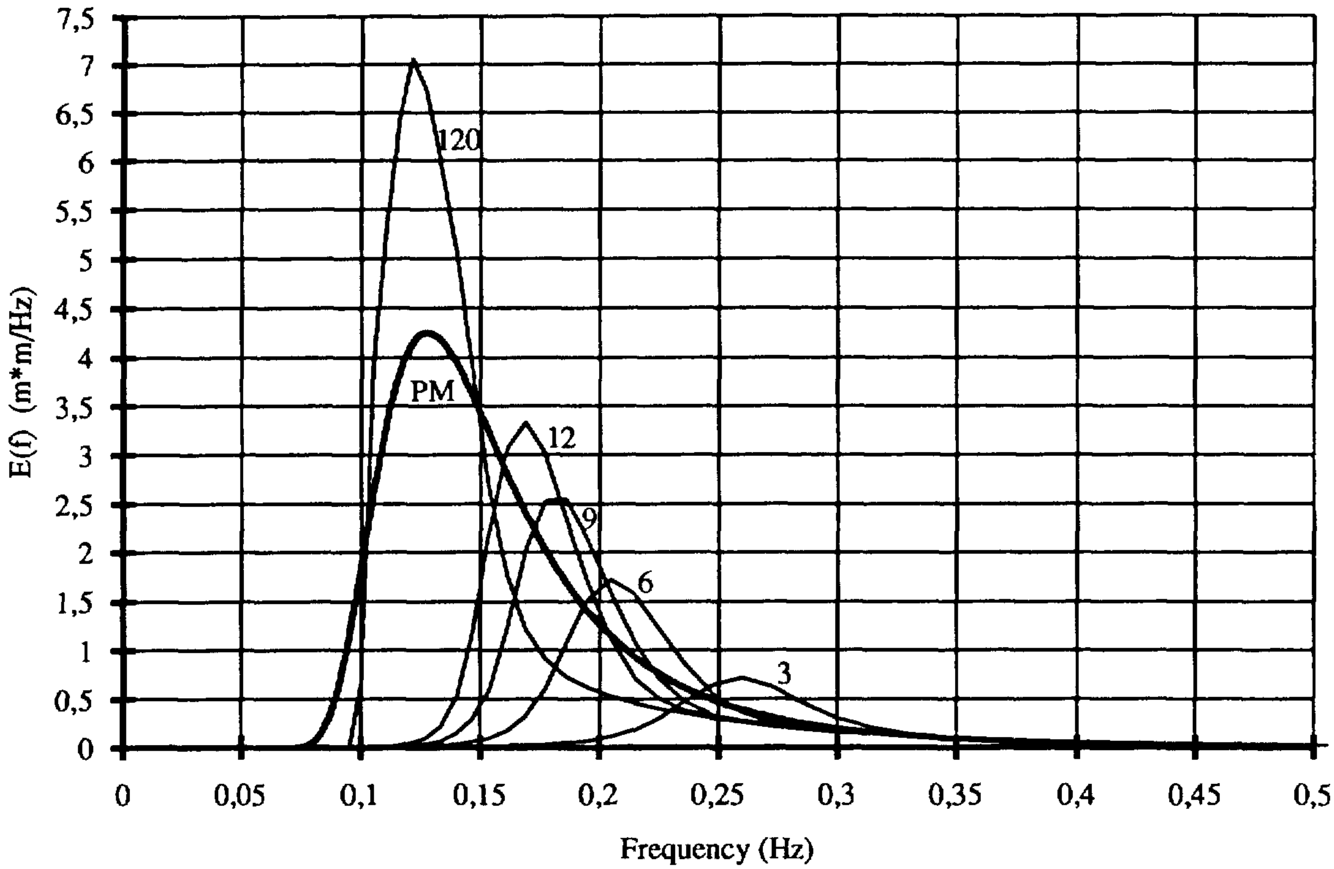

Fig.5 same as Fig.2, but with a dissipation constant γ as defined in (24).

The scaling of the dissipation by the relative wave number in (23) is not growth state dependent and therefore can not reduce the overshoot when the fully developed state is approached. This effect is related to the statistical nature of the forcing wind speed which is not covered by the formulation of the input source function (10). In particular the sharp cut by the maximum function does not allow growth for waves with phase speeds higher than the mean wind speed (Komen et al 1994).

Assuming Gaussian statistics for the fluctuations of the friction velocity with mean u_* and standard deviation σ_u, the mean input source function is calculated from (10) as

$$S_{in} = \beta\omega \left\{ \begin{array}{l} \frac{1}{\sqrt{2\pi}} \frac{\sigma_u}{c_*} e^{-\frac{(c_* - u_*)^2}{2\sigma_u^2}} \\ + \frac{1}{2}\left[\frac{u_*}{c_*} - 1\right] \cdot \left[1 - \phi\left(\frac{c_* - u_*}{\sigma_u}\right)\right] \end{array} \right\} N(k) \tag{25}$$

if

$$c_* = \frac{\omega}{28k\cos(\theta - \varphi)} \tag{26}$$

is positive, and zero otherwise, ϕ is the probability function

$$\phi(y) = \frac{2}{\sqrt{2\pi}} \int_0^y e^{-\frac{t^2}{2}} dt \tag{27}$$

The input source function (25) in combination with the dissipation source function (9) extended by (24) is used to calculate the duration limited growth again. After changing the parameters in (24) to γ_0=0.675, P_1=4.0, P_2=1.2 and q=8.0 and assuming 0.4 for the gustiness parameter $\sigma u/u_*$, the result of Fig. 6 is obtained. The agreement between the Pierson Moskowitz and the model spectrum is quite good and an overshoot is present in the growing phase. The shift of the peak frequency to lower values is comparable to Fig. 3 .

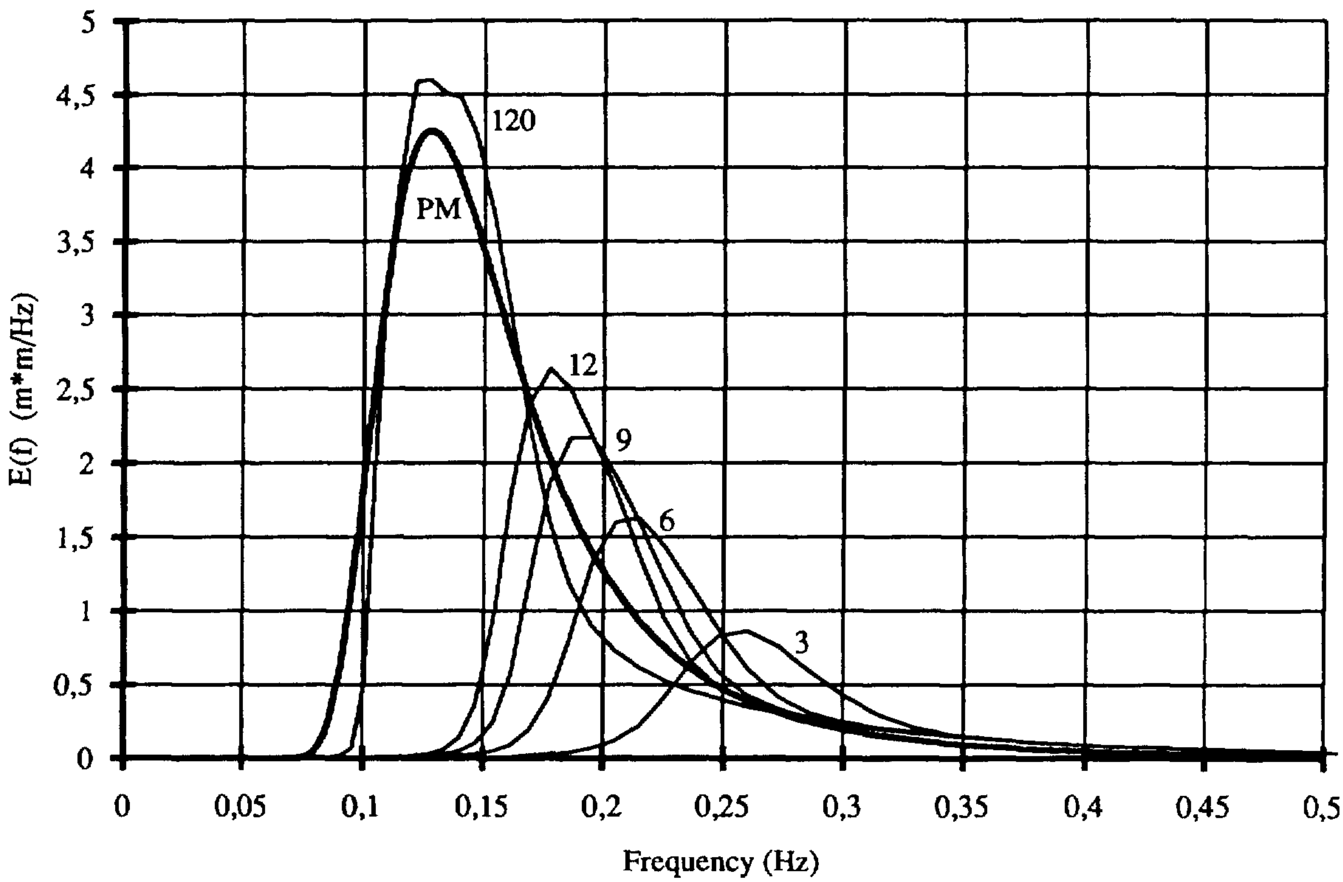

Fig.6 same as Fig.2, but with a dissipation constant γ as defined in (24) and input source function (25).

7. THE JONSWAP FETCH GROWTH

The most famous picture of fetch limited wave development is presented in Fig 25 (Hasselmann et al 1973). The reproduction in Fig. 7 shows wave spectra at 9.5 km (station 5), 20 km (station 7), 37 km (station 9), 52 km (station 10) and 80 km (station 11) measured under 'ideal' generation conditions. Unfortunately, the measured wind speed for this case is not given. It can be estimated roughly from

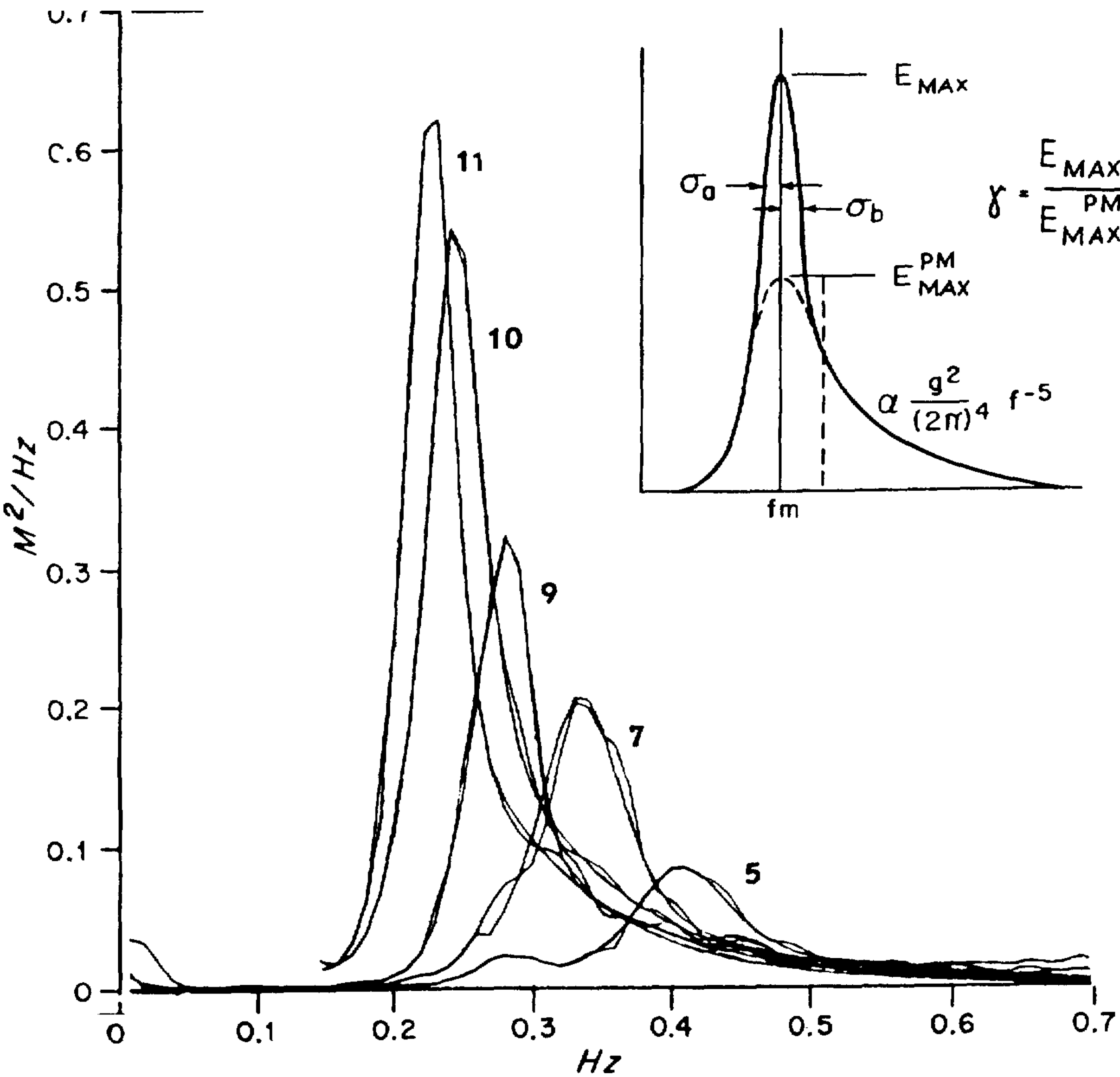

Fig.7 Evolution of wave spectrum with fetch for offshore winds (11h-12h, Sept. 15,1968). Numbers refer to stations (see text). The best-fit analytical spectra are also shown. The inset illustrates the definition of the five free parameters in the form. (Fig . 25 in Hasselmann et al 1973).

Müller (1976) to 8 m/s. Results of the coupled model as described in chapter 6 forced by u_{10} = 8 m/s are shown in Fig. 8 . The agreement of Fig.7 and 8 is remarkable, even more, if one takes into account the uncertainty in the wind speed and the fact, that the tuning of the model has only been done with the Pierson Moskowitz fully developed sea state. Fig. 8 shows that the fit with the JONSWAP spectral form is just as well as in Fig.7 , which means that the model is able to produce a self-similar spectral form.

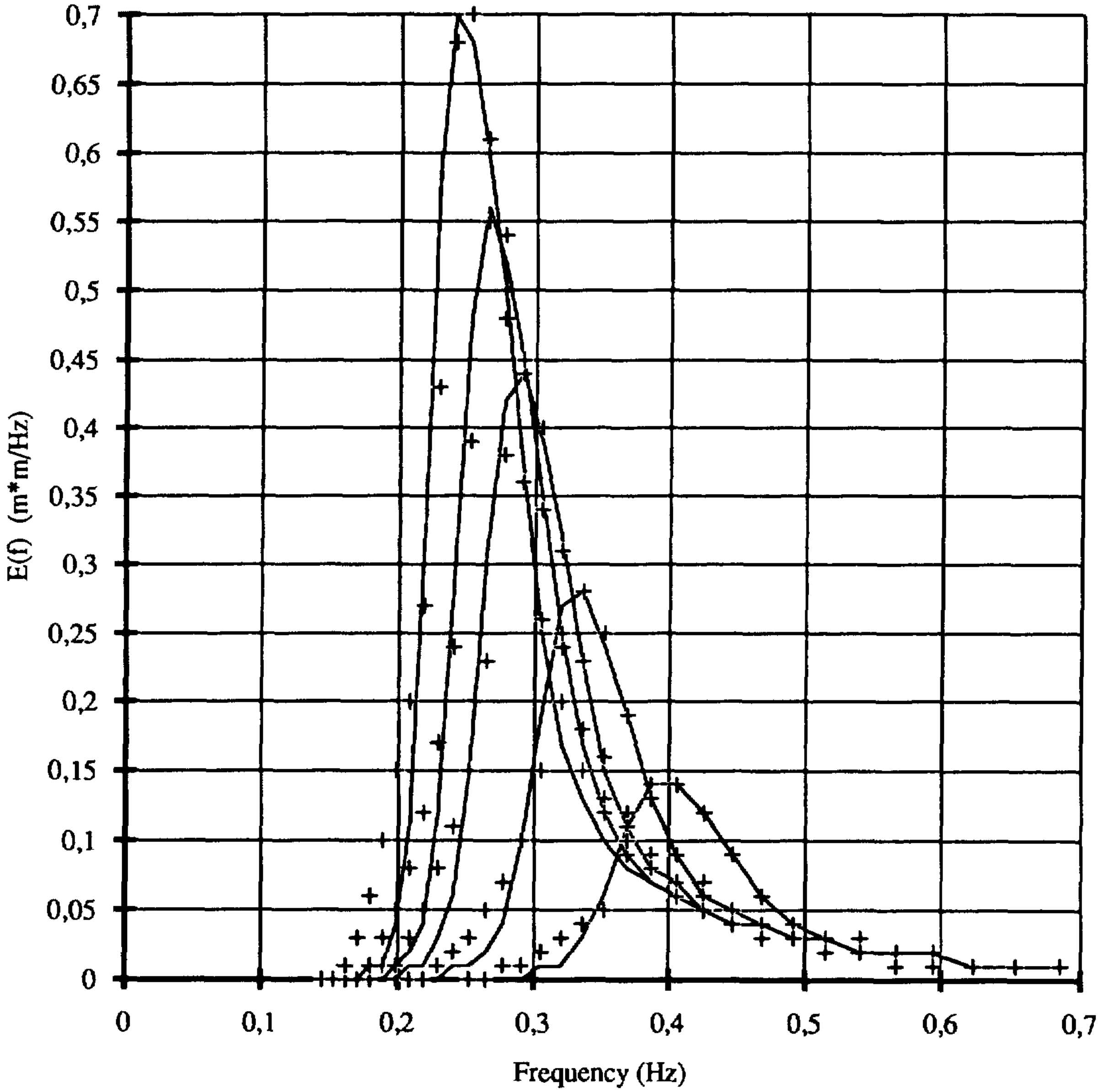

Fig.8 Fetch limited evolution of wave spectra computed with the coupled model forced by a 8m/s wind. Numbers refer to stations (see text). The full lines are the model spectra and the crosses indicate the fit with the analytical JONSWAP form.

The fetch development of the JONSWAP parameters are plotted in Fig. 9 . The dimensionless peak frequency fetch development is in good agreement with the JONSWAP curve. The fitted Phillips parameter α is higher than the JONSWAP curve but well inside the cloud of the measured data. The overshoot parameter γ and the left and right peak width parameter σ_a and σ_b are inside the range of measured values as well. Whereas γ and σ_a are close to the mean JONSWAP values of 3.3 and 0.07, respectively, the σ_b values are higher than the mean JONSWAP value 0.09. The scatter of the modelled peak parameters are caused by the fitting routine and the discrete frequency axis used in the computations (Günther 1981).

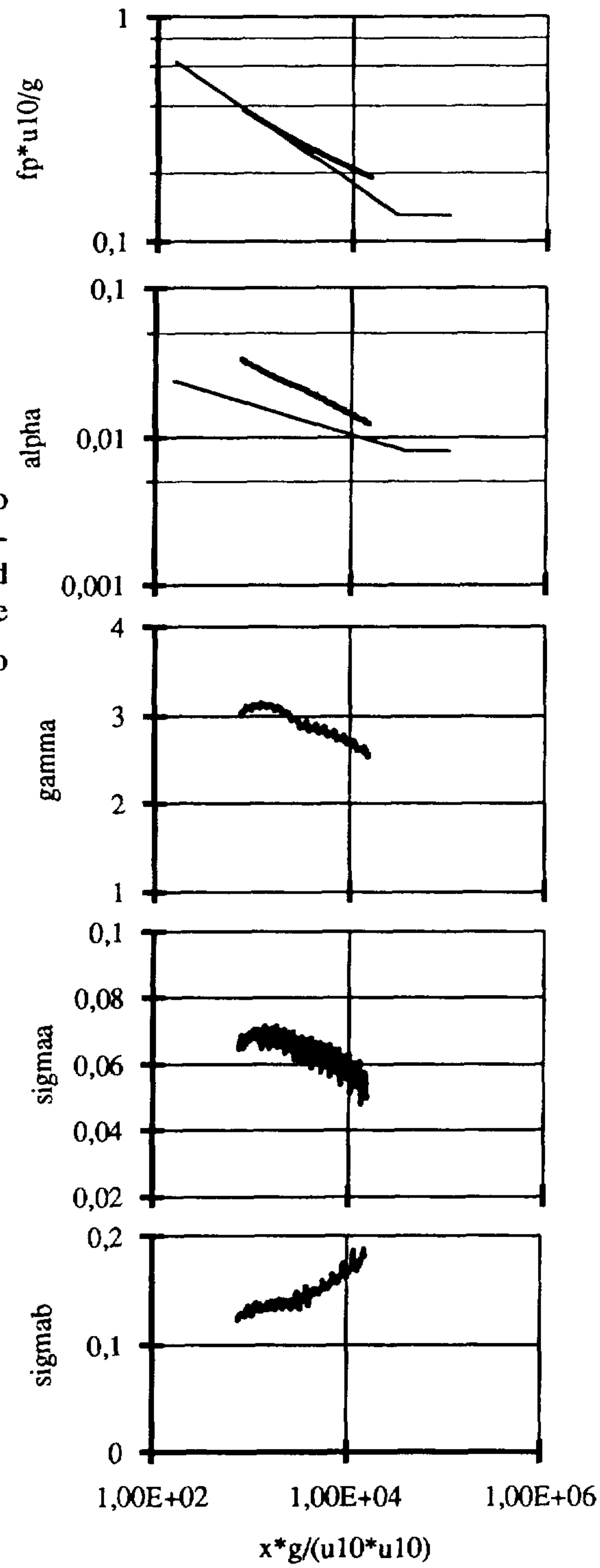

Fig. 9 JONSWAP parameters vs. fetch. From top to bottom are the dimensionless peak frequency, Phillips parameter α, overshoot factor γ and left and right peak width σ_a and σ_b as thick lines. The JONSWAP fetch relations are shown in the top two diagrams as thin lines.

8. SUMMARY

A decoupled and a coupled ocean wave model with a nonlinear dissipation source function have been presented. In both models the nonlinear interaction source term is neglected and the dissipation constant has been tuned to reproduce the total energy and peak frequency of the Pierson Moskowitz fully developed sea state correctly.

The decoupled version is able to model correctly energy the growth of integrated spectral parameters (eg. energy) and the shift of the peak frequency to lower values. The directional distribution of the spectra is consistent with observations. The 1-dimensional spectra are self similar but the observed overshoot is missing. The results of this model are typical for a first generation wave model (SWAMP 1985) even if the artificial limitation of the spectral growth is not present in the model.

The decoupled model has been extended to a coupled model by introducing a mean wave number dependent function in the dissipation 'constant'. This is necessary to generate a spectral overshoot. The overshoot disappears at the approach of the fully developed sea state when the gustiness of the wind is taken into account in the input source function.

It has been demonstrated that the coupled model is able to reproduce the JONSWAP fetch limited growth. Measured and model spectra are in excellent agreement.

The coupled model can be classified as a third generation model, because it has no prescription of the spectral form.

To investigate the behaviour of the model in nonstationary wind fields and in shallow water a number of tests have to be done in the future. First results not shown here in shallow water applications show that the TMA-spectra (Bouws et al 1985) are correctly modelled as well.

9. REFERENCES

Bouws, E., H. Günther, W. Rosenthal and C.L. Vincent, 1985: Similarity of the wind wave spectrum in finite depth water, Part 1. J. Geophys. Res. C90, 975-986.

Burgers, G. and V.K. Makin, 1992: Boundary layer model results for wind-sea growth. J. Phys. Oceanogr. 23, 372-385.

Günther, H., W. Rosenthal, T.J. Weare, B.A. Worthington, K. Hasselmann, J.A. Ewing, 1979: A Hybrid Parametrical Wave Prediction Model. J. Geophys. Res., 84, No. C9, 5727-5738.

Günther, H., 1981: A parametric surface wave model and the statistics of the prediction parameters. Hamburger Geophysikalische Einzelschriften, Reihe A, Nr. 55, 90 p.

Hasselmann, K., T.P. Barnett, E. Bouws, H. Carlson, D.E.Cartwright, K. Enke, J.A. Ewing, H. Gienapp, D.E. Hasselmann, P. Kruseman, A. Meerburg, P. Müller, DJ. Olbers, K. Richter, W. Sell, and H. Walden, 1973: Measurements of wind-wave growth and swell decay during the Joint North Sea Wave Project (JONSWAP), Dtsch. Hydrogr. Z. Suppl. A 8(12), 95p.

Komen, G.J., L. Cavaleri, M. Donelan, K. Hasselmann, S. Hasselmann, P.A.E.M. Janssen, 1994: Dynamics and Modelling of Ocean Waves. Cambridge University Press, Cambridge, UK, 560 pages.

Müller, P., 1976: Parametrization of one-dimensional wind wave spectra and their dependence on the state of development. Hamburger Geophysikalische Einzelschriften, Nr. 31, 177 p.

Rosenthal, W., 1989: Derivation of Phillips α-Parameter from Turbulent Diffusion as a Damping Mechanism. In: Radar Scattering from Modulated Wind Waves, Komen, G.J. and W.A. Oast (eds.), Kluwer Academic Publishers.

The SWAMP-Group: J.H. Allender, T.P. Barnett, L. Bertotti, J. Bruinsma, V.J. Cardone, L. Cavaleri, J. Ephraums, B. Golding, A. Greenwood, J. Guddal, H. Günther, K. Hasselmann, S. Hasselmann, P. Joseph, S. Kawai, G.J. Komen, L. Lawson, H. Linné, R.B. Long, M. Lybanon, E. Maeland, W. Rosenthal, Y. Toba, T. Uji, W.J.P. de Voogt. 1985: Sea Wave Modelling Project (SWAMP). Principal Results and Conclusions. In: Ocean Wave Modelling. Plenum Press, New York, 256 pages.

Toba, Y, 1973: Local balance in the air-sea boundary process, 3. On the spectrum of wind waves. J. Oceanogr. Soc., Japan 29, 209-220.

Tolman, H.L., 1990: Wind wave propagation in tidal seas. Comm. Hydr. Geotechn. Eng., Delft Univ. of Techn., Report No. 90-1, 135p.

SENSITIVITY OF WAVE MODEL PREDICTIONS ON SPATIAL AND TEMPORAL RESOLUTION OF THE WIND FIELD

Hans C. Graber[†] Robert E. Jensen* Vincent J. Cardone[§]

[†] Division of Applied Marine Physics
Rosenstiel School for Marine and Atmospheric Science
University of Miami
Miami, FL 33149, USA

* Coastal Engineering Research Center
Waterways Experiment Station
U.S. Army Corps of Engineers
Vicksburg, MS 39180, USA

[§] Oceanweather, Inc.
Cos Cob, CT 06807, USA

1 Introduction

It is well established that uncertainties in the wind forcing are the largest source of errors in model generated wave fields in operational implementations of contemporary wave models (e.g. Janssen et al., 1984; Cardone and Szabo, 1985), and are usually so large as to mask errors associated solely with deficiencies in the wave models physics or numerics. Intercomparison of ocean wave predictions forced with wind fields specified on grids with different spatial and temporal resolutions is further complicated by the fact that differences in the model predicted wave fields depend on errors associated with the physics and numerics of weather prediction models, the objective analysis schemes and the coarseness of the wind analysis products in time and space. Accurate simulations of mesoscale cyclonic events (e.g. frontal passages, storms and hurricanes) require not only more dynamically consistent fields, but also higher spatial and temporal resolution for more detailed studies of such mesoscale forcing events on ocean modelling, particularly wave prediction. Such simulations are often carried out in atmospheric general circulation models (Held and Phillipps, 1993) and in model sensitivity studies of cyclonic disturbances over data-sparse oceans (Orlanski et al, 1991). Standard real-time objective analysis products of numerical weather prediction centers do not provide higher resolution of either global or regional wind fields. However, re-analyses of special events can produce higher resolution wind fields over limited areas and for selective time periods (e.g. the duration of a storm (Sanders, 1 990)).

This study investigates the impact of the spatial and temporal resolution of a wind field on the simulations of the sea state provided by a skillful ocean wave model. The ocean wave model was forced with a high-resolution wind field which was derived by intensive manual kinematic reanalysis of the space-time evolution of three low-pressure systems moving in rapid succession off the South Carolina coast into the western North Atlantic (Cardone et al., 1995). This triple storm system occurred during the first intensive observation period (IOP-1) of the Surface Wave Dynamics Experiment (SWADE) in October 1990 (Weller et al, 1990). A detailed study for this IOP was carried out by Graber et al. (1991) and Cardone et al. (1995) to assess the contributions of errors in wind fields through evaluations of the hindcasted wave field made with the WAM model against the extensive SWADE measured wave data base.

The basic approach employed in this study is to evaluate the sensitivity of the wave hindcasts on resolution of the wind forcing field by successively degrading the temporal and spatial resolution of the high-resolution OW/AES wind field for SWADE IOP-1. The spatial and temporal resolutions were sub-sampled in such a way as to emulate the characteristic resolutions of the operational numerical weather prediction center and special reanalysis wind products. The results assess the accuracy of the degraded wind fields in terms of the accuracy of the resulting wave hindcast and provide estimates of the magnitude of the error incurred from poorer resolution. The results also show estimates of the percentage error caused by poorer resolution in the alternative wind fields.

2 Numerical Experiments

In this section, a brief description is given of the alternative wind fields and the strategy of the modelling experiment. In particular, we describe the characteristics of the alternative wind fields and the methodology in degrading the temporal and spatial resolution of the OW/AES wind fields. We also discuss the configuration and setup of the wave model simulations and how the alternative wind fields on a regional scale were combined with one wind field specified over the entire Atlantic basin for providing boundary conditions of spectra and propagation of swell from distant storms.

2.1 Wind fields

Six alternative wind fields were originally employed in the analysis of SWADE IOP-1 discussed in Graber et al. (1994) and Cardone et al (1995). Three of the wind fields were taken from the standard real-time objective analysis products of numerical weather prediction centers including the European Center for Medium Range Weather Forecasting (ECMWF), the U. S. Navy Fleet Numerical Meteorology and

Oceanography Center (FNMOC), the United Kingdom Meteorological Office (UKMO). Two wind fields were produced at the NOAA National Meteorological Center (NMC) and at the Goddard Space Flight Center (GSFC) of the National Aeronautic and Space Administration (NASA) from a special high-resolution objective reanalysis of real time and non-real time meteorological data. The sixth wind field was derived by intensive manual kinematic reanalysis by Oceanweather, Inc. with support by the Atmospheric Environment Service of Canada (OW/AES) using all conventional and special SWADE meteorological data. The intent of the OW/AES analysis is to resolve the "synoptic scale" wind field at hourly intervals on a grid of spacing 0.5 deg in latitude and longitude covering the SWADE REGIONAL domain. The wind fields were compared to the measured winds in the SWADE array off the middle-Atlantic East Coast, and to each other. Table 1 summarizes the characteristics of the six wind fields. A detailed description of the wind field analysis procedures and methodologies is given in Cardone et al. (1995).

Table 1
Wind Field Characteristics

Source	**Symbol**	**Wind Variable**	**Resolution**	
			$\Delta x, \Delta y$	**Δt**
OW/AES	O	U_{20}	0.5°	1-hr
ECMWF	E	U_{10}	1.125°	6-hr
FNMOC	F	τ	1.25°	6-hr
UKMO	U	$U_{19.5}$	1.5° 1.875°	2-hr
NASA/GSFC	N	U_{10}	0.25°	3-hr
NOAA/NMC	M	U_{10}	0.3° 0.5°	6-hr

Since the OW/AES wind fields were already specified at high spatial and temporal resolution we selected these winds to examine the effect of poor resolution on wave hindcasting of a mesoscale storm event. In order to avoid additional smoothing or introducing of noise from interpolation of the OW/AES winds onto the grids and domains of the alternative wind fields, we decided to simply subsample the fields in time and space to achieve resolution characteristics which closest match those of the alternative wind fields specified in Table 1 . Hence, we selected the following time steps, Δt: 1, 2, 3, 6, 12 hours. These five time steps were combined with a constant grid size, Δ_x, in latitude and longitude: 0.5, 1.0 and 1.5 degrees.

2.2 Wave model

The ocean wave model used in the simulations described here is the third-generation WAM model. A very detailed description of the physical framework of the WAM model and numerous applications can be found in Komen et al (1994). The version of the model implemented here is the Cycle-4 release of WAM, or WAM-4 in which the atmospheric boundary-layer is coupled to the wave model following Janssen (1991). In WAM-4, the evolution of the

directional wave spectrum $F(f,\Theta,\phi,\lambda,t)$ as a function of frequency, f, and direction, Θ, in spherical coordinates defined by latitude, ϕ, and longitude, λ, is determined from the integration of the energy balance equation

$$\frac{\partial F}{\partial t} + \frac{1}{\cos\phi}\frac{\partial}{\partial\phi}(c_\phi \cos\phi F) + \frac{\partial}{\partial\lambda}(c_\lambda F) + \frac{\partial}{\partial\theta}(c_\theta F) = S_{in} + S_{nl} + S_{ds} \tag{1}$$

Here C_ϕ, C_λ, and C_Θ are the appropriate deep water group velocities along a great circle path. The three source terms consist of S_{in}, an empirical wind input function based on the results of Snyder et al. (1981), S_{nl}, the nonlinear energy transfer integral following Hasselmann et al. (1985), and S_{ds}, the dissipation due to white-capping waves after Komen et al. (1984). WAM-4 incorporates a wind input which is quadratic in the ratio of friction velocity to wave celerity, $u_*/c(f)$, and a dissipation which is proportional to the fourth power of the frequency as described in Janssen (1990).

The wind input is given at standard height, usually 10 meters, and the surface stress is calculated internally within the wave model as a function of both wind speed at height and stage of wave development. Deep water physics only was considered in the propagation and the source terms.

2.3 Model Implementation and simulations

WAM-4 was implemented on a nested grid system to represent the BASIN and REGIONAL SWADE domains. The BASIN grid covers the entire

North and South Atlantic Oceans with a grid of 1 degree spacing (Figure 1a). The BASIN grid hindcast with WAM-4 was run first and only once, using the ECMWF 6-hourly wind fields as input. This simulation was started at 0000 UT 15 October and run through 31 October to provide overall spin up and continuous background wave conditions in the Atlantic ocean and provide directional spectra along the ocean boundaries of the REGIONAL model. The set of directional spectra at 0000 UT 20 October were used for initialization of the interior domain of the REGIONAL grid. The REGIONAL model covers the domain shown in Figure 1b with a grid spacing of 0.25 degree in latitude and longitude. Directional wave spectra are supplied from the BASIN grid to the eastern and southern rows of sea points of the REGIONAL grid at 1200 second intervals The spectral components are interpolated bi-linearly in space from the BASIN grid points to the REGIONAL grid points, except of course for coinciding points. Wave spectra on the boundary of the REGIONAL grid are temporally interpolated to the REGIONAL model time step (Δt = 240s). The REGIONAL run was spun up with ECMWF winds at 0000 UT 15 October and run to 0000 UT 20 October with input generated from the BASIN run. All REGIONAL wind fields were kept constant during the wave model integration over the respective time intervals listed in Table 1 or those intervals selected for degrading the OW/AES winds.

The six different wave simulations of the REGIONAL model as discussed in Cardone et al. (1995) were each driven by a different wind field and spanned the IOP-1 period from 20 to 31 October. In this study we performed fourteen additional runs using as input the temporally and spatially degraded OW/AES wind fields. All winds were kept constant for the duration of the wind time step.

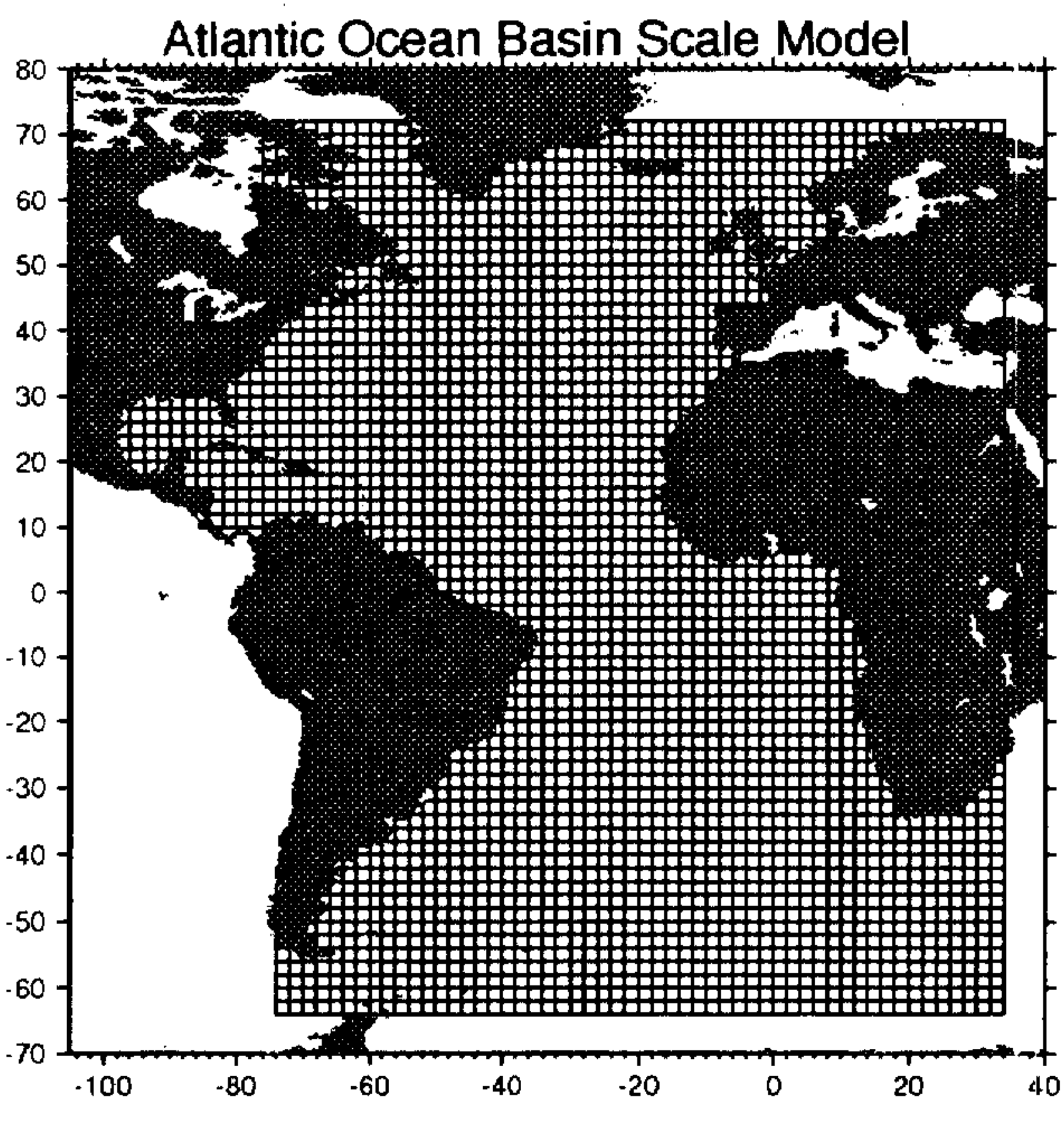

Figure 1a: The Atlantic BASIN model grid.

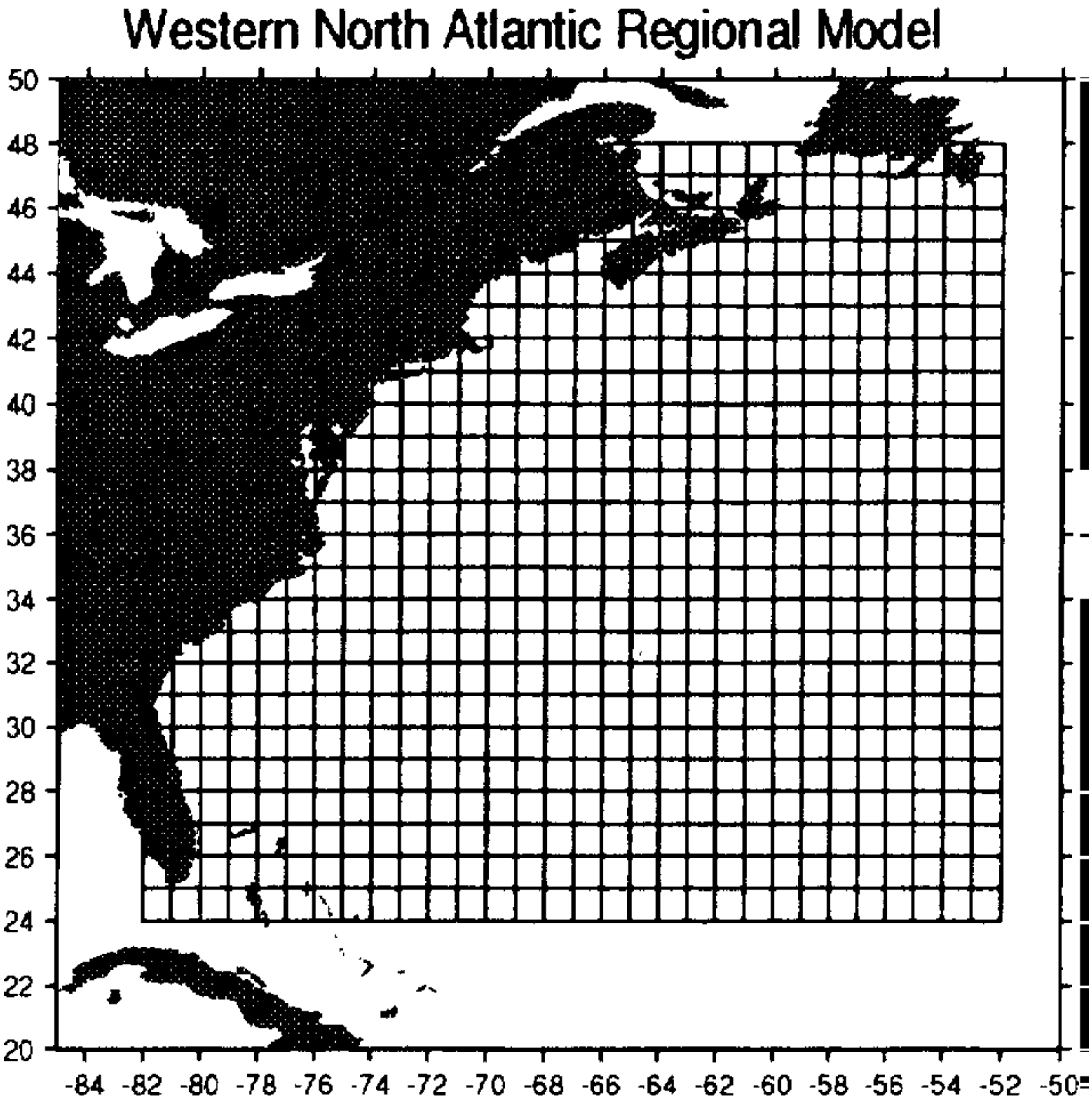

Figure 1b: The REGIONAL model grid for SWADE wave simulations.

The alternative wave hindcasts were evaluated against the extensive wave measurements acquired by the conventional NDBC buoys moored in intermediate and deep water off the US East Coast, and the special SWADE buoys moored in the SWADE FINE domain (Figure 2).

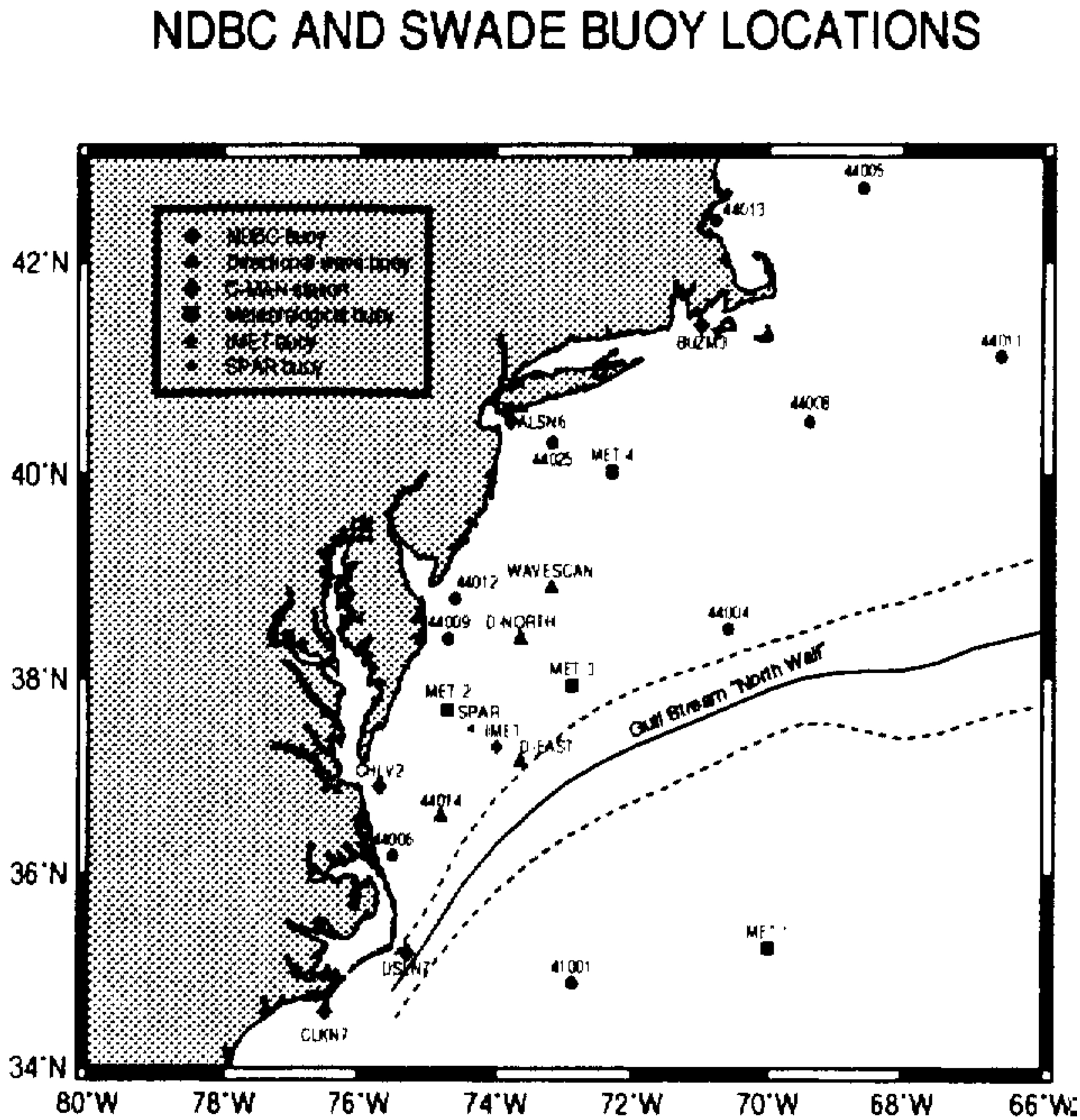

Figure 2: Location map and buoy positions of the SWADE experimental domain.

2.4 Buoy data preparation

The effect of "mesoscale" variations in the buoy measurements were minimized by smoothing hourly measurements of the 8.5 minute average wind to effective hourly means by averaging three successive measurements with a triangular filter. The averaging is done on meridional and zonal wind components of the wind to derive average wind direction, and on the scalar wind speed to compute average wind speed. The same smoothing algorithm is also applied to wave height and wave period.

The adjustment of measured average wind speed to a common reference level is carried out following the procedure originally suggested by Cardone (1969). The procedure uses stability-dependent surface wind profile laws and an assumed dependence of the roughness parameter on wind speed, to calculate an "effective neutral" wind speed at a reference height. The effective neutral wind speed, U_e, is that "virtual" wind speed which at height z_e, imparts, in neutral thermal surface boundary-layer stratification and for the assumed drag law, the same stress as imparted by the measured, U_m, measured at height z_m, in a thermally stratified boundary-layer:

$$U_e = U_m \frac{ln(z_e/z_0)}{ln(z_m/z_0) - \Psi(z_m/L)} \qquad (2)$$

where L is the Monin-Obukov length and Ψ is the "profile" stability function.

A direct evaluation of the accuracy of the wind fields is of course hampered by the absence of high quality wind data which have not already been assimilated into the wind fields as part of the analysis process. In contrast, the buoy wave measurements were not used in the wave hindcast process and therefore may be used to objectively evaluate the impact of the degraded wind fields on wave prediction and the accuracy of the alternative wave hindcasts. The relative skill in the wave hindcasts may then be considered to be an independent measure of the skill in the forcing wind fields, since there is no reason to believe that the WAM model favors wind fields produced by any particular wind analysis system. In that sense the traditional statistical measures of difference between the buoy winds and wind fields interpolated to the buoy locations, as well as the differences between hindcast and measured wave parameters provide a useful set of indicators about the predictive skill of the WAM model with a particular wind field.

3 Sensitivity of Wave Model Predictions

Our analysis was limited to only those buoys located either on the shelf break or in deep water (Table 2). The buoys can further be divided into two general classes: (1) well offshore, east and north of the SWADE array such as 44011, 44008 and 44005; and (2) within the SWADE FINE area such as 41001, 44014, 44015, 44001 and 44004. In addition all buoys except 41001 were located west of the quasi-stationary front (cf. Figure 4 of Cardone et al, 1995).

Table 2
Wind/Wave Stations in SWADE

Station	Name	LAT	LONG	Depth
41001	E HATTERAS	34.9 N	73.0 W	4,444 m
44001	D-NORTH	38.4 N	73.6 W	115 m
44004	HOTEL	38.5 N	70.6 W	3,231 m
44005	GULF OF ME	42.7 N	68.6 W	202 m
44008	NANTUCKET	40.5 N	69.5 W	60 m
44011	GEORGES BANK	41.1 N	66.6 W	87 m
44014	VA BEACH	36.6 N	74.8 W	48 m
44015	D-EAST	37.1 N	73.6 W	2,790 m

Figures 3 and 4 show families of curves (spatial resolution) of the scatter index (SI) of wind speed and significant wave height (SWH) as a function of temporal resolution for the entire SWADE IOP-1 in multi-panels for the offshore buoys. Here we define the SI as the rms difference divided by the mean of the observations. Superimposed are the discrete SI values of the alternative wind field sources. The errors in both wind speed and SWH grow nearly linearly with temporal degradation except for a small interruption of increase of the wind speed SI at Δt = 3hr at some of the buoys. This small reversal in trend may be related to the fact that a 3-hourly as a function of spatial and temporal resolution at smoothing was applied to the verification buoy data and that the 3-hourly sampling (ie., 00, 03, 06, 09, etc) matches exactly the analysis times for which the kinematic analyses were actually carried out and use digitized. This reversal would probably disappear if the 3-hourly winds had been sampled from the hourly winds at other times (e.g., 02, 05, 08, ...).

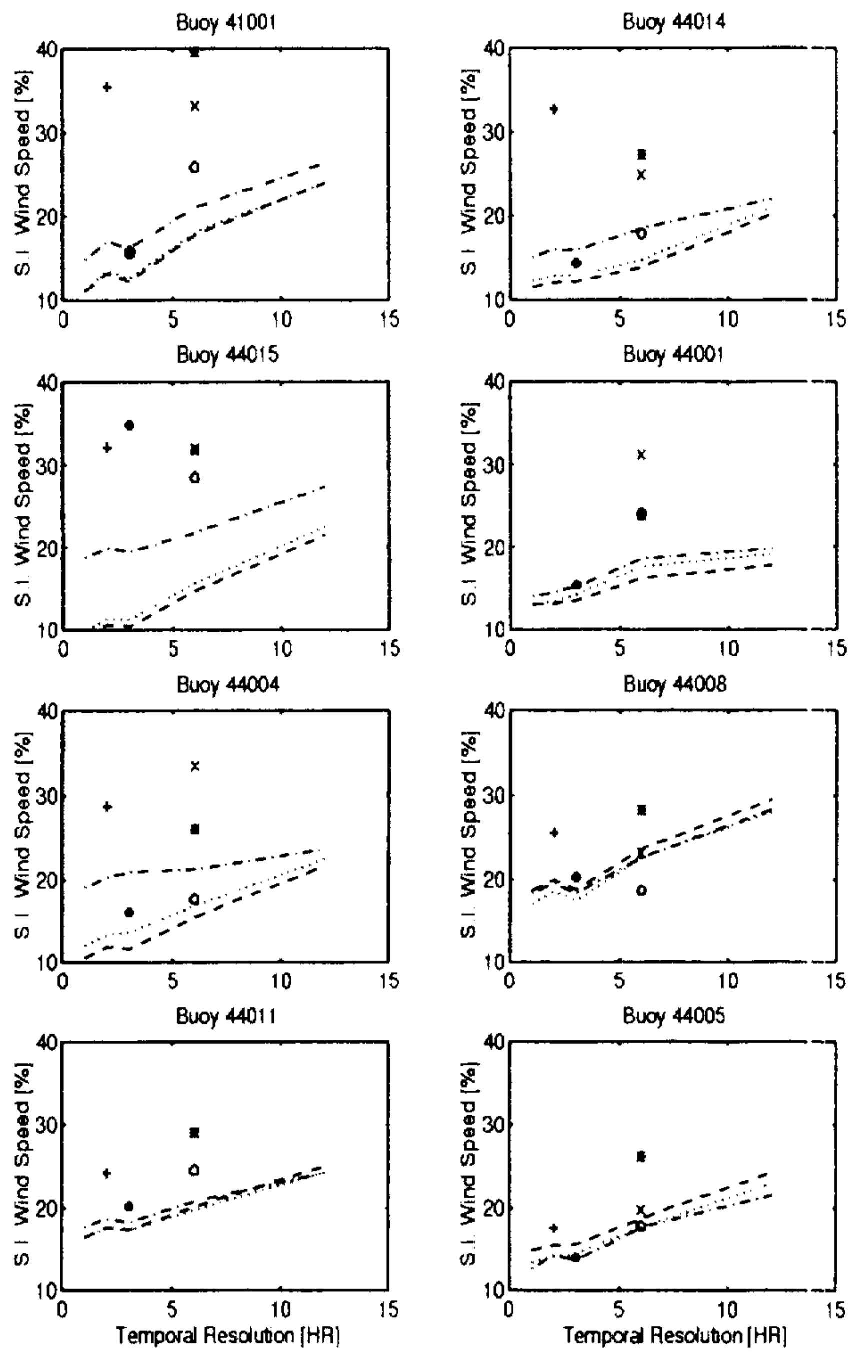

Figure 3: Variation of wind speed scatter index as a function of spatial and temporal resolution at eight offshore for SWADE IOP-1. Dashed line is $\Delta x = 0.5$, dotted line is $\Delta x = 1.0$ and dash-dotted line is $\Delta x = 1.5$. For the alternate wind fields we use: $\bullet$ = NASA; $\times$ = ECMWF; $*$ = FNMOC; $+$ = UKMO; o = NMC.

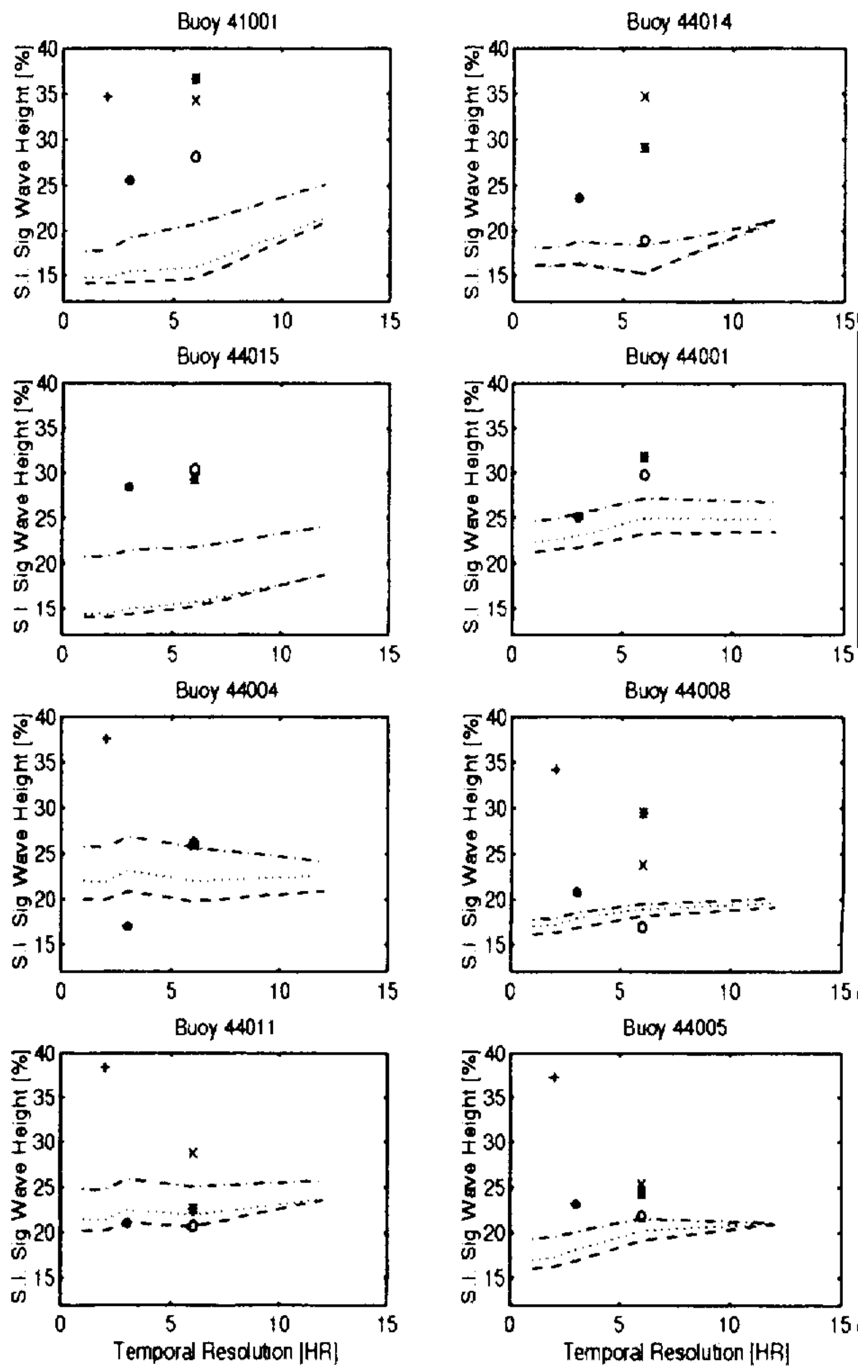

Figure 4: Variation of SWH scatter index as a function of spatial and temporal resolution at eight offshore for SWADE IOP-1. Dashed line is $\Delta x = 0.5$, dotted line is $\Delta x = 1.0$ and dash-dotted line is $\Delta x = 1.5$. For the alternate wind fields we use: $\bullet$ = NASA; $\times$ = ECMWF; $*$ = FNMOC; $+$ = UKMO; o = NMC.

It is also noteworthy that the error magnitude and growth are nearly identical for the cases Δx = 0.5 and 1.0 at all the buoys, while Δx = 1.5 appear to divide into the two classes mentioned above. At the buoys outside the SWADE FINE area (ie., 44011, 44008 and 44005) there is little difference among the curves with different spatial resolution. In contrast, the buoys inside the SWADE FINE domain (i.e., 41001, 44014, 44015 and 44004) exhibit a large spread between the spatial resolution at Δx = 1.5 and the other cases. This is most likely a result of the base winds not actually containing meso scales in the wind fields north and east of the SWADE array, because the average spacing of the buoys is 2 degrees and greater. Without other sources of accurate wind measurements these gaps cannot be filled. Cardone et al. (1995) also noted that just east of the SWADE array the wind errors in the SWADE winds rapidly degrade to levels more typical of the data sparse open ocean conditions. The other striking indication of Figures 3 and 4 is the fact that even at the resolutions of the alternative wind sources, the base SWADE winds are in general considerably more skillful. A notable exception is the NASA winds which closely tracked the buoy winds at the nearest model grid (Cardone et al., 1995). For the other wind field sources, wind errors are large even in the vicinity of the buoys which suggest that those errors do not arise simply in resolution effects.

It is also interesting to see that 44004 tracks more like a SWADE array location than an offshore location. This suggests that considerable high spatial frequency information is contained in the wind fields in the vicinity of 44004, but not further north or east. From this result we are led to conclude that the OW/AES wind analyses were able to propagate the data rich meteorological information in the SWADE area just a little further eastward by manual imposition of time-space continuity.

In Figure 5 the maximum SWH attained by the WAM model is plotted for the three spatial resolution as a function temporal resolution. The maximum SWH recorded by the buoy is superimposed on each panel. This mufti-panel graph reveals two basic patterns: (1) at buoys 41001 and 44015 a significant downward trend occurs with both spatial and temporal resolution, and (2) at 44001, 44008 and 44005 the lines of maximum predicted SWH are flat and with little separation about the observed maximum SWH. This figure reflects the big storm event which returned the maximum SWH at all buoys during the 11 days. The lack of sensitivity of maximum SWH at 44001, 44008 and 44005 is a result of a broad, slowly varying and nearly linear northeast air stream between the storm track and the US East Coast. In other words, the buoys experienced mainly fetch-limited conditions. On the contrary, the peak SWH just south of the primary low as it emerged offshore, at 41001 and 44015, was determined by a fast moving "jet streak", whose accurate spatial and temporal evolution required the finest spatial and temporal wind field resolutions.

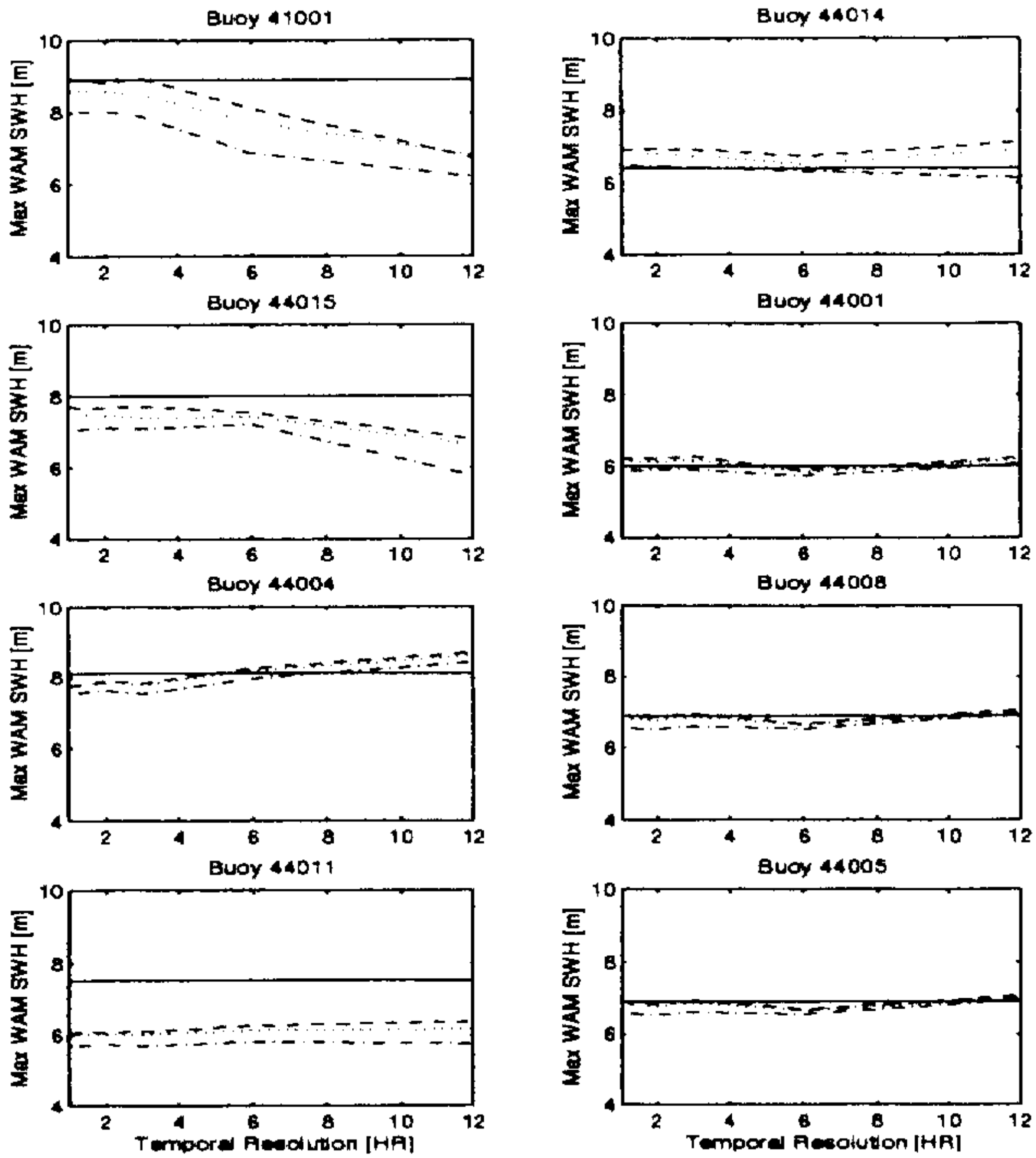

Figure 5: The maximum model-predicted SWH attained as a function of spatial and temporal resolution at eight offshore for SWADE IOP-1. Dashed line is $\Delta x = 0.5$, dotted line is $\Delta x = 1.0$ and dash-dotted line is $\Delta x = 1.5$. The solid line represents the maximum SWH observed at the buoy.

A snapshot of the "correct" SWH field is shown in Figure 6 as the "jet streak" induced maximum wave heights of 8-9 m are passing near 44015 and approaching 41001. In contrast, Figure 7 depicts the truncation of this region of maximum SWH from 9 to 7 m for the lowest resolution combination. This a general reduction of over 20%! Note, however, that away from this maximum, the SWH patterns for lowest and highest resolution cases are quite similar overall. Especially near the US East Coast (e.g. 44014 and 44001) where the wave field is strongly controlled by the physical fetch during this storm event.

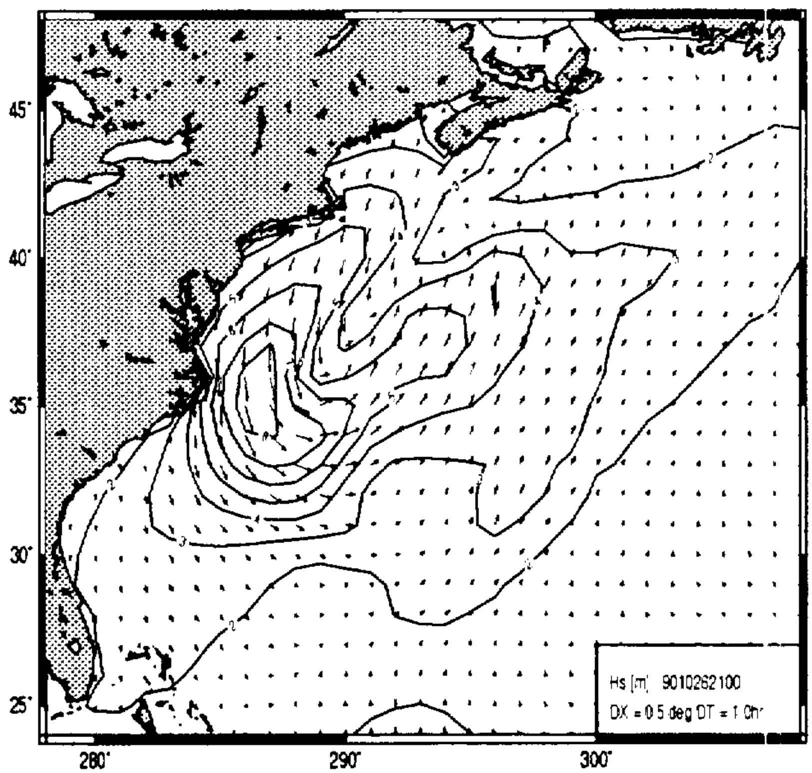

Figure 6: The SWH field from the reference OW/AES run ($\Delta t = 1hr$ and $\Delta x = 0.5°$) at 2100 UT, 26 October 1990.

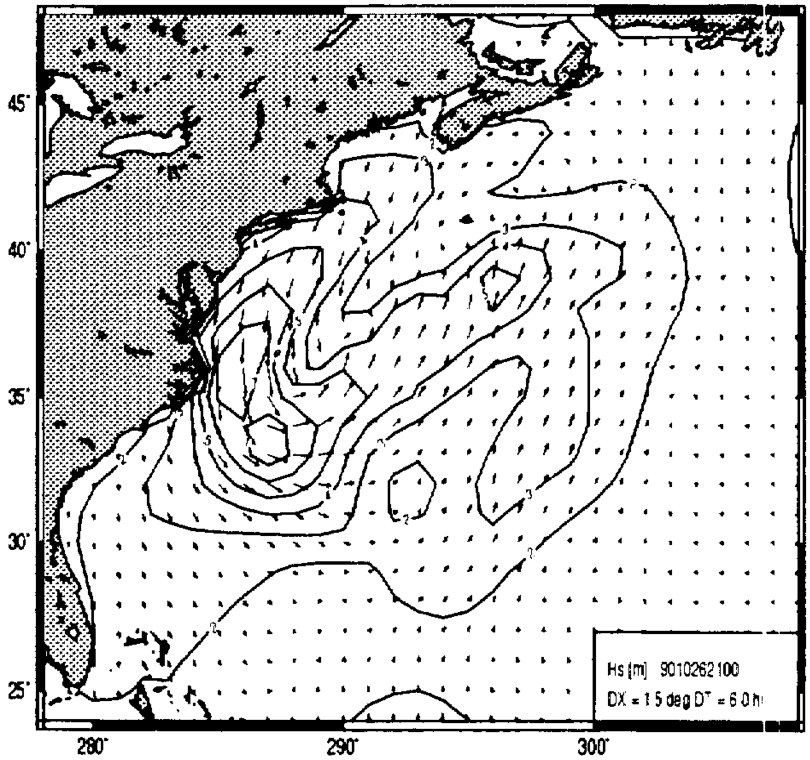

Figure 7: The SWH field from degraded resolution OW/AES run ($\Delta t = 6hr$ and $\Delta x = 1.5°$) at 2100 UT, 26 October 1990.

Finally, Figure 8 summarizes the general skill in the wave hindcasts. for all the alternative wind fields and a representative set of degraded wind fields. The correlation between the "site" wind errors and the "site" wave errors is consistent with respect to the degraded OW/AES winds. By this we mean that the various combination of temporal and spatial resolution leads to a gradual, but steady increase in wind and wave height errors. The points scatter about the dashed line which represents the theoretical relationship that a unit error in wind speed induces twice this error in significant wave height. There is reasonably high correlation between these errors for the alternative wind fields overall, with the notable exception of NASA, which as noted in Cardone et al. (1995) nearly matches the very low wind errors of the reference OW/AES but generally displays higher wave height errors. The other notable fact is that the errors of the operational center winds (e.g., ECMWF, UKMO and FNMOC) cluster between 25 - 40% for wind speed and SWH and do not overlap with those errors from the degraded OW/AES hindcasts; for similar combinations of spatial and temporal resolution.

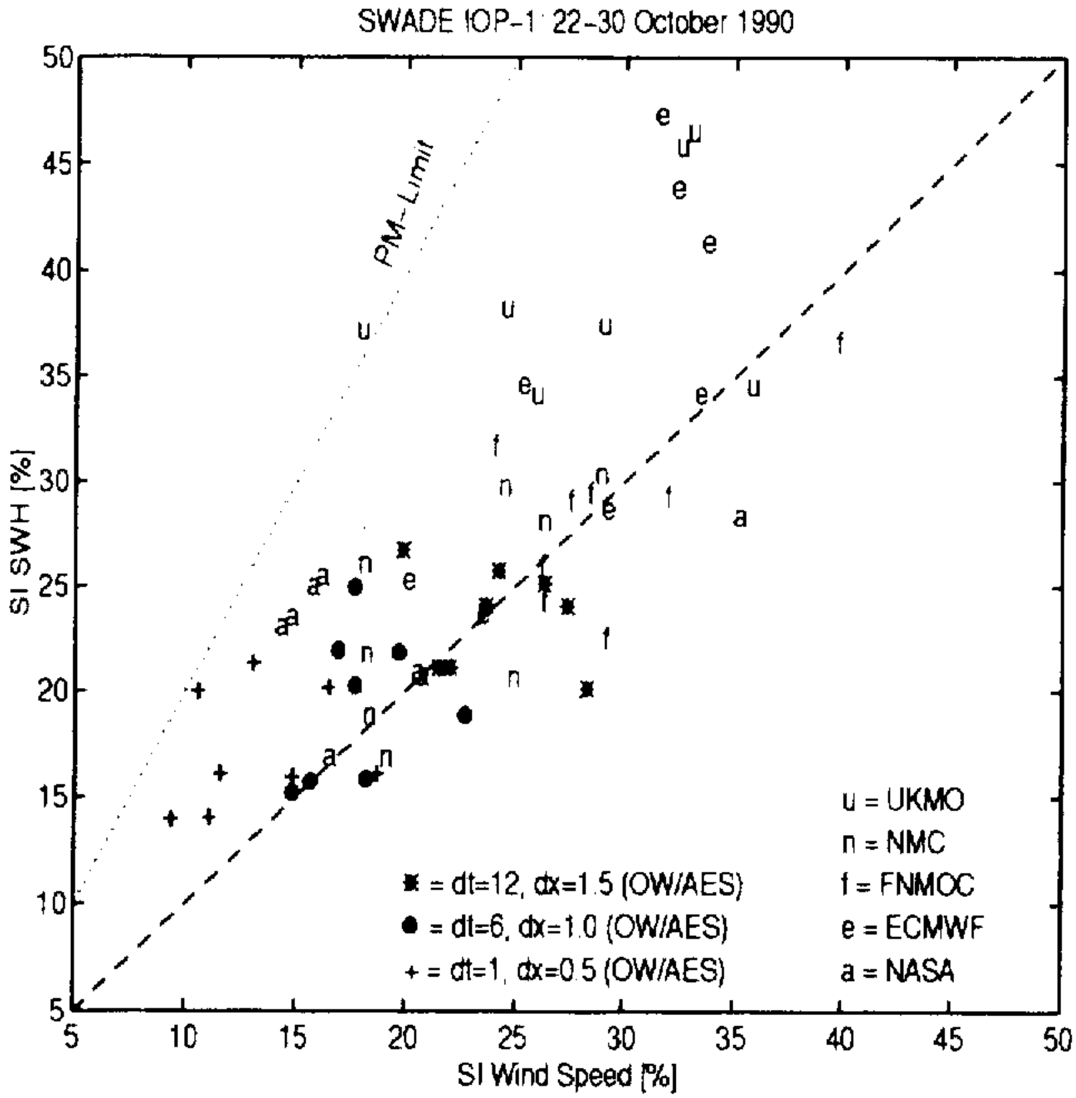

Figure 8: Comparison of wind speed SI and SWH SI for SWADE IOP-1 including the alternative and selected degraded wind fields. The dotted line shows the Pierson-Moskowitz relationship.

One of the objectives of this study was to estimate the error introduced in wave model predictions due to poor spatial and/or temporal resolution in the wind field. From the degraded OW/AES runs we can estimate the error solely contributed by the poor resolution in wind field. Hence, we define the rms error due to a particular combination of spatial resolution, Δx, and temporal resolution, Δt, as the root-mean-square difference between a given run and the reference run with the OW/AES winds:

$$\epsilon_{tx} = < (M - B) >^{1/2} \qquad (3)$$

where < ... > refers to arithmetic mean and the subscript of ε_{605}, refers to 6 hrs temporal and 0.5 degree spatial resolution. To quantify the contribution of poor resolution in the alternative wind fields, we divide the degradation error, ε_{tx}, which matches closest the space-time resolution of the alternative wind field, by the rms difference between the hindcast and observed SWH of the alternative wind field. Hence, we get

$$E = \frac{\epsilon_{tx}}{< (M - B) >^{1/2}} \cdot 100\% \qquad (4)$$

The percentages given in Table 3 reveal several interesting features. For the NASA winds only 10% or less of the total error when compared with the observed buoy SWH can be attributed to poor resolution. This is not surprising, because (i) the wind field was specified with similar space-time characteristics (cf. Table 1) and (ii) the model winds at the buoys were generally in good agreement. In contrast, the FNMOC winds appear to exhibit uniformly at the eight deep water, offshore buoys the largest fraction of error, 30-50%, due to coarser resolution in space and time. For the ECMWF winds this error is less than 201/6, except for two buoys, 44008 and 44005, where the degradation error increases to nearly 30%. These results, however, indicate that for typical synoptic-scale resolving (6 hours and 1.25 degrees), operational weather prediction products the error contributed by coarser resolution ranges between 20 - 40%. Furthermore, this implies that the remaining error of about 60 - 80% arises from the analysis and data assimilation schemes.

Table 3
Percentage Error Caused by
Spatial and Temporal Resolution

Station	NMC	NASA	FNMOC	UKMO	ECMWF
41001	20	9	42	31	23
44014	25	7	44	22	17
44015	19	5	50	29	16
44001	20	5	34	12	17
44004	16	9	37	22	13
44008	37	8	29	16	29
44011	21	9	42	20	19
44005	29	9	40	20	28

Curtis (et al, 1994) performed a similar study where only the temporal resolution of the OW/AES winds was reduced. Additional changes were included by using different wind time steps within the WAM model to examine the optimal time step for wind input for numerical ocean wave models. They also explored what differences exist in the hindcasts when the winds were kept constant over a time step or linearly interpolated in time. The simulations showed that differences in hindcast SWH were generally small, except during peak storm events where differences can be significant. It was also noted that reduced temporal resolution could lead to possible phase shifts in modelled wave height time series.

4 Summary and Conclusions

On October 1990 during the SWADE IOP-1, a series of three low pressure centers emerged over the Carolinas into the Northwest Atlantic. This region is known to be very cyclogenetic: and often shapes the local weather of the entire US East Coast. As the laws matured, they typically propagate along a frontal boundary which extends from the Carolinas to the Canadian Maritimes. The structure of this storm system was sufficiently intense to generate significant wave heights in excess of 8 m within the SWADE experimental array. A high-resolution wind field (OW/AES) derived by manual kinematic reanalysis formed the basis of the reference SWADE winds. Uncertainties in the wind field still remain the dominant source of errors in numerical wave prediction. The SWADE reference winds were employed to examine the impact of temporally and spatially degraded winds on the hindcast wave field for the SWADE IOP-1. The goals of this study was to investigate the effect of coarser resolution winds and to quantify the errors in sea state predictions which are attributable to spatial and/or temporal resolution in the wind forcing.

In a previous study by Cardone et al. (1995) we found that surface wind fields provided by operational centers generally performed poorer for mesoscale storm events. This implies that uncertainties in forecasting or even nowcasting the sea state during extreme storm events remain high and require re-analyses with finer resolution winds in space and time.

The results of this study show that even within a single cyclogenetic situation, the resolution required to accurately describe the wind field varies greatly. In areas of slowly evolving, nearly linear features, even 1.5 degree spacing and 6-hourly sampling appears to be satisfactory. However, in areas of fronts and rapidly propagating jet streak features, 0.5 degree spacing and no more than 3-hourly sampling are required to resolve strong gradients in the wave field and storm peak features.

It appears from our simulations of the storm scenario studied that the surface wind fields provided by the operational centers did not fully utilize the information contained in the enhanced buoy array off the East Coast. The difficulty is not merely one of grid and temporal resolution. The resolution degraded reference SWADE winds still outperformed the operational center winds for the matching resolution when used to force the ocean wave model WAM-4.

These results may be used to infer the design of satellite-based remote sensing system to monitor synoptic scale marine surface winds globally. For example, if such systems are to be relied upon to monitor storm maxima of wind speed, the requirement of three-hour temporal sampling implies a multi-satellite (at least three) operational configuration, even for wide-swath instruments such as a scatterometer.

Acknowledgments

The authors gratefully acknowledge funding support by the Office of Naval Research (ONR) under Grant No. N00014-92-J-1546 and the National Aeronautics and Space Administration under grants NAGW-2672 and JPL Contracts 957647 and 957652 (NSCAT Science Working Team). R. Jensen conducted his work at the Coastal Engineering Research Center of USAEWES under the Coastal Research and Development Program, "Modelling the Evolution of Wave Spectra in Shallow Water Work Unit". Permission was granted by Headquarters, U.S. Army Corps of Engineers, to publish this information.

5 References

Bauer, E., S. Hasselmann, K. Hasselmann and H.C. Graber, 1992: Validation and assimilation of SEASAT altimeter wave heights using the WAM wave model. J. Geophys. Res., **97**, 12,671-12,682.

Cardone, V.J., 1969: Specification of the wind distribution in the marine boundary layer for wave forecasting. Report **TR-69-01**, Geophys. Sciences Lab., New York University, 137pp. (Available from NTIS: Order AD 702 490).

Cardone, V.J. and D. Szabo, 1985: Impact of uncertainty in specification of offshore wind on accuracy of wave hindcasts and forecasts. Proc. Int. Workshop on Offshore Winds and Icing, Nova Scotia, 7-11 October, 1985. Publ. Environment Canada, Downsview, Ontario.

Cardone, V.J., H.C. Graber, R.E. Jensen, S. Hasselmann, and M. Caruso, 1995: In Search of the true surface wind field in SWADE IOP-1: Ocean wave modelling perspective. Accepted by The Global Atmosphere-Ocean System.

Curtis, W.R. and R.E. Jensen, 1994: Effects of temporal interpolation of wind fields in third generation wave modelling technology. EOS, Trans. Amer. Geophys. Union, **75**(3), 101.

Graber, H.C., M.J. Caruso and R.E. Jensen, 1991: Surface wave simulations during the October storm in SWADE. Proc. MTS '91 Conf., Marine Technology Society, New Orleans, LA, 159-164.

Graber, H.C., V. Cardone, R. Jensen, S. Hasselmann, H.L. Tolman and L. Cavaleri, 1994: The accuracy of wind field description. In: Komen et al., Dynamics and Modelling of Ocean Waves. Cambridge University Press, 285-293.

Hasselmann, S. and K. Hasselmann, 1985: Computations and parameterizations of the nonlinear energy transfer in gravity wave spectrum. Part I: A new method for efficient computations of the exact nonlinear transfer integral. J. Phys. Oceanogr., **15**(11),1369-1377.

Held, I.M. and P.J. Phillipps, 1993: Sensitivity of the eddy momentum flux to meridional resolution in atmospheric GCMs. J Climate, **6**, 499-507.

Janssen, P.A.E.M., G.J. Komen, and W.J.P. de Voogt, 1984. An operational coupled hybrid wave prediction model. J. Geophys. Res., **89**(C3), 3635-3654.

Janssen, P.A.E.M., 1991: Quasi-linear theory for wind-wave generation applied to wave forecasting. J. Phys. Oceanogr., **21**, 1631-1642.

Komen, G.J., S. Hasselmann and K. Hasselmann, 1984: On the existence of a fully developed wind-sea spectrum J. Phys. Oceanogr., **14**, 1271-1285.

Orlanski, I., J. Katzfey, C. Menendez and M. Marino, 1991: Simulation of an extratropical cyclone in the southern hemisphere: Model sensitivity. J. Atmos. Sci., **48**(21), 2293-2311.

Sanders, F., 1990: Surface weather analysis over the oceans - Searching for sea truth. Wea. Forecasting, **5**, 596-612.

Snyder, R.L., F.W. Dobson, J.A. Elliot and R.B. Long, 1981: Array measurements of atmospheric pressure fluctuations above surface gravity waves. J Fluid Mech., **102**, 1-59.

The WAMDI Group: Hasselmann, S., K. Hasselmann, E. Bauer, P.A.E.M. Janssen, G.J. Komen, L. Bertotti, P. Lionello, A. Guillaume, V.C. Cardone, J.A. Greenwood, M. Reistad, L. Zambresky and J.A. Ewing, 1988: The WAM model - a third generation ocean wave prediction model J. Phys. Oceanogr., **8**(12), 1775-1810.

Weller, R.A., M.A. Donelan, M.G. Briscoe and N.E. Huang, 1991: Riding the crest: A tale of two wave experiments. AMS Bulletin, **72**, No. 2, 163-183.

THE IMPACT OF WAVE MODEL GRID RESOLUTION ON OCEAN SURFACE RESPONSE AS REVEALED IN AN OPERATIONAL ENVIRONMENT

Roop Lalbeharry[1] and Madhav L. Khandekar[2]

Atmospheric Environment Service
4905 Dufferin Street, Downsview, Ontario, Canada M3H 5T4

[1] Meteorological Research Branch
[2] Climate Research Branch

1. INTRODUCTION

The state-of-the-art ocean surface wave model WAM (The WAMDI Group, 1988) is presently being tested for possible operational implementation in the AES (Atmospheric Environment Service) forecasting system. The version being tested is the Cycle-4 version of WAM in which the atmospheric boundary-layer is coupled to the wave model following Janssen (1991). A regional version of WAM Cycle-4 covering the northwest Atlantic is used and two grid resolutions, a coarse 1° x 1° grid (about 111 km x 111 km) and a fine 0.5° x 0.5° grid (about 55 km x 55 km) are being tested for possible implementation. In the present study the two grid versions of WAM are driven by the 10 m level winds obtainable from the RFE (Regional Finite Element) weather prediction model of the Canadian Meteorological Centre (CMC) in Montreal. The RFE model grid is a variable-resolution grid with a central window of 50 km resolution covering the region including the continental U.S.A., Canada and the Canadian Atlantic (Mailhot et al., 1995). The RFE model winds are interpolated on the two grids of the Warn model which is run in a forecast mode to generate products up to 36 hours. The wave model products using the two grid resolutions are generated for a selected storm case as well as for an arbitrarily selected period of 25 days. These wave products are evaluated against available buoy data in the northwest Atlantic and the results of this evaluation are presented and discussed in the following sections.

2. IMPACT OF TEMPORAL RESOLUTION IN THE WIND FIELD

A series of wave model simulations were obtained using RFE model 1-hourly as well as 3-hourly wind fields at the 10 m level. The simulations were obtained in respect of a storm case which pertains to the blizzard of March 1993, dubbed as the "storm of the century". The storm developed over the panhandle region of Florida, U.S.A., and moved rapidly through the U.S. Atlantic seaboard along a track from Florida to the Gulf of St. Lawerence in the Canadian east coast offshore (see Brugge, 1994). The storm generated extreme sea states with significant wave heights of 13-16 n at several buoy locations in the Scotian Shelf region of the Canadian Atlantic. Figure 1 shows the storm track and the locations of the buoys used in this study.

The coarse resolution grid (1° x 1°) of the WAM was used and the wave model was driven by both 1-hourly and 3-hourly wind fields. The wind fields for this experiment were based on a man-machine-mix (MMM) procedure using all conventional meteorological data as outlined in Cardone (1992). The MMM winds can be interpreted as providing the "ground truth" and would thus help minimize wind field errors in wave model products. In Figure 2 are shown two wave plots of temporal variations of wave heights at two selected buoy locations. The model generated wave heights using 1-hourly as well as 3-hourly wind fields are shown together with buoy-measured wave heights. The Figure shows that the model wave heights using the 1-hourly as well as 3-hourly wind fields are almost identical to each other throughout the time histories of the wave plots at both grid locations. Results of model simulations at other grid points (not shown) demonstrate quite conclusively that the use of 1-hourly versus 3-hourly wind fields produces negligibly small difference in wave model products. Consequently, the remaining simulation results in this study are discussed with respect to 3-hourly wind fields only.

3. IMPACT OF SPATIAL RESOLUTION ON SIMULATION OF STORM WAVES

Both the coarse and fine grid resolutions of the WAM model were used to obtain wave height simulations at selected grid points pertaining to the storm of the century, 13-17 March 1993. Once again, the wave model was driven by MMM winds prescribed at 3-hourly intervals and temporal variations of wave heights at two buoy locations are shown in Figure 3 . The wave plots at buoy 44137, which recorded a significant wave height (SWH) of 16.3 m at 0000 UTC on 15 March, show that that the model simulation with the finer grid resolution provides a better match with the peak value. The wave plot for buoy 44139 indicates that the model simulation with the finer grid resolution shows an excellent agreement with the buoy SWH, especially near the peak value of about 11.5 m. Model simulations (not shown) at other grid points show similar results. The impact of grid resolution can be clearly seen in the wave error statistics shown in Table 1 . The Table values reveal that for SWH > 6 m, the finer grid resolution produces improved error statistics.

The results of the storm simulation indicate that the WAM model with the finer grid resolution can provide improved wave height simulation during the peak of the storm.

4. IMPACT OF GRID RESOLUTION IN OPERATIONAL ENVIRONMENT

The two grid versions of the WAM model are run in a forecast mode in an operational environment twice daily at analysis times of 0000 UTC and 1200 UTC, respectively, using the RFE model 3-hourly forecast winds valid up to 36 hours for the period 1-25 August 1995. The WAM model forecast simulations valid at 12-, 24-, and 36-hour from the analysis times are validated against the observations available at all the buoys shown in Figure 1 . Figure 4 gives the time histories of the 12-hour forecast of the model simulations of SWH for the period 16-25 August 1995 at 3 selected buoys, namely, 44139 (top), 44141 (middle), and 44142 (bottom). An inspection of Figure 4 reveals that the wave heights generated by the coarse and fine grid versions of the WAM model are in close agreement with each other, the fine grid showing a slight improvement during the period (21-23 August) of high wave heights. For wave heights < 4 m the model simulations with the coarse and fine grids versions are almost identical.

In Table II are shown the 12-, 24-, and 36-hour forecast error statistics for the two grid versions of the WAM model. The verification covers the 25 day experimental period and uses all available data at buoys shown in Figure 1 . The Table shows marginal improvement for the fine grid wave height during the forecast period. Finally, Figure 5 gives a snapshot of the 12-hour forecast wave fields valid at 0000 UTC on 22 August obtained using the two versions of the WAM model. Both versions of the wave model generate wave height maxima in the same region. The fine grid version, however, shows a slightly larger area encircled by the 7 m SWH contour. It may be noted that the snapshot time of Figure 5 corresponds to the wave height peak (near buoy 44141 in Figure 4) on 22 August. Taking into account Figures 3 - 5 and Table 1 , it can be stated that the fine grid version of the wave model produces slightly better simulation of peak wave heights (> 6 m) associated with a storm.

5. SUMMARY AND CONCLUSIONS

This study uses a coarse grid version (1° x 1°) and a fine grid version (0.5° x 0.5°) of WAM Cycle-4 driven by MMM winds prescribed at 1-hourly and 3-hourly intervals in a hindcast mode for the storm of the century of March 1993, and by the RFE model winds prescribed at 3-hourly intervals in a forecast mode in an operational environment for the period 1-25 August 1995. The model results, when evaluated against buoy data, suggest that the fine grid version of the WAM model can produce an improved simulation of wave heights, especially during the peak of an intense storm. In an operational environment, the two (fine and coarse grids) versions of the WAM model produce almost identical simulations most of the time; during periods of high wave heights the fine grid version of the wave model can provide some improvement which may be of operational utility.

6. ACKNOWLEDGEMENT

Sincere thanks are expressed to Dr. Robert Jensen of NERC, Vicksburg, Mississippi, for his assistance in the setting up of the fine and coarse grid versions of the WAM model in an experimental mode and to David Brown, a Contractor with the Atmospheric Environment Service, for his computer support.

7. REFERENCES

Brugge, R., 1994: The blizzard of 12-15 March 1993 in the U.S.A. and Canada, Weather, Vol. 49, No. 3, 82-89.

Cardone, V., 1992: On the structure of marine surface wind field in extratropical storms. Preprints, Third Int. Workshop on Wave Hindcasting and Forecasting, 19-22 May 1992, Montreal, Quebec, Atmos. Environ. Serv, Downsview, Ont., pp. 54-66.

Janssen, P.A.E.M, 1991: Quasi-linaer theory for wind-wave generation applied to wave forecasting. J. Phys. Oceanogr., 21, 1631-1642.

Mailhot J., R. Sarrazin, B. Bilodeau, N. Brunet, A, Méthot, G. Pellerin, C. Chouinard, L. Garand, G. Girard, and R. Hogue, 1995: Changes to the Canadian regional forecast system: Description and evaluation of the 50-km version. Atmosphere-Ocean, 33, 55-80.

The WAMDI Group, 1988: The WAM model third generation ocean wave prediction model. J. Phys. Oceanogr. 18, 1775-1810.

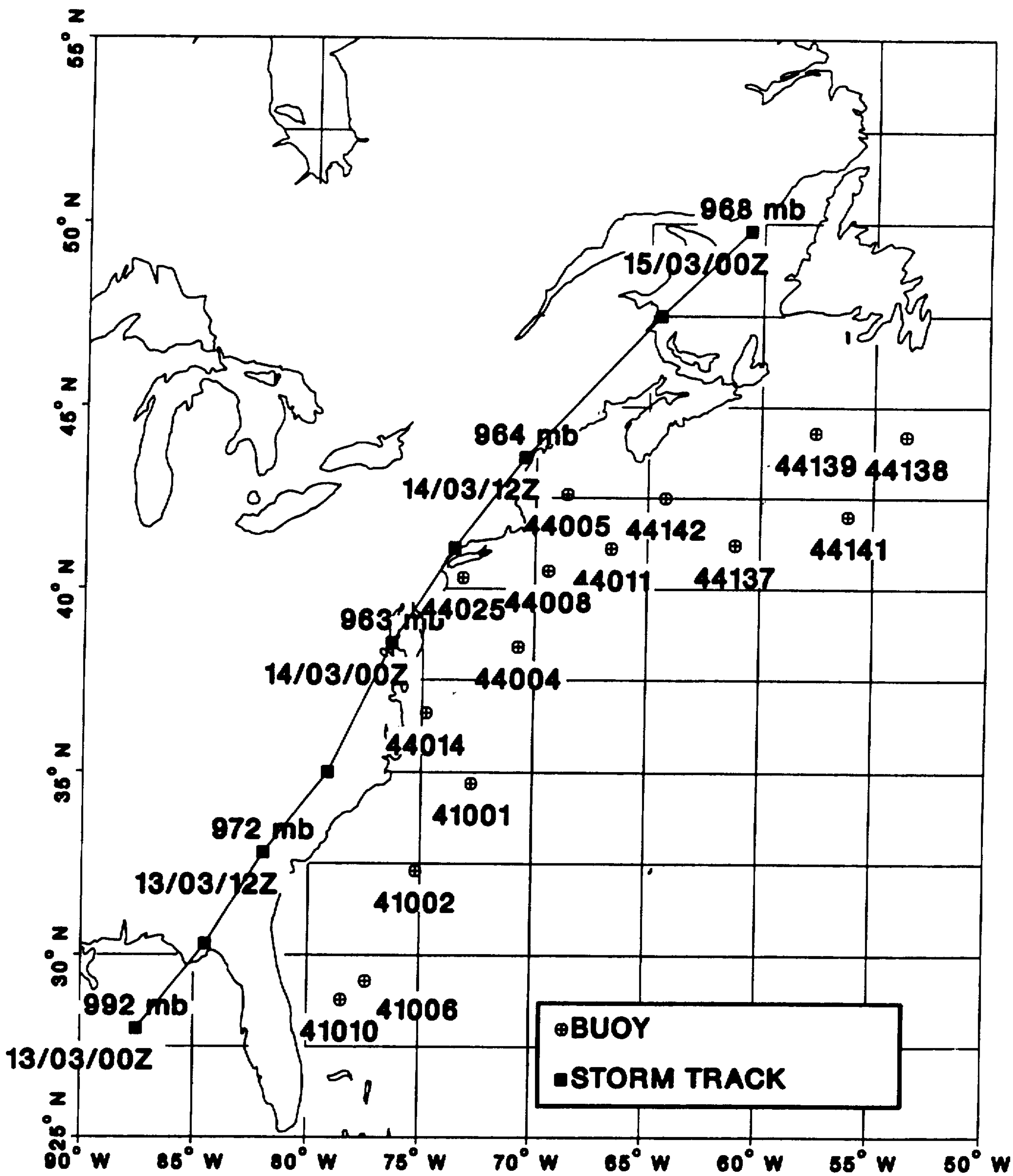

Figure 1: The track for the storm of the century, March 1993, together with the locations of the buoys where wave heights were measured during the the passage of the storm. The storm track shows 12-hourly positions of the storm centre beginning 0000 UTC on 13 March and central pressures in mb.

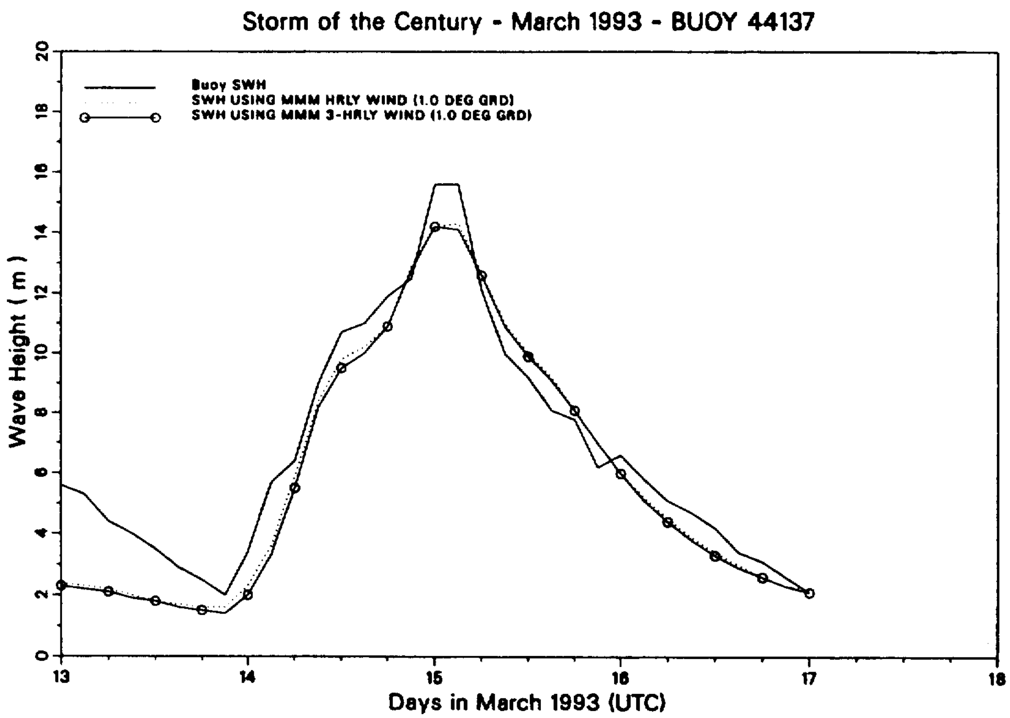

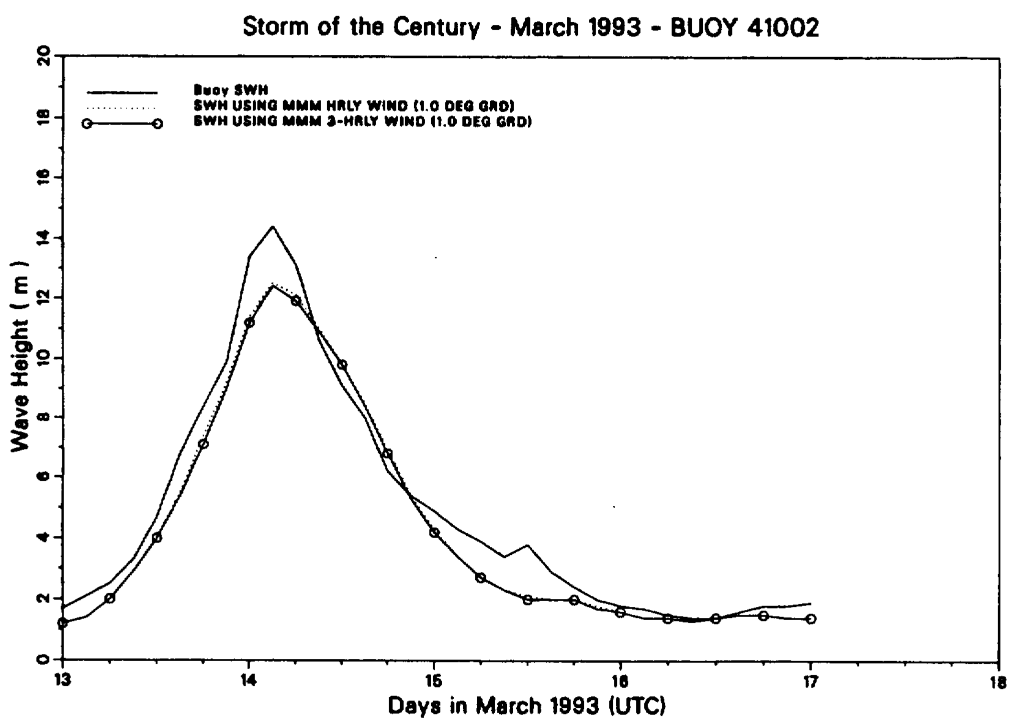

Figure 2: Temporal variation of wave height as measured at buoys 44137 (top) and 44139 (bottom) together with the model wave heights generated using 1-hourly (dotted line) and 3-hourly (line with circles) MMM wind input to the WAM model. The WAM model has a 1° grid spacing everywhere.

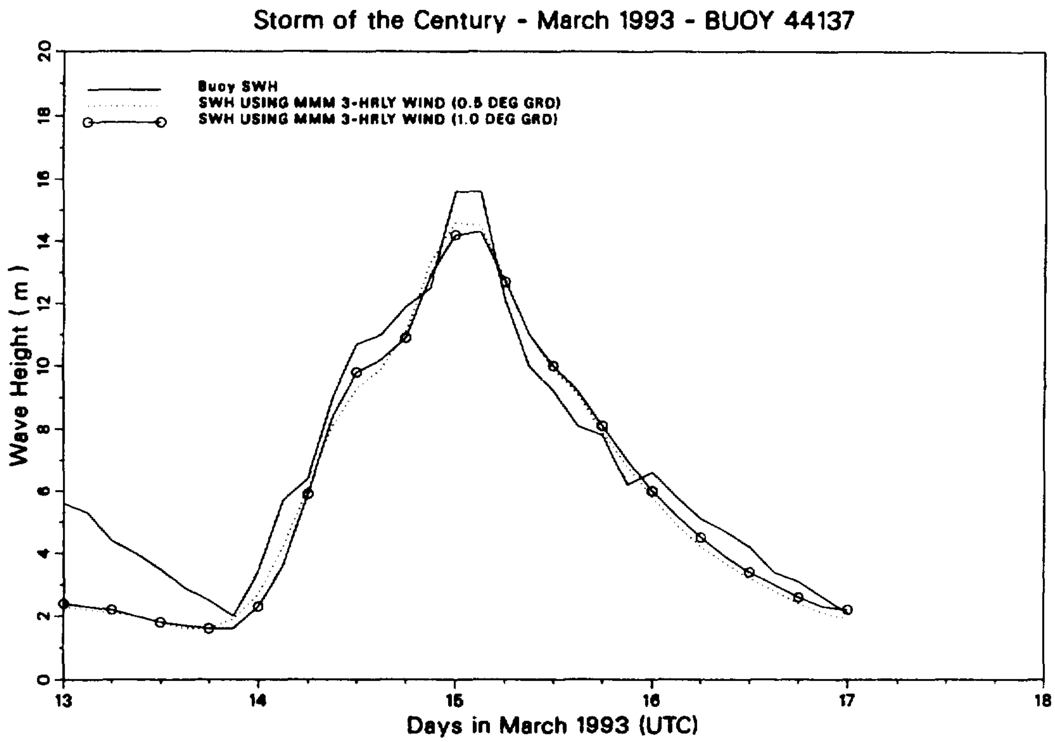

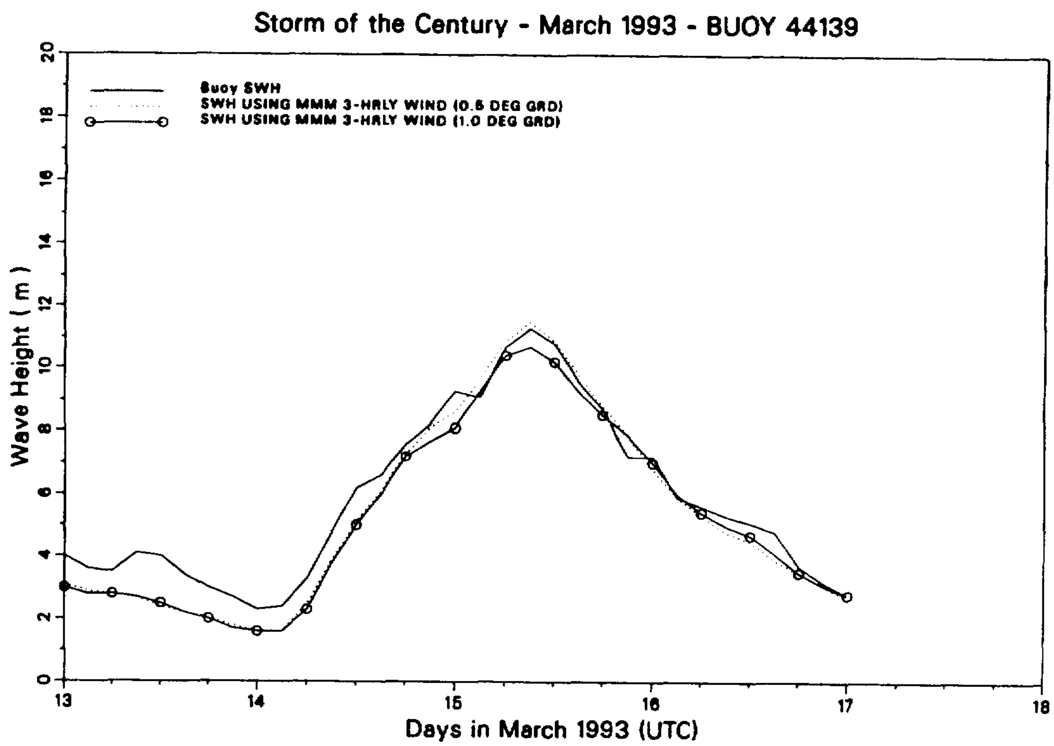

Figure 3: Same as Figure 2 but using fine grid (dotted line) and coarse grid (line with circles) versions of the WAM model. The WAM model is driven by 3-hourly MMM winds.

Table I; Wave error statistics for the storm of the century, 13-17 March 1993, based on 6 buoys (44137, 44138, 44139, 44141, 44004, 41002; see Figure 1)

	Grid 1° x 1°				Grid 0.5° x 0.5°			
	SWH Range (m)				SWH Range (m)			
	0-3	3-6	>6	All	0-3	3-6	>6	All
BIAS (m)	-0.26	-0.79	-0.31	-0.99	-0.36	-0.91	-0.20	-0.53
RMSE (m)	0.59	1.22	1.26	1.12	0.52	1.25	1.08	1.04
SI (%)	29	28	14	20	26	27	12	19
r	0.57	0.73	0.85	0.95	0.81	0.75	0.89	0.97
N	45	81	72	198	45	81	72	198

BIAS = 1/NΣ(Model – Buoy); RMSE = $\sqrt{(\Sigma(\text{Model} - \text{Buoy})^2/N)}$
SI (Scatter Index) = RMSE/Buoy mean value; N = Number of data points
r = Linear correlation coefficient between model and buoy SWH

Table II: 12-, 24-, and 36-hour forecast verification of wave error statistics using the two grid versions of the WAM model driven by the RFE model 3-hourly forecast winds for the period 1-25 August 1995. The statistics are based on the available observations at all 15 buoys shown in Figure 1 .

	Grid 1° x 1°			Grid 0.5° x 0.5°		
	Forecast Hour			Forecast Hour		
	12	24	36	12	24	36
BIAS (m)	-0.26	-0.44	-0.51	-0.37	-0.44	-0.52
RMSE (m)	0.74	0.79	0.85	0.72	0.78	0.84
SI (%)	34	35	37	33	35	37
r	0.77	0.76	0.74	0.79	0.77	0.75
N	206	206	206	206	206	206

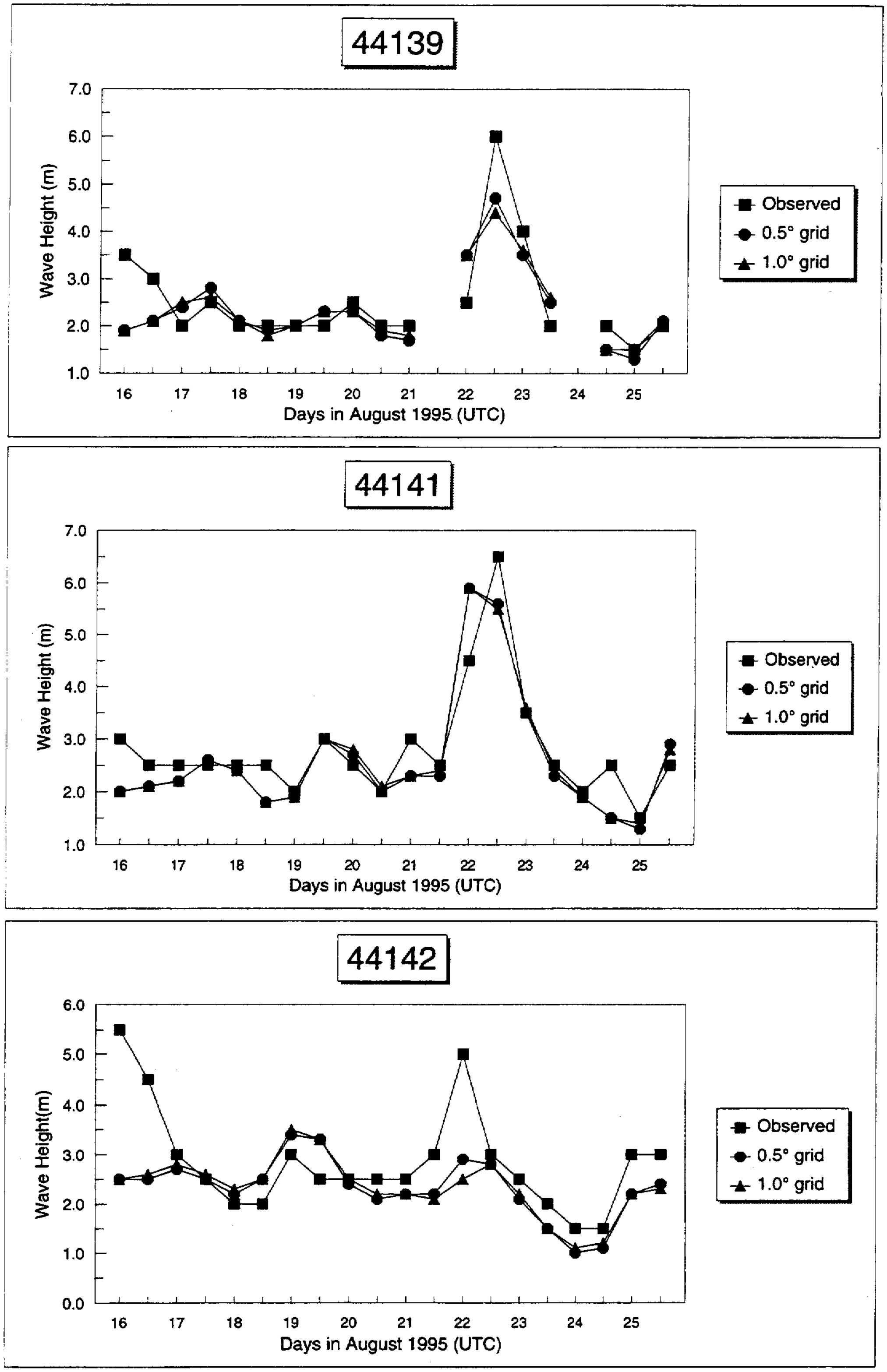

Figure 4: Comparison of the 12-hour forecast of wave heights for the fine grid version and the coarse grid version of the wave model WAM against observations at buoys 44139, 44141, and 44142 for the period 16-25 August 1995. Model wave heights are generated using the RFE model forecast winds provided at 3-hourly intervals.

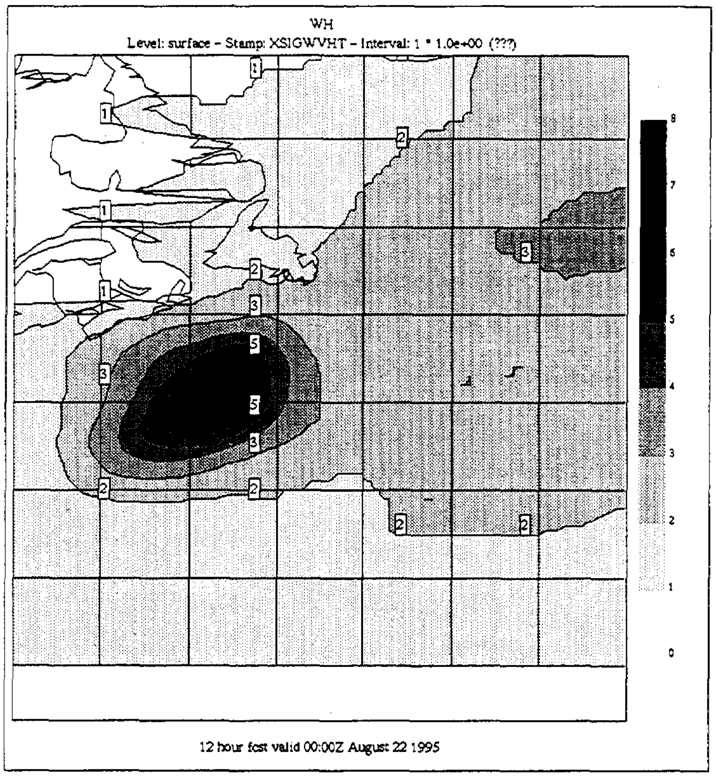

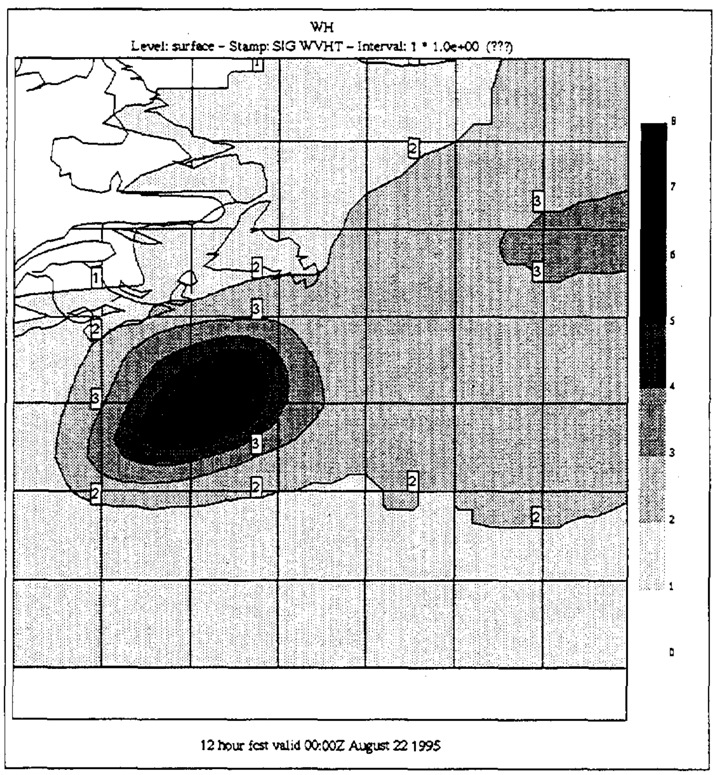

Figure 5: Snapshot of the 12-hour forecast of wave height (m) valid at 0000 UTC on 22 August 1995 for the fine grid version (top) and coarse grid version (bottom) of the wave model WAM driven by the RFE model 3-hourly forecast winds.

OPEN-OCEAN MEASUREMENTS OF THE WIND STRESS-SEA STATE RELATIONSHIP

F. W. Dobson, S. D. Smith and R. J. Anderson

Department of Fisheries and Oceans,
Bedford Institute of Oceanography,
P.O. Box 1006, Dartmouth, Nova Scotia B2Y 4A2

1. THEORETICAL AND EXPERIMENTAL BACKGROUND

The wind stress τ on the sea surface is a key parameter in studies of ocean and atmospheric dynamics, in numerical modelling of wind wave growth (Perrie and Toulany, 1990), and in the development of coupled models of surface wind and wave fields (de las Heras and Janssen, 1992). Remote sensing of marine winds requires a detailed understanding of the relations among wind speed, wave age and sea state; it is not the wind itself but the wind-driven waves that determine the microwave signature of the surface,

The wind speed U_z in the atmospheric surface layer has a logarithmic profile for neutral (adiabatic) stratification,

$$U_{ZN} - (u_*/k)\ \ln(Z/z_0) \qquad (1)$$

In neutral conditions U_z - U_{zN}. For stable (or unstable) stratification $U_z > U_{zN}$ (or $U_z < U_{zN}$), e.g. Smith (1988). Here Z is a reference height (usually 10 m), k - 0.4 is the von Karmen constant, and the friction velocity is $u_* - (\tau/\rho)^{1/2}$, where ρ is the air density. It follows that the aerodynamic roughness z_o of the sea surface is uniquely related to the "neutral" drag coefficient

$$C_{ZN} = (u_*/U_{ZN})^2 - [k/\ln(Z/z_0)]^2 \qquad (2)$$

The roughness and drag coefficient increase with wind speed (e.g. Smith, 1980, 1988) due to the growth of waves. There is also considerable variation in z_o and C_{10N} for a given "neutral" wind speed U_{10N}, and apart from experimental errors and sampling uncertainty this must be due to differences in the sea state (e.g. Donelan, 1990).

The short gravity waves that form initially on a smooth water surface (e.g. Kawai. 1979) travel much more slowly than the wind. With increasing duration and fetch, energy is transferred to longer, faster-travelling waves that approach and slightly exceed the wind speed. Wave "age" is here defined as the ratio $C_p/U_{10}\cos\Delta\theta$ of the phase velocity C_p at the peak of the wave slope spectrum to the component of wind speed at a 10 m reference height travelling in the direction of the waves, is the difference between wave and wind directions. (An alternative wave age is C_p/u_*.)

1.1 Wind stress and wave age in the absence of swell

Existing literature on the influence of sea state on wind stress (e.g. Charnock, 1955; Kitaigorodskii and Volkov, 1965; Phillips, 1985) has often been based on the premise that the aerodynamic roughness of a mature sea is controlled mainly by short gravity waves, which travel sufficiently slowly relative to the wind for flow separation to occur frequently. Since the shorter waves reach equilibrium fairly quickly, their contribution to the wind drag and surface roughness is related mainly to the local wind speed. These waves are normally "saturated" in the sense that any gain in their energy is accompanied, within only a few wave periods, by an increase in their rate of dissipation. The dissipation is accomplished by breaking on a wide variety of scales, and this breaking influences the surface roughness by inducing local separation of the air flow (Banner and Phillips, 1974). Except in very young seas these short waves differ greatly in frequency and wavenumber from the dominant waves, which travel at or near the wind speed. Similar arguments are used to relate radar backscatter, which is predominantly Bragg backscatter, to the wind stress and to the dominant waves in the ocean.

It has long been recognized that the roughness of the sea surface does not depend on wind speed alone. Correlations of air pressure and wave slope (e.g. Snyder et al., 1981) show that more wind momentum is absorbed by young, fast-growing waves than by older ones. The drag coefficient over the open sea (e.g. Smith, 1980, 1988; Large and Pond, 1981) is 10-15% lower than in coastal or shallower sites (e.g. Garratt, 1977; Wu, 1980; Donelan, 1982; Geernaert et al., 1986, 1987). This is believed to be linked to a difference in typical sea states, The drag of the wind on the dominant waves - those with frequencies near the spectral peak - is exerted by their gaining momentum and energy through an instability in the wind shear near the surface. This wave growth mechanism is a separate process from the flow separation mechanism that determines the drag on the short-wavelength gravity-capillary waves In the equilibrium range of the spectrum.

The goal of directly relating variations of the drag coefficient to sea state or wave age (e.g. Kitaigorodskii, 1970) has remained an elusive one. Smith (1980) found that at a site exposed to the open North Atlantic the "sea" peak in the one-dimensional wave spectrum was more often than not buried in the swell; a well-defined phase velocity C of dominant waves at the peak of the spectrum, as seen at sheltered sites (e.g. Hasselmann et al., 1973; Donelan, 1982), usually did not exist.

Donelan (1982) was one of the first to present a set of measurements of eddy wind stress and wave directional spectra which clearly showed a relationship between the state of development of the wave field and the wind stress. He divided the wave spectra so as to be the source of two types of roughness: waves near the peak frequency f_p of the wave spectrum which travel at nearly the wind speed, and waves in the "equilibrium range" of frequencies $f > 2f_p$ which travel much more slowly than the wind. His model was able to account for the much higher drag coefficients found in his experiment than were typical of the open sea (e.g. Smith, 1980; Large and Pond, 1981).

1.2 HEXOS

The HEXOS (Humidity Exchange over the Sea) data set includes one-dimensional wave spectra and eddy correlation wind stress measurements with three independent systems. Three approaches showed that "younger" waves were rougher than mature waves. Smith (1991) selected cases with single wave trains reported from observation of videotapes of the waves. The departure of the drag coefficient C_{10N} from the formula proposed for mature waves by Smith (1988) was called a "drag coefficient anomaly", ΔC_{10N}. A linear regression,

$$10^3 \Delta C_{10N} - 1.85 - 2.24\ C_p/(U_{10N}\ \cos\theta) \qquad (3)$$

with correlation coefficient r = 0.77 showed that 59% of the "scatter" in the drag coefficient was in fact explained by the influence of sea state. More often than not multiple wave trains were observed, and for these more complex cases no unique relation between wave age and wind stress was found.

A second approach related dimensionless surface roughness $z_* = g\ z_o/u_*$ to wave age in the form C_p/u_*; regression analysis on selected cases with single-peaked wave spectra (assumed to be mainly free of swell) showed z_* to be inversely proportional to wave age. Regression analysis gave

$$z_* = f u_*^{\ 3}/gC_p \quad (4)$$

with f = 0.48 (Smith et al. , 1992). This can be substituted in Equation 2, making the neutral drag coefficient a function of both wind speed and wave age. This second approach does not convincingly stand alone because both z_* and the wave age (in any form) are highly correlated with u_*, and the variability of u_* is greater than that of C_p in HEXOS (or in other data sets), giving rise to the possibility that the observed correlation is "spurious", i.e. introduced by the scaling.

In a third approach the roughness was scaled by the rms amplitude of the waves; z_o/σ is a measure of the ability of the waves to serve as roughness elements (Donelan, 1990). The HEXOS results for single-peaked wave spectra supported Donelan's results from Lake Ontario, and the combined data set gave

$$z_o/\sigma = 6.7 \times 10^{-4} \; (U_{10}/C_p) \quad (5)$$

(Donelan et al., 1993). Although u_* does not appear explicitly, both sides are highly correlated with u_* and the possibility of spurious correlation remains.

1.3 CASP-I

The Canadian Atlantic Storms Program (CASP-I) (Dobson et al., 1989) demonstrated that the variation of the wind with offshore fetch must be allowed for in the fetch-limited wave growth laws. Determination of the growth laws required separation of sea and swell components in the wave field: their separation algorithm remains the basis for the one used here. Whereas the CASP-I fetch limited growth laws for the open sea agreed within expected error limits with those determined by Donelan et al. (1985), neither agreed with the Hasselmann et al. (1973) JONSWAP laws unless the JONSWAP results were reformulated by removing all wave growth data taken in laboratory wind-wave tunnels. The fetch-limited wave growth relations were found to be sensitive to the formulation of the drag coefficient: a wave-age dependency based on the HEXOS data (Eq. 4) resulted in the highest degree of internal consistency among the relations (Perrie and Toulany, 1990).

The above work was conceptually based on the wave spectrum in the absence of swell, even if in some cases swell was present. Swell is known to influence the development of waves in wind-wave flumes (Phillips and Banner, 1974), even though it is thought to have negligible direct interaction with the wind (Kahma and Calkoen, 1992).

Dobson et al. (1994; hereafter DSA94) and Perrie and Toulany (1995, this Workshop; hereafter PT95) have used separate models to test the idea that separation of the sea from the swell in the observed wave height spectra will locate the rms amplitude and phase velocity of the sea alone, from which the wave age and hence a sea state-wind stress relation can be derived. In both studies the aerodynamic roughness tended to he greater for younger waves, but in DSA there was more scatter than in earlier experiments without swell.

The two studies differ on the fundamental point of whether the the sea-swell separation criterion should be based on the slope spectrum (DSA94) or the energy spectrum (PT95).

1.4 Objectives of present work

Wind stress and directional wave spectra were measured during the Grand Banks ERS-1 SAR Wave Spectra Calibration and Validation Experiment (Cal/Val) (Dobson & Vachon, 1994), the CASP-II Experiment (Smith et al., 1994), and the Sea Truth And Remote Sensing (STARS94) Experiment. In all these field experiments swell contributed most of the wave spectral energy most of the time. The present phase of this work will test the idea that removal of the swell from the full directional slope spectra would produce a more satisfactory sea state-wind stress relation. A spectral method for separating sea from swell has been adapted from a peak-finding algorithm based on hydrological catch basin delineation theory, The principle is to isolate the sea peak (and the phase velocity and direction), and to integrate over its territory in the directional wave spectrum to obtain the rms sea energy of the peak. It will improve upon earlier sea peak detection algorithms in the sense that the characteristics of the sea peak are here defined in both frequency and direction Instead of being averages over all directions, as was the case for both DSA94 and PT95.

We will be comparing our new 2-D results with the results from the small number of existing field experiments, expecting to find discrepancies from results at sites free of swell if the influence of the swell that we removed was significant, either in the analysis technique or in the development of waves in the open ocean.

2. THE MEASUREMENT SYSTEM

The requirement to measure wind stress in the open ocean at the times and places of satellite overpasses dictates a ship-based system. The "inertial-dissipation" method (e.g. Dobson et al., 1980; Large and Pond, 1981; Edson et al., 1991) estimates the wind stress from the spectra of downwind turbulence and of temperature fluctuations. A bow anemometer system developed for CSS Dawson (Anderson, 1993) has been adapted to make wind stress measurements from CSS Hudson and CSS Parizeau, A mast was mounted at the ship's bow (and another on the Parizeau's flying bridge for STARS94) carrying a Gill propellor-vane anemometer and two fast-response thermistors at a height of about 14 m above the waterline. These were interfaced to a 386 or 486 Personal Computer (PC) equipped with newly-developed software to automatically log and analyse the data.

2.1 Wind stress analysis: The dissipation technique

Sea surface wind stress and heat flux were calculated by the inertial-dissipation method as used by Anderson (1993). A PC was programmed to sample, calibrate, precondition and log the time series of wind velocity and air temperature at a rate of 16 Hz over runs lasting from 10-30 min, and fit an $f^{-5/3}$ power law to the wind and temperature power spectra in the inertial subrange region of the spectrum. If temperature fluctuation data were absent or failed to meet predefined criteria, the heat flux was estimated from wind speed and sea-air temperature difference by a bulk method (Smith, 1988). Empirical relations between the wind profile and stability were used to find U_{10N} and z_o from the wind stress and the heat flux.

Data were logged to coincide with all overpasses of ERS-1 during the experiment periods and at other times of interest.

2.2 Wave measurements

Two Datawell "Wavec" pitch/roll directional wave buoys (2m diameter) and/or a directional or nondirectional Datawell "Waverider" wave buoy with 90 cm diameter hulls were deployed for the experiments. These buoys were deployed on grid points of the Canadian Spectral Ocean Wave Model (CSOWM), in use at the Canadian Meteorological Centre, for experimental verification of the model. All wave buoys were calibrated at least once for each experiment, for heave (±10 cm), pitch and roll response and for directional accuracy (±15°).

In the (November 1991) ERS-1 CalVal experiment two Wavec and one nondirectional Waverider were deployed at separate model grid points in the Virgin Rocks area. During CASP-II (May 1992) one Wavec was deployed from CSS "Hudson" for 3-6 hourly at the ERS-1 and aircraft SAR overpass times. For the STARS94 experiment (December 1994) one Wavec buoy was deployed at a grid point in the centre of the line along which the ERS-1 SAR overpasses occurred, and in addition a directional Waverider was deployed from CSS "Parizeau" for each ERS-1 and aircraft SAR overpass.

2.3 Directional wave spectra

The wave spectra were computed using the Maximum Entropy Method (MEM) (Lygre and Krogstad, 1986); this technique provides the closest approximation to the directional resolution of the wave buoys, and matches the resolution of the SAR image spectra. The sampling interval was 0.78 s, and the runs were 34 min long. The directional spectra have been interpolated to a constant frequency bandwidth of 0.005 Hz. A STARS94 directional spectrum is shown in Figure 1 .

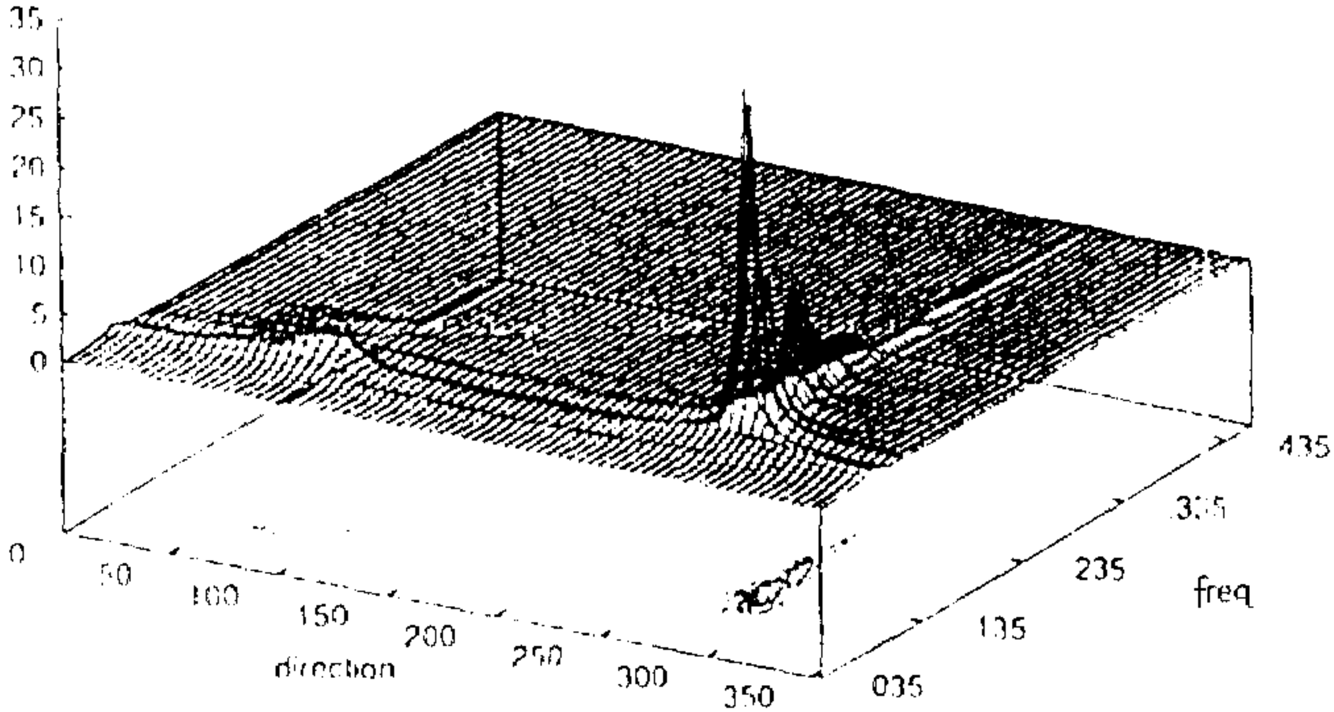

Figure 1. A typical directional wave spectrum from the STARS94 experiment. Direction is the direction from which the waves were travelling; the direction bins are at 5° intervals. The frequencies are at 0.005 Hz intervals, but the spectrum is smoothed with a weighted 3-point running mean in frequency. Wave energy is in m^2/radian/Hz.

2.4 Sea peak identification: Separation of sea from swell

The sea-swell separation technique described in Dobson et al. (1994) (DSA94) is summarised here for reference.

The buoy measurements provide spectral energy averaged over all directions and mean direction $\Theta(f)$ at each analyzed frequency. Peaks are sought in the wave slope spectrum, $f^4\phi(f)$. Swell is excluded if it is below a "critical" frequency f_c at which the component of the wind in the wave direction. $U_c = U \cos \Theta(f)$, becomes equal to the deep-water wave phase velocity $C(f) = g/2\pi f$; the highest peak in $f^4\phi(f)$ at frequencies above f_c is chosen as the "sea peak" frequency f_{sea}. The advantage in using the slope spectrum Is that peaks in the high-frequency region stand out more clearly, and so the younger seas that otherwise would be buried in the residual swell energy can be detected.

Next the 1-dimensional wave spectrum (that is the full directional spectrum averaged over all wave directions at each frequency) is integrated to obtain the sea energy

$$\sigma^2 = \sum_{f_t}^{f_{Ny}} \phi(f)\,\Delta f \tag{6}$$

and the rms sea amplitude σ. Here f_t is the trough frequency below f_{sea} and f_{Ny} is the highest (Nyquist) frequency analysed. The reciprocal wave age is the ratio U_c/C_p of wind speed in the wave direction to wave phase velocity C_p at the sea peak frequency.

This technique provides a basis for excluding the swell, so the results for complex sea states can be compared with existing results derived for sites or selected cases with sea only. It is not clear that the sea amplitude so derived is equivalent to the rms wave amplitude in the absence of swell - or that the mean sea direction coincides with the direction of the sea peak at the peak frequency. Although the procedure is objective, many decisions and choices have been built in: the highest peak of the slope spectrum does not always coincide with the highest peak of the heave spectrum, which biases the wave age and sea amplitude to value s smaller than would have been obtained by using the heave spectrum. Previous studies, which have made no attempt at all to consider the effects of swell, may contain an unknown contribution of swell to the rms wave amplitude. Furthermore, an unknown portion of the I-D spectral energy integrated over the selected frequency range is associated with the higher-frequency components of swell energy travelling in directions other than that of the wind, so that in some cases the sea energy may be overestimated. When no spectral trough exists another source of concern is the separation of swell from "older" sea-wave energy at frequencies < f_c, produced by winds no longer the same as those at the measurement site (a common occurrence during the passage of intense, fast-moving storm systems).

2.5 Sea-swell separation using the full directional spectrum

The present work is based on separating the sea from the swell in the full wave directional spectrum. The idea, originally proposed by Gerling (1992) and developed by S. Hasselmann for use in assimilating SAR wave spectra in the WAM model (see Komen et al., 1994), is derived from a hydrological catchment basin algorithm. The directional spectrum is smoothed and binned in frequency and direction, and each maximum is isolated using the catchment basin algorithm. A test is performed which determines whether the maximum is clearly swell (entire spectral peak propagates faster than the component of the wind vector in its mean propagation direction), clearly sea (as for swell but wave is slower than wind component in its direction) or mixed (parts of the peak are in the sea and other parts in the swell domain). Our version, as yet not completely tested on the data, will use the slope spectrum and will determine the sea energy by integrating over all maxima in the "sea" domain which have frequencies greater than or equal to the largest sea maximum. From a STARS94 directional spectrum (Figure 1), one of the peaks isolated by our technique is shown in Figure 2 .

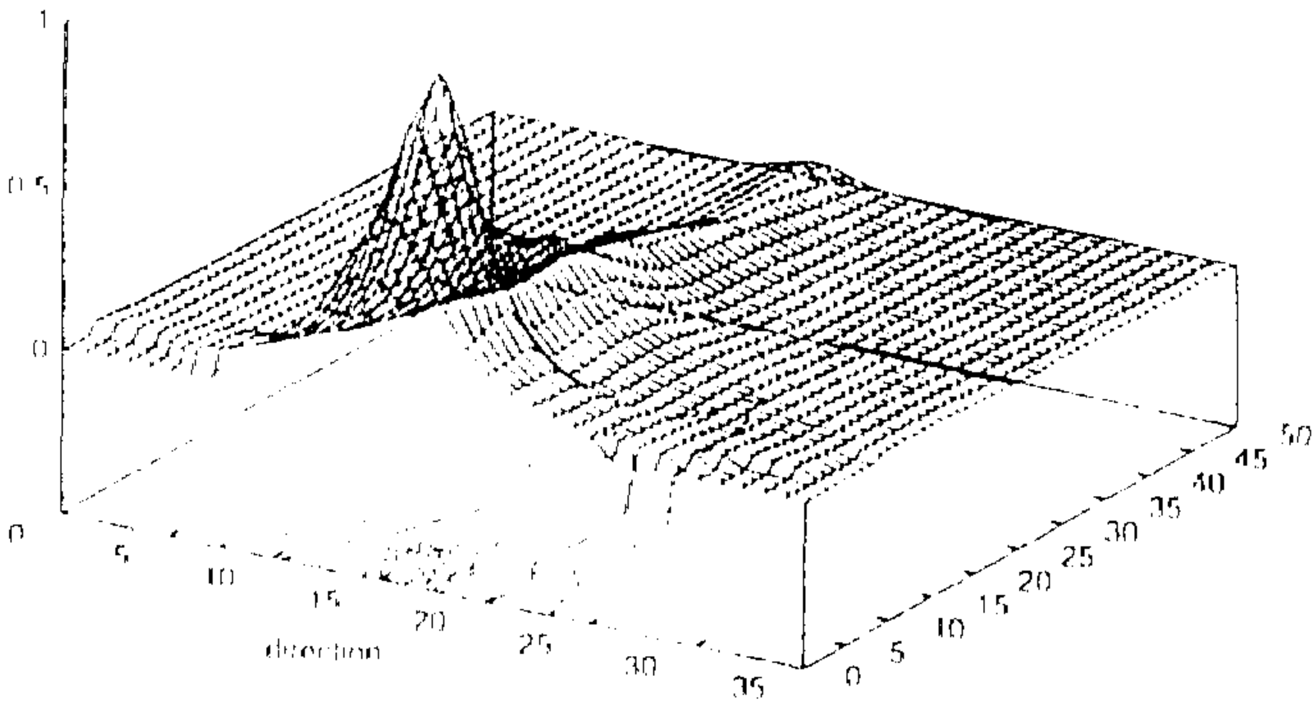

Figure 2. One of the sea peaks in the group coming from the NW (sea) from the STARS94 directional spectrum of Figure 1. It has been isolated with a neewly-developed catchment-basin algorithm. Energy is in m^2/radian/Hz as in Fig. 1, but the direction and frequency axes are bin numbers relative to the f, θ origin of the peak domain. It is such a peak which will be used to determine the age of the sea in the wave age analysis.

3. RESULTS

3.1 Wind stress

New data on neutral drag coefficients C_{10N} from CASP-II (Cruise 92-010 of CSS Hudson) and from STARS94 (Mission 94-034 of CSS Parizeau) are shown in Fig 3a and b , respectively.

Unless the wave ages are systematically different the distribution of the drag coefficients with wind speed ought to be nearly the same for each cruise. The STARS94 data from CSS Parizeau closely follow Anderson's (1993) dashed line from seven cruises of her sister ship, CSS Dawson. The values of C_{10N} from the two cruises of CSS Hudson are systematically higher by about 0.2 to 0.3 x 10^{-3}, although the variation with wind speed is nearly the same. This raises the possibility that flow distortion by the ship(s) has influenced the measured wind spectra, CSS Hudson has a higher bow and the ratio of our mast height to the height of the bow was less than for the other two ships; thus the Hudson data might be expected to be more influenced by distortion. On CSS Parizeau, winds blowing toward the bluff port side are expected to be distorted more, and in such cases higher values of C_{10N} are found (Figure 4). Taylor and Yelland (1994) have also recently reported differences among ships in C_{10N} derived by the dissipation method. This discrepancy is newly discovered and we are going to have to devise a method to remove differences between ships, for comparable wind speeds and wave ages.

At the time of writing the wave age analysis has not yet been combined with the wind stress data from the CASP-Il and STARS94 experiments. The influence of wave age (and possibly of swell) appears as scatter in Figures 3 and 4 .

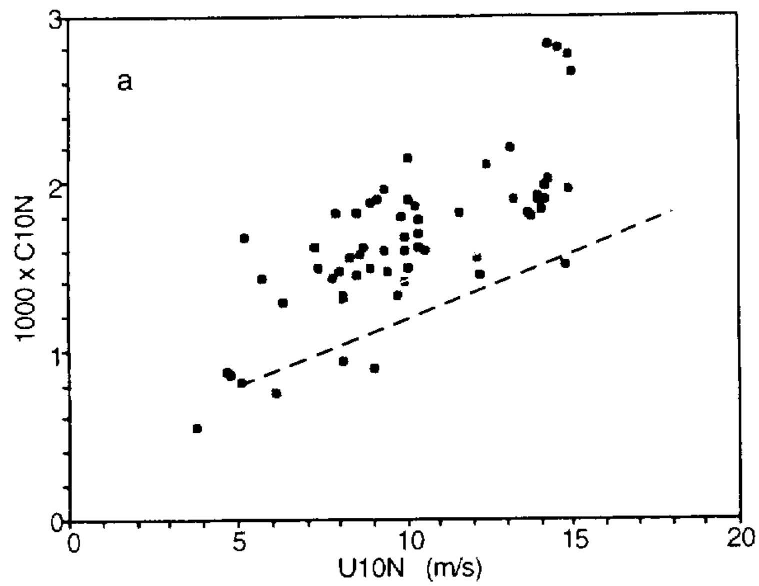

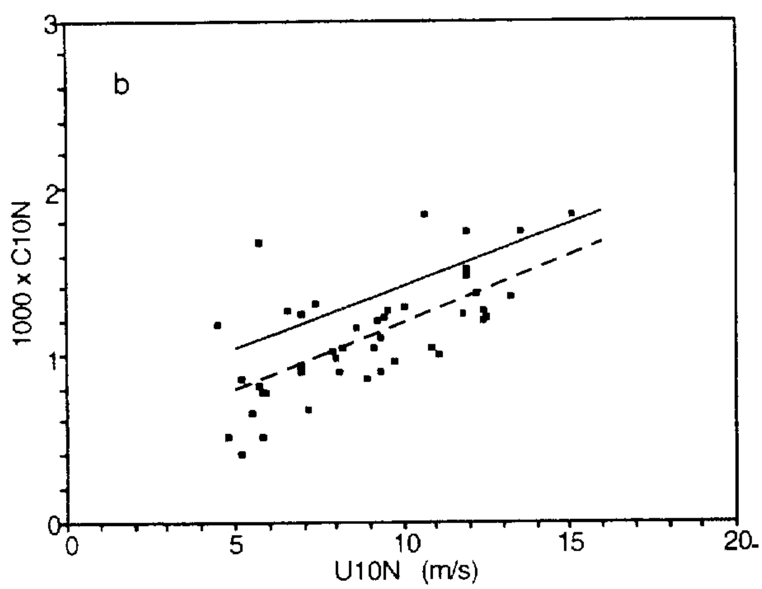

Figure 3. (a) Neutral 10 m drag coefficients measured from the bow mast of CSS *Hudson* during th CASP-II experiment against neutral 10m wind speed. Data runs with a relative wind direction outside ±60° from the bow may be influenced by flow distortion and have been deleted. The solid line (Eq. 6 and Fig. 3a from DSA94) is a regression on similar data from CSS *Hudson* Cruise 91-055 in the Grand Banks ERS-1 Cal/Val Experiment and the dashe line (Eq. 21 from Anderson, 1993) is based on seve cruises of CSS *Dawson* on the Grand Banks, Scotian Shelf and Labrador Shelf from 1982 to 1988.

(b) Same, from the bow mast of CSS *Parizeau* durin STARS94.

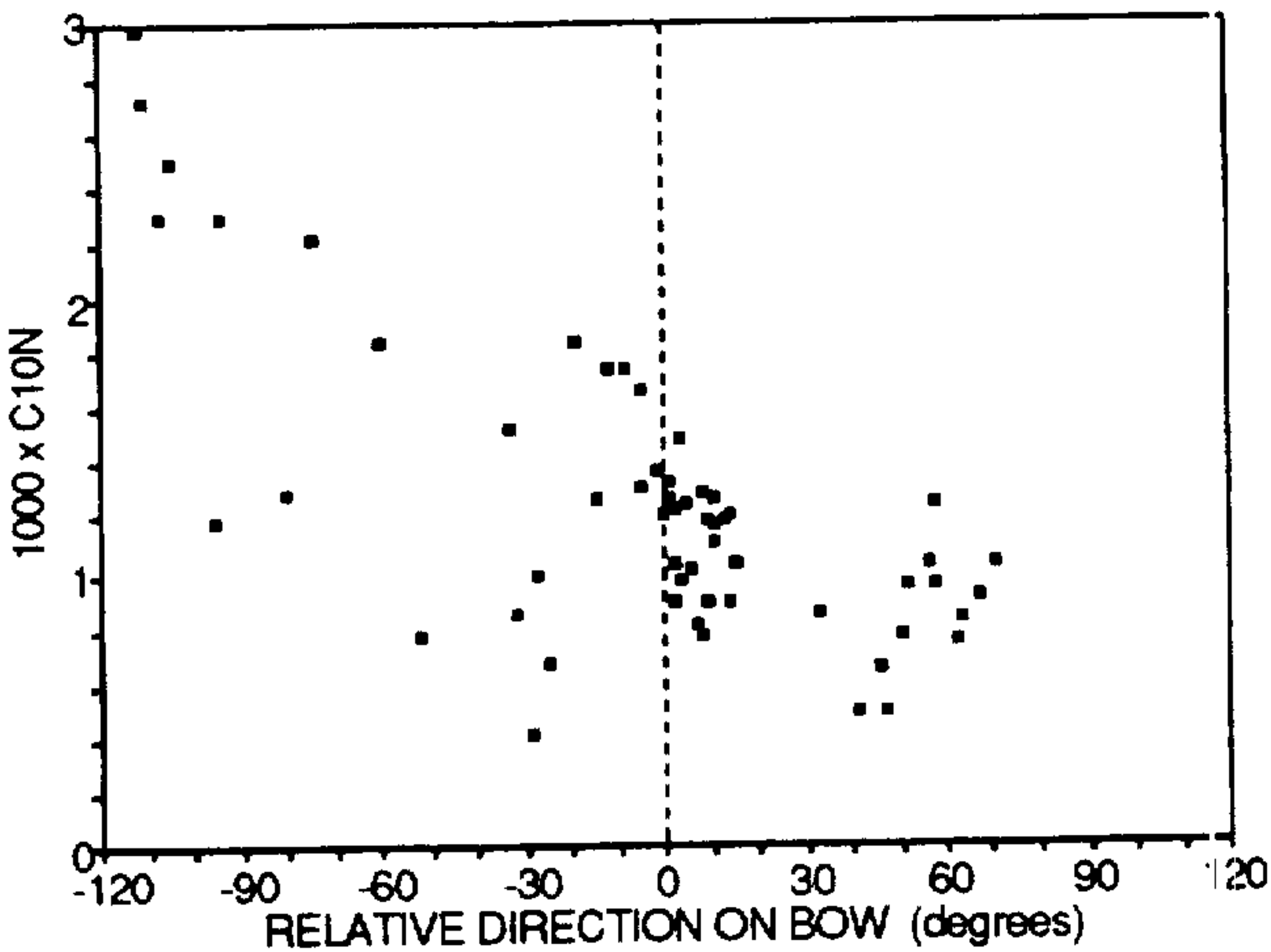

Figure 4. Neutral 10m drag coefficient measured from the bow mast of CSS *Parizeau* during STARS94, against the mean wind direction relative to the ship's bow.

6. CONCLUSIONS

This work is ongoing. At time of writing (September, 1995) we have:

1. developed and tested a new algorithm, based on catchment basin theory, which will allow a more precise determination of the sea peaR, the rms sea energy and the wave age from the full wave directional spectrum,

2. accumulated and processed a large set of high-quality directional wave spectra from an area of the North Atlantic Ocean dominated by intense, fast-moving atmospheric disturbances and complex patterns of sea and swell, and

3. accumulated and analysed a set of wind stress measurements concurrent with the wave spectra, using a shipboard system based on the dissipation technique.

Our next step will be to apply the sea-swell separation technique to the accumulated data sets Determining the optimum method of carrying out this process remains a central part of this research, and further iterations will be required before we can say what the best algorithm will be for use in coupling numerical forecast models of marine winds and waves.

7. REFERENCES

Anderson, R.J., 1993: A study of wind stress and heat flux over the open ocean by the inertial-dissipation method. J. Phys. Oceanogr. **23**, 2153-2161.

Banner, M.L. and O.K. Phillips, 1974: On the incipient breaking of small scale waves. J. Fluid Mech. **65**, 647-656.

Banner, M.L., 1990: Equilibrium spectra of wind waves. J. Phys. Oceanogr. **20**, 966-984.

Charnock, H., 1955: Wind stress on a water surface. Quart. J. Roy. Meteorol. Soc. **81**, 639-640.

De Las Heras, M.M. and P.A.E.M. Janssen, 1992: Data assimilation with a coupled wind-wave model. J. Geophys. Res. **97**, 20261-20270.

Dobson, F.W., L. Hasse and R. Davis (Eds), 1980; Air-Sea Interaction Instruments and Methods. Plenum Press, New York and London, 814 pp.

_____, Perrie and B. Toulany, 1989: On the deep-water fetch laws for wind-generated surface gravity waves. Atmosphere-Ocean **27**, 210-236.

_____, S.D. Smith and R.J. Anderson, 1994: Measuring the relationship between wind stress and sea state in the open ocean in the presence of swell, Atmosphere-Ocean **32**, 237-256.

Donelan, M. A., 1982: The dependence of the aerodynamic drag coefficient on wave parameters. Proc. 1st Int'l Conf. Meteorology and Air-Sea Interaction of the Coastal Zone. Amer. Meteorol. Soc., Boston, pp. 381-387.

_____, 1990: Air-sea interaction. In: The Sea, **98** LeMhaut and D.M. Hanes (Eds), J. Wiley and Sons, Inc., New York, pp. 239-292,

_____, J. Hamilton and W.H. Hui, 1985: Directiona spectra of wind-generated waves. Phil. Trans. Roy. Soc. London A, **315**, 509-562.

_____, F.W. Dobson, S.D. Smith and R.J. Anderson, 1993: On the dependence of sea surface roughness on wave development. J. Phys. Oceanogr. **23**, 2143-2149.

Edson, J.B., C.W. Fairall, S.E. Larsen and P.C. Mestayer, 1991: A study of the inertial-dissipation method for computing air-sea fluxes. J. Geophys. Res. **96**, 10689-10711.

Garratt, J.R., 1977: Review of drag coefficients over oceans and continents. Mon. Weather Rev. **105**, 915-929

Geernaert, G.L., K.B. Karsaros and K. Richter, 1986: Variation of the drag coefficient and its dependence on sea state. J. Geophys. Res, **91**, 7667-7679.

_____, S. E. Larsen and F. Hansen, 1987: Measurements of the wind stress, heat flux and turbulence intensity during storm conditions over the North Sea. J. Geophys. Res. **92**, 13127-13139.

Gerling, T.W., 1992: Partitioning sequences and arrays of directional wave spectra into component wave systems. J. Atmos. Ocean Techn. **9**, 444-458,

Hasselmann, K. et multi al., 1973: Measurements of wind-wave growth and swell decay during the Joint North Sea Wave Project (JONSWAP). Deutsch. Hydrograph. Zeit., Suppl. **A8**, No. 12, 22 pp.

Janssen, P.A.E,M.,1989: Wave-induced stress and drag of air flow over sea waves. J. Phys, Oceanogr. **19**, 745-754.

Kahma, K.K. and C.J. Calkoen, 1992: Recognizing discrepancies in the observed growth of wind-generated waves, J. Phys. Oceanogr. **22**, 1389-1405.

Kawai, S., 1979: Generation of initial wavelets by instability of a coupled shear flow and their evolution to wind waves. J. Fluid Mech. **93**, 661-703.
Kitaigorodskii, S.A., 1970: The Physics of Air-Sea Interaction. Hydrometeorological Press, Leningrad, 284 pp.; English translation, 1973. 237 pp., available as TT 72-50062 from U.S. National Technical Information Service, Springfield, VA 22151, USA.

_____, and Yu, A. Volkov, 1965: On the roughness parameter of the sea surface and the calculation of momentum flux in the near-water layer of the atmosphere. Izv. Atmos. Oceanic Phys. **1**. 973-988.

Komen, G.J., L. Cavaleri, M. Donelan, K. Hasselmann, S. Hasselmann and P.A.E.M. Janssen, 1994: Dynamics and Modelling of Ocean Waves. Cambridge U. Press, 532 pp.

Large, W.G. and S. Pond, 1981: Open ocean momentum flux measurements in moderate to strong winds, J. Phys. Oceanogr. **11**, 324-336.

Lygre, A. and H. E. Krogstad, 1986: Maximum entropy estimation of the directional distribution of ocean wave spectra, J. Phys. Oceanogr. **16**, 2052-2060.

Perrie, W. and B. Toulany, 1990: Fetch relations for wind-generated waves as a function of wind-stress scaling. J. Phys. Oceanogr. **20**, 1666-1681.

Phillips, O. M., 1985: Spectral and statistical properties of the equilibrium range in wind-generated gravity waves. J. Fluid Mech. **156**, 505-531.

_____ and M. L. Banner, 1974: Wave breaking in the presence of wind drift and swell. J. Fluid Mech. **66**, 625-640,

Smith, P. C., C. L. Tang, J. Ian MacPherson and R. F. McKenna, 1994: Investigating the Marginal Ice Zone on the Newfoundland Shelf. EOS, Trans. Amer. Geophys. Union **75**, 57, 60-62.

Smith, S. D., 1980: Wind stress and heat flux over the ocean in gale force winds. J. Phys. Oceanogr. **10**, 709-726. 1

_____, 1988: Coefficients for sea surface wind stress, heat flux and temperature as a function of wind speed and temperature. J. Geophys. Res. **93**, 15467-15472.

_____, 1991: Some early results of the Humidity Exchange over the Sea Main Experiment. In: Deep Convection and Deep Water Formation In the

Oceans, P.C. Chu and J.-C. Gascard (Eds.), Elsevier Science Publishers, Amsterdam, pp 377-382.

_____, R. J. Anderson, W.A. Oost, C. Kraan, N. Maat, J. DeCosmo, K.B. Katsaros, K. L. Davidson, K. Bumke, L. Hasse and H. M. Chadwick, 1992: Sea surface wind stress and drag coefficients: the HEXOS results. Boundary-Layer Meteorol. **60**, 109-142.

Snyder R.L., F.W. Dobson, J.A. Elliott and R.B. Long, 1981: Array measurements of atmospheric pressure fluctuations above surface gravity waves. J. Fluid Mech. **102**, 1-59.

Taylor, P.K. and M.J. Yelland, 1994: Wind stress measurements in the open ocean and the coastal zone. 2nd Int. Conf, on Air-Sea Interaction and on Meteorology and Oceanography of the Coastal Zone, Lisbon, Sept. 22-27, 1994

Wu, J. , 1980: Wind stress coefficients over sea surface near neutral conditions - a revisit. J. Phys. Oceanogr. **10**, 727-740.

4th International Workshop on Wave Hindcasting & Forecasting

ROLE OF OCEAN WAVE MATURITY IN SEA SURFACE ROUGHNESS

W. Perrie and B. Toulany

Ocean Sciences, Maritime Region
Department of Fisheries and Oceans, Bedford Institute of Oceanography
Dartmouth, Nova Scotia, Canada B2Y 4A2

1. INTRODUCTION

Wind stress on the sea surface is a key parameter in air-sea interaction dynamics. Its understanding is central to improvements to models for the dynamics of atmospheric and oceanic boundary layers. The boundary layers have impact on atmospheric and oceanic dynamics, and in critical cases influence the generation and evolution of baroclinic systems and larger scale circulation patterns. However, oceanic models typically represent wind stress τ by a constant drag coefficient C_d and the wind speed U evaluated at a reference height such as 10 m, ($\tau = \rho C_d U^2$, where ρ is the density of air and the wind speed U is given by an atmospheric model.

From dimensional analysis, Charnock (1955) suggested that that for mature ("old") seas the roughness Z_o, is proportional to the wind stress τ,

$$Z_0 = \Theta U_*^2 / g \qquad (1)$$

where U_* is the friction velocity. Wu (1980) suggested, from coastal data containing younger waves, that $\Theta \approx 0.0185$. Moreover, a recent understanding has emerged that wave development is a cause and effect of sea surface roughness. Smith et al (1992) derived a wave age C_p/U_* dependent relation for roughness, from the HEXOS (Humidity Experiment Over the Sea) experiment,

$$Z_0 \simeq 0.48 \frac{U_*^2}{g} \left(\frac{C_P}{U_*}\right)^{-1} \qquad (2)$$

Which is a extension of the Charnock (1955) relation. An alternate (Lake Ontario data) formulation for Z_o scaled by RMS wave amplitude $\sigma = \sqrt{E_{0_{Sea}}}$, is given by Donelan (1990), in terms of wave age denoted here as C_p/U,

$$Z_0/\sigma = 5.5 \times 10^{-4} (U/C_p)^{2.7} \qquad (3)$$

where E_{OSea} is the total energy in the wind sea, excluding swell.

The lack of consensus in these Z_o equations is notable. In Section 2 , we give relations for friction velocity U_* and drag coefficient C_d in terms of wave age, wave slope energy $< E_o > k^2$ and Phillips' (1985) a coefficient, derived from the fetch relations for growing waves. This model is verified with wind and wave measurements collected during the recent Grand Banks ERS-1 SAR Waves Validation (hereafter denoted GB) Experiment of Dobson et al (1993, 1994) in Sections 3 -4 .

2. THE DRAG COEFFICIENT

The average wave slope energy S may be expressed in terms of wavenumber k as,

$$S = <k^2>E_0 \tag{4}$$

where

$$< k^2 > \equiv \frac{1}{E_0}\int_{f_s}^{f_n}\int_0^{2\pi} k^2 \cdot E(f,\theta)d\theta df \tag{5}$$

and $E(f,\Theta)$ is the two-dimensional wave spectrum, f_n is a constant times the peak frequency f_p such as 2.5 or 3, sufficiently large that the integrals of equation (5) approximately cover the equilibrium range of the spectrum, f_s is the frequency which separates swell from local wind-generated waves, and Θ is the azimuthal angle, measured clockwise from north. Equation (4) may be related to Phillips' (1985) α coefficient, as in Perrie and Toulany (1995a), expressing α in terms of the one-dimensional energy $E(f)$,

$$\alpha = \frac{(2\pi)^3}{gU_*}\frac{1}{(f_n - 1.5f_p)}\int_{1.5f_p}^{f_n} f^4 E(f)\exp\left(\frac{f_p^4}{f^4}\right)df \quad . \tag{6}$$

where g is the acceleration due to gravity and U_*, U and C_d satisfy

$$U_* \equiv U\sqrt{C_d} \quad . \tag{7}$$

Perrie and Toulany (1995a) suggest $\exp(f_p^4/f^4) \approx 1$ for $1.5f_p < f < f_n$, and therefore

$$\int_{1.5f_p}^{f_n} f^4 E(f) \exp(f_p^4/f^4) df \approx \int_{1.5f_p}^{f_n} f^4 E(f) df \quad . \tag{8}$$

Introducing a coefficient $\mathcal{T}$

$$\mathcal{T} \equiv \int_{1.5f_p}^{f_n} f^4 E(f) df \bigg/ \int_{f_s}^{f_n} f^4 E(f) df \tag{9}$$

they argue that $\mathcal{T}$ is approximately constant.

Substituting equations (4), and (8)-(9) into equation (6) and assuming the deep water dispersion relation, $\omega^2 = gk$, gives

$$\alpha = \frac{g}{2\pi U_* \chi f_p} \mathcal{T} S \tag{10}$$

where $f_n = (\chi + 1.5)f_p$. In terms of phase velocity $C_p = \frac{2\pi f_p}{k}$, this is

$$U_* = \frac{C_p}{\alpha\chi} T S$$

or

$$C_d = \left(\frac{C_p}{U\alpha\chi} T S\right)^2 \quad .$$

Equations (11)-(12) are our drag model.

Wave slope energy S as described equation (4) measures part of the total mean square slope. From Cox and Munk (1954a-b), part of the mean square slope is in the short waves and cannot be sensed by the wave buoys. This is not important for the analysis considered here. From equation (6), it is only important that S as determined in equation (4) gives a stable estimate of α.

3. VALIDATION EXPERIMENT

A description of the GB experiment is given in Dobson and Vachon (1994) and Dobson et al (1994). The dissipation method was used to determine wind stress from the spectra of downwind turbulence and temperature fluctuations. Wind and wind stress measurements were made from the CSS Hudson for comparison with remotely sensed ERS-1 SAR images. Details of the measurement process are presented in *Dobson et al (1980), Large and Pond (1981), Edson et al (1991), Anderson (1993) and Dobson et al (1994)*. Sea surface wind stress and heat flux were calculated by the inertial-dissipation method described by *Anderson (1993)*.

A Datawell WAVEC pitch/roll directional wave buoy moored at 46°36.6’N, 50°25.0’W gave wave measurements. It functioned during November 10-15 and 17-24. The sampling interval was 0.78125 s, and the runs were 34 minutes long, every hour. It gave one directional wave spectrum per hour. As noted by *Dobson* et al (1994), the directional spectra were not corrected for the frequency response of the buoy. It was calibrated for heave, pitch, roll and compass direction prior to the experiment.

The GB experiment gave 56 measurements of wave spectra and corresponding wind stress. Of these measurements, comparison was made with the *drag* model, based on the criteria:

(i) To separate swell from wind sea, the directional wave spectra and the wind speed and direction were used to get the highest frequency f_s, at which the phase velocity equals the wind speed. The part of the spectrum below f_s was neglected as swell.

(ii) $E(f)$ at the peak f_p must have energy above $2m^2s$, else the spectra is noise.

(iii) Assuming the fetch-growth rules, f_p must satisfy $f_{p_{t+1}} < f_{p_t} + 0.01$ in succeeding hourly time steps.

(iv) f_p must have mean directions that are reasonably close to the wind direction, else the selected peak is swell.

A similar condition to (iii) was used in *Perrie and Toulany (1995b)*. The separation of swell from wind sea in (i) is described in *Dobson et al (1989)*. Regarding GB data, *Dobson et al (1994)* do not use (ii)-(iv). They determine the peak of the slope spectra, which they denote $f^4E(f)$, and estimate f_s as the first trough below the peak in $f^4E(f)$, or f_s as given in (i), whichever is higher. Thus Dobson et al (1994) select different data from what (i)-(iv) give.

4. MODEL VERIFICATION

In Figure 1 , U_* is correlated with C_p x S, following equations (11)-(12), using GB data, which implies

$$U_* = 2.5\ C_pS + 0.098 \qquad (13)$$

where the 95% confidence interval on the slope (regression coefficient) is ±0.5. The correlation coefficient $\mathcal{R}$ is 0.86, which is competitive with ($\mathcal{R}$) values reported by *Juszko et al (1995)* and exceeds that of *Dobson et al (1994)*. The latter regressed Z_o/σ against U_c/C_p, (where U_c is the component wind speed in the direction of the waves at f_p) and get $\mathcal{R}$=0.48. Constraints (i)-(iv) give a regression of Z_o/σ against U_c/C_p with $\mathcal{R}$ = 0.52.

The regression of U_* against C_pS in Figure 1 takes α as constant in equation (11). A fetch relation for α in terms of wave age U_*/C_p was found by *Perrie and Toulany (1990)*,

$$\alpha = 2.26 \times 10^{-2} \left(\frac{U_*}{C_p}\right)^{-0.67 \pm 0.13} \qquad (14)$$

Substituting equation (14) into equation (11) gives

$$U_* \approx 6.7 \times 10^3 C_p S^3 \qquad (15)$$

or in terms of C_d,

$$C_d \approx 4.5 \times 10^7 \left(\frac{C_p S^3}{U}\right)^2 \qquad (16)$$

assuming χ = 1.5 and $\mathcal{T}|$ ≈ 0.64, as estimated in *Perrie and Toulany (1995a)* using spectral parameterizations of *Donelan et al (1985)*. The linear regression of U_* against $C_p S^3$ implies

$$U_* \approx 8.7 \times 10^3 C_p S^3 + 0.3 \qquad (17)$$

with respect to GB data, which is consistent with equation (15) and $\mathcal{R}$ =0.90. The corresponding regression between C_d and $\left(\frac{C_p S^3}{U}\right)^2$ implies

$$C_d \approx 5.5 \times 10^7 \left(\frac{C_p S^3}{U}\right)^2 + 0.1 \times 10^7 \qquad (18)$$

where $\mathcal{R}$ =0.66, comparable to R obtained by Smith (1991) for the HEXOS derived C_d. We note that as all calculations of this sort, spurious self-correlation contributes to $\mathcal{R}$.

5. CONCLUSIONS

The *drag* model in equations (11)-(12), is shown to compare well with recently collected wind and wave data (GB) from the Grand Banks of Newfoundland. The correlation coefficient R is in the range 0.86-0.90, depending on pararmeterizations for Phillips' α coefficient. Dependency on wave slope is important. When wave slope is ignored, R is also reduced, with respect to the GB data. Alternate pararmeterizations, such as Z_o/σ against U_c/C_p, as suggested by Dobson et al (1994) and many others, have much lower values for R.

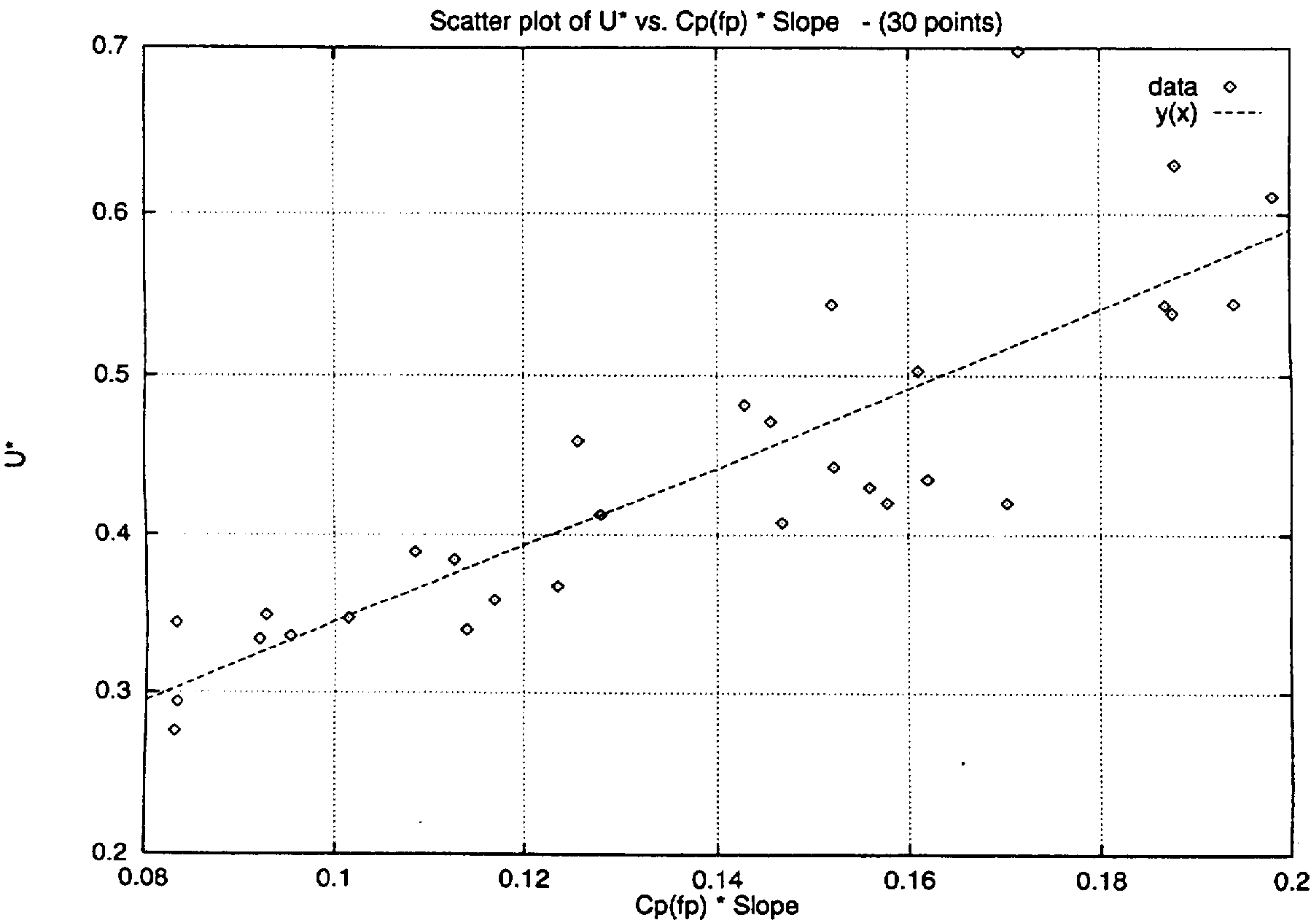

Figure 1 Comparison of GB data with the *drag* model given in equations (11)-(12), regressing measured friction velocity against C_pS.

6. ACKNOWLEDGEMENTS

The wave modelling program at BIO is funded by the Federal Panel on Energy Research and Development (Canada) under Project No. 6B3006. We want to thank F. Dobson, S. Smith and B. Anderson for very generously providing the wind and wave data from the Grand Banks ERS-1 SAR Waves Validation Experiment (GB), and in assisting in important phases of the analysis.

References

[1] Anderson, R. J. (1993) A study of wind stress and heat flux over the open ocean by the inertial-dissipation method. J. Phys. Oceanogr. **23**, p. 2153-2161.

[2] Charnock, H. (1955) Wind stress on a water surface. Quart. J. Roy. Meteorol. Soc. **81**, p. 639-640.

[3] Cox, C. and Munk, W. (1954a) Statistics of the sea surface derived from sun glitter. J. Mar. Res., **13**, 198-227.

[4] Cox, C. and Munk, W. (1954b) Measurements of the roughness of the sea surface from photographs of the sun's glitter. J. Opt. Soc. Am., **44**, 838-850.

[5] Dobson, F., Hasse, L. and Davis, R. (1980). (Eds). Air-sea Interaction Intruments and Methods. Plenum Press, New York and London, 814 pp.

[6] Dobson, F., Perrie, W. and Toulany, B. (1989) On the deep-water fetch laws for wind-generated surface gravity waves. Atmosphere-Ocean **27** (1), 210-236.

[7] Dobson, F.W., Smith, S.D. and Anderson, R.J. (1994) Measuring the relationship between wind stress and sea state in the open ocean in the presence of swell. Atmosphere-Ocean **32** (1), 237-256.

[8] Dobson, F.W., Smith, S.D., Anderson, R.J., Vachon, P.W., Vandemark, D., Buckley, JR., Allingham, M., Kandekar, M., and Lalbeharry, R. (1993) The Grand Banks ERS-1 SAR Wave Experiment. Eos, Trans. Am. Geophys. Union, **74**, No.4, p.41, 44-45

[9] Dobson, F.W. and Vachon, P. (1994) The Grand Banks ERS-1 SAR Wave Spectra Validation Experiment: Program Overview and Data Summary. Atmosphere-Ocean. **32**(1), p.7-29.

[10] Donelan M. A., Hamilton, J. and Hui, W. H. (1985) Directional spectra of wind-generated waves. Phil. Trans. R. Soc. Lond. A **315**, 509562.

[11] Donelan M. A. (1990) Air-Sea Interaction. In: The Sea, B. LeMehaute and D. M. Hanes (Eds), J. Wiley and Sons, Inc., New York, pp. 239-292.

[12] Edson, J. B., Fairall, C. W., Larsen, S. E. and Mestayer, P. G. (1991) A study of the inertial-dissipation method for computing air-sea fluxes. J. Geophys. Res. **96**. p. 1068910711.

[13] Juszko, B. A., Marsden, R. F., and Waddell, S. R. (1995) Wind stress from wave slopes using Phillips' equilibrium theory. J. Phys. Oceanogr. **25**, No. 2, 185-203.

[14] Large, W. G. and Pond, S. (1981) Open ocean momentum flux measurements in moderate to strong winds. J. Phys. Oceanogr. **11**. p. 324336.

[15] Perrie, W. and Toulany, B. J. (1990) Fetch relations for wind-generated waves as a function of wind-stress scaling. J. Phys. Oceanogr., **20**, 1666-1681.

[16] Perrie, W. and Toulany, B. J. (1995a) Relating friction velocity to spectral wave parameters. J. Phys. Oceanogr. **25**, No. 2, 266-279.
[17] Perrie, W. and Toulany, B. J. (1995b) The response of ocean waves to turning winds. J. Phys. Oceanogr. **25**, No. 6, 1116-1129.

[18] Phillips, O. M. (1985) Spectral and statistical properties of the equilibrium range in wind-generated gravity waves. J. Fluid Mech., **156**, 505-531.

[19] Smith, S. D. (1991) Some early results of the humidity exchange over the sea main experiment. In Deep Convection and Deep water Formation in the Oceans. P.C. Chu and J.C. Gascard (Editors). Elsevier. pp 377-382

[20] Smith, S.D., Anderson, R.J., Oost, W.A., Kraan, C., Maat, N., DeCosmo, J., Katsaros, K.B., Davidson, K.L., Bumke, K., Hasse, L and Chadwick, H.M. (1992) Sea surface wind stress and drag coefficients: The HEXOS results. Bound.-Layer Meteor. **60**, 109-142.

[21] Wu, J. (1980) Wind-stress coefficients over seat surface near neutral conditions: A revisit. J. Phys. Oceanogr., **10**, p. 727-740.

COUPLING ATMOSPHERIC AND OCEANIC WAVE DYNAMICS

W. Perrie and L. Wang

Ocean Sciences, Maritime Region
Department of Fisheries and Oceans, Bedford Institute of Oceanography
Dartmouth, Nova Scotia, Canada B2Y 4A2

1 INTRODUCTION

Although the balance relationship between the wind profile in the boundary layer and the seastate is important in understanding both atmospheric and oceanic dynamics, there is thus far no consensus as to its functional formulation. To attempt a formulation, it is important to recognise that the key parameter at the air-sea interface, in studies of oceanic and atmospheric dynamics, is the sea surface roughness. The sea surface roughness is directly related to the surface waves, which in turn are driven by the wind profile in the atmospheric boundary layer. However, the nonlinearity of the relationship makes it difficult to relate sea surface roughness to wave parameters in a simple quantitative manner.

Ultimately, the coupling of the boundary layer with a wave model must result in a derivation of the equilibrium state between winds and waves. 'Equilibrium' is understood in terms of implicitly consistent estimates for sea surface roughness Z_o in both the boundary layer model and in the wave model. In weather forecast offices using standard wave models, such as the WAM model of Hasselmann et al (1988), the wave model is not consistent with the models for the atmospheric boundary layer, in the sense that an 'equilibrium state', with respect to Z_o, is not achieved and involves the following considerations:

- (1) Given a wind speed U_{10} at a reference height (10m), the standard wave model uses empirical formulae to produce a friction velocity U_*, which in turn is used to estimate spectral wave energy $E(f,\Theta)$, as a function of frequency f and direction Θ. However, U_{10} is produced by a boundary layer model, which involves a formulation for U_*, the drag coefficient C_d, roughness Z_o and appropriate thermal conditions. Thus, U_* in the wave model differs from U_*, in the atmospheric model.
- (2) Roughness Z_o and C_d depend on the wind profile variation with height, rather than simply the wind

speed itself at a reference level such as 10 meters. The use of empirical formulae to estimate U_* and C_d as functions of U_{10}, implies that Z_o and C_d in the wave model differ from corresponding estimates in the atmospheric model.

- (3) The reaction of seastates on the wind profile with height also occurs because the interaction between the wind field and wind-generated ocean waves is strong. However, this is not taken into account in modern wave models or in operational meteorology.

In Section 2 , we present an empirically based model of Z_o, which couples ocean waves to the wind fields from a boundary layer model. Models for waves and the boundary layer are described in Sections 3 -4 . Verification with the observations from the CAL/VAL experiment of Dobson and Vachon (1994) are presented in Section 5 . This paper is a summary of Perrie and Wang (1995) and prepares for results given in Wang et al (1995).

2 SEA SURFACE ROUGHNESS

Numerous research efforts have been made to dynamically couple the atmosphere and the ocean, over the last few years. Although the effects of some characteristic properties are becoming clearer, the extremely complex processes of air-sea interaction are still not fully understood. The best known relation for Z_o, due to Charnock (1955), relates Z_o to only U_* without reference to characteristics of the wave field,

$$Z_o = C_o \times \left(\frac{U_*^2}{g} \right) \qquad (1)$$

where g is the acceleration due to gravity and C_o is a constant. Wu (1980) proposed a value of 0.0185 for C_o after averaging results from a wide range of data sets. Other values have also been proposed, over the years. The Charnock relation of equation (1) is therefore a composite description for Z_o under the varied seastate conditions that can exist. It follows that the Charnock relation is not capable of a good representation of specific dynamical processes such as young wind-generated waves or the response of waves to turning wind directions. A demonstration of the breakdown of the Charnock relation, in all but mature wave conditions, was given by Donelan (1982, 1990).

The variation of Z_o with wave parameters such as wave age C_p/U_* where C_p is the phase velocity at the peak of the wave spectrum, has proved difficult to determine. Following the recent HEXOS experiment in the North Sea, Smith et al (1992) suggested the relation,

$$Z_o = 0.48 \times \left(\frac{U_*^2}{g}\right)\left(\frac{C_p}{U_*}\right)^{-\frac{1}{2}} \qquad (2)$$

which has C_p/U_* dependence. This paper concerns the implementation of the Charnock relation (1), in comparison with the seastate-dependent formulation for Z_o given in equation (2). We hereafter denote the former as 'UNCOUPLED' and the latter as 'COUPLED'.

3 WIND AND WAVES

This section consists of a brief description of the wave model and boundary layer model components, which must be connected together to constitute our COUPLED and UNCOUPLED models.

- (A.) Boundary-layer model

Our boundary layer model is quite similar to the RPN, as documented by Delage (1988a, 1988b). It is a diagnostic model. Given U and Z_o it specifies boundary layer parameters at a given grid point. The vertical fluxes of momentum, sensible heat and latent heat are computed at the surface (denoted by subscript 's'), as

$$\overline{\mid w'V' \mid_s} = (C_M \mid V_a \mid)^2 \qquad (3)$$
$$\overline{\mid w'T' \mid_s} = c_p(C_M C_T \mid V_a \mid (T_s - T_a) \qquad (4)$$
$$\overline{\mid w'q' \mid_s} = L(C_M C_T \mid V_a \mid (q_s - q_a) \qquad (5)$$

The transfer coefficients for momentum and heat, denoted C_M and C_T, are functions of the bulk Richardson number R_{ib}, anemometer level Z_a and Z_o. Latent heat is L, specific heat at constant pressure, c_p, air temperature T_a, sea surface temperature T_s, the specific heat content of water vapour at the sea surface, q_a specific heat content of liquid water, q_s.

This boundary layer model implies C_d depends on Z_o under neutral conditions, satisfying the usual relation, $C_{dn} = \left(\frac{U_*}{U_z}\right)^{1/2}$ or

$$C_{dn} = \left(\frac{\kappa}{\ln\left(\frac{Z_o + Z_a}{Z_o}\right)} \right) \qquad (6)$$

rather than the wind speed at a desired anemometer level Z_a. Many empirical relations attempt to relate Cd or Z_o to U_a, only, without reference to seastate. An example is given in Hsu (1986). Numerous empirical relationships between the neutral drag coefficient and wind speed have been proposed. Donelan (1990) pointed out that the development of these relationships is due to differences in seastate during various experimental situations. In our boundary layer model, $C_M C_T$ may also be shown to be a function of Z_o, under near-neutral conditions.

- (B.) Wave Model

The spectral energy density for surface gravity waves in deep water $E(f,\Theta)$ approximately evolves according to the balance relation

$$\frac{\partial E(f,\theta)}{\partial t} + c_g \dot{\nabla} E(f,\theta) = S_{in} + S_{ds} + S_{nl} \qquad (7)$$

where S_{in} is the spectral energy input by the wind, S_{ds}, the dissipation due to wave-breaking and white-cap formation, S_{nl} the change in spectral energy due to non-linear transfer resulting from wave-wave interactions and c_g the propagation group velocity. The wave model constitutes an integration of the spectral balance equation (7) in space and time. We use the WAM model (cycle 3) of Hasselmann et al (1988) for parameterizations of S_{in}, S_{ds}, S_{nl} and propagation. In integrating the balance equation (7), $E(f,\Theta)$ is represented by 54 frequencies and 12 directions for a total of 648 spectral elements, at every grid point. The 54 frequencies range from 0.0417725 Hz to 0.65268 Hz, increasing with a constant ratio of 1.1.

4 COUPLED WIND-SEA

The Z_o pararmeterizations, the boundary layer model and the wave model are connected together iteratively. At a given timestep, we first use wind speed and direction (specified externally as forcing for the boundary layer / wave model dynamics), to compute the peak frequency f_p from the wave model. Assuming a first guess Z_o, then U_* and C_d are obtained from the boundary layer model. Thereafter a 'new' Z_o is calculated using either the Charnock formula (1) in the UNCOUPLED model or the Smith et al (1992) equation (2) in the COUPLED model. If the 'new' Z_o is within allowable error relative to the previous Z_o, we proceed to the next time step in the simulation. Otherwise we iterate it again. The boundary layer model then leads to a new estimates for C_d and U_*. Thus, equation (1) or equation (2) lead to a revised estimate of Z_o. When the iteration process converges, we go to the next time step. Although a given reference wind speed may be specified in these tests, it is implicit that as Z_o and U_* evolve and the seastate matures, the vertical wind profile also changes in time. This is evident in the COUPLED model. Of course, the vertical wind profile does not change in the UNCOUPLED model because changes in Z_o and U_* do not occur.

5 MODEL VERIFICATION

To provide model verification using observed data, implementation was made on the northwest Atlantic, on a transverse Mercator projection with an assumed equator at 51° W and a grid spacing of 119 km near Halifax, Nova Scotia. The grid consists of 160 points of which 139 are water points, at which model parameters are generated. Two operational wave buoys are located in this grid. Observations used to verify the model were collected during the ERS-1 Grand Banks Calibration/Validation experiment of Dobson and Vachon (1994). Wind data was provided every three hours for the experiment (8 to 25 November 1991) by RPN and linearly interpolated to hourly wind fields. The time step is 20 minutes for the one-dimensional model and one hour for three-dimensional model. The buoy data were provided by the Atmospheric Environment Service (AES) in Bedford Nova Scotia.

During the experiment a cyclone developed in the region between Nova Scotia and Newfoundland on November 15. Wind fields for 00 UTC on November 15 and 16 are shown in Figures 1a -b . Estimated Hs time series at the model grid point nearest buoy 44138 are shown in Figure 2 , for both the COUPLED and UNCOUPLED models. It is therefore demonstrated that at the peak of the storm, late on 15 November, the COUPLED model estimates for H_s are closer to measured H_s values than those of the UNCOUPLED model. Lower seastate conditions are less determinate. When observed wave heights H_s are in the range 2-3 m during November 12-15, errors of up to 1.7 m occur. This is not too serious because, whereas a fine-mesh wave model with high quality wind fields and more detailed physics may succeed in modelling these 2-3 m waves, we are using wind fields from an operational weather forecasting laboratory, a comparatively large grid and the operational WAM model of Hasselmann et al (1988). Thus, it is hardly surprising that these 2-3 m waves are not resolved.

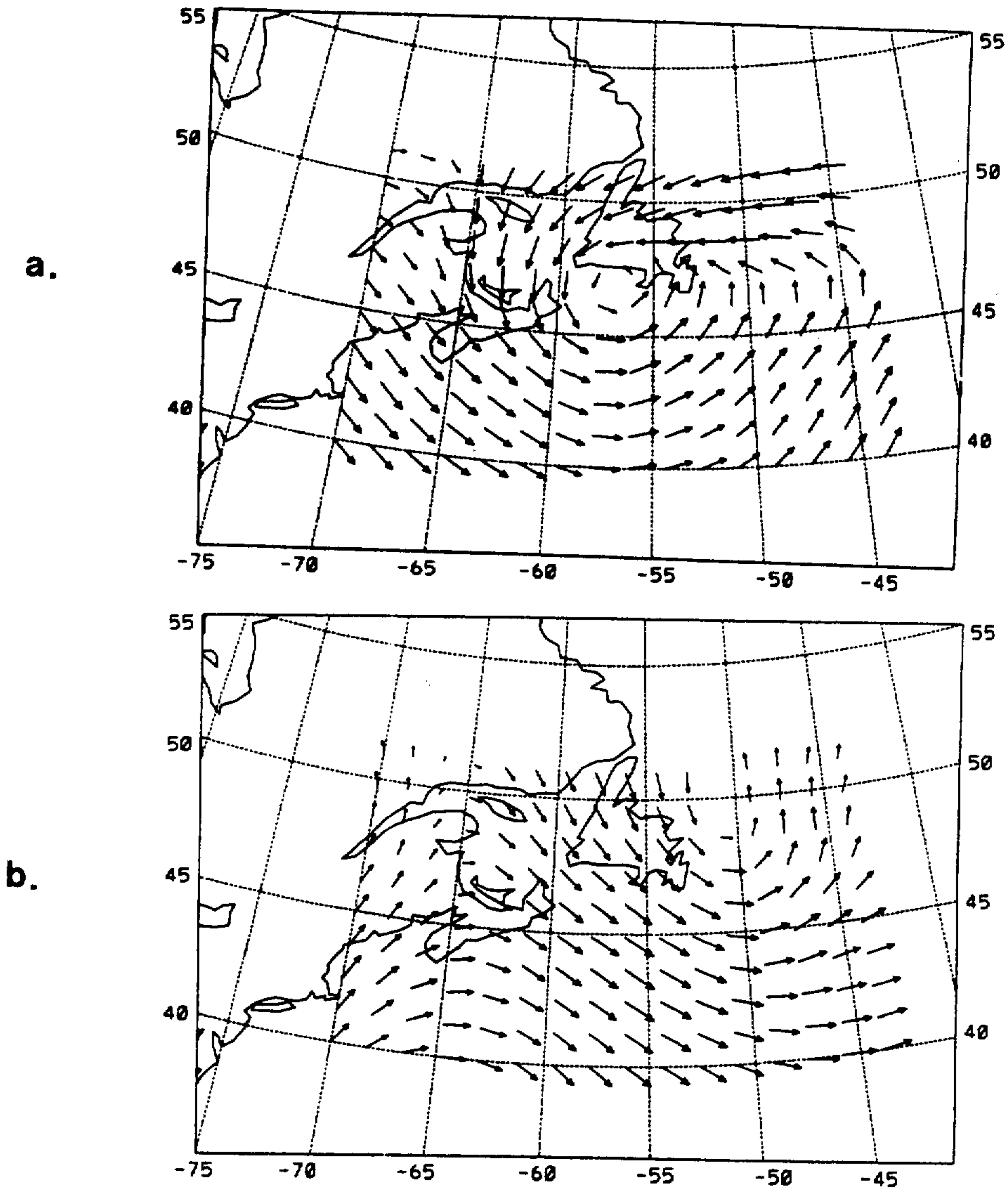

Figure 1 The wind velcity field at 00: UTC on (a) November 15, 1991 andl (b) on November 16, 1991.

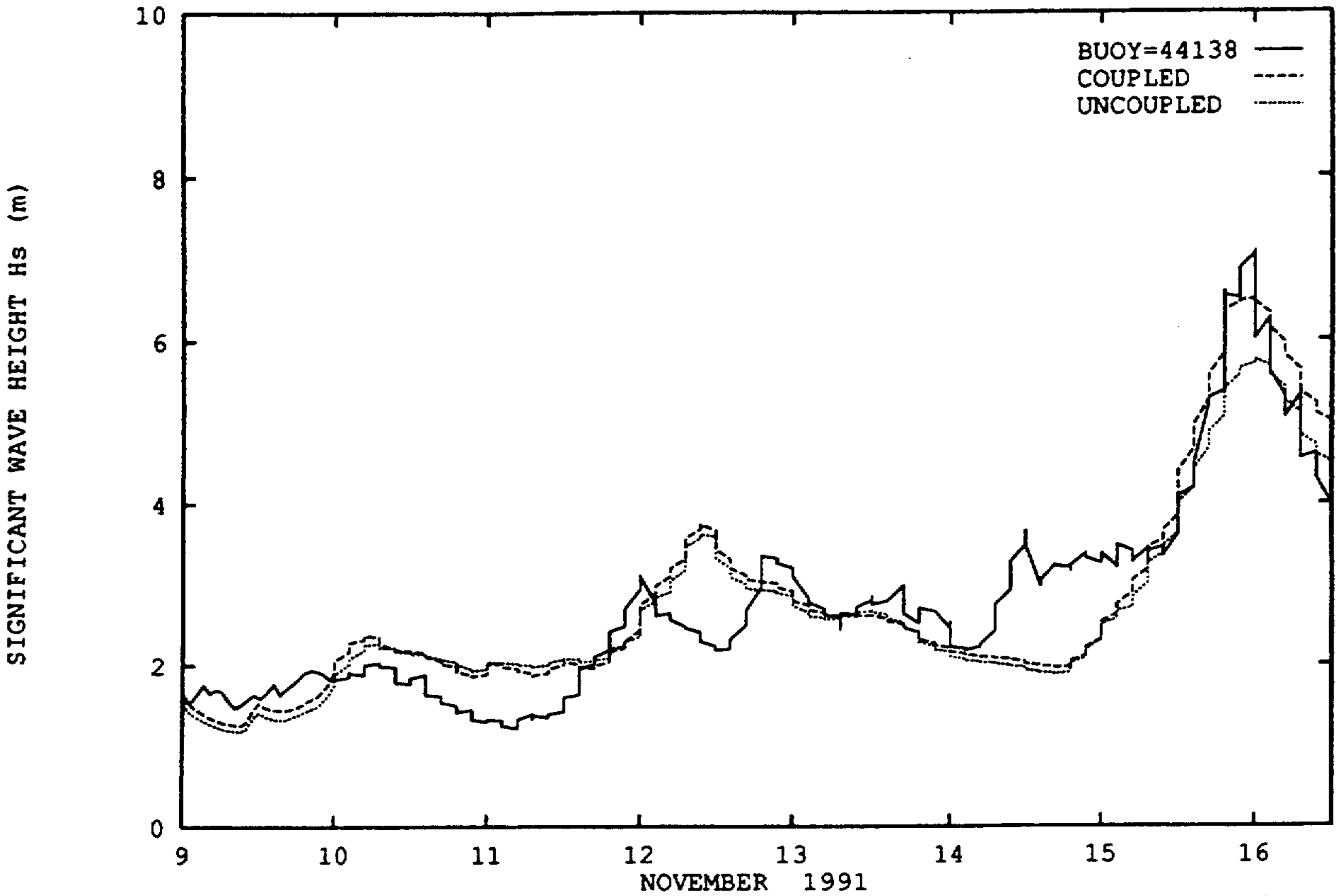

Figure 2 Time series of Hs as measured at buoy 44138 as estimated from the COUPLED and UNCOUPLED models.

6 CONCLUSIONS

The usual modelling of ocean waves and the atmospheric boundary layer assumes a Charnock relation (1), which assumes that the waves are mature. The corresponding wave age C_p/U_* is old. Thus, the atmospheric boundary layer is uncoupled from the seastate. This is at variance with parameterization of wind-wave maturity using variables such as wave age in specifying Z_o, as achieved by Smith et al (1992), which is the basis of our COUPLED model.

If the wind speed is not strong, the difference between the COUPLED and the UNCOUPLED models is negligible, because the wind-waves quickly become mature. If the wind speed is strong (> 20m/s) or if conditions are unstable. the waves take longer to mature and the reaction of the seastate on the boundary layer is important. The wave age-dependent C_d of Smith et al (1992), leads to a higher wind stress and a more rapid initial growth for young waves. Using an advanced wave model, we have demonstrated that this results in an ability to correct the (WAM model) tendency to under-estimate peak values for significant wave height during high seastate conditions. It is notable that this was achieved using the analysis winds from an operational weather forecast office, rather than kinematically analysed wind fields, specifically created for the experiment.

7 ACKNOWLEDGEMENTS

The wave modelling program at BIO is funded by the Federal Panel on Energy Research and Development (Canada) under Project No. 6B3006.

References

[1] Charnock, H. (1955) Wind stress on a water surface. Quart. J. Roy. Meteorol. Soc. **81**, p. 639-640.

[2] Delage, Y. (1988a) The position of the lowest levels in the boundary layer of atmospheric circulation models. Atmosphere-Ocean, **26**, 329-340.

[3] Delage, Y. (1988b) A parameterization of the stable atmospheric boundary layer. Boundary Laver Meteorol., **43**, 365-381.

[4] Dobson, F.W. and Vachon, P. (1994) The Grand Banks ERS-1 SAR Wave Spectra Validation Experiment: Program Overview and Data Summary. Atmosphere-Ocean. **32** (1) p.7-29.

[5] Donelan, M.A. (1982) The dependence of the aerodynamic drag coefficient on wave parameters. Proc. First Int. Conf. on Meteorology and Air-Sea Interaction of the Coastal Zone. the Hague, 381-387.

[6] Donelan, M.A. (1990) Air-Sea Interaction, in B. LeMéhauté and D.M. Hanes (Eds.), The Sea: Ideas and observations on Progress in the Study of the Seas, **9** , Wiley-Interscience, New York. pp 239-292.

[7] Hasselmann, S. et al (the WAMDI Group) (1988) The WAM model - A third generation ocean wave prediction model. J. Phys. Oceanogr., **18**, 1775-1810.

[8] Hsu, S. A. (1986) A mechanism for the increase of wind stress (drag) coefficient with wind speed over water surface: A parametric model. J. Phys. Oceanogr., **16**, 144-150.

[9] Perrie, W. and Wang, L. (1995) A coupling mechanism for wind and waves. J. Phys. Oceanogr., **25**, p. 615-630.

[10] Smith, S.D., Anderson, R.J., Oost, W.A., Kraan, C., Maat, N., DeCosmo, J., Katsaros, K.B., Davidson, K.L., Bumke, K., Hasse, L. and Chadwick, H.M. (1992) Sea surface wind stress and drag coefficients: The HEXOS results. Bound.-Layer Meteor. **60**, 109-142.

[11] Wang, L., Perrie, W., Toulany, B., Yang, J., Mailhot, J., Lee, V., Wilson, L. and Lalebeharry, R. (1995). This workshop.

[12] Wu, J . (1980) Wind-stress coefficients over sea surface near neutral conditions: A revisit. J. Phys. Oceanogr., **10**, p. 727-740.

RELATING MARINE WINDS TO OCEAN WAVE FORECAST MODELS

Wang, L., Perrie, W., Toulany, B., Yang, J.

Ocean Sciences, Maritimes Region
Bedford Institute of Oceanography, Department of Fisheries and Oceans
Dartmouth, Nova Scotia

Mailhot, J., Lee, V.

Recherche en Prévision numérique
Atmospheric Environment Service
Dorval, Québec

Wilson, L. and Lalbeharry, R.

Recherche en Prévision numérique
Atmospheric Environment Service
Downsview, Ontario

1 INTRODUCTION

The "Storm of the Century", which we hereafter denote SOC, occurred on March 12-17 1993 in the Northwest Atlantic. It was a severe extratropical storm which produced measurements of sea states of unprecedented magnitude, on the same scale as the "Halloween Storm" of 1991. During SOC, one of the Canadian buoys, moored southeast from Nova Scotia in deep water, measured a peak significant wave height (Hs) of more than 16 m. A NOAA buoy measured a peak Hs of 15.7 m, a record high for NOAA buoys. These deep water measurements provide a critical testing of ocean wave models, far beyond the parameterization and tuning they receive in their original development and implementation.

Cardone et al (1995) recently used SOC and the Halloween Storm to intercompare four wave models: the 1st and 3rd generation Cardone models, the 2nd generation Resio model and the 3rd generation WAM cycle 4 model. The wind fields were constructed by a careful manual kinematic analysis using all conventional data, including ship and buoy observations received too late for use in real-time. They evaluated wave hindcasts against time series of measured Hs, dominant wave period and wave spectra at nine US and Canadian deep water buoys moored offshore, between Georgia and Newfoundland. As they could demonstrate considerably greater skill than was exhibited by real time analysis derived from *some of the same wave models* operating in Canadian, US and European forecast centers, they suggested that large errors in operational surface marine wind field analysis are the *dominant* source of errors in operational wave analyses and forecasts. However, all models they considered show a tendency to underpredict the most extreme sea states, i.e. when Hs is above 12 m and they could not discern if this was due to remaining errors in the wind fields, or inadequacies in the wave models during high sea state conditions. Despite large differences in model physics among the 1st, 2nd and 3rd generation models of their study, differences in skill in estimating Hs averaged over all buoys, were slight.

Given a wind speed U_{10} at a reference height (10m), the standard practice in operational marine weather forecasting, uses empirical formulae to produce a friction velocity U_*, which in turn is used to estimate spectral wave energy $F(f,\Theta)$ from a wave model, as a function of frequency f and direction Θ. However, U_{10} is produced by a boundary layer model, which involves a formulation for U_*, the drag coefficient C_d, roughness Z_o and appropriate thermal conditions. Thus, U_* in the wave model differs from U_* in the atmospheric model. Moreover, roughness Z_o and C_d depend on the wind profile variation with height, rather than simply the wind speed itself at a reference level such as 10 meters. The use of empirical formulae to estimate U_* and C_d as functions of U_{10}, implies that Z_o and C_d in the wave model differ from corresponding estimates in the atmospheric model. Furthermore, the reaction of seastates on the wind profile with height also occurs because the interaction between the wind field and wind-generated ocean waves is strong.

In Perrie and Wang (1995a,b), the importance of sea state dependence is explored, in the estimation of sea surface roughness Z_o. The key to coupling the atmospheric boundary layer to ocean waves is Z_o. An 'uncoupled' wave - boundary layer model was constructed by Perrie and Wang (1995a,b), using the WAM wave model, an RPN atmospheric boundary layer model and Z_o specified by the Charnock (1955) relation, which relates Z_o to U_* without explicit reference to wave parameters,

$$Z_o = C_o \times \left(\frac{U_*^2}{g} \right) \qquad (1)$$

where g is the acceleration due to gravity and C_o is a constant, taken as 0.0185. The Charnock relation is not capable of a good representation of rapidly evolving processes such as young wind-generated waves or the response of waves to turning wind directions (Donelan: 1982, 1990). Perrie and Wang (1995a,b) constructed a 'coupled' model using the wave age C_p/U_* dependent Z_o suggested by Smith et al (1992),

$$Z_o = 0.48 \times \left(\frac{U_*^2}{g}\right)\left(\frac{C_p}{U_*}\right)^{-1} \qquad (2)$$

More complete descriptions of the 'uncoupled' and 'coupled' models are given in Perrie and Wang (1995a,b).

This study considers the implementation and application of third generation wave models with respect to the SOC data. We show that significant differences can arise depending on details of model physics. In section 2 , we give descriptions of the models. Section 3 compares these models for SOC winds and measured Hs, implemented for the North Atlantic. The wind fields used are the same as those of Wilson et al (1995). These are forecast winds from the Regional Finite Element (RFE) atmospheric model at RPN. These winds were output on a polar stereographic grid at a resolution of 50 km, which was then projected onto a lat-long grid at every 0.5 degrees. They are not analysis winds.

2 WIND-WAVE MODELS

The model physics is briefly described below. The wave model component of the modelling was largely architected by Tolman (1991, 1992) in formulating global third generation wave model studies at NMC (National Meteorological Center, Washington). We do not present results for all models described here. The models are listed to make connections with results achieved by other research groups.

- (A.) WAM Cycle 3

  The first third generation wave model to be widely distributed and implemented at operational forecast centers was WAM cycle 3, hereafter denoted WAM3. It is documented by Hasselmann et al (1988). A distinctive of WAM3 is that it uses an early dissipation formulation motivated by Hasselmann (1974),

$$S_{ds} = -2.33 \times 10^{-5}\hat{\sigma}\frac{k}{\hat{k}}\left(\frac{\hat{\alpha}}{\hat{\alpha}_{PM}}\right)^2 F(f,\theta) \qquad (3)$$

  where k is wavenumber, the relative frequency is $\sigma = (gk \tanh kd)^{1/2} = \omega - \vec{k}\,\vec{U}$ for a given current U, $F(f,\theta)$ is the energy spectral density as a function of frequency f and direction $\theta, \omega \equiv 2\pi f$, with

$$\hat{\sigma} = \overline{\sigma^{-1}}^{-1}$$
$$\hat{k} = \overline{1/\sqrt{k}}^{-2}$$
$$\hat{\alpha} = E_o \hat{k}^2 g^{-2}$$

and E_o, is the total energy integrating over f and Θ.

- (B.) WAM Cycle 4

The current WAM state-of-the-art is cycle 4, which is documented in Komen et al (1994), hereafter denoted WAM4. WAM4 retains a first order propagation scheme with an explicitly or implicitly defined integration timestep. It also considers the wave-induced stress τ_w, motivated by Janssen (1989, 1991). As in WAM3, the wind input S_{in}, is

$$S_{in}(f,\theta) = \beta \frac{\rho_a}{\rho_w} \left(\frac{U_*}{c}\right)^2 max[0, \cos(\theta - \theta_w)]^2 \sigma F(f,\theta); \tag{7}$$

where ρ_a , and ρ_w are air and water densities, U_* is the friction velocity, c is the phase speed of the waves at frequency f, Θ is the wave direction and Θ_w is the wind direction. The Miles constant β is tuned in WAM3 to an appropriate value. In WAM4, β is evaluated at nondimensional critical height λ,

$$\beta = \frac{1.2}{\kappa^2} \lambda \ln^4 \lambda \tag{8}$$

$$\lambda = \frac{g z_e}{c^2} e^{\kappa c / |U_* \cos(\theta - \theta_w)|} \tag{9}$$

where k = 0.4 is the Von Karman constant and z_e, is the effective sea surface roughness due to both wave-induced stress

τ_w and turbulent stress τ_t, and where $\tau = \tau_w + \tau_t$ and by definition $U_*^2 = \tau/\rho_a$. The effective sea surface roughness z_e, the (usual) sea surface roughness Z_o and the corresponding wind profile U(z) are given by

$$z_e = \frac{Z_o}{\sqrt{1 - \tau_w/\tau}} \tag{10}$$

$$Z_o = \frac{C_o U_*^2}{g} \tag{11}$$

$$U(z) = \frac{U_*}{\kappa} \ln\left(\frac{z + z_e + Z_o}{z_e}\right) \tag{12}$$

where the Z_o equation is due to Charnock (1955). The wave stress τ_w may be computed from the source terms as

$$\tau_w = \rho_w \int_0^\infty \int_0^{2\pi} \sigma\left(S_{in} + S_{ds} + S_{nl}\right) d\theta df \quad . \tag{13}$$

Given wind speed U at reference height z = 10m and wave spectra $E(f,\Theta)$, equations (7)-(13) can in principle be solved iteratively, using U_* and Z_e from the previous time step.

However, this iteration has thus far not been implemented in WAM4, (which assumes that wave and wind conditions vary slowly, compared to time steps). WAM4 uses the dissipative source term

$$S_{ds} = -2.25\hat{\sigma}\hat{k}^4 E_o^2 \left[\frac{k}{\hat{k}} + \left(\frac{k}{\hat{k}}\right)^2\right] F(f,\theta) \tag{14}$$

in combination with S_{in} given in equations (7)-(13)

- (C.) Coupling to the Boundary Layer

The basis for our 'UNCOUPLED' and 'COUPLED' models, is WAM3, the RPN atmospheric boundary layer model of Delage (1988a,b), and either the Charnock relation (1) or the sea state dependent HEXOS relation (2) due to Smith et al (1992). The Charnock relation is associated with the UNCOUPLED model because it has no explicit dependence on sea state parameters. The HEXOS relation, dependent on wave age C_p/U_* is basic to the COUPLED model. The wave model, boundary layer model and Z_o components are connected together iteratively at any timestep, using wind speed and direction to compute the peak frequency f_p from the wave model. Assuming a first guess Z_o, then U_* and C_d are obtained from the boundary layer model. Thereafter a 'new' Z_o is calculated. If the 'new' Z_o, is within allowable error relative to the previous Z_o, we proceed to the next time step in the simulation. Otherwise we iterate again. The boundary layer model then leads to a new estimates for C_d and U_*. Thus, equation (1) leads to a revised estimate of Z_o. When the iteration process converges, we go to the next time step. Although a given reference wind speed may be specified in these tests, it is implicit that as Z_o and U_* evolve and the seastate matures, the vertical wind profile also changes in time. This is evident in the COUPLED model (but not the UNCOUPLED model).

- (D.) Source Term Integration Models

The simplest integration scheme for source terms is straightforward explicit (Euler) integration, with a time step equal to that of the propagation time step. The change in energy density per time step ΔF for this scheme is simply

$$\Delta F(f,\theta) = S(f,\theta)\Delta t \qquad (15)$$

Smoother spectra and source terms can be obtained from a semi-implicit integration scheme implemented in WAM3 and WAM4,

$$\Delta F(f,\theta) = \frac{S(f,\theta)}{1-0.5D(f,\theta)\Delta t}\Delta t \qquad (16)$$

where D is determined from the source terms, as discussed in Hasselmann et al (1988), and $S = S_{in} + S_{ds} + S_{nl}$. The problem with the schemes of equations (15)-(16) is that the propagation time step is too large to allow the source term integration to adjust to fast changes in wind. As discussed in Tolman (1992), this results in under-estimates for growth rates and turning rates of wave spectra. A dynamically adjusted source term integration scheme, as described by Tolman (1991, 1992) for both explicit and implicit schemes, can largely correct the problem. This method first propagates the entire wave field for a fixed time step Δt. The propagated solution is used as the starting point of the source term integration, which is performed for a number of dynamic time steps until Δt_d until $\Sigma t_d = \Delta t$, recalculating source terms each time step. The time step Δt_d is calculated for each grid point separately, because source terms at different grid points are essentially uncoupled. Thus the time step for source term integration is reduced for selected grid points only. Dynamic time integration schemes based on both the explicit and implicit scheme are available. For the explicit scheme, dynamic integration implies

$$\Delta t_d^n = \min\left[\Delta t - \sum_{i=1}^{n-1} \Delta t_d^i,\ \min_{\substack{\forall\theta \\ f < f_{h_f}}} \left(\frac{\Delta F_m(f,\theta)}{|S(f,\theta)|}\right)^n\right] \quad (17)$$

$$F(f,\theta)^n = \max\left[0, F(f,\theta)^{n-1} + (S(f,\theta)\Delta t_d))^n\right] \quad (18)$$

where i is the local dynamic time step counter, n is the present time step, ΔF_m is the maximum change of energy density per dynamic time step and E^0 is the initial energy density. The implicit-dynamic scheme is

$$\Delta t_d^n = \min\left[\Delta t - \sum_{i=1}^{n-1} \Delta t_d^i, \min_{\substack{\forall\theta \\ f < f_{h_f}}} \left(\frac{\Delta F_m(f,\theta)}{|S(f,\theta)|} \left[1 + 0.5 D(f,\theta) \frac{\Delta F_m(f,\theta)}{|S(f,\theta)|} \right]^{-1} \right)^n \right] \quad (19)$$

$$F(f,\theta)^n = \max\left[0, F(f,\theta)^{n-1} + \left(\frac{S(f,\theta)\Delta t_d}{1 - 0.5D(f,\theta)\Delta t_d} \right)^n \right] \quad (20)$$

The maximum change of energy density ΔF_m is determined by a parametric change of energy density ΔF_p, as in the stability condition limiting energy density change to some fraction of the Pierson-Moskowitz equilibrium level,

$$\max(|\,\Delta F(f,\theta)\,|) = 0.3 \times 10^{-4} \frac{(2\pi)^5}{g^2} c_g^{-1} k^{-3} \quad (21)$$

A filtered relative change ΔF_r is given by

$$\Delta F_m(f,\theta) = \min\left[\Delta F_p(f,\theta), \Delta F_r(f,\theta)\right] \quad (22)$$

$$\Delta F_p(f,\theta) = 0.825^{\mu-5} 10^{-3} \pi C_g^{-1} k^{-(\mu+1)/2} X_p^{-1} \quad (23)$$

$$\Delta F_r(f,\theta) = X_r \max\left[F(f,\theta), F_f\right] \quad (24)$$

$$F_f = \max\left[F_p(f_{max},\theta), 0.05 \max_{\forall f,\theta} F(f,\theta)\right] \quad (25)$$

where μ defines the power law relation for the parametric maximum change F_p (which for deep water reduces to an $f^{-\mu}$ shape), X_p is a reduction factor for this parametric level, X_r is the maximum relative change per time step and F_f is a filter level. Of these, n, X_p and X_r are model input parameters, whose effects are discussed in Tolman (1991, 1992). In this study, results from WAM4 with implicit integration and dynamic time stepping are reported.

3 MODEL VERIFICATION

The storm of the Century (SOC) developed as a slowly evolving cyclone, having its genesis off the southern US coast and moving northwards, along the US-Canada coastlines. During March 12-17 1993, SOC reached its maximum intensity, as observed by NDBC and AES buoys. To provide model verification, using observed data, implementation was made on the northwest Atlantic, on a spherical coordinates ½ x ½° projection. The grid extended from 20°N to 65°N and from 80°W to 10°W, including 91 x 141 lat-long points over land and sea. Of these, 10305 were active sea points. The propagation time step for the models was 20 minutes, for this study.

Wind data was provided every hour for the entire grid by the RFE atmospheric model at RPN. In Figure 1 , we show these wind fields as compared with winds measured at buoy 44137. The original buoy wind data that was received were averaged hourly from about 10 min. recorded data. If there was missing data then the closest hour was taken for the required hour. The maximum buoy wind speeds were also given hourly and these represent the maximum speed recorded within that hour. These are denoted GUST-Buoy winds in Figure 1 . Figure 1 demonstrates that the RFE modelled winds are high compared to estimates from buoy winds, denoted OBS-Buoy, during much of March 14 as Hs is building to it maximum value at about 00UTC on March 15. What is most interesting about this comparison is that the apparent buoy winds OBS-Buoy are low. The Pierson-Moskowitz equilibrium Hs corresponding to 20 m/s is about 10 m. For the Gust-Buoy winds of 25 m/s, which are close to the RFE model estimates for the period just preceding the peak of the storm, the Pierson-Moskowitz equilibrium significant wave height is about 15.4 m which is comparable to the observed 16 m. This suggests that the Pierson-Moskowitz Hs parameterizations may not be reliable for extremal SOC-type storms.

In Figure 2 , we present a comparison of observed Hs, as measured at buoy 44137, with estimates produced by three models using implicit integration and dynamic time stepping: WAM4, COUPLED and UNCOUPLED. Qualitatively, the COUPLED model appears to give the closest match to measured Hs values. This is verified by the RMS error of Hs, calculated hourly for the duration of the storm, denoted here as RMSHD. With respect to observed Hs, the UNCOUPLED model has a RMSHD of 1.06, the WAM4 model has a RMSHD of 1.01 and the COUPLED model has a RMSHD of only 0.90. We note that the study of Cardone et al (1995) reports RMSHD of 1.35 at buoy 44137, calculated three-hourly for the duration of SOC, using no dynamic time-steping and alternate wind fields from what we have used here.

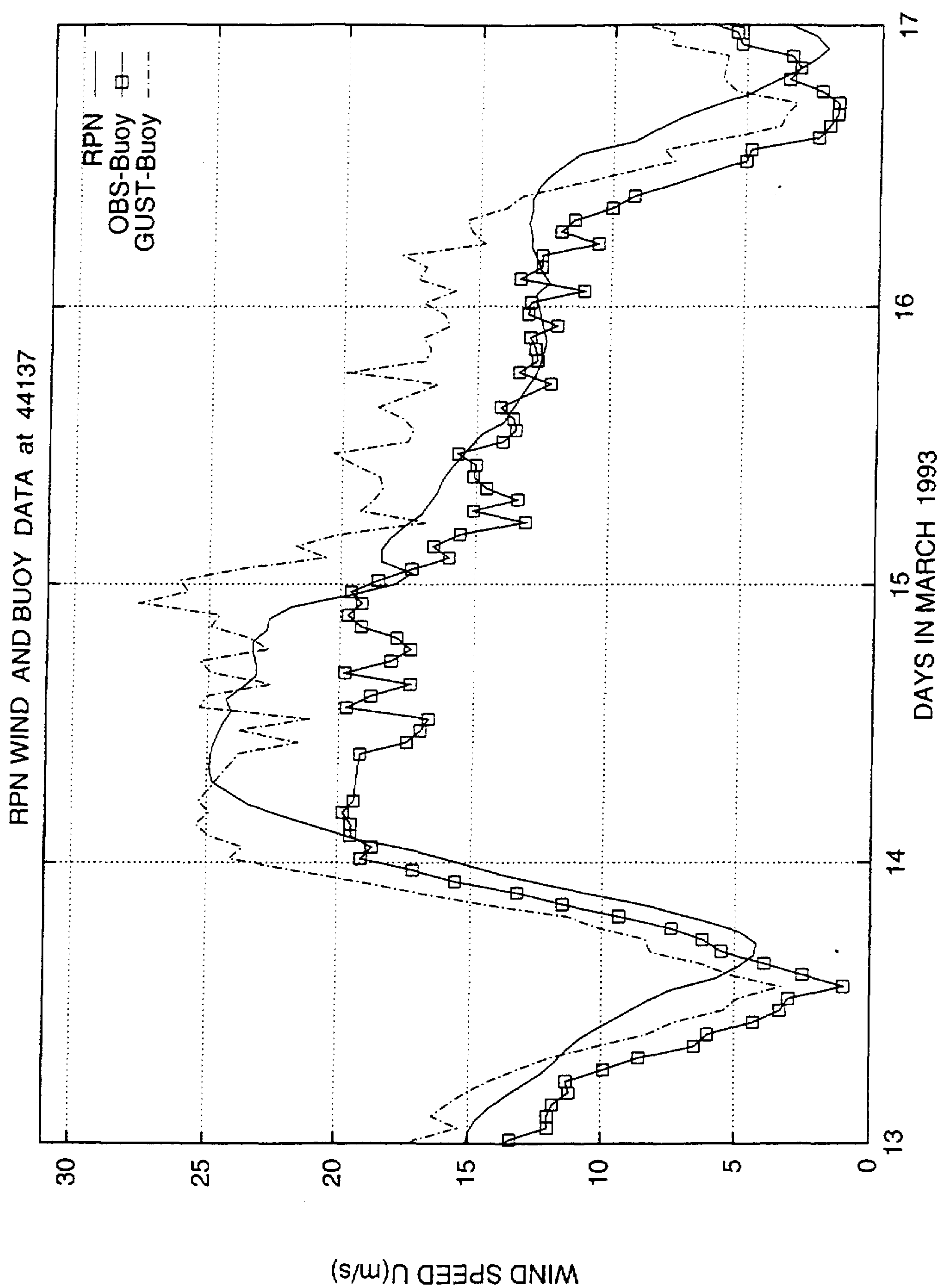

Figure 1 The wind speed at buoy 44137.

4 CONCLUSIONS

It is generally understood that the key to improved wave modelling is improved wave model physics. In this regard, WAM4 made a great step forward by considering the sea state reaction to the wind. This was accomplished by introducing the wave-induced stress τ_w. However, this still does not coincide with coupling waves to a boundary layer model. We have developed a coupled wind-wave model and obtained good agreement with measured significant wave height Hs collected during the Storm of the Century (SOC), as implemented in our COUPLED model. The COUPLED model differs from WAM3 and WAM4 in its modelling of the coupling mechanism between waves and the atmospheric boundary layer. This specically demonstrates the importance of improvements in modelling the coupling between waves and the atmospheric boundary layer.

The winds used in this study were RFE atmospheric model winds, which are in principle, operational. These wind fields were used to get good agreement between the COUPLED model and with measured Hs from SOC. Therefore, it follows that enhanced modelling of Hs, for operational forecasting, is possible without extensive kinematic analysis of wind fields.

5 ACKNOWLEDGEMENTS

The wave modelling program at BIO is funded by the Federal Panel on Energy Research and Development (Canada) under Project No. 6B3027.

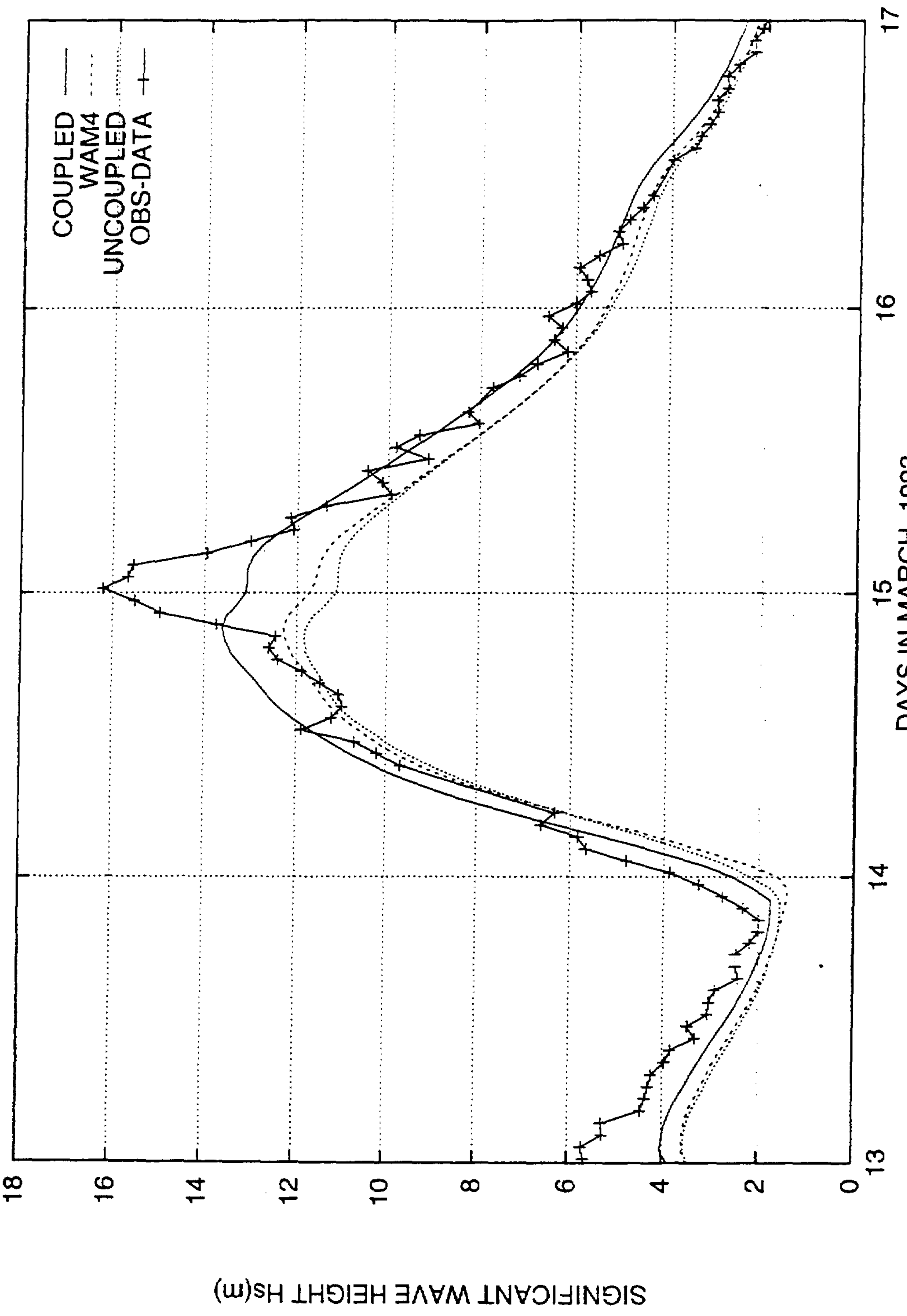

Figure 2 Time series of Hs as measured at buoy 44137 as estimated from WAM4, the COUPLED and UN-COUPLED models.

References

[1] Cardone, V.J., Jensen, R.E., Resio, D.T., Swail, V.R. and Cox, A.T. (1995) Evaluation of Contemporary Ocean Wave models in Rare Extreme Events: "Halloween Storm" of October, 1991; "Storm of the Century" of March, 1993. In press in J. Atmos. Oceanic Tech.

[2] Charnock, H. Wind stress on a water surface. Quart. J. Roy. Meteorol. Soc. **81**, p. 639-640.

[3] Delage, Y. (1988a) The position of the lowest levels in the boundary layer of atmospheric circulation models. Atmosphere-Ocean, **26**, 329-340.

[4] Delage, Y. (1988b) A parameterization of the stable atmospheric boundary layer. Boundary Layer Meteorol., **43**, 365-381.

[5] Donelan, M.A. (1982) The dependence of the aerodynamic drag coefficient on wave parameters. Proc. First Int. Conf. on Meteorology and Air-Sea Interaction of the Coastal Zone, the Hague, 381-387.

[6] Donelan, M.A. (1990) Air-Sea Interaction, in B. LeMéhauté and D.M. Hanes (Eds.), The Sea: Ideas and observations on Progress in the Study of the Seas, **9**, Wiley-Interscience, New York. pp 239-292.

[7] Hasselmann, K. (1974) On the spectral dissipation of ocean waves due to whitecapping. Bound. Layer Meteorol. **6**, 107-127.

[8] Hasselmann, S. et al (the WAMDI Group) (1988) The WAM model - A third generation ocean wave prediction model. J. Phys. Oceanogr., **18**, 1775-1810.

[9] Janssen, P.A.E.M. (1989) Wave-induced stress and the drag of air flow over sea waves. J. Phys. Oceanogr. **21**, 1631-1642.

[10] Janssen, P.A.E.M. (1991) Quasi-linear theory of wind-wave generation applied to wave forecasting. J. Phys. Oceanogr., **21**, 1631-1642.

[11] Komen, G.J., Cavaleri, L., Donelan, M., Hasselmann, K., Hasselmann, S. and Janssen, P.A.E.M. (1994) Dynamics and Modelling of Ocean Waves. Cambridge University Press, 532 pp.

[12] Perrie, W. and Wang, L. (1995a) A coupling mechanism for wind and waves. J. Phys. Oceanogr., **25**, p. 615-630.

[13] Perrie, W. and Wang, L. (1995b) Coupling atmospheric and ocean wave dynamics. This workshop.

[14] Smith, S.D., Anderson, R.J., Oost, W.A., Kraan, C., Maat, N., DeCosmo, J., Katsaros, K.B., Davidson, K.L., Bumke, K., Hasse, L. and Chadwick, H.M. (1992) Sea surface wind stress and drag coefficients: The HEXOS results. Bound.-Layer Meteor. **60**, 109-142.

[15] Tolman, H. A third-generation model for wind waves on slowly varying, unsteady and inhomogeneous deptha and currents. J. Phys. Oceanogr. **21**, 782-797.

[16] Tolman, H. Effects of numerics on the physics in a third-generation wind-wave model. J. Phys. Oceanogr. **22**, 1095-1111.

[17] Wilson, L., Lalbeharry, R., Mailhot, J., Lee, V., Perrie, W., Wang, L. and Toulany, B. Towards a consistent boundary layer formulation in operational atmospheric and wave models. This workshop.

TOWARDS A CONSISTENT BOUNDARY LAYER FORMULATION IN OPERATIONAL ATMOSPHERIC AND WAVE MODELS

R. Lalbeharry, L. Wilson

Recherche en prévision numérique
Atmospheric Environment Service, Downsview, Ontario, Canada

J. Mailhot, V. Lee

Recherche en prévision numérique
Atmospheric Environment Service, Dorval, Quebec, Canada

W. Perrie, L. Wang, and B. Toulany

Bedford Institute of Oceanography
Department of Fisheries and Oceans, Dartmouth, Nova Scotia, Canada

1. INTRODUCTION

The Canadian Spectral Ocean Wave Model (CSOWM) produces sea state forecasts up to 36 hours for most of the North Atlantic in an operational environment (see Khandekar et al., 1994). The wave model is forced by surface winds obtained from the atmospheric model using its own stress formulation in the surface layer. From an atmospheric perspective, a proper determination of the stress in the surface layer is needed to provide reliable estimates of ocean wave heights and fluxes of momentum, heat and moisture. In the wave model CSOWM, the wind input source term uses the surface stresses to generate the wind waves so that the wave model converts internally the surface wind field to stress field using its own boundary layer stress formulation. These two stress formulations may or may not be consistent. It they are consistent, then by forcing the wave model with the surface stress from the atmospheric model, there is no longer a need to worry about the level at which the atmospheric model output wind field is valid, and the process of converting stresses to winds at a specified level for input to the wave model and the winds back to stresses by the wave model is eliminated.

The present study uses surface stresses as well as 10 m level surface winds produced by the regional finite-element (RFE) weather prediction model of the Canadian Meteorological Centre (CMC) to drive the Cycle-4 version of the ocean wave model WAM described by the WAMDI Group (1988) in which the atmospheric boundary-layer is coupled to the wave model following Janssen (1991). The WAM model is the state-of-the-art wave model and a regional version of the WAM is at present being tested for operational implementation at CMC. The RFE model generates surface stress and the 10 m level winds on a variable-resolution horizontal grid having a central window with uniform resolution of 50 km covering the continental US, Canada, and the Canadian Atlantic (Mailhot et al., 1995). Both the RFE model hourly surface stress and wind fields are interpolated onto the WAM grid with a grid spacing of 0.5 degree in both latitude and longitude and extending from 25°N to 70°N and from 80°W to 15°W in the North Atlantic.

The WAM model is run in a hindcast mode using both the wind and surface stress fields obtained from the RFE model to simulate the sea states associated with the extremely powerful winter storm of March 1993 called the "blizzard", and dubbed as the "storm of the century" briefly described in Section 4.1 . These runs are compared with the run made for the same storm but with winds obtained from a man-machine-mix (MMM) procedure using all conventional meteorological data, including ship and buoy observations received too late for use in real-time. (Cardone, 1992). The MMM wind field was produced at hourly intervals on 0.5° x 0.5° latitude/longitude grid over the area covered by the WAM grid and represents the best possible winds close to the "ground truth".

The purpose of this study is to assess the consistency in the stress formulations of the RFE model and the wave model WAM and the possibility of coupling the two models. Section 2 briefly describes the RFE model and the dataset produced by the model, while Section 3 gives a brief description of the wave model WAM. Results and discussion are presented in Section 4 , followed by summary and conclusions in Section 5 . Improvements in modelling the coupling mechanism between the WAM model and the RFE boundary layer are investigated in a companion paper (Wang et al., 1995).

2. THE RFE MODEL AND DATASET

The version of the RFE model used to generate the surface fields for the WAM model is similar to the 50-km version currently operational at the CMC since November 1993 (Mailhot et al., 1995). In order to focus on the area of interest, the central domain with high resolution has been displaced toward the Atlantic (Fig. 1). The present version also includes modifications to the formulation of the surface layer stability functions according to Delage and Girard (1992). Over the ocean, the roughness parameter, z_o, is given by the Charnock (1955) relation (see section 3).

To generate a continuous dataset to drive the WAM model during the period of 10-17 March 1993, the following procedure was used. A series of successive 24-h forecasts at 50 km were performed, with each forecast initialized with the CMC archived regional analyses

(Chouinard et al., 1994). In contrast to the MMM analyses, these operational regional analyses use only the conventional meteorological data available in real-time. Furthermore, the regional analyses were done at a resolution of 100 km in March 1993, and the moisture field was not enhanced with satellite data. Therefore, to cover the period of 10-17 March 1993, overlapping integrations of 24 hours with the 50-km model were performed, starting every 12 hours. In order to minimize the initial moisture and precipitation spin-up problems related to the utilization of lower-resolution analyses, for each integration, only the fields resulting from the last 12 h of the forecasts were used.

3. THE WAM MODEL

The Cycle-4 version of WAM used in this study describes the evolution of the directional wave spectrum $F(f,\theta,\phi,\lambda,t)$ by solving the wave energy transfer equation. Here, f is frequency, θ is wave direction, ϕ is latitude, λ is longitude, and t is time. The net source term consists of the wind input term from Snyder et al. (1981), the nonlinear wave-wave interaction term from Hasselmann et al. (1985), and the dissipation term due to whitecapping from Hasselmann (1974) modified by Komen (1984). In the present Cycle-4 of the wave model the wind input and dissipation terms represent a further development based on Janssen's quasi-linear wind-wave generation (Janssen, 1991). In this formulation the wind input term includes the square of the inverse of the wave age defined as c/u_*, c being the wave phase velocity and u_* the friction velocity, and the dissipation term is proportional to the fourth power of the frequency.

The wave model consists of 25 frequency bands logarithmically spaced from 0.042 Hz to 0.41 Hz at intervals of $\Delta f/f$ = 0.1 and 24 directional bands 15 degrees apart. Deep water physics only was considered in the propagation and the source terms so that evaluation of the basic model parameters is done against 6 buoys located in deep waters in the northwest Atlantic in Table I .

In the current Cycle-4 version of the WAM model the roughness parameter, z_o, given by the Charnock's equation (Charnock, 1955) in terms of the friction velocity, u_*, and the acceleration due to gravity, g, as

$$z_o = \beta u_*^2/g \qquad (1)$$

is modified to include the wave-induced stress. Here, the Charnock's constant β is given as

$$\beta = \alpha/\sqrt{\{1-(\tau_w/\tau)\}} \;;\; \alpha=0.01 \qquad (2)$$

in which the sea state dependence is reflected through the wave-induced stress, τ_w,, obtained from the integration of the model wind-input source term over all frequencies and wave directions. In (2) τ is the total kinematic stress defined as the sum of the turbulent stress provided by the RFE model and the wave-induced stress. Without any sea state dependence, $\beta = 0.018$, which is the value used by the RFE model in the determination of z_o, over the ocean. Given the modified z_o, the 10 m neutral drag coefficient, C_{10}, is given by

$$C_{10} = \{\kappa/(\ln(10/z_0))\}^2 \qquad (3)$$

where κ is the von Karman constant (= 0.4), while the WAM internally-derived 10 m level wind speed U_{10} is obtained from

$$\tau = C_{10}U_{10}^2 \qquad (4)$$

Given τ_w and the RFE U_{10}, or given τ_w and the RFE model stress, τ, z_o, C_{10} and the WAM U_{10} can be determined using an iterative procedure.

Use of the surface stress directly in the wave model is attractive because it avoids ambiguity about the actual height the wind output represents and is a first step towards the full coupling of the atmospheric and wave models. The wave model can, therefore, act as a subroutine to the RFE model, providing the latter at each integration time step the parameter, z_o. The RFE model, in turn, provides the wave model a corrected value of the turbulent surface stress which now includes the effect of the wave-induced stress for use in the determination of a new z_o, for the RFE model next integration time step.

Table I: Locations of buoys used in model verification.

Buoy	Latitude (°N)	Longitude (°W)
44137	41.2	61.1
44138	44.2	53.6
44139	44.3	57.4
44141	42.1	56.2
44004	38.5	70.7
41002	32.3	75.2

4. RESULTS AND DISCUSSION

4.1 Simulation of the "Storm of the Century", or the Blizzard", during the period 13-17 March 1993

An extremely powerful winter storm which started as a closed low pressure system in the Gulf of Mexico on 12 March 1993 moved rapidly during the next two days along a track from the Florida panhandle to the Gulf of St Lawrence in the Canadian east coast offshore. The storm, dubbed as the "Storm of the Century" and the "Blizzard", was predicted remarkably well, almost 4 days ahead of time by the U.S. National Meteorological Centre in Washington and the CMC. The storm produced winter weather in many southeastern states of the U.S. with heavy snowfall reported at many locations from Georgia to Maine (see. Brugge, 1994). As the storm moved through the northeastern U.S. and eastern Canada, it produced extreme sea states over the Scotian Shelf region of the Canadian Atlantic with the buoy 44137 measuring wave heights close to 16 m at 0000 UTC on 15 March 1993.

4.2 Results from the RFE model

Detailed comparisons with observations (not shown) indicate that the general evolution of the storm is quite well predicted by the model. During its entire life cycle, errors in the storm central pressure did not exceed 1 hPa, a remarkable result considering that the cyclone deepened from 1000 hPa to 969 hPa in 24 hours. However, the movement of the storm predicted by the model is a bit too slow with a track slightly inshore, especially near the end of the period. Figure 2 shows a comparison of the 10-m level RFE winds with the wind measurements at three selected buoy locations. Generally, the agreement is quite good and the model shows a tendency to capture the extreme wind values generated by the passage of the storm. The main discrepancy appears to be a lag of a few hours between the observations and the RFE model winds. This is probably related to the slow track predicted by the RFE model. It is also worth noting that the maximum wind is underpredicted at buoy 41002 by some 5 m/s, but the wind maxima are apparently overpredicted at other locations, especially at buoy 44137. However, as discussed by Wang et al. (1995), this observation appears too low and a value of 25 m/s is more in agreement with the observed significant wave height of 16 m and the recorded maximum wind speed at the buoy.

4.3 Results from wave model WAM

The wave model was run in a hindcast mode starting from a flat sea (zero wave energy everywhere). A spin-up time of 48 hours from 0000 UTC on 11 March to 0000 UTC on 13 March 1993 was used before the wave model products were generated for the duration of the storm. The input wind and surface stress fields are at hourly intervals while the model integrated output parameters are at 3-hourly intervals for evaluation against the 3-hourly buoy observations. The wave model products evaluated at the 6 buoy locations in Table I were obtained through bi-linear interpolation of the parameters at the 4 model grid points surrounding the buoy location.

A comparison of the 10 m level wind speed input to WAM and the corresponding WAM internally-derived 10 m level wind speed output is presented in Figure 3a for the MMM winds and in Figure 3b for the RFE winds for fifteen buoy locations. It is seen that the WAM U_{10} derived in this way coincides very closely with the U_{10} provided to WAM. Similar results were obtained also by Cardone et al. (1995). Since the differences are rather small, wind speed distributions presented are the WAM internally-derived U_{10}.

Figure 4 presents the scatter plot of the WAM winds derived from the inputs of RFE model surface stresses and the 10 m level winds at the same fifteen buoy locations. The WAM stress-derived winds are slightly overestimated for winds below about 16 m/s and underestimated for winds above 16 m/s when compared with the WAM winds derived from the RFE winds to WAM. Figure 5 gives the corresponding scatter plot of model significant wave height (SWH) generated using the RFE stresses versus that generated using RFE winds. It is seen that the WAM SWH based on surface stress is overestimated at wave heights below about 6 m and underestimated for wave heights above 6 m when compared with that using RFE winds. There is some inconsistency in the determination of the SWH based on the RFE model surface stress and wind fields, which may be related to the fact that the stress formulations in the two models (RFE and WAM) may not be consistent. This inconsistency may be removed through the coupling of the RFE and WAM models.

The temporal variation of SWH as measured by buoys 44137 and 41002 is compared against model-generated SWH using MMM winds, RFE winds, and RFE stresses as shown in Figures 6 and 7 . The model underestimates the measured peak wave heights at both buoys (about 15.5 m at 44137 and 14.5 m at 41002). The only significant difference between the results obtained with MMM and RFE winds is the representation of the peak wave height at buoy 44137. The peak at buoy 41002 is underestimated by both MMM and RFE wind fields. The RFE stress- and wind-generated wave heights are in close agreement with each other, but the RFE winds are better able to simulate the peak wave heights at both buoys. Also, in agreement with the results of Figs. 4 and 5 , the SWH are larger (smaller) with the RFE winds than RFE stresses for strong (light) winds.

The spatial distributions of SWH generated using MMM winds, RFE winds, and RFE stresses are shown in Figures 8a , 9a , and 10a respectively for 0000 UTC on 15 March 1993, the time at which buoy 44137 recorded the maximum wave height close to 16 m. Figures 8b , 9b and 10b give the corresponding distributions of WAM derived U10 for 2100 UTC on 14 March, 3 hours prior to the peak wave height observed at buoy 44137. The MMM winds did a better job in simulating the extreme sea state (existence of a 15 m SWH contour in Figure 8a) than both the RFE winds and stresses as illustrated in Figures 9a and 10a . The 12 m contour encircled a smaller area in Fig, 10a than in Fig. 9a . This is in agreement with Fig. 6 where the SWH obtained with the RFE winds are larger than with the RFE stresses in the extreme sea state. The better simulation of the extreme SWH by the MMM winds is due to the more accurate MMM winds in the periphery of the storm as the latter moved northeastward. A close comparison of the MMM and RFE wind fields indicates the presence of a core of very strong winds, or a jet streak, that propagates northeastward along the east coast in the cold air behind the cold front. Figure 8b shows that the jet streak reaches 26 m/s in the MMM wind fields. This jet streak passed directly over the location of buoy 44137. However, in the WAM wind fields derived from the RFE wind and stress fields shown in Figures 9b and 10b , this jet streak is weaker (about 24 m/s) and propagates nearer to the coastline (farther away from buoy 44137). This may be due to the inshore storm track in the model, as discussed before. Therefore, it appears to be very important to resolve accurately such mesoscale storm features for the correct simulation of extreme sea state.

The model generated wave height values are further analysed to obtain various error parameters such as bias, root mean square error (RMSE), etc., between the model and the observed values. The various error parameters are calculated using wave height values at all the buoy locations in Table I and Table II shows these error parameters obtained using the MMM winds, RFE winds, and RFE stresses for 3 wave height categories. It is seen that the MMM winds have outperformed both the RFE winds and stresses for SWH > 6 m while the RFE winds have outperformed the RFE stresses for the same SWH range. Table III gives the SWH statistics for the individual buoys 44137 and 41002. For buoy 41002, both the RFE wind and stress give better BIAS scores than MMM winds while MMM winds have a smaller RMSE. At 44137, there is a marked advantage with the MMM winds.

5. SUMMARY AND CONCLUSIONS

Three different hourly inputs, namely, MMM winds, RFE model winds, and RFE model surface stresses were supplied to the Cycle-4 version of the WAM model to simulate the sea states associated with the extremely powerful winter storm dubbed as the "storm of the century" as well as the "blizzard" of March 1993. The evaluation suggests that the MMM wind field has better simulated the storm peak wave height at one buoy location than the other two fields. The evaluation also indicates that extreme sea state results from very strong wind cores, or jet streaks, that propagate in a coherent fashion for a period of time. Thus, it is crucial to correctly simulate these mesoscale wind patterns to better represent the extreme wave heights associated with these spectacular storms. The results also show that the SWH obtained using the RFE model stress field are smaller than those obtained using RFE 10 m level wind field in the wave height range greater than about 6 m. This inconsistency in SWH based on RFE winds and stresses may be due to the fact that the stress formulations in the two models (RFE and WAM) may not be consistent and may be removed through the coupling of the RFE and WAM models through the roughness parameter, z_o, over the ocean.

6. ACKNOWLEDGEMENT

Sincere thanks are expressed to Dr. Robert Jensen of NERC, Vicksburg, Mississippi, for his assistance to us (RL) in the setting up of the WAM model in an experimental mode, to Dr. Madhav Khandekar of the Atmospheric Environment Service (AES) for his helpful comments and suggestions, and to David Brown, a Contractor with AES, for his computer support.

7. REFERENCES

Brugge, R., 1994: The blizzard of 12-15 March 1993 in the U.S.A. and Canada, Weather, Vol. 49, No. 3, 82-89.
Cardone, V.J., H.C. Graber, J.E. Jensen, S. Hasselmann, and M.J. Caruso, 1995: In search of the true surface wind field in SWADE IOP-1: Ocean wave modelling perspective. The Global Atmosphere-Ocean System, Accepted for Publication.
----------, 1992: On the structure of marine surface wind field in extratropical storms. Preprints, Third Int. Workshop on Wave Hindcasting and Forecasting, 19-22 May 1992, Montreal, Quebec, Atmos. Environ. Serv, Downsview, Ont., pp. 54-66, Charnock, H., 1955: Wind stress on a water surface. Quart. J. Roy. Meteor. Soc., 81, 639-640, Hasselmann, K., 1974: On the spectral dissipation of ocean waves due to white capping, Boundary-Layer Meteorol. 6, 107-127.
Chouinard, C., J. Mailhot, H.L. Mitchell, A. Staniforth and R. Hogue, 1994: The Canadian regional data assimilation system: Operational and research applications. Mon. Wea. Rev. 122, 11306-1325.
Hasselmann, S. and K. Hasselmann, 1985: Computations and parameterizations of the nonlinear energy transfer in gravity waves.

Part I: A new method for efficient computations of the exact nonlinear transfer integral. J. Phys. Oceanogr, 15(11), 1369-1377.
Janssen, P.A.E.M, 1991: Quasi-linear theory for wind-wave generation applied to wave forecasting. J. Phys. Oceanogr., 21, 1631-1642.
Khandekar, M.L., R. Lalbeharry, and V. Cardone, 1994: The performance of the Canadian Spectral Ocean Wave Model (CSOWM) during the Grand Banks ERS-1 SAR wave spectra experiment. Atmospher-Ocean, 32, 31-60.
Komen, G.J., S. Hasselmann, and K. Hasselman, 1984: On the existence of a fully developed wind sea spectrum. J. Phys. Oceanogr. 14, 1271-1285. Mailhot J., R. Sarrazin, B. Bilodeau, N. Brunet, A. Méthot, G. Pellerin, C. Chouinard, L. Garand, C. Girard, and R. Hogue, 1995: Changes to the Canadian regional forecast system: Description and evaluation of the 50-km version. Atmosphere-Ocean, 33, 55-80.
Snyder, R.L.. F.W. Dobson, J.A. Elliot, and R.B. Long, 1981: Array measurement of atmospheric pressure fluctuations above surface gravity waves. J. Fluid Mech. 102, 1-59.
WAMDI Group, 1988: The WAM model - A third generation ocean wave prediction model. J. Phys. Oceanogr. 18, 1775-1810.
Wang, L., W. Perrie, B. Toulany, J. Yang, J. Mailhot, V. Lee, L. Wilson and R. Lalbeharry, 1995: Relating Marine Winds to Ocean Wave Forecast Models. This workshop.

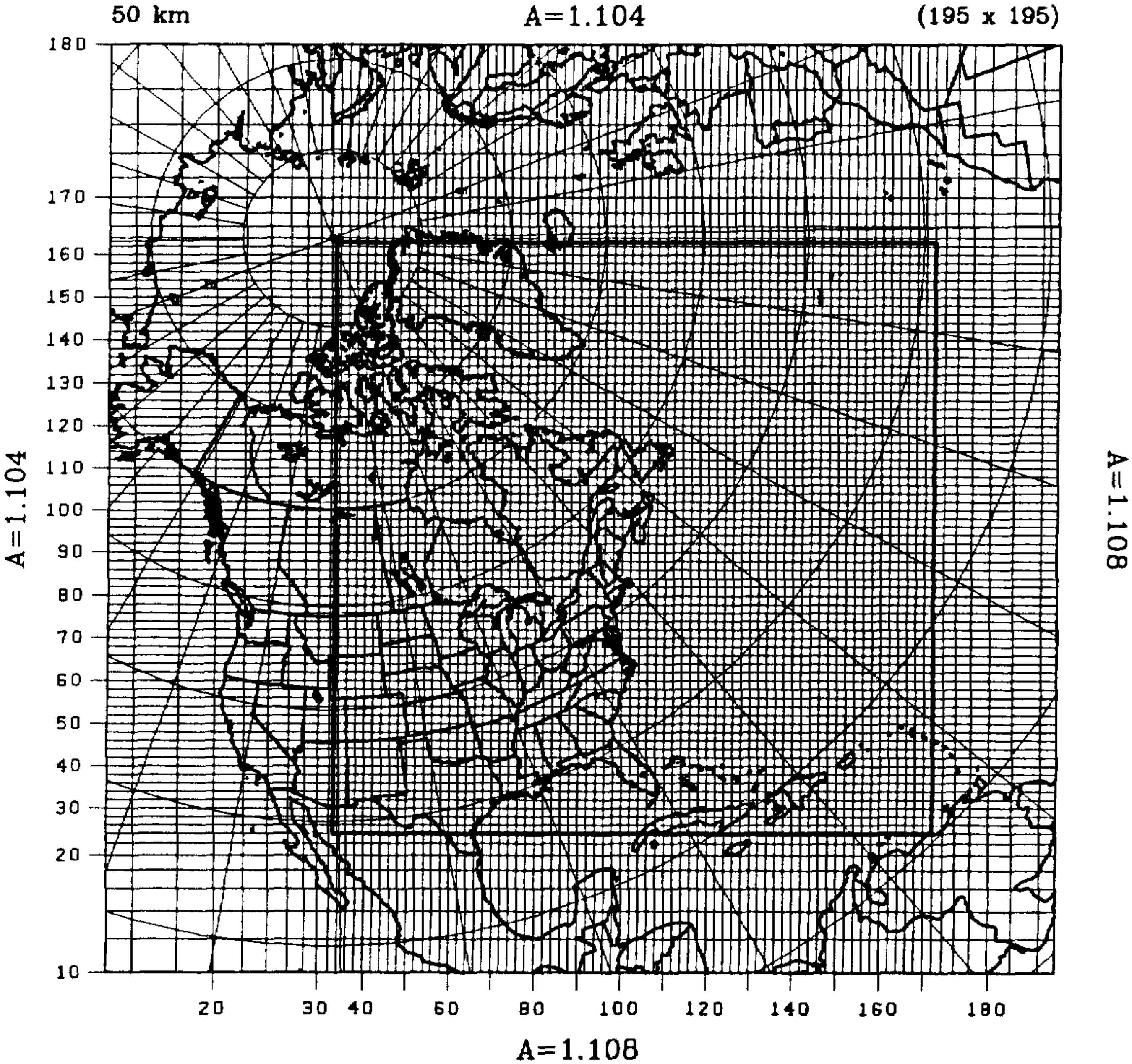

Fig. 1: The 195 x 195 variable-resolution horizontal grid on a polar stereographic projection used by the RFE model: the resolution is 50 km in the central window (heavy rectangle).. Only every other meshline in each direction is plotted.

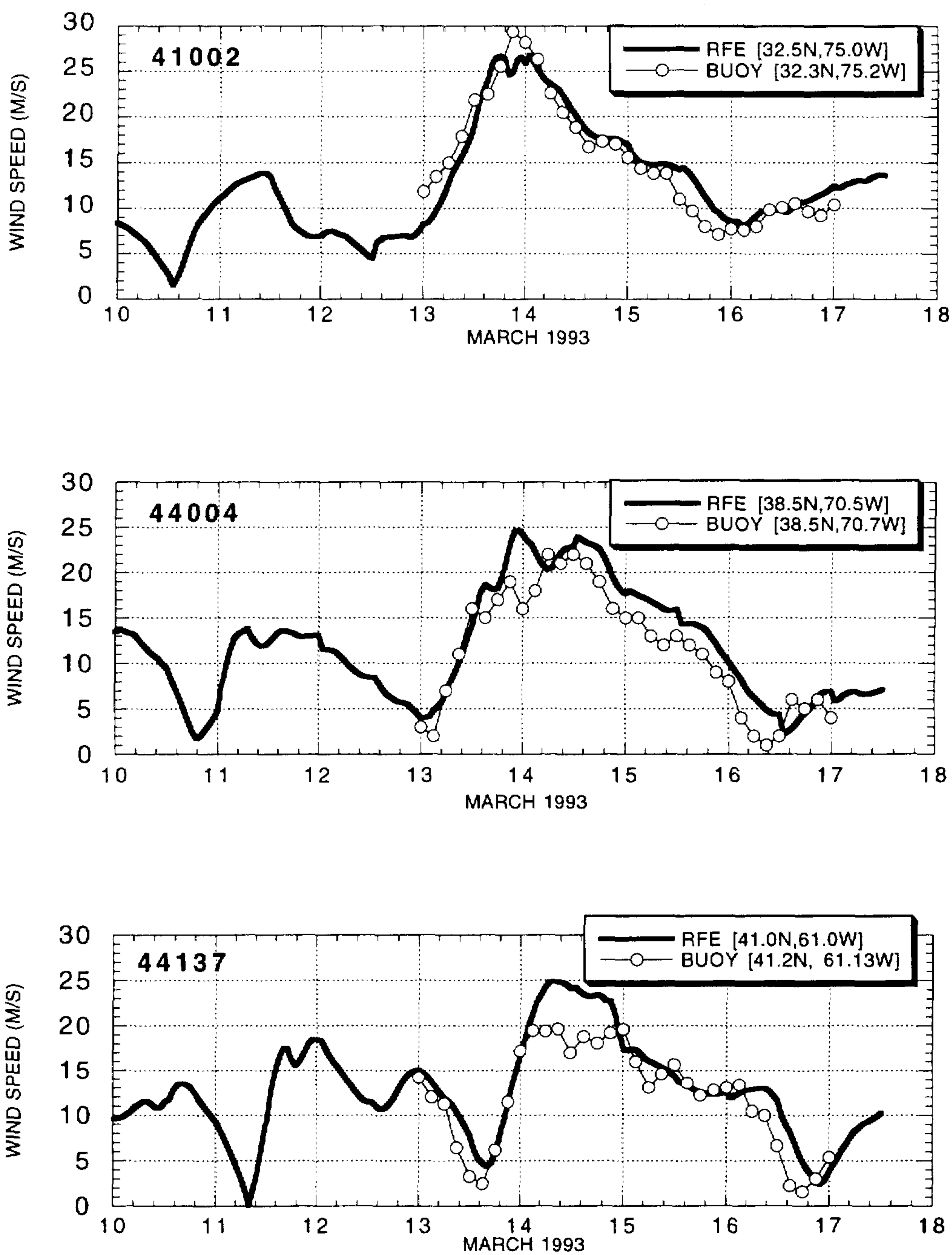

Fig. 2: Comparison of measured wind speed (open circle line) at buoys 41002, 44004 and 44137, and RFE model 10-m level wind speed (solid line) at the nearest grid point for the period 10-17 March 1993. Wind speeds are in m/s.

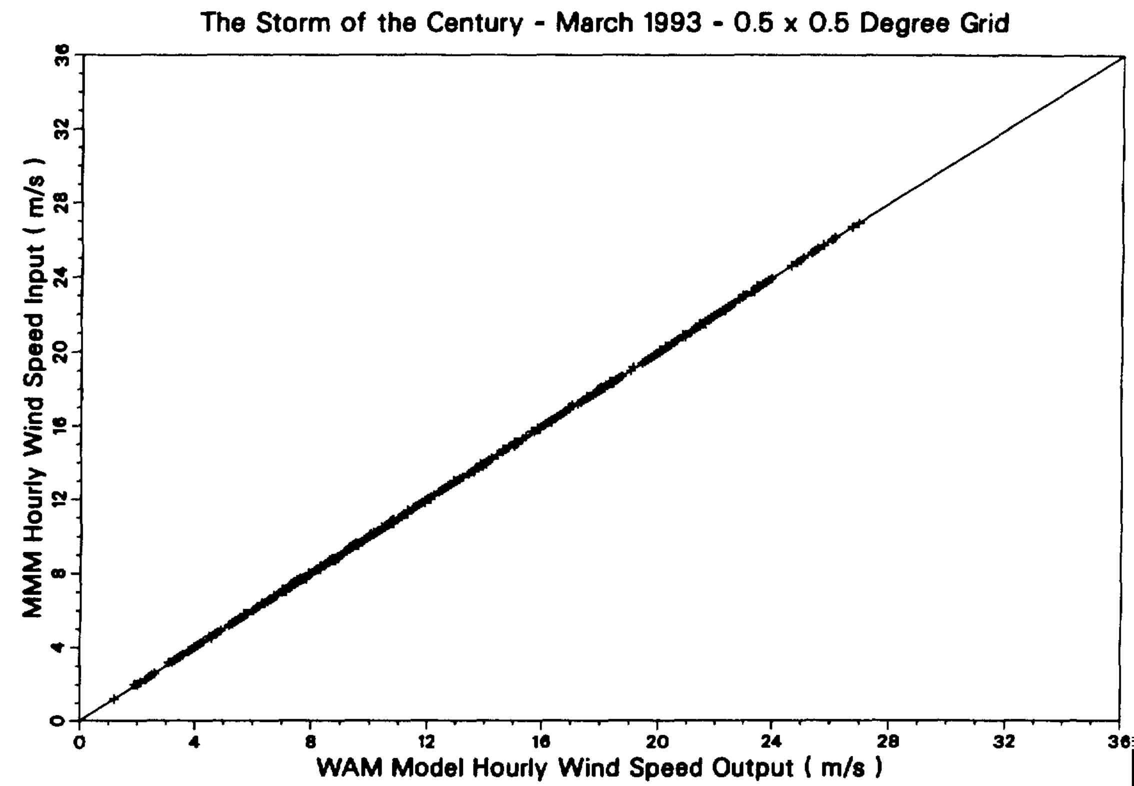

Figure 3a: Comparison of the MMM 10m level wind speed input to WAM with the WAM internally-derived 10m level wind speed output at the fifteen buoy locations.

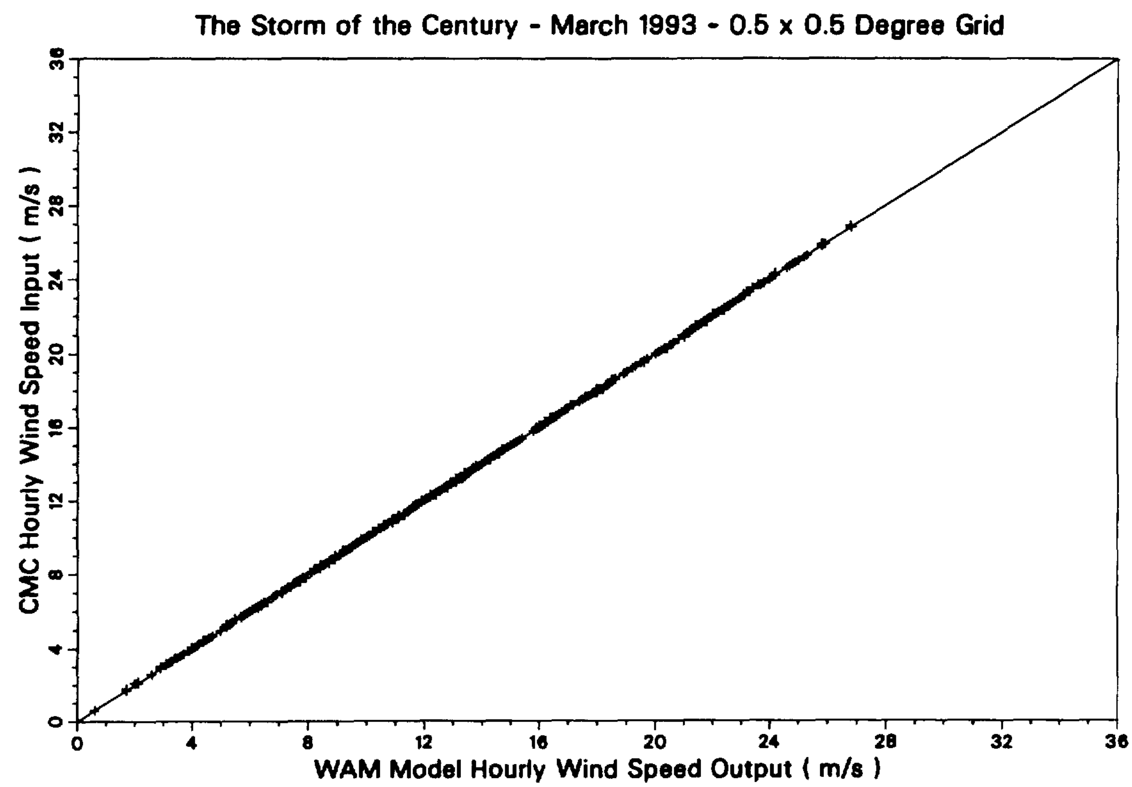

Figure 3b: Same as Figure 3a, but RFE model wind speed input to WAM.

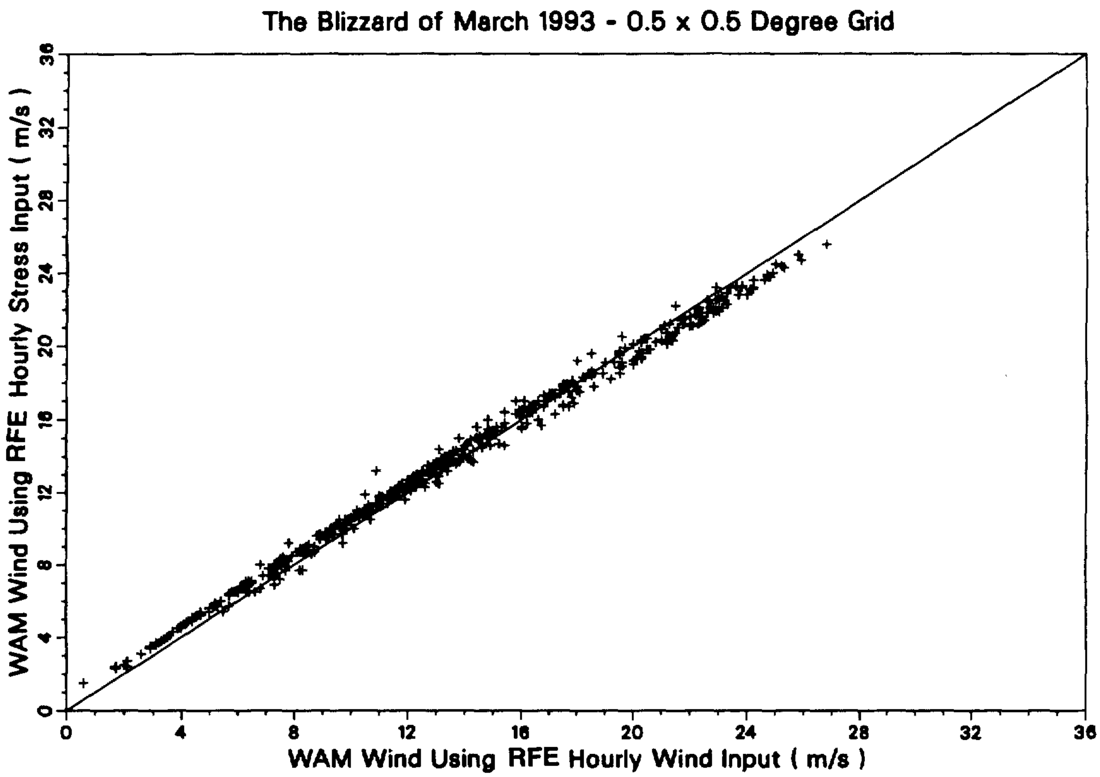

Figure 4: Scatter plot of WAM winds derived from inputs of RFE model surface stress and RFE model 10m level winds at fifteen buoy locations.

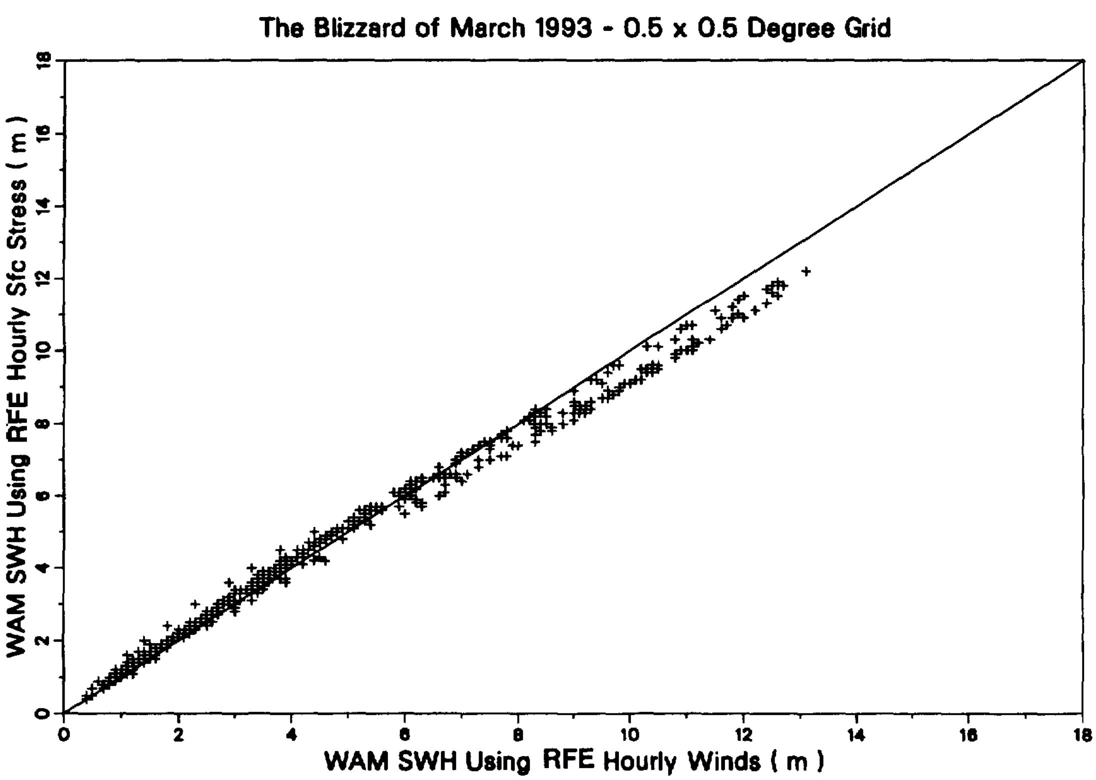

Figure 5: Scatter plot of model SWH generated using as inputs RFE model surface stress and RFE model 10m level wind at fifteen buoy locations.

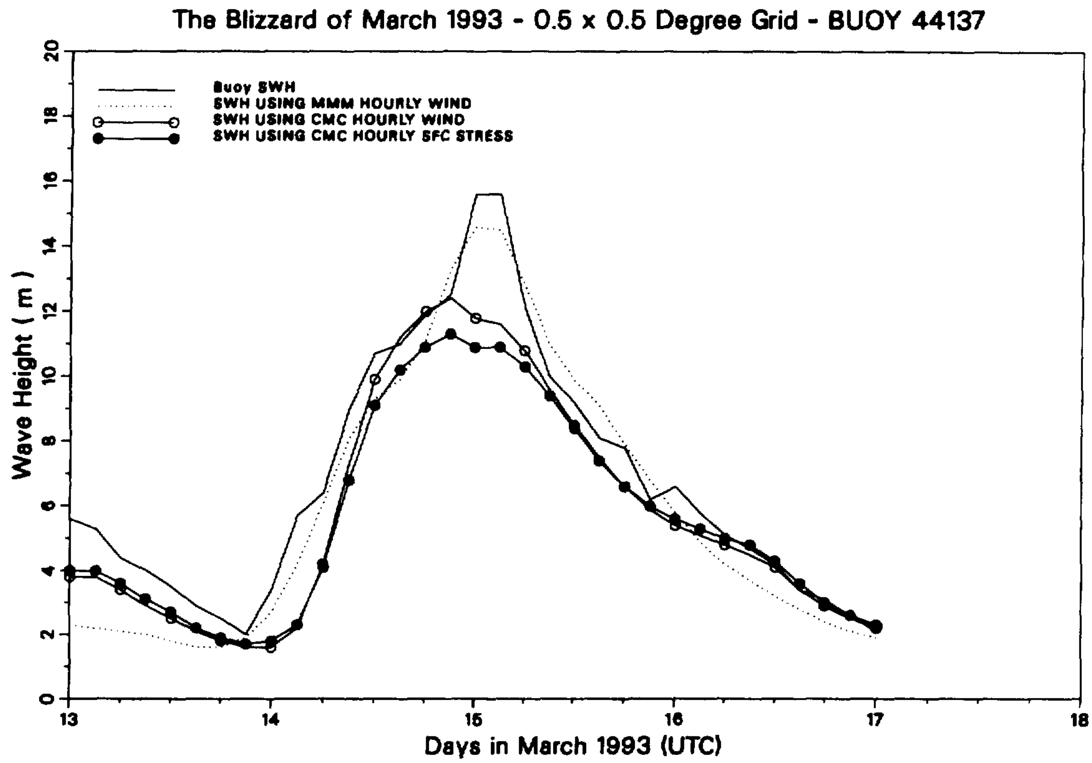

Figure 6: Comparison of buoy SWH (solid line) and model SWH using MMM winds (dotted line), RFE model stress (solid circle line), and RFE model winds (open circle line) at buoy 44137.

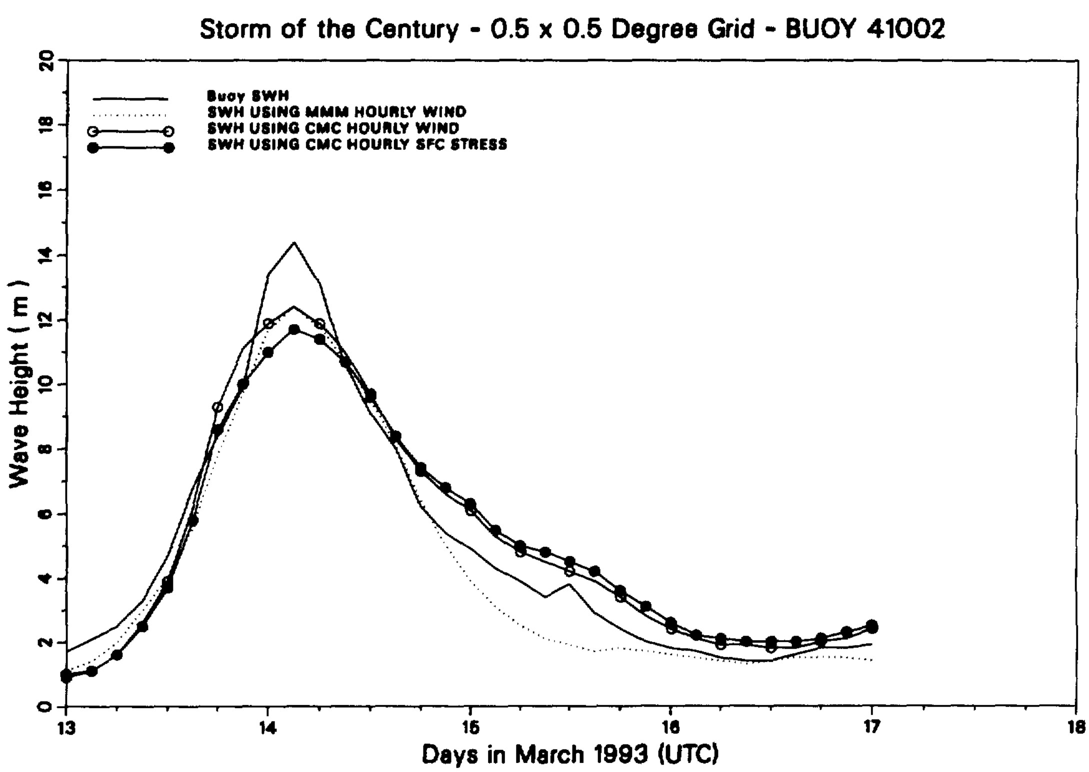

Figure 7: Same as Figure 6, but at buoy 41002.

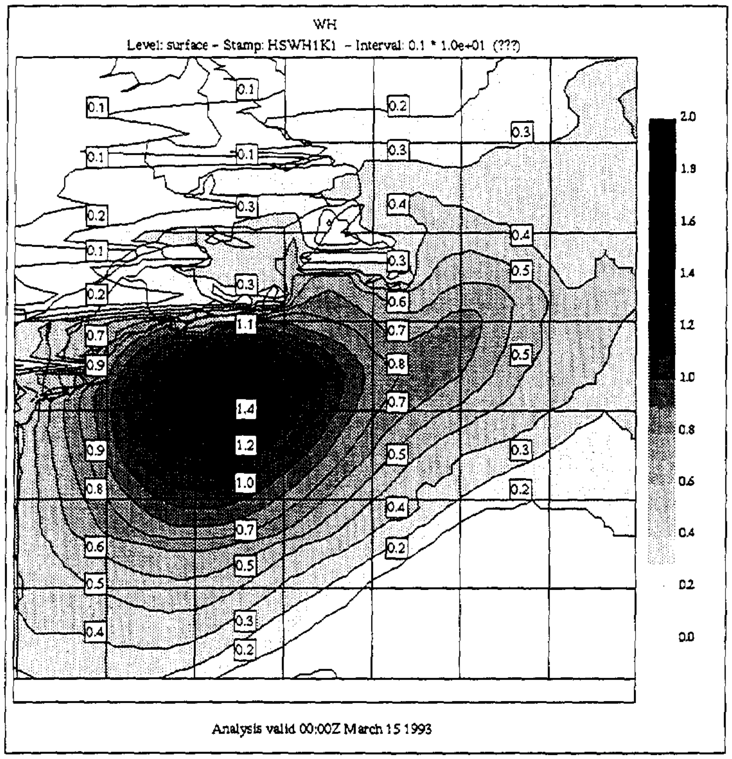

Figure 8a: SWH field generated using MMM winds for 0000UTC on 15 March 1993. Labelled values of SWH are in units of 10 metres.

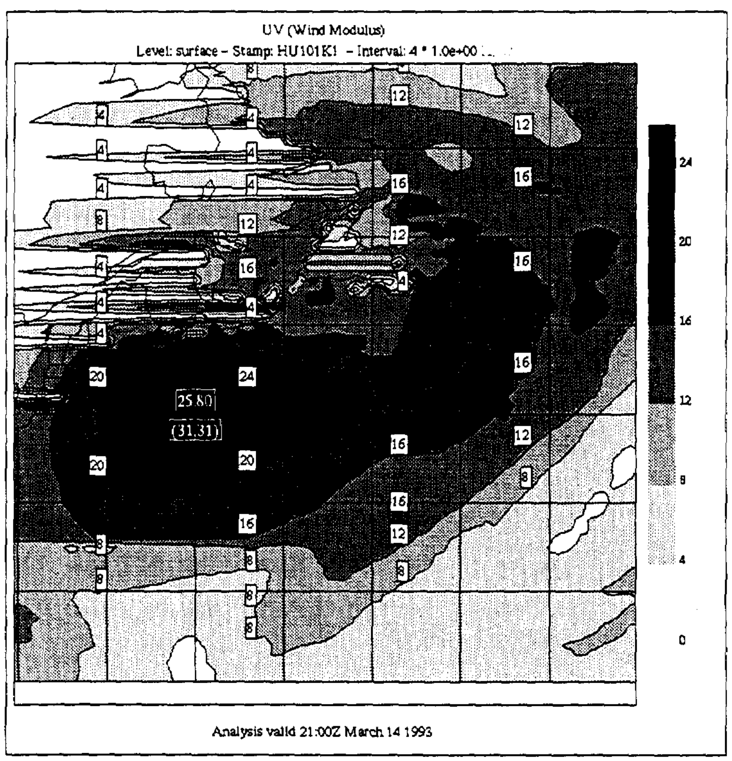

Figure 8b: MMM wind speed field in m/s for 2100UTC on 14 March 1993.

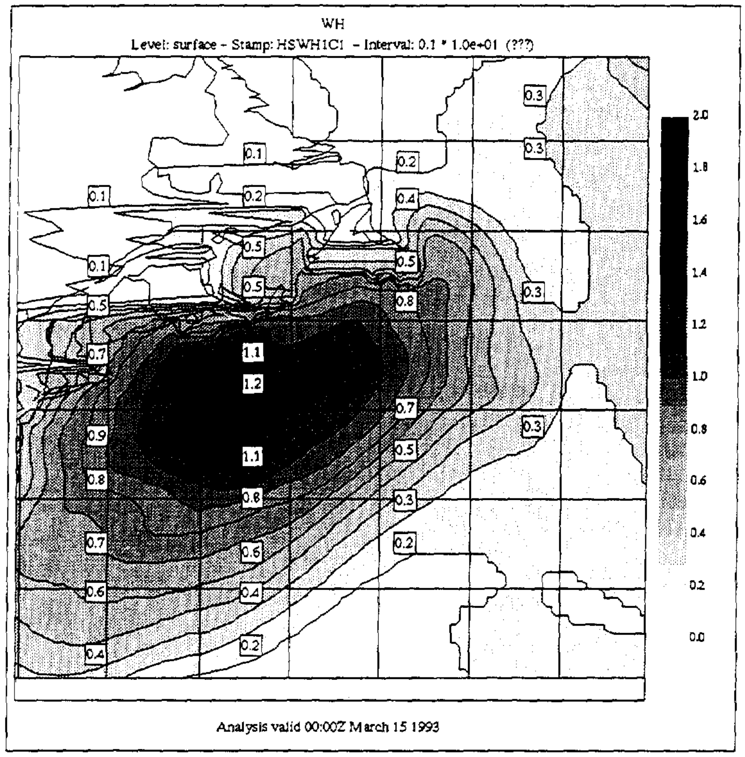

Figure 9a: Same as Figure 7a but using RFE model winds.

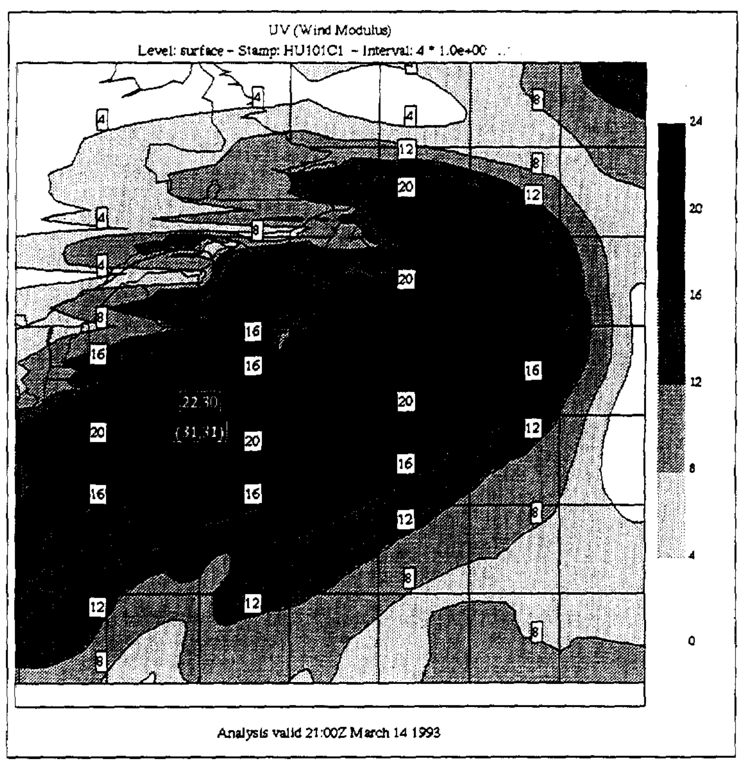

Figure 9b: Same as Figure 7b but for RFE model wind field.

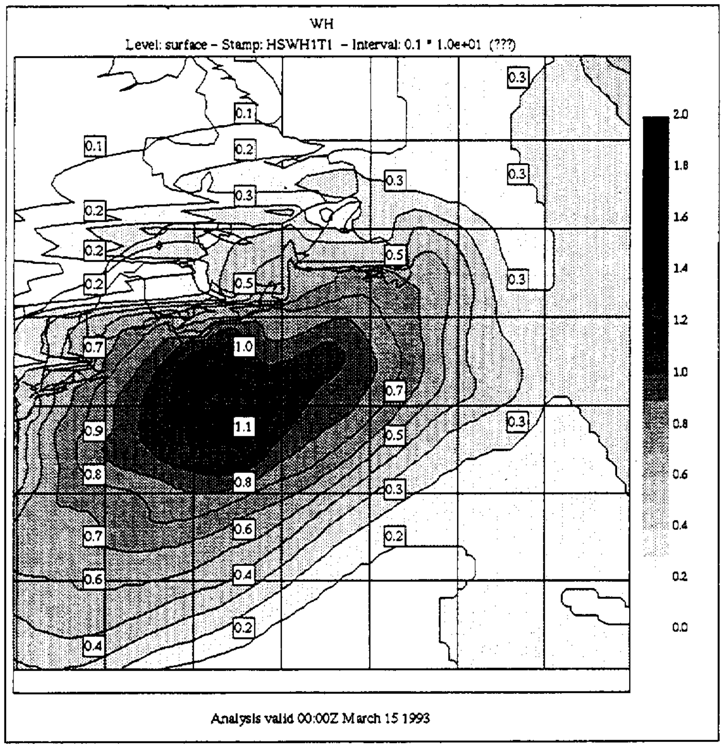

Figure 10a: Same as Figure 7a but using RFE model surface stress field.

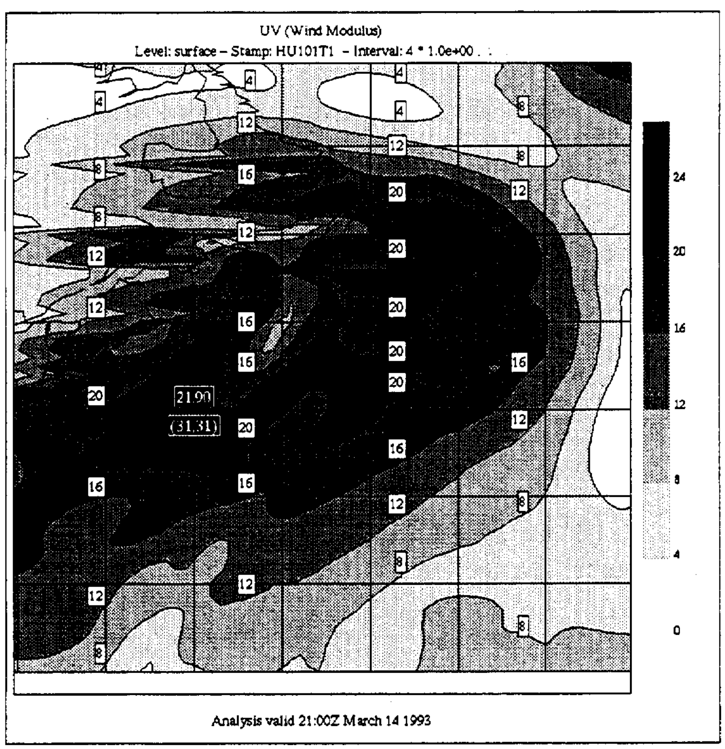

Figure 10b: Same as Figure 7b but for WAM internally-derived 10m level wind field using the RFE model surface stress field as input to WAM.

Table II: Verification for various ranges of significant wave height (SWH) values for the WAM model driven by MMM winds, RFE model winds, and RFE model surface stress for the storm of March 1993. Wave heights at six buoy locations (Table I) are used in the verification.

WAM INPUT	MMM Winds			CMC Winds			CMC Sfc Stress		
	SWH Range (m)			SWH Range (m)			SWH Range (m)		
	0–3	3–6	>6	0–3	3–6	>6	0–3	3–6	>6
BIAS (m)	–0.35	–0.89	–0.10	–0.09	–0.42	–0.26	0.06	–0.27	–0.78
RMSE (m)	0.52	1.19	1.03	0.55	1.00	1.33	0.58	0.95	1.47
SI (%)	26	27	11	27	23	14	29	22	16
r	0.80	0.75	0.90	0.68	0.64	0.83	0.67	0.63	0.84
Buoy Mean (m)	2.01	4.42	9.24	2.01	4.42	9.24	2.01	4.42	9.24
Model Mean (m)	1.65	3.53	9.14	1.92	4.00	8.98	2.06	4.15	8.46
N	45	81	72	45	81	72	45	81	72

BIAS = $1/N\Sigma(\text{Model-Buoy})$; RMSE = $\sqrt{\Sigma(\text{Model-Buoy})^2/N}$
r = Linear correlation coefficient between model and buoy SWH
SI (Scatter Index) = RMSE/Buoy mean value; N = Number of data points

Table III: Verification of significant wave height (SWH) values at locations of buoy 44137 (41.2N/61.1W) and buoy 41002 (32.3N/75.2W) for the WAM model driven by MMM winds, RFE model winds, and RFE model surface stress for the storm of March 1993.

	Buoy 44137			Buoy 41002		
WAM INPUT	MMM Winds	CMC Winds	CMC Sfc Stress	MMM Winds	CMC Winds	CMC Sfc Stress
BIAS (m)	-0.76	-1.00	-1.12	-0.61	0.22	0.18
RMSE (m)	1.28	1.46	1.64	0.86	0.89	1.09
SI (%)	19	22	24	18	18	22
r	0.97	0.96	0.96	0.99	0.97	0.96
Buoy Mean (m)	6.76	6.76	6.76	4.91	4.91	4.91
Model Mean (m)	5.99	5.75	5.64	4.30	5.13	5.09
N	33	33	33	33	33	33

DETAILED MEASUREMENTS OF WINDS AND WAVES IN HIGH SEASTATES FROM A MOORED NOMAD WEATHER BUOY.

S.G.P. Skey[1], K. Berger-North[1] and V.R. Swail[2]

[1] Axys Environmental Consulting Ltd., Sidney, B.C.
[2] Environment Canada, Downsview, Ontario

1. INTRODUCTION

The data gathered from remote weather buoys have both climatological and operational uses. Climatological uses include climate change analysis, calibration of satellite and airborne remote sensors, and forecast and hindcast wave models. For all climatological analyses, the precision of the measurement of winds and waves is becoming increasingly important, As more and more reliance is placed on satellite-based observations, it is essential that their measurements are well understood and accurately calibrated. Present efforts in developing high wind speed algorithms for remotely sensed data require accurate wind speed data for ground truthing.

The forecasting and hindcasting of wave heights during storms require accurate descriptions of the wind field. Since wave heights are a function of the square of the wind speed, the precision to which wind speed is measured and modelled is important. The ability to accurately forecast wave heights during storm conditions is a prime objective for increasing marine and coastal safety, and the development of improved engineering design criteria requires accurate hindcasting of wave heights during storms.

Given the importance of precise wind and wave measurements especially in high seastates, concern has been raised, based on the experiences of the Halloween Storm of 1991 and others, that the wind speeds reported from the weather buoys in high seastates are undervalued. A number of factors may affect wind measurement on buoys, but little is known of the magnitude of these effects during high wind and wave conditions.

To maximize the use and understanding of the data that are transmitted from the buoys in high seastate conditions, a 6m ship-shaped Environment Canada NOMAD (Navy Oceanographic Meteorological Automated Device) weather buoy was instrumented to measure a variety of parameters at a sampling interval of 2Hz (without averaging) in seastates exceeding 8m significant wave height. The additional payload that was integrated onto the buoy is referred to as SWS-1. This paper describes the SWS-1 field program, the data quality control and preparation, the preliminary analysis, the detailed analysis plan and recommendations for further work.

2. FIELD PROGRAM

2.1 Platform Description

The SWS-1 NOMAD buoy was deployed from 22 October 1994 to 29 July 1995 at a location about 10 miles southwest of Cape St. James at the southern tip of the Queen Charlotte Islands off Canada’s west coast. The site is referred to as the South Moresby location, and the buoy has the WMO ID Number 46147. The water depth is approximately 2,000m.

The SWS-1 package is contained within a standard Environment Canada NOMAD buoy. The NOMAD hull is welded aluminum, weighs about 20,000 lbs (including ballast) and measures 6m by 3.1m. There are four watertight compartments available for housing the sensor electronics, batteries, etc. In addition to the two masts on a standard NOMAD, a 0.61m extension boom is added to the rear mast to accommodate the additional SWS-1 wind sensors and radio antennae (Figure 1). The SWS-1 package of sensors, electronics, computers. radios and batteries is independent of the payload sensor package already in the buoy. A microcontroller on the SWS-1 passively monitors the output to the GOES satellite for activation criteria.

The NOMAD buoy in which the SWS-1 package is installed provides regular weather data to Environment Canada through a link with the GOES satellite. The SWS-1 package allows for some additional sensors to be installed on the buoy, but s primarily a data acquisition and transmission package.

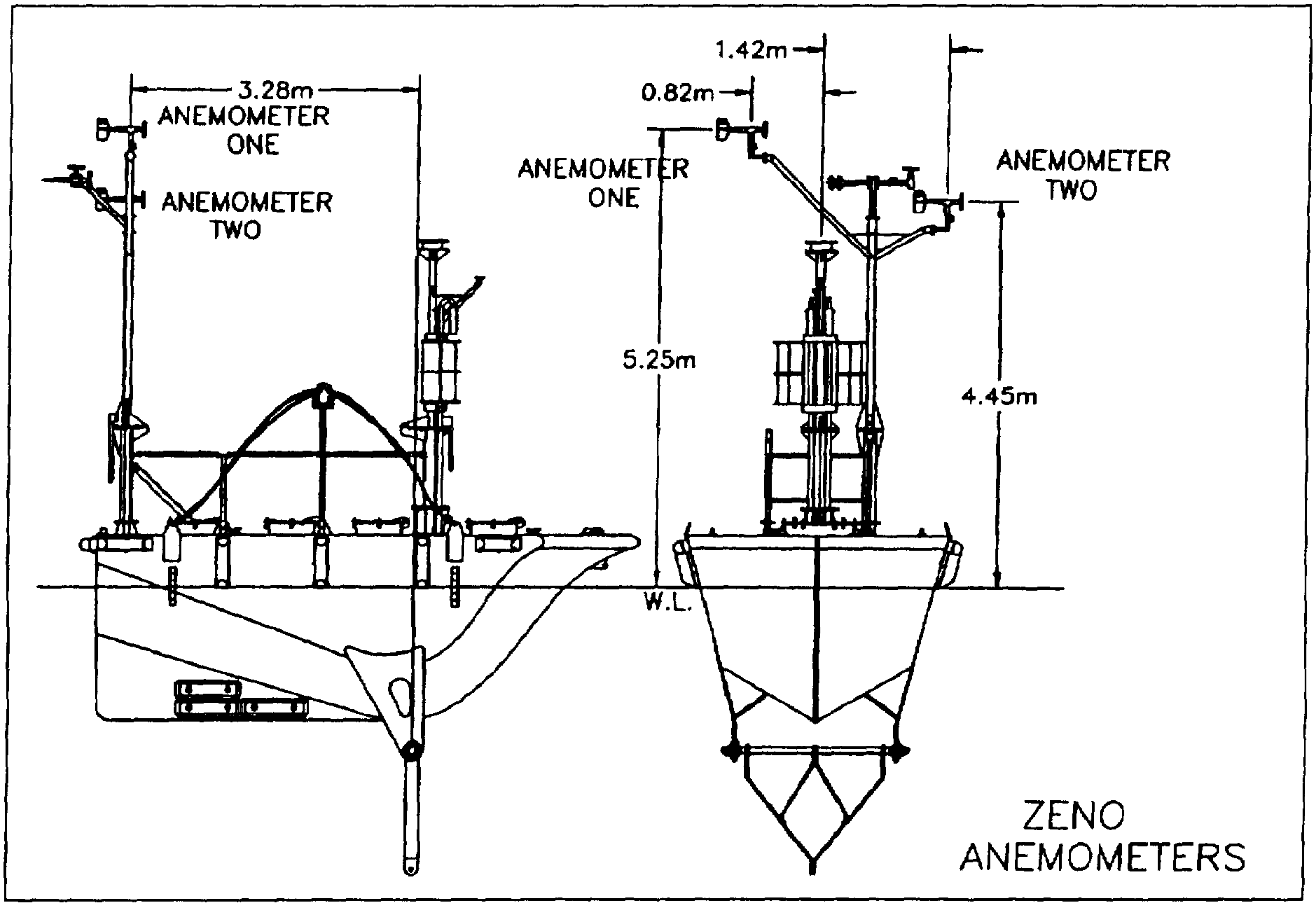

Figure 1.

2.2 SWS-1 Functions

The SWS-1 data acquisition package consists of two laptop computers (386SX, 20MHz, 60 MB HDD), and interface and controller cards. The second laptop is programmed identically to the first one for data back-up. Only the first laptop is connected to the radio link. SWS-1 is programmed to read the value of the significant wave as sensed by the Datawell sensor and reported in the GOES message. When the sea state exceeds 8m significant, SWS-1 records data at 2 Hz for all of the parameters listed in Table 1 , without averaging. SWS-1 stops sampling either (i) when the wave heights decrease below 6m for two consecutive hours, or (ii) when 12 hours have elapsed since the start of the sampling period, whichever comes first. After the end of the sample period, the SWS-1 waits six hours before transmitting the data via VHF radio link to the unmanned station at Cape St. James. SWS-1 is also programmed to sample data in low sea states for comparison with data from high sea states. There are 19 events recorded by SWS-1 between deployment and recovery. The details of each event are given in Table 2 .

Table 1

Configuration of NOMAD SWS-1 Buoy (#46147)

Parameter/System	Normal System for WMO Buoy 46147	Extra Systems for SWS-1
Horizontal Wind Speed and Direction	Two R.M.Young anemometers (model # 05103) at 4.45m and 5.25m above sea level (ASL).	
Vertical Wind Speed		R.M.Young anemometer (model #05103), without vane, fixed vertically on horizontal axis 4.82m ASL.
Vertical Wind Direction		R.M.Young anemometer (model #05103) pivoted on horizontal axis 4.82 m ASL.
Air temperature	YSI (model #703) with radiation shield at 4.27m ASL.	Increased sampling rate from 0.5Hz to 2Hz.
Buoy Attitude		General Oceanics Inc (model #6011 TAMS) three axis magnetic sensor
Wave Height and Period	Datawell Mark II heave sensor (single axis gimbaled accelerometer)	Columbia Research Lab (SA 107B) single axis strap down accelerometer
Barometric Pressure	Atmospheric Instrumentation Research Ltd. (model AIR-SB-2A)	
Water Temperature	YSI (model 44203) mounted in a s/s bolt below sea level.	
Compass	Two Syntron (model FHS-AV-1) fluxgate compasses (one for each anemometer).	One Syntron (model FHS-AV-1) fluxgate compass.
Mooring Strain		Metrox TL101-25K tension load link mounted immediately below bridle.
Data Processing	ZENO 1200	SWS-1
Data Transmission	GOES and ARGOS.	Repco RDS 1200 VHF transceiver.
Power	Primary, solar and secondary batteries.	Primary, and secondary batteries.

Table 2

Summary of Recorded Seastate Events

Date	[1]Hours	[2]Max 10m mean Vector Windspeed (m/s)	[3]10m mean Scalar Windspeed (m/s)	[4]Max 8s Gust (m/s)	[5]Max Hs (m)	[6]Max Hmax (m)
Nov 04/94	12	13.5	14.1	18.1	9.5	14.6
Nov 06/94	5	9.6	9.8	12.6	8.4	13.2
Nov 12/94	4	9.3	9.5	13.2	8.2	13.5
Nov 14/94	1	8.9	no data	10.9	3.6	6.1
Nov 27/94	12	12.7	13.1	15.7	9.2	14.2
Nov 30/94	12	14.9	15.3	18.8	7.6	12.4
Dec 02/94	8	11.2	11.6	15.8	9.0	13.7
Dec 05/94	8	17.4	18.0	22.1	8.3	14.2
Dec 06/94	2	10.0	10.2	12.7	7.9	14.1
Dec 07/94	10	9.1	9.8	14.6	8.3	12.5
Dec 19/94	12	13.2	13.6	16.2	7.7	12.6
Dec 22/94	12	16.7	17.1	20.9	9.0	15.5
Dec 30/94	1	7.1	7.2	9.1	3.7	5.9
Jan 15/95	11	11.2	11.4	10.4	2.5	5.0
Jan 18/95	1	10.7	10.9	14.0	5.4	10.5
Jan 24/95	6	7.2	7.3	8.7	2.1	3.9
Feb 10/95	1	6.9	7.2	8.9	3.1	5.5
Mar 06/95	1	7.1	7.2	9.7	1.2	2.4
Mar 29/95	1	1.4	1.5	2.1	2.2	4.0

1 Hours: The length of the storm recorded by SWS-1.
2 Vector Wind: The maximum value for the storm as reported in the GOES message.
3 Scalar Wind: The value corresponding to the time of the maximum vector mean.
4 Max 8s Gust: The maximum value for the storm as reported in the GOES message.
5 Max Hs: The maximum value for the storm as reported in the GOES message.
6 Max Hmax: The maximum value for Hmax (see Table 3) as reported in the GOES message.

2.3 Rationale for Sampling Thresholds

The data from three Pacific weather buoys were reviewed to determine the initiation and cut-off threshold values for use during the SWS-1 field program. Winter season data from 1989-90 and 1990-91 were analyzed for buoys 46004, 46207 and 46208. 46207 (water depth 2,125m) and 46208 (depth 2,950m) are 3m Discus buoys located 75 miles SE and 60 miles NW of the SWS-1 location respectively. 46004 is a NOMAD (depth 3,600m) approximately 150 miles west-southwest of SWS-1. Three sets of threshold values were chosen for analysis (initiation/cut-off): 8m/7m, 8m/6m, and 7m/6m. For each winter period, the event start and end date/times, the length of the event in hours, the maximum and minimum wave height, and the interval between events were determined. The analysis showed that we could expect eight to 10 events with maximum significant waves in excess of 8m, and only four to five events in excess of 9m. The number of events doubles when the initiation threshold drops from 8m to 7m. Since the hard drive capacity in SWS-1 is such that it can store about 10 to 15 events, we set the thresholds at 8m/6m.

The length of the events is generally less than 12 hours. An analysis of the events which exceeded 12 hours showed that the maximum significant wave occurred during the first 12 hours of the period. Therefore, using a maximum event length of 12 hours would not likely jeopardize the event including the maximum wave height. The interval between events was generally much greater than 24 hours. Therefore waiting for 6-12 hours after the cut-off threshold is reached would generally place the buoy in more favourable weather conditions for transmission purposes.

3. DATA QUALITY CONTROL AND PREPARATION

3.1 Signal Conditioning

Most of the SWS-1 sensor outputs were conditioned to produce a 0-5V DC signal at the input stage of a 12-bit A/D (analog to digital) converter. The discretization of a 0-5V signal into 4096 elements results in the equivalent to a mV (0.025% full scale) signal resolution at the output stage of the A/D converter.

Wind direction and temperatures have frequency outputs which were measured with digital pulse counters to produce 8 bit digital values. The discretization into 256 elements results in the equivalent to a 0.4% full scale signal resolution at the output stage. Heave measurements were processed with a 12 bit A/D converter for computing wave parameters. The digital output of barometric pressure provides 10 bits of resolution. All raw data were logged to the hard disk drives at full frequency, before the application of calibration information.

3.2 Calibration

All sensors were calibrated prior to deployment. Signal output was plotted as a function of known inputs for each sensor to produce linear calibration coefficients. These calibration coefficients were applied to the raw data to produce calibrated output. Post deployment calibration was performed as necessary to the sensors in order to verify proper functioning of the sensors and to monitor sensor drift.

Table 3
Processing Details of standard met and ocean parameters as reported from the Environment Canada Buoy Network

Parameter r	Processing	Location in WMO Message	Record Length	Samples in Record	Time of Record Relative to Transmission
Average Wind Speed & Direction	Vector Average	Section 1: dddfff[1]	600s	300	Immediately prior
	Scalar Average	Section 4: Analog Data Group A8ffffff	600S	300	Immediately prior
Maximum Wind Gust	Value of maxi-mum moving scalar average	Section 3. 921fff	8s	4	Completed immediately prior to start of wind sample
Wave Height and Period	FFT for T. Hsig Hmax[2] Detailed waves	Section 2– 1kkkeee Section 3:WAVEyyy Section 5:$ppp..pp	8*256[3]	2048[3]	Completed immediately prior to start of wind sample
Atmospheric Pressure	Arithmetic Mean	Section 1: 4pppp	20s	20	Mid–point of wind sample
Air Temperature	Arithmetic Mean	Section 1: 1nttt	600s	300[4]	Coincident with wind sample
Sea Surface Temperature	Arithmetic Mean	Section 2: Onwww	600s	300	Coincident with wind sample

[1] The higher of the two anemometers is reported first. The second anemometer is reported in parentheses (dddfff).

[2] Hmean = numerical mean of the 2048 data points
Hh = the maximum positive value of the wave height.
H_{max} = (Hh–Hmean)*2.

[3] In any one wave record there are 8 blocks of 256 one–second samples. This accounts for 2048 samples, There is a 24 sec period between each 256 sec sample for FFT analysis.

[4] SWS–1 sampled the air temperature at 2Hz.

3.2.1 Magnetometer

When a magnetometer is used to determine buoy attitude, the buoy has to be spun in place to allow the alignment of the magnetometer output to the compass output. Additionally the magnetometer needs to be removed from its bracket and rotated through all of its axes (one at a time), both continuously and in discrete steps of 30 degrees. These calibrations provide an indication of magnetometer output as a function of attitude in the magnetic environment in which the data were captured.

Since it was not possible to carry out these procedures at the SWS-1 site due to timing and weather problems, they will be carried out outside Victoria harbour. The buoy and mooring configuration will be exactly as they were during the deployment. Allowances will be made for the difference in the earth’s magnetic field between the two sites.

3.3 Post-Processing

SWS-1 collects the raw wind sensor output directly from the anemometers which are aligned to the buoy such that north is directly in line with the bow. After correcting the SWS-1 compass output for local magnetic variation to produce true heading, this heading is added to the raw wind direction in order to produce true wind direction.

The mean value from the wave sensors is used to provide a zero value for the estimated sea surface. This value is applied as an offset incorporated into the sensor calibration coefficients, and is -14.78m for the Datawell heave sensor and -14.71 for the accelerometer. These means are computed as a single value for each storm, with typical variation of less than 1cm. Zero crossing analysis is used to define wave events.

3.4 Data on CD-ROM

Once all the data have been properly calibrated and sorted, they will be made available on CD-ROM. The purpose of this is to provide other researchers with this unique data set for their own research purposes. If you are interested in receiving a copy of the CD-ROM please contact one of the authors of this paper.

4. PRELIMINARY ANALYSIS

4.1 Buoy Data Processing

The preceding Table 3 indicates how the data from the various sensors on the buoy are gathered and processed by the buoy payload. The data are transmitted via GOES in a standard WMO format.

4.2 Preliminary Analysis

At the time of submission of this paper only preliminary analyses have been done. Some of these are presented here. To compare the effects of high seastates on the buoy measurements, we have chosen to represent the data from three storms of high, medium and low seastates. The dates of these storms are November 4, December 19 and March 6. The summary details of these storms are given in Table 2 .

4.2.1 Intercomparison of Wave Sensors

Figures 2a , 2b and 2c show two-minute time series plots of wave heights as recorded by the Datawell and strap-down accelerometer. Figure 2a is taken from the high seastate condition, Figure 2b from the medium seastate condition, and Figure 2c from the low seastate condition.

The plots for the accelerometer are not corrected for roll or pitch, and the effects of this can be seen in the high seastate condition where roll and pitch would be expected to be high. As the seastate becomes less severe the peak to peak agreement between the sensors improves.

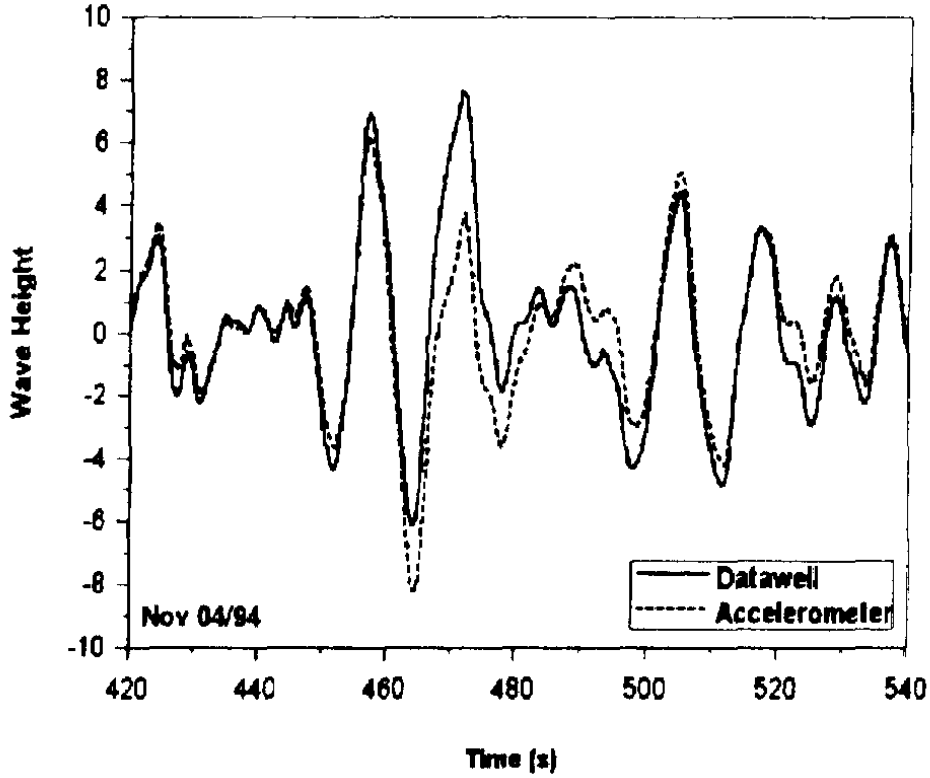

Figure 2a.

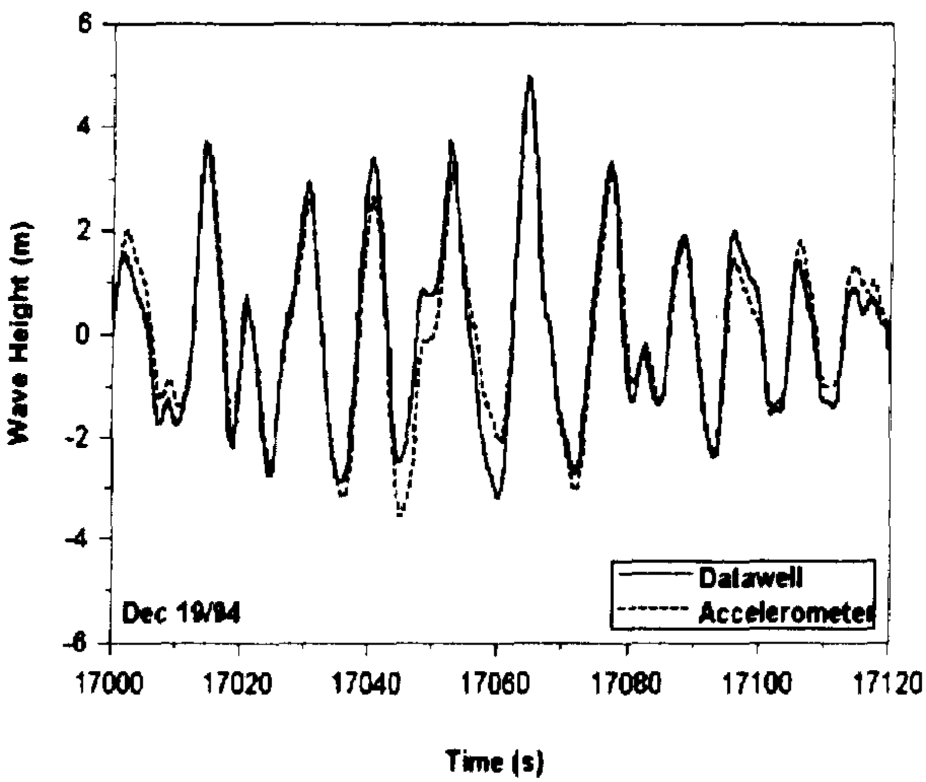

Figure 2b.

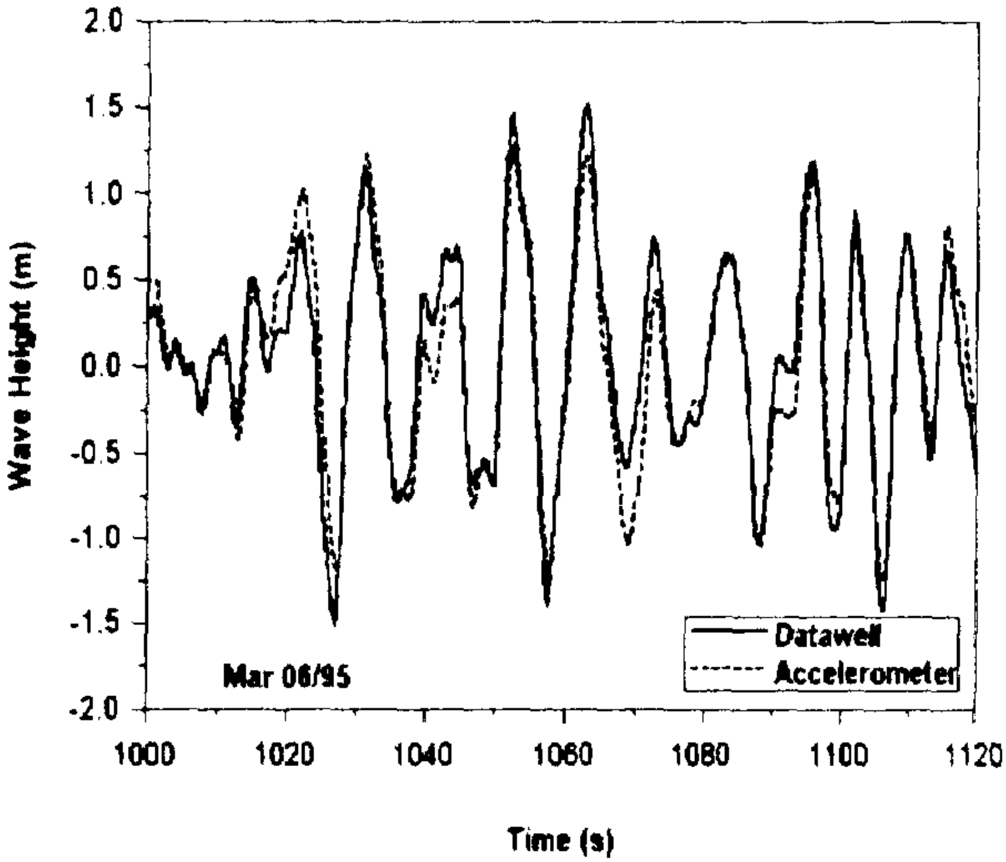
2.0
1.5
1.0
0.5
0.0
-0.5
-1.0
-1.5
-2.0
Wave Height (m)
Mar 06/95
Datawell
Accelerometer
1000
1020
1040
1060
1080
1100
1120
Time (s)

Figure 2c.

Figure 3 shows the scatter plot between the two sensors for the complete November 4 storm and represents over 86,000 data points. The accelerometer data, uncorrected for roll and pitch, consistently gives a lower value than the Datawell. Scatter plots for medium and low seastate conditions show similar results.

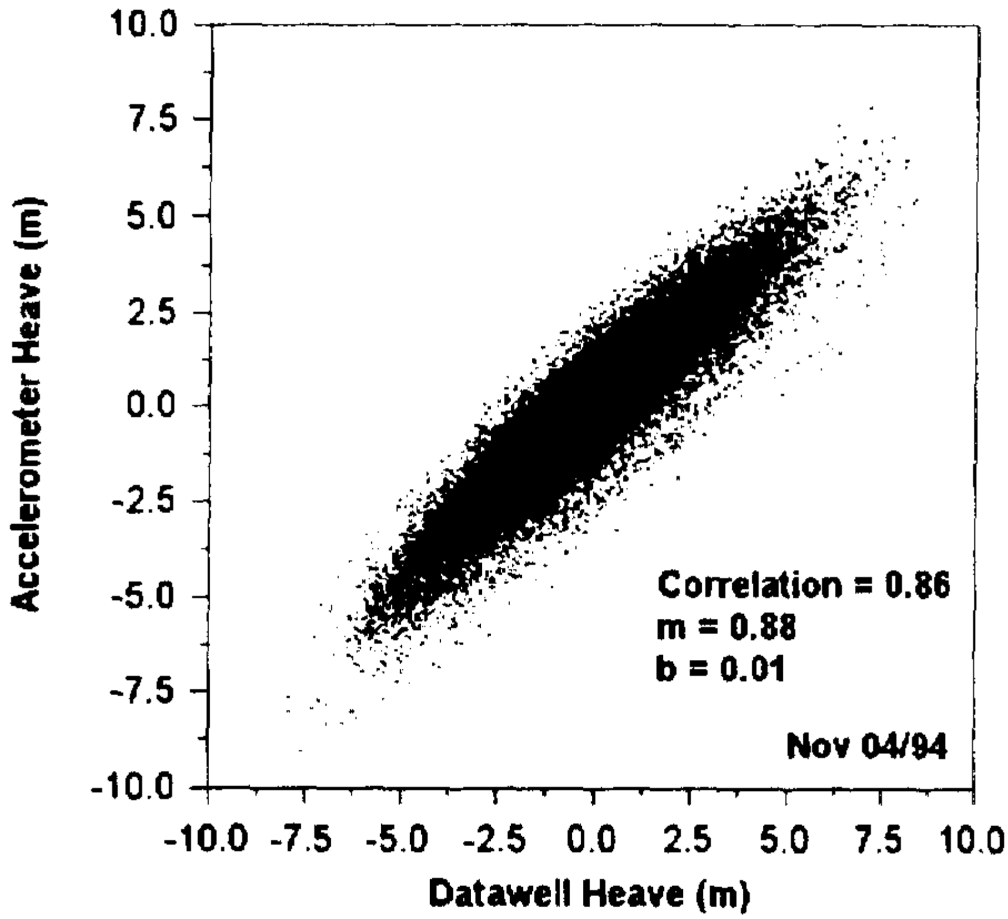

Figure 3.

4.2.2 Gust Analysis

The gust factors produced from a gust analysis of each of the three sample storms are shown in Figure 4 . The length of time over which the gust speeds is calculated ranges from 0.5s to 30s. The values are calculated by taking the mean value of all the gusts of the same length over a ten minute sample and dividing by the mean wind speed for that sample. This process is repeated for each ten minute sample period for the duration of the storm. The values in the figure are then the mean values of all the ten minute samples.

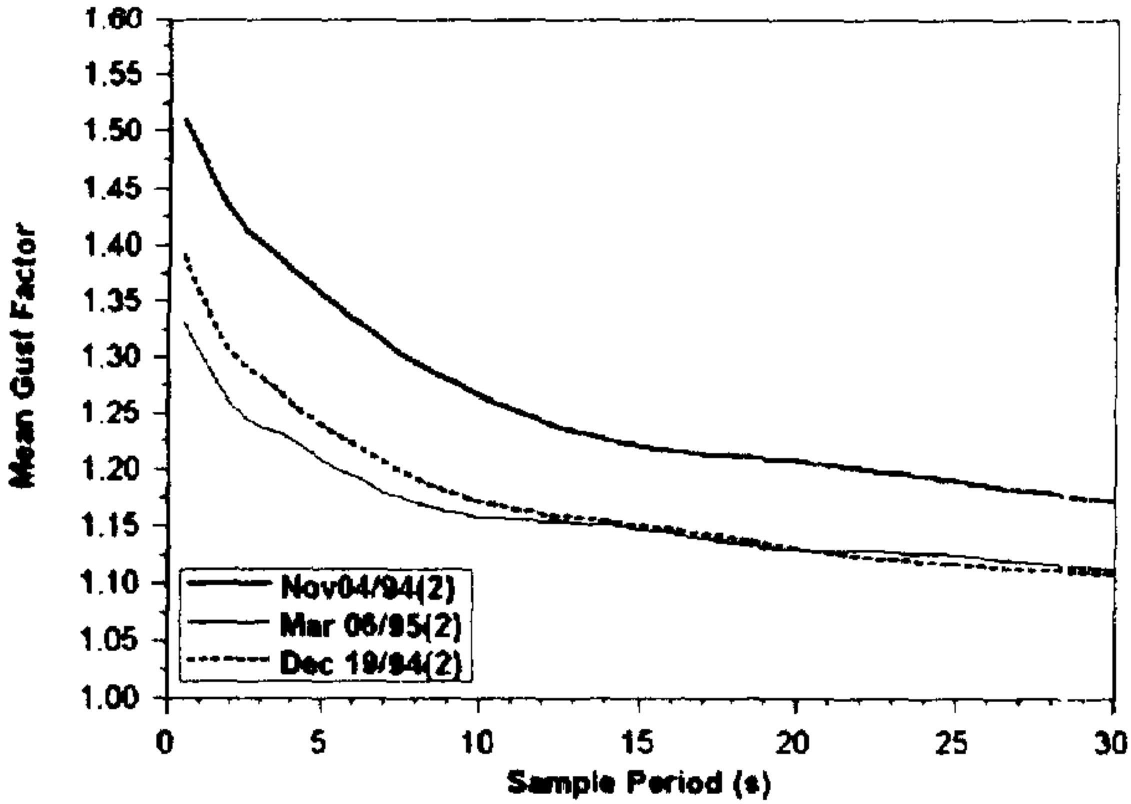

Figure 4.

4.2.3 Wave Height vs Wind Measurement

4.2.3.1 Wind Speed

Figures 5a , 5b and 5c show the instantaneous wind speed measurements over the same two-minute period shown in Figures 2a , 2b and 2c . For this short record length, the variation in wind speed is very marked in the high seastate condition, with an apparent relationship between peak wind and peak wave. This relationship becomes less marked as the seastate decreases (Figures 5b and 5c).

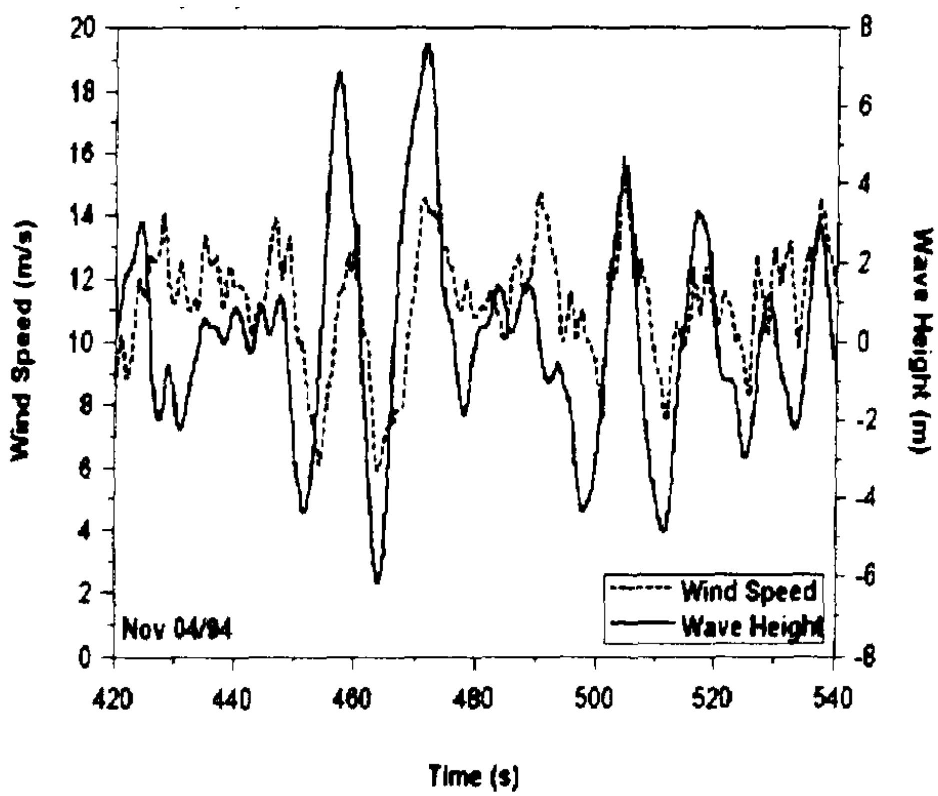

Figure 5a.

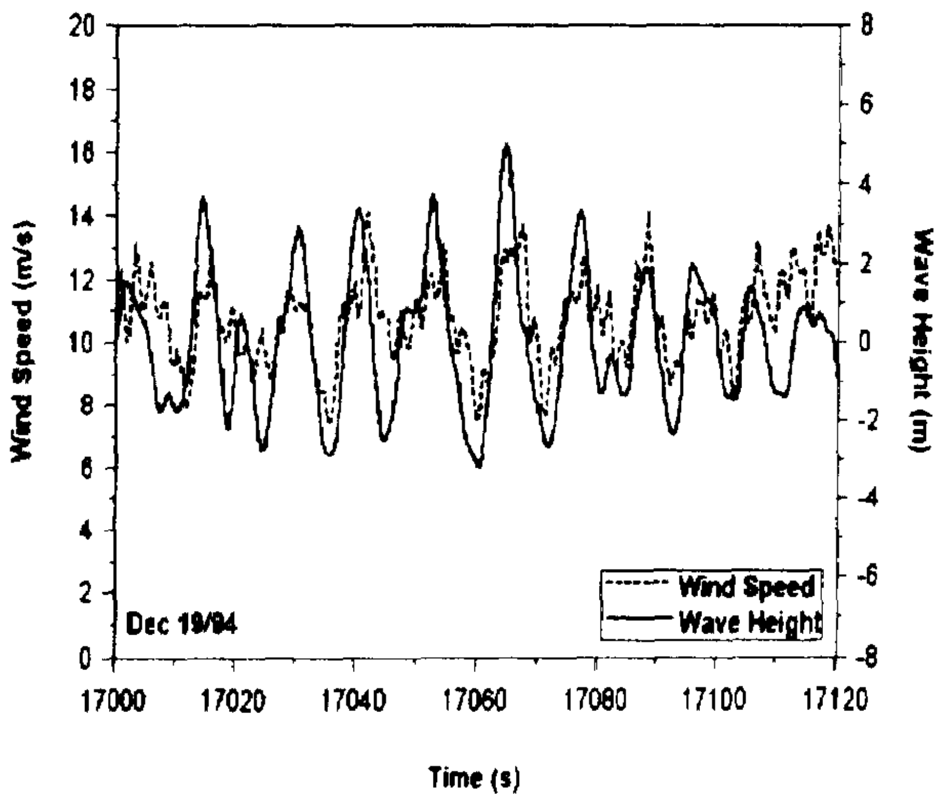

Figure 5b.

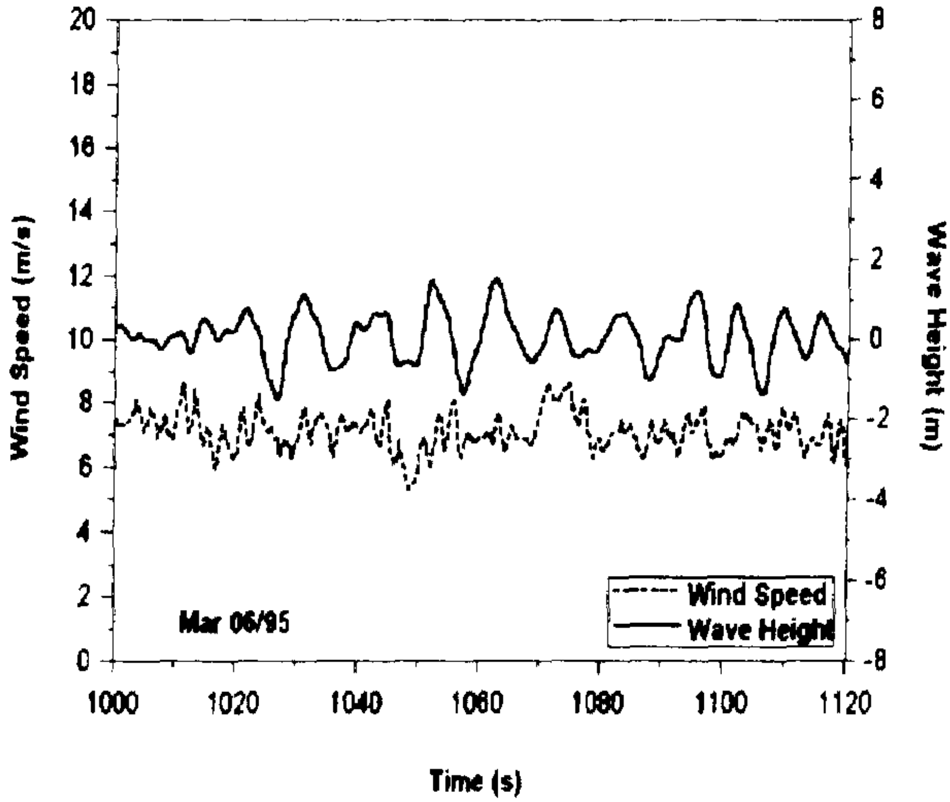

Figure 5c.

4.2.3.2 Wind Direction

Figures 6a , 6b and 6c show the instantaneous variation in wind direction over the same time intervals. Again, over this short record length, there appears to be a strong correlation with wave height.

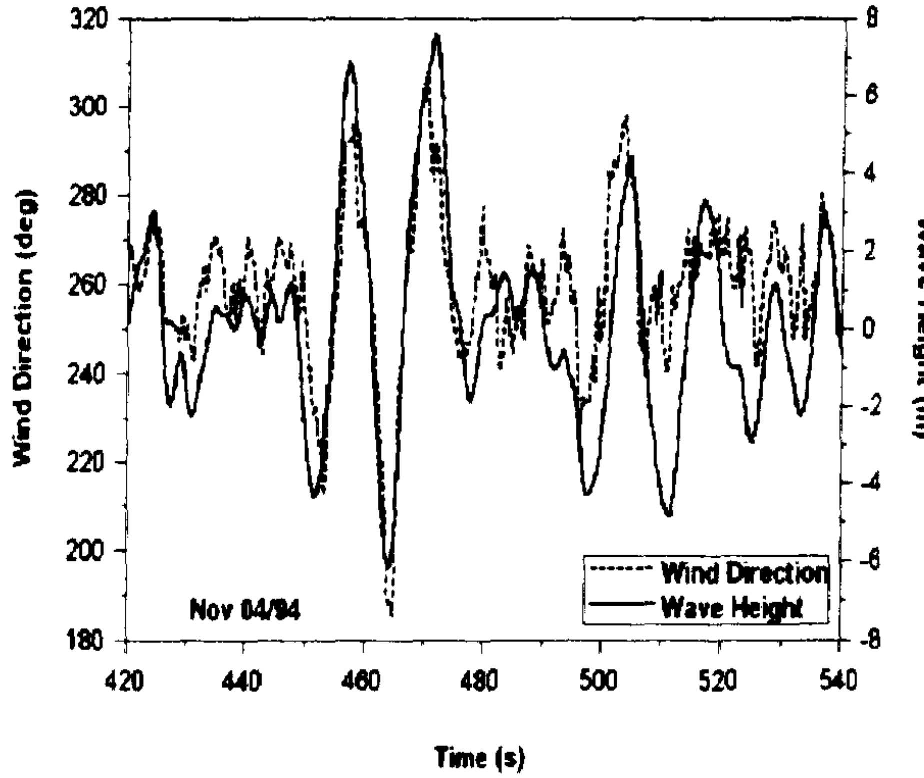

Figure 6a.

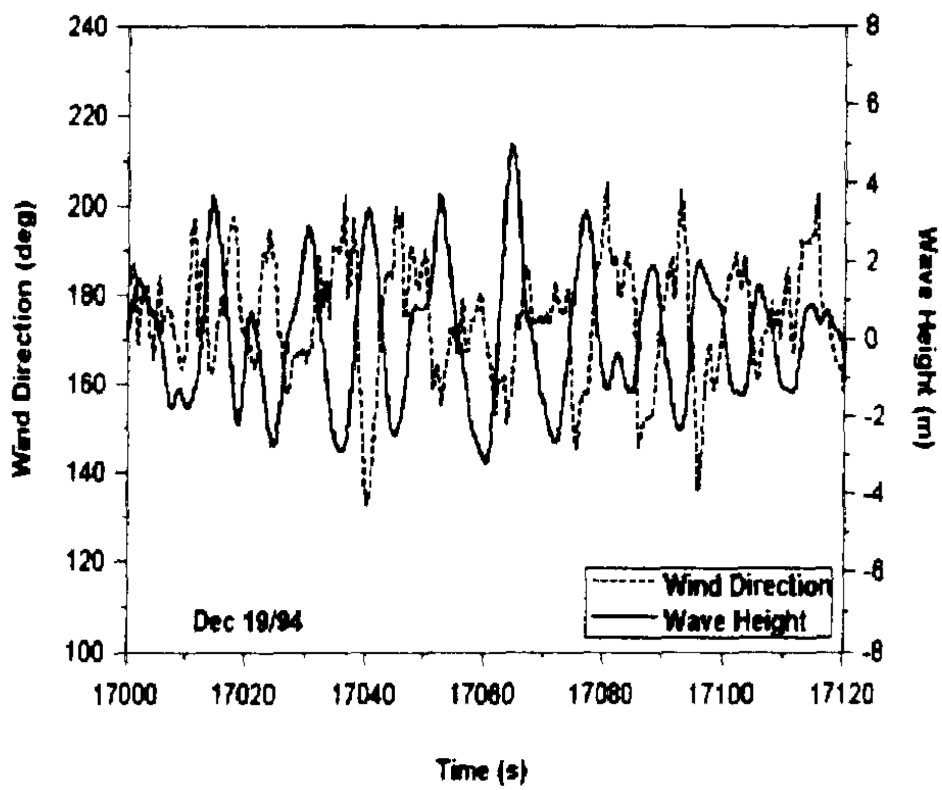

Figure 6b.

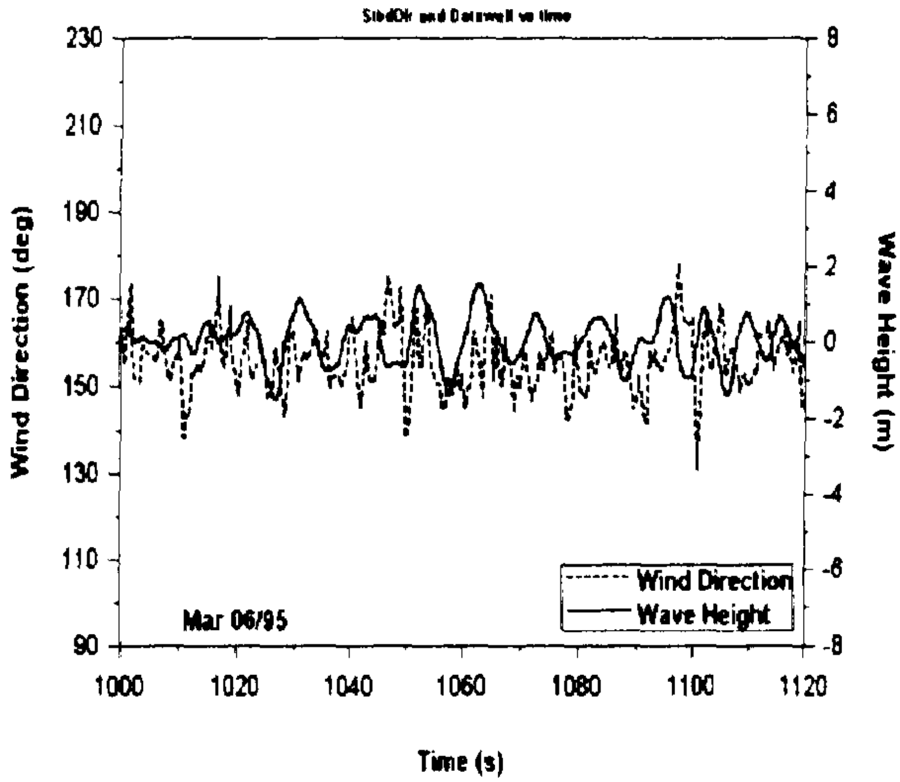

Figure 6c.

4.2.3.3 Buoy Heading

Figures 7a , 7b and 7c show the instantaneous buoy headings for the same storm intervals.

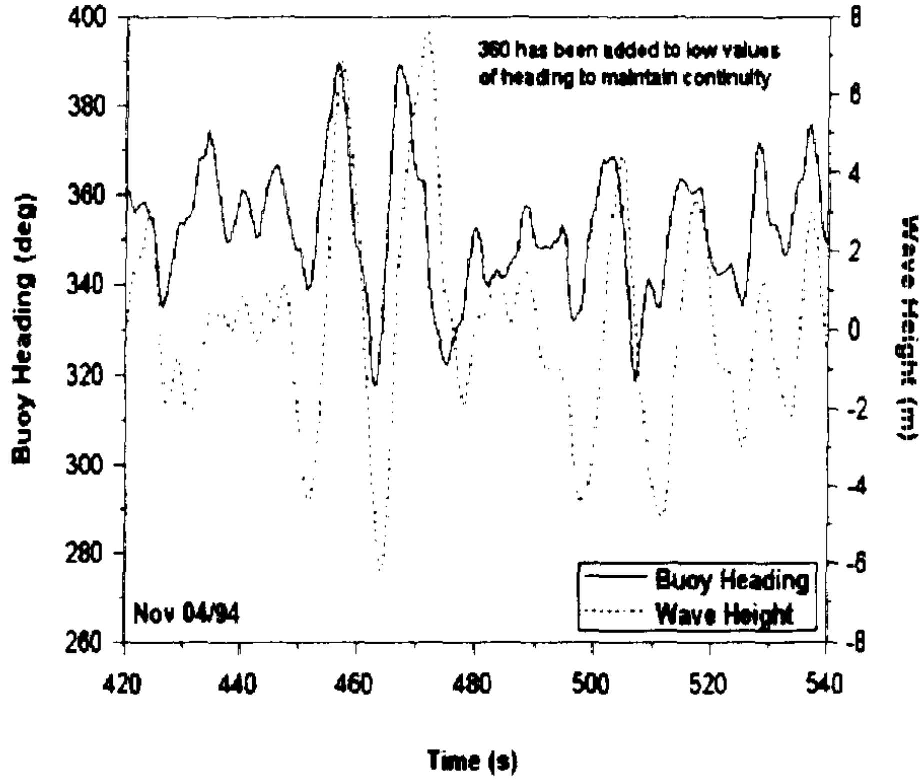

Figure 7a.

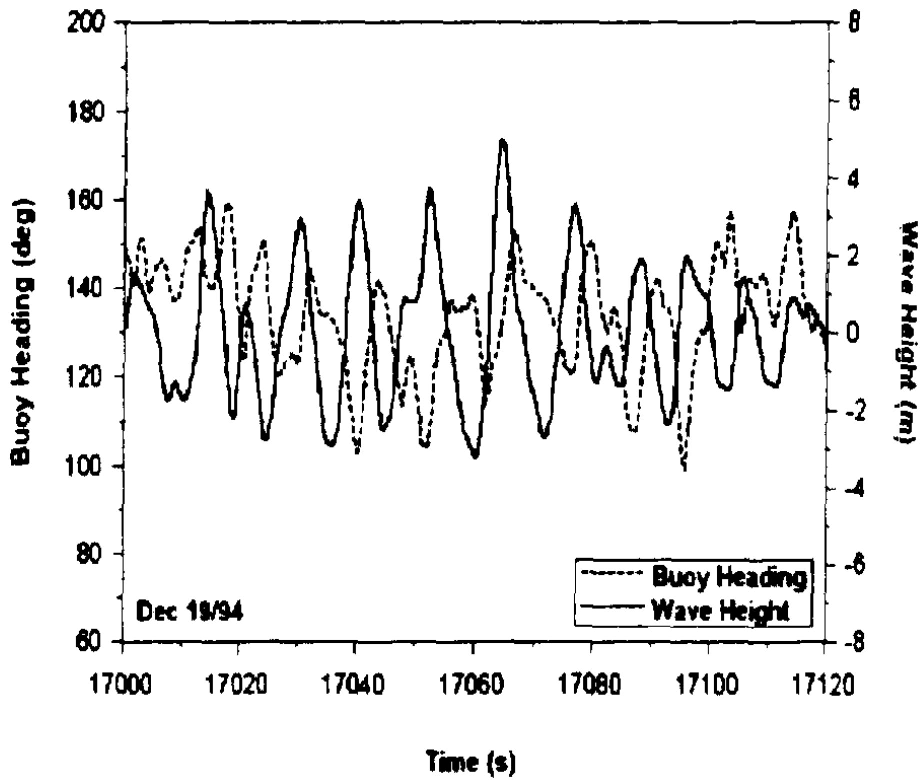

Figure 7b.

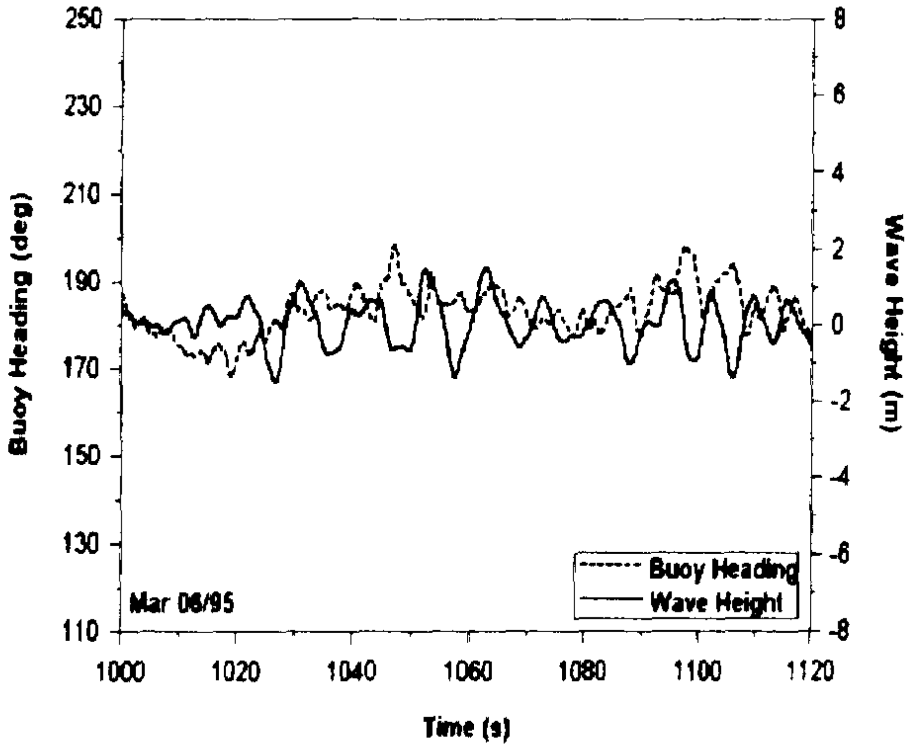

Figure 7c.

4.2.4 Air Temperature Analysis

Figures 8a , 8b and 8c show the instantaneous values of air temperature for the same storm intervals.

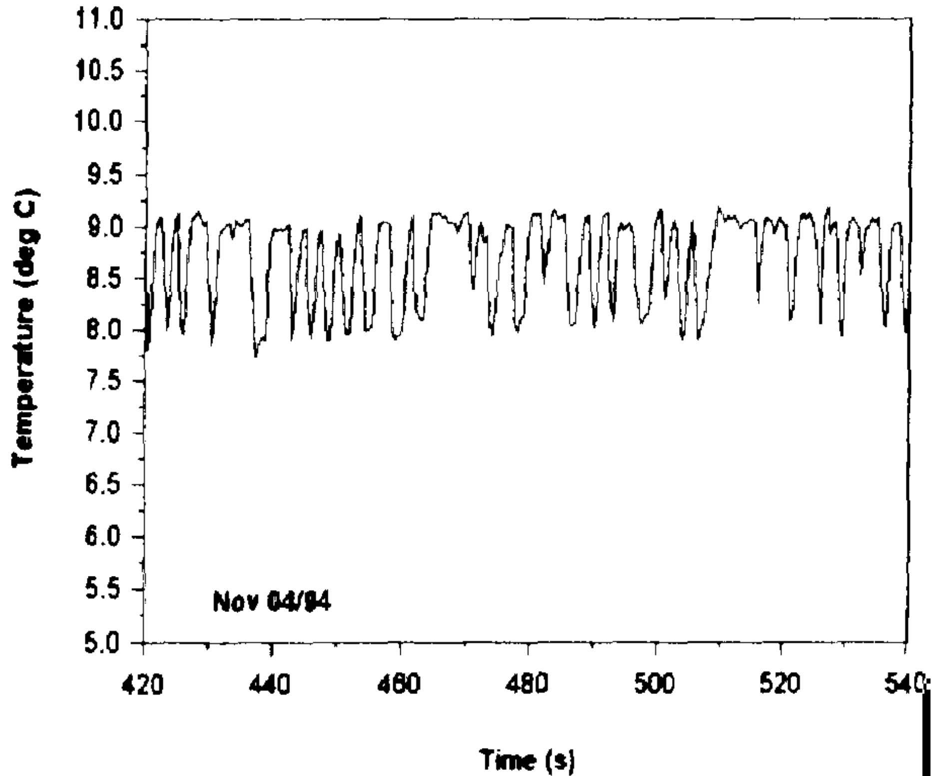

Figure 8a.

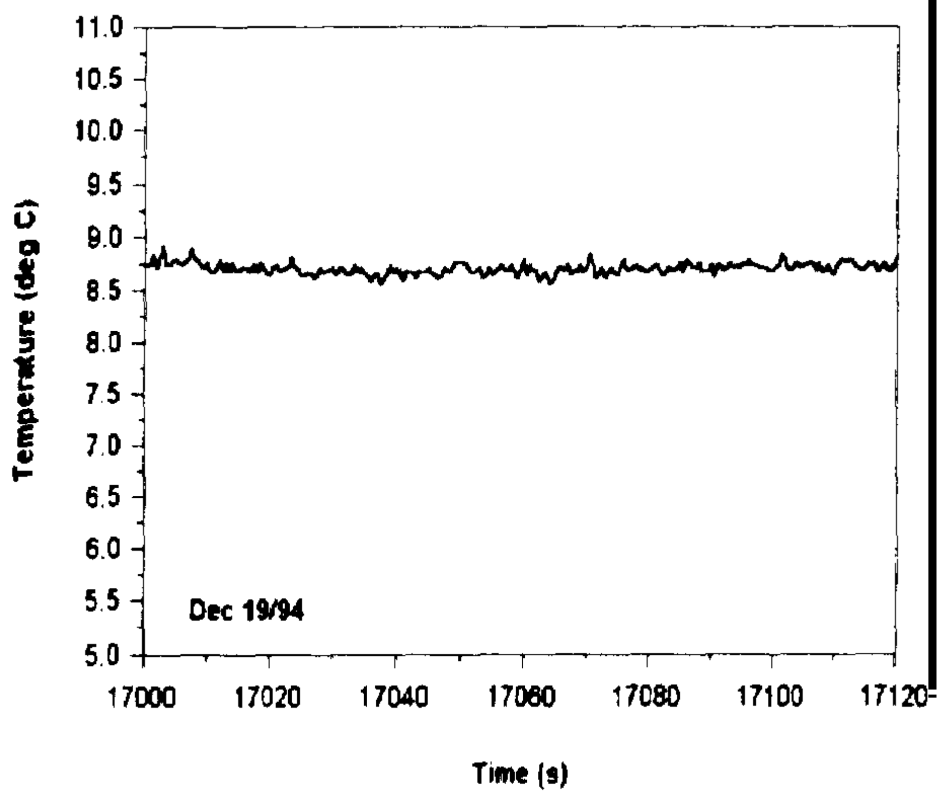

Figure 8b.

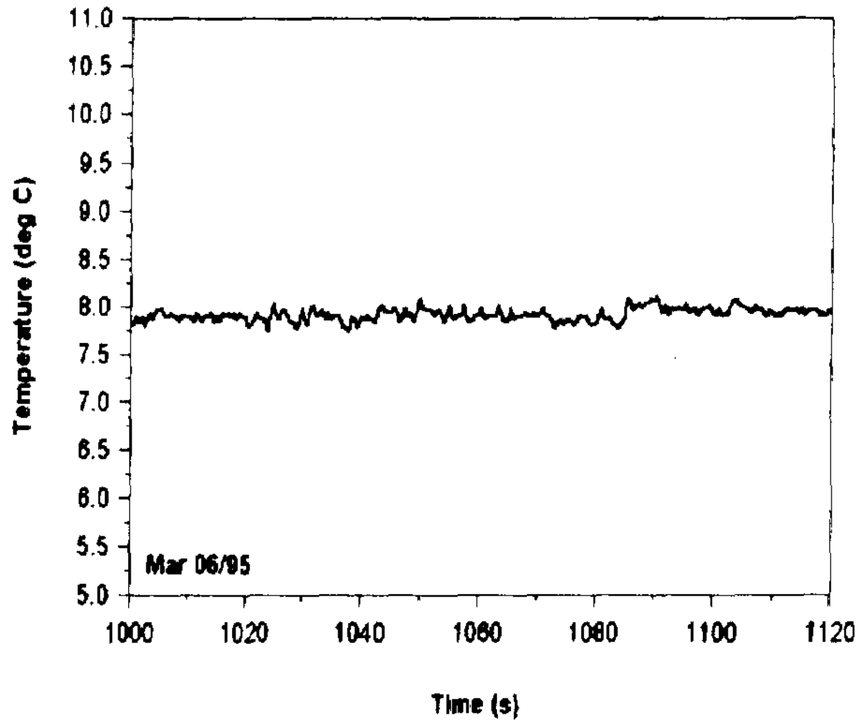

Figure 8c.

5 DETAILED ANALYSIS PLAN

5.1 Projected Analysis

Detailed analysis will be done on the following topics:

- Buoy motions (Wave sensor intercalibration)
- Vector vs Scalar averaged winds
- Effects of high sea states on reported wind speeds.

5.1.1 Accelerometer Tilt Analysis

Preliminary analyses show an agreement of 0.86 when the accelerometer is compared to the Datawell Mark II sensor. In our projected analyses we propose to:

- Correct the acceleration values from the buoy for buoy attitude (i.e., normalise the output so that the effect of the roll and pitch angles of the buoy are removed from the accelerometer output).

- Investigate the relationship between the corrected wave heights and the degree to which the two sensors give comparable results.

5.1.2 Scalar vs Vector Winds

- Since the vector analysis is affected by the degree in variation of the wind direction, we will look at this parameter and how it varies with wave height. The justification that the error is small (Gilhousen, 1987) can be determined for increasing wave heights. This will enable users of the wind data to assess the size of the error introduced by the vector average.

5.1.3 Effect of Wave Height on Wind Measurement

We can see from the preliminary analyses of time series (Figure 9) from the November 4th storm that the instantaneous wind speed varies greatly between peak and trough. We propose to:

- Correct the reported wind speed for buoy motion, so that the true wind speed is determined;

- We will average the wind speeds over the peaks separately from over the troughs. We will vary the length of each average period from, say, 2 sec to 4 sec for different wave height regimes and wind directions.

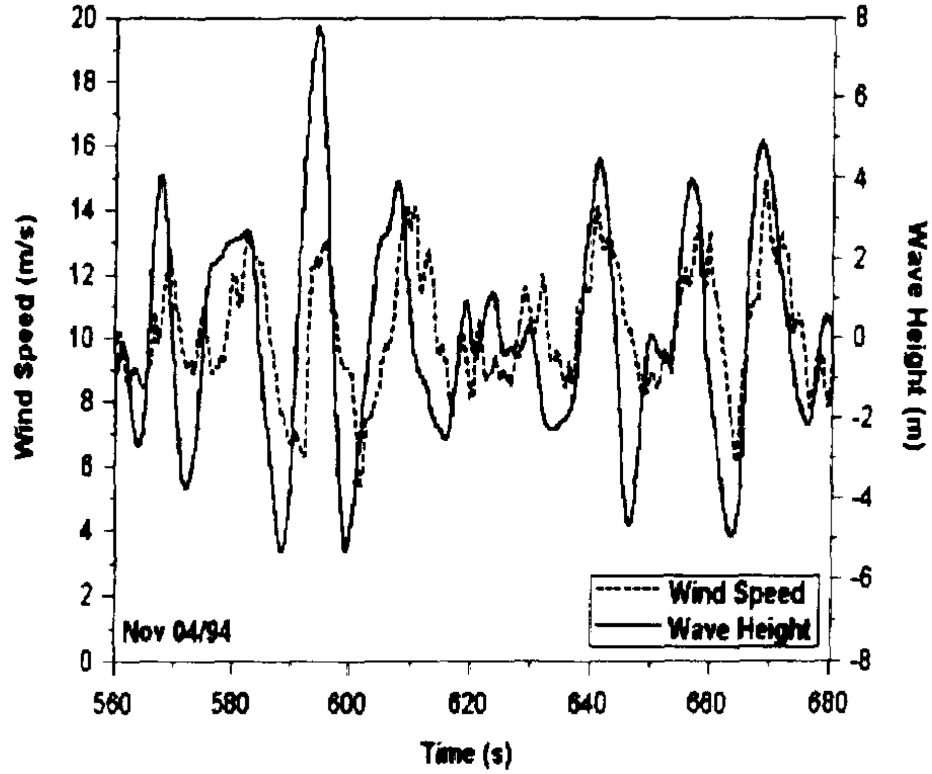

Figure 9a.

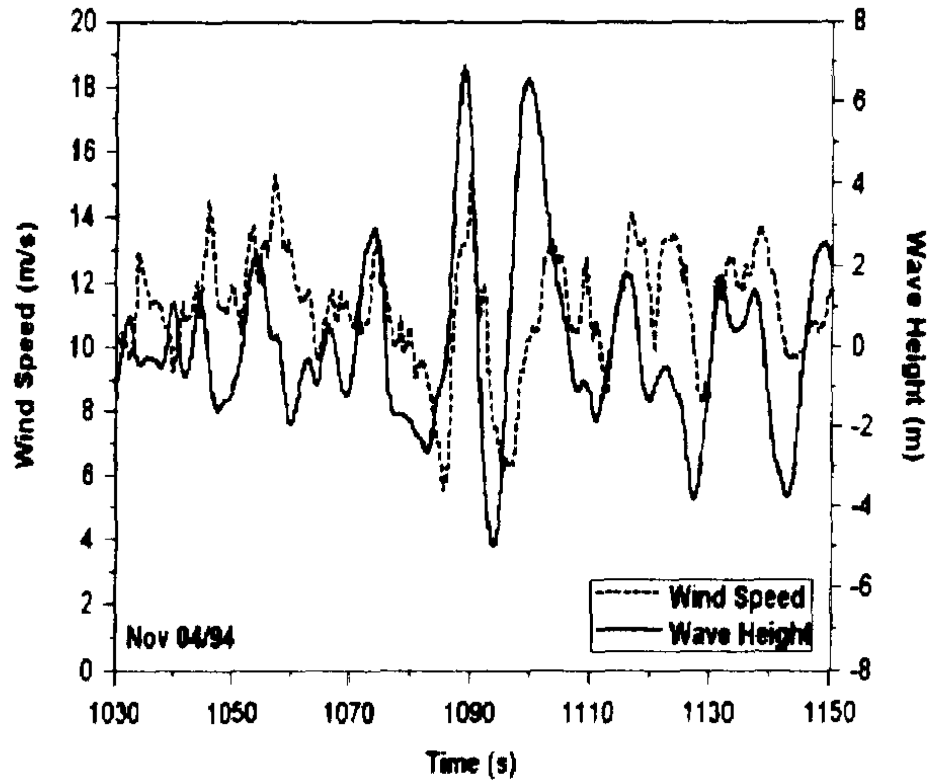

Figure 9b.

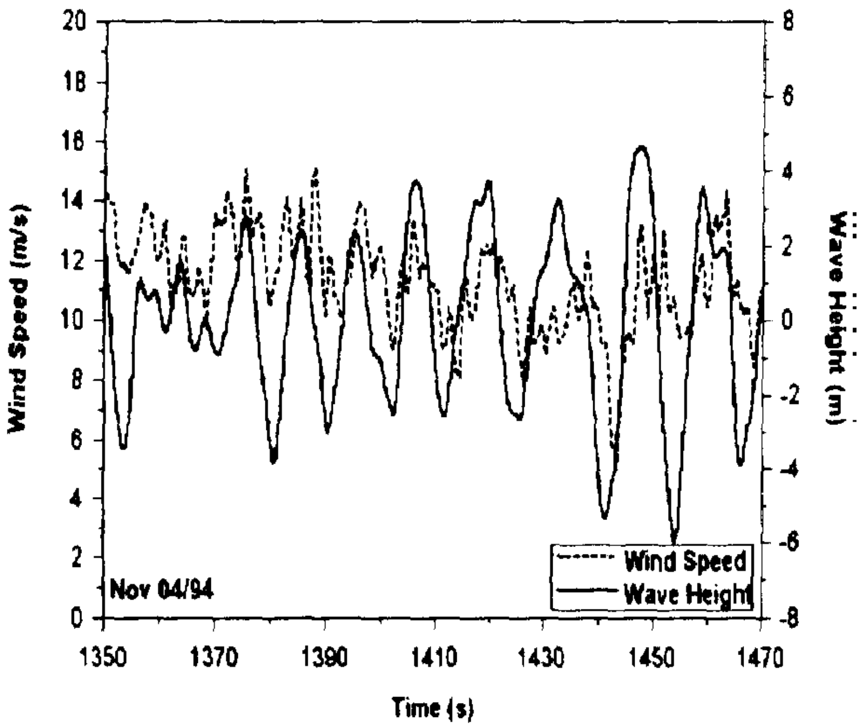

Figure 9c.

6. SUMMARY AND RECOMMENDATIONS

6.1 Summary

The data from the SWS-1 platform, gathered during an eight-month deployment, have been recovered and a preliminary analysis has been carried out for (i) an intercomparison between the gimbaled vs non-gimbaled wave sensors, (ii) a gust analysis, (iii) effects of wave height on wind speed measurements, and (iv) measurement of air temperature.

The preliminary results indicate:

- Values from the strap-down accelerometer, uncorrected for pitch and roll, are consistently about 10% to 15% lower than the Datawell values in all sea conditions.

- The gust factors have a direct relationship with seastate conditions, the 8-sec gust being about 1.3 times the mean wind speed in high seastate conditions and reducing to 1.2 in calmer conditions.

- In the time series shown, the wind speeds measured at the peak of the waves is noticeably higher than that in the troughs. This is particularly true for the high seastate conditions in the November 4 storm where the wind speed varies between 14 m/s and 6 m/s.

- Wind direction measurements also show considerable change with seastate condition. In the high seastates of the November storm the variation is over 120°. This drops to about 70° for the December storm, and 40° for the March storm. However these large variations did not have the expected impacts on the difference between the reported vector and scalar wind speeds (see Table 2). Further analysis of the SWS-1 high frequency data will provide more insight into the magnitude of these differences.

- Buoy heading variations are also dependent on seastate conditions, and vary between 70° for high seastates and 15° for low seastates.

- An unexpected rapid variation in air temperature in high seastate conditions may be due to highly variable conditions within the radiation shield.

- The data indicate that in high seastate conditions there is great variability both in wind speed and direction and that the use of averaged data masks events that may affect the climatological and operational use of the data.

6.2 Recommendations

Because the analysis of the SWS-1 data is not yet completed, firm recommendations are not possible. However, from the preliminary results we conclude that the following further research may be beneficial:

- Adapt SWS-1 for a 3m Discus buoy;
- Include directional wave sensors on the buoy;
- Improve the mooring strain recording devices;
- Independent measure of winds and maybe waves as well. This would pre-suppose that the buoy be moored close to an offshore platform. This would provide a ground truth calibration that is not possible for a buoy moored at a remote location on its own.

The proposed program by the NDBC at the Texaco "Harvest" field off the Californian coast during the winter of 1995 (October 1995: Pers Corn. Teng, NDBC) may address some of these suggestions.

7. REFERENCES

Skey, S.G.P., K.C. Heidorn, S. Jarvin and V.R. Swail. 1993. "The measurement of wind speed in high seas by meteorological buoys". Proc. Oceans '93, Vol II, pp. 100-104.

Gilhousen, D.B. 1987. "A field evaluation of NDBC moored buoy winds." J. Atmos. Ocean. Technol., 4:94-104.

Teng, C. 1995. "NDBC Directional Wave buoy supports the DUCK94 field experiment." NDBC Tech. Bull. Vol. 21, No. 1, 1995.

USE OF RADARSAT SAR FOR OBSERVATIONS OF OCEAN WINDS AND WAVES: VALIDATION WITH ERS-1 SAR AND SIR-C/X-SAR

Fred W. Dobson[1], Paris W. Vachon[2], and R. J. Anderson[1]

[1.] Ocean Sciences Division,
Dept. of Fisheries and Oceans,
Bedford Institute of Oceanography,
P.O. Box 1006, Dartmouth, NS, B2Y 4A2

[2.] Canada Centre for Remote Sensing,
588 Booth Street,
Ottawa, ON, K1A 0Y7

1. INTRODUCTION

Over the past four years a series of field experiments have been conducted in the area of the Grand Banks of Newfoundland with the general purpose of comparing *in situ* measurements of sea surface parameters associated with winds and waves with coincident measurements of radar backscatter by Synthetic Aperture Radar (SAR). The experiments were the Grand Banks ERS-1 SAR Wave Spectra Calibration and Validation Experiment (ERS-1 Cal/Val or Cal/Val henceforth) (Dobson & Vachon, 1994), the second Canadian Atlantic Storms Programme (henceforth CASP-II), (Smith et al, 1994), the Gulf of St. Lawrence Shuttle Imaging Radar Experiment (henceforth SIR-C/X-SAR) (Vachon et al, 1995), and the Sea Truth and Radar Systems Experiment (henceforth STARS '94).

We are using the ERS-1 Cal/Val, CASP-II, SIR-C/X-SAR and STARS '94 field experiments to compare in situ (ship + buoy) wind vectors with normalized radar backscatter from SAR images containing the in situ measurements. The SARs considered include the ERS-1 Advanced Microwave Imager (AMI) SAR mode and Canada Centre for Remote Sensing Convair 580 (CCRS CV-580) SAR for the ERS-1 Cal/Val, CASP-II and STARS '94 experiments and the NASA C-and L-band SARs and the DLR X-SAR for SIR-C/X-SAR. The combination of the four experiments gives us a useful number of SAR image - in situ ship measurement collocations for statistical reliability.

The purpose of this presentation is to demonstrate that useful quantitative sea surface information is available from spaceborne SAR such as Canada's RADARSAT, scheduled for launch in October 1995 - when assimilated into a numerical wind-wave forecast model which has been designed to use it. We begin with a validation of the ERS-1 SAR as a sensor of wind velocity. Under some circumstances it is possible to retrieve the wind vector (Vachon & Dobson, 1995b). The wind speed retrieval is based upon the CMOD4 C-band VV polarization scatterometer wind speed models (see eg. Stoffelen & Anderson, 1994) while the wind direction estimate (with a 180° ambiguity) is estimated by noting that the large-scale structures in the SAR images tend to align themselves with the wind (Gerling, 1986).

We then demonstrate how the direction of wave propagation can be resolved from SAR data by processing individual look cross spectra. The cross spectrum technique is based upon the concept that each look represents a slightly different observation time (Vachon & Raney, 1991). The cross spectrum accounts for this, allowing resolution of the propagation direction as well as elimination of speckle noise in the image spectrum (Engen & Johnsen, 1995). SAR image cross spectra have been calculated for the ERS-1 SAR (Engen & Johnsen, 1995), and for SIR-C/X-SAR (Vachon et al, 1995). In principle, these directionally-resolved SAR image spectra may be autonomously inverted to directional wave spectra and assimilated into a wave forecast model.

We first describe in Section 2 how these techniques might be combined and used in a coupled numerical marine wind and wave forecast model to provide estimates of wind stress and sea state from a SAR system like RADARSAT. We then describe in Sections 3 & 4 the field validations which make such a combination feasible.

2. ASSIMILATION OF SAR DATA IN COUPLED WIND-WAVE MODELS

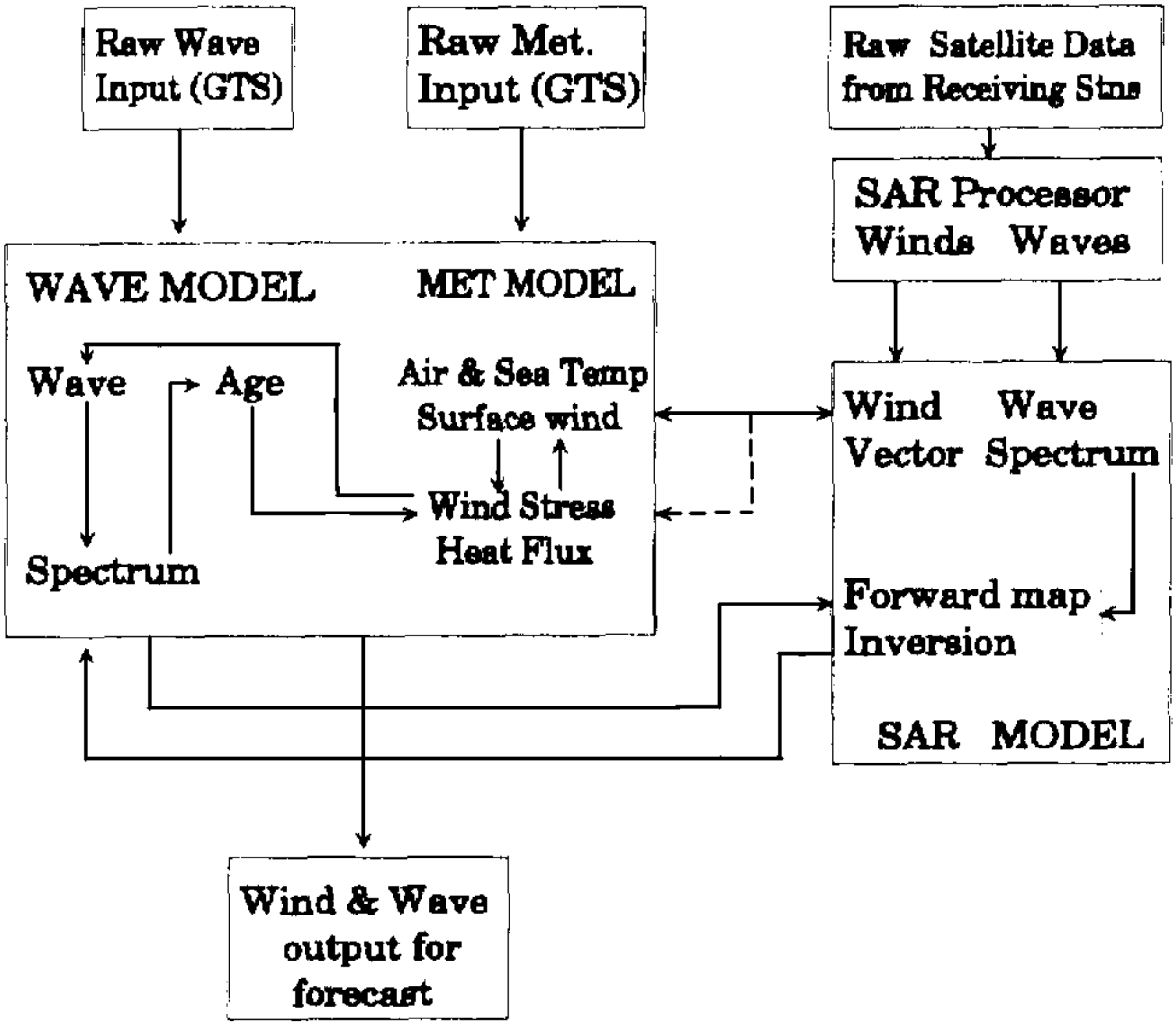

Figure 1. Schema of coupled numerical meteorological and wave forcast model system capable of using sea surface data from a satellite–borne SAR to its fullest potential. Raw data inputs are at the top and the final outputs for the forecast are at the bottom. Such a system would provide a forecast for the marine conditions and the waves at a predetermined set of grid points over the sea at a set of forecast times, usually spaced at 12 hour intervals. Arrows in both directions indicate iterative procedures, solved at each time step of the model. The dotted arrow from the SAR model to the Meteorological model wind stress is feasible but not yet validated. The heat flux is not well–determined by the system: it is a secondary parameter in the wind stress–wave age iteration, and can be used in determining the wind speed from SAR data in low–wind conditions. The SAR processor is located at the receiving station; the SAR model is incorporated in the coupled forecast model.

A schema (Figure 1) indicates the complex set of pathways involved in the assimilation of SAR data in operational forecast models. As they stand now, it is only the meteorological models which make significant use of data up to forecast time: the wave models, lacking all but the crudest wave data (visual sea state estimates from an extremely sparsely distributed set of ships), are initially "spun up" from a small, uniform wave field for 48 hours using forecast winds, and thereafter are initialized with the last forecast. It is therefore expected that the SAR wave data will have the greatest influence on the initialization of the wave model. This influence, if it modifies the waves forecast at a given grid point of the wave model, carries meaning for the meteorological model: the winds are inconsistent with the observed waves. The simplest solution (to ignore that meaning and not correct the model winds) leads to a rapid decay - typically one timestep - of the usefulness of the SAR wave measurement.

The problem can be dealt with in three independent ways. First, if the SAR wave spectrum contains no direction ambiguity (and there is output for presently no existing SAR system capable of performing the interlock cross spectra which remove the ambiguity) then the SAR spectrum can be given much more weight than is presently possible. The reason for this is simple: if it is necessary for the model to resolve the SAR wave direction ambiguity, then the model must perforce throw away all SAR wave information where any uncertainty at all exists that the wrong branch of the ambiguity might be chosen. Otherwise, the assimilation of the SAR data becomes pathological, introducing larger errors than existed in its absence. Second, if the model wind stress is constrained by a built-in relationship between wind stress and the state of development of the waves (see the other papers in this session), then the SAR measurements' influence is preserved in as far as the wind stress so constrained is made consistent with the meteorological model's wind stress computation scheme. Third, if the SAR provides a wind to the meteorological model during its initialization, and if the model's wind prediction is assimilated and made compatible with the SAR-measured wave spectrum, then the wind-wave coupling in the models is strengthened and optimum use can be made of both the SAR winds and the SAR waves.

3. THE FIELD EXPERIMENTS

The ERS-1 SAR Calibration and Validation Experiment (Cal/Val) took place in the Virgin Rocks area of the Grand Banks from November 10-24, 1991 (Dobson & Vachon, 1994). The principal goals of the experiment were to use a combination of in situ wave and meteorological measurements from ships and buoys, SAR measurements from aircraft and satellites, and numerical modelling of the winds and waves, to provide an in-depth look at the relationship between conditions at the sea surface and the images produced by radars viewing the same sea surface at the same time. A total of 12 overpasses of the ERS-1 SAR, 7 of the CCRS CV-580 SAR, and one overpass of the (then) USSR "Almaz" SAR over the CSS "Hudson" location were analyzed. The results have been published in a Special Issue of the journal ATMOSPHERE-OCEAN (Volume **32**(1), 1994): they include a validation of a technique for extracting wave height and wind speed from a comparison of expected and observed SAR wave spectrum azimuth cutoff wavenumbers (Vachon et al, 1994) and an exposition of several SAR wave inversion schemes (in particular Krogstad et al, 1993).

The second Canadian Atlantic Storms Programme (CASP-II: see Smith et al, 1994) included a field programme on the Grand Banks from May 8-25, 1992. A meteorological buoy (Coastal Climate "Minimet") was moored in the Hibernia area of the Grand Banks, near 47° 20' N, 48° 25' W. A total of four overflights of the ship CSS "Hudson" - were made with the CCRS CV-580 C-band SAR, three of which were coincident with ERS-1 SAR overpasses. In each of the three a comparison is available among the aircraft SAR, the ERS-1 C-band SAR and an in situ wind vector from either the Minimet buoy or the ship. Directional wave spectra are also available from a "Wavec" buoy deployed from the ship, and surface current measurements are available from an "Ametek-Straza" acoustic Doppler current profiler (ADCP) mounted on the ship.

The Gulf of St. Lawrence SIR-C/X-SAR Experiment (Vachon et al, 1995a) took place from October 1-7, 1994 in conjunction with the second NASA Space Shuttle SAR Experiment (SRL-2). Meteorological and directional wave measurement buoys were placed 24 km south of the southern tip of the Isles de la Madeleine; in situ measurements were made during 6 overpasses of the Space Shuttle L-, C- and X-band SAR systems. The data are still being analyzed; SAR-wave spectrum coincidences are being used to extend the existing (ie CMOD4) C-band VV polarization scatterometer wind retrieval models for use with SAR images to other SAR frequencies and polarizations.

The Grand Banks 1994 Radar Validation Experiment (STARS '94) took place on the southeastern Grand Banks from 1-6 December, 1994. As with the other experiments, in situ meteorological and directional wave buoys were deployed from CSS "Parizeau" and their results compared with the SAR imagery from the CCRS CV-580 and ERS-1 C-band SARs. The CV-580 overpasses were made on Dec 3, 4 and 6, and the ERS-1 overpasses with concurrent in situ and aircraft data were on Dec 3 and 4.

4. VALIDATION OF THE SAR AS A SENSOR OF THE MARINE WIND VECTOR

For moderate incidence angles, Bragg scattering is the dominant microwave backscatter mechanism from the ocean surface at C-band (5.7

cm radar wavelength). A measure of the magnitude of the backscatter is the radar cross section σo, which is dependent upon the amplitude of the Bragg-scale waves which in turn may be affected by many ocean processes such as wave-wave interaction, wave-current interaction, and wind stress. It is usually assumed that the dominant influence on the radar cross section is the wind stress.

In the context of ocean scatterometery, many empirical models have been developed which relate the expected radar cross section (for a particular radar frequency and polarization) to the wind stress (usually represented as an empirical drag coefficient times the square of the neutral-stability wind speed at 10 m height) and the radar geometry (specifically, the incidence angle and the angle between the antenna look direction and the wind vector.)

Recently, there has been considerable interest in the ERS-1 C-band VV polarization scatterometer. The ERS-1 scatterometer CMOD (C-band Model) wind retrieval models have evolved over the years. Currently, CMOD4 (Stoffelen & Anderson, 1994) is used operationally for ERS-1 scatterometer wind retrieval.

There also exists the potential to extract the wind speed directly from SAR images. This potential role of SAR as an imaging scatterometer requires that the following three issues be addressed: first, the SAR images must be calibrated; second, there must exist a model which relates the radar cross section derived from the SAR image to the wind speed and geometry; and third, the angle between the look direction and the wind vector must be known.

In the case of the ERS-1 SAR, the first issue has been fulfilled since the system has been shown to be radiometrically stable to within 0.2 dB over several years of operation. Also, corrections for analogue to digital converter (ADC) saturation (which is important for a distributed target with large radar cross section, such as the ocean surface for moderate to high wind speeds) have been developed (Laur et al, 1993).

We propose that the requirement for a wind retrieval model may be met for the C-band VV polarization ERS-1 SAR by using the CMOD4 model. This model requires the assumption that the radar cross section over the ocean is only influenced by local changes in wind speed and direction. The wind direction is the more difficult parameter to obtain, but as a worst case, it could come from a surface analysis chart, and as a best case, it could be derived from the long-wavelength structure in the SAR image (Gerling, 1986).

In Figure 2 , we present a validation of wind vector extraction from ERS-1 SAR images. We compare the radar cross section derived from

ERS-1 SAR images with that predicted by CMOD4 when driven by accurate in situ wind vector measurements. The data are from the ERS-1 Cal/Val and STARS '94 programs. On the left side there is good agreement between the observed and modelled σo in each of the 12 cases considered. We have found that, for wind speeds > 4 m/s, the ADC power loss correction is essential.

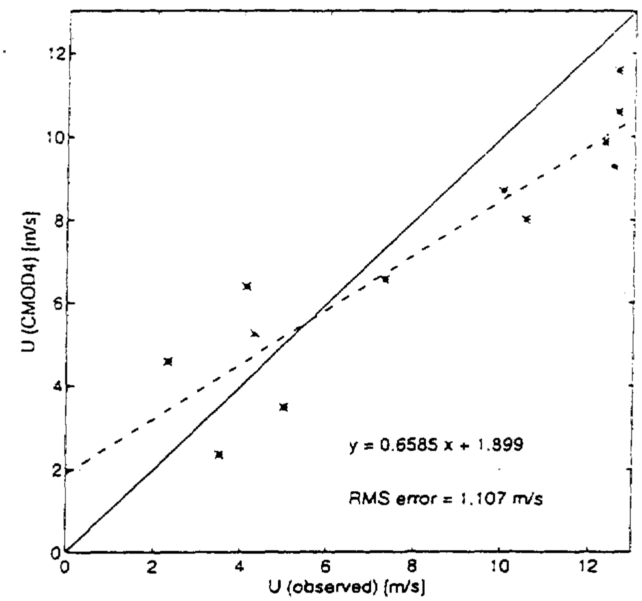

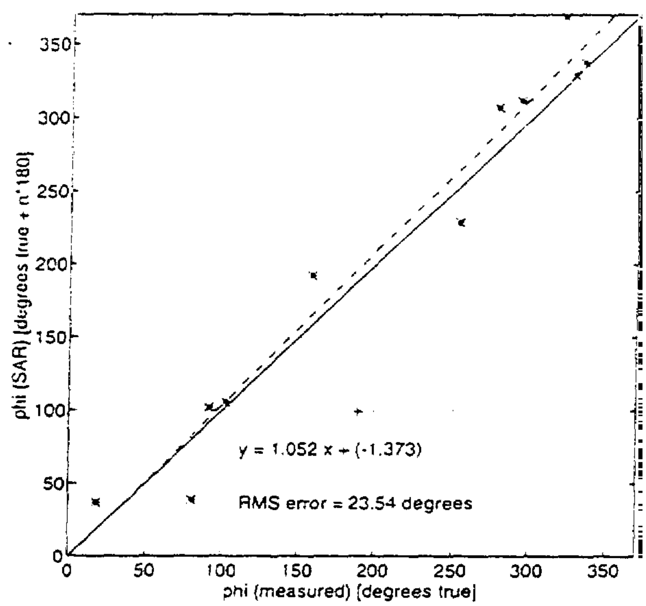

Figure 2 (Left). Validation of wind vector retrieval from ERS-1 SAR images. The figure above shows a regression of estimated radar cross section based upon *in situ* measured wind vector against measured radar cross section from the ERS-1 SAR image after correction for analogue to digital converter saturation powerloss. The figure on the right shows a regression of the *in situ* measured wind direction against the wind direction estimated from the low wavnumber portion of the SAR image spectrum (after correcting for the 180° direction ambiguity by adding multiple of 180°.)

Figure 2 (Right)

Under some circumstances, it is possible to extract the wind direction directly from the SAR image based upon the orientation of the large-scale image structure, under the assumption that such structure is caused by boundary-layer rolls. On the right side of the figure we have plotted the regression of SAR-derived wind direction against the measured wind direction. If we ignore the outlying point of 15 Nov. 1991 (the low-wavenumber spectrum was very nearly symmetrical for this low wind speed case), the RMS wind direction error is less than 24 degrees.

Although the SAR-derived wind direction is less robust than the SAR-derived wind speed, we have demonstrated the feasibility of extracting wind vectors from SAR images over the ocean. This validates the role of SAR as an imaging scatterometer and affirms quantitative use of ERS-1 SAR imagery to study kilometer-scale secondary atmospheric flow phenomena over the ocean by deriving their associated surface wind speed modulation using CMOD4.

It should also be feasible to operationally extract wind vectors from C-band HH polarization SAR images such as those from RADARSAT. This should be a simpler exercise than for ERS-1 since RADARSAT data will be operationally calibrated. Furthermore, RADARSAT will have an automatic gain control which will eliminate the requirement for the ADC saturation correction. On the other hand, there is not, so far, a well-developed wind retrieval model for a C-band HH polarization radar. An essential aspect of the RADARSAT validation activities will be the development of such a model based upon validation data sets such as those we have acquired in the field programs analyzed in this paper.

5. RESOLUTION OF THE SAR WAVE DIRECTION AMBIGUITY

The conventional approach to calculation of a SAR image spectrum starts from a multiple look SAR image of the ocean surface, with the looks already summed. In this case, the effect of speckle noise is being reduced by the multiple look processing, at the expense of degraded spatial resolution. However, with spacecraft SARs flown to date, the effects of speckle noise cannot be eliminated. Thus, the estimated SAR image spectrum is characterised by a broadband noise spectrum due to the image speckle. This speckle spectrum must be properly compensated. Furthermore, it is known that the individual looks, formed by bandpass filtering the Doppler spectrum, essentially correspond to images of the scene taken at discrete intervals of time. Since the waves move with time, the direction of wave travel should be resolvable if the individual looks are suitably processed. Some processing scenarios are presented by Vachon & Raney (1991).

More recently, it has been shown (Engen & Johnsen, 1995) that the individual look cross spectrum can overcome both of these problems simultaneously. If the individual looks are processed such that they are from statistically independent parts of the Doppler spectrum, then each look has statistically independent speckle noise, which cannot appear in the cross spectrum. Also, since the wave images may propagate between looks, there will be a phase shift associated with the cross spectral energy for each wave mode imaged. The sign of the phase shift determines the wave mode which is propagating in the correct direction.

The key requirement for resolution of wave propagation direction is that the SAR integration time be long enough to observe a measurable wave movement. Thus, longer wavelength, higher altitude SARs will provide better wave direction information. Resolution of wave propagation direction is possible for low altitude SIR-C/X-SAR, L-band data and similarly for ERS-1 higher altitude C-band data. However, even if resolution of the propagation direction is not possible (as is the case for SIR-C/X-SAR C-band and X-band data) the removal of the speckle noise spectrum is still an advantage of this technique.

In Figure 3 , we present examples of image spectra and cross spectra for ERS-1 and SIR-C/X-SAR L-band data. In each case, we started from a single look complex image and band pass filtered and detected the complex image to produce the individual looks for cross spectral analysis.

Autonomous inversion (ie without any other outside information such as a first guess wave spectrum) of these cross spectra is possible. A methodology has been proposed by Engen & Johnsen (1995) as an extension of the Hasselmann & Hasselmann (1991) SAR image spectrum inversion formalism.

Furthermore, the speckle-free image spectra so derived present an ideal starting point for the estimation of the real aperture radar modulation transfer function (the contributions of local tilting and hydrodynamic straining) to the SAR ocean wave imaging process.

6. DISCUSSION

We have demonstrated that, with proper processing, a SAR can provide, at the location of each SAR image acquired, independent estimates of:

1. the wind speed (if the SAR is well-calibrated, not subject to ADC saturation powerless, and a suitable wind retrieval model exists),

2. the wind direction, subject to a 180° ambiguity which must be resolved with independent information (if the long scale structure present in the SAR image can be related to the wind direction), and

3. A calibrated and fully (directionally) resolved wave directional spectrum (that is, in m2/Hz/radian) at all vector

wavenumbers less than an ”azimuth cutoff” wavenumber associated with the geometry of the SAR and its satellite (the azimuth cutoff plagues all SARs with a large range-to-velocity ratio: useful information outside of the passband cannot be retrieved).

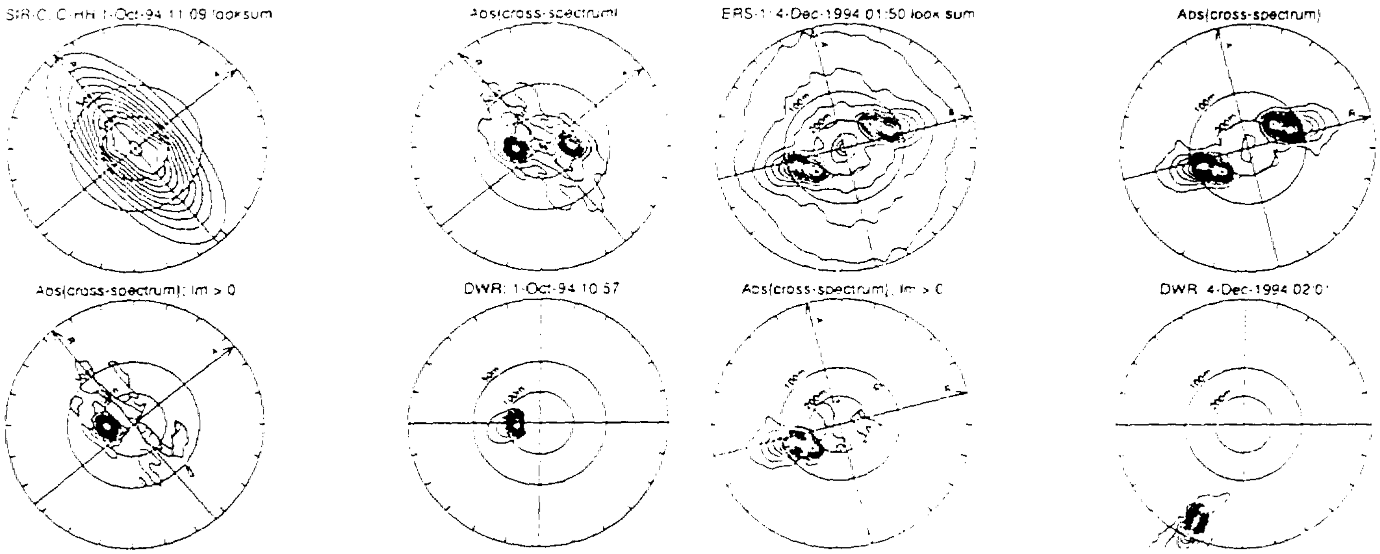

Figure 3. Examples of SAR image cross spectra from (a, left) SIR-C/X-SAR (C-band HH mode) and (b, right) ERS-1 SAR (from STARS '94). In each case, the spectrum in the upper left is the conventional multi-look SAR image spectrum. Note the broadband noise associated with the speckle contribution to the image spectrum. The spectrum in the upper right is the magnitude of the cross spectrum. The cross spectrum is largely immune from the speckle noise of the multi-look SAR image spectrum. The spectrum in the lower left is those portions of the cross spectrum which have positive phase (i.e. are propagating in their true direction). The emphasized peak is the correct one of the otherwise ambiguous pair. The spectrum in the lower right is the collocated directional wave rider (DWR) spectrum. Comparing the lower spectra illustrates that the wave propagation direction has been correctly resolved in the two cross spectra. For each spectrum, north is up, A is the azimuth (velocity vector) direction, and R is the range direction. Circles of constant wavelength are plotted and labelled. Note that there is good agreement between wavelength and direction from the SAR and DWR for the low altitude SIR-C/X-SAR spectrum (R/V = 32 s), but the agreement is rather poorer for the higher altitude ERS-1 spectrum (R/V = 115 s) due to its more severe azimuth cutoff.

Figure 3b (Right)

6.1 Model Assimilation of SAR Wave Image Spectra

Such information appears at first blush ideally suited for assimilation in a wave forecast model (see e.g. Figure 1 and Dobson, 1995): normally such models begin with a smooth sea or at best with the last valid forecast field. The model wind field (converted by a bulk formula to wind stress or friction velocity) is then applied to forecast the wave field at the next time step, allowing any residual swell to propagate with the dispersion relation and very little damping. The SAR information allows the insertion of measurements, at least at the SAR acquisition locations, which can be assimilated and in the process used to evaluate the model predictions of winds and waves at the SAR locations.

Past attempts at utilizing the SAR information have been severely limited by four important considerations:

a) the SAR information is only available for any given forecast hour at a small fraction of the total number of model grid points,

b) model-SAR differences are difficult to handle realistically, because giving the SAR spectra too much weight in the data assimilation procedure leads to pathological model behaviour (adjacent model spectra are forced to be dynamically incompatible with both the model input winds and with the model's wave field),

c) SAR observations assimilated at one place and time lose their influence very quickly (the next time step) if the model winds used to predict the waves are inconsistent with the SAR measurements,

and

d) information from satellite-borne SARs is limited by the SAR imaging geometry to only the larger wavenumbers, so that for a typical polar-orbiting spaceborne SAR, except in the range direction, waves with lengths less than about 100 meters (periods < 8 sec) are not imaged at all.

Consideration c) is a very difficult matter for the modellers because the model winds are computed from the model pressure field (via the geostrophic relation), and applying corrections based on the SAR wind and wave measurements means correcting the model pressure field, with only one isolated set of surface measurements. Practically speaking, d) limits satellite-borne SARs to the longer-wavelength swell components except in very special circumstances (storms producing long-wavelength seas and/or wind seas travelling in the SAR range direction).

At the end, it is worth noting that the SAR, which provides accurate information on the longer-wavelength components of the waves (ie swell), is an excellent complement to the model, which predicts the wind sea best (often swell from locations where there are no meteorological data is missed completely).

7. THE POTENTIAL OF RADARSAT

We have demonstrated the type of ocean surface information which is available from a SAR and discussed how such information might be used in conjunction with an operational coupled wind/wave forecast model. In principle, this sort of information will be available from RADARSAT SAR images. RADARSAT will carry an operationally calibrated C-band HH polarization SAR instrument.

Unfortunately, we need to attach a number of caveats to this assertion:

1) With respect to wind speed retrieval, there does not exist, so far, a C-band HH polarization wind retrieval model (such as CMOD4 which exists for C-band VV polarizations). Development of such a model will be a necessary element of early post-launch RADARSAT validation objectives.

2) With respect to resolution of the wave propagation direction, the performance of RADARSAT "standard beam 1" (see Raney, 1995) images should be similar to that of ERS-1 (having similar resolution and range-to-velocity ratio). For larger incidence angle beams (hence range-to-velocity ratios) the directional resolution ability should improve. However, this is in direct conflict with an increased degree of azimuth cutoff (information on shorter wavelengths is lost). RADARSAT "standard beam 1" is likely the best compromise between allowing the ability to resolve the wave propagation direction and minimising the degree of azimuth cutoff. Selection of the best RADARSAT beam mode for wave observation will also be an important validation program objective.

8. CONCLUSIONS

1. Spaceborne SAR, if processed knowledgeably at source, can provide marine forecast models with much of the information they need to base real-time operational forecasts on measured data in the open ocean.

2. The principal problems to be overcome are

a) resolving the wind direction ambiguity,

b) determining the best form for the wind-wave coupling term (see the Sessions dealing with the topic at this meeting),

c) determining the optimum weights to apply to the model and the SAR image wave spectra when performing the inversion,

d) estimating the real wave spectrum in areas where the SAR provides no data (outside the azimuth cutoff wavenumber in each SAR image spectrum, and outside the physical area containing data from current SAR satellite passes),

e) assimilating SAR surface winds in the marine forecast model.

3. RADARSAT should be capable of supplying this type of information on a routine basis, following a successful validation program.

9. REFERENCES

Dobson, F.W., 1995: The Simultaneous Assimilation of Satellite Radar Data in Coupled Wind and Wave Forecast Models, In Oceanographic Applications of Remote Sensing, Eds. M. Ikeda and F. Dobson. CRC Press, 512 pp.

Dobson, F.W. and P.W. Vachon, 1994: The Grand Banks ERS-1 SAR Wave Spectra Validation Experiment: Program Overview and Data Summary. Atmosphere-Ocean, **32**(1), 7-29.

Engen, G., and H. Johnsen, 1995: Analysis and Inversion of ERS-1 Image Cross-Spectra, Proc. IGARSS 1995, 1863-1865.

Gerling, T.W., 1986: Structure of the surface wind field from the Seasat SAR. J. Geophys. Res. **91**(C2), 2308-2320.

Hasselmann, K. and S. Hasselmann, 1991: On the nonlinear mapping of an ocean wave spectrum into a SAR image spectrum and its inversion. J. Geophys. Res. **96**(C6), 10,713-10,729.

Laur, H., P. Meadows, J.I. Sanchez, and E. Dwyer, 1993: ERS-1 SAR radiometric calibration. Proc. CEOS SAR Calibration Workshop, 20-24 September 1993, ESTEC, Noordwijk, The Netherlands, **ESA WPP-048**, 257-281.

Krogstad, H.E., O. Samset and P.W. Vachon, 1994: Generalizations of the Nonlinear Ocean-SAR Transform and a Simplified SAR Inversion Algorithm. Atmosphere-Ocean **32**(1), 61-82.

Raney, R.K., 1995: SAR Systems, In Oceanographic Applications of Remote Sensing, Eds. M. Ikeda and F. Dobson. CRC Press, 512 pp.

Smith, P.C., C.L. Tang, J.1. MacPherson and R.F. McKenna, 1994: Investigating the Marginal Ice Zone on the Newfoundland Continental Shelf. Eos, Trans. Amer. Geophys. Union **75**(6), 57, 60-62.

Stoffelen, A. and D.L.T. Anderson, 1993, ERS-1 scatterometer data characteristics and wind retrieval skill. Adv. Space Res., **13**, 553-560.

Vachon, P.W., and R.K. Raney, 1995: Resolution of the ocean wave propagation direction in SAR Imagery. IEEE Trans. Geoscience Rem. Sens., 29(1), 105-112.

Vachon, P.W., H.E. Krogstad and J.S. Patterson, 1994: Airborne and Spaceborne SAR Observations of Ocean Waves. Atmosphere-Ocean **32**(1), 83-112.

Vachon. P.W., F.W. Dobson and R. Lalbeharry, 1995a: SIR-C/X-SAR Wind and Wave Observations in the Gulf of St. Lawrence. Proc. IGARSS 1995, 1314-1316.

Vachon, P.W. and F.W. Dobson, 1995b: Validation of Wind Vector Retrieval from ERS-1 SAR Images over the Ocean. The Global Atmosphere-Ocean System, MS submitted April 1995.

4th International Workshop on Wave Hindcasting & Forecasting

AN EVALUATION OF TWO EXTREME STORM EVENTS IN THE MID-ATLANTIC COASTAL WATERS: MEASUREMENTS AND 3GWAM ASSESSMENT

R. E. Jensen, C. M. Holmes, and C. L. Doiron

USAE Waterways Experiment Station
Coastal Engineering Research Center
Vicksburg, MS 39180-6199

1. INTRODUCTION:

The evolution of an ocean wave spectrum transforms significantly once it enters shallow water. These transformations are based on specific mechanisms: spatially-dependent changes termed shoaling and retraction processes; and time-dependent source/sink terms such as the atmospheric input, nonlinear wave-wave interactions, high-frequency dissipation, bottom effects, and depth-induced spectral breaking. These mechanisms simultaneously act on a spectrum when it enters shallow water. The relative magnitude of each mechanism, its resulting changes in the spectrum, and the time required for the change are not well understood.

In order to study these processes, sufficient high-resolution 1- and 2-D wave spectra are required to adequately investigate the problem. Presently, there are no wave data bases that contain such information on the required scales. A timely large-scale field experiment called DUCK94 occurred at the Field Research Facility (FRF) in Duck, North Carolina from August - October 1994 (Birkemeier, 1994). DUCK94's principal concerns were with sediment transport and quantification of the hydrodynamics in the extreme nearshore region (1-1000 m from shore). Other studies in the overall umbrella of DUCK94 were sponsored by the Coastal Ocean Processes Experiment (CoOP, Butman, 1994), the Office of Naval Research, and the Naval Research Laboratories. These wave measurement programs were commensurate with the spatial and temporal scales required to evaluate shelf zone wave transformation processes.

In the fall of 1994, two unique and extreme storm events took place along the central Atlantic seaboard. These storm scenarios included a large, synoptic-scale northeaster and Hurricane Gordon, which produced measured significant wave heights in excess of 5 and 10 m, respectively. In the nearshore zone, significant wave heights ranged from 4-5 m in a water depth of 8.5 m. These events prove timely due to DUCK94's experiment, and provided a unique set of measurements from which directional spectral transformation studies could be made. Processes including local wind-wave generation, transformation across the shelf, and the interaction between multiple wave systems were studied.

As a counterpart to this study, a third-generation discrete spectral wave model called 3GWAM (Komen et al. 1994) was used in the simulation of these storms. Model output is compared to in-situ measurements for intermediate and shallow-water depths.

2. WAVE MEASUREMENT DEVICES:

Three National Data Buoy Center (NDBC, Steele and Mettlach, 1994) 3 m buoys were selected as the most reliable measurement devices for the water depth requirements in this study (20-40 m). NDBC has been testing their 3m buoys to resolve higher frequency energy (0.475 Hz) beyond what it had historically processed. Longer time series and analysis packages have partitioned the analysis into distinct sector's dependent on the frequency range. This results in the selection of a consistent number of degrees of freedom and does not bias any frequency band or range over a neighboring one. With this new analysis package, accuracy in the wave estimates was vastly improved without increasing the overall data set size.

The three NDBC 3 m buoys were deployed the week of 25 July 1994 and retrieved in late April 1995 (Figure 1). Each of these buoys had a sensor suite which included a Datawell Hippy 40 sensor that measured earth-vertical acceleration, pitch, and roll. The azimuthal angle was measured by two axes of a triaxial magnetometer. Onboard algorithms (enhanced Value Engineered Environmental Payload) as well as the Directional Wave Analyzer were used to estimate the directional wave data and to process the information for transmission via a satellite network (Steele and Mettlach 1993). In addition to the wave measurements, meteorological information such as wind speed, direction, barometric pressure, and air/sea temperatures were analyzed and transmitted. All data were generated on an hourly basis.

Each buoy was outfitted with a Time Series Data Recorder (TSDR) consisting of an optical disk system which continuously self-recorded all wave parameters (15 channels in all) at approximately 1.76 seconds. Meteorological time series were also recorded on the TSDR. Thus, the TSDR showed the ability to identify small-scale temporal features such as wind gustiness, cold air outbreaks, and movement of wind-driven current patterns from the sea surface temperatures. This type of device was successfully used in the Surface Wave Dynamics Experiment (SWADE, Weller et al. 1991). A fourth 3 m directional NDBC buoy was located approximately 90 km directly offshore of the FRF (CERC-44014) and was operational during the DUCK94 field experiment as shown in Figure 1 .

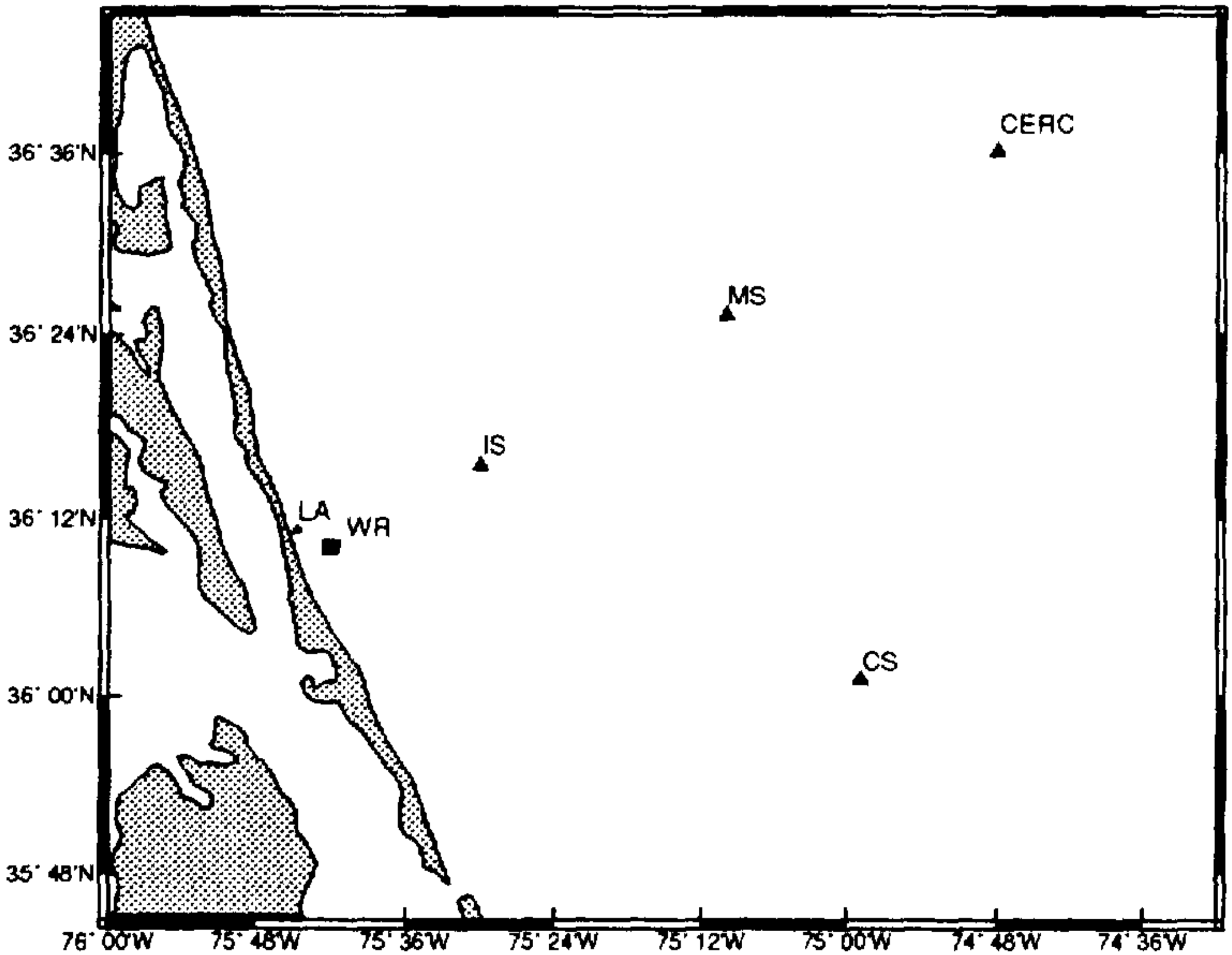

Figure 1. Position of NDBC DUCK94 Buoys (CS-44010, MS-44019, IS-44006, CERC-44014, the FRF waverider WR, and Linear Array LA).

In addition to the four NDBC buoys, the Field Research Facility maintained two measurement devices within 5 km of the shoreline. The Waverider buoy (FRF-WR) was located approximately 5 km from shore in approximately 18 m of water. Frequency spectra were estimated from a double integrated acceleration time series caused by the motions of the free surface. These records were produced every thirty-four minutes. The Linear Array (FRF-LA) consisted of orthogonally bottom-mounted pressure transducers where the shore parallel array was in approximately 8 m water depths (e.g. Long and Ottman-Shay 1991). By employing phase lags of the free surface, high resolution directional spectra were estimated nominally on a three hour basis. In addition to the wave measurement devices, meteorological information such as wind speed, direction (from anemometers atop the FRF building and one located at the end of the FRF pier), barometric pressure, and air/sea temperatures were recorded.

3. DUCK94: IOP-2 METEOROLOGICAL AND WAVE CONDITIONS:

Meteorological conditions varied greatly during the three week period (8 - 22 October 1994) of DUCK94 IOP-2 (Figure 2). In early October a modest low pressure system was accompanied by a warm front which developed south of Cape Hatteras. This system was short lived; however, wind speeds reached 12 m/s and waves peaked slightly above 3 m. Over the next five days, a high pressure system developed. Wave heights diminished to slightly less than 0.5 m.

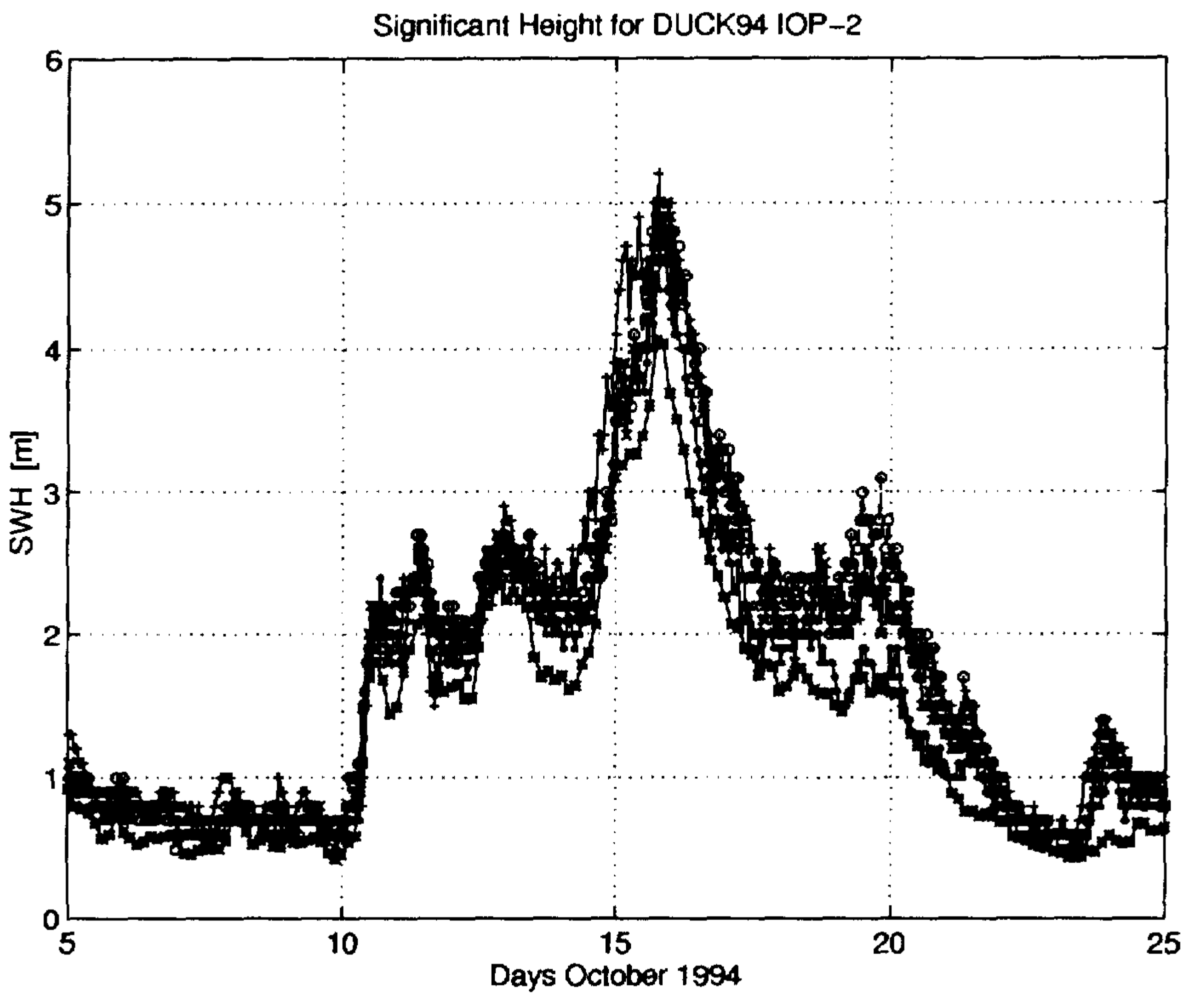

Figure 2. Significant height time plot for DUCK94 buoys IOP-2 storm (-o- 44014, -+- 44010, -x- 44019, -•- 44006, -*- FRF/LA).

A significant storm event dominated the wave environment for nearly a ten-day period much like October storms do in the western Atlantic ocean basin. On 10 October, a cold front passed the FRF bringing with it a five-fold increase in wind speeds in excess of 10 m/s. In addition to the increase in wind speed there was an extreme temperature inversion. The air temperature dropped suddenly creating an unstable thermal boundary layer. Working in concert, these two effects elevated the conditions for wind-wave growth, as indicated by nearly a 1 m increase in wave height at all four buoys. This passage was very rapid (about three hours). These winds continued from the northeast for the next twenty-four hours. During that time, another low pressure center formed in the Carolinas. By 15 October, this storm moved to a position southeast of the FRF with winds in excess of 15 m/s. Wave heights at the four NDBC; buoys peaked at 4.8 m, and a maximum significant wave height of 4.05 m at the linear array. This storm system moved rapidly in a northeasterly direction bringing with it longer period swell waves. It was not until 20 October that significant wave heights were recorded under 2 m, while the weather pattern was dominated by a strong high-pressure center. This persisted for the remainder of IOP-2. Another frontal passage occurred on 27 October. Wind speeds increased from near calm conditions to 12 m/s. This brought wave heights nearing 3 m in the area. This storm had characteristics similar to the 15 October storm; however, it was lower in magnitude and was shorter in duration.

4. HURRICANE GORDON METEOROLOGICAL AND WAVE CONDITIONS

Hurricane Gordon was an extremely complex storm that eventually had a significant impact on the measurement program offshore the FRF. This storm developed north of Panama on 6 November. Ten days later, after traveling through the Caribbean Sea into the Gulf of Mexico and crossing Florida, it entered the Atlantic Ocean north of Vero Beach, Florida around 2200 UTC on 16 November. Wind measurements of 27 m/s were reported. Gordon’s northeasterly motion accelerated on 17 November and strengthened into a hurricane. If this track had been followed, it would have placed Gordon harmlessly out to sea. However, on 18 November the storm slowed and turned in a northerly, then northwesterly, and then west-northwesterly direction threatening the outer banks of North Carolina. A ten-minute average wild speed of 31 m/s was recorded at Diamond Shoals, North Carolina (south of Cape Hatteras) and south of the DUCK94 array. During this twelve-hour period, NDBC buoy 41001 recorded wave heights increasing from 6 m to approximately 11 m, and peak wind speeds of nearly 25 m/s. Within the DUCK94 array similar trends were found. Significant wave heights started at 4-5 m and rapidly increased to 8-10 m as shown in Figure 3 . The wind speed traces did not emulate the wave height traces with a characteristic peak. They did show a broad time period (eighteen-hours or more) of nearly constant 15-18 m/s wind speeds for the offshore buoys CERC, CS, and MS. The IS aid meteorological data at the FRF displayed ±4 m/s variations in wind speed traces, where maxima of 12 and 10 m/s were observed. The only constant in these records was the wind direction where observations at the five locations were between 240-260°. The center of Gordon came within 150 km of the Outer Banks at 1200 UTC on 18 November before turning in a southerly direction. Over the next three days Gordon weakened, and on 20 November it was downgraded to a tropical depression.

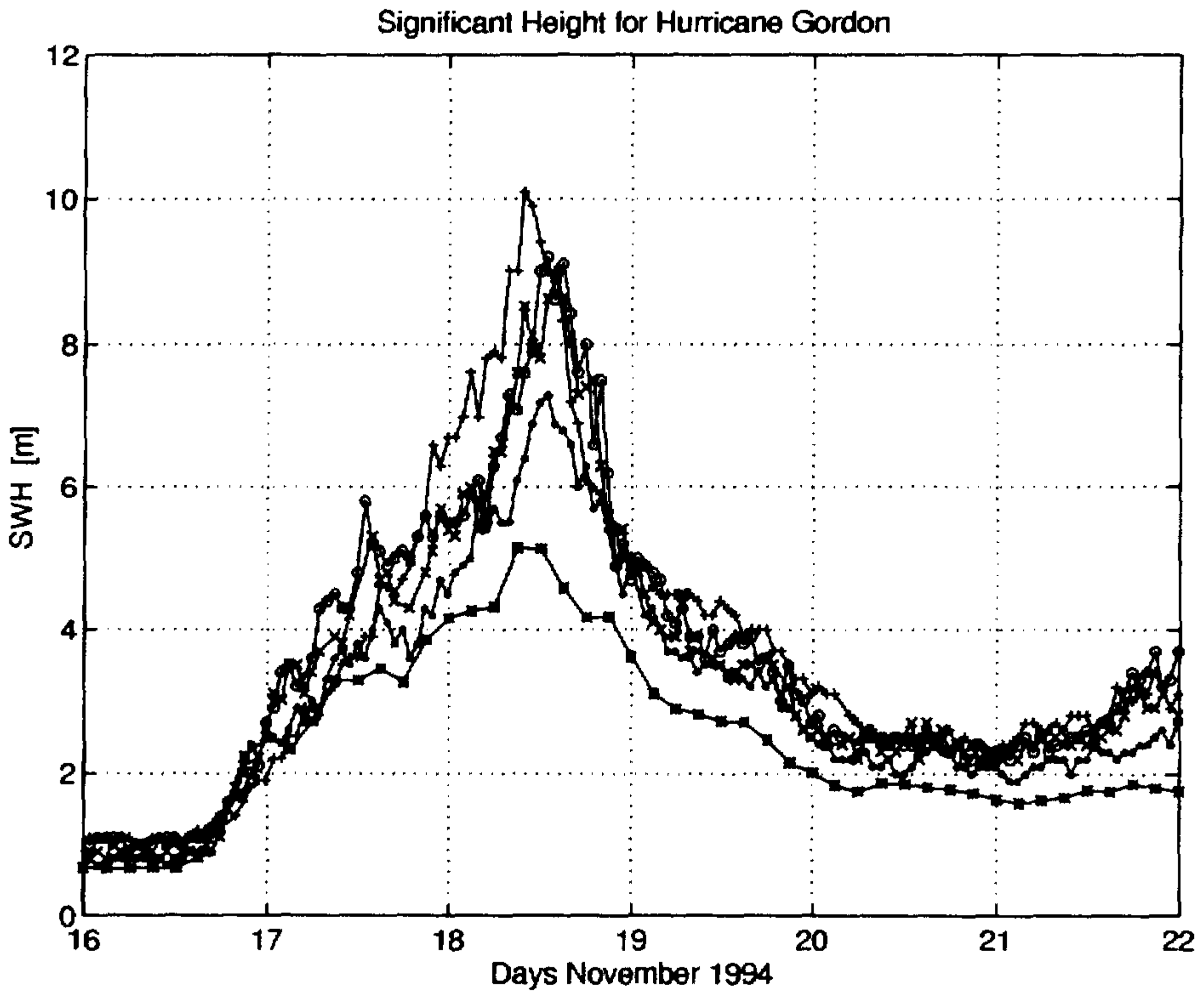

Figure 3. Significant height time plot for Hurricane Gordon (-o- 44014, -+- 44010, -x- 44019, -•- 44006, -*- FRF/LA).

5. ANALYSIS OF STORM IMPACTS

In retrospect, the IOP-2 northeaster and Hurricane Gordon were extreme events, as indicated by comparison of the resulting wave height conditions over the eight-month deployment period (Figure 4). The maximum observed wave heights for the data set at CERC were a result of Gordon. The IOP-2 northeaster was the third-highest event.

These two storms impacted the shelf region offshore of the FRF in a very similar manner. Both storm tracks were comparable as they began off the Florida coastline and rapidly headed in a northerly direction. Gordon and IOP-2 became stationary, imparting wind speeds in excess of 15 m/s for nearly six to twelve hours just offshore of the FRF. Gordon had winds nearly double that of the IOP-2 storm; however, the area impacted was south of Cape Hatteras. The ensuing wave conditions generated from these storms were quite different. IOP-2 brought locally generated wind-seas and the spectra were nearly uni-modal at the peak of the storm. These wave heights scaled more toward the fully developed Pierson-Moskowitz limit (Pierson and Moskowitz, 1964) than the data derived from Hurricane Gordon indicative of swell energy, and plotted to the left of the P-M limit in Figure 4 .

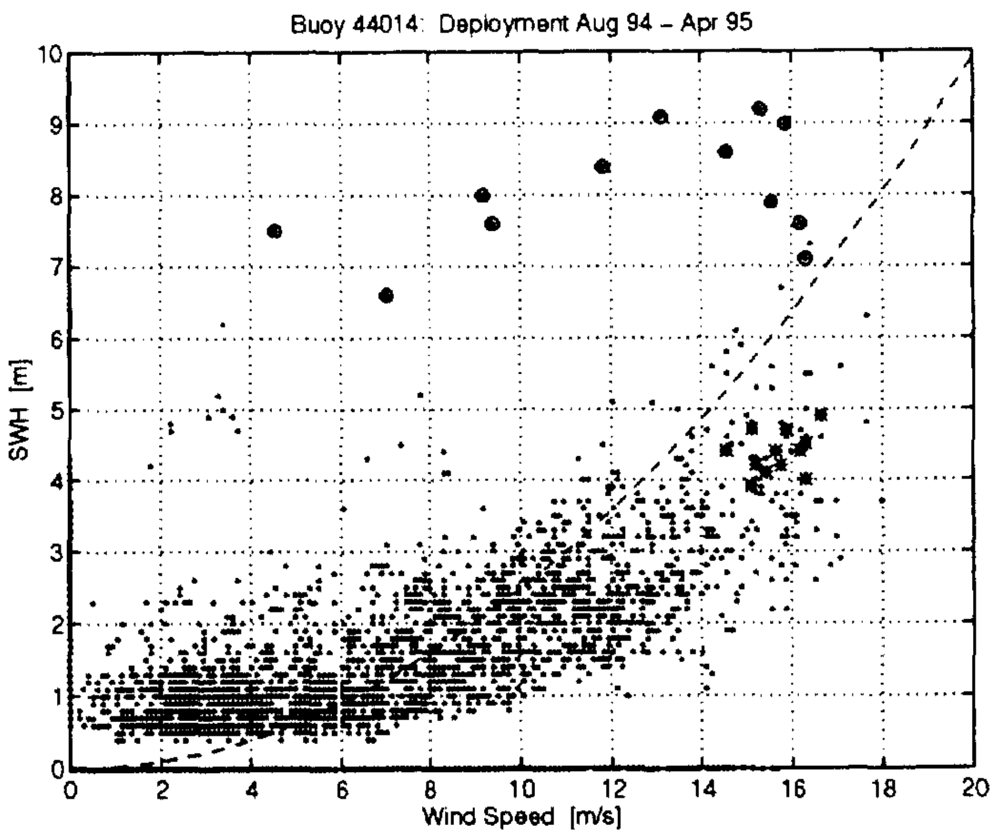

Figure 4. Scatter plot of wind speed versus significant wave height at 44014 (o Hurricane Gordon, ★ IOP-2, and - - PM fully developed).

In general, the IOP-2 storm displayed a rather uniform characteristic in the DUCK94 array. To get a better perspective of this uniformity, frequency spectra were closely examined. The spectra estimates derived from the peak of the IOP-2 storm are plotted in Figure 5 . The storm produced peak periods of 10 sec and maximum energy densities of 30 M2 -sec. The frequency spectra are very similar in the rear face as well as the very steep forward face. The change in energy density from the offshore gage (CERC) to the FRF/LA is very small. Although the change in significant wave height between these two locations is only 1 m, the distance from CERC to the FRF/LA is 90 km and the water depths vary from 48 m to 8.5 m. The CS buoy is the outlier with an amplified peak energy nearly double that of the other three offshore buoys and a significant wave height elevated by 0.5 m. Based on the wind direction (15-20° measured clockwise from north) and the relative location of the CS gage, additional growth could be expected. Along the onshore transect (CERC to FRF/LA) it is apparent that the wind-sea is saturated. The source/sink terms such as wave-bottom effects are in balance with the atmospheric input and the nonlinear wave-wave interactions.

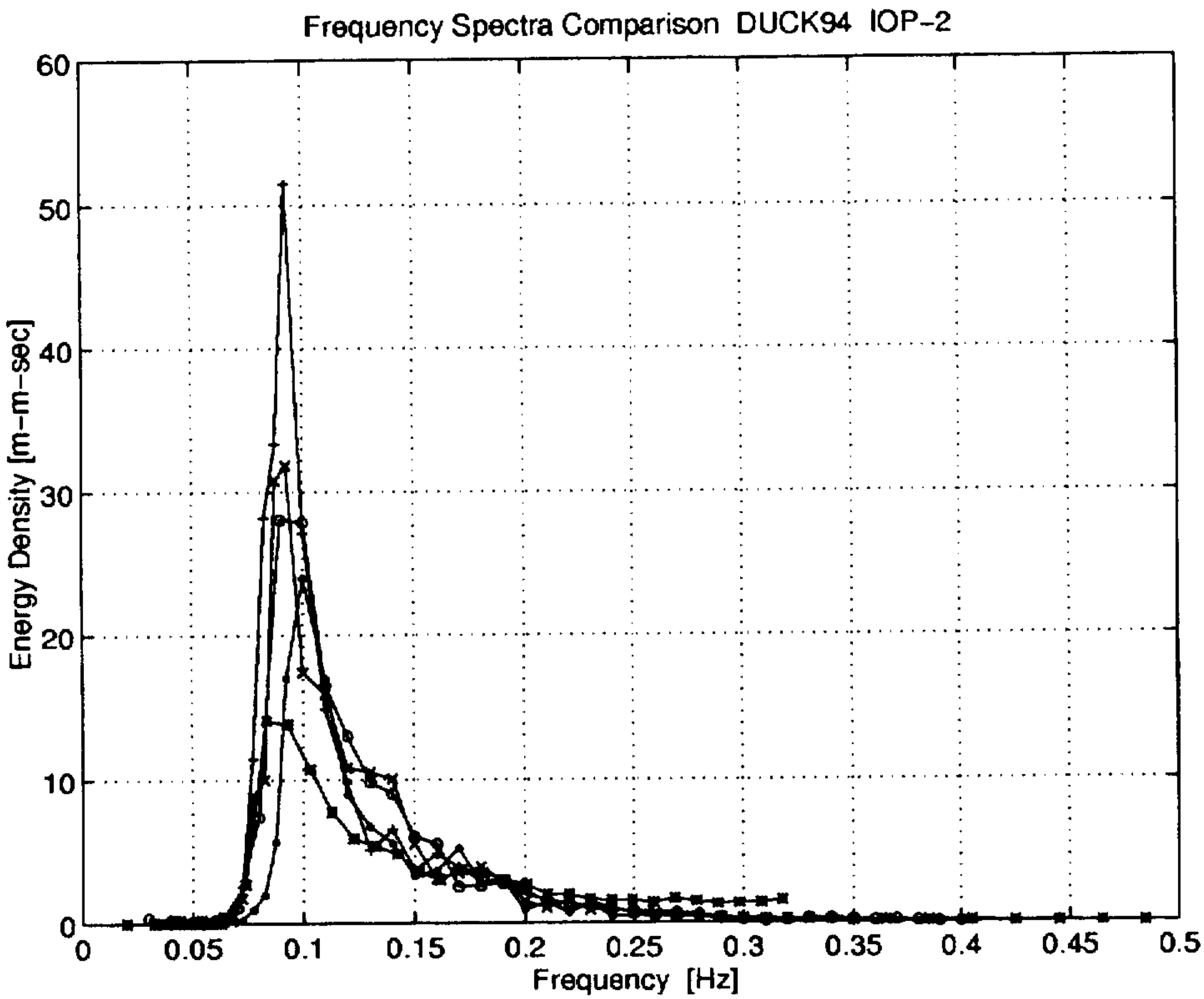

Figure 5. Spectral estimates at the peak of the IOP-2 storm (-o- 44014, -+- 44010, -x- 44019, -•- 44006, -*- FRF/LA).

Changes in the mean and peak wave directions would be expected because of the changes in the water depth and carrier frequency; however, this was not the case during the IOP-2 storm. From the CERC buoy to the IS, only a modest a 5° changes in the mean and peak wave directions were observed, despite a change in water depth of 20 m. This left the major energy lobe nearly 50° from a shore normal wave approach angle. In a distance of about 20 km between the IS and FRF/LA, and a difference in water depth of about 15 m, a rotation of nearly 200 for both the mean and peak directions occurred. Visual observations of waves breaking over the FRF/LA occurred; however, the net effect on the measurements was not quantified. This illustrates the relative impact of the primary forcing functions between the atmospheric input and depth-induced changes observed in directional wave spectra. Under growth and saturated conditions it appears that the atmospheric input dominates over depth-induced mechanisms such as refraction.

Data obtained from Hurricane Gordon were vastly different from the measurements observed in the IOP-2 storm. The area defined by wind-wave growth falls outside the relative region of the four offshore buoys. Swell energy dominated as indicated by wind speed significant wave height data plotted in Figure 4 . The characteristics of the frequency spectra also diverge from the IOP-2 storm. Plotted in Figure 6 are the frequency spectral estimates at the peak of Gordon. The peak periods are much longer (14-15 sec) and the maximum energy density is nearly an order of magnitude higher than observed in the IOP-2 storm. Hurricane Gordon's spectra are quite uni-modal, displaying steep forward and rear face features of monochromatic, unidirectional waves. The observed differences between the CERC buoy and all other spectra can be attributed to differences in analysis packages. Directional spreads of ±45° were estimated from the two-dimensional spectra. At the CS and MS locations, a secondary lobe of energy in a northerly direction was evident; however, it only lasted one hour. The IS buoy was most likely sheltered by Cape Hatteras from southerly propagating swells. The CERC buoy did not observe energy from the south for nearly six hours after the storm peak. Based on these observations, it is not unreasonable to assume that the observed energy was derived from a point source from the far field. Rather than coming from the southeast quadrant the waves appeared to be propagating from an easterly direction. Despite the southerly location of Gordon at its peak intensity, the mean and peak wave directions from the offshore buoys indicate the energy source was slightly north of a near easterly direction. The maximum estimated winds derived from preliminary data sources by the Hurricane Research Division/NOAA were 20-25 m/s and extended over 400 km east of the DUCK94 array. The peak frequency and spectral shape seemed to be nearly invariant to changes in the water depth. In addition to this, the mean and peak wave directions showed a change of 15° from CERC to IS. The winds steered the spectra to some degree at the offshore buoys (i.e. ±5° variation between the peak wave direction and the wind direction); however, these directions were well established by initial growth defined in the far field by Gordon's winds. This effect was reduced shoreward where at the IS the observed differences were on the order of 20° and the wave directions were rotating toward shore normal. At the FRF/LA the mean and peak wave directions departed by about 10° from shore normal.

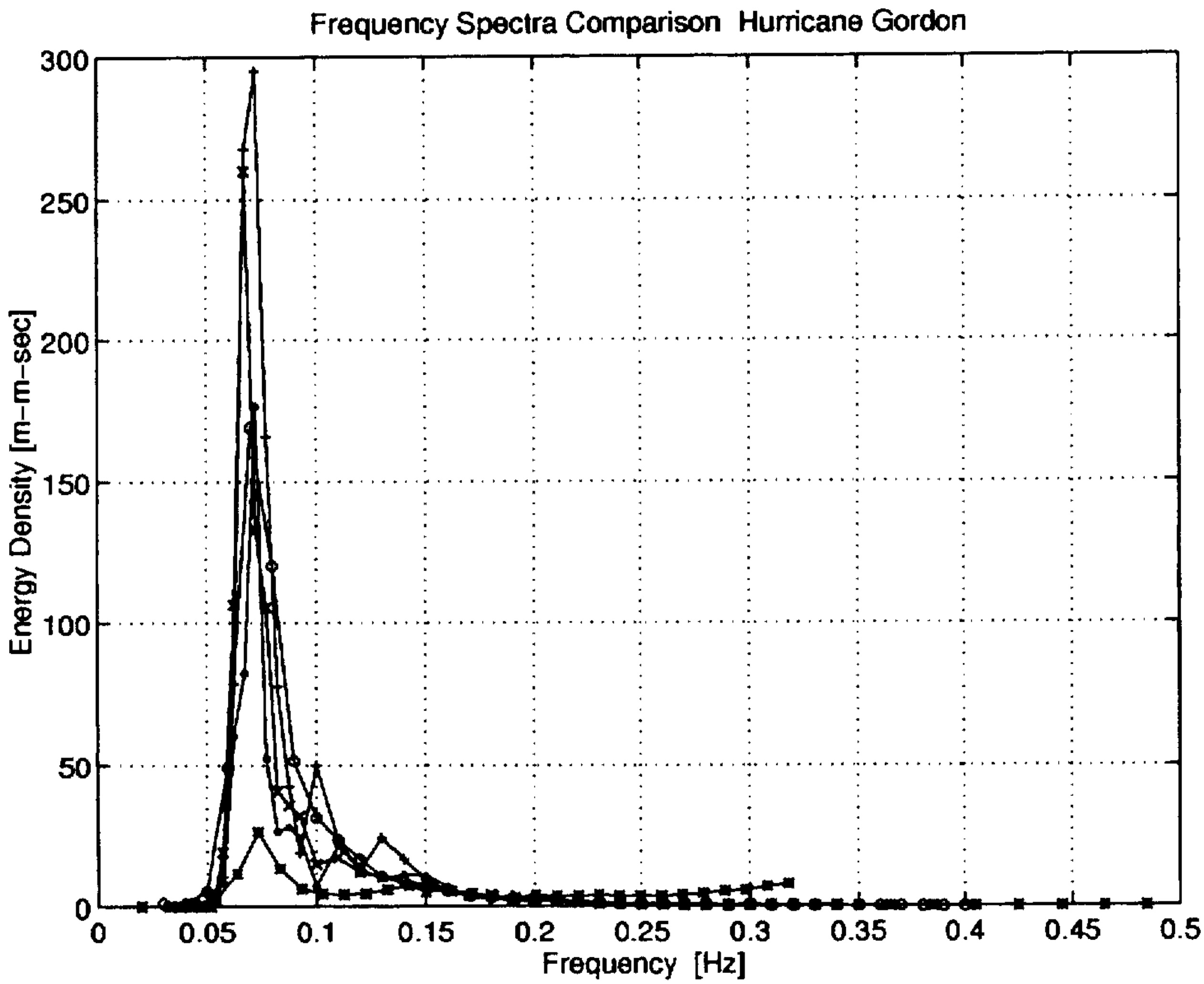

Figure 6. Spectral estimates at the peak of Hurricane Gordon (-o- 44014, -+- 44010 -x- 44019, -•- 44006, -*- FRF/LA).

These two storm scenarios offer a rather unique look at the important role of various mechanisms depicting spectral transformations over the continental shelf. The IOP-2 storm was clearly a local wind generation problem, forced by a synoptic scale meteorological event. Wave characteristics (e.g. height, period, direction) were dominated by the source/sink terms (atmospheric input, nonlinear wave-wave interactions, and wave-bottom effects), and invarience of the changing bathymetry, The effects caused by Hurricane Gordon were significantly different. The active mechanisms defined in the Gordon case became dependent upon depth effects such as refraction, shoaling and wave-bottom interactions. Steering of the directional spectra became invariant of the winds, and the contribution from the atmospheric input showed little effect.

6. 3GWAM ASSESSMENT

A wave forecasting system was developed and implemented for the FRF-DUCK94 region. This forecasting system used 3GWAM (WAMDIG, 1988, Komen et al. 1994) in a multi-nested grid system (0.25° regional grid, nested to a 0.083330° FRF grid) implemented with shallow-water effects (refraction and shoaling) and forced by the Fleet Numerical Meteorological and Oceanographic Center (FNMOC) global stress fields (1.25° spatial and three-hour temporal resolution). The regional grid extended to 310° E longitude, south to the Florida Keys, and to Nova Scotia, Canada as the northern boundary. Any far field energy generated outside this region was not accounted for. However, for the IOP-2 storm and Hurricane Gordon this was not the case.

The system was run twice a day and provided a forty-eight-hour wave forecast for planning of daily operations during IOP-1 (August 1994) and IOP-2. Taking advantage of the most recent analyzed stress fields, each wave forecast was initiated six hours prior to each watch cycle. For example, the 12Z watch cycle was started at 06Z and run to 18Z. A restart file was saved for the next watch cycle and the forecast continued to 60Z (12Z + forty-eight-hour forecast period). Hence, selecting the first twelve hours from each watch cycle produced wave model results that would be have been identical to that generated in a hindcast mode and used for this assessment. Hurricane Gordon fell outside the forecast period and was run in a hindcast mode using only the analyzed stress fields.

During the forecast period, daily observations from the NDBC buoys and the FRF databases were used for quality control. An in-depth comparison of model-to-measurement estimates of the wind and wave characteristics was undertaken much later in the study. A battery of statistical tests was used in the assessment of 3GWAM wave results such as the bias, root mean square (rms) error, scatter index, skill score, linear regression, correlation, and systematic error (e.g. Cardone et al. 1995). With these results a better understanding of the model’s performance can be made for the estimation of wave characteristics in a continental shelf region. All analyses conducted used wave estimates obtained from the fine-scale grid. Although the resolution of the FRF grid was about 9 km, co-location of the FRF/WR and FRF/LA (4.5 km and 1 km from shore) could not be performed. Hence, this assessment will be restricted to the offshore buoys and a reduced assessment of 3GWAM will be made to the FRF/LA.

6.1 DUCK94 IOP-2 Assessment

The quality of wave model results is dictated by the accuracy of the wind fields, Because the IOP-2 storm was a synoptic-scale feature, the FNMOC global stress fields were able to resolve this meteorological situation quite well. In all wind-related comparisons, the FNMOC stress fields were transformed to 10-m winds. Root mean square errors were generally less than 2 m/s at all buoy locations, the bias was between 1.4-3.5 m/s (at IS and CERC, respectively), with skill scores of 30%. Errors encountered in the wave model results may be difficult to isolate between wind and wave model deficiencies because of the potential errors in the wind fields.

A summary of a partial set of the statistical tests is shown in Table 1 . This provides an overview of the degree to which 3GWAM performed. There is a general trend of 3GWAM to estimate the significant wave height very well. Biases of less than 0.05 m were found to be the case, and the rms error was found to be less than 0.5 m. Correlation results of 0.95 were the general case, with slopes near 1.0 and intercepts close to zero. Scatter index values ranged near 20%. The peak (Tp) and mean (Tm) results were less accurate; however, they tended to follow historical patterns of 3GWAM (Cardone et al. 1995). Wave periods for DUCK94 IOP-2 were under-estimated by 3GWAM. The bias results ranged from 0.8 to 1.4 sec; rms errors from 1.0 to 2.0 sec; scatter index values were found to be slightly greater than 20%. Correlation coefficients were generally near 0.80, with slopes based on a linear regression less than 1.0 and intercepts that ranged from near zero to a 1.0-sec offset.

Time plots are another useful way to evaluate 3GWAM's performance for IOP-2. This discussion is limited to significant wave height, mean wave direction and directional spread results compared to three sites, CERC-44014, IS-44006, and the FRF/LA (Figures 7 -15). 3GWAM performed well in the estimation of the growth (a positive wave height gradient) and decay stages of the two storms in IOP-2 at the CERC buoy (Figure 7). The model underestimated both storm peaks by about 40 cm. At the IS location (Figure 8) the model results displayed similar trends. Significant wave height results again followed the growth and decay stages remarkably well. The storm peaks were also underestimated, and the model shows modest attenuation of the wave heights, similar to the measurements.

The mean wave direction trace derived from 3GWAM followed the measurements very well (Figure 9). Differences between the model results were on the order of about 20°, until the decay of the major IOP-2 storm. Dramatic changes in the mean wave direction occurred soon after 10 October, where a 100° shift was resolved by 3GWAM. The IS data (Figure 10) showed only modest rotation toward shore-normal compared to the CERC buoy in the mean direction despite a 20 m change in the water depth. 3GWAM results exhibit larger depth effects where the trace in the mean directions was focused more toward a shore-normal direction of 250°. At both locations (CERC, Figure 9 , and IS, Figure 10) 3GWAM departed from the measurements soon after the IOP-2 storm peak. At this time, the IOP-2 storm was moving in a northeasterly direction, and the wind speed decreased from 15 m/s to 7.5 m/s. It seems as though 3GWAM preferentially treated the wind-sea over the swell energy, and rotated in the direction of the winds.

The directional spread (defined by Yamartino, 1984) comparisons reveal some striking differences between 3GWAM and the measurements (Figures 11 and 12). In all cases, and at both buoy locations, there is a 30° offset between the model and buoy results. The general trends were followed by 3GWAM relatively well, displaying expansion and contraction of the two-dimensional spectra similar to CERC (Figure 11). The only time when this trend is not followed is in the lee of the IOP-2 storm near 18 October. This is the same location where the mean wave direction from 3GWAM rotated opposite to that of the CERC buoy. The directional spread results at IS (Figure 12) show similar trends established from the CERC data, with one exception. On 15 October the data indicated a strong increase in spread of about 15° that occurred over about four hours at the same time the peak wave conditions occurred at IS. After that time there was an oscillation in the buoy data of nearly 20°. The 3GWAM results show only modest changes in the directional spread for this time period, and tend to be approximately 20° low in comparison to the data. The times where major changes do occur, (e.g. 10, 20, 22 and 24 October), 3GWAM reacts; however, not to the degree at which the IS data indicate.

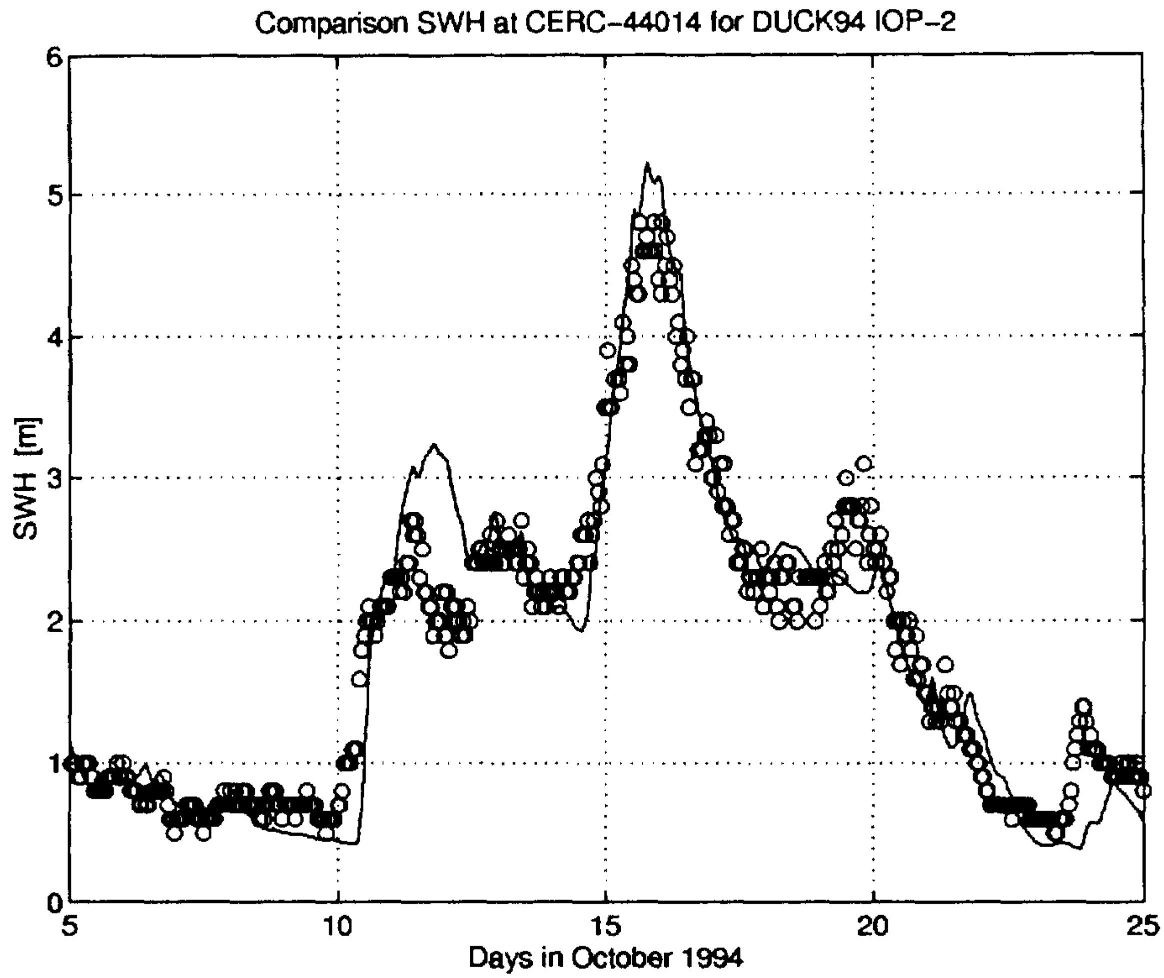

Figure 7. 3GWAM comparison of significant wave height at 44014 for DUCK94 IOP-2 (— 3GWAM, o CERC-44014).

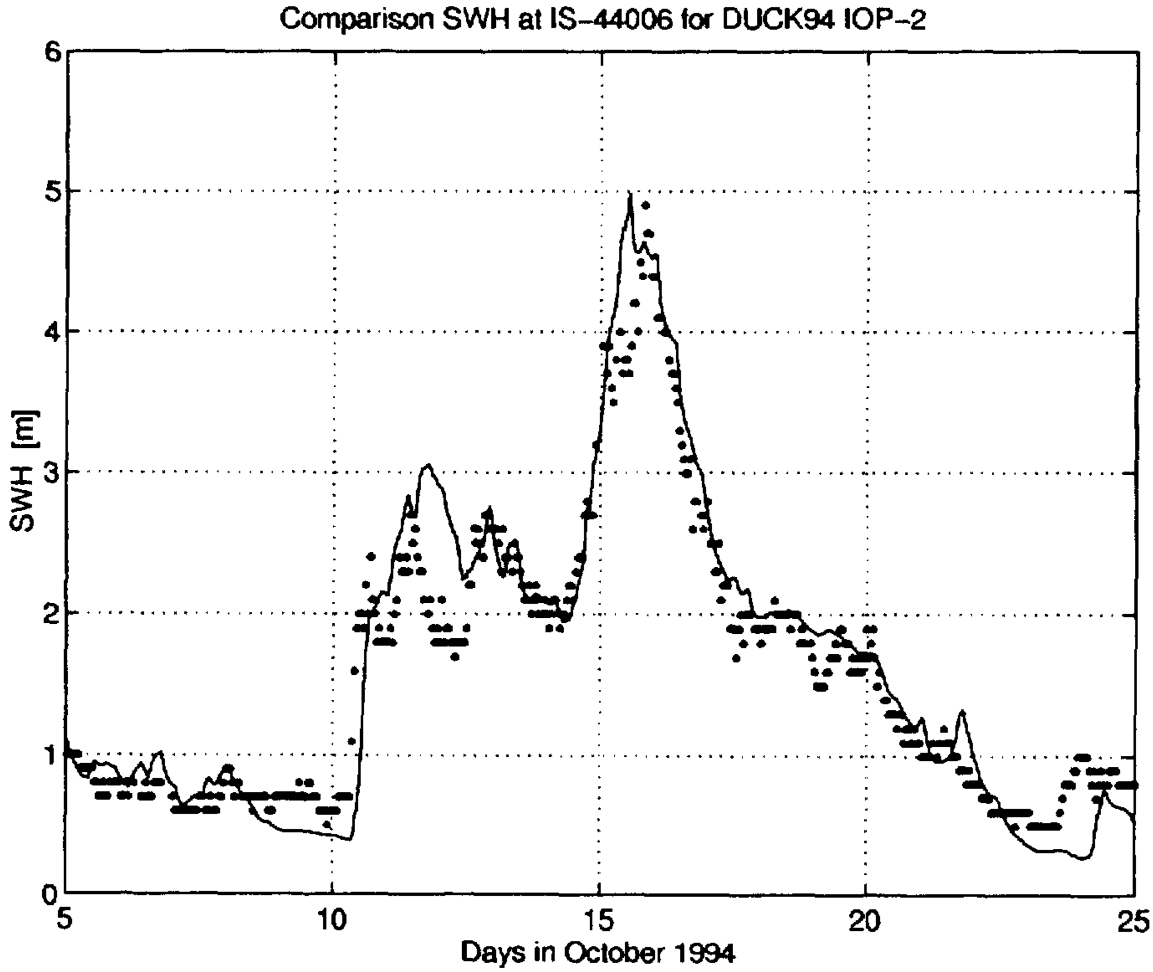

Figure 8. 3GWAM comparison of significant wave height at 44006 for DUCK94 IOP-2 (— 3GWAM, • IS-44006).

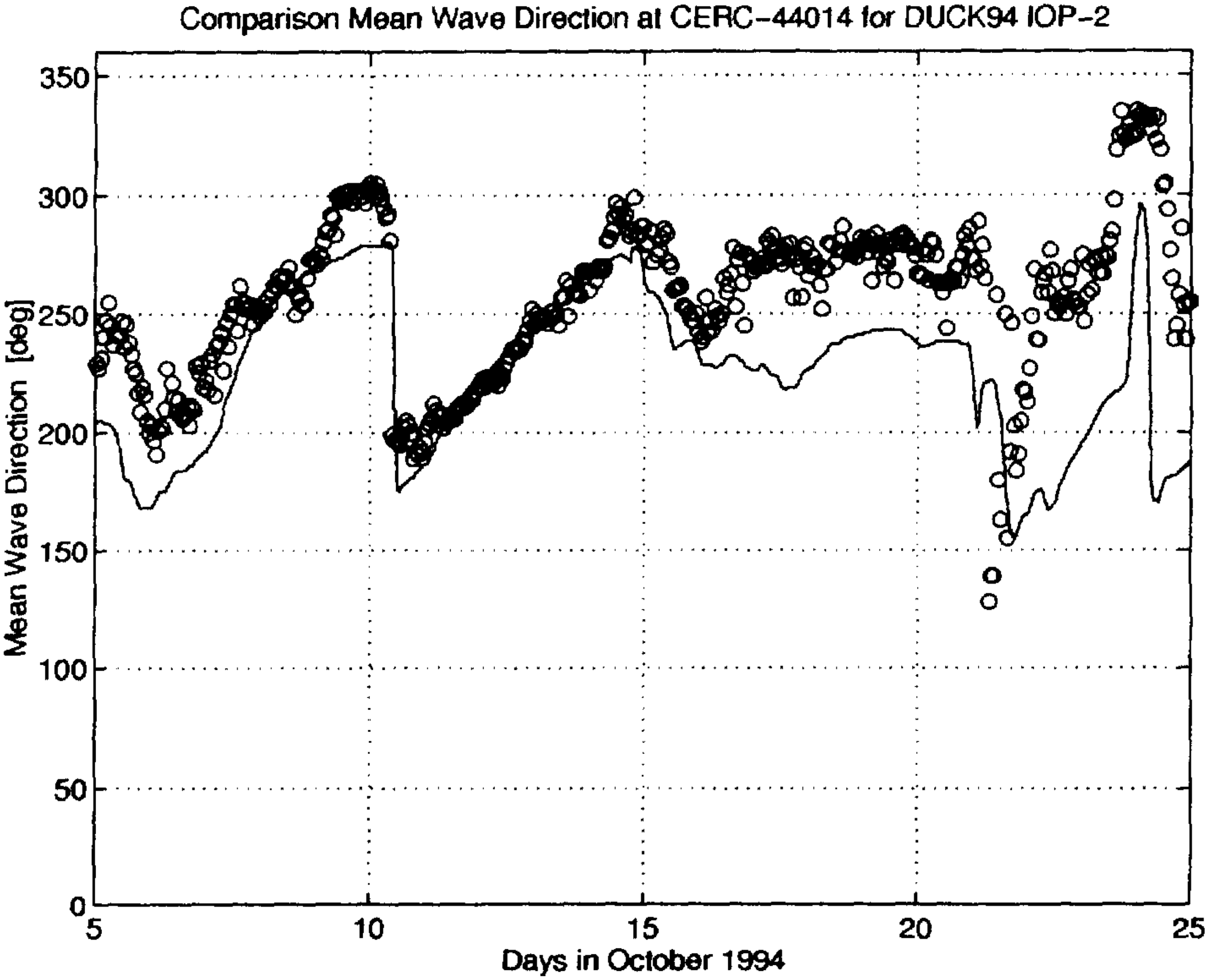

Figure 9. 3GWAM comparison of mean wave direction at 44014 for DUCK94 IOP-2 (— 3GWAM, o CERC-44014).

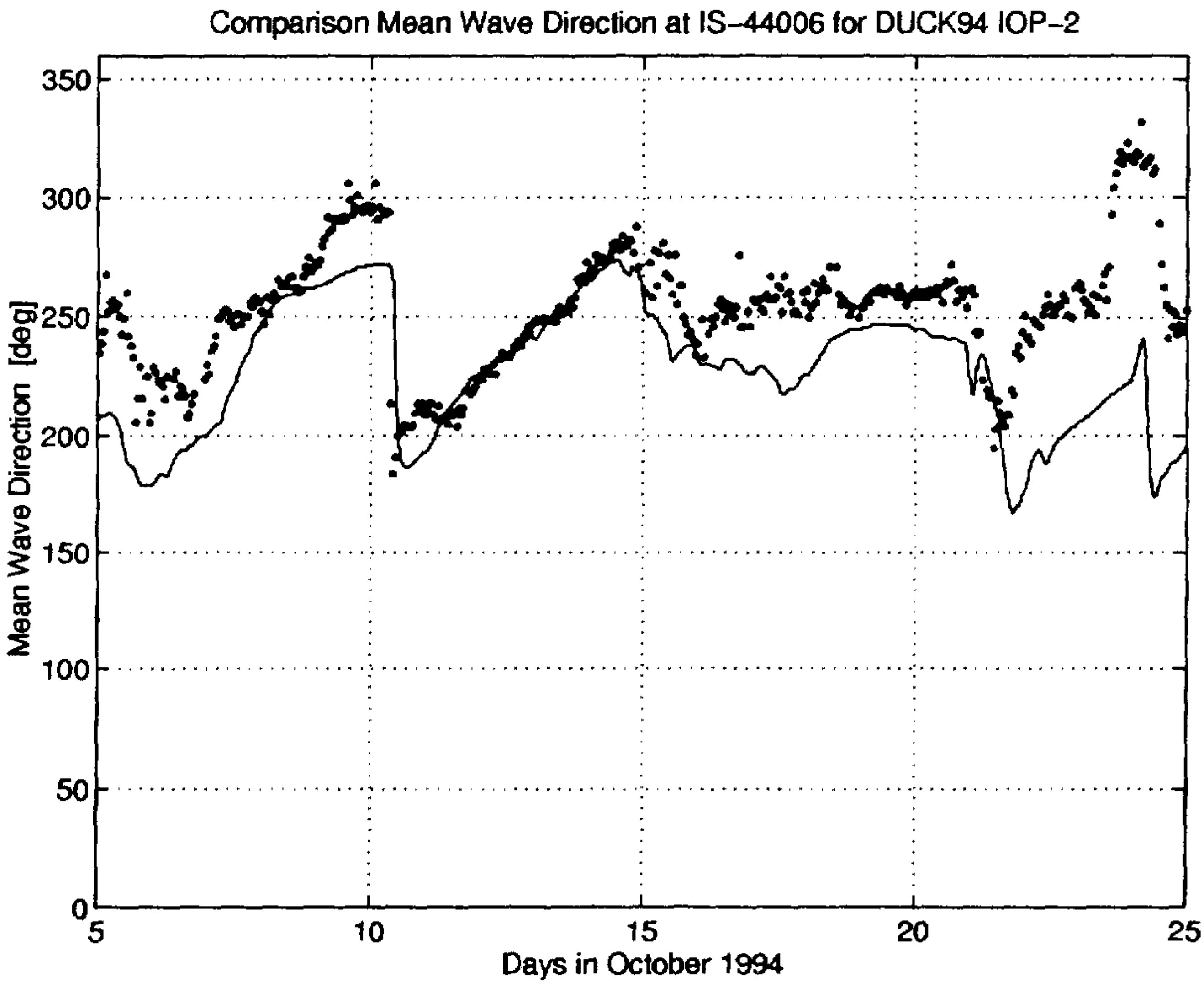

Figure 10. 3GWAM comparison of mean wave direction at 44006 for DUCK94 IOP-2 (— 3GWAM, • IS-44006).

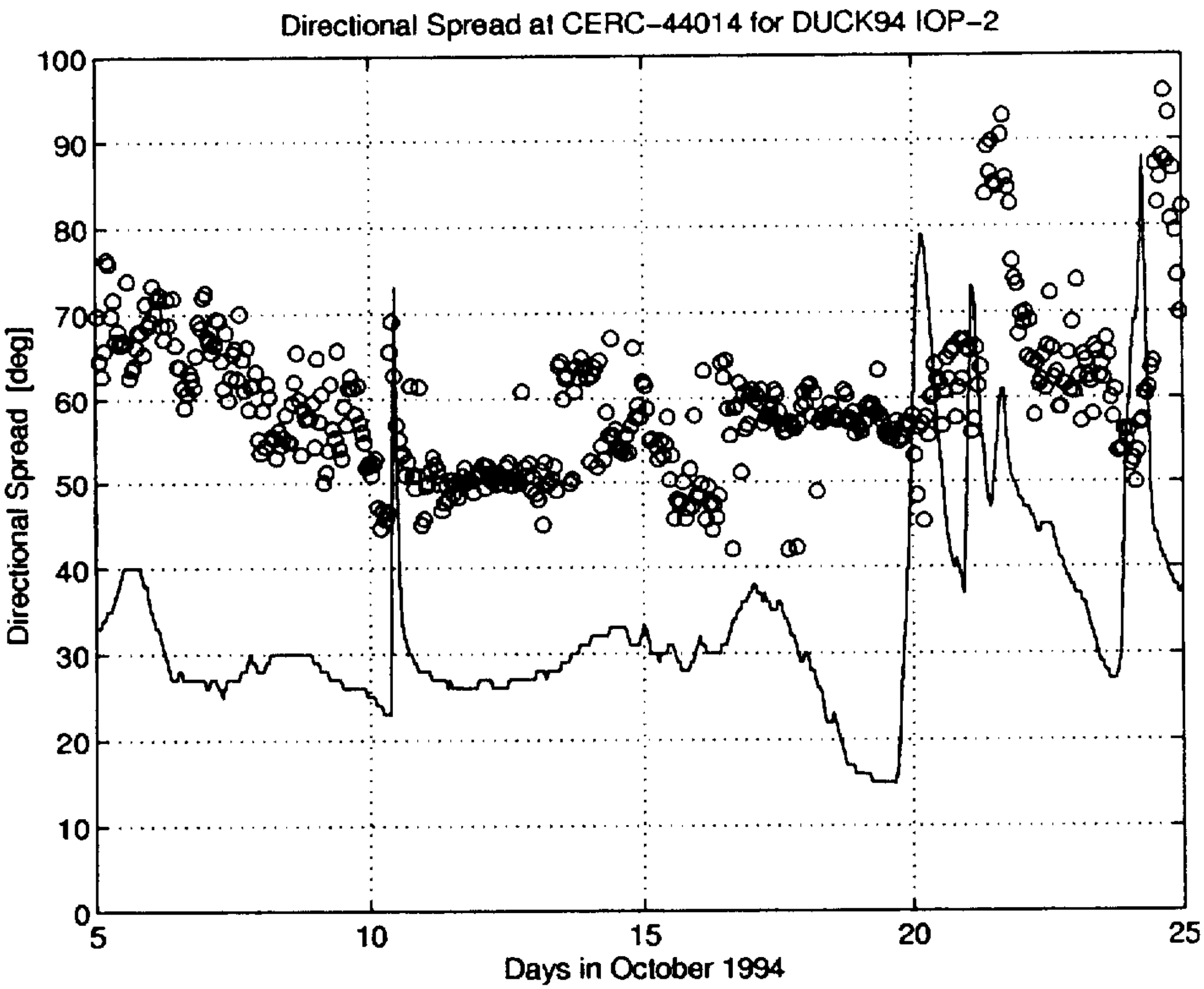

Figure 11. 3GWAM comparison of directional spread at 44014 for DUCK94 IOP-2 (— 3GWAM, o CERC-44014).

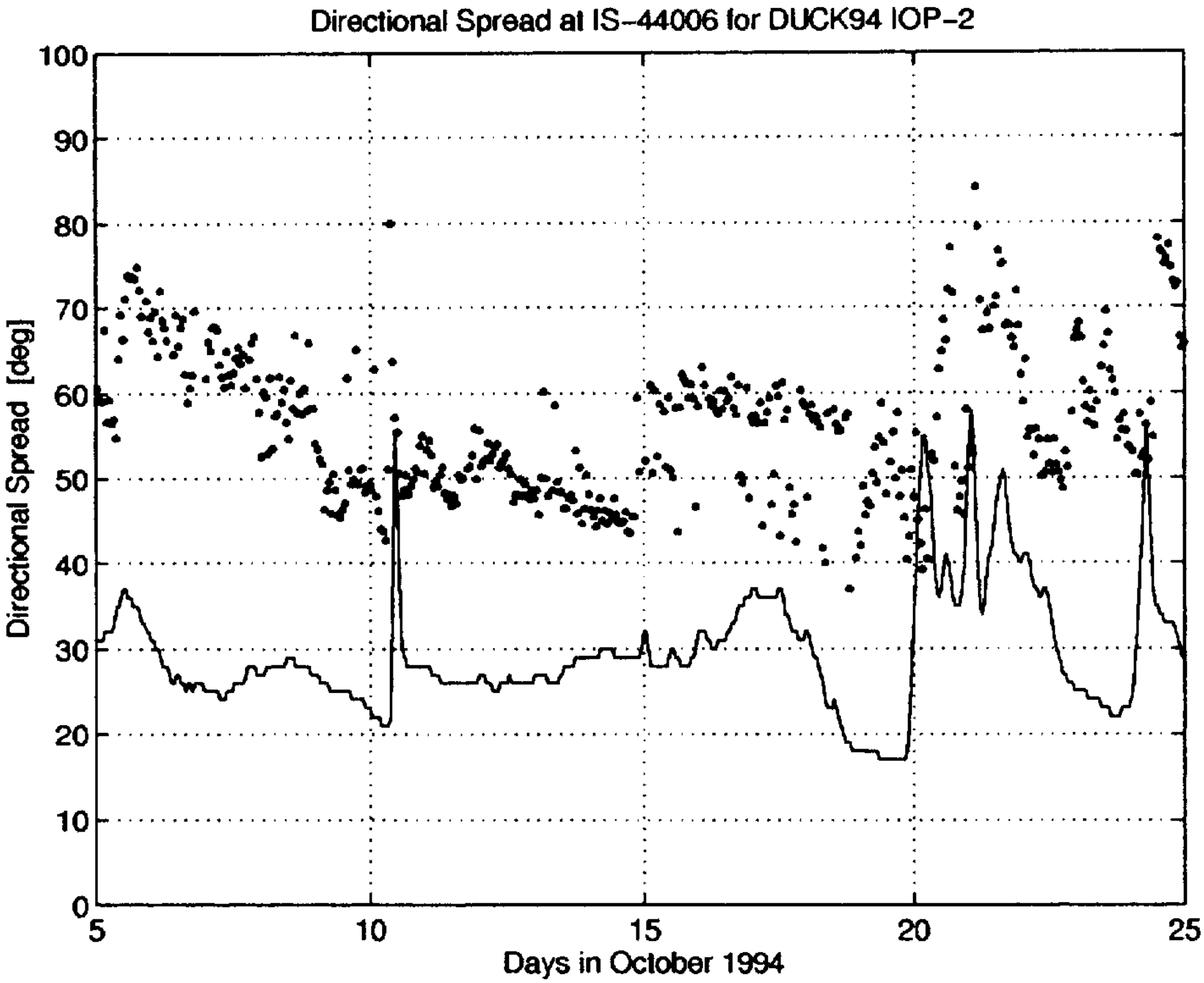

Figure 12. 3GWAM comparison of directional spread at 44006 for DUCK94 IOP-2 (— 3GWAM, • IS-44006).

Lastly, wave model results were compared to the FRF/LA gage site (Figures 12 -15). The model significant wave height results (Figure 12) follow the measurements despite the lack of a depth induced wave breaking sink term. Based on these comparisons improvements to 3GWAM can be gained with this addition because of the overestimation at the storm peaks. The mean wave direction comparison (Figure 14) clearly shows the relative importance of refraction and shoaling. The measurements collapse toward a shore-normal direction; 3GWAM follows this tendency. Again there is a divergence in the directional response between the model results and FRF/LA after the IOP-2 storm. As waves propagate into shallow water, it has been assumed that the mean direction becomes aligned to a shore normal direction, and the directional spread is reduced. This is confirmed in the FRF/LA data (Figure 15), where directional spreads were rarely greater than 30°. 3GWAM compared better to the data at this location than the previous two offshore sites. The model's directional spread did not significantly change from CERC to IS and finally to the FRF/LA, the measurements changed. Thus conclusions regarding the performance of 3GWAM in shallow water (less than 10 m) cannot be simply stated.

6.2 Hurricane Gordon Assessment

A preliminary assessment of 3GWAM's performance was made at the five gage sites. In all cases the model under-estimated wave height by nearly 3 m. These poor results were directly caused by the spatial resolution in the FNMOC global stress fields compared to the size of Hurricane Gordon. Modeled wind speeds of the magnitudes described by Hurricane Gordon were not evident. Despite the lateral extent of tropical wind speeds extending some 400 km from the storm's center, a maximum of three grid points in the FNMOC global stress fields (1.25° resolution) would have been affected. Three points at wind speeds of 30 m/s could not produce the driving forces necessary to produce wave heights of the magnitudes found in the data. It is anticipated that Hurricane Gordon will be reanalyzed once higher-resolution wind fields become available.

7. SUMMARY AND CONCLUSIONS

In the fall of 1994 two unique storm events took place along the central Atlantic seaboard. Because of the DUCK94 field experiment, these storms could be studied in great detail. Five wave measurement sites were in operation and recorded the directional response due to changing meteorological and water depth conditions. The two storms, IOP-2 and Hurricane Gordon, showed a direct correlation between the relative effects of source/sink term mechanisms and depth effects. During the IOP-2 storm, atmospheric input controlled the response in the directional spectra, whereas in Hurricane Gordon depth effects were predominant.

3GWAM was used in the simulation of both storm events. The model replicated the spatial variation compared to the measurements at the five sites. Significant wave height, and peak and mean wave period results showed biases of 0.04 m and 0.8 sec, respectively. Time plot comparisons of the mean wave direction and directional spread showed that 3GWAM is capable of estimating these parameters quite well. However, there did appear to be a positive bias in the directional spread of about 200. In shallow water, it was shown that 3GWAM requires a depth-induced breaking mechanism to better replicate measured significant wave heights.

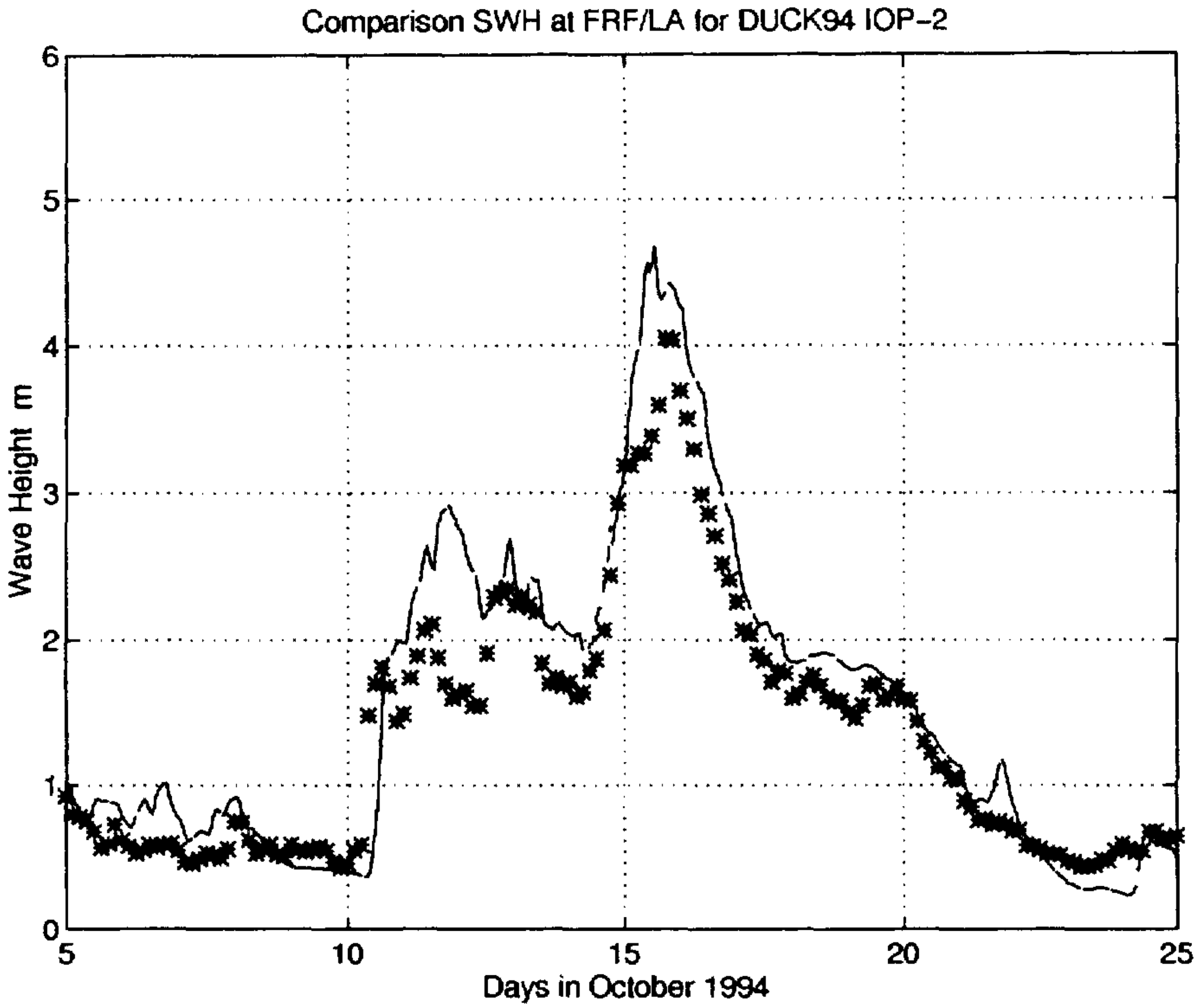

Figure 13. 3GWAM comparison of significant wave height at FRF/LA for DUCK94 IOP-2 (— 3GWAM, ⋆ FRF/LA)

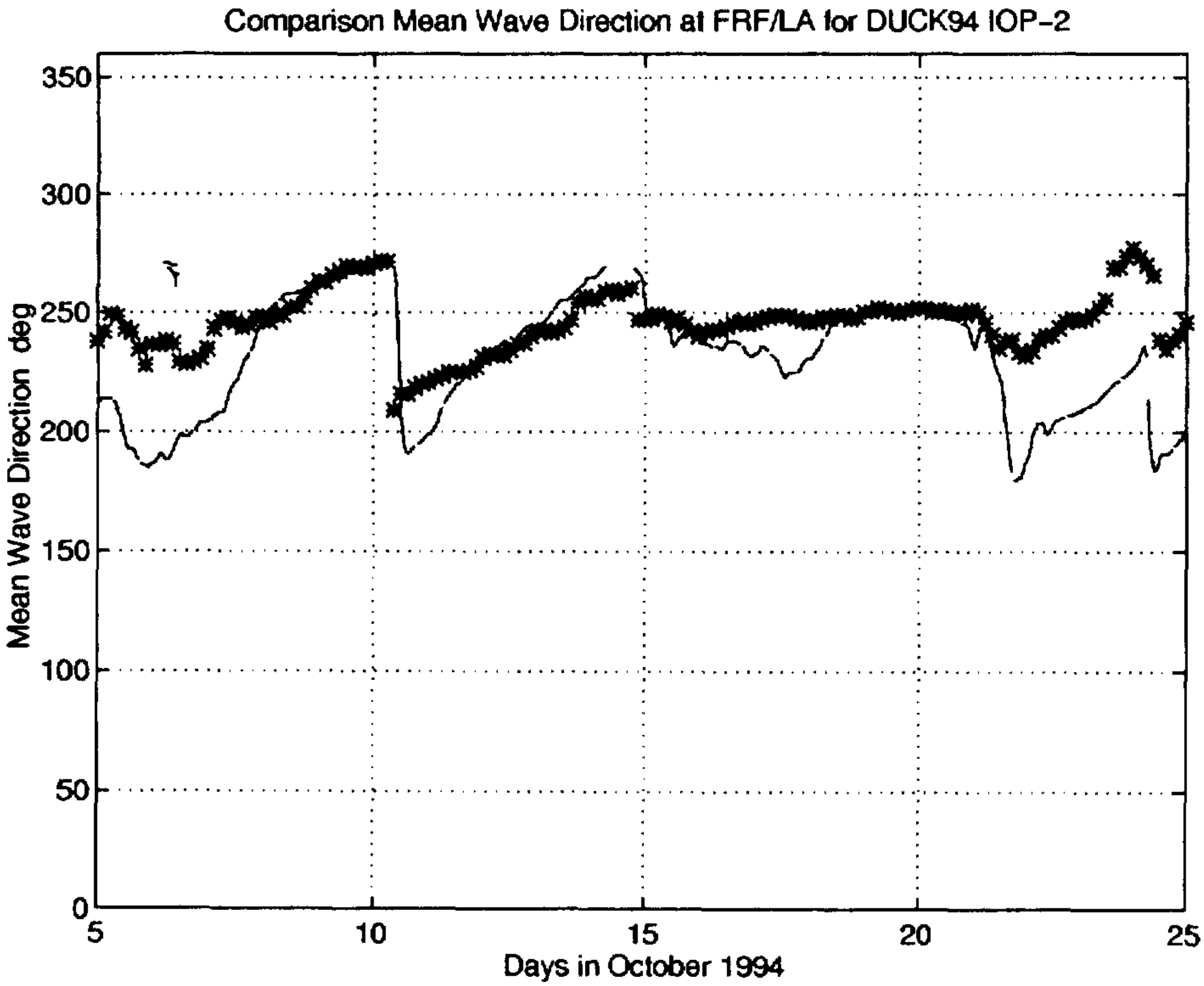

Figure 14. 3GWAM comparison of mean wave direction at FRF/LA for DUCK94 IOP-2 (— 3GWAM, ⋆ FRF/LA).

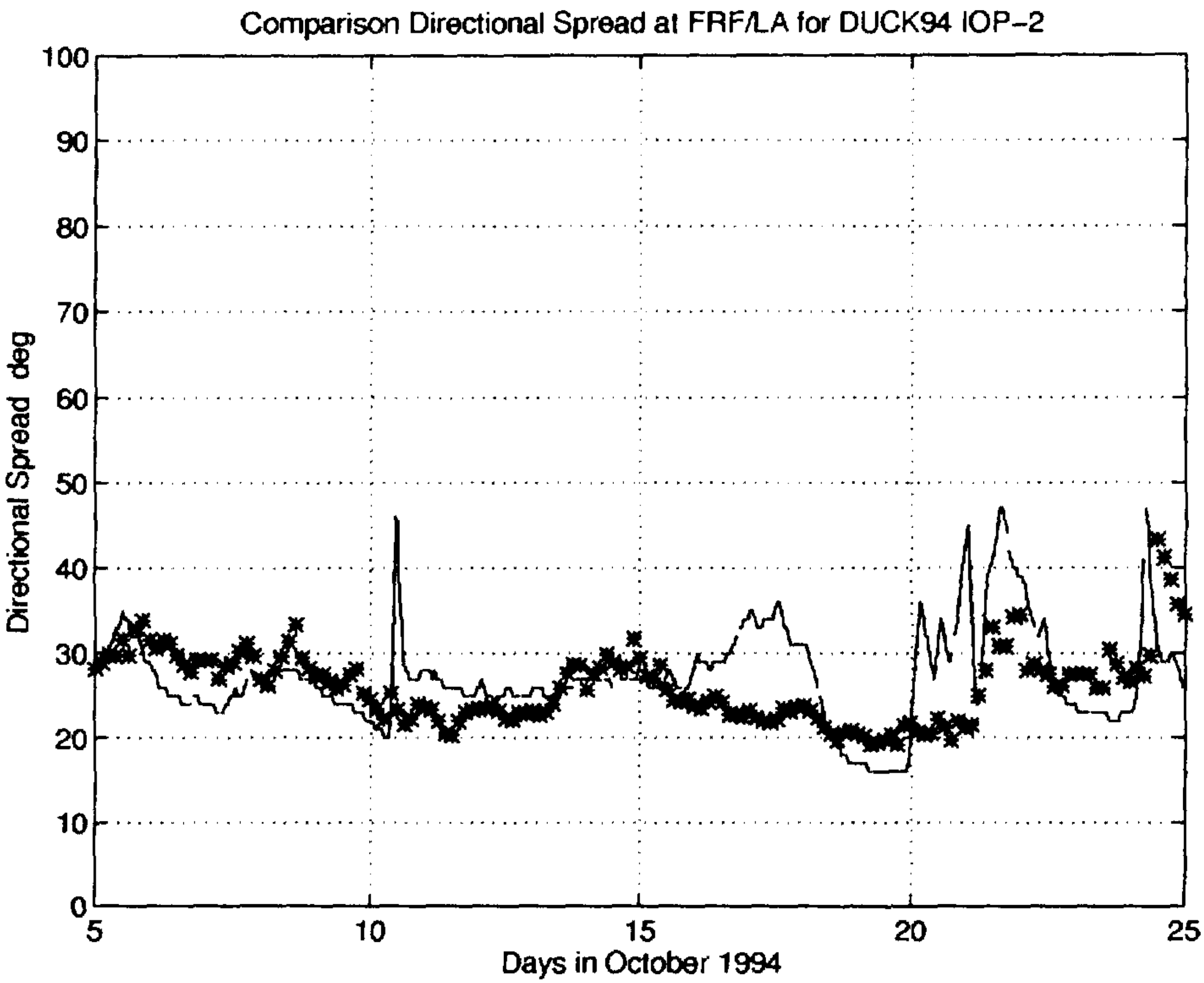

Figure 15. 3GWAM comparison of directional spread at FRF/LA for DUCK94 IOP-2 (— 3GWAM, ⋆ FRF/LA).

Table 1. Wave Parameter Statistics for DUCK94 IOP-2

BUOY	VAR	MEAN buoy	BIAS	RMSE	S.I	SLOPE	INT	CORR
CERC	SWH	1.77	0.01	0.34	19	1.07	–0.11	0.96
44014	Tp	8.15	–0.61	1.61	20	0.85	0.61	0.83
	Tm	7.22	–0.78	1.15	16	0.96	–0.52	0.84
CS	SWH	1.85	0.05	0.43	23	1.09	–0.11	0.94
44010	Tp	8.53	–0.84	1.60	19	0.91	–0.07	0.83
	Tm	7.72	–1.18	1.19	15	0.86	–0.14	0.84
MS	SWH	1.48	–0.02	0.32	21	1.08	–0.13	0.94
44019	Tp	8.30	–0.92	2.03	24	0.77	0.95	0.78
	Tm	7.66	–1.40	1.27	17	0.87	–0.44	0.83
IS	SWH	1.58	0.05	0.31	19	1.10	–0.11	0.96
44006	Tp	8.16	–0.66	1.88	23	0.80	1.01	0.78
	Tm	7.54	–1.20	1.22	16	0.85	–0.09	0.83

8. ACKNOWLEDGEMENTS

This work was carried out under the Coastal Flooding Research and Development Program, Modelling the Evolution of Wave Spectra in Shallow Water work unit.. The author acknowledges Headquarters, U.S. Army Corps of Engineers for authorizing publication of this paper.

9. REFERENCES

Birkemeier, W.A. 1994: The DUCK94 nearshore field experiment. US Army Engineer Waterways Experiment Station, Vicksburg, MS.

Butman, C.A. 1994: CoOp: Coastal ocean processes, Sea Technology, vol 35, No. 1, 44-49.

Cardone, V.J. Graber, H.C., Jensen, R.E., Hasselmann, S., and Caruso, M. 1995: In search of the true wind fields in SWADE IOP-1: Ocean wave modelling perspective. Submitted to the Global Atmosphere and Ocean System.

Komen, G.J., Cavaleri, L., Donelan, M., Hasselmann, K., Hasselmann, S., and Janssen, P.A.E.M. 1994: Dynamics and Modelling of Ocean Waves, Cambridge Press.

Long, C.E., and Oltman-Shay, J.M. 1991: Directional characteristics of waves in shallow water. Tech. Rep. **CERC-91-1**, US Army Engineer Waterways Experiment Station, Vicksburg, MS.

Pierson, W. J., and Moskowitz, L. 1964: A proposed spectral form for fully developed wind seas based on the similarity theory of S.A. Kitiagordskii. J. Geophys. Res. **9**, 5181-5190.

Steele, K.E., and Mettlach T. 1993: NDBC wave data: current and planned. Proceedings of 2nd International Symposium Ocean Wave Measurement and Analysis, Waterways, Port, Coastal and Ocean Division ASCE, 198-207.

Yamartino, 1984: A comparison of several "singlepass" estimators of the standard deviation of wind direction. J. Climate Appl. Meteor, **23**, 1362-1366.

WAMDIG 1988: The WAM model - a third generation ocean wave prediction model. J. Phys. Oceanogr., 18, 1775-1810.

Weller, R.A., Donelan, M.A., Brisco , M.G., and Huang, N.E. 1991: Riding the crest: a tale of two wave experiments. Bull. Amer. Met. Soc., **72**, No. 2, 163-183.

ANALYSIS OF EXTREME WAVES IN SEVERE SEAS

David Wei-Chi Wang

Computer Sciences Corporation
Stennis Space Center, Mississippi 39529-6000

1. INTRODUCTION

Studies of in situ measured wave data have contributed greatly to the development of wave spectral models and parametric relations (Pierson and Moskowitz, 1964; Hasselmann et al., 1973), Due to logistic difficulties and great costs, most field data studies have been limited to measurements from modest sea states in nearshore areas, which were often under a relatively uniform and stationary wind field. However, most extreme seas are generated by a fast moving storm, which hardly has a uniform and stationary wind field. Analysis of well documented and reliable storm-generated extreme wave data is, hence, of great practical importance for wave model verifications and the enhancement of our understandings of wind-wave evolution.

At 1200 UTC, March 12, 1993, an extratropical cyclone formed over the western Gulf of Mexico off the southeastern Texas coast with a central pressure of 1000 hPa. The storm swept through the Florida panhandle and kept moving northeastward as the central pressure continued to drop. At 0000 UTC, Match 14, 1993, the storm center was located near the Delaware Bay with a central pressure of 960 hPa. At 1200 UTC, March 14, 1993, 48 hours after the storm was formed, the center was located over New England with a central pressure of 966 hPa. Extensive damage along the track was reported (Kraft, 1993; Zahn and Grim, 1995). Many National Data Buoy Center (NDBC) offshore buoy stations reported record-breaking high winds and waves. The maximum reported significant wave height reached 15.66 m, which is the largest significant wave height ever reported by any NDBC buoy station along the east coast of the United States.

This study presents an analysis of a set of storm-generated extreme wave data containing the wave growing and decaying stages of the 15.66 m, significant wave height. This analysis examines the validity of various wave spectral models and parametric relationships under extreme weather conditions.

2. DATA ANALYSIS AND RESULTS

Along the storm track, 14 NDBC buoy stations (Table 1) reported high winds and severe sea conditions. Table 1 displays the reported maximum significant wave height and the associated wave and meteorological parameters. The significant wave height, H_s, and average wave period, T_z, are derived from the spectrum, $S(f)$, by

$$H_s = 4\sqrt{m_0} \qquad (1)$$

and

$$T_z = \sqrt{\frac{m_0}{m_2}} \qquad (2)$$

where m_o and m_2 are the n^{th} spectral moment defined as

$$m_n = \int_a^b f^n\, S(f) df \qquad (3)$$

where a is 0.03 Hz and b is 0.4 Hz. The peak frequency, f_p (or peak period T_p), is the frequency associated with the maximum value of $S(f)$. The spectrum is estimated from a 20-min buoy heave acceleration measurement each hour. Details of NDBC buoy measurements can be found in Steele and Mettlach (1993). The wind speed and direction are average values of an 8-min measurement each hour at approximately 5 m above the buoy hull design waterline. The representativeness of the wind measurements from a constantly moving buoy platform in severe weather conditions is beyond the scope of this study.

In this study, measurements from station 41002 over a period of three days (March 13 to 15, 1993, were analyzed. This station is located about 300 km south of Cape Hatteras in a water depth of 3,658 in (Figure 1). The time series of hourly measured wind speed, wind direction, and significant wave height are shown in Figure 2 . In this 72-hour period, the wind speed and direction were constantly changing. The wind speed increased approximately from 10 to 25 m/s within the first 24 hours, then gradually decreased to approximately 5 m/s. The wind direction gradually shifted clockwise approximately from 140 degrees (southeast) to 50 degrees (northeast). In the meantime, the sea state, represented by the significant wave height, increased from 2 to 15.66 m at 0400 UTC, March 14, and then gradually dropped back to approximately 2 m.

2.1 Wave Energy, Wave Period, and Wind Speed

Based on the Pierson-Moskowitz (PM) spectral model for a fully developed sea (Pierson and Moskowitz, 1964), the wave energy, represented by H_s, and wave period, represented by T_p, increase as the wind speed increases, which can be expressed as

$$\frac{gH_s}{U^2} = 0.24 \tag{4}$$

and

$$\frac{gT_p}{U} = 7.69 \tag{5}$$

where g is the gravitational constant, and U is the wind speed at a level of 10 m. Figure 3 shows the scatter-plot of the wind speed versus the significant wave height. Figure 4 shows the scatterplot of the wind speed versus the peak period. For a given wind speed, the wave height and peak period of the PM model, shown as the solid lines in the figures, are greater than those of the growing stage and smaller than those of the decaying stage. This is because during the growing stage, the time duration of a given wind speed is too short to result into a fully developed sea. During the decaying stage, the presence of swells adds wave energy and may slow the shift of peak period.

Based on the local balance assumption of waves under the action of wind, Toba (1972) first derived the three-second power law to represent the relation between the nondimensionalized wave energy, ε, and the nondimensionalized peak wave frequency, ν. Toba (1978) used 1.0 x 10^{-3} for the drag coefficient, C_d, and derived

$$\epsilon = 7.1 * 10^{-6} \nu^{-3} \quad , \tag{6}$$

where

$$\epsilon = \frac{g^2 m_0}{U^4} \quad , \quad \nu = \frac{Uf_p}{g} \tag{7}$$

Similar results were also obtained by Mitsuyasu et al. (1981). Hasselmann et al. (1976) proposed a slightly different empirical relation, which is

$$\epsilon = 5.3 * 10^{-6} \nu^{-10/3} \tag{8}$$

Donelan et al. (1985) showed a very similar result. Figure 5 shows a scatterplot of the nondimensionalized wave energy versus the nondimensionalized wave frequency. As can be shown in the figure, the data from the growing and decaying stage show a strong and consistent correlation. Equation (6), displayed as the dash-dotted line (marked with T), underestimates the data but shows a very similar slope, which was also observed by Liu (1985). Equation (8), displayed as the dashed line (marked with H), shows a better fit to the data of the decaying stage than that of the growing stage. The average relation can be visually approximated by the solid line in the figure, which is

$$\epsilon = 13 * 10^{-6} \nu^{-3} \tag{9}$$

The coefficient is much higher than that in Equation (6).

2.2 Significant Wave Height Versus Average Wave Period

A scatterplot of the significant wave height versus the average wave period is shown in Figure 6 . The two curves in the figure represent the relation between H_s, in m and T_z, in s, which is

$$H_s = C{T_z}^2 \tag{10}$$

where C = 0.11 and C = 0.09. In the growing stage, the relationship between the significant wave height and the wave period can be represented by C = 0.11. final stage of wave growth and the earlier stage of wave decay, in which wave height exceeded 10 m, the wave height exceeded 10 m, the wave height and period relation can be fitted with C = 0.1. During The rest of the decaying stage, the relation can be represented by C = 0.009. It is noted that, based on PM spectral model, the value of C is 0.092.

2.3 High Frequency Wave Energy Versus Wind Speed

Based on the study of hurricane-generated waves, Stacy (1974) showed that the high-frequency portion of wave spectrum is wind speed dependent. High-frequency wave energy, represented by the integration of $S(f)$ from 0.33 to 0.4 Hz versus the wind speed, is shown in Figure 7 . In general, as the wind speed increases, the high-frequency wave energy increases. It is noted that as the wind speed reaches 15 m/s, the wave energy drops significantly and, then, increases as the wind speed increases. The relation between the high-frequency wave energy, E_h, in m^2 and wind speed, U, in m/s can be approximately represented by

$$E_h = AU^{1.1} \tag{11}$$

where A = 0.0003 for U is greater than 15 m/s. The drop of wave energy as the wind speed reaches 15 m/s, and the slower wave energy increase at higher wind speeds, could be due to increasing energy dissipation caused by wave breaking.

2.4 Peak Wave Energy Versus Peak Frequency

According to the PM spectral model, the peak wave energy, $S(f_p)$, is related to peak frequency by

$$S(f_p) = \alpha(2\pi)^{-4} g^2 f_p^{-5} e^{-1.25} \qquad (12)$$

where the α is the equilibrium range parameter and has a constant value of 0.0081 for the PM model. Figure 8 shows the plot of the peak wave energy versus the peak frequency. The peak wave energy increases as the peak frequency decreases. It is also noted that a given peak frequency, the corresponding peak wave energy of the growing stage is generally higher than that of decaying stage. This indicates that the wave spectrum during the growing stage has a sharper peak than that of the decaying stage. The PM model, shown as the dashed line, displays a very similar pattern but underestimates the data noticeably. The average relation of the peak wave energy and the peak frequency can be approximated by the solid line, which is the PM model multiplied by a factor of 3.3.

2.5 Spectral Shape of Equilibrium Range

Phillips (1958) showed, based on similarity considerations, that wave spectrum in deep water in equilibrium range should vary as f^{-5} , which is

$$S(f) = \alpha\, g^2 f^{-5} \qquad (f > f_p) \qquad (13)$$

where α is a universal constant. Many field measurements, however, showed an f^{-4} characteristic (Forristall, 1981; Donelan et al., 1985). Figure 9 shows the spectra of the significant wave height greater than 10 m. To show the slope characteristic of the spectrum rear face, the spectra have been multiplied by f^{-4} and normalized by the average value of high-frequency spectral density multiplied by f^{-4} in the range between $1.5f_p$ and $3f_p$ (Donelan et al., 1985). The f^{-4} shape characteristic is indicated by the straight dashed line of a value of 1. The f^{-5} shape characteristic is represented by the dash-dotted line. As can be seen in the figure, at frequencies less than $3f_p$, the spectra exhibit an f^{-4} shape. At frequencies larger than $3f_p$, the spectra show an f^{-5} shape. This suggests that the rear face of wave spectrum follows the or shape characteristics depending on the relative frequency range with respect to the f_p

2.6 Equilibrium Range Parameter

The parameter α is considered the shape parameter related to the equilibrium range of wave spectrum, which can be estimated by (Hasselmann et al., 1973)

$$\alpha = \frac{(2\pi)^4 \int_a^b f^{-5} e^{1.25\left(\frac{f}{f_p}\right)^{-4}} S(f)\,df}{0.65 g^2 f_p} \tag{14}$$

where a = 1.35f_p and b = 2f_p Hasselmann et al. (1976) showed that α is related to the nondimensional peak frequency by

$$\alpha = 0.033\, \nu^{2/3} \tag{15}$$

Figure 10 shows the computed α versus the nondimensional peak frequency and a dashed line representing Equation (15). The correlation is significant and consistent through the wave growing and decaying stages. The proposed relation in Equation (15) shows a similar slope but underestimates the data.

Because the spectral shape is primarily controlled by the nonlinear energy transfer, Huang et al. (1981) suggested that the parameter α should be related to a parameter describing wave nonlinearity, which is the significant slope defined as

$$s = \frac{m_0^{1/2}}{L_p} = \frac{2\pi\, m_0^{1/2} f_p^{\,2}}{g} \quad 16)$$

Huang et al. (1981) pointed out that the relation between α and the significant slope was implicitly shown by Hasselmann et al. (1976) as

$$\lambda = \frac{\epsilon \nu^4}{\alpha} = 1.6 * 10^{-4} \tag{17}$$

Based on Equations (16) and (17), Huang et al. (1981) derived

$$\alpha = 16.04\, \pi^2 s^2 \tag{18}$$

Figure 11 shows the scatterplot of α versus the significant slope, and a dashed line representing Equation (18). The data of the decaying stage have a better agreement with the proposed relation in Equation (18) than that of the growing stage.

3. CONCLUDING REMARKS

A detailed examination of a set of extreme wave data caused by a fast moving storm was presented. The high-frequency spectral shape at frequencies less than $3f_p$ shows an f^{-4} characteristic. At frequencies higher than $3f_p$ an f^{-5} shape is more evident. During the growing and decaying stages, the high-frequency wave energy increases as the wind speed increases.

A significant correlation between the nondimensionalized wave energy and the nondimensionalized wave peak frequency is shown. The shape parameter, α, was related to the nondimensional peak frequency and the significant slope. These parametric relations are consistent through the wave growing and decaying stages.

In general, the parametric relations shown from this data set are consistent only qualitatively with those proposed in many previous studies. Realizing the complexity and variety of the storm-generated waves and only a very small portion of extreme wave data from the 14 buoy stations were analyzed, more studies and analyses are needed before any definitive conclusions about the characteristics of storm generated extreme waves can be reached.

Acknowledgements. The author would like to thank NDBC for supporting this study. The valuable comments by Ted Mettlach and Ian Palao of Computer Sciences Corporation and Paul Liu of the Great Lakes Environmental Research Laboratory are appreciated.

REFERENCES

Donelan, M.A., J. Hamilton, and W.H. Hui, 1985: Directional spectra of wind generated waves. Phil. Trans. Roy. Soc. London, A315, 509-562.

Forristall, G.Z., 1981: Measurements of saturated range in ocean wave spectra. J. Geophys. Res. 86, 8075-8089.

Hasselmann, K., T.P. Barnett, E. Bouws, H. Carlson, D.E. Cartwright, K. Enke, J.A. Ewing, H. Gienapp, D.E. Hasselmann, P. Kruseman, A. Merrburg, P. Muller, D.J. Olbers, K. Richter, W. Sell, and H. Walden, 1973: Measurements of wind-wave growth and swell decay during the Joint North Sea Wave Project (JONSWAP). Deut. Hydrogr. Z. A12.

Hasselmann, K., D.B. Ross, P. Mill and W. Sell, 1976: A parametric wave prediction model. J. Phys.Oceanogr. 6, 200-228.

Huang, N. E., S.R. Long, C.C. Tung, and L.F. Bliven,1981: A unified two-parameter wave spectral model for a general sea state. J.Fluid Mech. 112, 203-224.

Kraft, A.J., 1993: The evolution of jet features during the 1993 east coast "White Hurricane": A case study using the global spectral model. Thesis, Naval Postgraduate School, Monterey, CA.

Liu, P., 1985: Testing parametric correlations for wind waves in the Great Lakes. J. Great Lakes Res. 11(4), 478-491.

Mitsuyasu, H., F. Tasi, T. Suhara, S. Mizuno, M. Ohkusu, T. Honda, and K. Rikiishi, 1980: Observation of the power spectrum of ocean waves using a cloverleaf buoy. J. Phys. Oceanogr. 10, 286-296.

Phillips, O.M., 1958: The equilibrium range in the spectrum of wind-generated waves. J. Fluid Mech. 4, 426:434.

Pierson, W.J., and L. Moskowitz, 1964: A proposed spectral form for fully developed wind seas based on the similarity theory of S.A. Kitaigorodskii. J. Geophys. Res., 69, 5181-5190.

Stacy, R.A., 1974: Spectral analysis of high frequency gravity waves generated by a hurricane. Ph.D. Dissertation, New York University, 63 p.

Steele, K.E. and T. Mettlach, 1993: NDBC wave datacurrent and planned. Proc. 2nd International Symposium on Ocean Wave Measurement and Analysis, New Orleans, 198-207.

Toba, Y., 1972: Local balance in the air-sea boundary processes, I. J.Oceanogr. Soc., Japan, 28, 109-120.

Toba, Y., 1978: Stochastic form of the growth of wind waves in a single-parameter representation with physical implications. J. Phys. Oceanogr. 8, 494 507.

Zahn, P.B. and M. Grim, 1995: Determination of extreme seas encountered by operational ships. J. Naval Engineers, May, 197-2 IS.

Table 1. Maximum significant wave height and related wave and meteorological measurements from 14 NDBC buoy stations.

Station	Hs (m)	Tp (s)	Tz (s)	U (m/s)	Wdir (°)	Atmp (°C)	Wtmp (C°)	Bare (hPa)	TIME day/ UTC
41002	15.66	16.67	12.50	22.5	257	12.1	22.2	998.3	14/04
41009	4.17	7.14	6.31	20.9	261	12.1	20.3	1003.5	13/22
41010	8.29	11.10	8.64	21.4	254	16.0	22.2	1008.0	13/20
42001	9.11	12.50	9.77	21.6	321	11.9	21.0	1018.3	13/12
42002	7.82	11.11	9.07	18.0	342	12.4	20.5	1015.9	13/10
42003	9.10	12.50	9.47	20.7	307	13.5	25.2	1011.6	13/18
42019	5.66	8.33	7.31	17.6	346	9.9	21.5	1020.2	13/06
42020	6.06	9.09	7.81	17.8	328	10.4	22.0	1026.5	13/05
44004	13.52	16.67	12.07	22.1	243	2.8	9.7	986.6	14/12
44005	9.15	12.50	9.53				4.0	971.5	14/15
44007	6.98	11.11	8.73	18.0	30	–3.8	0.9	975.3	14/14
44013	6.01	11.11	8.92	15.8	22	2.4	1.3	974.1	14/02
44014	7.78	14.29	10.43	12.7	190	12.5	6.7	972.0	13/20
44025	7.27	14.29	9.64	16.5	188	6.0	2.9	965.9	14/04

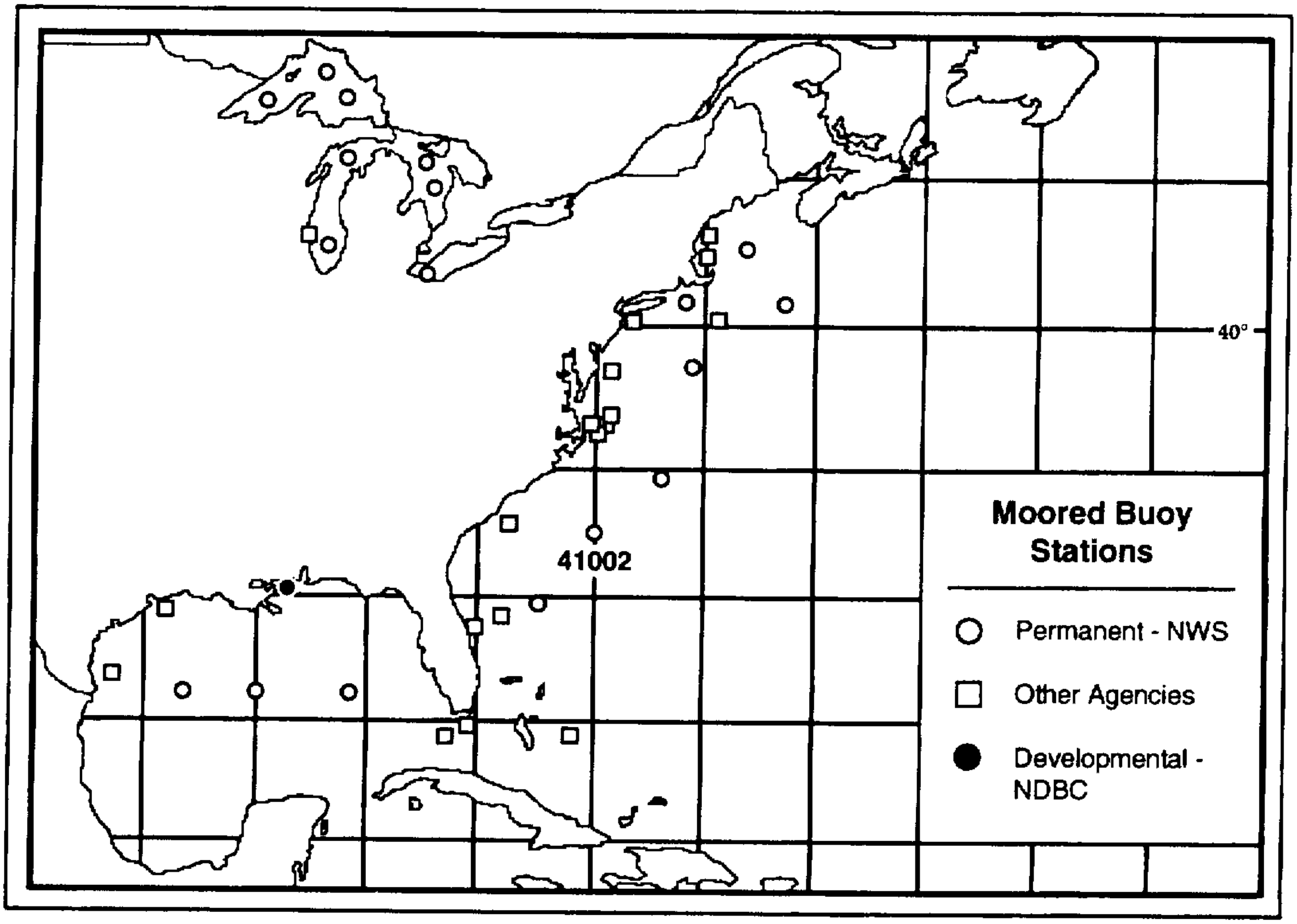

Figure 1. Location maps of NDBC buoy stations during the storm.

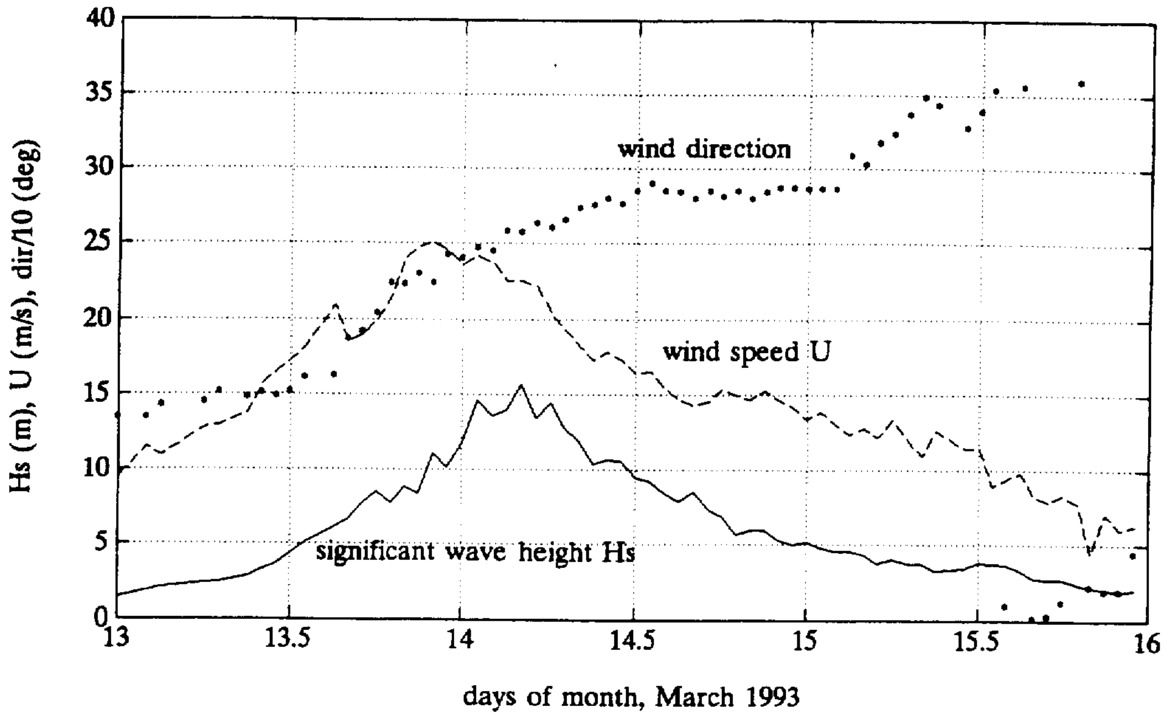

Figure 2. Time series of significant wave height, wind speed, and wind direction during the storm..

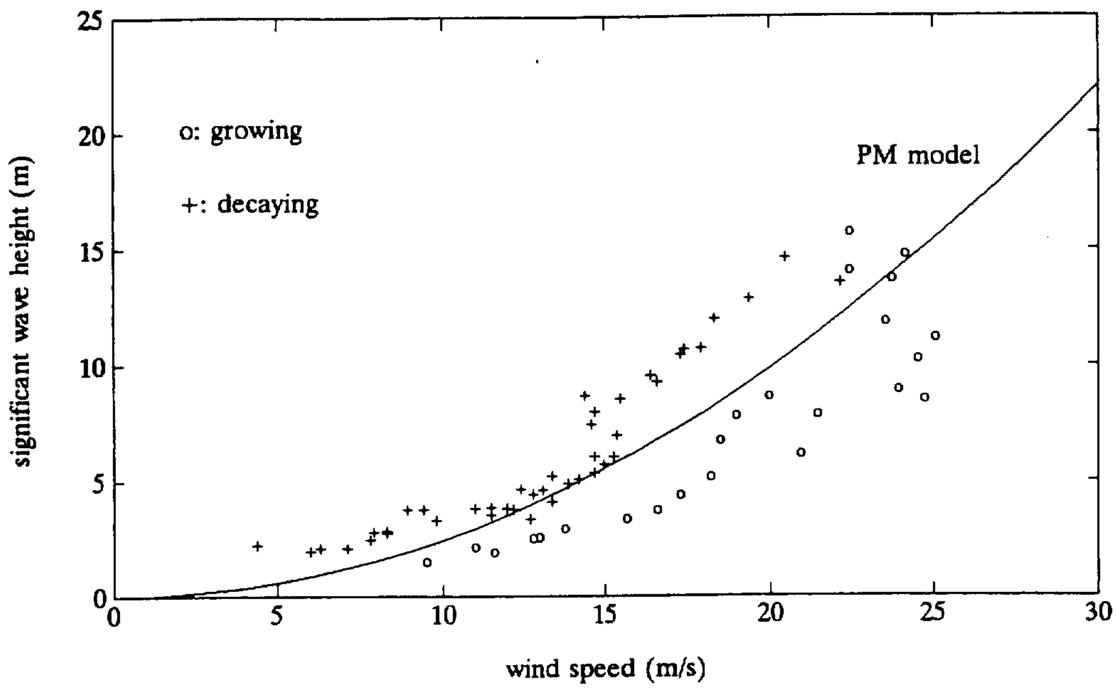

Figure 3. Significant wave height versus wind speed.

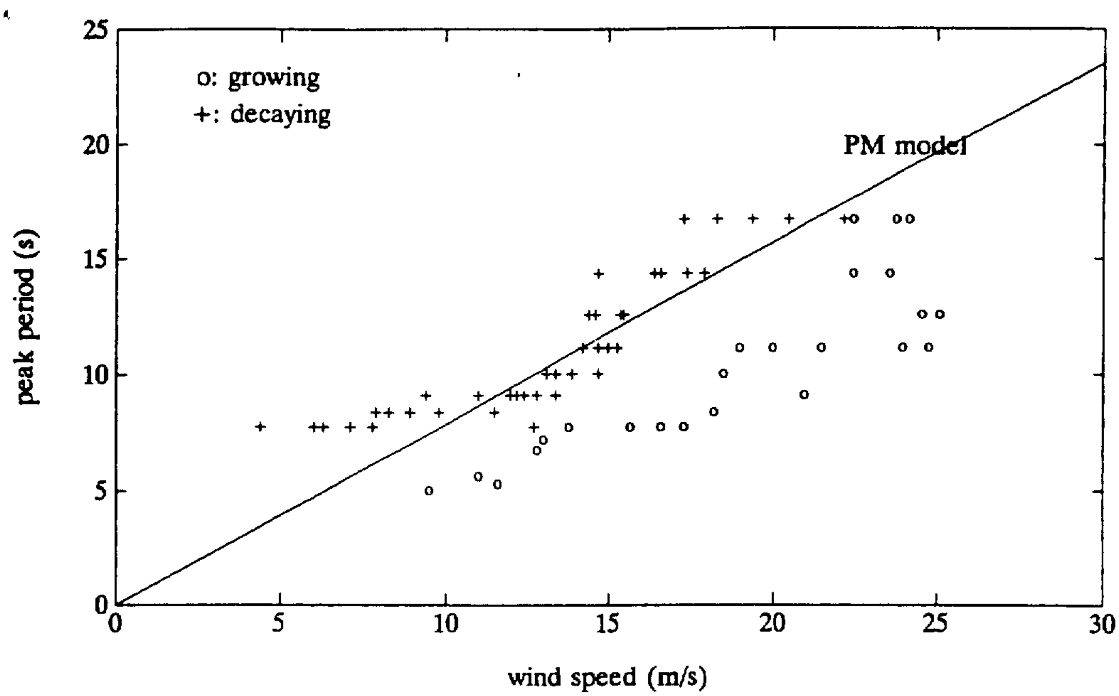

Figure 4. Peak wave period versus wind speed.

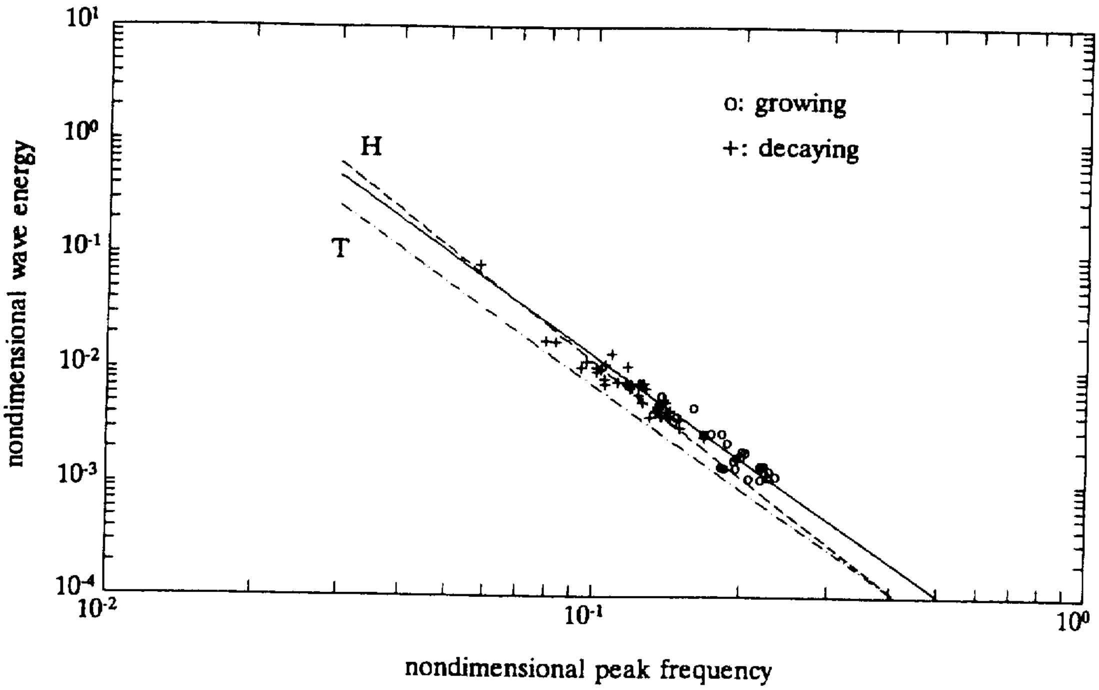

Figure 5. Nondimensional wave energy versus nondimensional peak frequency.

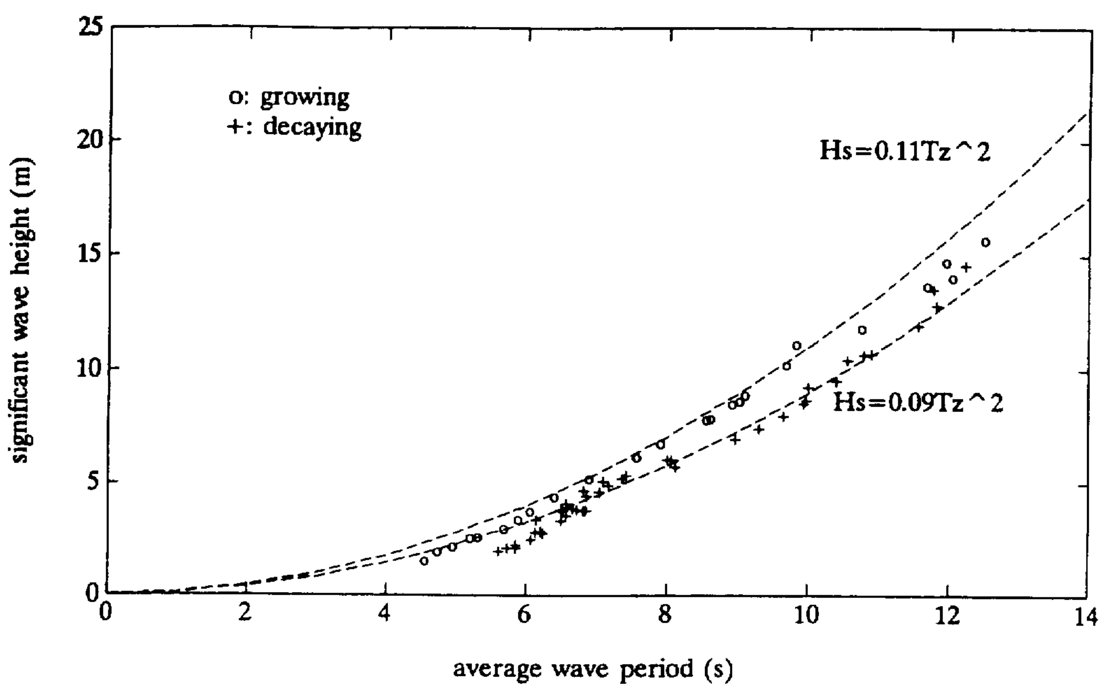

Figure 6. Significant wave height versus average wave period.

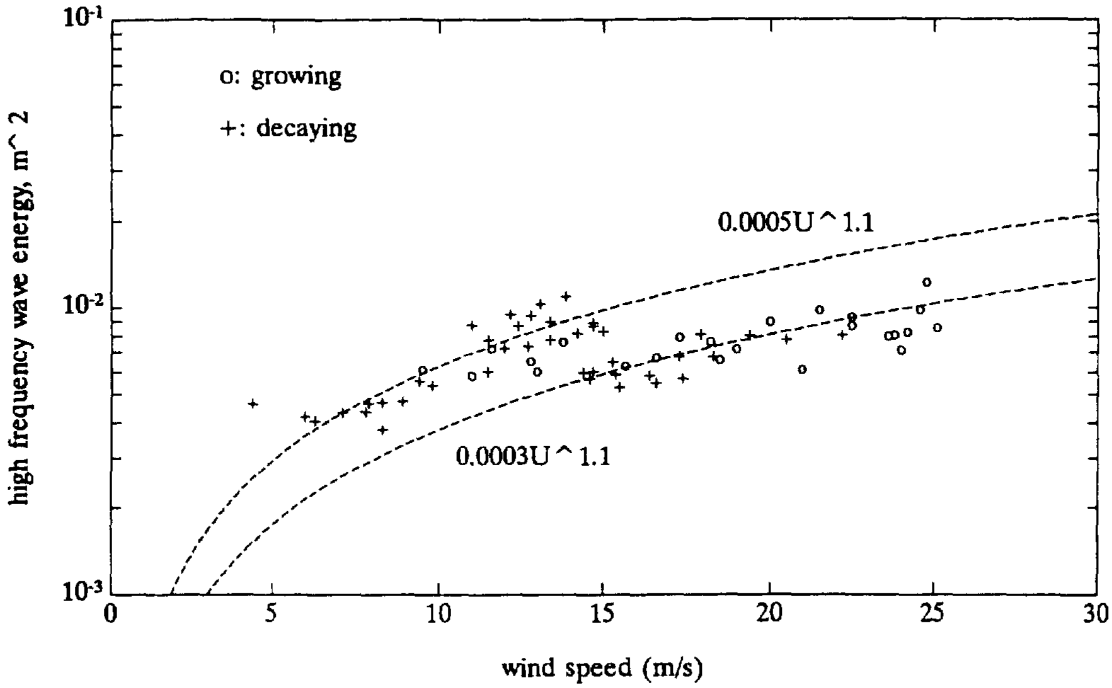

Figure 7. High-frequency wave energy versus wind speed.

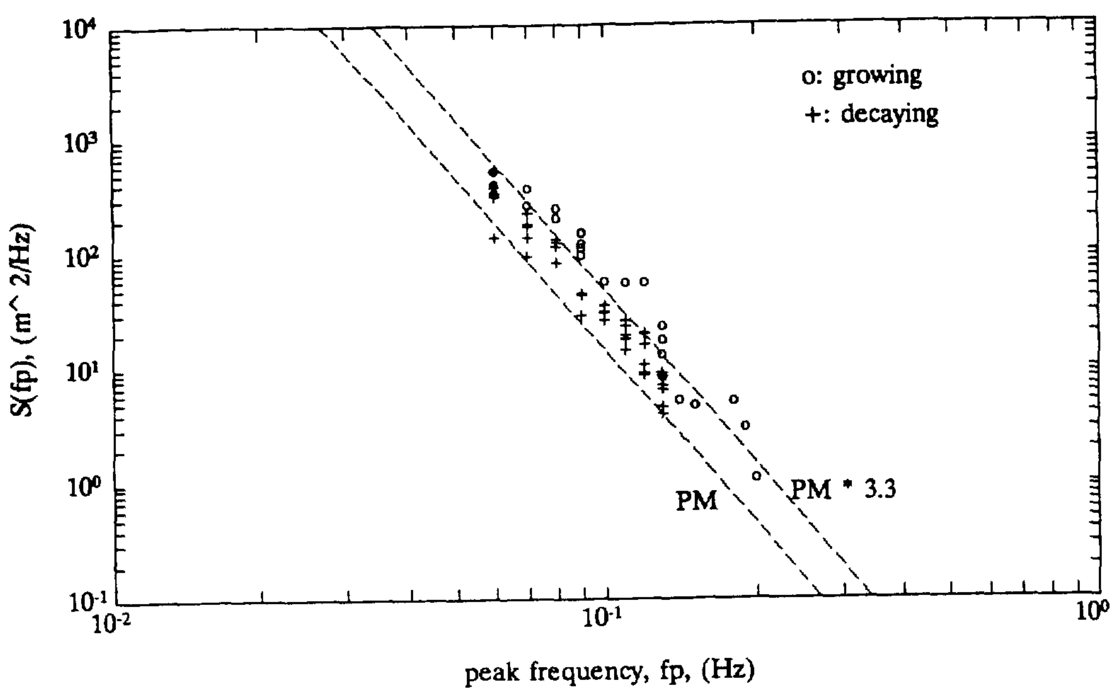

Figure 8. Peak wave energy versus peak frequency.

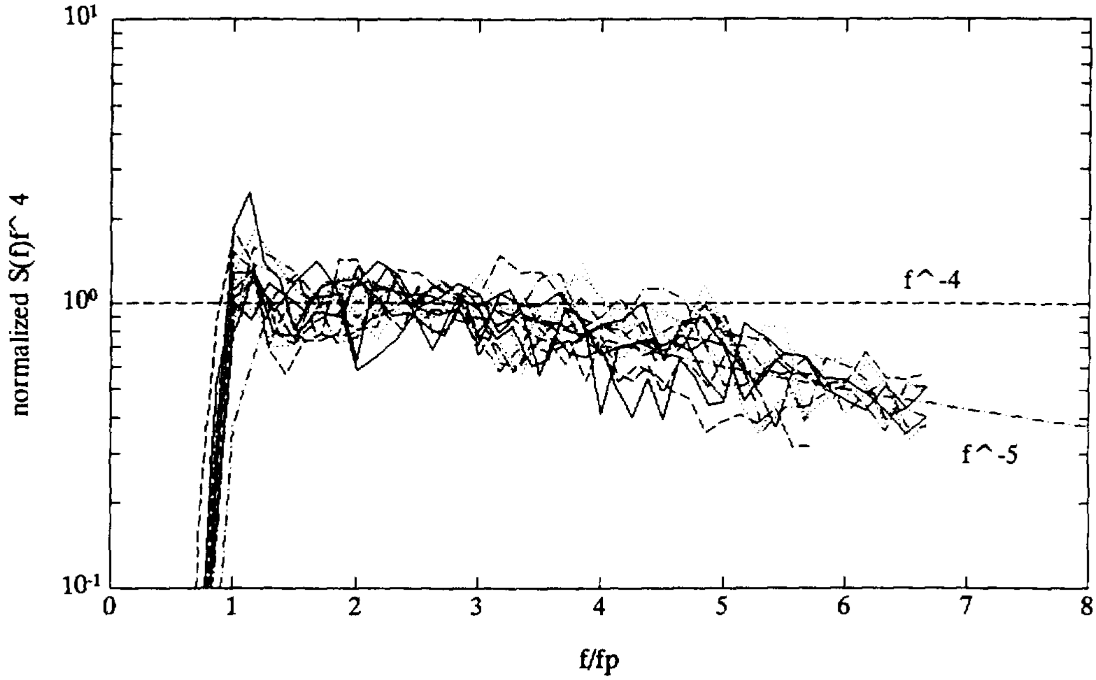

Figure 9. Normalized wave spectra.

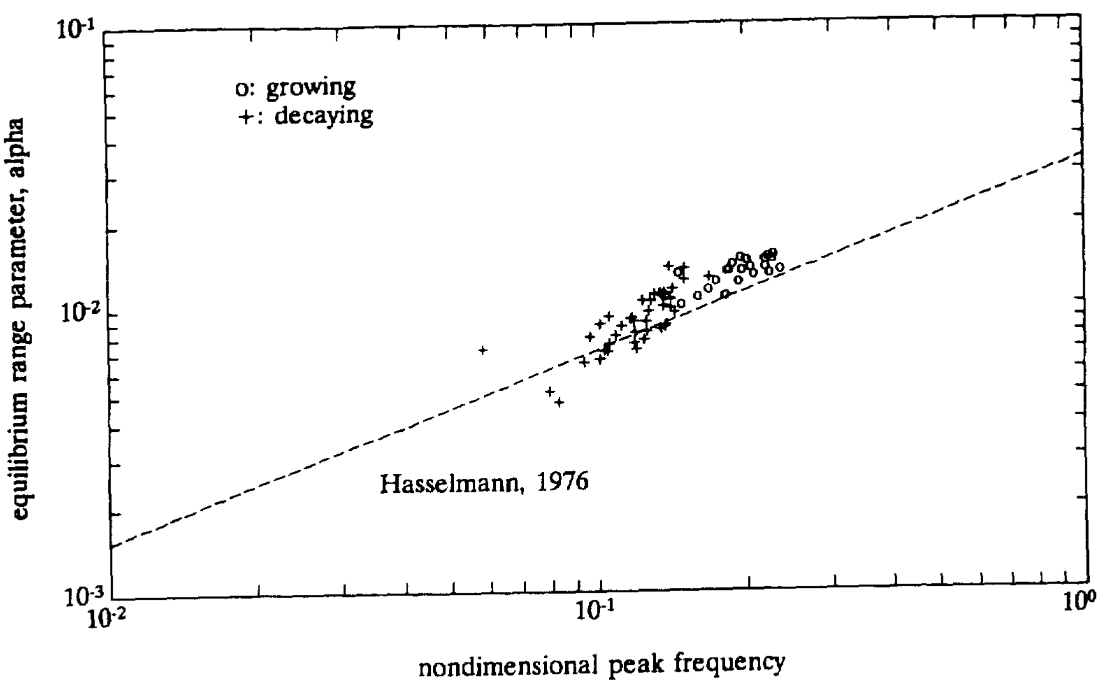

Figure 10. Equilibrium range parameter versus nondimensional peak frequency.

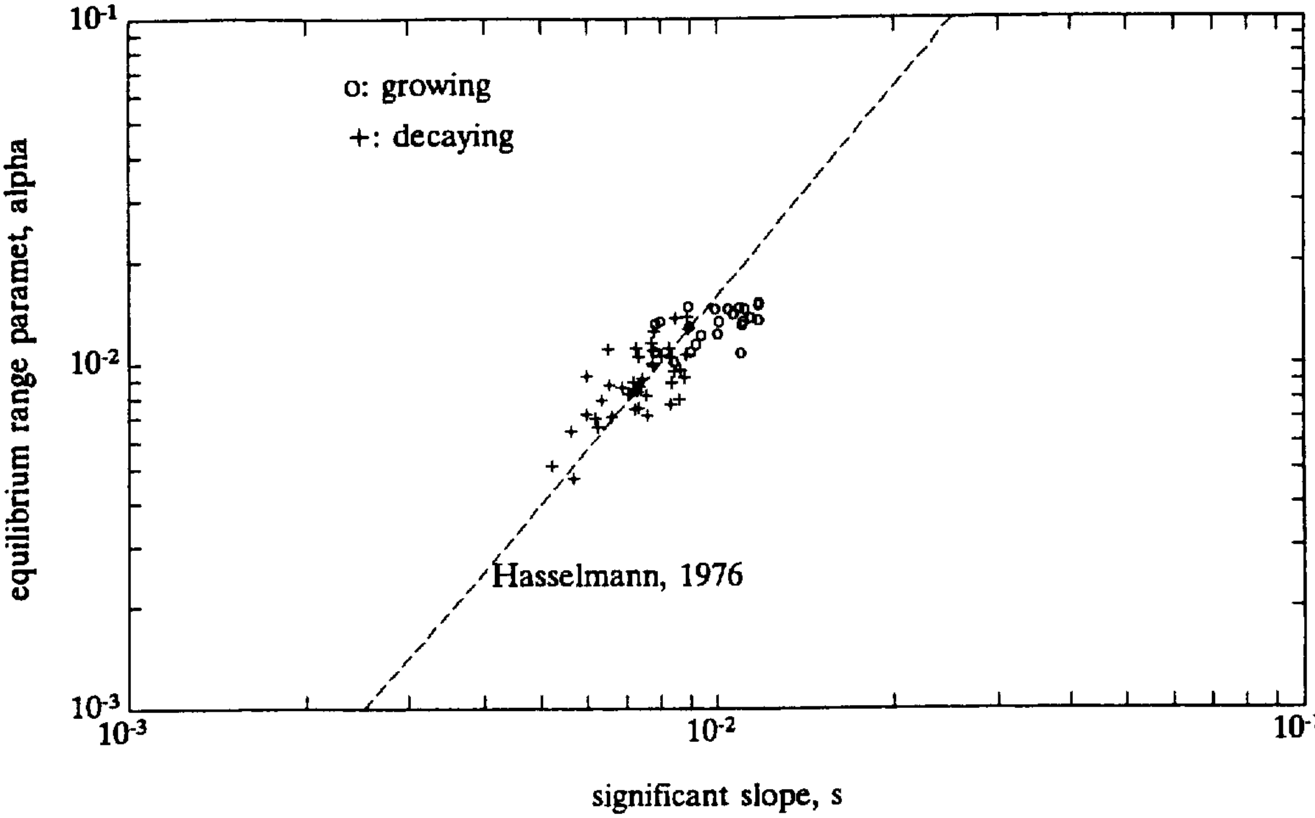

Figure 11. Equilibrium range parameter versus significant slope.

OBSERVATIONS OF THE DIRECTIONAL SPECTRUM OF FETCH-LIMITED WAVES OFF THE WEST COAST OF NEW ZEALAND

K.C. Ewans

Shell Internationale Petroleum Maatschappij B.V.
The Hague, The Netherlands

1. INTRODUCTION

Many offshore applications require information on the directional characteristics of the wave field. These characteristics can be conveniently specified by the directional wave spectrum. Like the omnidirectional case our understanding of the nature of the directional wave spectrum is best studied when some of the many variables which contribute to the general sea state are constant. Fetch-limited sea states provide this situation, and the directional distribution of fetch-limited sea states has been the subject of a number of studies. More significant are those of Mitsuyasu et al. (1975), Hasselmann et al. (1980),and Donelan et al, (1985), each providing parameterisations of a unimodal directional distribution. Young et al. (1995), report an interesting study of fetch-limited waves in Lake George, Australia, where they observed a bimodal directional distribution at frequencies above the spectral peak.

This paper reports observations of fetch-limited directional spectra, made near to the site of the Maui-A platform off the West Coast of New Zealand (Figure 1). An earlier study (Ewans and Kibblewhite, 1990) showed that at this location southeast wind events, which funnel through Cook Strait and the Manawatu Gorge and may persist for just a few hours or for several days and sometimes reach gale force, produce well defined fetch-limited wind-seas at the Maui location. The study showed that the omnidirectional spectrum associated with these "southeast events" conformed closely to the JONSWAP (Hasselmann et al., 1973) spectral shape, and the fetch-dependencies of the parameters of the spectrum were quite similar to those observed in the JONSWAP experiment.

Similarly, the southeast winds, which occur ,approximately 25% of the time at the Maui location, provided a number of well-defined fetch-limited conditions during a subsequent wave directional measurement programme. The corresponding sea states, which were measured with a WAVEC heave-pitch-and-roll buoy are the basis of this paper.

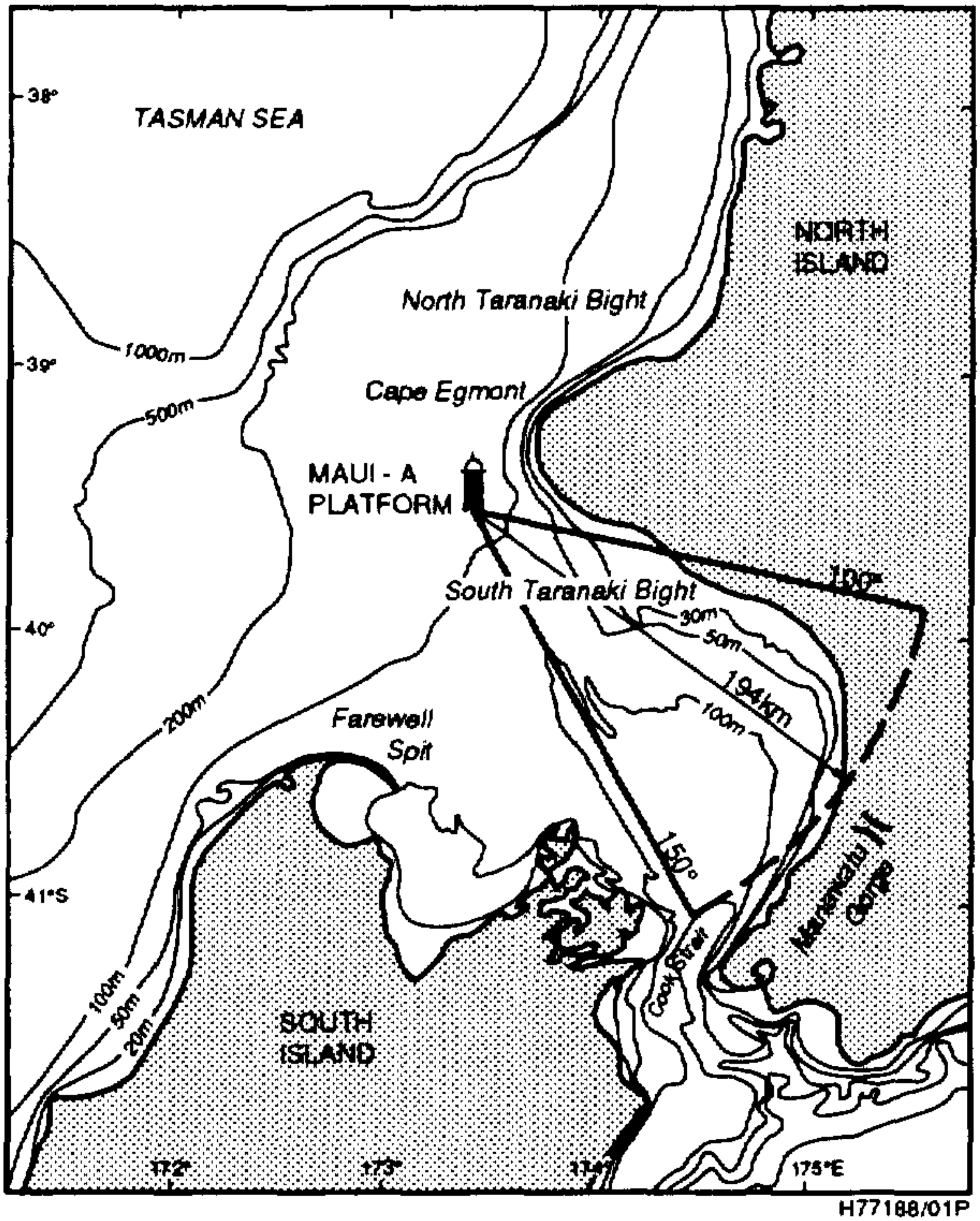

Figure 1: The Greater Cook Strait region of New Zealand. The WAVEC buoy was installed close to the Maui-A platform.

Section 2 describes the measurement programme and data processing. Sections 3 and 4 describe the data and analyses. Section 5 gives a comparison of the observed spreading with previously published parameterisations of directional distributions. Section 6 presents the directional distributions derived from the Maui data and a comparison with the Young et al. (1995) results. A parameterisation of the Maui directional distributions is also given in Section 6 ; this is discussed in Section 7 , and conclusions are given in Section 8 .

2. MEASUREMENT PROGRAMME AND DATA PROCESSING

The wave measurements were made with a Datawell WAVEC buoy moored near to the Maui-A platform 32 km off the west coast of the North Island of New Zealand, in a water depth of 110 m. Measurements commenced in November 1986 and concluded in November 1987. Wind measurements were made with a Lambrecht anemometer instilled on the Maui-A platform at a height of 95 m above sea level.

The signals of heave,and pitch and roll angles were digitized at 1.28 Hz and each half hour co-incident and co-quadrature spectra (co-quad spectra) were computed from the previous 20 minutes of recordings. Spectral analysis followed the Welch (1967) technique with the final spectrum being in average of 6 sub-series of 200 s length, and having approximately 12 degrees of freedom. The co-quad spectra were corrected for the buoy heave filter and then smoothed from 0.16 Hz to 0.50 Hz, resulting in spectra with 0.005 Hz resolution from 0.03 Hz to 0.155 Hz and 0.010 Hz resolution from 0.16 Hz to 0.50 Hz.

The co-quad spectra corresponding to the fetch-limited southeast sea states were further averaged over 3 hours, resulting in estimates with approximately 72 degrees of freedom. From these 3-hourly averages, the first four Fourier coefficients of the directions spectrum were calculated in the standard way (e.g. Long, 1980), and subsequently spectra for the mean wave direction, $\bar{\theta}(f)$, and the circular rms spreading, $\sigma(f)$, were calculated from the first pair of Fourier coefficients (see Equation (1)), following Kuik el at. (1988). This process is further described in Section 3 .

The wind data were recorded on a strip chart, from which the 10 minute mean speed and direction were obtained at hourly intervals. The wind speeds were reduced to an equivalent wind speed at 10 in above sea level using a neutral wind profile.

3. SELECTION & PROCESSING OF STEADY SEA STATES

A population of southeasterly spectra was established by selecting all those spectral for which the wind direction was from the southeast and the mean wave direction was within the sector 100° to 150°. From this population a sub-selection of steady spectra was made on the basis that:

(i) the wind speed was steady to within 1 m/s for at least 4 hours (based on the last 5 wind estimates), and

(ii) the omnidirectional, $E(f)$, circular rms, $\sigma(f)$, and mean direction, $\bar{\theta}(f)$, spectra were approximately constant for the last 3 hours (based on the last 7 half hourly spectra).

This selection process resulted in a sub-population of 77 groups of co-quad spectra.

A feature of the wave climate at the Maui location is the presence of a more or less persistent swell from the southwest. Fortunately, this component occurs at low frequency, generally having a peak frequency of around 0.080 Hz (Ewans and Kibblewhite, 1992), is well separated from the wind-sea frequency band, and can easily be removed from the analysis by restricting further calculations and analysis to the high frequency band width corresponding to the local southeast wind-sea. In a few cases it was not possible to apply this simple filter because the southeast sea band width extended to low-frequency into the swell band, but these cases corresponded to large local sea states, in which the local wind-sea component completely swamped the southwest swell component. In these cases, in the frequency region in which the two components overlapped, the spectral levels associated with the wind-sea were at least an order of magnitude larger than the swell component, and the mean wave direction at these frequencies was equal to the wind-sea mean direction. The selection of the low-frequency cut-off of the wind-sea component was done by eye, based on plots of the omnidirectional, mean direction, and circular rms spreading spectra.

A number of parameters were calculated over the band width of the local southeast wind-sea, including the following parameters.

- The maximum of the omnidirectional spectrum, $E(f)_p$, and the frequency of the maximum, f_p.

- The significant wave height, $H_s = 4\sqrt{(m_0)}$, and the mean wave period, $T_2 = \sqrt{(m_0/m_2)}$ where the m_i are the moments of the omnidirectional spectrum.

In addition the vector average wind speed and direction, averaged over the last three hours were stored for each spectrum.

The 77 spectra had significant wave heights ranging between 0.54 m to 4.2 m, mean wave periods between 3.3s and 6.9s, and had associated vector average wind speed ranging from 4.6 m/s to 18.3 m/s, and inverse wave ages, ranging from 0.70 to 1.4.

4. ESTIMATION OF THE DIRECTIONAL DISTRIBUTION

An estimate was made of the directions Distribution from the Fourier coefficients at each frequency, using both the Maximum Entropy Method (MEM) (Lygre and Krogstad, 1986) and the Maximum Likelihood Method (MLM) (Isobe et al., 1984). Both of these techniques are model independent and allow for the possibility that the distribution may be bimodal.

The resulting MEM and MLM estimates at each frequency were subjected to further analysis, and the following parameters were computed for each:

- The local maxima and minima and the directions of the local maxima. For each estimate there may be either one or two local minima/maxima, depending on whether the particular distribution had respectively one or two peaks.

- Three directional distribution shape parameters as defined by Kuik et al. (1988): p, the ratio of the area of the distribution from θ_{max} to $\theta_{max} - \pi$ to the area of the distribution from θ_{max} to $\theta_{max} + \pi$; q, the ratio of the largest minimum to the smallest maximum (if the distribution is bimodal); and r, the ratio of the area of the secondary lobe over the area of the main lobe. Kuik et al., 1988, used these parameters to evaluate whether directional distributions could be categorised as unimodal and symmetric or nearly unimodal and symmetric if either a distribution was unimodal but not exactly symmetric or a distribution was strictly bimodal but the secondary lobe was relatively insignificant compared with the main lobe.

- A unimodal/symmetric parameter ,U_{pqr}, which is set to 1 if the distribution can be categorised as unimodal and symmetric or nearly unimodal and symmetric (based on the criteria specified in Appendix B of Kuik et al. 1988) and 0 if not. This parameter was computed for the MEM and the MLM estimates.

5. COMPARISON WITH OTHER DISTRIBUTIONS

5.1 <u>General</u>

The two dimensional frequency-direction spectrum, $E(f,\Theta)$, is often expressed as the product of the omnidirectional variance density spectrum, $E(f)$ and the directional distribution, $H(f,\Theta)$, as follows:

$$E(f,\Theta) = E(f)H(f,\Theta)$$

The directional distribution has the properties of a probability distribution, vis.

$0 \leq H(f,\Theta) \leq 1$

and

$$\int_0^{2\pi} H(f,\Theta) = 1$$

In turn $H(f,\Theta)$ is frequently expressed as a Fourier series

$$H(f,\theta) = \frac{1}{\pi}\left\{\frac{1}{2} + \sum_{n=1}^{\infty}\left[a_n(f)\cos n\theta + b_n(f)\sin n\theta\right]\right\} \quad (1)$$

5.2 Published Distributions

Mitsuyasu et al. (1975), Hasselmann et al. (1980), and Donelan et al. (1985) have independently estimated the form of the directional distribution from directional wave measurements.

5.2.1 Mitsuyasu Distribution

Mitsuyasu et al. (1975) measured directional wave spectra, with a cloverleaf buoy, at open sea locations in the Sea of Japan and the Pacific Ocean and in a bay on the east coast of Japan. Meteorological data were collected from a (ending ship near each observation station. They chose 5 data sets for estimating the directional distribution, with wind speeds ranging from 7 to 10 m/s and significant wave heights from 0.74 to 2.34 in. The cloverleaf buoy enables the first four pairs of the coefficients in Equation (1) to be calculated. However, the higher order coefficients which are available from the measurement of the wave curvature were not used because they were thought to be inaccurate. Thus, the data used by Mitsuyasu et al. (1975) were the same as if the measurement instrument was a heave-pitch-and-roll buoy.

The Mitsuyasu distribution is based on the so-called 'cosine2s' form.

$$H(f,\theta) = A(s)\cos^{2s}\left(\frac{\theta - \overline{\theta}(f)}{2}\right) \quad (2)$$

where A(s) is a normalisation factor to ensure condition (ii) above is met, and $\overline{\theta}(f)$ is the mean wave direction at frequency f. The parameter s is a function of frequency.

Based on their data, Mitsuyasu et al. (1975) proposed the following parameterisation for s.

$$s = \begin{cases} s_p\left(\dfrac{f}{f_p}\right)^{5} & f < f_p \\ s_p\left(\dfrac{f}{f_p}\right)^{-2.5} & f \geq f_p \end{cases} \qquad (3)$$

where s_p is the value of s at the frequency of the spectral peak, f_p, given by

$$S_p = 11.5\left(\frac{U_{10}}{C_p}\right)^{-2.5} \qquad (4)$$

where U_{10} is the wind speed at 10 m above sea level and $C_p = g/(2\pi f)$ is the deep-water phase speed at the spectral peak. The directional distribution defined by Equations (2), (3), and (4) will be referred to as the Mitsuyasu distribution in the remainder of this paper.

5.2.2 Hasselmann Distribution

Hasselmann et al. (1980) report an analysis of data recorded during the JONSWAP experiment. The directional wave data were collected with a heave-pitch-and-roll buoy located in 22 m of water 52 km off the island of Sylt in the North Sea. Meteorological data were also collected at this site and with a meteorological buoy located 27 kin offshore in a water depth of 18 m. The data set chosen for analysis ranged in wind speed from 6.8 to 15.0 m/s and significant wave heights from 0.55 to 1.88 m.

The Hasselmann distribution is also based on the ‘cosine2s’ form with the following parametrisation for s.

$$s = \begin{cases} 6.97\left(\dfrac{f}{f_p}\right)^{4.06} & f < 1.05 f_p \\ 9.77\left(\dfrac{f}{f_p}\right)^{\mu} & f \geq 1.05 f_p \end{cases} \quad (5)$$

where μ has a dependence on wave age as follows:

$$\mu = -2.33 - 1.45\left(\frac{U_{10}}{c_p} - 1.17\right) \quad (6)$$

The directional distribution defined by Equations (2), (5), and (6) will be referred to as the Hasselmann distribution in the remainder of this paper.

5.2.3 Donelan Distribution

Donelan et al. (1985) report an analysis of data recorded with an array of 14 wave staffs in Lake

Ontario and a similar, scaled down version in a large laboratory tank. The wave staffs were mounted on tower 1 km offshore in a water depth of 12 m. Meteorological data were also collected from the tower and with a buoy 11 km from the tower in deeper water. Eighty five field recordings and 7 laboratory recordings were used in the analysis. Donelan et al. (1985) do not report the absolute range of wind speed and significant wave heights associated with their analysis data set, but the field data were in the range $0.83 < U_{10}/C_p < 4.6$ and the laboratory data in the range $7.2 < U_{10}/C_p < 16.5$.

Based on the theoretical directional characteristics freely propagating, second-order Stokes wave groups, and analysis of their data, Donelan et al. (1985) proposed the following directional distribution:

$$H(f,\theta) = 0.5\beta \operatorname{sech}^2 \beta(\theta - \overline{\theta}(f)) \quad (7)$$

$$\beta = \begin{cases} 2.61\left(\dfrac{f}{f_p}\right)^{1.3} & 0.56 < f/f_p < 0.95 \\ 2.28\left(\dfrac{f}{f_p}\right)^{-1.3} & 0.96 < f/f_p < 1.6 \\ 1.24 & f/f_p > 1.6 \end{cases} \qquad (8)$$

The Donelan et al. (1985) data set only extended to $f/f_p = 1.6$. Thus, the constant value of $\beta = 1.24$ for frequencies greater than 1.6 was assumed.

The directional distribution defined by Equations (7) and (8) will be referred to as the Donelan distribution in the remainder of this paper.

5.2.4 Donelan/Banner Distribution

Based on high frequency stereo photography, Bann (1990) concluded that ß was not a constant at value of $f/f_p > 1.6$ as specified by Donelan et al. (1985) and proposed that

$$\beta = 10^{\left\{-0.4+0.8393\exp\left[-0.567\ln\left(\left(\frac{f}{fp}\right)^2\right)\right]\right\}} \qquad f/fp > 1.6$$

Thus, the distribution referred to as the Donelan/Banner distribution in this paper consists of the Donelan distribution to $f/f_p = 1.6$ and the Banner value for β for $f/f_p > 1.6$.

5.3 Comparison of Proposed Distributions with the Maui Data

The s parameter in the 'cosine2s' distribution can be estimated directly from the circular rms spreading as

$$s = \frac{2}{\sigma^2} - 1 \qquad (9)$$

where

$$\sigma = \sqrt{2 - 2\sqrt{a_1^2 + b_1^2}} \qquad (10)$$

This parameter was calculated for all 77 Maui spectra and is plotted as a function of non-dimensional frequency, f/f_p, in Figure 2 . Figure 2 shows that the data are in qualitative agreement with previous observations of this parameter - the spreading is a minimum (s maximum) at the spectral peak but increases with increasing and decreasing frequency.

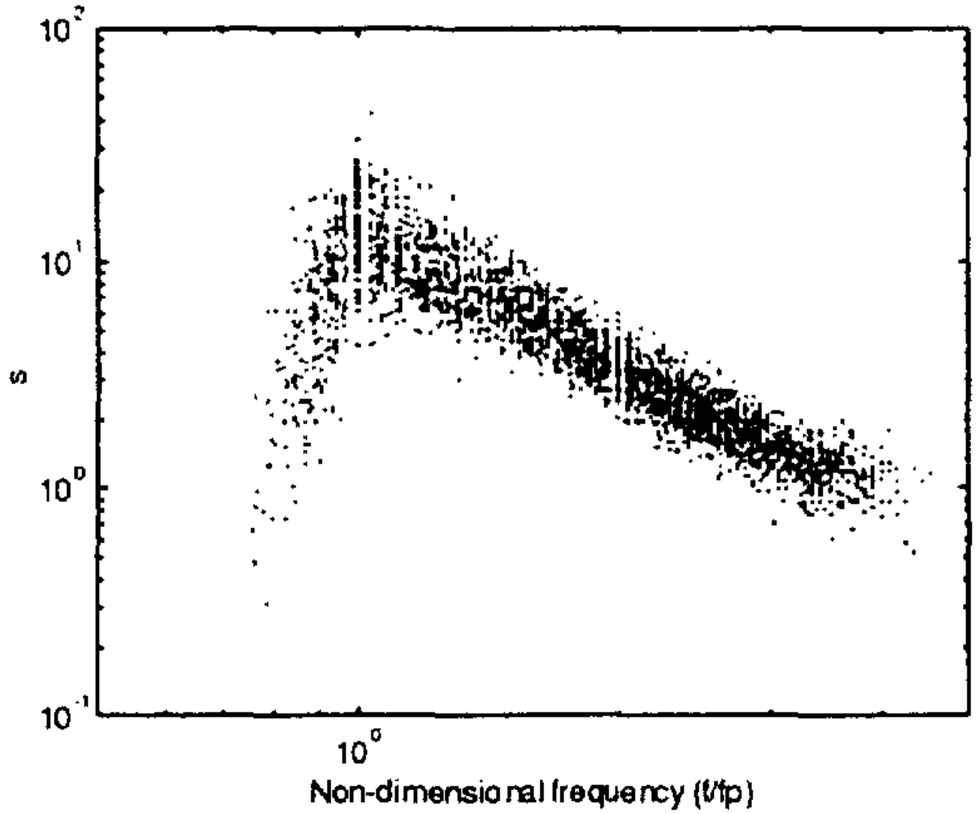

Figure 2: Plot of s against f/f_p for the southeast fetch-limited Maui sea states.

Hasselmann et al. (1975) argue that if the directional spreading is controlled pre-dominantly by nonlinear wave-wave interactions then s should depend mainly on f/f_p, while if atmospheric input was the controlling process, then s should depend mainly on U/c_p. To investigate the behaviour of the Maui data in this respect, the spectra were categorised into groups of inverse wave age, the frequency nondimensionalised and binned, and an average s value calculated for each f/f_p, bin. This resulted in average s curves for each category. These curves are plotted in Figure 3 . Also plotted in Figure 3 are the s values from the Mitsuyasu and the Hasselmann distributions for U_{10}/C_p = 0.8 and 1.2.

Figure 3 shows good agreement between the shape of the Maui distributions and the previously published s values, although the Maui distributions, with higher s values, show less directional spreading than the other distributions over the high frequency range of the spectrum, and have a more rapid increase in spreading with decreasing frequency below f_p. The Maui curves also show no significant evidence of a dependency of s the on U_{10}/C_p.

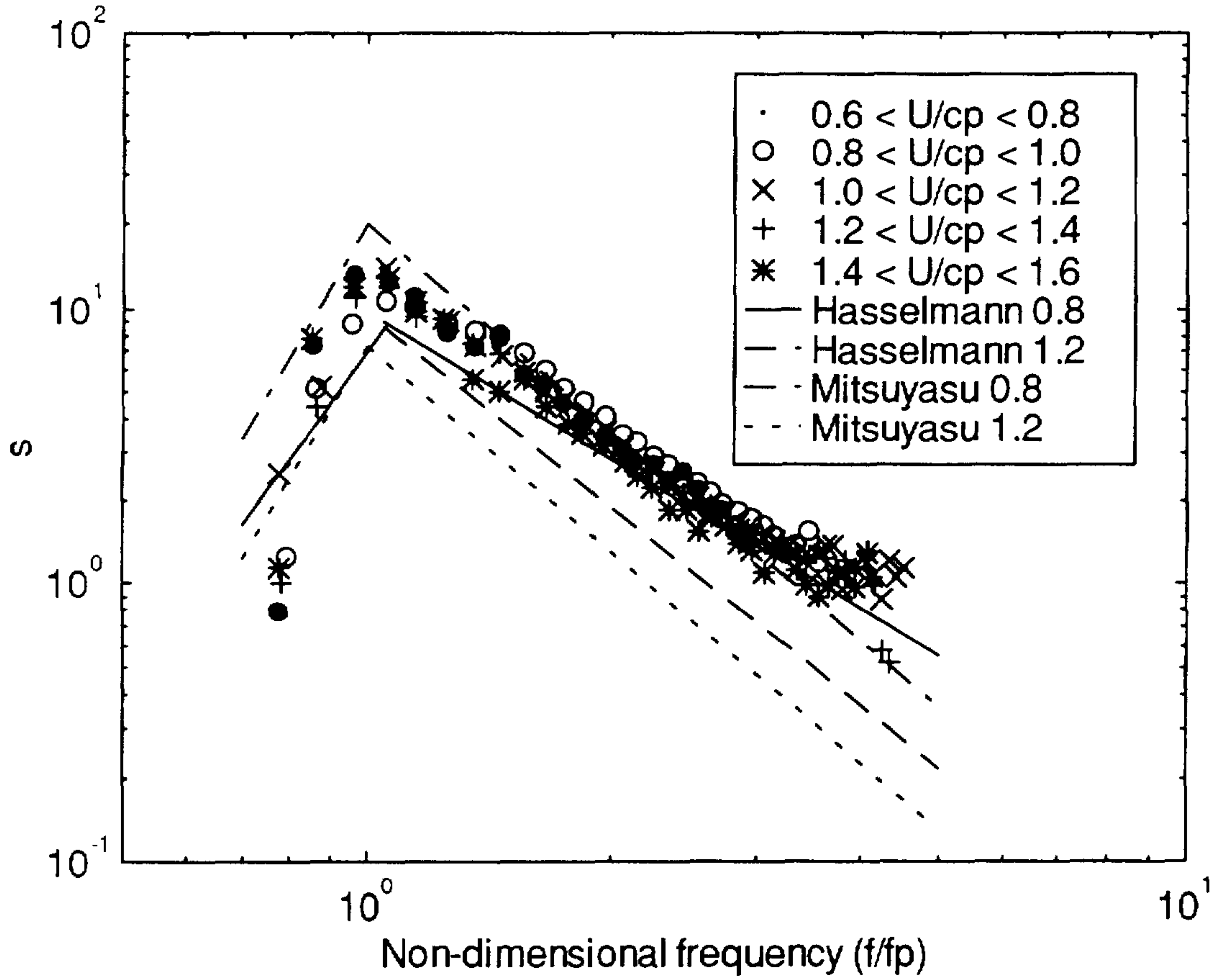

Figure 3: Plot of s against f/f_p for the southeast fetch-limited Maui sea states, grouped by U_{10}/c_p. The Hasselmann and Mitsuyasu s functions for $U_{10}/c_p = 0.8$ and 1.2 are also given.

A similar plot of the circular rms spreading, $\sigma(f)$, allows comparison with the Donelan and Donelan/Banner curves. This is given in Figure 4 . The Mitsuyasu and Hasselmann curves have been included by applying Equation (9); while the Donelan and Donelan/Banner curves have been determined from Equation (10) through the calculation of the

Fourier coefficients derived from the respective distributions. Again good general agreement is seen between the Maui and other distributions, but at the peak frequency the Maui σ values are closer to the Donelan and Donelan/Banner distributions than to the Mitsuyasu (U_{10}/C_p = 1.2) and Hasselmann distributions (both of which suggest more spreading in the region of the peak). The Mitsuyasu (U_{10}/C_p = 0.8) curve shows the least spreading in the region of the peak, but Young (1994) has questioned the validity of the strong wave age dependence of the Mitsuyasu distribution when the data they based their distribution on covered only a small range of wind-sea wave ages (1.0 to 1.2). At higher frequencies, f/f_p > 1.4, it is clear that the spreading is not constant as given by the Donelan distribution.

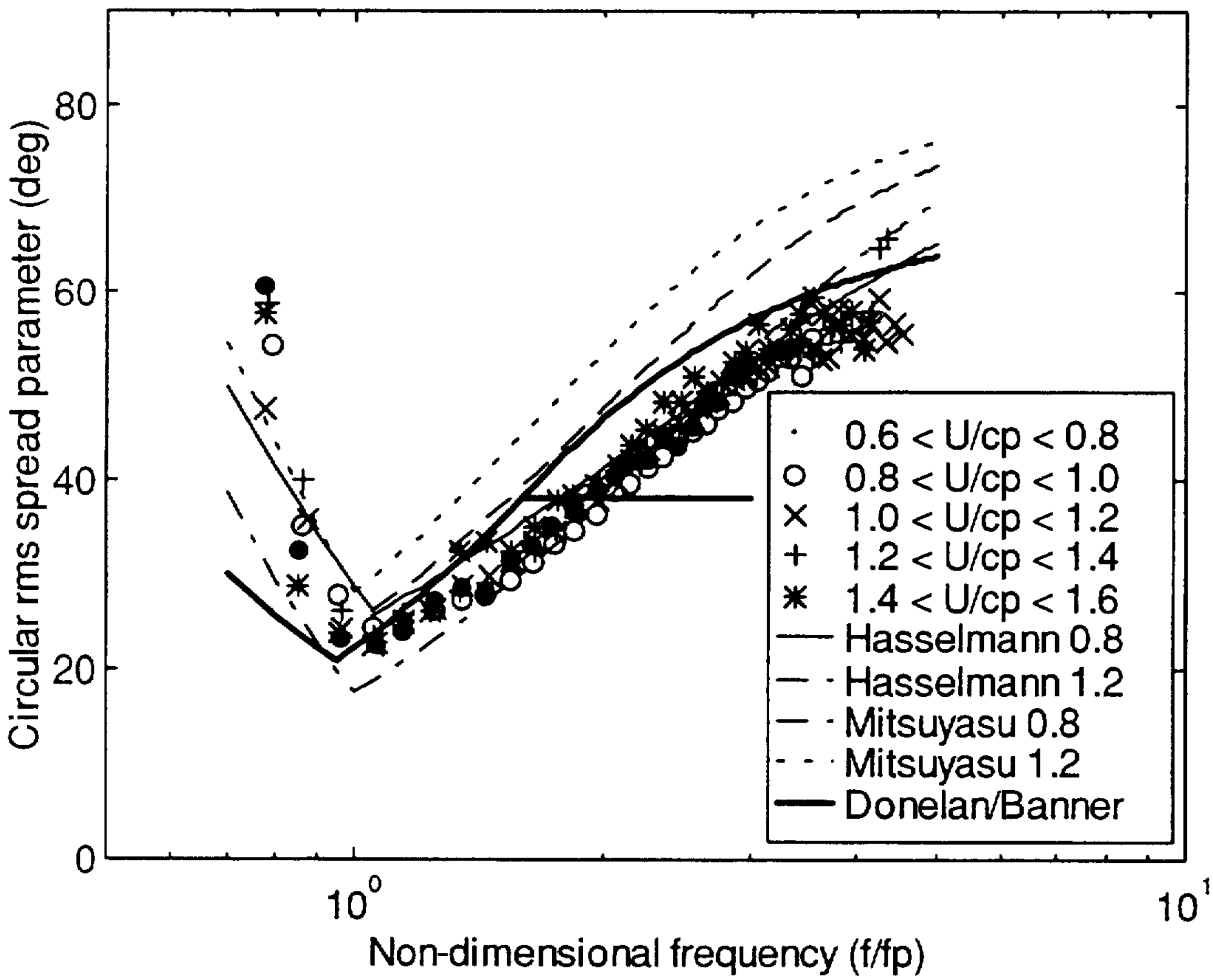

Figure 4: Plot of σ against f/f_p, as for Figure 3.

5.4 Parameterisation of the Maui s parameter

For direct comparison with the Mitsuyasu and Hasselmann functions a parameterisation for s was established. Following the same approach as

Mitsuyasu et at. (1975) and Hasselmann et al. (1980), it was assumed that s could be determined by a relation of the form

$$s = k\left(\frac{f}{f_p}\right)^m \tag{11}$$

and the constants, k and m determined by linear regression analysis of $\log_{10}(s)$ versus $\log_{10}(f/f_p)$.

The linear regression was performed on the data for $f/f_p \geq 1$ and for $f/f_p < 1$. On the basis of the lack of a dependence of the Maui s parameter on U_{10}/C_p , all 77 spectra were included in the regression.

The analysis resulted in the following s parameterisation for the Maui data.

$$s = \begin{cases} 13.1\left(\dfrac{f}{f_p}\right)^{-1.94} & f/f_p \geq 1 \\ 15.5\left(\dfrac{f}{f_p}\right)^{9.47} & f/f_p < 1 \end{cases}$$

The constants k and m are similar to those of the Mitsuyasu and Hasselmann distributions but without a wave age dependence.

6. THE MAUI DIRECTIONAL DISTRIBUTION

6.1 Characteristics of the Maui Directional Distribution

The 'cosine2s' parameterisation of the Maui data in Section 5.4 , permit a directions distribution function to be ascribed to the Maui fetch-limited data, which is unimodal, symmetric but based only on the first pair of Fourier coefficients in Equation (1). The estimates of the directions distribution using the Maximum Entropy and Maximum Likelihood Methods, make use of all four Fourier coefficients available from heave-pitch-and-roll buoy data. The resulting distributions showed that a simple 'cosine2s' form is not appropriate for the fetch-limited Maui data. In particular, the estimates show that for frequencies above the spectral peak, it unimodal, symmetric distribution is not appropriate.

Figure 5 is an example of the MEM and MLM estimates for one of the spectra (H_s = 3.8 m, T_2 = 6.4 s). Both distributions are unimodal at the peak frequency but become bimodal at frequencies above the spectral peak, with the MEM estimate becoming bimodal at around 0.17 Hz and the MLM at around 2.5 Hz ($\approx 2f_p$).

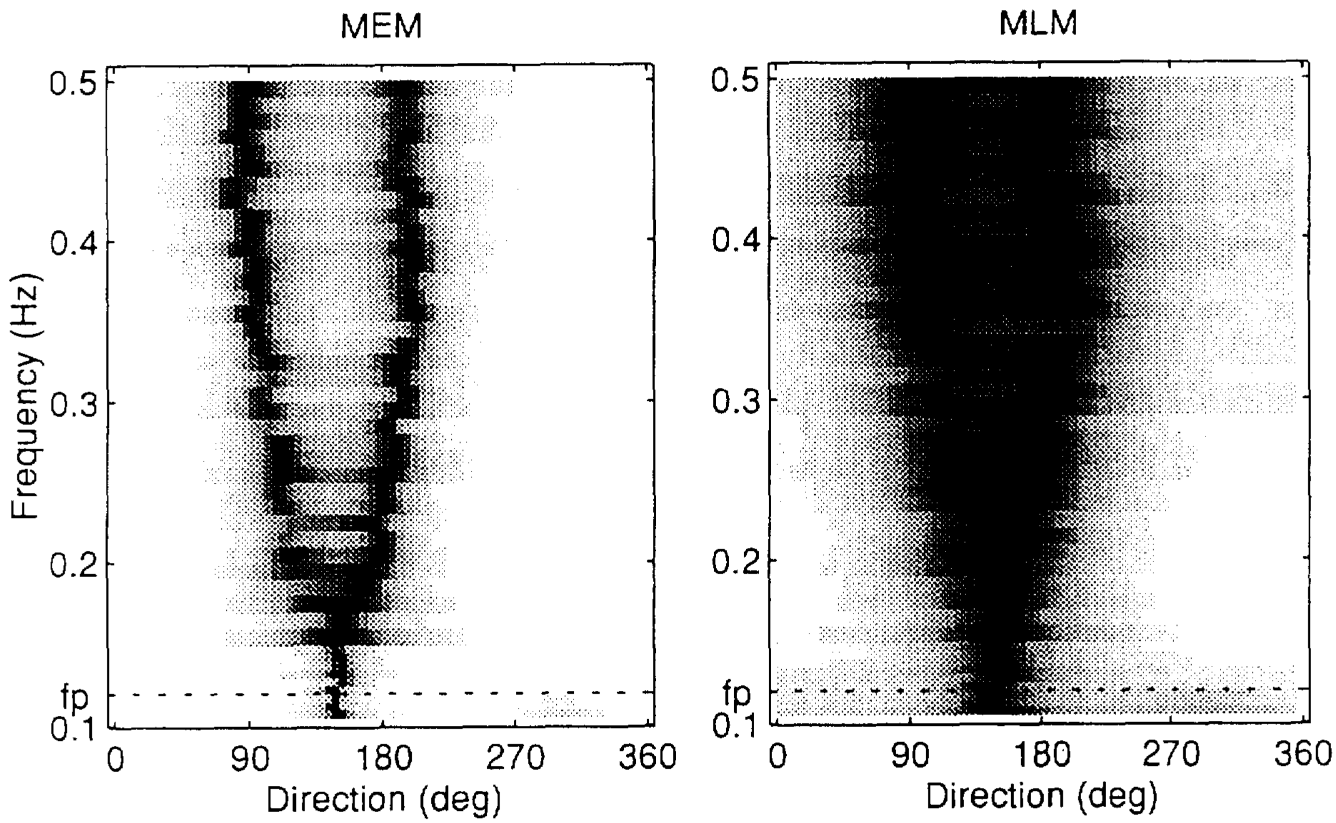

Figure 5: Shaded image of the directional spreading of a southeast fetch-limited Maui sea state. The spectral level at each frequency is normalised to one.

The observation that fetch-limited sea states have bimodal distributions at frequencies greater than the spectral peak has previously been reported by Young et al. (1995), who showed that their directional spectra recorded with a wave gauge array demonstrated bimodality at frequencies greater than f/f_p = 2. This provided experimental confirmation of earlier work by Banner and Young (1994) who showed that the directions distribution of components irk the equilibrium range of the spectrum were bimodal when calculations were made using the full solution to the nonlinear wave-wave interaction source term at those frequencies. Young et al. (1995) presented a comparison between a directional spectrum calculated in this way with their spectra and showed that there was very good agreement. Accordingly, they concluded that the bimodal effect they observed was caused by nonlinear wave-wave interactions, and speculated why the phenomenon had not been previously reported. They cited a number of publications in which the effect was visible but apparently given little or no attention, and observed that the effect will clearly not be observed in studies based on analyses where the directional distribution has been assumed to be unimodal, such as reported by Mitsuyasu et al. (1975).

The Young et al. (1995) data were collected with a wave gauge array in Lake George, Australia. The lake had a water depth of 20 m and the reported waves were in the range $1.7 < U_{10}/C_p < 3$. The Maui spectra show that the effect is also present in open ocean conditions. In addition as the effect his been observed with a heave-pitch-and-roll buoy, it can be concluded that a 3-element system, which provides estimates of the first two pairs of Fourier coefficients in Equation (1), are capable of resolving the bimodality, contrary to the conclusion of Banner and Young (1994). In addition, the circular rms spreading results presented in Figure 4 show that the Maui data show even less spreading than those of Donelan et al. (1985) who used a 14-element array. This is in contrast to conclusions made by Young (1994) that the directional spectra derived from heave-pitch-and-roll buoys will be excessively broad.

A feature of the estimates, and which is also evident in Figure 6 , was that the MEM estimate always gave an apparent improvement in the resolution of the bimodal effect. Previous studies (e.g. Nwogu et al., 1987) have noted the high resolving power of the MEM estimate by comparison with the MLM estimate, while others (e.g. Brisette and Tsanis, 1994), based on synthetic data, have concluded that the MEM estimate may at times provide two peaks when there is actually only one. Krogstad (1989) argues that this observation is not necessarily a weakness of the MEM estimate, on the grounds that if the form of the directional distribution is already known then additional information is known and the MEM estimate is no longer an optimal estimate. While such a result has not been reported for the MLM estimates, it has been observed to artificially broaden the spectrum (Young, 1994). Of course when we are estimating directional spectra from data measured in the open ocean we do not know the directional distribution a priori, and therefore we can not dismiss either of the estimates. However, it should be noted that the author has a preference for MEM estimate because of its higher resolving power and because it preserves the Fourier coefficients - i.e. the Fourier coefficients calculated from the estimate are identical to those used to estimate it; this is not the case for the NILM estimate. Nevertheless, in the analysis of the Maui directional data both MEM and MLM estimates were investigated in parallel.

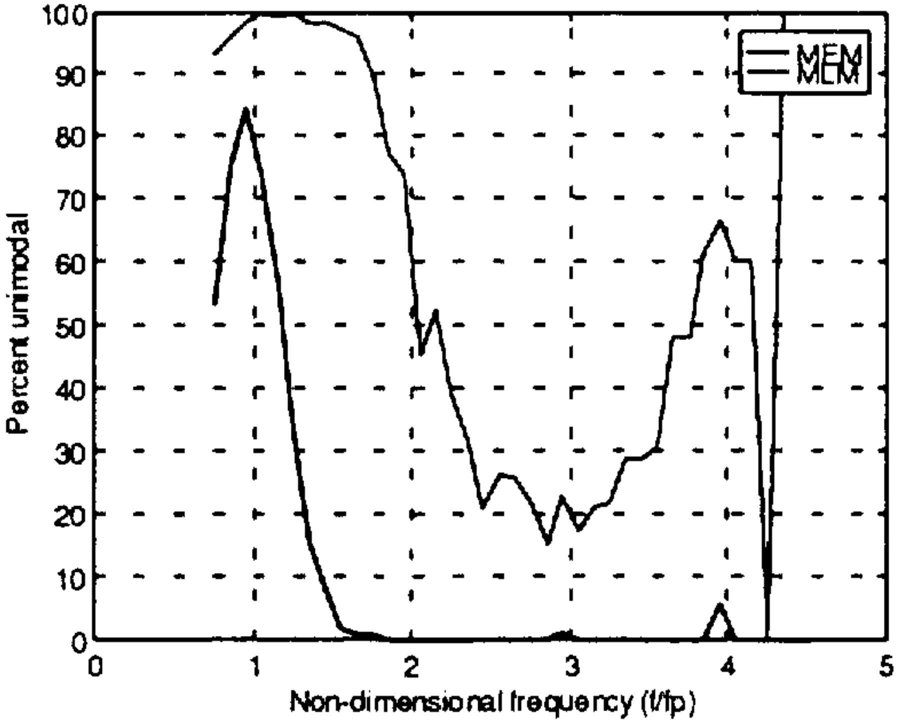

Figure 6: Percent of spectral estimates which are unimodal/symmetric plotted as a function of non-dimensional frequency f/f_p.

The behaviour of the MEM and MLM estimates was investigated by examining various features of the peaks identified by their local maxima and minimal as described in Section 4 . The percentage of unimodal/symmetric estimates, as given by the U_{pqr}, is plotted as function of f/f_p in Figure 6 . The figure shows that in the region of the peak frequency both estimates produce predominantly unimodal/symmetric distributions. However, while this occurs through to around $f/f_p \approx 1.7$ in the case of MLM, the percentage of MEM unimodal/symmetric distributions quickly diminishes with increasing f/f_p, and there are effectively no occurrences above $f/f_p \approx 1.7$. Against this trend, the percentage of unimodal/symmetric MLM distributions increases above $f/f_p \approx 3$, and appears to increase again with f/f_p. The figure also indicates occurrences of distributions which are not unimodal/symmetric below, $f/f_p = 1.0$ for both distributions, indicating the existence of bimodal distributions at frequencies below the peak, something which was noted by Young et al. (1995) in the theoretical estimate of the directional spectrum.

A scatter plot of the angular separation between the two peaks plotted as a function of f/f_p is given for both the MEM and MLM estimates is given in Figure 7 . When plotted in this way the angular separation for each spectrum essentially collapse onto a single curve, indicating that it can be considered a function f/f_p only. The peak shapes of the directional distribution were investigated by dividing them into a left and right peak (relative to the largest local minimum), and the circular rms spreading and amplitude of each peak was calculated. While there were individual differences between the comparative rms spreading and amplitude of the respective peaks, no systematic difference was observed, leading to the conclusion that on average the peaks have the same shape and the distribution is symmetric about the mean wave direction.

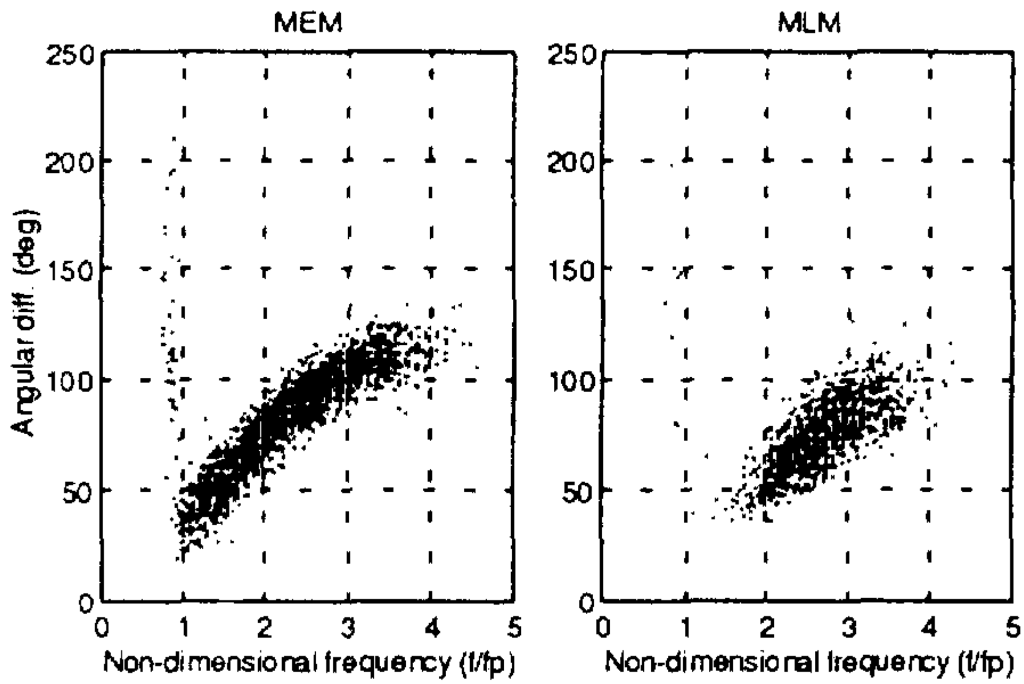

Figure 7: Plot of angular difference between peak maxima of the bimodal distributions, plotted against f/f_p for the MEM and MLM estimates

6.2 Parameterisation of the Maui Directional Distribution

The results presented in the previous section clearly indicate that at high frequency a bimodal representation is more appropriate than a unimodal one. A model of the directional distribution of fetch-limited sea states should therefore give a bimodal distribution at frequencies greater than the peak frequency. An analysis of the Maui data was undertaken to establish such a distribution.

First, the Fourier coefficients were averaged in bins of $f/f_p = 0.1$ and an MEM and MLM estimate produced for each set of average Fourier coefficients at each f/f_p. The resulting MEM and MLM estimates were then fitted with a so-called Voigt function which is a combination of a Gaussian and Lorentzian (or Cauchy) distribution. The combination of the Gaussian and Lorentzian distribution allows for a flexible fit to a peak, the Lorentzian distribution allowing for a broad distribution and the Gaussian distribution accommodating a peaked distribution. Thus an equation of the following form was fitted to each distribution.

$$H(\theta, f/f_p) = \sum_{i=1}^{n} A_i(f/f_p)\left\{(1-F)P_G(\theta) + F.P_L(\theta)\right\} \tag{12}$$

where

$$P_G(\theta) = \sum_{k=-\infty}^{\infty} \exp\left[-2.77\left(\frac{\theta - \theta_p - 2k\pi}{\Gamma}\right)^2\right]$$

and

$$P_L(\theta) = \sum_{k=-\infty}^{\infty} \frac{1}{\left(\frac{2(\theta - \theta_p - 2k\pi)}{\Gamma}\right)^2 + 1}$$

where $A_i(f/f_p)$ is the amplitude of the local peak,
F is the fraction of Lorentzian to Gaussian function, Θ_p is the direction of the local peak, and Γ is the half-width of the local peak (the width of the distribution at half the maximum).

The summation in Equation (12) allows for the possibility of one (n = 1) or two peaks (n = 2) in the spectrum, and the summation over k in the Gaussian and Lorentzian functions ensures the distributions are wrapped over 2π. In practice a good fit to each distribution was achieved with k = 0, and it was not necessary to include the summation in the curve-fitting process.

Thus, the Voigt function allows for a possibility of two peaks with each peak being described by four parameters.

Average Fourier coefficients were available for values of f/f_p ranging from 0.80 to 0.43. The MEM estimates were unimodal for $f/f_p \leq 1.0$ and bimodal for $f/f_p > 1$. The MLM estimates did not show a discernible splitting into two peaks until $f/f_p \approx 2$ but from $f/f_p = 1.4$ a better fit was achieved with two peaks rather than one.

The parameters resulting from the curve-fitting are plotted in Figure 8 . Figure 8a shows the plot of the peak- directions, including an estimation of the peak directions of the theoretical distribution presented in Young et al. (1995), which shows very good agreement with the Maui results. The results show larger separation of the peaks fitted to the MEM estimates by comparison with the MLM estimates, with the theoretical distribution somewhere in between. The fitted peaks also show some asymmetry, with one peak being closer to the mean direction (the direction of the peak) than the other. It is not clear what is responsible for this. One possible conclusion to make is that the asymmetry is due to some asymmetry in the fetch, but if so one would expect the asymmetry to reduce at higher frequencies (larger f/f_p), but this is not the case. The measured directional distributions reported by Young et al. (1995) also show some asymmetry, but they believed this to be due to sampling variability.

The asymmetry in the regular separation of the peaks is also generally seen in the other parameters. Figure 8b is a plot of the ratio of the peak amplitudes, showing a systematic increase of the MEM ‘peak 2’ amplitude relative to ‘peak 1’ with increasing f/f_p but essentially equal MLM peak amplitudes. The plots of the peak half widths in Figure 8c show that the peak half width of ‘peak 2’ is generally larger than that of ‘peak 1’, and the plots of F show that this parameter is generally larger for ‘peak 2’ than ‘peak 1’.

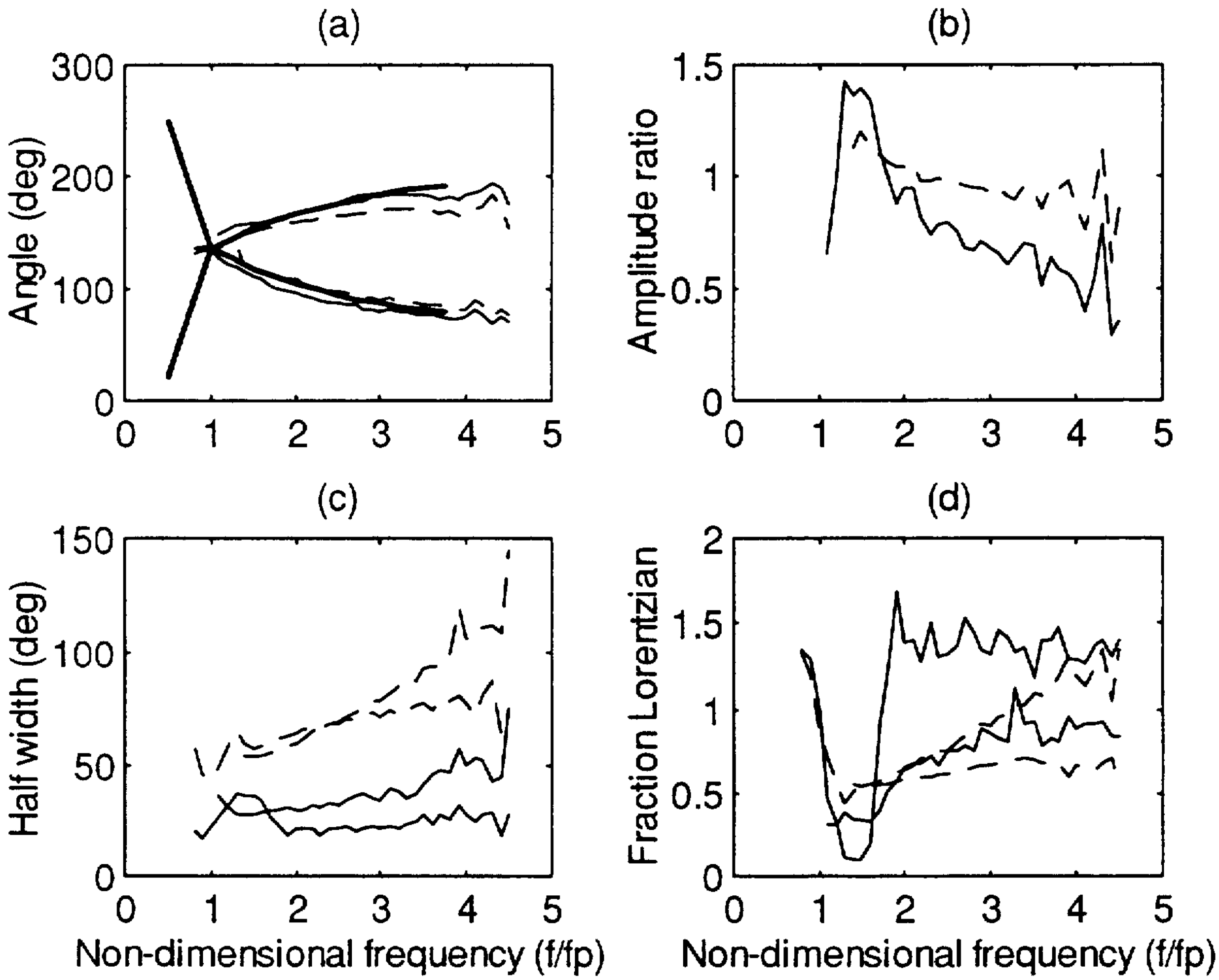

Figure 8: Plots of the Voigt function parameters, as a function of f/f_p, resulting from curve-fitting the average Maui spectrum: (a) angle of peak maximum, MEM estimate - continuous line, MLM estimate - dashed line, Young *et al.* (1995) prediction for $U_{10}/c_p = 3$ - thick line; (b) ratio of peak amplitudes; (c) peak half-width, Γ; (d) fraction Lorentzian, F.

The parameters plotted in Figure 8 were used to establish a functional form for each as a function of non-dimensional frequency. On this basis the distribution should be unimodal at the peak frequency and lower frequencies, and bimodal above the peak frequency. As the exact form of the directional distribution is not known (it is not known whether the MEM or MLM produces the better approximation), but the MEM data were used as the basis for the parameter values simply on the grounds that Fourier coefficients are consistent for this distribution. It was however assumed that the bimodality displayed by the distributions above the peak should be symmetric; the bimodality is a robust feature of non-linear wave-wave interactions, and the examination of individual spectral peaks showed no systematic differences.

To obtain a parameterisation of the peak separation, the angular separation of the peaks divided by two (assuming the mean to lie in the middle) was curve fitted with a simple non-linear function and forced to go through zero at $f/f_p = 1$. For simplicity, a straight line was fitted to the half-widths and fraction Lorentzian for the frequency ranges above and below $f/f_p = 1$. For $f/f_p > 1$ the parameters associated with each peak were averaged before fitting. This analysis provided a 'first estimate' parameterisation; modification to the parameters was then made to ensure the resulting circular rms spreading, σ, was consistent with the data, resulting in some parameters deviating from their fitted values plotted in Figure 8 . This process resulted in the following parameterisation:

For $f/f_p \leq 1$

$$\Delta\theta = 0$$

$$\Gamma = -15\left(\frac{f}{f_p}\right) + 35$$

$$F = -10.2\left(\frac{f}{f_p}\right) + 10.7$$

For $f/f_p > 1$

$$\Delta\theta = 1.02 - 2.77\exp\left[-\left(\frac{f}{f_p}\right)\right]$$

$$\Gamma = \frac{-20\left(\frac{f}{f_p}\right) + 50}{3.5}$$

$$F = 0.5$$

This parameterisation produces a circular rms spreading that is consistent with other forms (Figure 9) but for frequencies greater than $f/f_p = 1$, the directional distribution is bimodal.

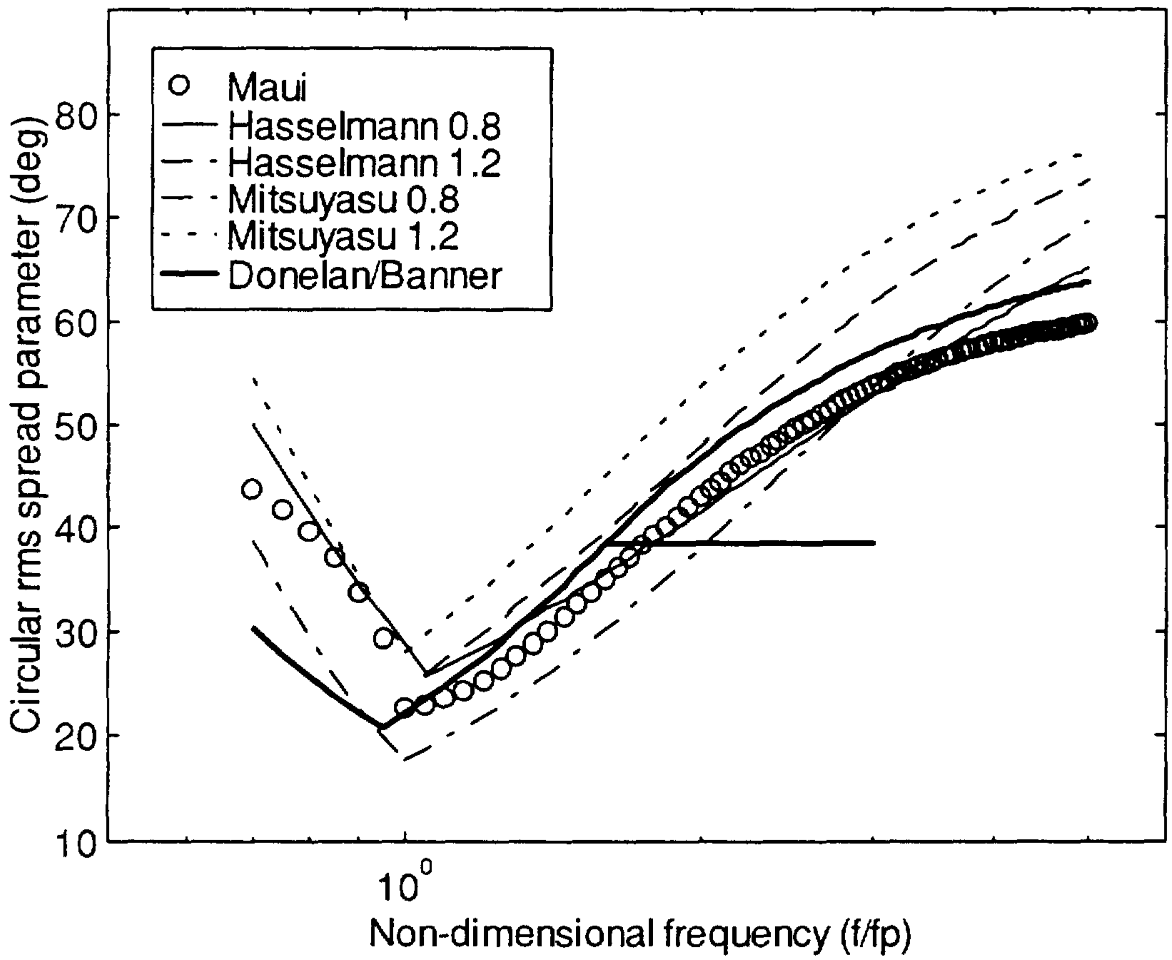

Figure 9: Circular rms spreading parameter, σ, as function of f/f_p, for published parameterisations and the Maui parameterisation.

7. DISCUSSION

The proposed parameterisation can be used to estimate the significance of the bimodality for practical purposes. Accordingly, a model fetch-limited sea state was constructed for a fetch of 200 km, and a wind speed of 10 m/s. The omnidirectional spectrum was modeled with a JONSWAP spectrum, and a frequency-direction spectrum computed for the Hasselmann, Donelan/Banner, and Maui distributions. Figure 10 is a plot of the directional spectrum, the integration of the frequency-direction distribution over frequency, for each distribution type. The figure shows that the overall directional distribution of energy of Maui sea state remains unimodal; the more energetic components in the region of the peak of the spectrum therefore dominate the higher frequency, bimodal components. Of course at specific frequencies, such as f = 0.2 Hz (Figure 11), bimodality will be important.

Banner and Young (1994) conclude that the bimodality is a robust feature of predictions made using the full solution to the non-linear wave-wave interaction source term. For computational efficiency, operational numerical wave models employ various approximations to the source terms. In 1G-models the nonlinear wave-wave interaction source term is not considered; in 2G-models the nonlinear source term is considered through a parameterisation of the non-linear spectral energy transfer and by constraining the spectral shape; and in 3G-models the non-linear interactions are approximated with a parameterisation. Clearly, the 1G and 2G models, which assume a unimodal parameterisation for the directional spreading, will not predict directional bimodality at $f/f_p > 1$. It is however not clear whether the 3G-models will predict directional bimodality; but the results in Young et al. (1987) casts some doubt on this, particularly their Figure 5 , which shows differences in the directional spectra derived from the EXACTNL model and the 3G-WAM models.

Figure 10 shows that overall whether or not bimodality is predicted is probably not that significant within the active sea state, but one can speculate that due to dispersion it might become more significant in the prediction of swell at a location some distance from the source and at relatively large angles from the direction of the wind field of the source. At such a location, the swell could be larger than predicted by current numerical models. Even at a location directly in line with the wind field of the source it might be expected that due to dispersion, the energy of the swell might attenuate more quickly with time than predicted by current numerical models.

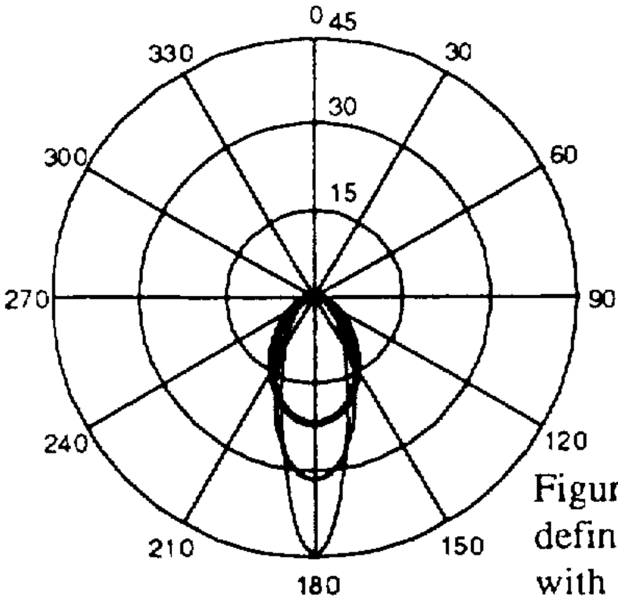

Figure 10: Directional spectrum of a sea state defined by a JONSWAP omnidirectional spectrum, with fetch = 200 km, wind speed = 20 m/s, and mean direction 180°. Maui direction distribution parameterisation - thin line, Donelan/Banner direction distribution parameterisation - medium line, Hasselmann direction distribution parameterisation - thick line.

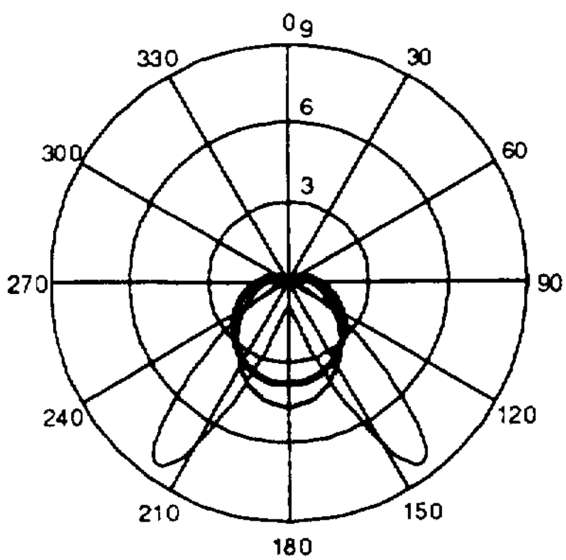

Figure 11: Directional distributions at $f = 0.20$ Hz of the sea state with directional spectrum given in Figure 10.

8. CONCLUSIONS

The integrated properties of the moments of the Maui directional distribution, and in particular the circular rms spreading are consistent with previously published results of Hasselmann et al. (1980) and Donelan et al. (1985) but are closer to the Donelan et al. (1985), which has a narrower spreading than Hasselmann et al. (1980).

However, unlike the earlier results which are associated with a unimodal directional distribution at all frequencies, the Maui data provide convincing evidence for the presence of bimodal directional distributions at frequencies higher than the peak frequency. This supports the work of Young et al. (1995) who observed the same phenomenon, but with observed bimodality occurring for $f/f_p > 2$. The Young et al. (1995) data were recorded in Lake George, Australia. The Maui data were recorded over a large range of wind and wave conditions, with wind speeds to 20 m/s and significant wave heights to 4.1 in, and the bimodality remained a dominant feature of all of these conditions; thus the observations of the effect are extended to open ocean scales by the Maui data.

The proposed parameterisation for the Maui directional distributions reproduces the essential features, of directional distribution, giving a consistent circular rms spreading over frequency, at the same time as reproducing the bimodality at higher frequencies and approximating the peak width of the two peaks in the high frequency directional distribution. This parameterisation is useful for evaluating the qualitative aspects of the directional spreading and is probably as good as previously proposed distributions for quantitative evaluation, but it is expected that data sets acquired with higher resolution instrumentation together with more rigorous analysis of the distributions than has been possible in this study, will ultimately lead to a more precise parameterisation of the distribution.

The parameterisation has shown however, that because the bimodality occurs at higher frequency with lower spectral levels, the total directional distribution of energy of a sea state remains unimodal. It therefore seems likely that unless there is a particular application which has a strong frequency dependence, engineering calculations which make use of a simple unimodal description of the directional distribution are adequate. It is possible however that the existence of a bimodal directional distribution in real sea states may produce levels of swell at certain locations which are not well predicted by current numerical models.

ACKNOWLEDGMENTS

The wave directional data used in this study were provided by Shell, Todd Oil Services Ltd, New Plymouth, New Zealand. Their contribution is gratefully acknowledged.

REFERENCES

Banner, M.L., 1990: Equilibrium spectra of wind waves. J. Phys. Oceanogr., **20**, 966-984.

Banner, M.L. and I.R. Young, 1994: Modelling spectral dissipation in the evolution of wind waves, 1, Assessment of existing model performance, J. Phys. Oceanogr., **24**, 1550-1671

Brissette, F.P., and I.K. Tsanis, 1994: Estimation of wave directional spectra from pitch-roll buoy data. J. Waterway, Port, Coastal, and Ocean Eng., 93 -115.

Donelan, M.A., Hamilton, J. and W.H. Hui, 1985: Directional spectra of wind-generated waves. Phil. Trans. R. Soc. Lond., **A315**,509-62.

Ewans, K.C. and A.C. Kibblewhite, 1990: An examination of fetch-limited wave growth off the west coast of New Zealand by a comparison with the JONSWAP results. J. Phys. Oceanogr., **20**, 1278-1296.

Ewans, K.C.and A.C. Kibblewhite, 1992: Spectral features of the New Zealand deep-water ocean wave climate. N.Z.J. Mar. and Fresh. Res., **26**, 323-338.

Hasselmann, K., et al., 1973: Measurements of wind-wave growth and swell decay during the Joint North Sea Wave Project (JONSWAP). Dtsch. Hydrogr. Z, **8** (Suppl. A), 5-95.

Hasselmann, D.E., Dunckel, M., and J.A. Ewing, 1980: Directional wave spectra observed during JONSWAP 1973. J. Phys. Oceanogr., **10**, 1264-1280.

Isobe, M., Kondo, K., and K. Horikawa, 1984: Extension of MLM for estimating directional wave spectrum. Symp. on Description and Modelling of Directional Seas. DHI and MMI, Copenhagen.

Long, R.B., 1980: The statistical evaluation of directional spectrum estimates derived from pitch/roll buoy data. J. Phys. Oceanogr., **10**, 944952.

Mitsuyasu, H., et al., 1975: Observations of the directional spectrum of ocean waves using a cloverleaf buoy. J. Phys. Oceanogr., **5**, 750-760.

Nwogu, O.U., Mansard, E.P.D., Miles, M.D., and M. Isaacson, 1987: Estimation of directional wave spectra by the maximum entropy method. Proc. Wave Analysis and Generation in Laboratory Basins, IAHR Seminar, 363-376.

Krogstad, H.E., 1991: Reliability and resolution of directional wave spectra from heave, pitch, and roll data buoys. In Directional Ocean Wave Spectra, Ed. R.C. Beal, 66-71.

Kuik, A.J., Van Vledder, G. Ph., and L.H. Holthuisen, 1989: A method for the routine analysis of pitch-and-roll buoy wave data. J. Phys. Oceanogr., **18**, 1020-1034.

Welch, P.D., 1967: The use of the fast Fourier transform for the estimation of power spectra: A method based on time averaging over short modified periodograms. IEEE Trans. Audio Electroacoust., AU-15, 70-73.

Young, I.R., 1994: On the measurement of directional wave spectra. App. Ocean Res., **16**, 283-294.

Young, I.R., Verhagen, L.A., and M.L. Banner, 1995: A note on the bimodal directional spreading of fetch-limited wind waves. J. Geophys. Res., **100**, C 1, 773-778.

EXTREME WAVES IN COASTAL WATERS

Diane Masson and Richard E. Thomson
Institute of Ocean Sciences
Sidney, B.C.

1. INTRODUCTION

Wind waves result in a random displacement of the ocean surface, forming a succession of crests and troughs of varying dimensions. The extreme displacements of this random surface are commonly known as rogue, giant or freak waves, and constitute a serious marine hazard. Extreme wave events have been linked to numerous marine accidents and losses of life. They are also of crucial importance to naval architects for the design of ships and marine structures. For example, an important engineering design parameter is the likelihood of encountering a sequence of unusually high waves.

Mariners' logs show that abnormally large waves occur with little prior warning and appear "to come out of nowhere". In the open ocean, giant waves are regularly reported in regions of strong western boundary currents, suggesting that the likelihood of extreme wave events is enhanced by wave-current interactions. Rogue waves are also known to occur along exposed coastlines, and incidents involving such large waves are routinely reported on the coast of British Columbia (e.g. Nickerson, 1986).

Despite the scientific and engineering interest in these waves, they are rarely the focus of oceanographic measurement programs. Part of the difficulty of investigating extreme waves is that the events are highly elusive in space and time. This makes them difficult to document and study in any consistent statistical manner. In 1993 a field program was initiated to collect an extensive data set from which a large sample of extreme wave events have been extracted. Three wave buoys were moored on the inner continental shelf off southwestern Vancouver Island on the west coast of Canada (Figure 1). Time series of surface elevation were continuously recorded throughout the 1993/94 winter. Extreme wave events, defined here as statistical maxima, are identified in the heave data from the three wave buoys. The wave profile around these large events are compared with predictions derived from the linear Gaussian theory as well as the heights of neighboring waves, and large wave period.

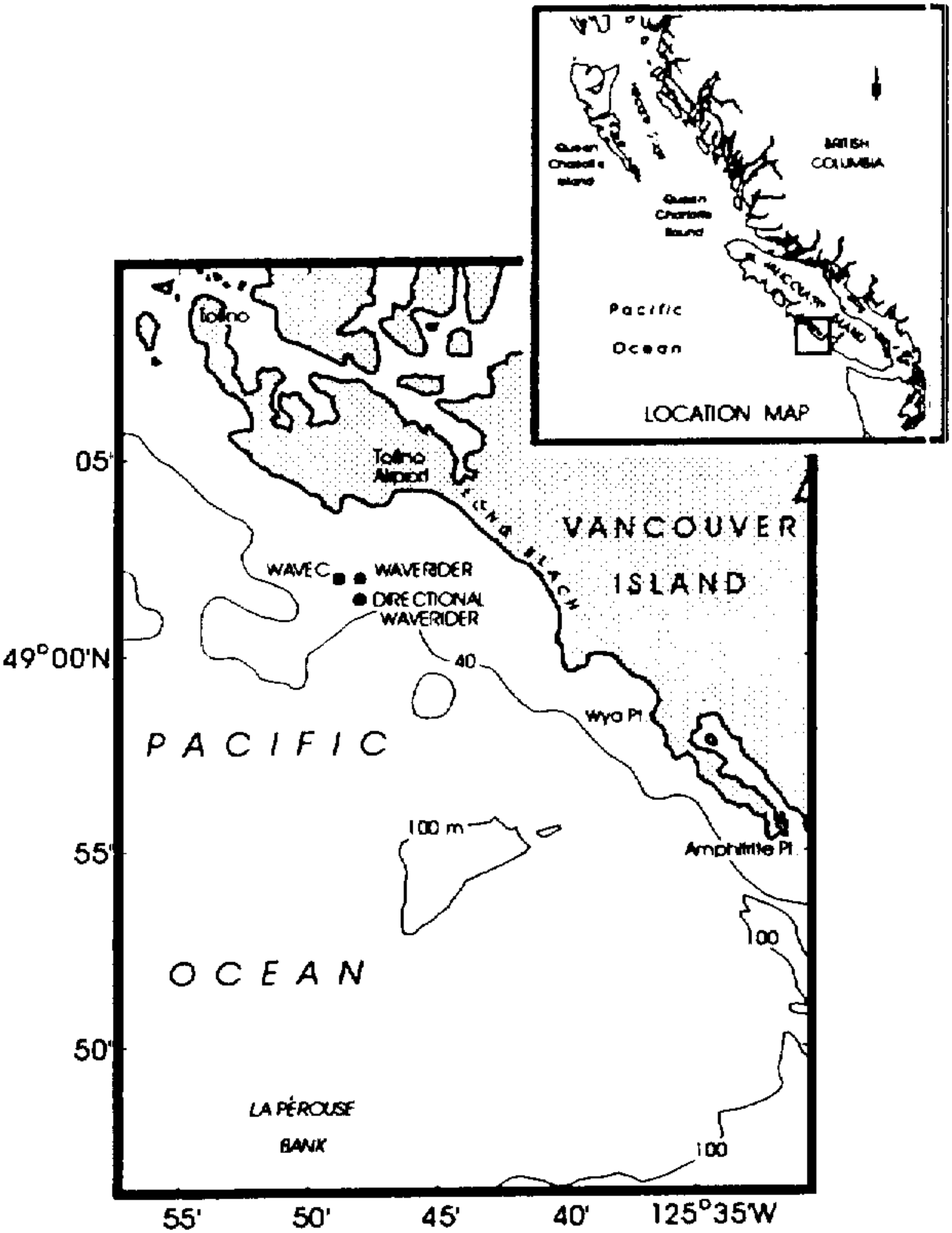

Figure 1. Study area with locations of the three wave buoys.

2. DATA COLLECTION AND PROCESSING

Three buoys, provided by the Marine Environment Data Services (MEDS) of Canada, were deployed in a water depth of about 30 m, forming a triangle with sides of approximately 1 km (Figure 1). The two offshore buoys, a Wavec and a Directional Waverider, had directional measurement abilities. The inshore buoy was a standard Waverider and, therefore, only recorded the heave motion. The data from the three buoys were telemetered to a shore station and the raw data were simultaneously stored on 90 MB Bernouilli disks at a sample interval of 0.78125 s. From October 19, 1993 to March 17, 1994, a total of about 1.1 GB of data were collected.

Throughout the winter, a series of moderate storms with a significant wave height, H_s reaching values above 4 m (Figure 2) passed through the study area. On one occasion, December 13, 1993, a more intense low system caused Hs, to exceed 7 m. Overall, the data return was quite good but, as seen in Figure 2 , some data gaps were caused by occasional power failures at the shore station or by buoy telemetry problems.

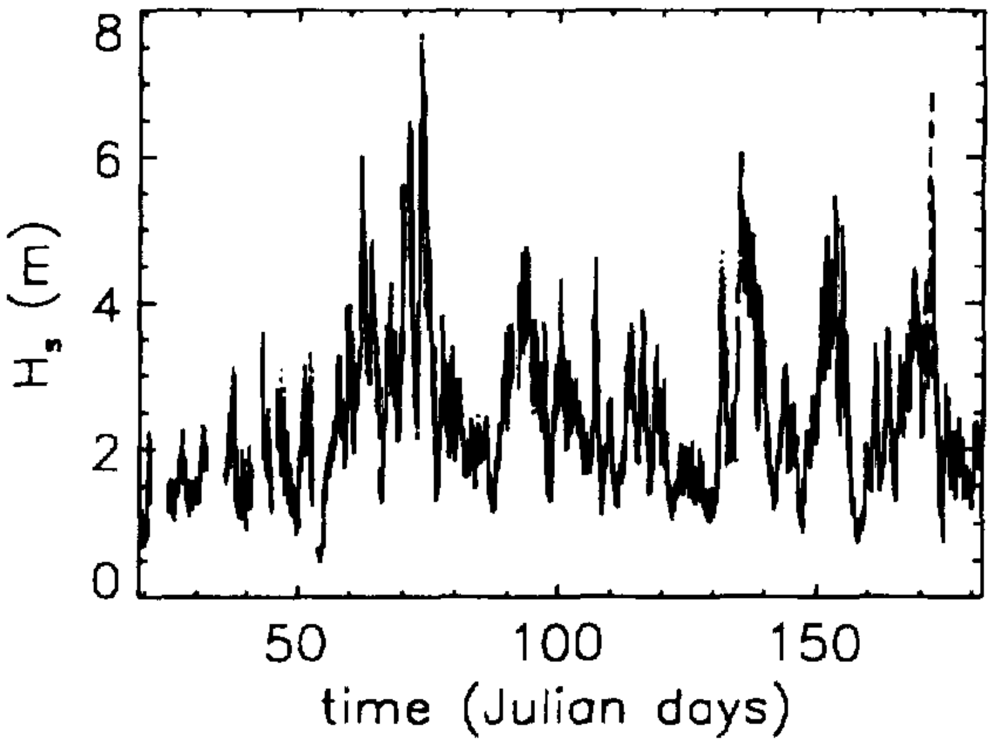

Figure 2. Significant wave height for the three buoys: Wavec (solid line), Directional Waverider (dotted line), and Waverider (dashed line). The time is given in Julian days from October 19, 1993.

The heave time series from the three buoys were first carefully despiked. Then, because the focus of the study is on the specific nature of large wave events, the heave time series were corrected using the low-frequency instrument transfer function specific to each of the three buoys: for the Wavec,

$$H = \frac{1}{(1 - p^2 - pq\sqrt{2}) + i(p^2 q - q - p\sqrt{2})}$$

$$p = T/30.8$$

$$q = T/170,$$

the Directional Waverider,

$$H = \frac{1}{(1 + 2ip - 2p^2 - ip^3)}$$

$$p = T/30.8,$$

and the Waverider,

$$H = \frac{1}{(1 - ip\sqrt{2} - p^2)(1 - iq)^3}:$$

$$p = T/30.8$$

$$q = T/460.$$

3. PRELIMINARY DATA ANALYSIS

The existence of extreme waves are often explained within the framework of the linear Gaussian model in which extreme waves are the statistical maxima of a random sea state. In this approach, the wave field is represented as a linear superposition of components with random phase. Accordingly, the surface displacement at a fixed location on the ocean surface is given as a function of time, $\eta(t)$, and its distribution takes the standard form

$$p(\gamma) = \frac{1}{\sqrt{2\pi}} \exp\left(-\frac{1}{2}\gamma^2\right) \qquad (1)$$

with $\gamma = \eta/\sigma$. In the above, the surface displacement, is normalized by the standard deviation of the distribution, σ. For all buoys, the data closely follow the Gaussian model. As an example, the Gaussian distribution (1), along with the measured distributions for all the data collected on December 2 are presented in Figure 3 . It can be seen that the number of measured events in each interval is quite close to the Gaussian curve and within three times the estimated standard deviation for the number of events in one interval.

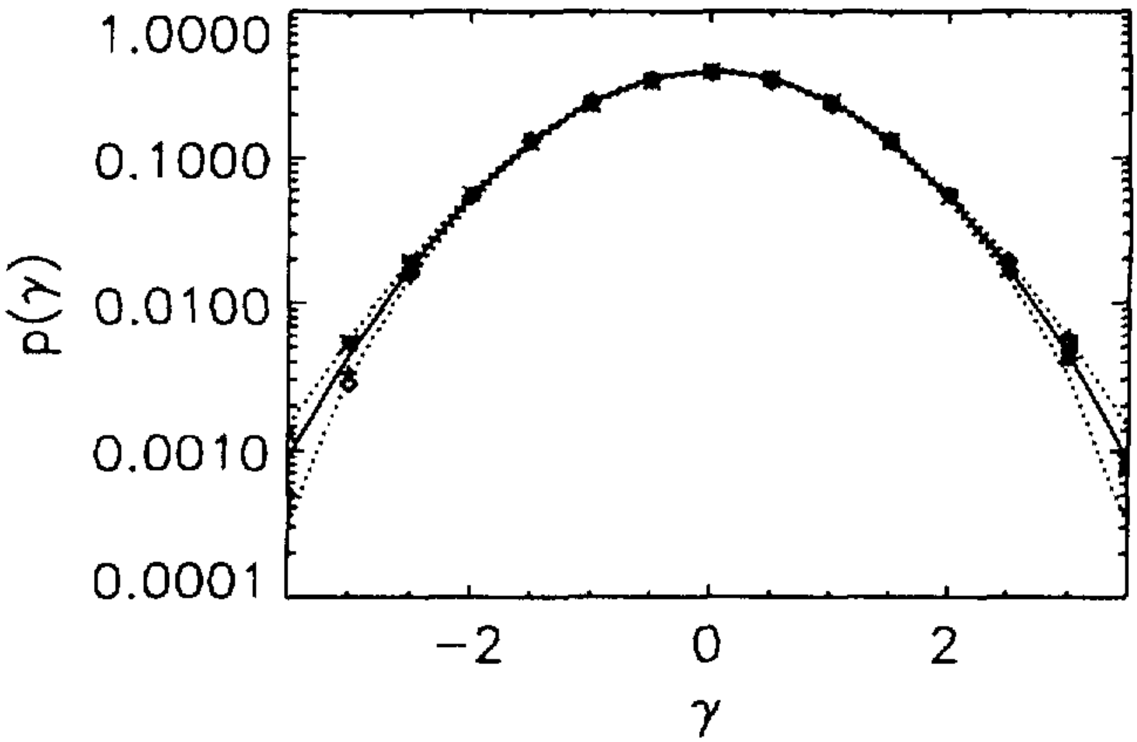

Figure 3. Probability distribution of the normalized heave signal measured by the three buoys: Wavec (⋄), Directional Waverider (∗), and Waverider (+). The Gaussian distribution is the solid line and the dotted lines give the interval of ±3 times the estimated standard deviation for the number of events in one interval.

As seen in the above figure, most of the surface displacement values are reasonably well represented by the linear Gaussian distribution. However, what is of interest here is the far tall of the distribution composed of the unusually large events. How well do these extreme events fit the Gaussian model? To examine the problem, all the heave time series were scrutinized in order to identify extreme events. The choice of a criterium used to define extreme events is somewhat arbitrary, having to be severe enough to be identified with extremes but not too severe to allow meaningful statistics. A value of $|\gamma| = 4.4$ was chosen as the lower limit for the selection, leading to a total of 339 events over the winter. These selected events can undoubtedly be qualified as extremes, with the Gaussian model giving a very small value for the cumulative probability of $P(|\gamma| \geq 4.4) \approx 1.08 \times 10^{-5}$. Of these cases, 202 are crests and only 137 are troughs, indicating some possible effects of nonlinearity in the tail of the distribution. An example of large crests measured by the Wavec buoy is given in Figure 4 for which the parameter, γ , takes a maximum value of 5.8.

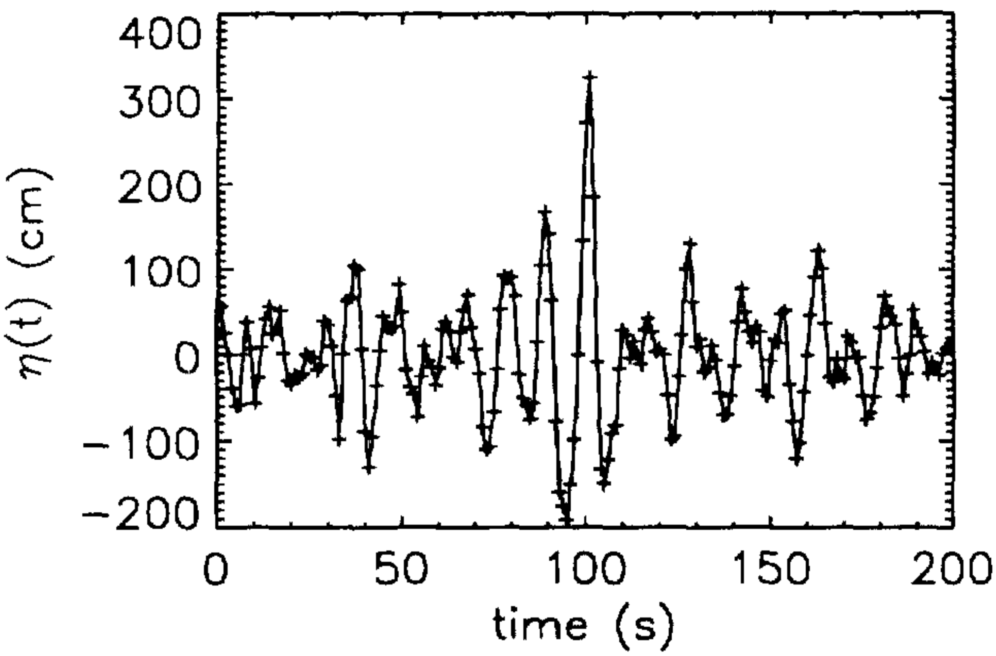

Figure 4. Heave signal from the Wavec buoy measured on November 21, 1993 at 1800GMT. At the time, $H_s = 2.2$ m.

Using the Gaussian theory, it has been shown that, at a fixed location, the expected profile surrounding an extreme event of a random wave field can be approximated in terms of the autocorrelation function of the surface displacement,

$$\rho(\tau) = \frac{\langle \eta(t)\eta(t+\tau) \rangle}{\langle \eta(t)^2 \rangle}$$

The symbol $\langle\rangle$ is used to indicate an ensemble average. Boccotti (1989) derived an expression for the expected profile around a large crest which can be written in the form:

$$\frac{\langle\eta(\tau)\rangle}{\beta} = \frac{[\rho(\tau) - \rho(\tau^*)\rho(\tau - \tau^*)]}{1 - \rho(\tau_*)^2} + \frac{\xi\,[\rho(\tau - \tau^*) - \rho(\tau^*)\rho(\tau)]}{1 - \rho(\tau_*)^2} \qquad (2)$$

It is assumed that the surface elevation takes a large value, β, at time $\tau = 0$, and that the autocorrelation function has a first minimum, $\rho(\tau^*) = \xi\beta$. Although not mentioned by Boccotti (1989), because of the linearity of the Gaussian model, the above expression also applies to large troughs. More recently, Phillips et a]. (1993) followed a similar approach and derived, for the expected profile around extreme events, a simpler approximation, which is only a function of $\rho(\tau)$:

$$\frac{\langle\eta(\tau)\rangle}{\beta} = \rho(\tau). \qquad (3)$$

The above expression simply states that the expected wave profile around a large crest can be approximated by the autocorrelation function. It is interesting to relate the above results to some known characteristics of groups of large waves. It is well known that the mean number of large waves in a group is a direct function of the correlation parameter between consecutive wave heights (e.g. Kimura, 198)). Those results predict that, for high correlation parameter values, it is more likely that large waves will come in groups. Going back to the present analysis, relation (3) also indicates that, in a time series for which the autocorrelation does not decay rapidly (high correlation parameter), the crests and troughs surrounding a large wave will also take large values.

The expected profiles (2) and (3) are compared with the extreme event of Figure 4 . A measured mean profile around the large crest is computed as the average of the displacement measured on both sides of the large crest located at $\tau = 0$ (Figure 5). Phillips et al. (1993) derived an approximation for the variance about (3) for various realizations of extremes:

$$\langle[\eta(\tau) - \langle\eta(\tau)\rangle]^2\rangle \approx \sigma^2\left[1 - \rho(\tau)^2(1 - \gamma^{-2})\right] \qquad (4)$$

when $\gamma \gg 1$. The shaded area in Figure 5 indicates the above estimated uncertainty. Although the estimated variance close to the large crest is quite small, it increases rapidly as τ increases to become as large as the standard deviation of the surface displacement, σ, in this case, near the second crest. Also, it is important to note that, according, to (4), the expected deviation of the measured profile from the predicted one decreases as the parameter, γ , increases.

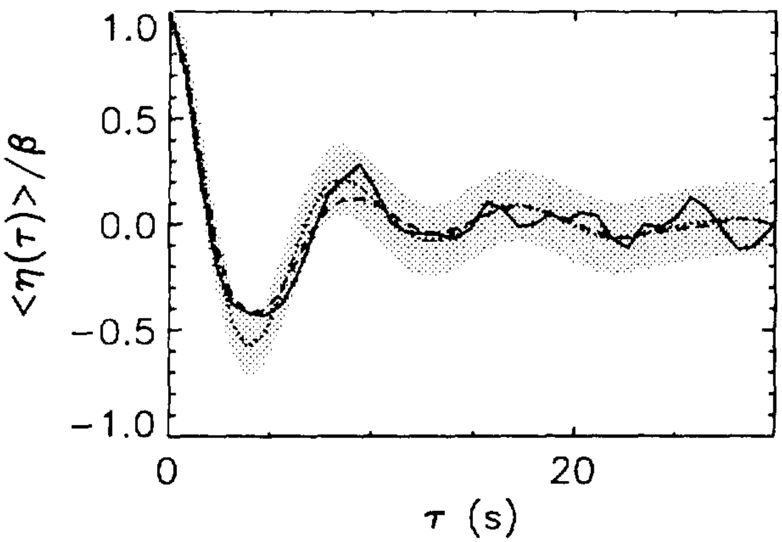

Figure 5. Mean measured profile (solid line) and expected profiles as given by (2) (dashed line) and (3) (dotted line) for the event in Figure 4. The shaded area is delimited by ± one standard deviation of the expected profile as in (4).

In order to evaluate the applicability of the simple model derived by Phillips et al. (1993) to the present data set, the 339 extreme events were examined in terms of two characteristics: the amplitude of the trough (crest) just before or after the large crest (trough), and the period of the extreme waves. To simplify the discussion, given the symmetry of the Gaussian model relative to the mean water level, all large events will be simply referred to as large crests, and the measured profile around

large troughs is inverted. According to (3), the predicted normalized profile will take a minimum value of $\rho(\tau_*)$ on either side of the large crest. All the profiles were processed and the two troughs on each side of the large crests are compared with the model predictions. The points are grouped in 6 intervals of $\rho(\tau_*)$ values. For each interval, the mean value and the standard deviation are given for the preceding and the following troughs separately. The two populations of preceding and following troughs have quite similar characteristics, in agreement with the model which predicts a symmetry of the profile on each side of the crest. The results also indicate that, for all intervals except the lowest one, all the measured mean values of $\eta(t)_{min}/\beta$ are within one standard deviation of the model value. The disagreement for the first interval may be due to the small sample size (only 10 events).

The standard deviation of $\eta(t)_{min}/\beta$, indicated as error bars in Figure 6 , are quite large. How do these values compare with expected variance of the model's profile given by (4)? Substituting an average value of $\rho(\tau_*)$= 0.6 and γ = 4.8 into (4) gives a standard deviation of about 0.2 for the normalized predicted profile, in agreement with the large measured variance of Figure 6 .

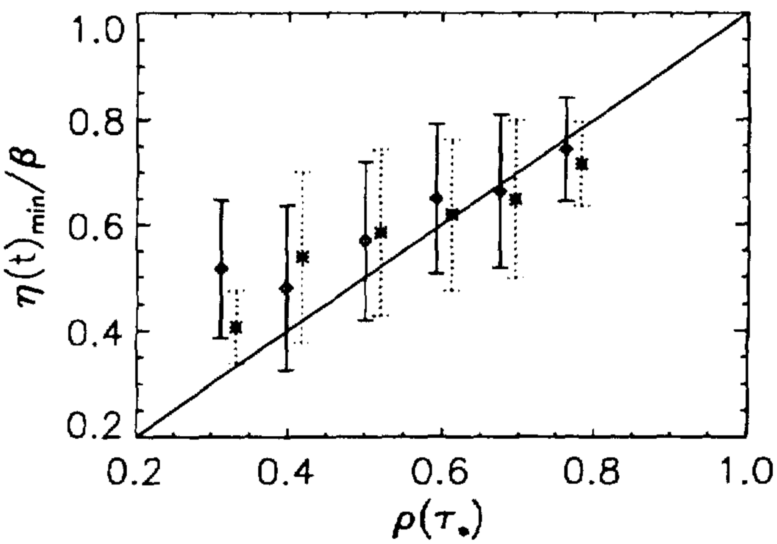

Figure 6. Mean value of the preceding (*) and following (◇) troughs of the normalized profile for 6 intervals of $\rho(\tau_*)$ values. Error bars indicate the standard deviation for each interval.

The wave period of each extreme event is then compared with the model predictions. Here, the period of the wave associated with each extreme event is defined as the time interval between the trough before the large crest and the trough following it. A trough is defined in the standard way as a minimum value of the surface displacement between a zero downcrossing and a zero upcrossing. This measured wave period is compared with the period of the predicted wave profile taken as $2\tau_*$, twice the time at which the autocorrelation function takes a first minimum value. Results are given in Figure 7 . For most of the 339 cases, the two periods are in close agreement, with a relatively high value of the correlation coefficient, r=0.73. However, in some cases, the difference between the measured and the predicted periods is quite large. This happens when the spectrum is quite broad and for which it is well known that the standard zero crossing method of defining individual waves is not ideal (e.g. Longuet-Higgins, 1984).

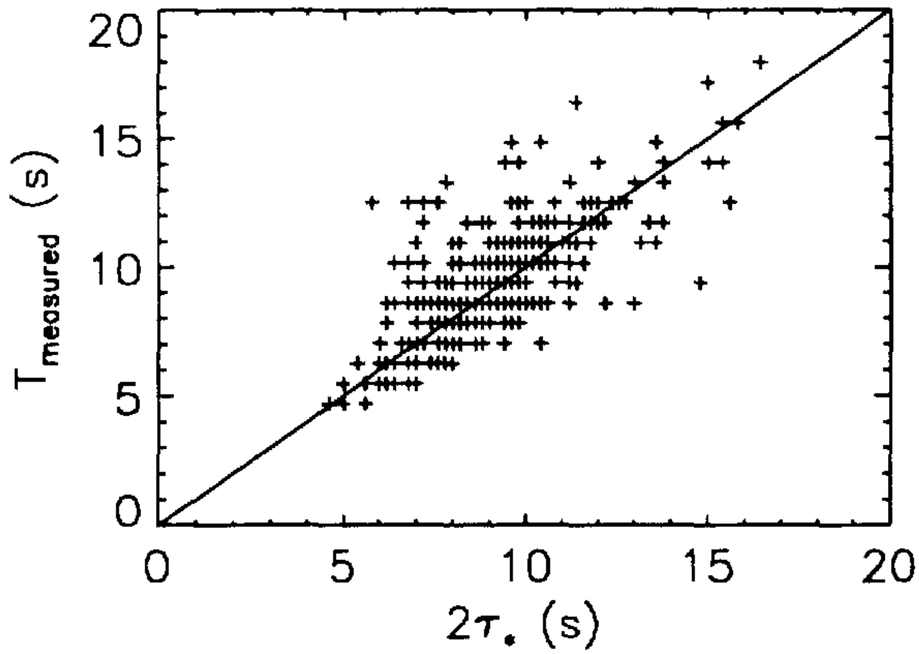

Figure 7. Measured period of extreme waves ($T_{measured}$) in terms of predicted period $2\tau_*$.

CONCLUSION

Wave data were collected over the 1993/94 winter using three wave buoys. The buoys were deployed in a tight triangular array off the west coast of Vancouver Island, British Columbia. The heave time series were despiked and corrected for the instruments' transfer functions. The heave signal from the three buoys closely followed the standard Gaussian distribution except for a slight excess of large crests on deep troughs. Statistical extreme wave events were then identified by searching for cases with an unusually large value of the surface elevation normalized by the standard deviation, $\gamma \geq 4.4$. A total of 339 extreme events were analysed.

The wave profile around one particular event was first qualitatively compared with the predictions of two models based on the linear Gaussian approach (Boccotti, 1989; Phillips et al., 1993). For a more quantitative comparison, the heights of the neighboring crests and the periods of the extreme waves were compared with the predictions of the simple model of Phillips et al. (1993). The comparison showed a reasonable agreement between measurements and the expected values predicted by theory. The scatter of the data about the predictions is, however, quite large as, indeed, is predicted by the simple linear approach.

References

Boccotti P., 1989: On mechanics of irregular gravity waves. Atti della accademia nazionale dei lincei, Serie **VIII** (19), 111-170,

Kimura, A., 1980: Statistical properties of random waves. In: Proc. 17th ICCE, 2955-2973.

Longuet-Higgins, M.S., 1984: Statistical properties of wave groups in a random sea state. Phil. Trans. R. Soc. Lond., **A 312**, 219-250.

Nickerson J.W., 1986: "Three Sisters" Mar historic. Mariners Weather Log, **30(4)**, 190-196.

Phillips, O.M., D. Gu, and M. Donelan, 1993: Expected structure of extreme waves in a Gaussian sea. Part 1: Theory and SWADE buoy measurements. J. Phys. Oceanogr., **23**, 992-1000.

AN INVESTIGATION OF APPARENT GIANT WAVES OFF THE WEST COAST OF CANADA

B. R. Thomas

Atmospheric Environment Service
Bedford, Nova Scotia

1. INTRODUCTION

On December 10, 1993, during an intense storm in British Columbia coastal waters, one of Environment Canada's buoys reported a maximum wave height of 30.8 in. The observation at the East Dellwood buoy (ID 46207) generated considerable interest because of its apparent record value. Gower and Jones (1994) discussed this event, and showed that there have been other recent observations of supposedly rare giant waves.

Some doubt was expressed about the reliability of the measurement, because the 30.8 m report was considerably more than twice the significant wave height of 12.8 m. Typical estimates of maximum wave height are up to about 2.0 Hs (Thomson, 1981).

Gower and Jones discussed factors that might cause errors in the measurement of maximum wave, such as the accelerometer confusing horizontal and vertical accelerations in heavy seas, calibration of the accelerometer, and the possible tendency of the buoy to skirt around the highest peaks of waves. Also, the buoys were designed to measure waves with a vertical range of about 15 m, corresponding to a maximum wave of about 30 m. Measurements near 30 m could have been clipped by this limit.

This study examines the wind and wave buoy data, and the results of a wind and wave hindcast of the storm, in an attempt to understand the conditions associated with the report of the 30.8 m wave.

Table 1 shows the largest significant wave height and largest maximum wave height reported at each buoy during the storm, along with the time of the report of largest significant wave height. The buoys which reported significant wave heights of 11 m or more were selected for further study. The highest significant wave heights at these 6 buoys ranged from 11 to 13 m, and except for the 30.8 m report at the East Dellwood buoy, the highest maximum wave heights ranged from 19 to 23 m.

Table 1 Largest reported and modelled significant wave height (H_s) at each buoy, with largest reported maximum wave height (H_{max}) and time of report of largest H_s.

Buoy Name	Buoy ID	Lat. (_N)/ Long. (_W)	Depth (m)	Hmax (m)	Hs Buoy (m)	Hs Model (m)	Time Hs Buoy (hr/dy)
East Dellwood	46207	50.9/ 129.9	2125	30.8	12.8	11.8	07/10
South Nomad	46036	48.4/ 133.9	3500	21	12.4	10.1	01/10
W. Sea Otter	46204	51.4/ 128.7	224	21.3	11.6	10.8	10/10
S.Hecate Strait	46185	52.4/ 129.8	226	19.5	11.1	10.7	12/10
South Moresby	46147	51.8/ 131.2	2000	21.2	11	11.6	05/10
West Moresby	46208	52.5/ 132.7	2950	22.7	11	9.8	07/10
South Brooks	46132	49.7/ 127.9	2040	18.7	10.2	–	09/10
Middle Nomad	46004	51.0/ 135.8	3658	18.3	9.5	10.3	14/10
West Dixon Ent.	46205	54.2/ 134.3	2675	17.7	8.8	7.4	20/10
La Perouse Bank	46206	48.8/ 126.0	73	13.9	8.3	8.8	12/10
N.Hecate Strait	46183	53.6/131.1	58	17	7.4	8.1	03 10
North Nomad	46184	53.9/138.9	3600	13.1	6.9	7.1	13 10
Cent.Dixon Ent.	46145	54.4/132.4	257	9	4.5	6.9	03 10

The storm hit British Columbia coastal Waters; with storm to hurricane force winds on December 9 and 10. The low had deepened rapidly as it moved eastward across the Pacific and was already below 960 hPa when it neared the outer edge of the buoy network (shown in Fig. 1) on December 9. It reached its lowest depth of 950 hPa as it tracked just northwest of the Middle Nomad buoy (46004) at 00 UTC 10 December. Thereafter the low moved northward and began to fill slowly. All buoys except the North Nomad buoy (46184) were east of the centre's track. Figures 2 -4 show the Pacific Weather Centre (PWC) analyses for 18 UTC 9 December, 00 UTC and 06 UTC 10 December.

The strongest winds reported by the buoys occurred on December 9 in the southeasterlies ahead of the advancing low, while the highest waves occurred on December 10 in the southerlies. The East Dellwood buoy (46207) reported the maximum wave of 30.8 in at 07 UTC 10 December.

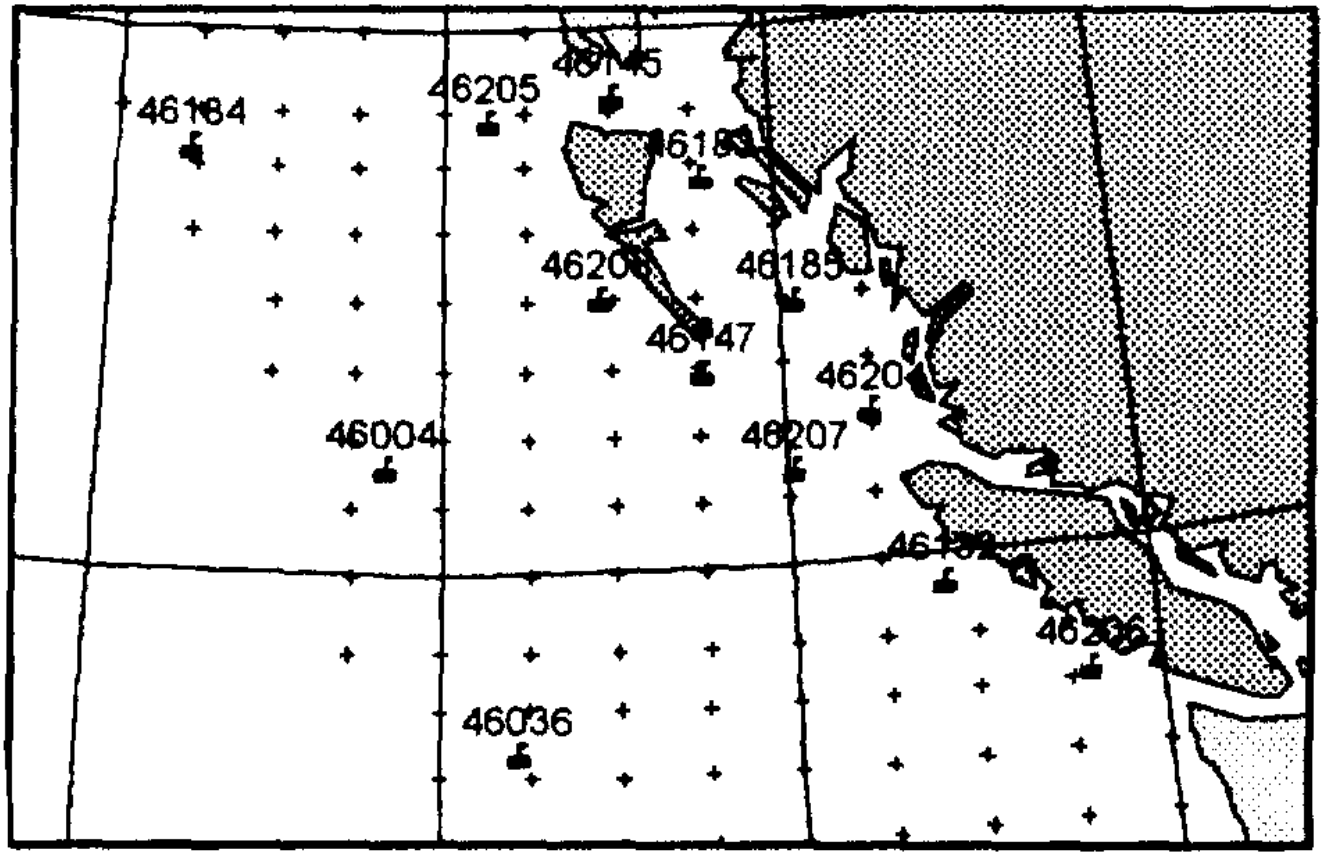

Figure 1 Buoy locations and wave model fine grid points

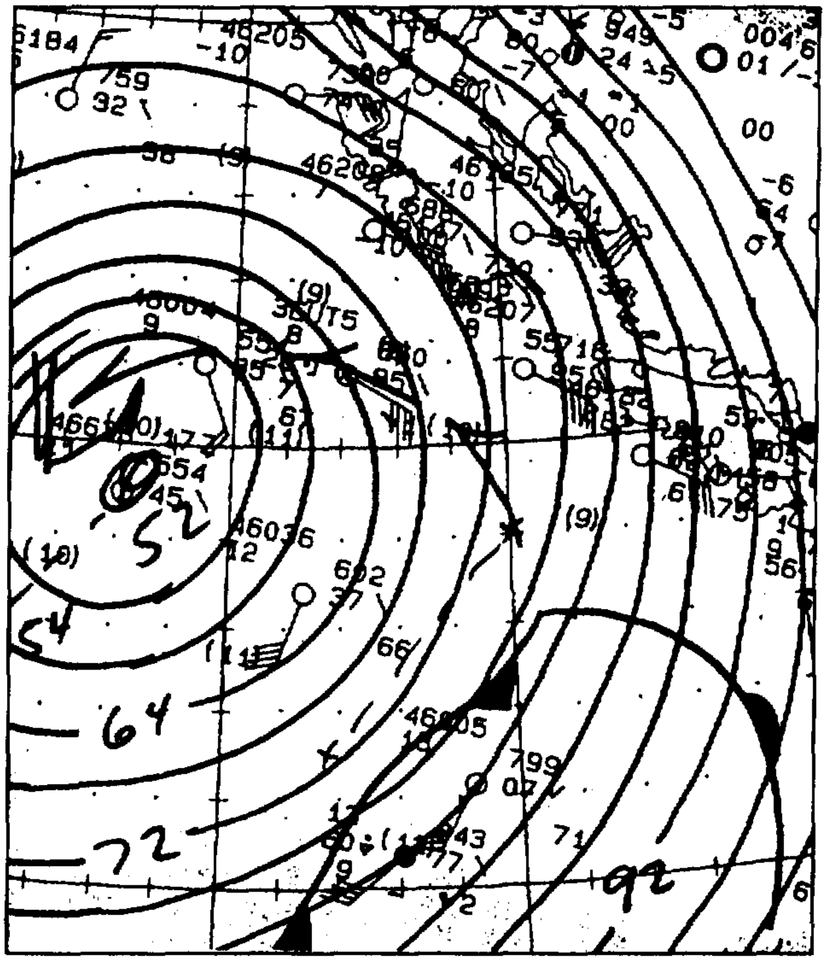

Figure 2. PWC analysis for 18 UTC 9 December 1993.

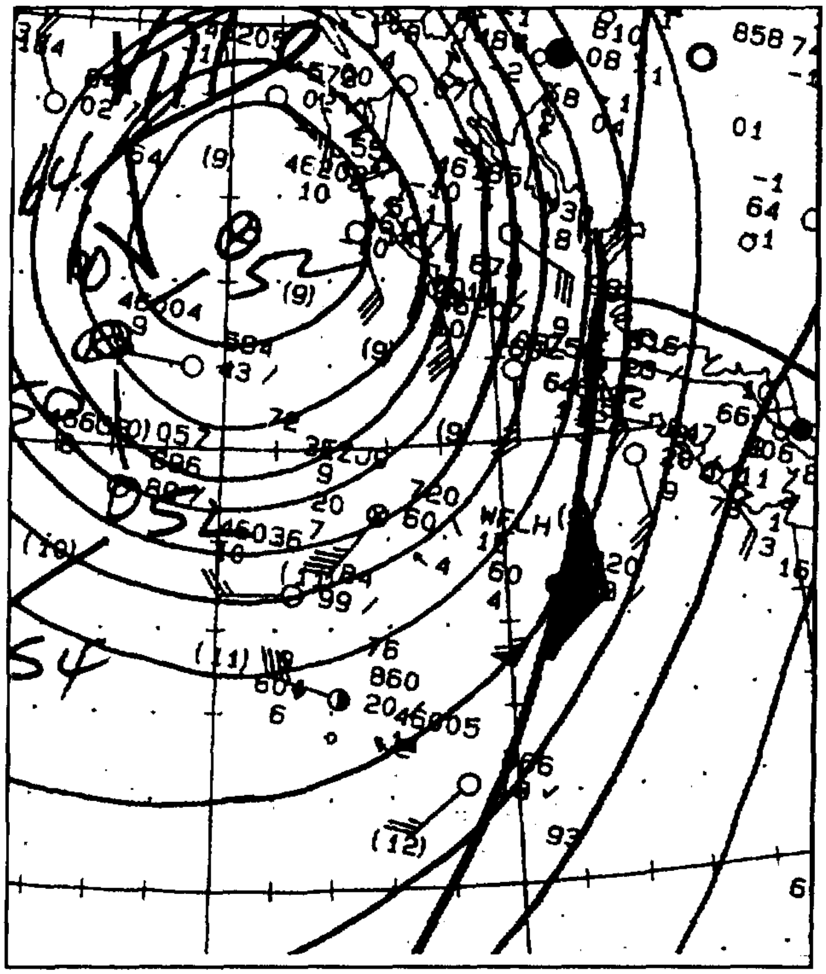

Figure 3 PWC analysis for 06 UTC 10 December 1993.

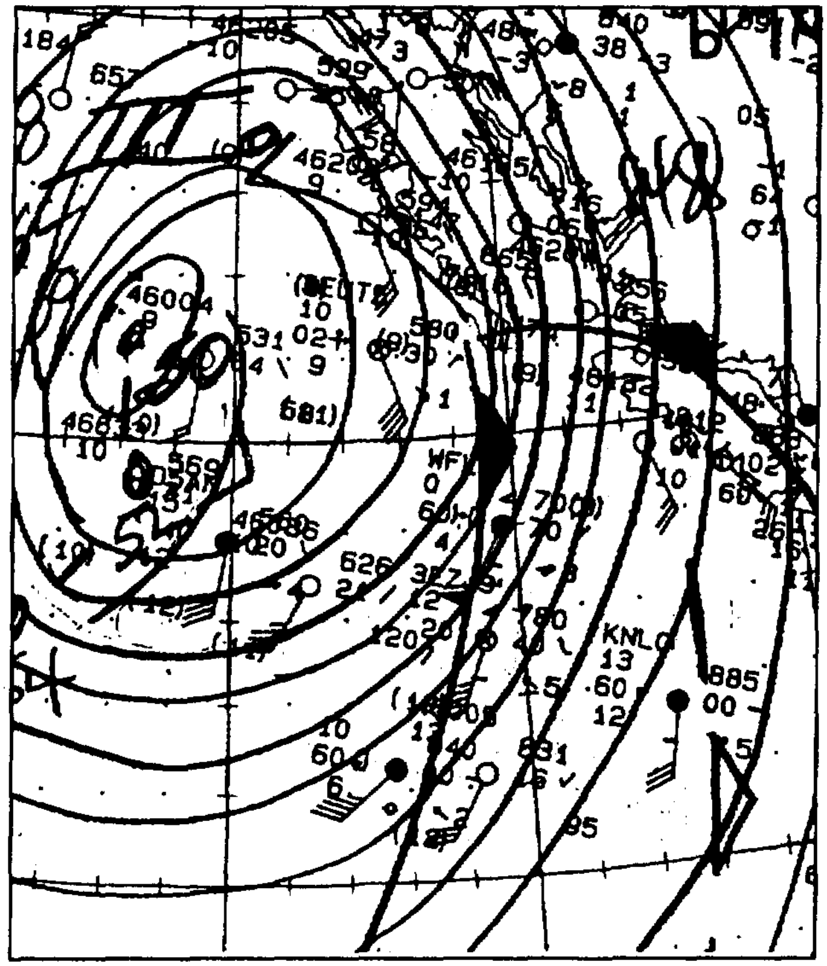

Figure 4 PWC analysis for 00 UTC 10 December 1993.

2. WIND AND WAVE HINDCAST METHOD

The Forecast Production Assistant (FPA) software (de Lorenzis, 1988; Swail, et. al., 1992), running on an HP 9000 workstation, was used to prepare the data fields and run the wind and wave models. The Canadian Meteorological Centre's GLOBAL model provided gridded binary files of objectively analyzed surface pressure, air temperature, and sea temperature at six hourly intervals. FPA was used to display and modify the pressure fields which were used in the wind calculations. The FPA system displays gridded data as contoured fields using the method of cubic spline interpolation. An internal resolution of 400 km was used.

The pressure fields were edited by comparing the central pressures of high and low pressure systems displayed with FPA to those on the Pacific Weather Centre surface analyses, and deepening or raising the central pressure as necessary. No other editing of the pressure or temperature fields was done. FPA then interpolated the fields to two hourly time steps, calculated the winds at the wave model grid points, and ran the wave model. No subjective corrections were made to the objectively modelled winds. The wave model was started with a flat ocean (no waves) on 00 UTC 4 December 4, five days before the storm began to affect the west coast buoys, and it ran until 18 UTC 12 December. The wave model produced detailed data at the grid points nearest the buoys.

The winds used to drive the wave model were calculated at the 19.5 m level using the marine planetary boundary layer (MPBL) model of Cardone (1969, 1979). The MPBL model uses the surface pressure, air and sea temperature fields to calculate the "effective neutral winds", so called because they are the winds in a neutral atmosphere that would have the same effect on the ocean surface as the winds in the real atmosphere with a given stratification.

The wave model run by FPA is the ODGP first generation, deep water spectral ocean wave model described by Cardone et. al. (1976), with 15 frequency hands and 24 direction bands. PACWAVE is the north Pacific implementation of the model. It is run with a two hour time step. The coarse grid extends from Japan to the west coast of North America, with a grid spacing of 1.25° lat. by 2.5° long.. The fine grid covers a much smaller area off the coast of B.C, with a grid spacing of .625° lat. by 1.25° long. (shown in Fig. 1).

3. BUOY MEASUREMENTS OF WIND SPEED AND WAVE HEIGHT

The East Dellwood buoy, which reported the 30.8 m maximum wave, was a 3-m discus buoy. The 3-m discus buoys are round hulled with anemometers at 4.9 m and 3.7 m (Gilhousen, 1987). Most near and inshore buoys on the west coast of British Columbia are 3-m discus buoys. The South Moresby, North, Middle, and South Nomad buoys are 6-m NOMAD buoys with boat shaped hulls and anemometers at 4.9 and 4.1 in. The buoys report a 10 minute vector mean wind speed and an 8 second scalar peak wind speed. The data from the first (slightly higher) anemometer is presented, unless noted. In order to compare the observed buoy wind to the model wind at the nearest grid point, the observed winds from the buoys were adjusted to "effective neutral 19.5 m winds" using the MPBL model described by Cardone (1969,1978), which uses the observed air-sea temperature difference to estimate the stability of the boundary layer.

The buoys report significant wave height, peak wave period, maximum wave height, and wave spectral information. On the west coast NOMAD buoys, wave information is determined from a Datawell gimballed accelerometer which senses vertical acceleration, regardless of buoy attitude. Strapped-down accelerometers are used on the 3-m discus buoys, which measure acceleration along an axis perpendicular to the deck of the buoy. Tipping or rocking of a buoy with a strapped-down accelerometer can result in additional accelerations being interpreted as wavelike motion. In both types of sensors, the acceleration is electronically integrated to a voltage corresponding to displacement. The voltage is then processed by an analogue to digital converter which is limited in both kinds of sensors to a range of ± 15.36 m. Measurements above the limit are "clipped" (Skey et. al., 1995).

The maximum wave height reported by the buoy is interpreted as the maximum peak to trough distance. [t is actually computed as twice the maximum positive excursion (displacement above mean sea level) (Skey et, al., 1995). The displacements are measured every second in the roughly 34 minute sampling interval. This method assumes that the highest wave peak will have a similar magnitude as the deepest wave trough. The value of maximum wave height that ran be reported is limited to twice the range of the sensor, or about 30.7 m. A small value, representing the mean height, is subtracted from the maximum excursion, to remove any offset. A 30.8 m maximum wave height would be reported if the mean height was -.05.

4. BUOY REPORTS OF WINDS AND SIGNIFICANT WAVE HEIGHT DURING THE STORM

4.1 Wind Speed Adjustments

Figures 5 to 10 show time series of the observed and modelled wind and wave data at the buoys that reported significant wave heights of 11 m or more during the storm. The adjusted buoy wind speeds are plotted. At the East Dellwood buoy (Fig. 5) the first anemometer wind speeds dropped to almost zero after 07 UTC. The second (backup) anemometer continued to send wind observations that looked reasonable, and it showed wind speeds diminishing after 06 UTC.

The time series of adjusted wind speed show values of 45 to 55 kt (mean) and 55 to 75 kt (peak) during the storm on December 9 and 10. The adjustment factor was 1.16 to 1.2. The stability of the boundary layer was generally neutral to slightly unstable during the storm, with sea surface temperatures of about 10° C and air temperatures between 5 to 10° C, so most of the difference in the adjusted winds was due to the change in height from 5 m to 19.5m. The adjustment increases gale to storm force wind speeds by about 10 knots. For example, the highest wind report from the East Dellwood buoy was at 18 UTC December 9. The observed mean and peak speeds were 45 and 60 kt, and the adjusted winds were 53 and 72 kt. The air sea temperature difference was -2° and the significant wave height was 8.2 m. The adjustment factor was 1.18 to 1.2. The adjustment factor given by Smith (1988) is similar: 1.22 to adjust 50 kt from 5 m to 20 m with an air sea temperature difference of -2°C.

As discussed in the next section, the hindcast wind speeds were close to the adjusted peak buoy wind speeds, during the very high waves of the storm, when hindcast wave heights verified reasonably well. This result was noted by Thomas (1993) in other hindcast studies. The 10 minute vector mean wind may be reduced by sheltering effect of the high waves, when the buoy is in the troughs. This effect was discussed by Skey et. al. (1995).

The adjustment process did not take into account .the way in which the high waves would modify the wind speeds in the lowest levels, or the effect on the anemometer height of the buoy riding up and down through the boundary layer wind profile.

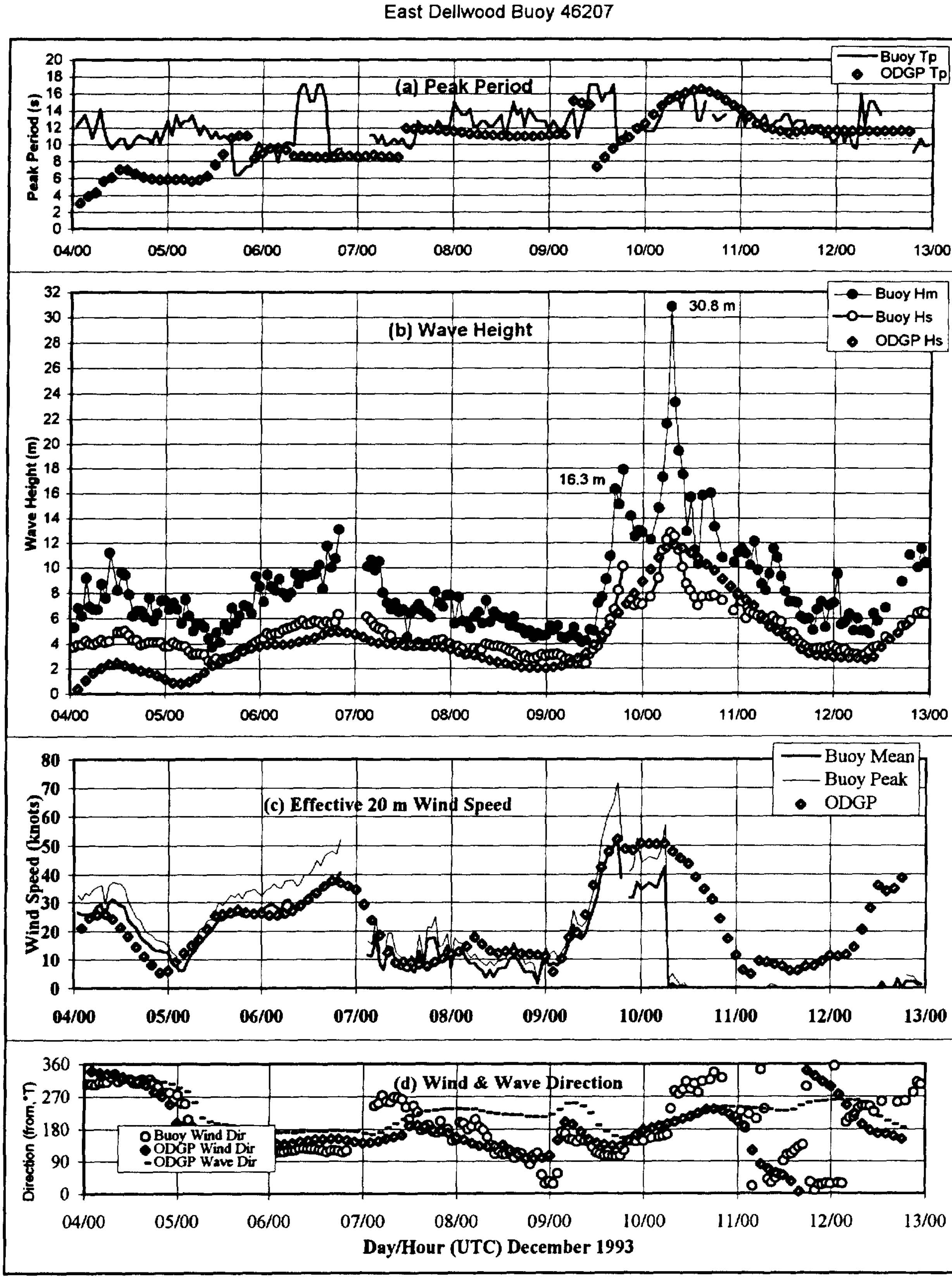

Fig. 5 Time series of observed (buoy 46207) and modelled (ODGP) wind and wave data.
Buoy wind speed and dir. bad after 06 UTC 10 Dec.

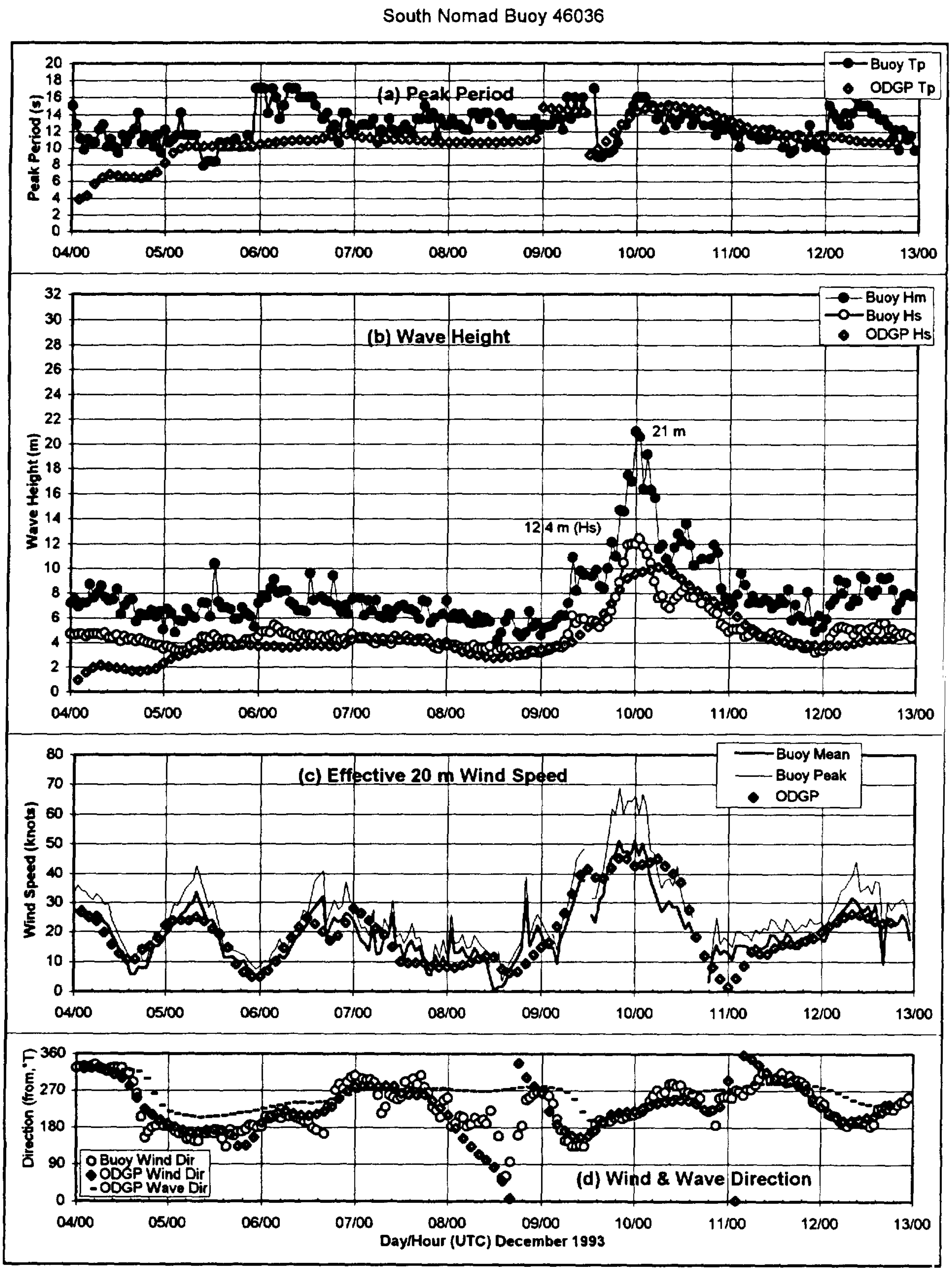

Fig. 6 Time series of observed (buoy 46036) and modelled (ODGP) wind and wave data.

West Sea Otter Buoy 46204

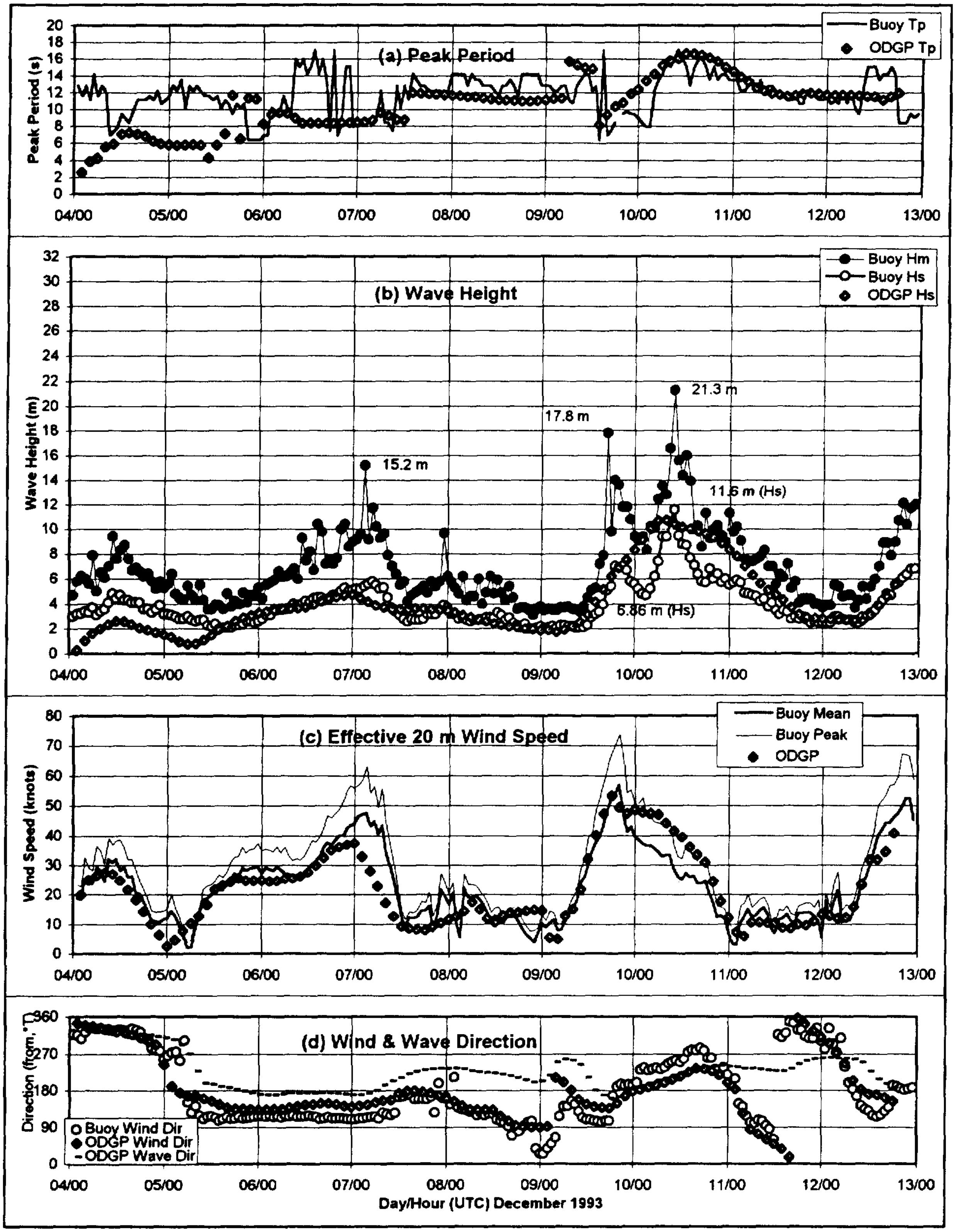

Fig. 7 Time series of observed (buoy 46204) and modelled (ODGP) wind and wave data.
Buoy wind dir. out (veered) by 80° after 18 UTC 9 Dec.

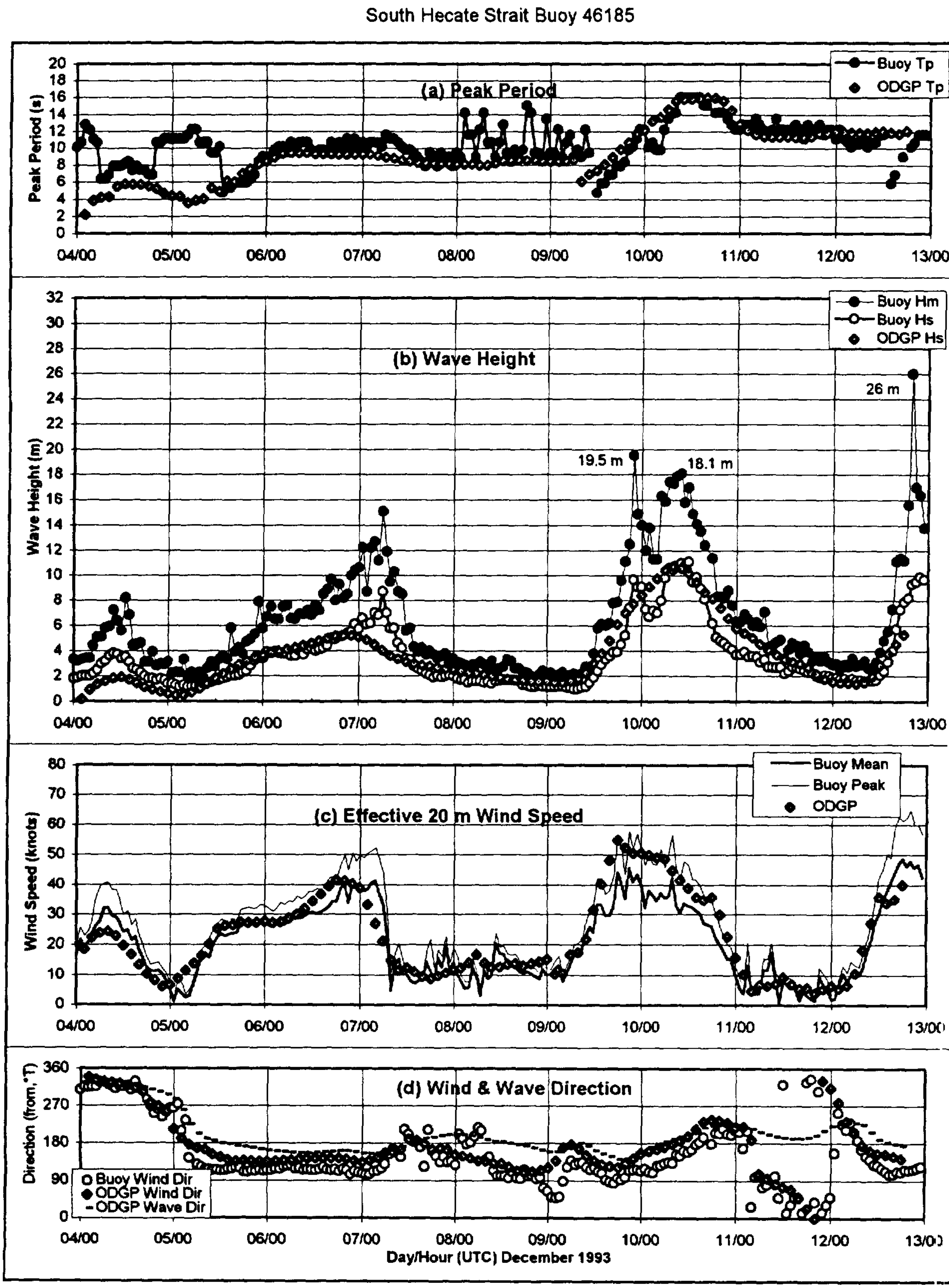

Fig. 8 Time series of observed (buoy 46185) and modelled (ODGP) wind and wave data.

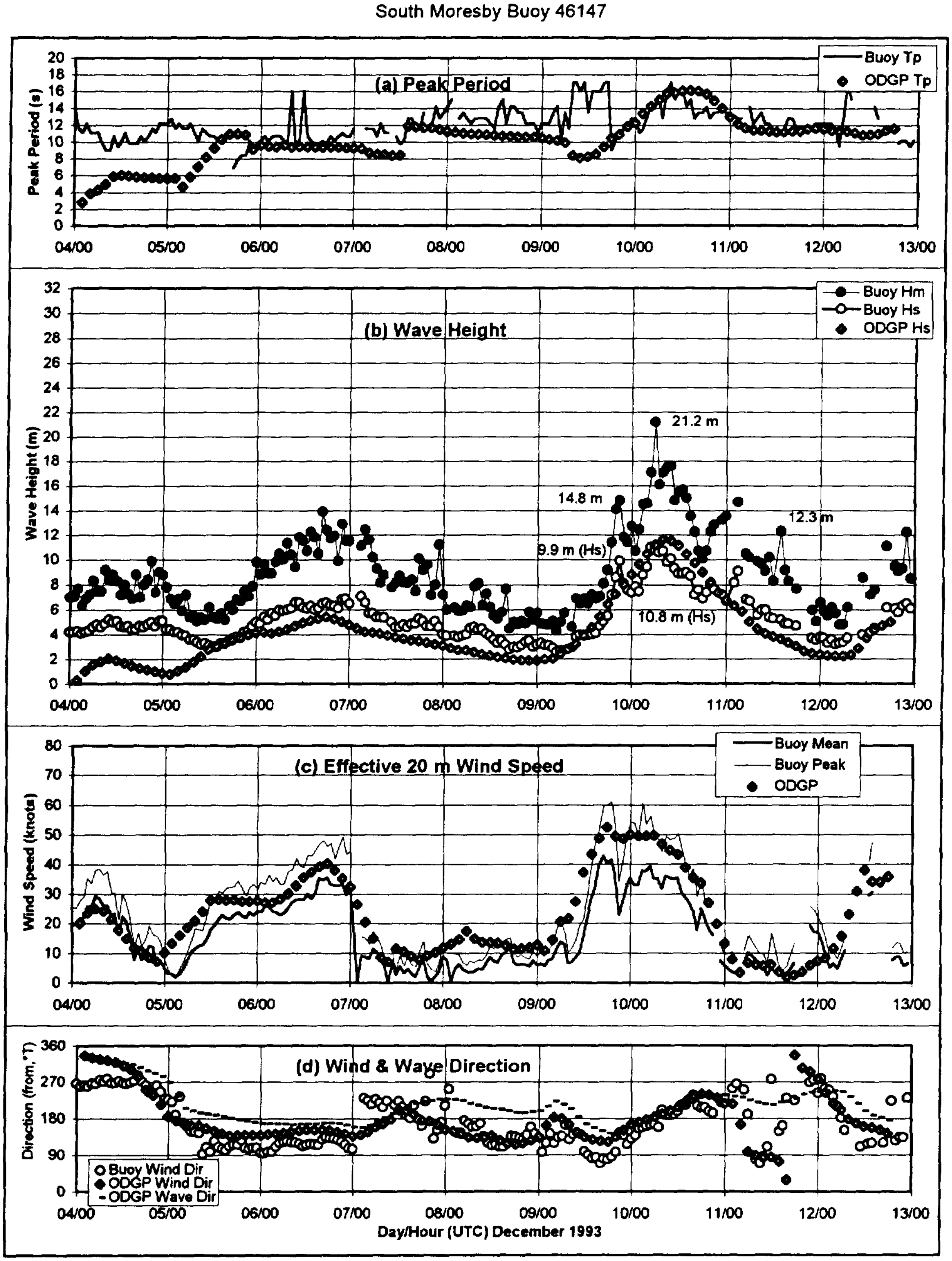

Fig. 9 Time series of observed (buoy 46147) and modelled (ODGP) wind and wave data.

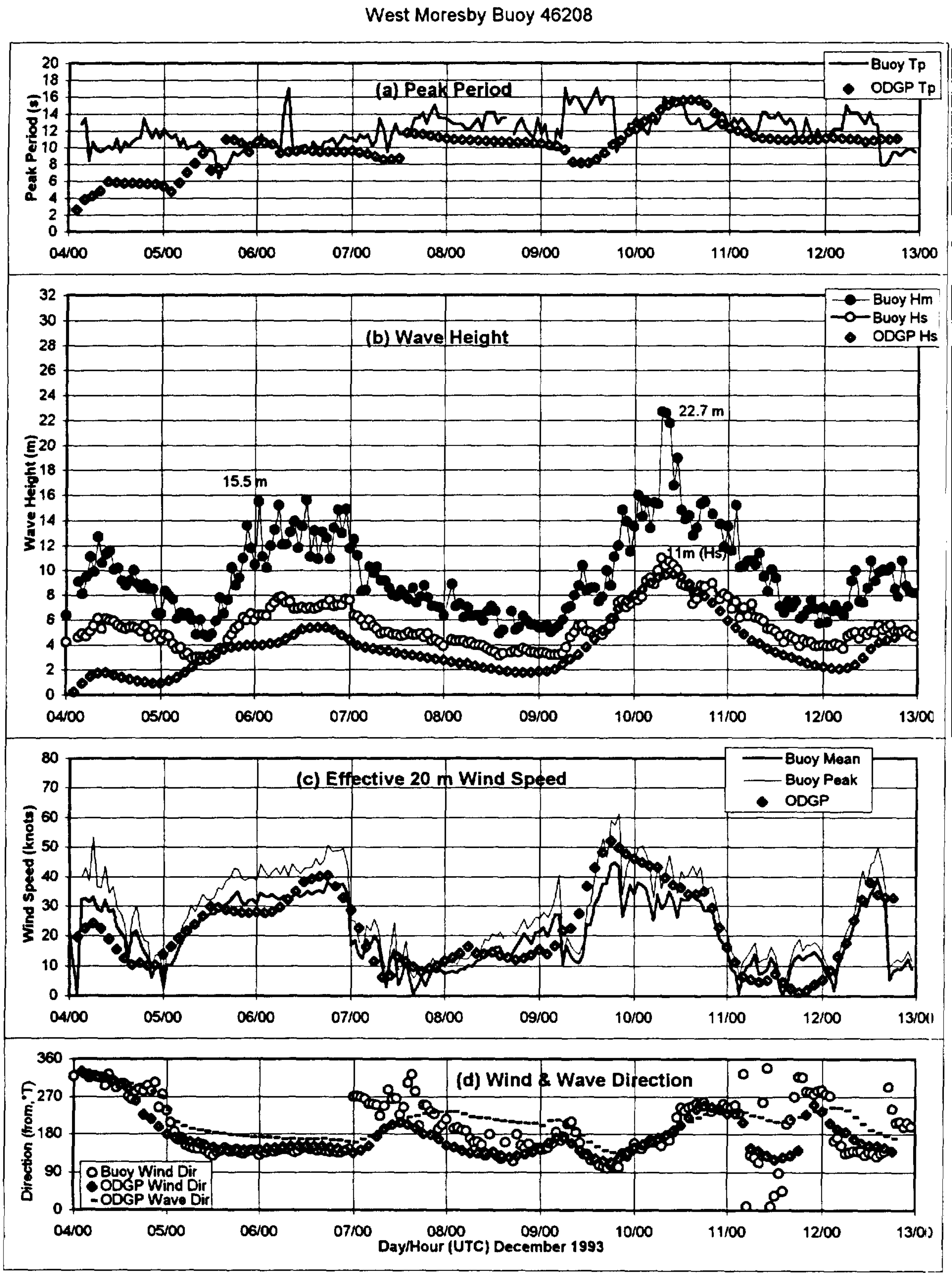

Fig. 10 Time series of observed (buoy 46208) and modelled (ODGP) wind and wave data.

4.2 Winds and Wave Heights During the Storm

At the 4 buoys in the area between Moresby Island and Vancouver Island, including East Dellwood (Fig. 5), West Sea Otter (Fig. 7), S. Hecate Strait (Fig. 8), and S. Moresby (Fig. 9), there are two distinct peaks in the time series of significant wave height. These correspond to a period of strong east southeast winds, following by a period of strong southerly winds.

The highest waves in the first regime were observed between 18 and 23 UTC on December 9. They were generated by winds from the east southeast, and were extremely steep. In only 12 to 18 hours the winds increased dramatically, from light to at least storm force. The West Sea Otter Buoy reported the highest speeds, with east southeast mean and peak wind speeds of 48 and 62 kt (adjusted, 57 and 74), at 20 UTC 9 December. The fetch was limited by the presence of the mainland coast and Vancouver Island in the upstream direction, and the duration was limited, as the winds had increased so rapidly. Significant wave heights built rapidly to 7 to 10 metres, with peak wave periods increasing to about 11 seconds.

Wave heights diminished slightly as the winds veered, then the second wave regime developed in the southerly winds, with a considerably longer fetch. The highest significant wave heights in this regime were 9 to 13 metres. High waves with the southerly winds reached the South Nomad buoy first, at 00 UTC 10 December. At the East Dellwood and neighboring buoys, these waves occurred between 06 and 12 UTC 10 December. Peak wave periods were about 16 seconds.

The East Dellwood and neighboring buoys reported somewhat lighter winds in the southerly pressure gradient, rather than the southeast gradient, even though the southerly pressure gradient was twice as strong at 00 and 06 UTC 10 December as the southeast gradient was at 18 UTC 9 December (see pressure analyses, Figs 24). The highest mean and peak wind speeds reported by the East Dellwood buoy in the southerly gradient were 37 and 49 kt (adjusted, 43 and 57), at 06 UTC 10 December 10. However there was a report of 66 kt (estimated) from the ship Sealand Reliance, identifier WFLH, about 300 km south of East Dellwood in a similar pressure gradient. The southerly pressure gradient was extremely strong, indicating a geostrophic wind of at least 125 knots. A typical wind in that gradient might be 50% of the geostrophic speed, which would give a value consistent with the ship report.

At the West Sea Otter buoy the winds diminished rapidly while the waves built up for the second time. The gradient was beginning to weaken as the low moved further north, and the waves were arriving as swell.

5. HINDCAST WIND AND WAVES

The time series in Figures 5 to 10 show the modelled wave height, wind speed, peak period, wind direction and wave direction. The modelled values are from the wave model grid point nearest to each buoy. The storm was fairly well modelled. Table I compares the highest modelled and reported significant wave heights. At most sites the difference was fairly small, about a metre or less (hindcast either too high or too low). However, at the South Nomad buoy, the error was just over two metres. At East Dellwood the highest modelled significant wave height was one metre less than the observed value, and occurred at nearly the same time (one hour apart). The error between time of occurrence of the highest modelled waves, compared to that of the observations was within six hours in most cases.

East Dellwood and the three neighboring buoys reported two peaks on the time series of wave height. The modelled wave heights showed only one peak, so although the general pattern and the magnitude of the highest significant wave heights were fairly well modelled, some of the finer details were not.

The modelled winds were typically somewhere between the mean and peak buoy wind speeds (adjusted to effective neutral 19.5 m winds). In the highest waves at East Dellwood, South Hecate Strait, West Sea Otter, and South Moresby buoys, the modelled wind speed were close to the adjusted peak wind speeds. At the South Nomad buoy the modelled winds appear too have been too low. They were only slightly less than the mean buoy winds at the time of the highest waves, but the hindcast waves were two metres too low.

Peak periods were generally reasonably well modelled, with the highest values within a second or so of the observed highest values.

Wind direction was modelled moderately well. However at East Dellwood, South Moresby, West Sea Otter and South Hecate buoys the observed wind is backed more (by as much as 45°) than the modelled wind. This is particularly pronounced around 12 UTC 9 December, when the storm is approaching and winds are from the east. During the southerly winds early on December 10 the modelled winds were more southwesterly. This suggests that the modelled wave directions may also be out (veered) by up to 45°. Wind directions were modelled better at the West Moresby and South Nomad buoys.

A sensitivity study of the wind/wave hindcast system on the east coast (Thomas, 1993) found that very intense storms, with the wave maximum in the southeast quadrant of the low, were fairly well modelled For these storms the low pressure centres were edited (typically deepened a few mb) but little or no correction was made to the objectively modelled winds. The storm of December 9 and 10 was that type of storm, and the hindcast results are consistent with that type. The low centre was deepened between one to five mb during the worst part of the storm; the objectively modelled winds were not corrected.

However, for the storm preceding the one of December 9 and 10, the hindcast results were not so good. There was a prolonged period of southeast winds on December 5 to 7, from a sharp nearly stationary trough extending southeastward off the BC coast from a low in Gulf of Alaska. A low pressure centre was analyzed in the trough. The winds strengthened steadily to a maximum early on December 7, and the modelled winds were much too light around that time, particularly at the W. Sea Otter buoy (Fig. 7) and the S. Hecate Strait buoy (Fig. 8). In this case simply editing the pressure centres was not adequate.

6. BUOY REPORTS OF MAXIMUM WAVE HEIGHT

The maximum wave of 30.8 in was reported at East Dellwood at 07 UTC on December 10. It was measured during the highest significant wave heights of the storm, in southerly winds. The maximum wave height was considerably higher than the other reports of between 19 and 23 metres at the East Dellwood buoy and at the other buoys. In the southeasterlies on December 9 the highest reports of maximum wave height were between 15 and 20 metres. The significant wave height at the time of the 30.8 in report was 12.8 in, yielding a ratio of maximum wave height to significant wave height of 2.4.

Thomson (1981) cited Van Horn (1974) in discussing the estimate of the most probable maximum wave. It is a function of $\sqrt{E}$ where E has the dimensions of height squared and is a measure of the average wave energy during the time the record was taken (or the significant wave height) and the total number of waves encountered. The chance of meeting a giant "rogue" wave are increased as greater energy is fed into the ocean waves by the wind and as more waves pass by. The significant wave height is calculated from $H_s = 2.83\sqrt{E}$. For every 200 waves there is a 5% chance that one will exceed $5.8\sqrt{E}$ (or 2.0 H_s). At the time of the 30.8 in report, the peak wave period was 15 seconds, so about 140 waves would pass in the 34 minute sampling interval. Thus the chance of exceeding 2.0 Hs would be even less than 5%. However, Thomson cautions that the estimate is based on a fully developed sea. It will under estimate the extreme wave heights in a rapidly growing sea. This was the situation at the East Dellwood buoy, where significant wave heights had increased 5.4 m in the previous 6 hours.

Data from the buoys shows that the ratio of 2.0 was exceeded surprisingly often, in the period from December 4 to 12. Figure 11 shows time series of the ratio of reported Hmax to Hs for each buoy. Most ratios were between 1.5 and 2.0, but there were several reports above 2.5, and one was as high as 3.5 Hs. The ratio of 2.0 was exceeded more frequently at the 3m discus buoys (8 to 12% of the reports) than at the 6 in NOMADS (46036 and 46147) (2 to 5% of the reports). The high ratios did not necessarily correspond to high values of Hs.

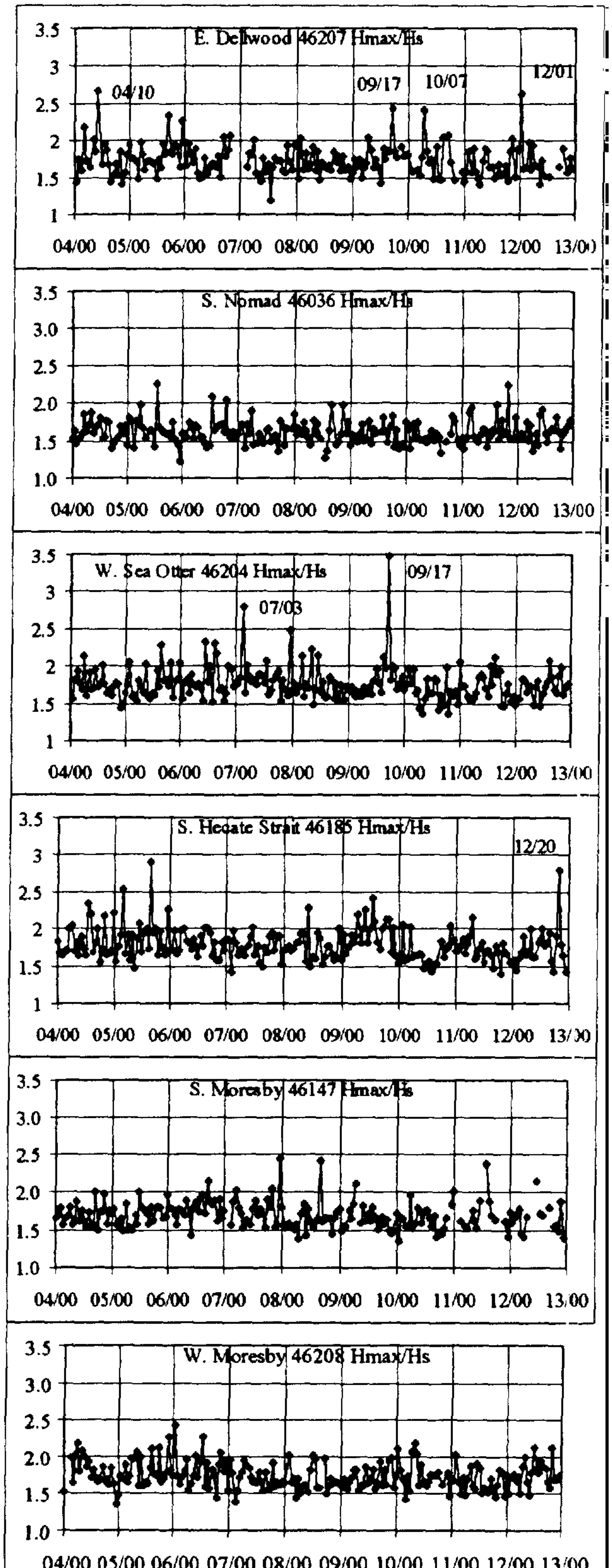

Figure 11 Time series of ratio of Hmax to Hs at each buoy, Dec. 4-12/93.

The events where the ratio exceeded 2.3 and the significant wave height exceeded 5 m are shown in Table 2 . Besides the case of the East Dellwood (46207) buoy with 30.8 m, two other events stand out. At the West Sea Otter buoy at 17 UTC 9 December the maximum reported wave height of 17.8 m was 3.5 times the significant wave height of only 5.1 m. At the South Hecate Strait buoy (46185) at 20 UTC 12 December, the maximum wave was 26.0 m, 2.8 times the significant wave height. This event occurred in the storm that followed the one of December 9 to 10. There was a deep low over the Gulf of Alaska, with an intensifying southeasterly pressure gradient along the BC coast ahead of an approaching frontal system. As on December 9 and 10, the winds and waves were increasing very quickly. The system on December 7 was also a storm with increasing southeast winds.

Table 2 Observations with high ratios of maximum (H_{max}) to significant (H_s) wave height. Day/hour in Dec. 1993, and peak period are also shown.

Buoy	D/H	Ratio	H_{max}	H_s	T_2
46207	09/17	2.4	16.3	6.7	9.8
46207	10/07	2.4	30.8	12.8	15.1
46204	07/03	2.8	15.2	5.4	8.4
46204	09/17	3.5	17.8	5.1	7.4
46185	12/20	2.8	26.0	9.3	10.7
46147	11/14	2.4	12.3	5.2	11.6
46208	06/01	2.4	15.5	6.4	11.6

Figure 12 shows the significant wave heights plotted against peak period, for the reports listed in Table 2 . The location of the points can be compared to the maximum steepness curve to get an estimate of the steepness of the individual waves during these events. The maximum steepness curve was determined by Buckley (1988) and cited by Gilhousen (1993). Buckley searched the entire archive of National Data Buoy Centre data for extreme events. He derived the maximum wave steepness curve by empirically fitting the function that describes steepness from linear wave theory to these extreme events. The curve is defined by

$$H_s = 0.00776 g T_p{}^2 \quad ,$$

where g is gravity. The events of December 7, 9, and 12 lay near or to the left of the extreme steepness curve. They indicate very steep waves and phenomenal wave growth.

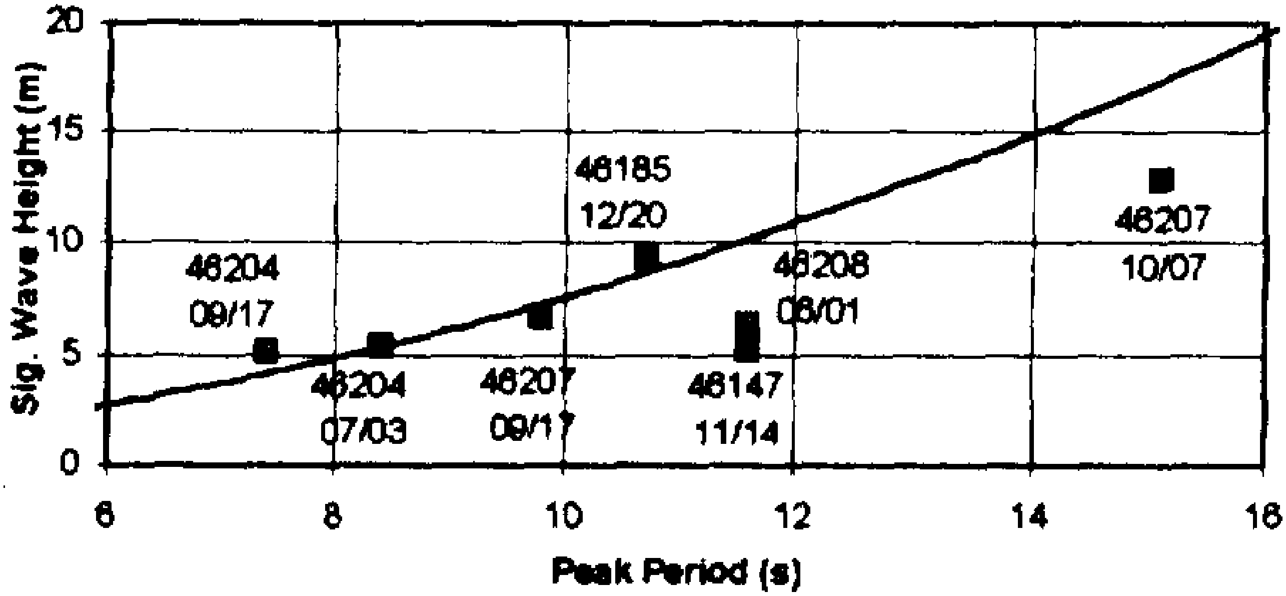

Figure 12 Observations of significant wave height and peak period from Table 2. Labels are buoy ID and day/hour of observation. Also plotted is a solid curve depicting maximum wave steepness.

During two of these events, buoy anemometers were damaged. The East Dellwood buoy's first anemometer began reporting near zero wind speeds and erroneous directions , starting at 07 UTC, the time of the 30.8 m report. Of the observations sent by the East Dellwood between 18 UTC on December 9 and 06 UTC on December 10, four were incomplete, possibly indicating data transmission problems as a result of the rough seas, The West Sea Otter buoy reported the maximum wave height of 17.8 m at 17 UTC 9 December. Two hours later, at 19 UTC, the wind direction measured by the first anemometer shifted, with respect to the second. They had been within 3°, and after the change they were 80° apart. The direction from the first anemometer was veered too much to the west.

7. WAVE SPECTRAL DATA

7.1 Observed Wave Spectra

Figure 13 shows the wave frequency spectra measured at the East Dellwood buoy, at various times on December 9 and 10. The spectral density is related to the variance of displacement about the mean sea level, which is related to the potential energy of the sea surface, thus the plots give an indication of the energy of the wave frequency components. The spectra show the shift to lower frequencies and rapid increase in energy associated with a growing sea. The peak wave period reported by the buoy gradually increased from 11 seconds on December 9 (.09 Hz), in the southeasterlies, to 15 seconds on December 10 (.066 Hz). Some of the spectra are bimodal, with energy in two components, at frequencies of about .07 Hz and.09 Hz. This might be a result of the waves generated in the southerly fetch moving in the same direction as the low, so that waves with slightly longer wavelengths, generated further upstream, are also present in the wave spectra. The waves generated by the east southeast winds may have already moved past the buoy, as the east southeast winds peaked 12 hours before 07 UTC, and the fetch was somewhat limited.

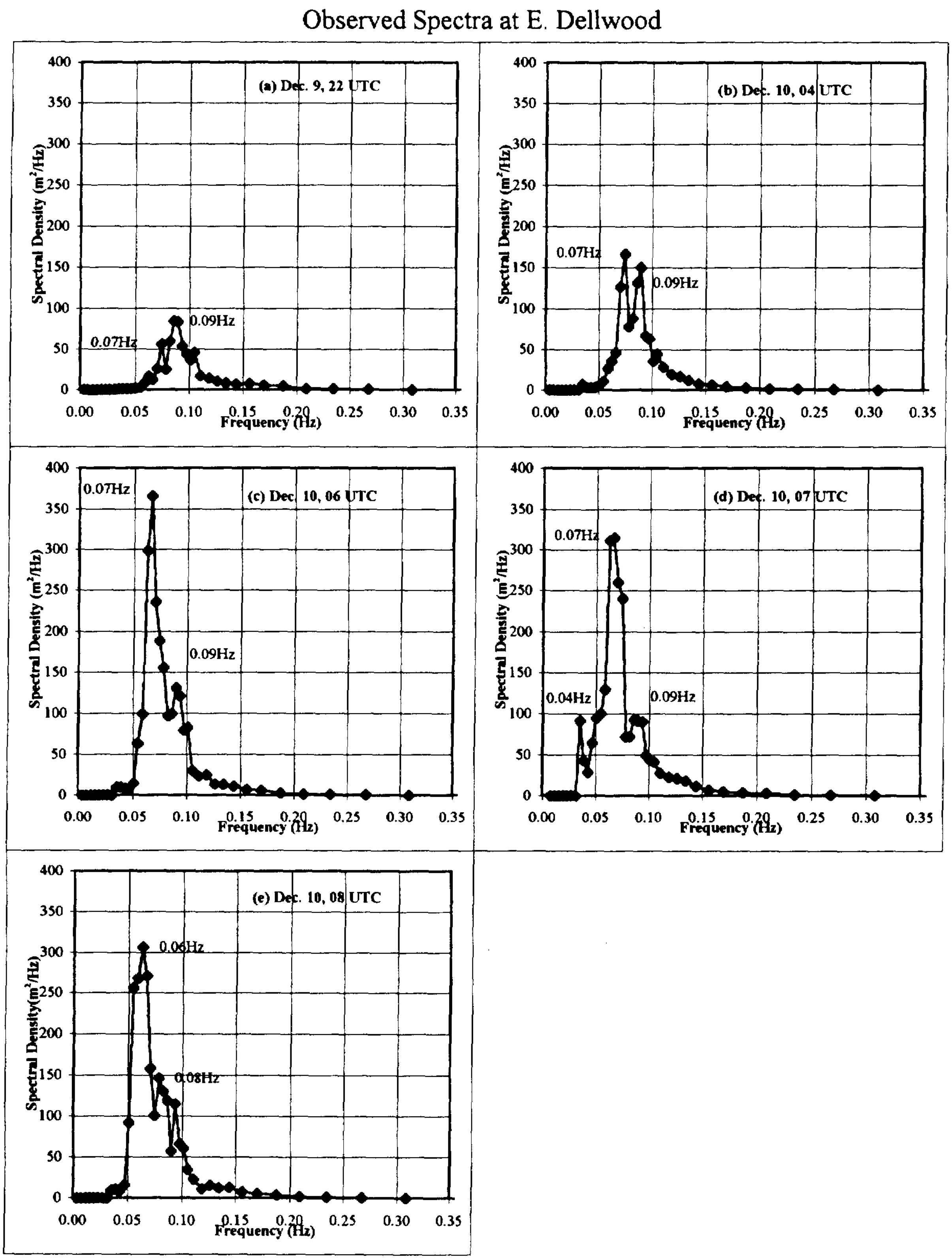

Fig. 13 Observed wave spectra (spectral density vs frequency) at buoy 46207.

The wave spectrum at 07 UTC 10 December 10 (Fig. 13d), when the maximum wave of 30.8m was reported, had a third spike at low frequencies (.035 Hz), corresponding to a period of 28 seconds. It was not present in the spectrum one hour before or one hour after. Most of the wave energy was in the frequency component of .066 Hz at this time, with a corresponding peak wave period of 15 seconds.

This additional low frequency spike suggests there was a problem with the accelerations sensed by the buoy. A wave period of 28 seconds seems unrealistic given the conditions that were present at the time (wave periods generally 16 seconds). It might conceivably have been caused by swell coming from a considerable distance, but it seems unlikely that it would show up for only one wave sampling period, coincident with the worst storm conditions. Gower and Jones speculated that very rough seas may hit the buoy and cause horizontal acceleration to be measured as well as vertical, which could confuse the determination of maximum wave height. The period corresponding to the third low frequency spike was roughly double that of the waves with the most energy. This may be a case of the non-linear phenomenon of period doubling, when a system is driven beyond linearity (Gleick, 1987). For instance, the buoy may have been repeatedly hit by breaking waves and driven sideways or tipped over each time, but it may not have recovered in time to be hit by each subsequent wave. If the horizontal accelerations were driven by every second wave, repeatedly during the sampling period of this observation, then the additional frequency mode might be detectable and have roughly double the wave period. Under this scenario, the measurement of significant wave height might not have been affected, as the significant wave height is calculated from the area under the curve of the wave spectral plot (the total variance), and the additional area from the third low frequency mode was relatively small.

7.2 Hindcast wave spectra

Figure 14 (a)-(d) shows the hindcast spectra (spectral density by frequency) corresponding to the times of the observed spectra. The hindcast spectra are much smoother, with only one mode. The peak frequencies fit fairly well with the observed values. The magnitude of the hindcast spectral density is close to the observed values in the early part of the storm on December 9 and 10, but it is too low when the highest significant waves were reported,

Figure 14 (e) and (f) show the hindcast directional spectra (variance by direction). Most of the wave energy is from a south southwest direction at 22 UTC 9 December, becoming, more southwest by 08 UTC 10 December. The 08 UTC spectrum is skewed somewhat, indicating a wave component from the south. However as discussed earlier, the modelled wave direction may have been veered too much to the southwest, as the modelled winds were. Thus the skewness may actually indicate a wave component from the southeast.

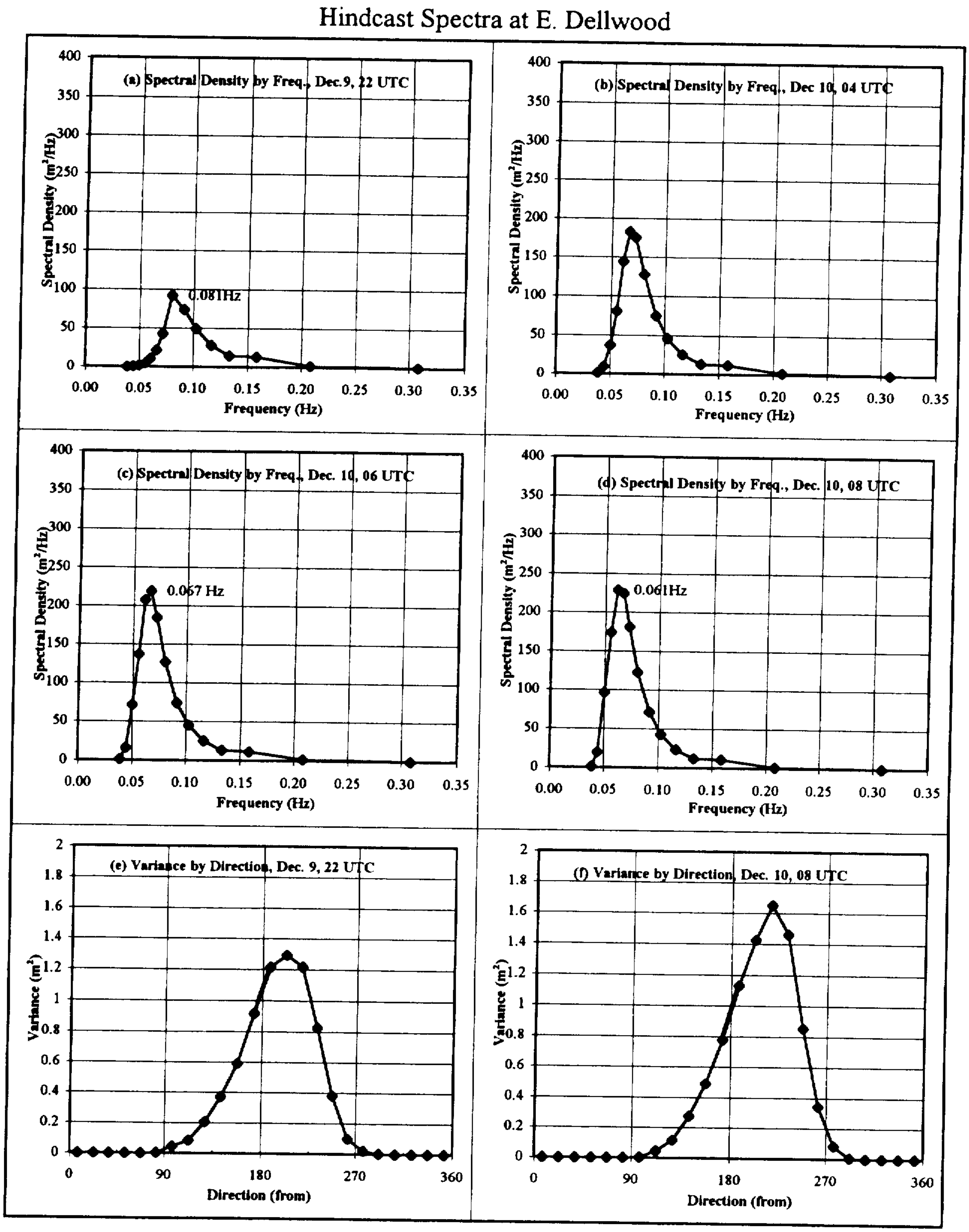

Fig. 14 Hindcast wave spectra for buoy 46207: (a)-(d) spectral density by frequency, (e) and (f) variance by direction.

8. SUMMARY AND CONCLUSIONS

Except for the 30.8 m maximum wave reported at the East Dellwood buoy, the intense storm on December 9 and 10 produced maximum wave reports in the low twenties and significant wave heights of 12 to 13 in. The high waves were generated in an area of storm to hurricane force southerly winds, with long fetch, following a shorter period of storm to hurricane force east southeast winds.

It is not clear if the reported 30.8 m giant wave was real, or an erroneous measurement due to something happening to the buoy. Some possible explanations for observation of the giant wave include waves from lower frequency and higher frequency wave trains from the south combining together for a brief moment, or a similar combination of crossing wave trains from the southeast and south. However, there were some indications that the report was an over estimate of the maximum wave.

The 30.8m report from the 3 in discus East Dellwood buoy was unusually high for the conditions of the storm. The ratio of maximum to significant wave height of 2.4 exceeded the typical limit of 2.0. However, it appears that maximum wave heights more than twice the significant wave height may be more common than was previously thought. Some of the more extreme events corresponded to very steep wave conditions and or rapidly increasing winds and waves, when the probability of getting a higher maximum wave increases. There were ratios of greater than the 2.4 corresponding to the report of 30.8 in, but that event is the most sulking since the significant waves were already exceptionally high. Higher ratios of Hmax to Hs were reported more frequently froze, the 3 in discus buoys. This could indicate the reports of Hmax are in error, as a result of the smaller buoys responding to the rough seas, but it could also be a true result of more complicated wave patterns as a result of rapidly building seas or coastal effects. These extreme wave conditions may be sufficient to capsize the buoy or force other unusual motion, such as repeated sideways accelerations. Wave spectral data at the East Dellwood buoy at the time of the giant wave report supports the idea that the buoy was undergoing unusual forcing by the exceptionally high seas. Further investigation into the validity of maximum wave reports from the buoys is warranted.

The adjusted (to 19. 5 in) 8 second scalar peak buoy wind speed appeared to be more representative of the prevailing winds than the adjusted 10 minute vector mean wind in very high seas. Ms conclusion is supported by the hindcast wave results, which generally verified fairly well, while the modelled wind speeds were close to adjusted peak wind speeds. There was a substantial difference, of about 20 knots, between the reported mean wind speed and the adjusted peak wind speed in the very high seas.

ACKNOWLEDGMENTS

This work was directed by V.R. Swail and supported by the Federal Panel on Energy Research and Development.

REFERENCES

Cardone, V. J. 1969. Specification of the wind field distribution in the marine boundary layer wave forecasting. Report TR-69- 1, Geophys. Sci. Lab., New York University.

Cardone, V.J., W.J. Pierson and E.G. Ward. 1976. Hindcasting the directional spectrum of hurricane generated waves. J of Petroleum Technology 28: 385-394.

Cardone, V.J. 1978. Specification and prediction of the vector wind on the United States continental shelf for application to an oil stick trajectory forecast program. Final Report, Contract T35430 NOAA, US Dept. of Commerce, Silver Spring, Maryland.

de Lorenzis, B. 1988. Interactive graphics editor. Proc. of AMS 4th International Conference on Interactive Information Processing and Processing Systems for Meteorology, Oceanography, and Hydrology, Feb. 1-5, 1988, Anaheim, CA. 143-145.

Gilhousen, D. B. 1994. The value of NDBC observations during March 1993's "Storm of the Century", Weather and Forecasting, 9, 255-264.

Gleick, J. 1987. Chaos: Making of a New Science, Viking Penguin Inc., New York, NY, US, 352 p.

Gower, J., and D. Jones. 1994. Canadian West Coast Giant Waves. Mariners Weather Log, 38, 4-8.

Skey, S.G.P., K. Berger-North, and VR. Swail. 1995. Detailed measurements of winds and waves in high sea states from a moored NOMAD weather buoy. Proc. 4th Int'l Workshop on Wave Hindcasting mid Forecasting, Oct. 16-20, 1995, Banff, AB.

Smith, S.D. 1981. Factors for adjustment of wind speed over water to a 10 metre height. Report Series/Bl-R-81-3/March 1981. Bedford Institute of Oceanography.

Swail, VR., B. de Lorenzis, C. Doe, R. Bigio, C. Calnan. 1992. An Interactive Graphics Approach to Wave Analysis and Forecasting, Proc. of 3rd International Workshop on Wave Hindcasting and Forecasting, May 19-22, 1992, Montreal, QB, 333-338.

Thomas, B.R. 1993. Sensitivity Study of an Interactive Graphical Wind and Wave Analysis and Forecast System, Climate Adaptation Branch Bulletin 93-07, Environment Canada, Downsview, Ont, 85 p.

Thomson, R. E., 1981. Oceanography of the British Columbia coast. Can. Spec. Publ. Fish. Aquat. Sci. 56: 291 p.

Van Dom, W.G. 1974. Oceanography and seamanship. Dodd, Mead and Co., New York. 481 p.

ASSIMILATION OF SAR WAVE DATA INTO AN OPERATIONAL SPECTRAL WAVE MODEL

L. J. Wilson

Atmospheric Environment Service
Downsview Ontario

E. Dunlap

ASA Consulting
Halifax, Nova Scotia

R.B. Olsen

Satlantic, Inc.
Halifax, Nova Scotia

S. de Margerie

ASA Consulting
Halifax, Nova Scotia

1. INTRODUCTION

Canada's soon-to-be operational spectral ocean wave model, a version of the WAM (WAMDIG, 1988), is driven solely by the 10m wind field, which is obtained from analyses or forecasts or a combination thereof. In real time operations, forecast winds will be used and will be taken from the operational atmospheric model. Thus, wave forecasting has so far been treated primarily as a boundary value problem rather than in initial value problem. This situation has been encouraged by two factors: First, wave models have been proven to do quite a good job of simulating the wave field if they are fed a good quality wind field. Second, until recently, wave observations were so few and far between that it wasn't worth the effort to try to use them to initialize the wave field. Even observations that were available, were usually in the form of summary parameters such as significant wave height, or at best one-dimensional spectra.

With the launch of ERS-1 in 1991, this situation began to change. ERS-1 has provided wave observations in two forms, an estimate of the significant wave height Hs from the radar altimeter, and spectral wave information from the AMI instrument operating in SAR mode. The latter source represents the first opportunity to obtain on a regular basis, two-dimensional spectra of the wave field. This is attractive to wave modellers since spectral wave models attempt to predict the evolution of the complete two dimensional spectrum of waves.

Beginning in March 1993, we have been developing a first data assimilation system for SAR spectra. Our strategy has been to mount a full system as quickly as possible, keeping it as simple as possible. Then, it can be used as a platform to test enhancements, and to evaluate different candidate strategies for optimal use of SAR data in wave models.

The first prototype system has been completed and fully tested on one case, the Storm of the Century, March 1993. Sensitivity tests have also been carried out to determine better values for some of the control parameters of the assimilation and thus optimize the impact. We are currently modularizing the code to facilitate further tests, and beginning a longer term verification of the system performance. Different strategies for interpretation of SAR data into wave spectra are being set up for comparison using the system.

The next section describes the assimilation system, and the following section shows test results. Section 4 describes the sensitivity test results. Finally, future plans are examined in light of research and development trends in related areas.

2. THE SAR DATA ASSIMILATION SYSTEM

The overall goal of a sequential assimilation system is to inject new data into the model's present state forecast, altering the model state to produce a best-fit to the data consistent with known or estimated error characteristics of both model and observations. After many forecast assimilation cycles, it is hoped the accumulation of information will ultimately provide an accurate estimate of the sea state (Thacker, 1988). At each data insertion time, it is necessary to determine what changes to make to the model state at all the model grid points to produce the best fit.

Ideally, the increments to the model state are determined at all the grid points at once, using all the available data at assimilation time. Both the optimum interpolation method (used operationally in many meteorological centers) and multidimensional forms of variational assimilation operate this way. These methods must be supported by estimates of the error correlation of both observations and the model trial field (the "background" field). In the case of ocean wave spectra, little is known about the error structure of forecasts from the wave model.

For SAR data, the problem is complicated by the fact that the "observations" taken by the instrument are of back scattered radar signal, not wave amplitude and direction. A highly non-linear and not fully understood transfer function must be applied to the back scatter data to estimate the wave spectrum.

Since we had available to us at the start of the project a pointwise SAR inversion algorithm which uses the model state and processed SAR data to obtain a best fit spectrum at the observation point, we decided to divide the assimilation problem into two steps for the first prototype system: The first step is a variational inversion of the SAR image (O D Var) to determine the analysis increments at the data points, followed by spreading of the increments to adjacent grid points within a predefined influence region.

Although the inversion procedure processes the entire spectrum, we chose to assimilate parameters of the spectrum, to help ensure physically reasonable results, and to minimize the adverse effects of noise on the assimilation. Parameters assimilated are the significant wave height Hs, the peak period Tp and the propagation direction of separable wave systems.

Figure 1 shows the components of the assimilation system. The entire system forms a component of the wave model, accepting trial spectra from the model, and returning modified spectra to the model. The first step, the inversion, is shown in the upper right; all the rest of the components comprise the spreading of corrections to adjacent grid points. The principal features of the system are described briefly in the following two sections; a more complete description is given in Dunlap et. al., 1994.

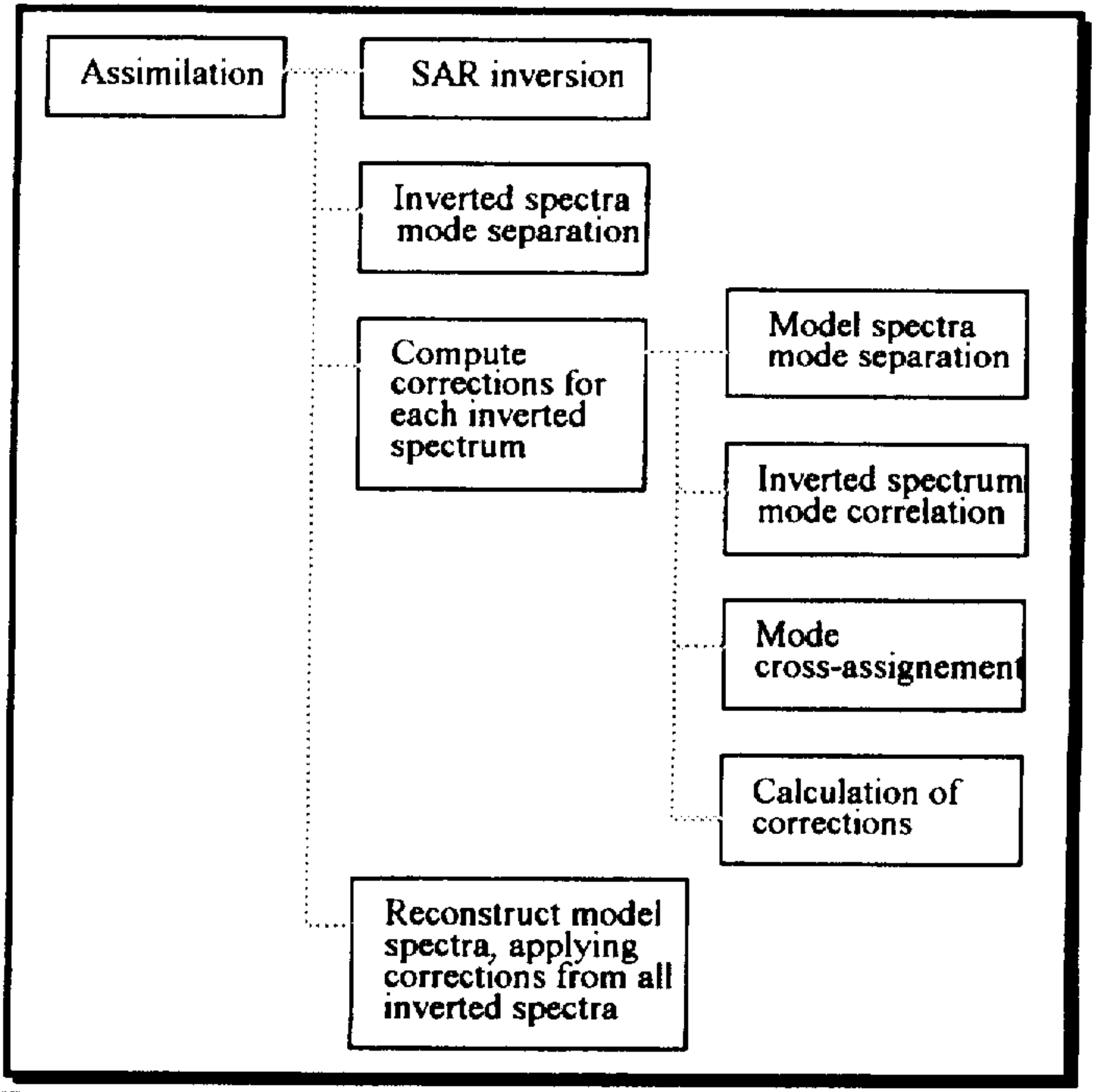

Figure 1. Main components of SAR data assimilating system

2.1 The SAR inversion

The process begins with selection of all the ERS-1 SAR spectra that are within the model domain, and which are within a three-hour window centered at the assimilation time. For each SAR observation, the nearest model grid point is identified, to provide the first guess spectrum for the inversion. The SAR spectra are then preprocessed in two ways: First, the spectrum is converted from the original polar coordinates to Cartesian coordinates in wave number space, oriented with axes along and across the satellite track. Second, the SAR spectra are scaled according to a computed background noise level for each spectrum. The modeled first guess spectrum is also converted to Cartesian space with axes oriented along and across the satellite track. Both spectra are then ready for the inversion step.

The inversion algorithm is currently that of Hasselmann and Hasselmann (1991), although other methods are being investigated.

The goal of the inversion is to find a "best-fit" spectrum S^{wav} by minimizing the cost function,

$$\mathbf{J} = \int \left(\lambda \cdot \mathbf{S}_{sim}^{SAR}(\vec{\mathbf{k}}) - \mathbf{S}_{obs}^{SAR}(\vec{\mathbf{k}})\right)^2 \mathbf{S}_{obs}^{SAR}(\vec{\mathbf{k}}) \cdot d\vec{\mathbf{k}}$$
$$+ \int \mu(\vec{\mathbf{k}}) \cdot \left(\mathbf{S}^{wav}(\vec{\mathbf{k}}) - \mathbf{S}_{mod}^{wav}(\vec{\mathbf{k}})\right)^2 \cdot d\vec{\mathbf{k}}$$

where λ is an optimal normalization factor given by,

$$\lambda = \frac{\int \left(\mathbf{S}_{obs}^{SAR}(\vec{\mathbf{k}})\right)^2 \cdot \mathbf{S}_{sim}^{SAR}(\vec{\mathbf{k}}) d\vec{\mathbf{k}}}{\int \mathbf{S}_{obs}^{SAR}(\vec{\mathbf{k}}) \cdot \left(\mathbf{S}_{sim}^{SAR}(\vec{\mathbf{k}})\right)^2 d\vec{\mathbf{k}}}$$

S_{obs}^{SAR} is the observed SAR spectrum, S_{sim}^{SAR} is the model counterpart (forward mapped) of the SAR spectrum, S_{mod}^{wav} Swavmod is the model first guess spectrum, and μ is a weighting function that expresses the relative confidence in the observed vs. the model spectrum. The first guess is needed because the SAR data contains some ambiguity, that is, more than one wave spectrum can give rise to the same SAR spectrum. The two main sources of ambiguity are the 180° ambiguity in the direction and uncertainties associated with Doppler shifting of the moving scattering elements in the return (called velocity bunching). Reliance on the model first guess also means, however, that wave trains that are missing in the model simulation cannot be entered even if they are well-represented in the SAR data. Serious mismatches between the model trial field and the SAR observation cause the inversion to fail, and the data is not given any further consideration in the assimilation. Figure 2 is an example of the inversion.

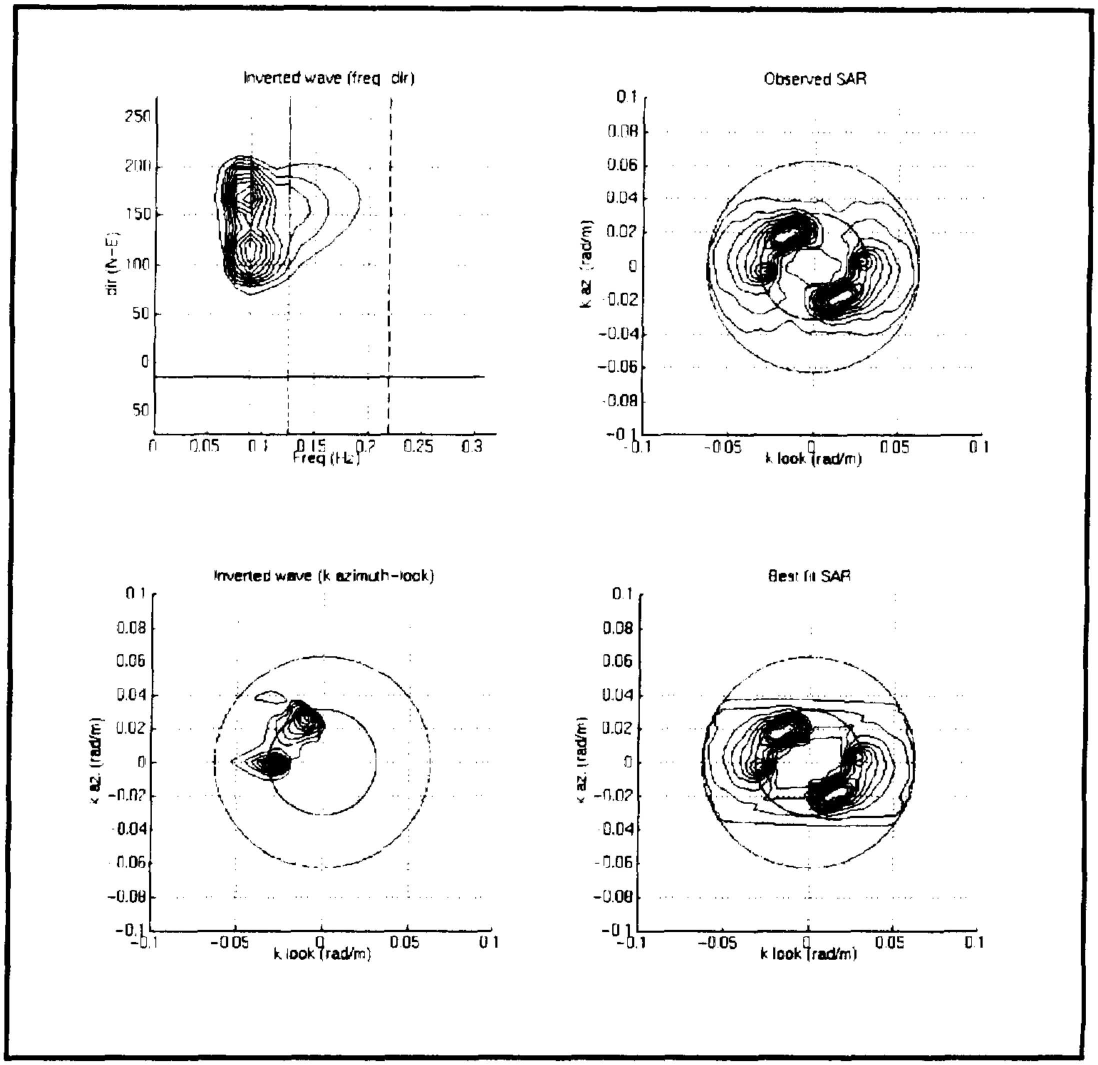

Figure 2. Inverted wave data, 15 March 1993, 13:11 GMT. Vertical lines in upper left panel indicate frequencies corresponding to 100m, 200m and SAR cut-off wave lengths. Horizontal line indicates the satellite flight direction.

2.2. The assimilation step.

The output of the inversion step is a best-fit full two- dimensional spectrum which is in general different from the model spectrum at the observation point. The second step in the process - the assimilation step - involves the adjustment of model spectra according to the differences at the observation points. First, both the inverted and the model spectra are split into non-overlapping partitions associated with local peaks. The following are the delimiting characteristics of the partition separation:

1. Each partition contains a local maximum of energy.
2. All wind-sea partitions are combined into one wind-sea mode, where "wind-sea" applies to all partitions where the ratio of the phase speed of the peak frequency to the wind velocity component in the direction of the wave is less than 1.5.
3. Partitions are merged if the separation of their peaks is less than half of the smallest within-partition variance.
4. The minimum significant wave height for a partition is 0.2m.
5. Two peaks are combined if the valley between them is not less than 0.85 of the lower of the two.
6. Peaks which are not wind-sea, but which lie in the two highest frequency bins are combined with the nearest partitions at lower frequency.

Although the partitioning means rejecting some of the detail in the original SAR observation, it should also eliminate any noise present in the inverted spectrum. The model spectrum is subjected to the same partitioning, and the parameters total energy, mean frequency and mean direction are retained for both model and inverted spectra.

Next, the inverted spectral modes are merged it necessary and cross-assigned to corresponding model modes. Merging is necessary when there is more than one SAR mode that is "close" in wave number-direction space to a single modeled mode. Merging was frequently needed in our experiments. Modes are then cross-assigned, that is associated one-to-one with modeled modes. Two criteria must be met: The modes must be sufficiently close (less than (0.0017 rad m-2) in wave number-direction space and the relative energy difference must be less than 50%. Modes of all model spectra within the influence region (about 11 model grid points) are scanned for cross-assignment.

The corrections are spread laterally in the vicinity of the observation point by a simple interpolation method which consists of calculating a net correction to each of the three spectral parameters for each cross-assigned mode within the range of influence. The method follows that of Francis and Stratton (1990). The corrected values P_j at grid point j are:

$$P_j^{new} = P_j^{model} + \sum_{i=1}^{N_{obs}} w_{ij} \cdot \frac{\left(P_i^{obs} - P_i^{model}\right)}{1 + \sum_{k=1}^{N_{obs}} w_{kj}}$$

where i denotes the spectrum at the observation point, and w_{ij} are weights that decrease with distance between the observation point i and the grid point j. The weights are the first order term in the series expansion of the exponential spreading function. See Francis and Stratton (1990) for details.

To complete the assimilation, the modified modes must be recombined into a complete spectrum and put back into the model.

3. TEST OF THE IMPACT OF THE SAR ASSIMILATION

First tests of the assimilation system were carried out with the old operational model, CSOWM, a first generation spectral model. Two test runs were done:

a) A hindcast run, continuous through the period March 11 to 20, 1993, using all available SAR data, and analyzed wind fields valid at each 12 hours. Intermediate three hourly steps used 3, 6, and 9h forecast winds from the operational atmospheric model (RFE). This run was used to assess the impact of the assimilation on the analysis.

b) A forecast run, consisting of a series of 36 h forecast runs initialized from the analysis each 12h. During the forecast simulation, no assimilation was done. By comparing forecasts initialized from analyses with assimilation to those initialized without assimilation, the impact on the forecast can be estimated.

The case used for the impact study is referred to as the Storm of the Century because of the associated blizzard conditions and record snowfalls that accompanied it throughout the Eastern US. However, it also produced extreme wave conditions south of Nova Scotia. One buoy registered a maximum significant wave height of 16.3 m at the height of the storm.

The SAR data used in the test are ERS-1 fast delivery wave mode data, from the low bit rate (LBR) data stream. The wave mode data was used in its "imagette" form; each imagette covers a 5 km by 5 km area. All data within the domain of the model (most of the North Atlantic north of 25 degrees N) were made available to the assimilation.

We can first assess the performance of the system in terms of its ability to use the data. Figures 3 , 4 , and 5 show this type of performance information. Figure 3 is a histogram of the number of SAR imagettes available to the system at each 3 hour assimilation time. Due to the sunsynchronous orbit of ERS-11, there is a tendency for most reports to be available near 1200 and 0000 UTC, with fewer reports available at intermediate times. Figures 4 and 5 show numbers and percentages of data that were used at each step in the assimilation. Of the 1145 reports available, nearly 20% were rejected because the noise level was too high and/or wave heights too low to give a reliable signal. Of the remaining 80% that were fed to the inversion, one third failed to invert, either because the inversion was unstable or because it did not converge. Of the 615 spectra that successfully inverted, about one third of those were not assimilated because the assimilation algorithm failed to correlate the inverted spectral modes with the modeled modes. As a result, only 45.6% of the spectra that were used in the inversion were assimilated, about 45 per day on average, or only about 6 per 3h assimilation window. For a domain covering most of the north Atlantic, this amounts to a rather small amount of data. However, it is spectral wave data and even this amount is much greater than what was available before the launch of ERS-1.

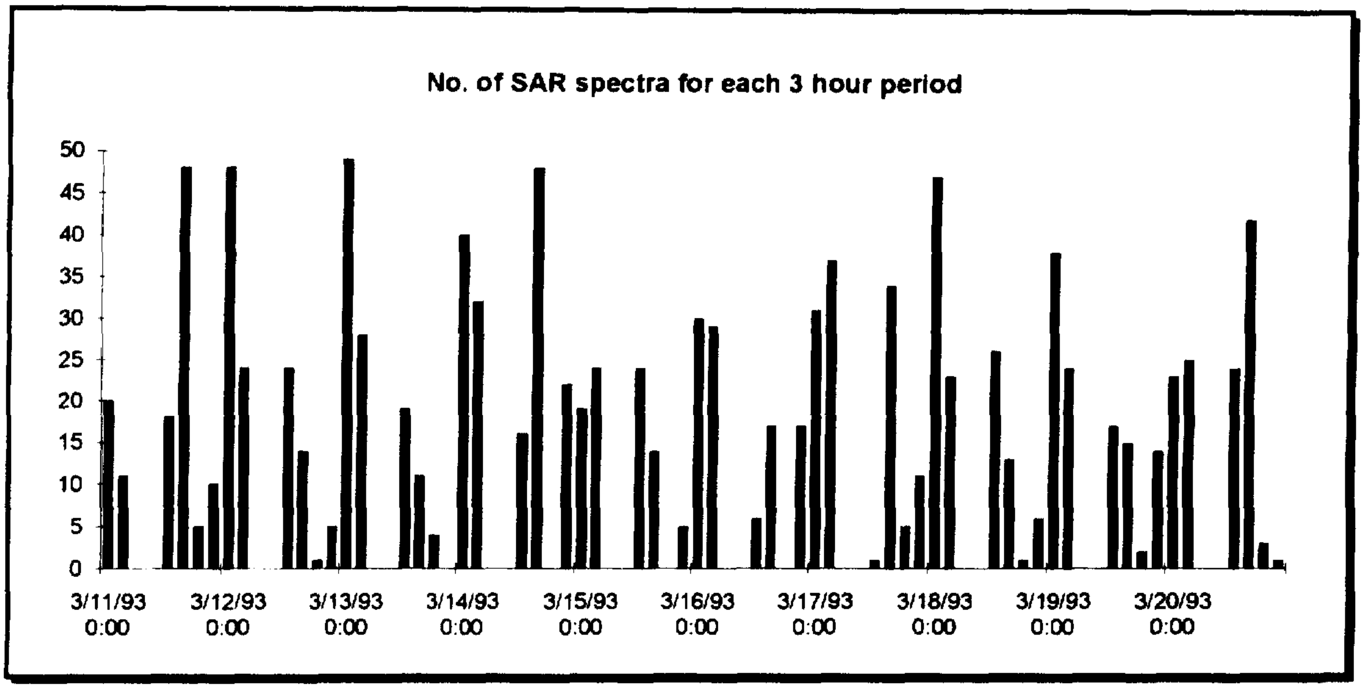

Figure 3. Distribution of SAR observations for each 3 hour period

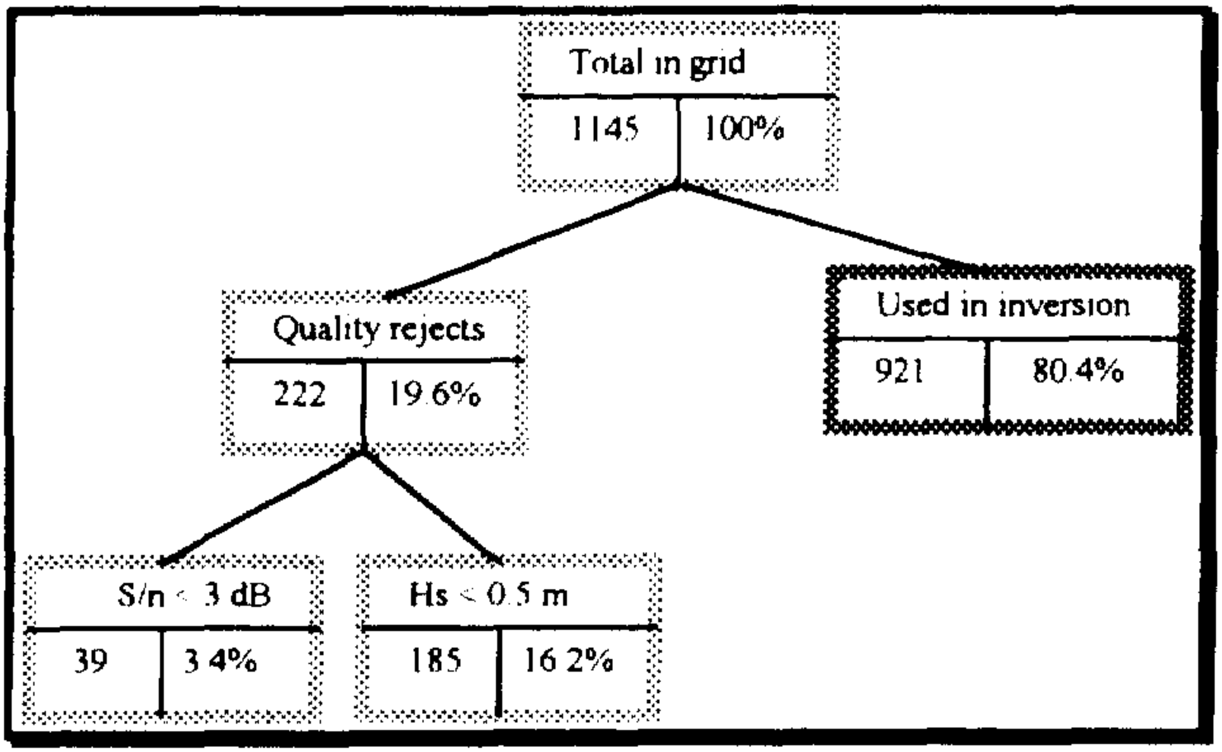

Figure 4. Number of inverted and rejected SAR data.

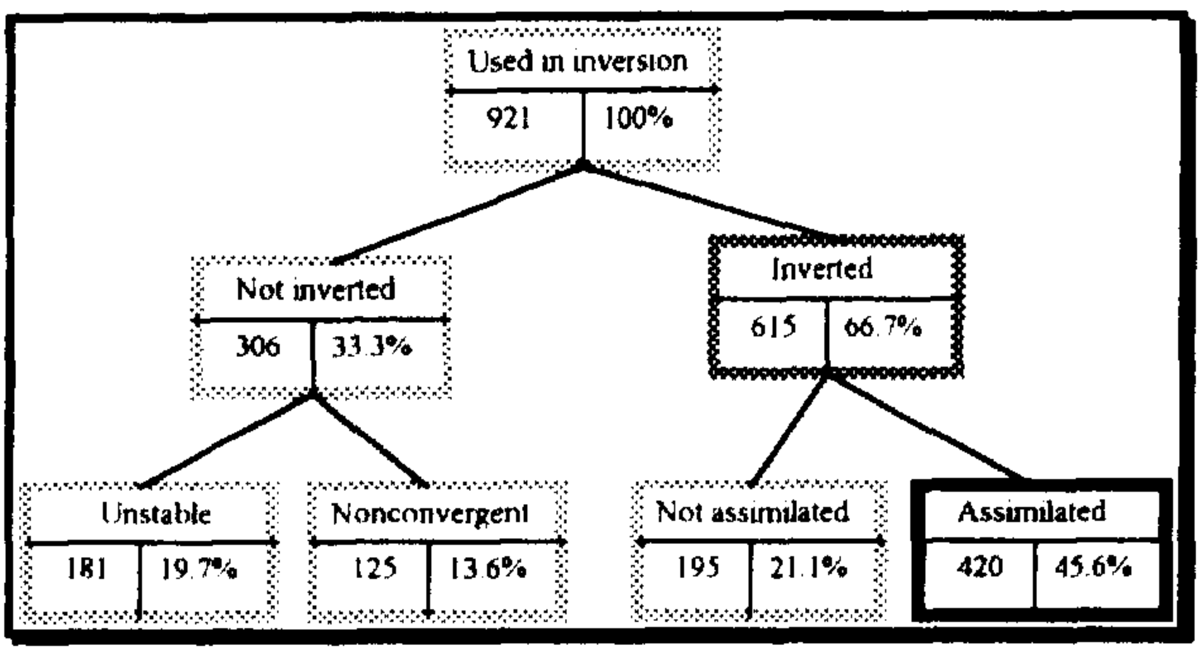

Figure 5. Number of inverted and assimilated SAR data

A second step in the evaluation was to compare the hindcast run with and without assimilation. This gives an overall measure of the impact of the data on the analyzed wave field. Over the whole period and over the whole model domain, the average rms change in Hs was only 0.071 m which seems disappointing until it is realized that the data points are widely spaced in time and space. The average rms change in Hs at all points within the influence region of the data was 0.96 m, which is more significant.

A third evaluation was to compare forecast runs with and without assimilation, to determine the rate of loss of impact and to trace the spatial evolution of the impact. Figure 6 shows the overall change in impact during the 36h forecast run. Degradation is steady from time 0, but there is still some impact on the forecasts after 36 h. The e-folding time for relaxation of the correction is about 40h. Figure 7 traces the spatial evolution of the impact for one case, the forecast initialized at March 15, 00 UTC. Assimilation was carried out up until time 0, then stopped for the forecasts run. The comparison was done with respect to the hindcast run with no assimilation. It can be seen from the figure that the corrections tend to propagate eastward with the predominant swell direction, and they also spread out, so that nearly half the grid is affected by the end of the forecast period.

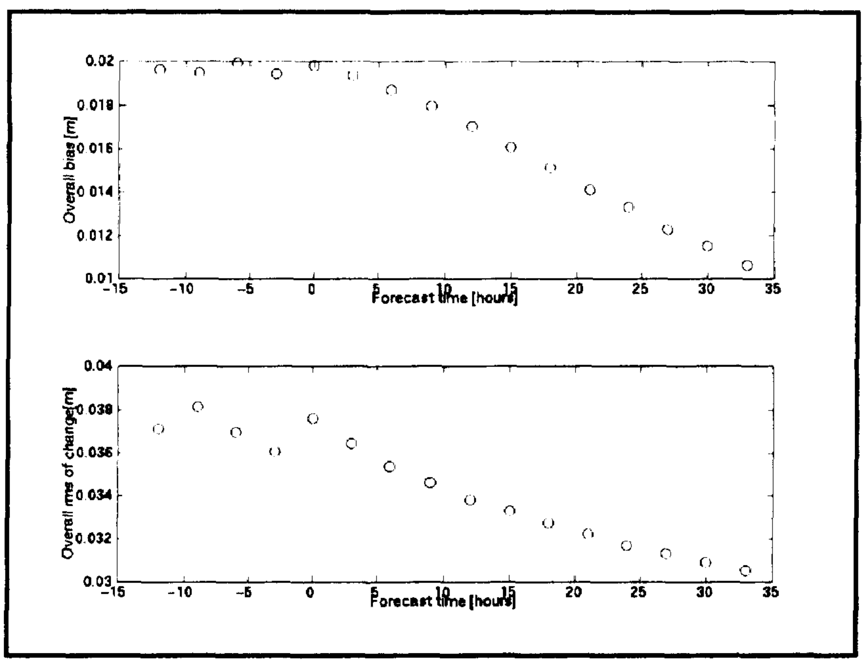

Figure 6. Decay of impact of assimilation on forecast results, measured by overall bias and rms difference between assimilation and baseline run.

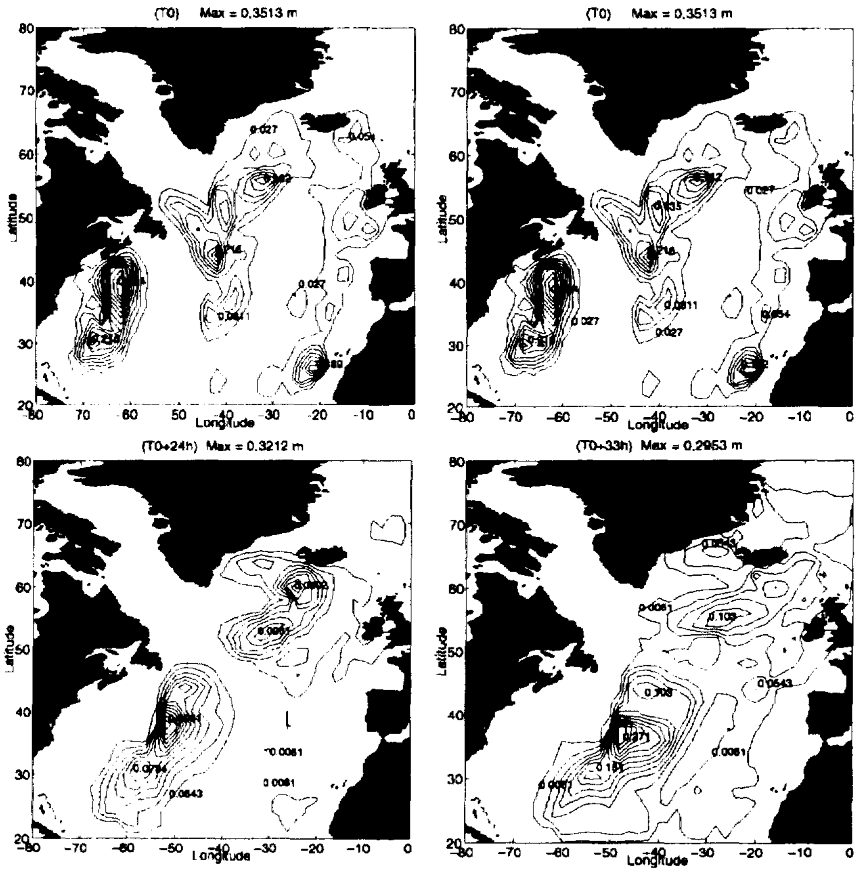

Figure 7. Fields of difference in significant wave height between assimilation and baseline run.

This first assessment identified the magnitude of changes in wave height, peak period and wave direction produced by the assimilation. Results shown so far have concentrated on Hs. For peak period, the assimilation appears to have relatively greater impact: The e-folding time for Tp changes due to the assimilation is greater than 40 hours. The impact reduces only by about 1/3 during the 36 hour forecast.

We were not able to determine whether the direction of the changes is correct compared to independent data (That is, observational data that was not used in the assimilation). The reason is that there were very few in situ observations within the influence range of the satellite observations. Both data sources are sparse enough that one has to be lucky to have the satellite pass over a buoy at or near observation time. The exception to this are calibration/validation field experiments where it is arranged that in situ observations will be taken at the time of satellite overpasses. Such experiments provide extremely valuable data for assessment of assimilation systems.

4. SENSITIVITY TESTS

The test results described above show that the impact of the SAR data is not large. Although the paucity of available data is undoubtedly a major cause of its low impact, there are many control parameters on the assimilation and inversion which could perhaps be adjusted to increase the system's ability to extract useful information from the SAR data that is available and increase its impact. For example some of the parameters express the confidence in the data vs. the model trial field. With little information available to estimate these confidence factors (weights), we have so far simply guessed at appropriate values to make the system work.

To determine if the impact of the observation data could be increased, we conducted some sensitivity tests on some of the adjustable parameters. Since the operational wave model is being changed to WAM, we decided to carry out the sensitivity tests using WAM rather than CSOWM. We don't believe the model used is important to the sensitivity test results; they should be similar for all models with similar overall accuracy.

4.1 Parameters used in the sensitivity tests

The specific tests that were carried out are as follows:

1. Use of the quasi-linear approximation in the forward mapping portion of the inversion module, instead of the full non-linear mapping used to date.
2. Use of old versus new inversion parameters suggested by the Max Planck Institute. The most important of these is a significant reduction in the weight of the model trial spectrum compared to the observation. In the new version, the model spectrum is used essentially only to determine which of the two SAR peaks is the real one.
3. A change in the limiting ratio of phase speed to wind speed to separate sea from swell. The ratio was lowered in the test, so that, at a given wind speed the minimum phase speed for a swell wave is lowered.
4. A change to the maximum allowed distance in wave number space between observed and modeled wave modes to declare a match. This parameter was made more restrictive; modes have to be closer together to be considered a match.
5. A change to the parameter expressing the relative confidence of the corrected spectrum and the model spectrum at the observation point. In the original system, model and corrected spectrum were weighted equally, which meant that the final correction was a simple average of the two at the observation point. This is "double jeopardy" for the observation, since there is a similar weighting scheme in the inversion step. In effect, it meant that only one quarter of the real difference would be passed through to the final analysis, and it is not surprising

therefore that the impact of the data was so low. The tested value for the relative weight is 1000, which essentially replaces the model spectrum with the observed spectrum at the observation point.

6. A relaxing of the energy ratio criterion for matching of modes. In the original system, the energies of the observed and modeled modes had to be within a ratio of 0.5 to 2. This implicitly limited possible corrections to Hs to 41%. The tested value is 10, that is, observed energy must lie between 0.1 and 10 times the modeled value.

Table 1. Sensitivity analysis results: Changes with respect to the non-assimilating run, averaged over the period March 11 to 16, 1993, for all grid points of WAM. H_s values in m, T_p in s, and direction in degrees.

	base	Exp 1	Exp2	Exp3	Exp4	Exp5	Exp6
rms ΔH_s	0.10	0.03	0.11	0.10	0.08	0.18	0.25
rms ΔT_p	O.22	0.08	0.25	0.22	0.19	0.39	0.46
rms Δdir	5.41	2.43	6.62	5.38	4.55	7.73	10.3
bias ΔH_s	0.03	0.01	0.03	0.03	0.03	0.07	0.10
bias ΔT_p	0.08	0.02	0.08	0.08	0.06	0.16	0.20
bias Δdir	0.16	0.06	10.32	0.25	0.22	-.29	-.72
# inverted	470	320	559	473	1472	1465	453
# changed	3576	1744	4922	3500	2952	3745	5086

Table 2. Sensitivity test results. Percentage changes with respect to the base run, averaged over the period March 11 to 16, 1993 for the North Atlantic WAM grid. (%)

	base	Exp1	Exp2	Exp3	Exp4	Exp5	Exp6
rms ΔH_s	0	-63	16	3	-15	85	149
rms ΔT_p	0	-62	14	1	-15	80	112
rms Δdir	0	-55	22	-1	-16	43	90
bias ΔH_S	0	-80	-8	-4	-24	120	212
bias ΔT_P	0	-82	12	0	-18	112	153
bias Δdir	0	-65	102	58	37	-284	-557
# inverted	0	-32	19	1	0	-1	-4
# changed	0	-51	38	-2	-17	5	42

For the purposes of the test, a ”base run” was made which used the newest inversion system supplied by the Max Planck Institute. Runs were then made with each of the changes listed above, referred to as ”exp 1” to ”exp 6”. Average rmsd and average difference (bias) were computed for all 7 runs over the test period March 10 to 16, 1993 (Storm of the Century) for the three spectral parameters Hs, Tp and direction, with respect to the run without assimilation. Then, percentage changes were tabulated with respect to the results for the base run.

4.2 Results of the tests

The results of the tests are summarized in Tables 1 and 2 . Examination of the tables suggests the following:

1. The number of successful inversions is lower in the base run (new inversion parameters) than in the old system (exp 2). The new inversion is stricter; it can be assumed that the inversions which are successful are of higher quality.
2. The quasi-linear approximation is not worth using. Not only does it reduce the number of successful inversions by 30% or so,

the savings in computational time are not great (not shown), amounting to only about 16%.

3. Exp 3 and exp 4 show little impact; the assimilation results are not sensitive to the seaswell threshold, nor are they particularly sensitive to the distance criterion for matching, although the number of assimilated spectra was clearly reduced by the stricter matching criterion.

4. Exp 5 shows a significant impact, as expected. The rms change in Hs is nearly doubled as is the rms change in Tp. Impact on the direction is more modest. This is expected: exp 5 gives full weight to the observation at the observation point.

5. Exp 6 also shows a significant impact, even greater overall than exp 5. The impact is attributable to the fact that relaxing the energy ratio criterion has increased the number of assimilated modes by 42%.

We are not in a position to state whether the changes represent improvement in the analysis, because we do not have independent collocated data to evaluate the accuracy of the changes. This experiment, and all the tests done so far, have assessed the impact only.

Figure 8 shows the impact of the new inversion compared to the old (exp 2) for a specific case. In the case shown, the model does not resolve the two peaks in the spectrum that are indicated by the SAR. The old inversion fits both peaks, but the new one does so more sharply and clearly.

The "best fit" SAR is closer to the observed SAR image.

Figures 9 , 10 and 11 show the areal distribution of the rms change for the base run, exp 5 and exp 6 respectively. In all three cases, changes are greatest in the south and east portions of the grid, and the changes in exp 5 and exp 6 are generally greater in magnitude, consistent with tables 1 and 2 . When the observational data is allowed to dominate, as in the base run and especially exp 5, one can expect the largest corrections to be in area where the model simulation is least accurate. Since we are assimilating mainly swell data (the longer wavelengths) which also propagates over longer distances, we expect the model to be least accurate near the grid boundaries. Thus, one possible explanation for the higher impact in the southeast portion of the grid is the addition of observed swell which has been missed by the model. The quality of the wind data near the southeast grid boundary is also lower, which also will reduce the accuracy of the model simulation in these areas.

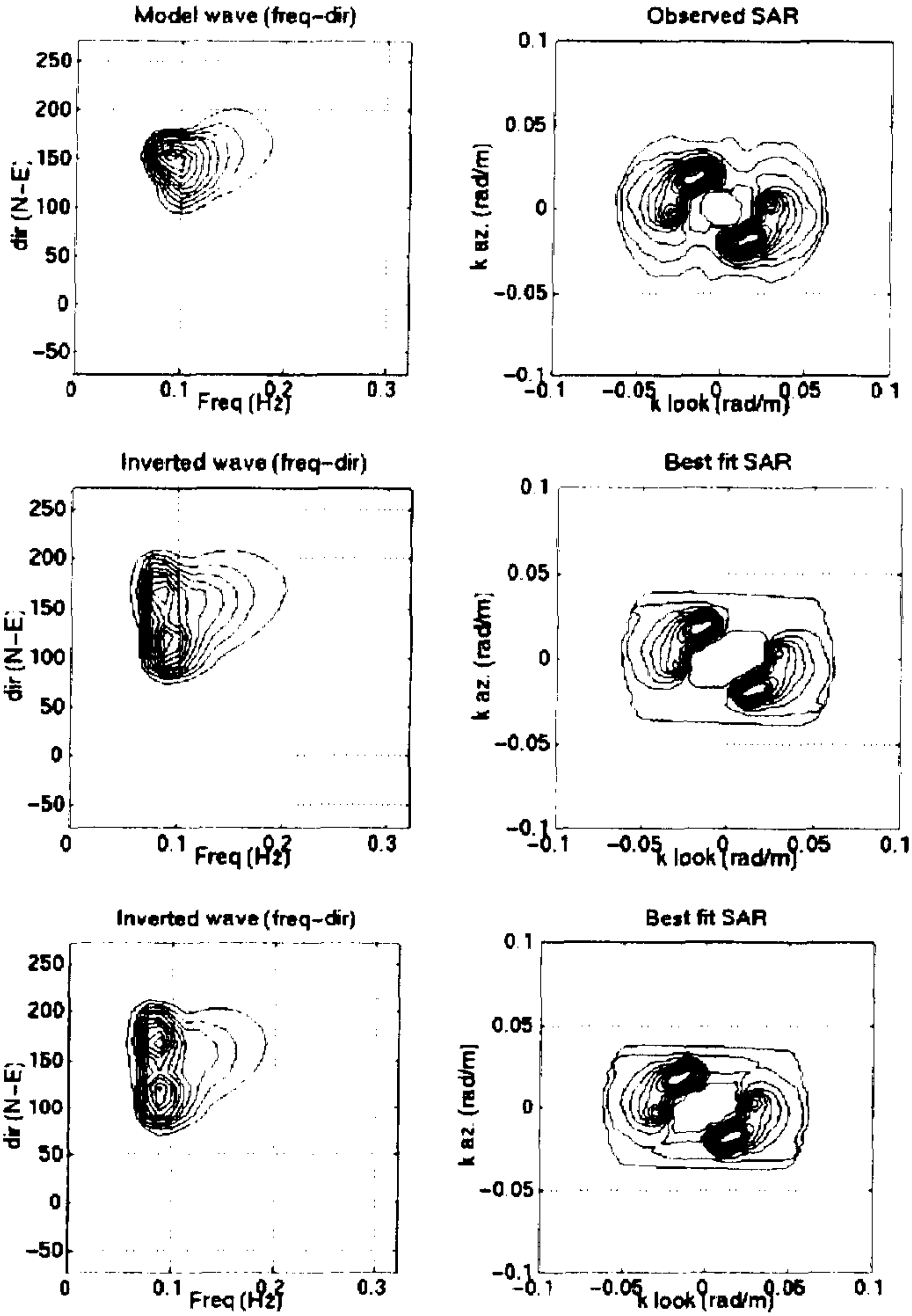

Figure 8. SAR data inversion results: Input data (top), inversion results for old SAR parameter values (middle) and for the base run values (bottom). 15 March 1993, 13:30 UTC, grid point 700.

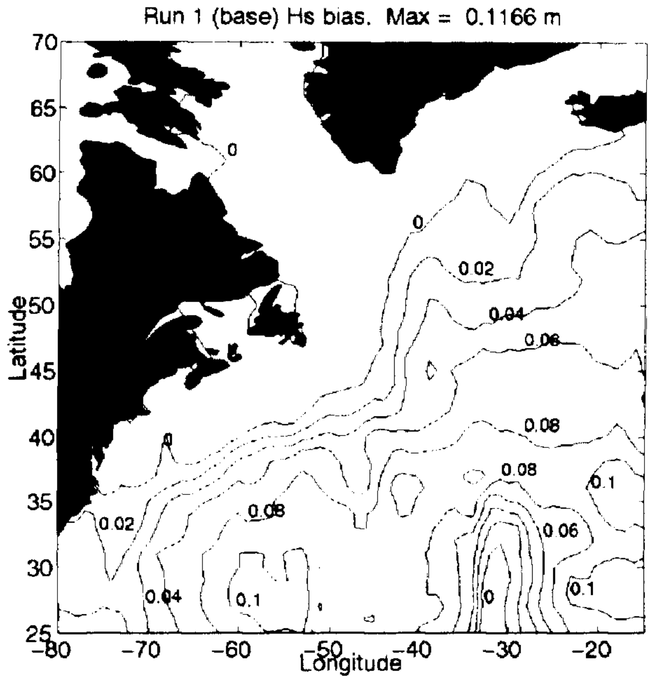

Figure 9. Bias and rms difference for assimilation impact, base run.

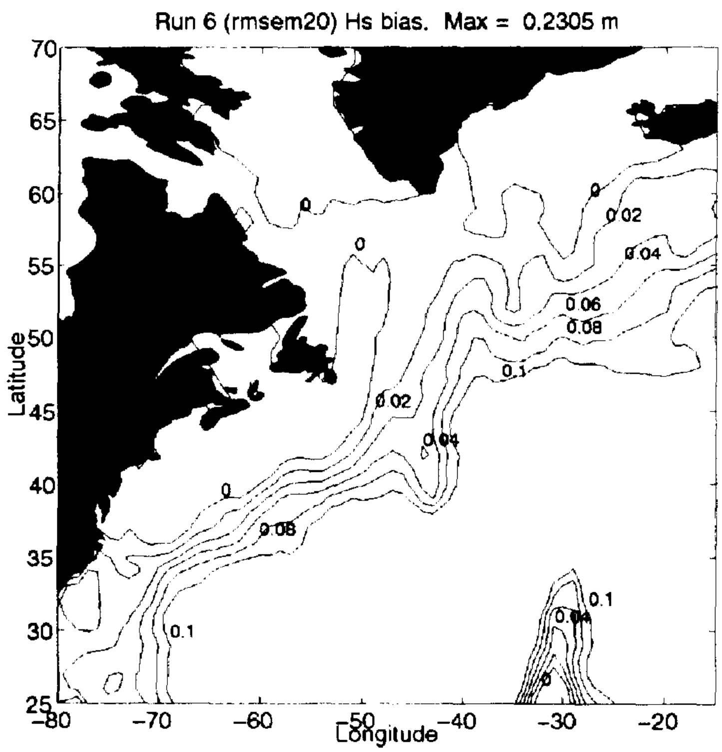

Figure 10 Bias and rms difference for assimilation impact, exp 5

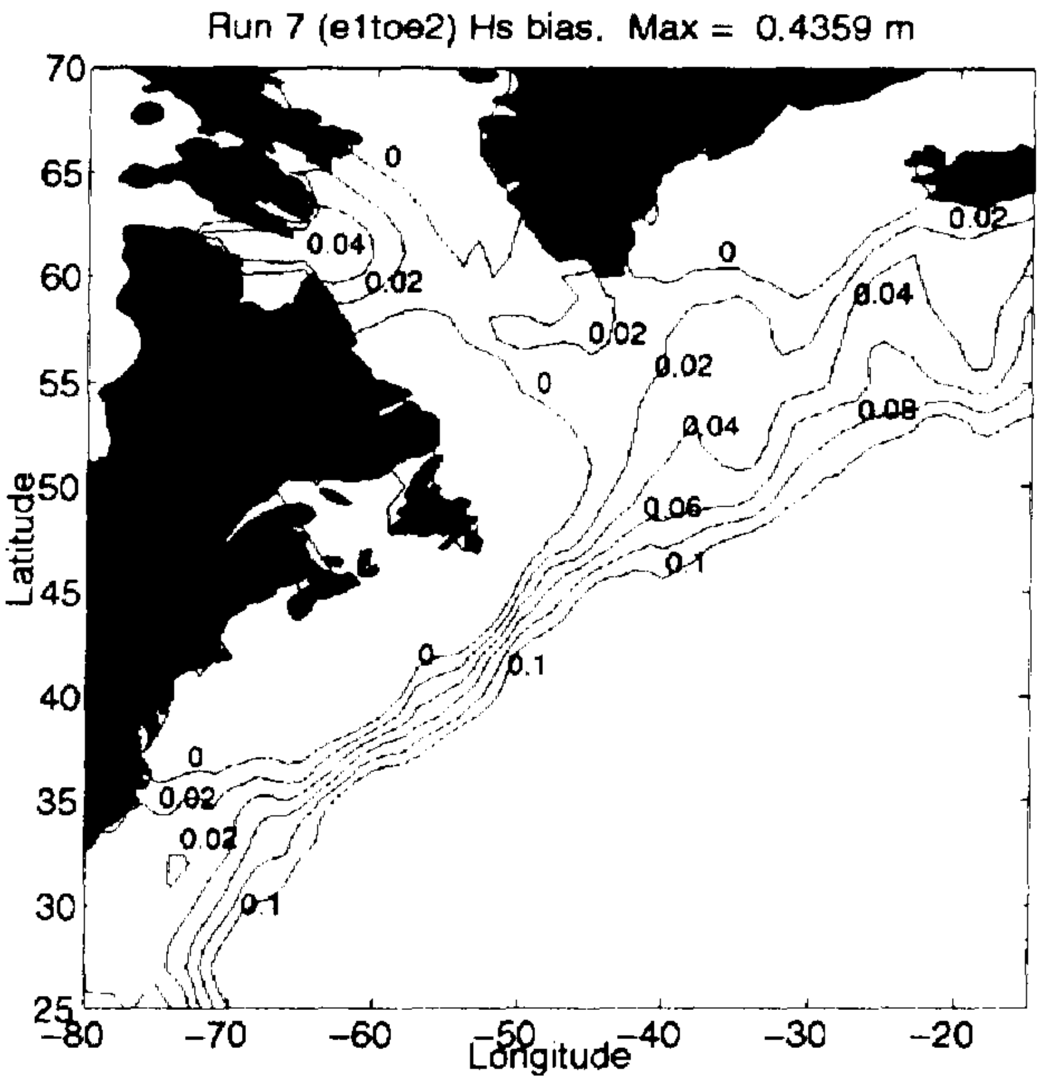

Figure 11 Bias and rms difference for assimilation impact, exp 6

5. DISCUSSION

We have developed a prototype data assimilation system for SAR wave data, and have done some testing to assess the impact of the SAR data on wave analysis and forecasting. The system has also been subjected to sensitivity tests, to search for more optimal values of some of the parameters of the assimilation. The impact of the data is small when considered over a domain the size of the North Atlantic, but large enough to be considered significant in the vicinity of the observations.

So far, we have made no attempt to consider the wind field in the assimilation. Generally, ignoring the winds that drive the wave forecasts will lessen the potential impact of the wave observations because the wind field will tend to "wipe out" changes to the wave spectra that are not consistent with the winds, so that the impact of the data may be lost within a few hours. However, in our system, we believe that this problem is not significant because the SAR data that is assimilated is (mostly) limited to the swell portion of the spectrum, which is decoupled from the winds, and which has a relatively long lifetime. For this reason, we believe that, for a first step, we can ignore the winds. So far, our results are consistent with this idea; the impact of the data extends beyond the 36h forecast run of the model.

The longer term goal of this work is to develop and operate a fully coupled wind-wave assimilation system, as input to a fully coupled atmospheric-wave model. Work is proceeding towards this goal along separate fronts. (See, for example, the papers by Wilson et. al. and Perrie et. al in this volume). A parallel project on surface marine wind assimilation is also beginning.

Ideally, the final assimilation system will be able to ingest all available surface marine wind and wave data, from ships, buoys, satellites, extract the signal about the winds and sea state in an optimal way, consistent with the wave model, Such a system will likely need to use variational assimilation techniques because they are most flexible for use with mixed sources of data that are irregular and incomplete representations of the physical field under consideration, and because it is easiest to ensure consistency with the model's representation of the physics of the evolution of the sea state. Since each data source must be associated with its own "data model", or transfer function that relates the observation to the physical field being observed, there is a great amount of development work to do to achieve the ultimate system.

The next steps for development of the SAR data assimilation are first to carry out a verification for a long enough period that sufficient collocated independent data will be available to determine whether the impact is positive or not. Second, we are moving toward a variational formulation to replace the two-step system.

Finally, the imminent launch of RADARSAT will increase considerably the amount of SAR data available. Tests with RADARSAT data are planned as soon as it becomes available. We hope to be ready in a year or so for a full operational test demonstration of the system using real time satellite data.

6. REFERENCES

Dunlap, E., R. Olsen, and S. de Margerie, 1994: Assimilation of SAR data in the Canadian Spectral Ocean Wave Model, Phase 2 Report, ASA Consulting Ltd., Halifax, NS.

Francis, P.E., and R.A. Stratton, 1990: Some experiments to investigate the assimilation of SEASAT altimeter wave height data into a global wave model. Quart. J. Roy. Meteor. Soc., 116, 1225-1251.

Hasselmann, K. and S. Hasselmann, 1 991: On the nonlinear mapping of an ocean wave system into a synthetic aperture radar image spectrum and its inversion. J. Geophys. Res., 96, 10713-10729.

Thacker, W.C., 1988: Three lectures on fitting numerical models to observations. Internal document GKSS 87/E/65, GKSS Forschungszentrum Geeshacht GmbH, 64pp.

WAMDIG, 1988: The WAM model - a third generation ocean wave predation model. J. Phys. Oceanogr. 18, 1775-1810.

AN EXPERIMENT TO ESTIMATE THE POTENTIAL IMPACT OF ASSIMILATION OF WAVE DATA FROM MORE THAN ONE SATELLITE

R.B. Olsen

Satlantic, Inc.
Halifax, Nova Scotia

L. J. Wilson

Atmospheric Environment Service
Downsview Ontario

E. Dunlap and S. de Margerie

ASA Consulting
Halifax, Nova Scotia

1. INTRODUCTION

One important reason for the relatively low overall impact of satellite wave data on ocean wave analyses and forecasts is that the coverage in space and time is quite sparse. For example, the 10 day period from March 11 to 20, 1993 yielded an average of about 100 observations per day from ERS-1 over a domain consisting of most of the North Atlantic Ocean, or about one per day per 200,000 km2. With a three-hourly data ingest cycle, there will be on average only 12 observations to consider at each three-hourly assimilation. Since the wave model WAM (WAMDIG, 1988) that is used operationally comprises over 3000 grid points, it is clear that few of them will be affected by each assimilation, unless the influence region of the data is unrealistically large.

Studies using our SAR assimilation system (Dunlap et al., 1994) indicate that the most important impact of the assimilation is correcting under predicted wave heights in storm situations. Satellite observations are sparse enough that one has to be quite lucky to have the satellite pass overhead when the data is most needed.

Data coverage rates may improve in future with the launch of additional satellites such as RADARSAT and ERS-2. Both these satellites have SAR instruments aboard and can provide wave spectra, along with ERS-1. Thus it is conceivable that the amount of wave data available could treble in the near future. For the purposes of wave data assimilation into wave models the ideal strategy would be to synchronizer the satellite orbits to provide uniform coverage in space and time. In practice, this ideal will not be achieved and data will tend to be available with somewhat uneven distribution.

To try to estimate the potential impact of data from more than one satellite compared to data from only one satellite, we conducted an experiment using synthetic "ideal" data. This experiment was designed to shed some light on the question of the value of additional data. For instance, given that we already have access to ERS-11 wave mode data and could use it operationally in an assimilation system, could additional data from RADARSAT have a significant additional impact on the wave analysis?

The method and assumptions are discussed in the next section, and results are presented in the following section. Finally, the results are discussed in light of the assumptions.

2. METHOD AND ASSUMPTIONS

2.1 Generation of "observations"

Two wind datasets were available for this experiment. One of these is the standard CMC surface windfield, consisting of analyses each 12 hours, and forecast winds from the RFE model for 3, 6, and 9 hours. Together, this produces a time series of wind fields at three hour intervals. The analyses use ship and buoy data, but no satellite wind data. The lowest analysis level is 1000 mb; surface analyses of winds are produced by extrapolation from the 1000 mb level.

The other wind dataset was obtained by careful kinematic hand analysis, which fits all the available buoy and ship data. These kinematic winds are for each three hours, and are adjusted to the required height (10m) by a boundary layer model for input to the wave model. For the purposes of this experiment, the kinematic winds are considered to be perfect while the CMC winds are assumed to be imperfect.

The next step was to run the wave model using the kinematic winds as input, to generate a set of wave spectra at all the grid points. The period selected for the experiment was November 8 to 24, 1991, the period of the Grand Banks Calibration/Validation experiment. The WAM was spun up for the period 8 to 11 November and the rest of the period was used for the experiment. Given the 3 hourly kinematic winds as input, the model produced a time series of wave spectra at all the gridpoints. These spectra were then used as "observations" in the experiment.

2.2 Selection of satellite orbits

For wave modelling purposes, it is best if the observation points are evenly spaced in space and time, and ideally should have a density roughly equivalent to the resolution of the wave model. However, it the observation system cannot see the shorter length waves, which are also the most perishable and the least consistent in space, it is less important to sample at the resolution of the model. The longer swell portion of the spectrum can be resolved with fewer observations. For this synthetic data experiment, we have all the power to specify exactly which orbits to use for our ”satellites”.

We decided to simulate data for up to 4 satellites operating concurrently. For simplicity, the four satellites were all put in the same (polar) orbit, selected to be representative of the ERS-1 orbit, but offset in time by 3 hours. This means that the data swaths from the different satellites will be separated in space by approximately 45 degrees longitude at the equator and lesser amounts further north, as the earth turns under the orbit, so that one can expect two satellites at least to cross some part of the grid during each 3 hour window. Half the passes will be ascending orbits and half descending. A typical orbital period of somewhat less than 1.5 h means that about 4 swaths may lie over some part of the grid domain during each 3 h window.

If we select a typical sampling interval of 200 km along the track, the maximum number of data points that lie over the grid for a single pass will be about 50 for the chosen orbit, given the domain of the model. Since the orbital period is not an exact fraction of a day, the locations of the swaths will vary from day to day.

Figure 1 shows the average daily number of data points within the grid domain for each 3 h assimilation period, averaged over the 13 days of the experiment. Figure 2 shows an example of the data coverage over a 12 hour period of the experiment, for 4 satellites.

The synthetic observational dataset was defined simply by selecting the spectrum for the nearest model gridpoint to each point along the satellite track. These spectra, defined by the model run using kinematic winds, formed the dataset used in the assimilation.

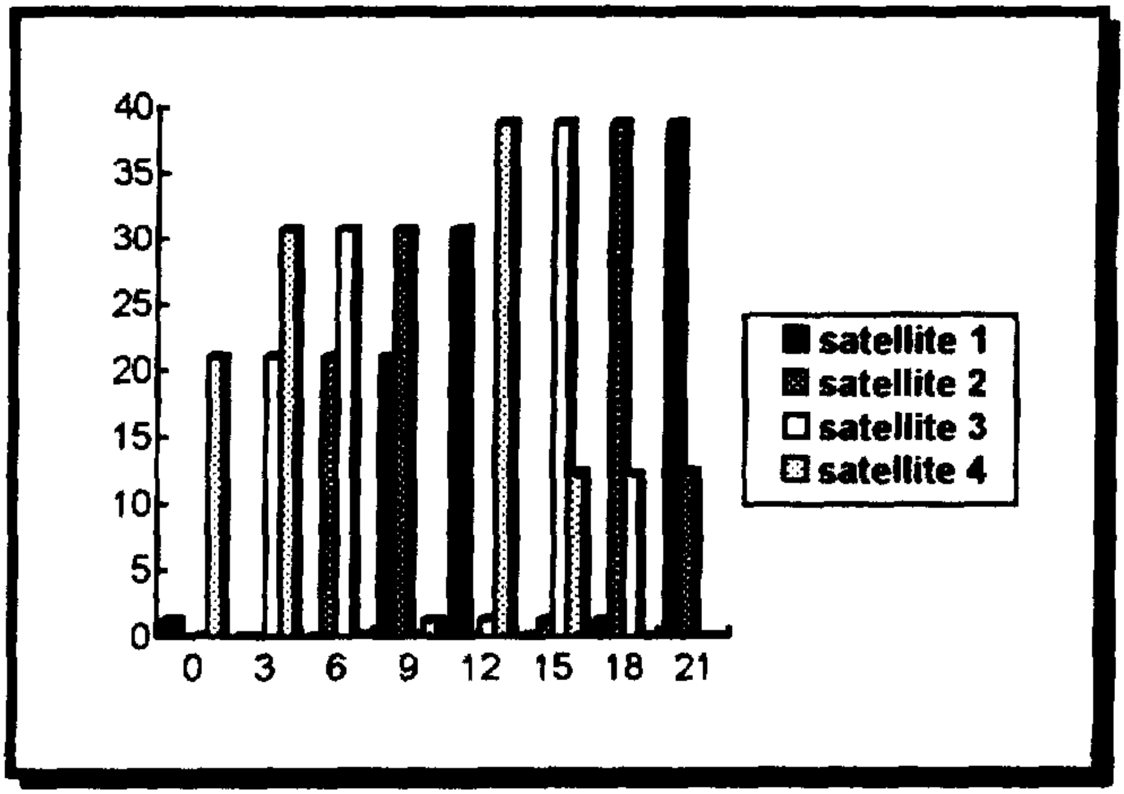

Figure 1. Average daily number of data points for each 3 h period.

2.3 Assimilation experiment

Our assimilating spectral wave model, AWAM was run in hindcast mode through the 13 days of the experiment period, using CMC winds as described above. Synthetic data were made available from the run with the kinematic winds, according to the orbital scenario described in the previous section.

Four assimilating runs were carried out, to simulate the presence of one, two , three and four satellites. For comparison, a control run was made using CMC winds, but without assimilation.

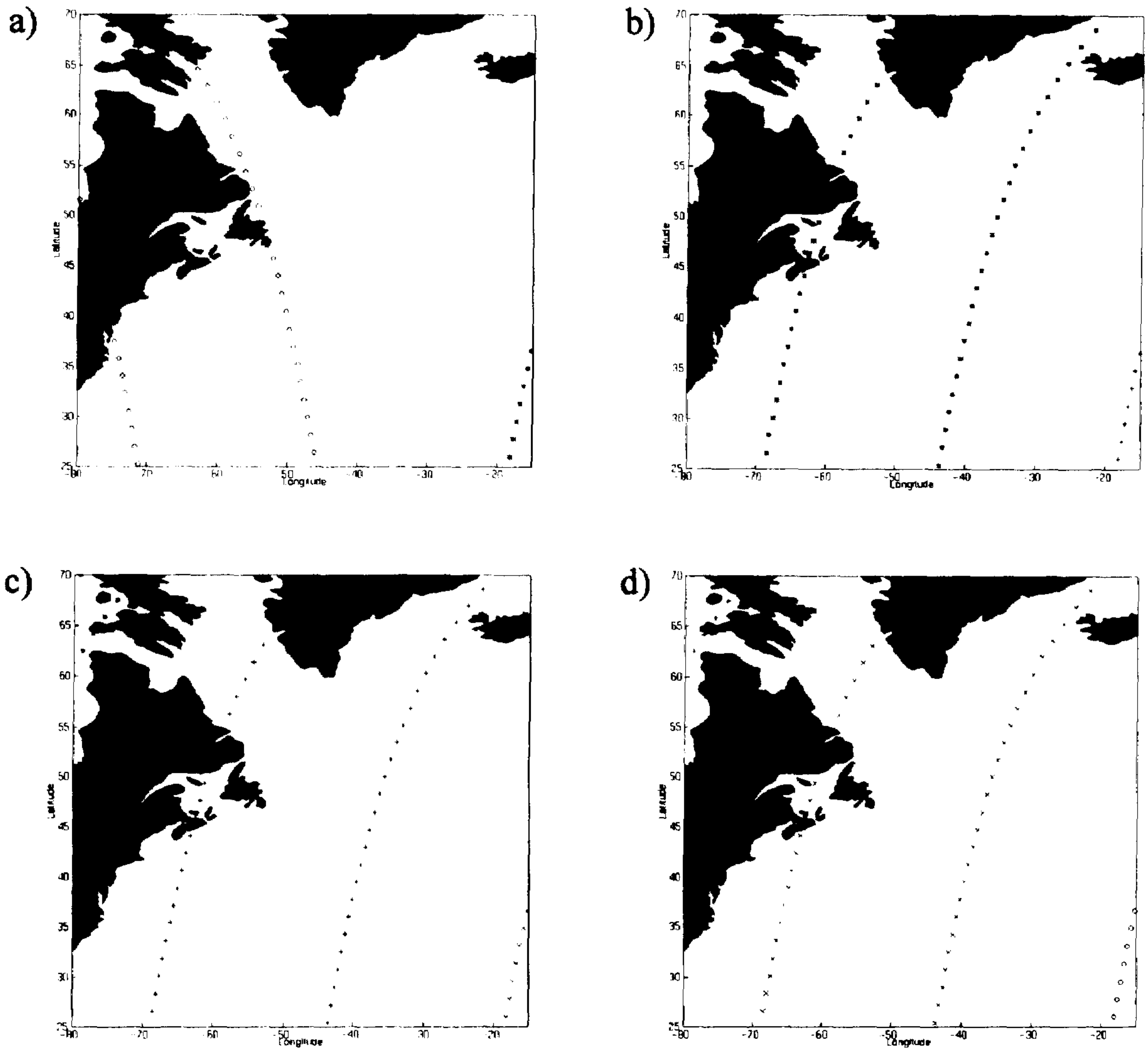

Figure 2. Example of satellite data coverage for assimilation cycles at 3 hour intervals: a) 00:00, b) 03:00, c) 06:00, d) 09:00. Satellites 1,2,3 and 4 are marked 0,x,+ and *.

Tables 1 to 4 show the numbers of spectra available to the assimilation at each 3 hour assimilation time for each of the 4 satellites individually. For the experiment, data was added cumulatively in order for satellites 1 to 4, to evaluate the additional impact of each.

Table 1. Number of synthetic observational spectra available in the WAM domain for satellite 1 during the ERS-1 cal/val experiment.

	0	3	6	9	12	15	18	21
11/11	28	0	0	7	45	0	0	48
12/11	9	0	0	22	22	1	0	36
13/11	12	0	0	22	28	0	0	25
14/11	22	0	0	17	40	0	2	35
15/11	18	0	0	9	45	0	0	50
16/11	10	0	0	24	19	0	0	41
17/11	11	0	0	23	27	0	3	22
18/11	10	0	0	18	40	0	2	41
19/11	7	0	0	28	27	0	0	49
20/11	10	0	0	25	20	0	0	42
21/11	11	0	0	23	25	0	7	26
22/11	15	0	0	18	41	0	2	40
23/11	5	0	0	36	19	0	0	49
24/11	9	0	0	-	-	-	-	-

Table 2: Number of synthetic observational spectra available in the WAM domain for satellite 2 during ERS-1 cal/val experiment.

	0	3	6	9	12	15	18	21
11/11	0	0	7	45	0	0	48	9
12/11	0	0	22	22	1	0	36	12
13/11	0	0	22	28	0	0	25	22
14/11	0	0	17	40	0	2	35	18
15/11	0	0	9	45	0	0	50	10
16/11	0	0	24	19	0	0	41	11
17/11	0	0	23	27	0	3	22	19
18/11	0	0	18	40	0	2	41	11
19/11	0	0	28	27	0	0	49	10
20/11	0	0	25	20	0	0	42	11
21/11	0	0	23	25	0	7	26	15
22/11	0	0	18	41	0	2	40	5
23/11	0	0	36	19	0	0	49	9
24/11	0	0	26	-	-	-	-	-

Table 3. Number of synthetic observational spectra available in the WAM domain for satellite 3 during ERS-1 cal/val experiment.

	0	3	6	9	12	15	18	21
11/11	0	7	45	0	0	48	9	0
12/11	0	22	22	1	0	36	12	0
13/11	0	22	28	0	0	25	22	0
14/11	0	17	40	0	2	35	18	0
15/11	0	9	45	0	0	50	10	0
16/11	0	24	19	0	0	41	11	0
17/11	0	23	27	0	3	22	19	0
18/11	0	18	40	0	2	41	7	0
19/11	0	28	27	0	0	49	10	0
20/11	0	25	20	0	0	42	11	0
21/11	0	23	25	0	7	26	15	0
22/11	0	18	41	0	2	40	5	0
23/11	0	36	19	0	0	49	9	0
24/11	0	26	19	-	-	-	-	-

Table 4. Number of synthetic observational spectra available in the WAM domain for satellite 4 during ERS-1 cal/val experiment.

	0	3	6	9	12	15	18	21
11/11	7	45	0	0	48	9	0	0
12/11	22	22	1	0	36	12	0	0
13/11	22	28	0	0	25	22	0	0
14/11	17	40	0	2	35	18	0	0
15/11	9	45	0	0	50	10	0	0
16/11	24	19	0	0	41	11	0	0
17/11	23	27	0	3	22	19	0	0
18/11	18	40	0	2	41	7	0	0
19/11	28	27	0	0	49	10	0	0
20/11	25	20	0	0	42	11	0	0
21/11	23	25	0	7	26	15	0	0
22/11	18	41	0	2	40	5	0	0
23/11	36	19	0	0	49	9	0	0
24/11	26	19	0	-	-	-	-	-

3. RESULTS

Results are shown in terms of the "base run", which is the model run using kinematic winds, Since the experiment consists of assimilation of a portion of the data from this run into the run which uses CMC winds, the assimilation run should look more and more like the base run as more of the data from it is made available to the assimilation. Therefore the difference between the two runs, however expressed, should decrease as more data is added. Theoretically, if 100% of the data would be assimilated, all the information from the base run should be recovered and there should be no difference between assimilation and base runs. We did not test this assumption because the assimilation system was not designed to handle such large quantities of data.

Figure 3 shows bias (mean difference) and root mean square difference (rmsd) in significant wave height (Hs) between the base run and the CMC run. The indicates the differences that are produced solely by using the two different wind datasets to drive the wave model, without any assimilation. It can be seen that differences are small over the southern portion of the domain, but larger in the north, near Greenland and Iceland. These differences, averaged over the 13 days of the run, are undoubtedly dependent on the particular characteristics of the flow regime that existed during the experiment period.

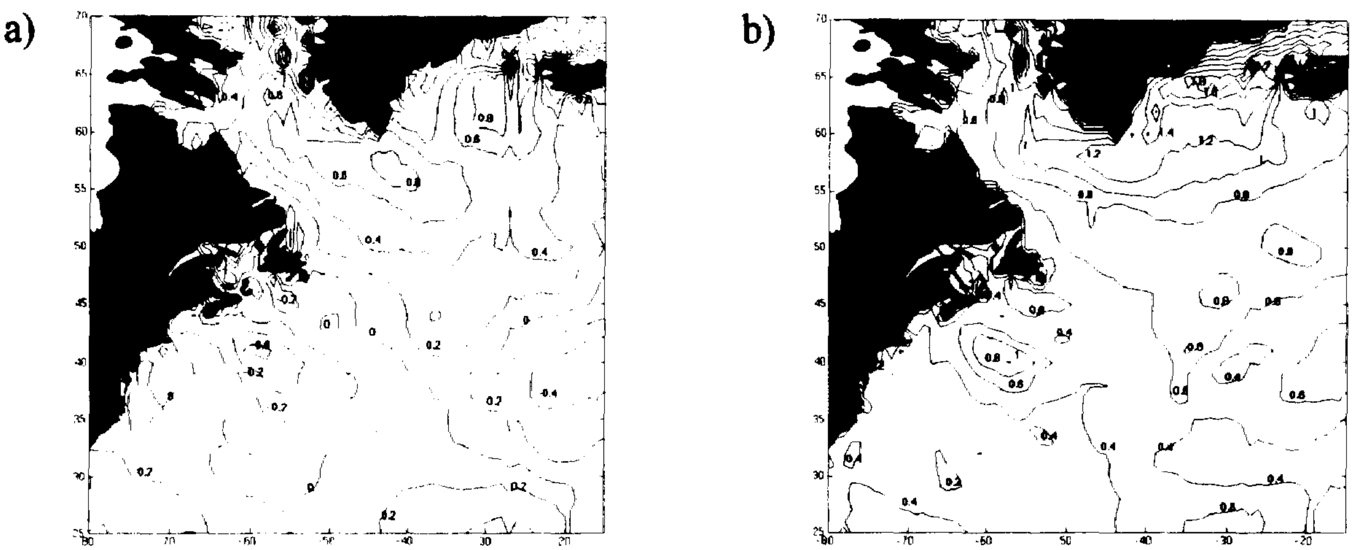

Figure 3. Bias (a) and rms difference (b) between base run and CMC run.

A different data period would produce a different distribution of differences.

Figure 4 shows bias and rmsd for Hs with data assimilation from one satellite. Comparison with Figure 3 reveals that the magnitude of the differences has indeed been reduced by the assimilation, as expected. Figure 5 shows the corresponding statistics for the assimilation run with 4 satellites. Once again, the magnitudes of the differences have been reduced, but more modestly than for one satellite.

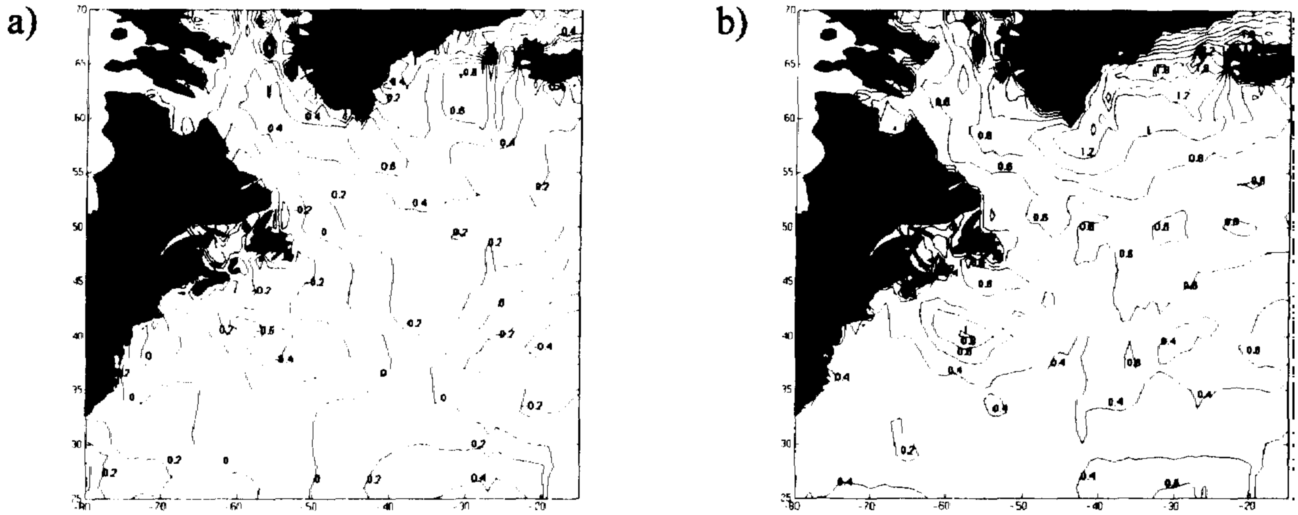

Figure 4. Bias (a) and rms difference (b) with data assimilation from one satellite

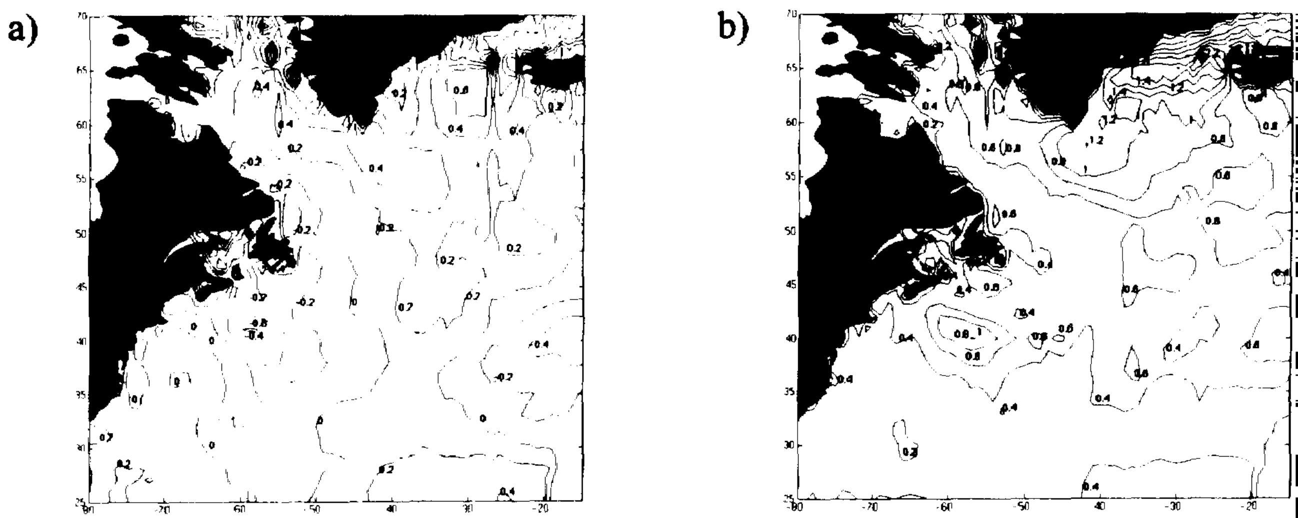

Figure 5. Bias (a) and rms difference (b) with data assimiation from 4 satellites

Figure 6 and Table 5 summarize the results over the whole 13 day period and over the whole grid. In terms of bias, the first satellite provides the greatest change, reducing the bias by 35% of the total difference. In terms of rmsd, however, the changes are more modest, with a reduction of 6.75% for one satellite increasing to 13.4% for four. When it is considered that the total number of data points is a smaller fraction of the total number of gridpoints, ranging from about 2.2% for one to 9% for four, these results look more encouraging.

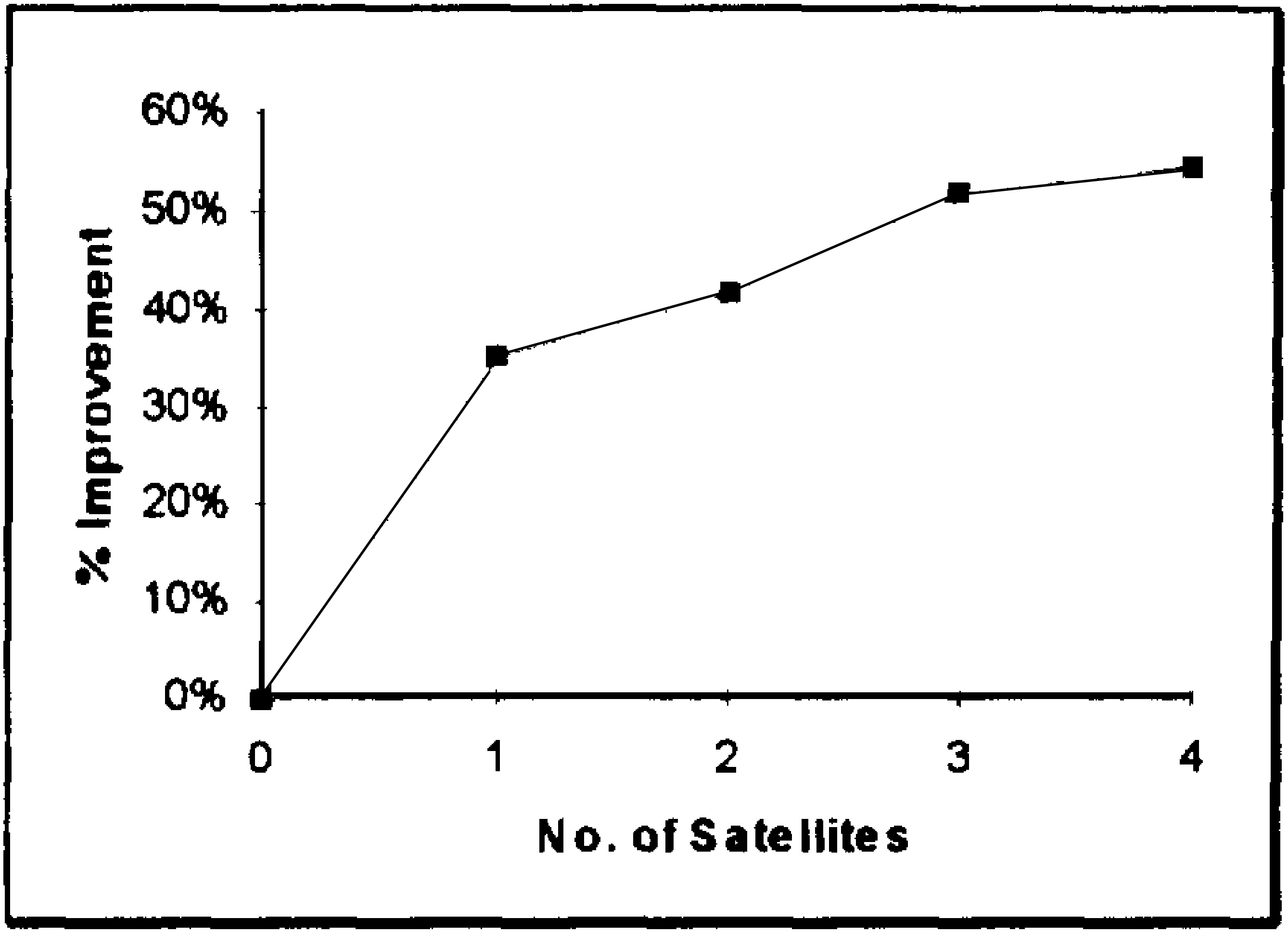

Figure 6. Illustration of improvement in Hs prediction, as measured by reduction in overall bias.

For the peak period, Tp, changes are greater, both in terms of bias and rmsd. For example, with one satellite, 14.8% of the difference could be reinstated, rising to 22.7% for four satellites. The percentages for bias in Tp are also consistent with those for Hs, a little greater in magnitude throughout. The discrepancy in percentage of bias compared to rmsd is probably related to an overall correction of systematic under-or-over-prediction of waves due to biases in the driving windfield. Although correction of the wave field is an indirect way of correcting for biases in the surface windfield, if is nevertheless an important use of wave observations in an operational sense.

Although the impact is greatest for the first satellite, the additional contribution tends to be a little greater with the addition of the third satellite than the second or the fourth. We believe that is a consequence of the orbital distribution. With only two satellites offset in time by three hours, there is still a significant data gap at 0300 h and 1500 h. The third satellite fills this in for the first time, providing a more even distribution of data over all the assimilation times.

Table 5. Summary statistics for synthetic data assimilation experiment, for significant wave height and peak period.

11-24 Nov. WAM		Base Run CMC	Assimilation runs: Satellite Numbers			
			1	1,2	1-3	1-4
Hs (m)	bias	.156	.101	.091	.075	.071
	%	0	35.3	41.7	51.9	54.5
	rms	.726	.677	.660	.643	.629
	%	0	6.7	9.1	11.4	13.4
Tp (s)	bias	.300	.181	.161	.127	.122
	%	0	39.7	46.3	57.7	59.3
	rms	1.033	.880	.851	.819	.798
	%	0	14.8	17.6	20.7	22.7
Sample size			248,026			

4. DISCUSSION

This experiment is intended to give an idea of the potential additional contribution of SAR wave data from additional satellites to an assimilating wave model. It is important first to compare the synthetic data to "real" data that might be obtained from SAR. The SAR instrument does not measure the wave spectrum directly; it must be inferred from the radar backscatter using a highly non-linear transfer function. Furthermore, it is not possible to retrieve the full spectrum from the radar signal; only the longer wave portion, the swell part of the spectrum and the longest wave portion of the wind sea spectrum can be obtained. Also, the signal contains noise which must be separated from the wave information via the transfer function. Processing of SAR data is carried out image by image at present; there is no spatially distributed information used in the SAR data processing to ensure physical consistency between the wave field observations at nearby points. The effect of the noise in the data is to reduce the effective information content of the data about the wave field, and to reduce the average spatial and temporal consistency of the analysis. A fuller discussion of the SAR transfer function and inversion process is contained in (Hasselmann and Hasselmann, 1991).

The wave model on the other hand, simulates the entire wave spectrum, and, through its ability to simulate the processes of wave growth, propagation and decay, implicitly ensures horizontal physical consistency of the wave field, and temporal consistency of its evolution, subject above all to the accuracy and consistency of the wind field that is used to drive the model.

The synthetic data produced by the model using the best available wind data is therefore as close to "perfect" an observation dataset as is possible, noise-free, spatially and temporally consistent, and consisting of complete spectra. Assimilation of such a dataset into a run of the same model represents an ideal that will not be achievable in practice with real data. For these reasons, the results shown here represent the best that would be achievable.

However, is there reason to believe that the results are not representative in a relative sense? Perhaps an additional contribution of one-fifth to one-third the impact of the first satellite is a reasonable estimate for a second satellite in real conditions. In fact, if the information content from the first satellite is lower in practice, there is every reason to believe that the contribution from a second satellite will be more of an independent second look than can be obtained from time-offset model output. Therefore, this estimate of the additional impact of a second satellite is more likely an underestimate than an overestimate.

It is important to note that this experiment applies only to the actual assimilation portion of the process. It would be possible to forward map the "perfect" spectra into a simulated SAR spectrum, using known relationships. Then, the SAR spectra could be inverted using the inversion portion of the assimilation system, and the CMC run of the model as the trial field. This would have been more realistic, for the short wave portion of the spectrum would be eliminated, but the simulated spectra would still be noise-free and consistent. This was not done because of lack of computer time.

Now that ERS-2 has been launched, it will be possible to repeat this study for one and two satellites using real data. This should be an interesting comparison.

5. ACKNOWLEDGEMENTS

This work was carried out under contract to the Atmospheric Environment Service. The authors wish to thank the Panel on Energy Research and Development (PERD) and the Canada Center for Remote Sensing for their financial support.

6. REFERENCES

Dunlap, E.M., R.B. Olsen, and S. de Margerie, 1994: Assimilation of SAR data in the Canadian Spectral Ocean Wave Model. Phase 2 report, ASA and Satlantic, 66p.

Hasselmann, K. and S. Hasselmann, 1991: On the Nonlinear Mapping of an Ocean Wave Spectrum Into a Synthetic Aperture Radar Image Spectrum and its Inversion. J. Geophys. Res. Vol 96, No. C6, 10,713-10,729.

WAMDIG, 1988: The WAM model - a third generation ocean wave prediction model. J. Phys. Oceanogr. 18, 1775-1810.

THE INFLUENCE OF SEA SURFACE TEMPERATURE DISTRIBUTION ON MARINE BOUNDARY LAYER WINDS

Serge DesJardins

Atmospheric Environment Service
Bedford, Nova Scotia

1. INTRODUCTION

A number of studies have been carried out on the impact of the mesoscale structure of the sea surface temperature, and especially on the influence of the Gulf Stream on east coast cyclogenesis (Mailhot and Chouinard, 1989; Nam and Kuo, 1991; Perkey and Lapenta, 1991). They showed that interaction of the sea surface temperature with the atmosphere through the marine boundary layer plays a major role in the early stage of cyclogmesis. Odier researchers have studied the mesoscale circulations generated by the sea surface distribution in the marine boundary layer especially, in vicinity of the Gulf Strewn (Nuss, 1989; Warner et al., 1990), but there has been little investigation of the influence of the mesoscale structure of sea surface temperature on larger-scale surface wind fields.

The present study was conducted to see if the Gulf Stream and the sea surface temperature distribution create mesoscale patterns in the synoptic wind field which could eventually influence the generation of ocean waves. It was carried out with the help of the MC2 model, which by its versatility allowed the author to make various high-resolution simulations of the Storm of the Century described by Huo et al., (1995) and Cardone et al., (1995). By using a detailed SST field and varying its resolution through different filtering, the influence of the sea surface temperature distribution was tested.

After the Introduction, the present paper is structured as follows: a theoretical discussion of the stability of the marine boundary layer is presented in section 2 . Section 3 describes the Storm of the Century and its wind field, while section 4 contains information on the numerical model used, followed by the methodology. Section 5 includes test results made to insure that the CMC analysis and the 50 km MC2 were valid representations of the real situation before proceeding to higher-resolution simulations. Results of the effect of the resolution and the implantation of a more detailed SST field are discussed in section 6 . Results of various higher-resolution simulations showing the influence of the Gulf Stream and the sea surface temperature distribution on surface winds are presented in section 7 . Finally, section 8 makes the link between the numerical results and the observations. A summary of the conclusions is contained in section 9 .

2. THEORY

The sea surface temperature, particularly in the region of the Gulf Stream, by virtue of its strong air-sea interaction, modifies the marine boundary layer above it. Vertical exchange of mass, momentum, moisture and heat occur continually above the ocean. However, the degree of air-sea interaction depends principally on the stability (Garratt, 1992, pp. 36-38, and Arya, 1988, pp. 74-8 1). As will be shown in the present paper, the influence of the Gulf Stream and the sea surface temperature distribution on surface wind is entirely controlled by the stability of the marine boundary layer. The stability of the marine boundary layer will be measured, in the present study, by the remainder of the vertical lapse rate of temperature derived as follows (Holton 1992, pp. 52-53):

For an ideal gas undergoing a **dry** adiabatic process, from the first law of thermodynamics, one can define the Poisson equation as:

$$\theta = T(P_s/P)^{R/C_p} \qquad (1)$$

where Θ is the potential temperature, p is the pressure, p_s is chosen at 1000 hPa, R is the dry gas constant and c_p is the specific heat at constant pressure. Taking the logarithm of (1) and using the ideal gas law, one can find a relationship between the lapse rate of temperature and the rate of change of potential temperature with respect to height. This gives as a result:

$$\boxed{\frac{T}{\theta}\frac{\partial \theta}{\partial z} = \frac{\partial T}{\partial z} + \frac{g}{c_p}} \qquad (2)$$

Defining the dry adiabatic lapse rate as

$$-\frac{dT}{dz} = \frac{g}{c_p} = \Gamma_d \qquad (3)$$

and the vertical lapse rate of temperature as $\Gamma \equiv -\partial T/\partial z$ by using the latter definition and (3), (2) can be rewritten as:

$$\boxed{R_\Gamma = \frac{T}{\theta}\frac{\partial \theta}{\partial z} = \Gamma_d - \Gamma} \qquad (4)$$

where R_Γ is defined as the **remainder of the adiabatic vertical lapse rate of temperature.** If $\Gamma<\Gamma_d$ so that Θ increases with height, the atmosphere is said to be stably stratified, since a parcel that undergoes an adiabatic upward displacement from its equilibrium level will tend to return to its equilibrium level. R_Γ defines 3 possible conditions of the marine boundary layer (summarizes in [5]):

$$\boxed{\begin{array}{l} R_\Gamma>0 \rightarrow \Gamma<\Gamma_d \rightarrow \textit{STABLE conditions} \\ R_\Gamma<0 \rightarrow \Gamma>\Gamma_d \rightarrow \textit{UNSTABLE conditions} \\ R_\Gamma=0 \rightarrow \Gamma=\Gamma_d \rightarrow \textit{NEUTRAL conditions} \end{array}} \qquad (5)$$

3. SYNOPTIC SITUATION

3.1 Description of the storm

From March 13 to 15, 1993, the east coast of North America was hit by one of the deepest extratropical low pressure systems affecting this part of the world. The Blizzard of 1993, also known as the "Storm of the Century", deepened explosively in the Gulf of Mexico and over the southeastern U.S. On March 13 at 0000 UTC, a strong cyclonic low pressure system at 996 hPa was located in the Gulf of Mexico. It tracked northeastward and continued to intensify rapidly over the following 24 hours. On March 14 at 0000 UTC, the storm reached the state of Delaware, where the pressure at the low center bottomed out at 963 hPa. It continued to track northeastward along the east coast and slowly filled to reach Anticosti Island by 0000 UTC March 15, with a pressure center value of 968 hPa.

An intense hyperbarochnic zone was one of the thermodynamic: sources of the storm. Its southern edge was delimited by a surface warm front extending eastward from the low and a surface cold front extending south-southeastward from a wave. Because of the well-developed cyclonicity of the storm, no significant surface trough was present, resulting in a rather gradual change in wind direction. However, the passage of the surface cold front was well marked by a drastic fall in temperature and a rise in pressure, A picture of the synoptic situation is given in Figure 1 . For a more complete description of the storm, the reader is referred to Cardone et W., 1995, Thomas, 1995 and Huo et al., 1995.

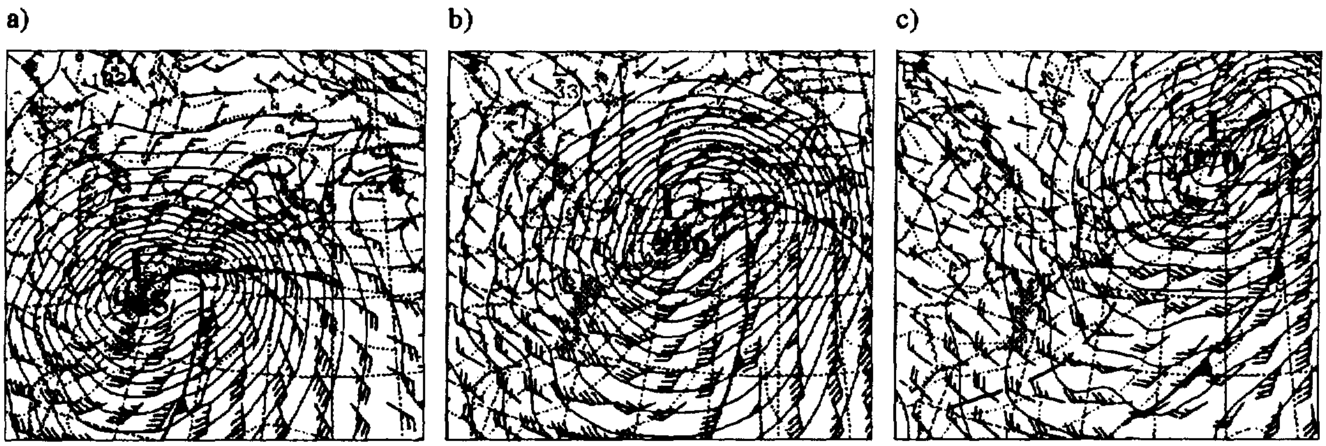

Figure 1: Synoptic surface situation from CMC analysis at 0000 UTC on March 14 1993 to March 15 1993 at 0000 UTC.. Solid lines represent pressure at sea level [4 hPa]. Dashed lines represent 1000 hPa temperature [5° C]. Windbarbs are: knots. Hours represented are a) 14/00z, b) 14/12z, c) 15/00z.

3.2 Description of the storm's wind field

The surface pressure gradient around the storm was very intense throughout its duration. At the deepest stage of the storm, at 0000 UTC on March 14, corresponding surface geostrophic winds of 75 to 125 knots surrounded it. The strongest geostrophic winds were found in the northwest sector of the low, in a narrow band north of the warm front, and in the warm sector ahead of the cold front. North of the warm front, easterlies 45 to 65 knots (50-60% of the surface pressure gradient, or SPG) were reported by numerous coastal stations. Ahead of the surface cold front, a surface jet of south-southeasterlies at 50 to 65 knots (65% of the SPG) was present. Behind the surface cold front, although the pressure gradient slightly slackened, southwesterlies at 40 to 60 knots (50 to 70% of the SPG) remained.

Continuous cold air advection behind the surface cold front destabilized the marine boundary layer and allowed downward momentum transfer, creating geostrophic to supergeostrophic wind conditions. On March 15 at 0000 UTC, southwesterly winds at 40 to 50 knots (100 to 130% of the SPG) were blowing over the southern waters of Nova Scotia. For a more complete description of the storm's wind field, the reader is referred to Thomas, 1995 and Cardone et al., 1995.

4. METHODOLOGY

4.1. MC2 model

All numerical simulations were done with the Mesoscale Compressible and Community (hereinafter MC2) model developed at Environment Canada's numerical modelling centre (RPN). The MC2 model is based on the full-elastic nonhydrostatic model of Robert, Tanguay and Laprise (1990). The model solves a full set of Euler equations on a limited area Cartesian domain of the polar projection with time-dependent nesting of the lateral boundary conditions supplied by a large-scale model or an analysis. The MC2 model uses numerical algorithms of semi-Lagrangian advection and semi-implicit time differencing. It has so far proven to be quite a versatile modelling tool that allows excellent simulations over a wide spectrum of scales. For further information about the MC2 model, the reader is referred to Desgagne, Benoit and Chartier (1994), Bergeron, Laprise and Caya (1994) and Mailhot (1994).

4.2 Numerical simulations

The MC2 model was run on an HP 9000 series 755 with 160 RAM. All simulations were done using the RPN full physics package (Mailhot, 1994). The lid of the model was set at 25km. Vertical levels were distributed automatically according to an RPN algorithm, although the first two thermodynamic levels were set at zero and 20m to fix the first momentum level at 10m. Different numbers of levels were tested. However, a set of 20 computational levels was chosen because of the presence of half of the levels below 2.5 km, with 6 in the first km. By switching vertical acceleration on and off, hydrostaticity was tested very easily. Finally, simulations at different resolutions -- 50, 25 and 10km -- were carried out. The MC2 50 km output was generated by using the Canadian Meteorological Center (CMC) 50 km analysis. Higher-resolution runs were obtained by cascade, using the previous run at lower resolution as a ”pilot file” to supply the boundary conditions. Figure 2 shows the grids employed during the cascade process, which is summarized in Figure 4 .

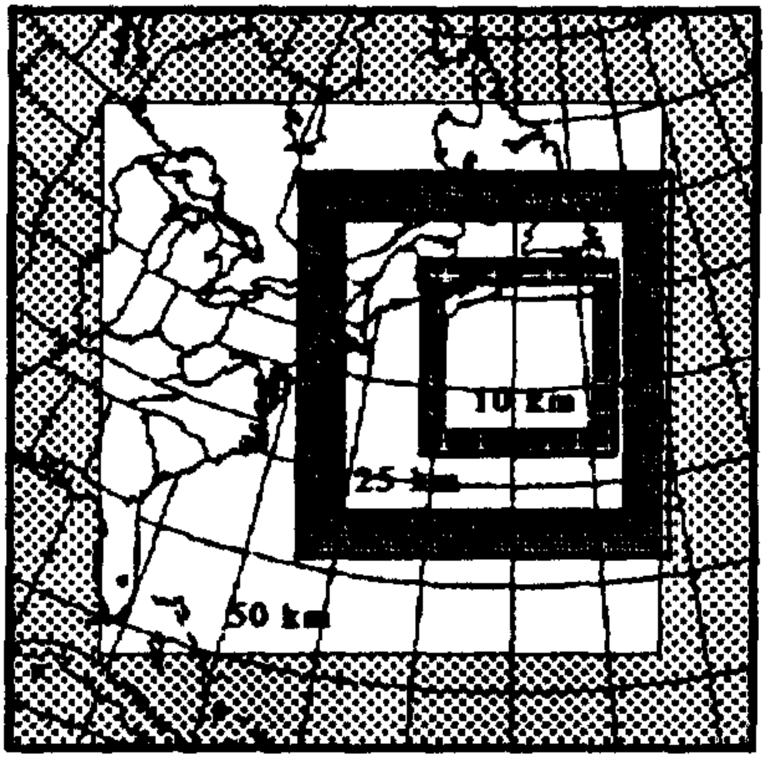

Figure 2: Grids for different resolutions used during the cascade process. Shaded areas correspond to the pilot–buffer zone of each grid.

The MC2 50km simulations used the Sea Surface Temperature (hereinafter SST) field from the CMC analysis, an SST field smoother than the real SST. Higher-resolution simulations used a digitized (by hand) 25 km SST analysis from the Canadian Forces Meteorological and Oceanographical Centre Halifax (METOC), valid from March 12/0000z to March 15 at 2100z. For 25km and 10km resolutions, a Shuman filter (Shuman, 1957) was applied to the digitized SST field to test the influence of the SST distribution. The first filtering eliminated the short wave variations in the SST field in order to preserve the main meanders and eddies (hereinafter S1). In fact, this field was very similar to the SST from the analysis. The second filtering produced a SST field without eddies and a Gulf Stream with practically no meanders and eliminated all eddies north of it (hereinafter S2). Figure 3 shows the various SST fields used. Table 1 summarizes a simulations carried out.

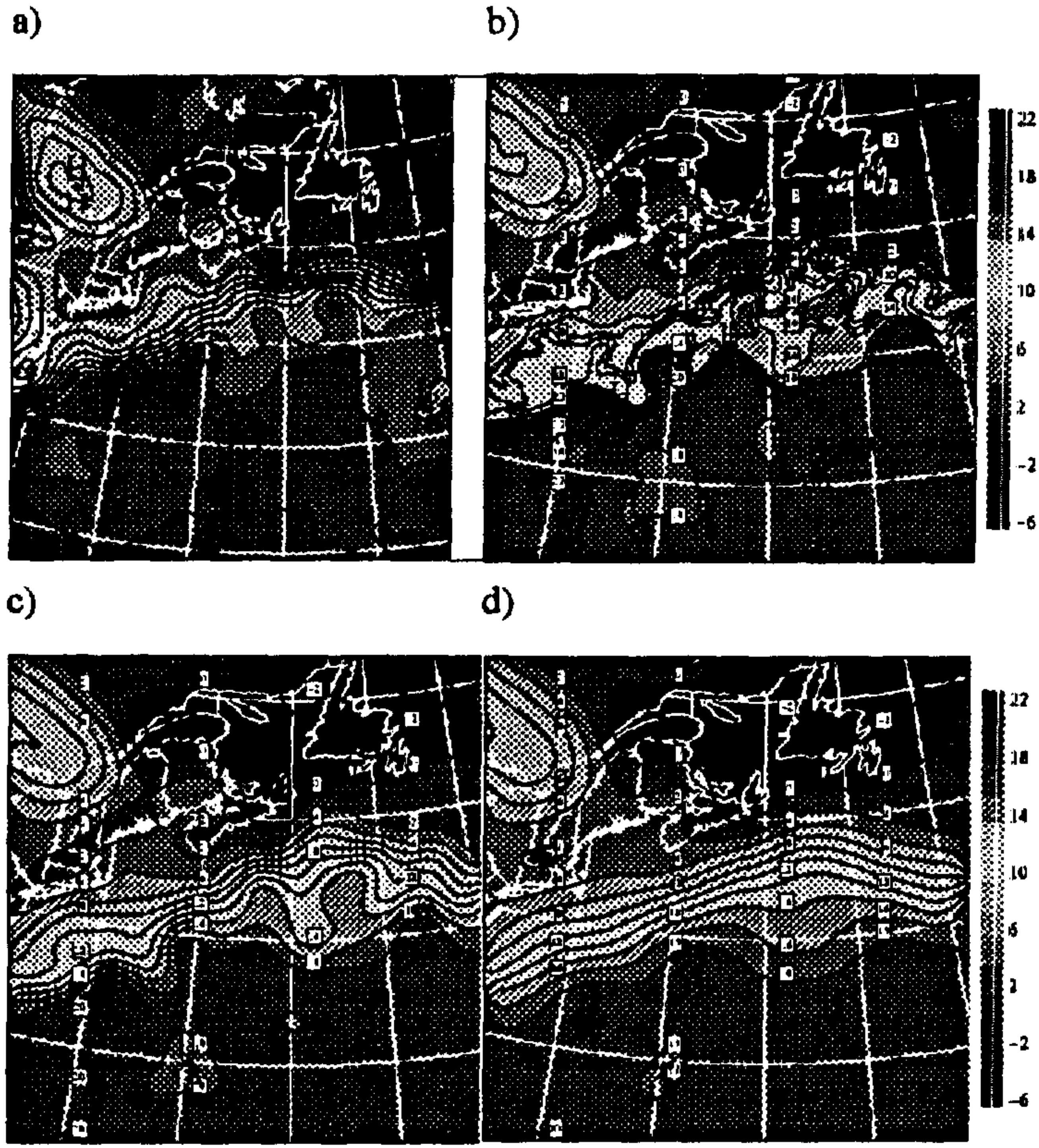

Figure 3: Sea surface temperature (2° C) at a) 50km from CMC analysis; and b) 25 and 10km from digitized METOC SST analysis {S0}. Digitized METOC SST analysis filtered c) 250 times {S1} and d) 2500 times {S2}.

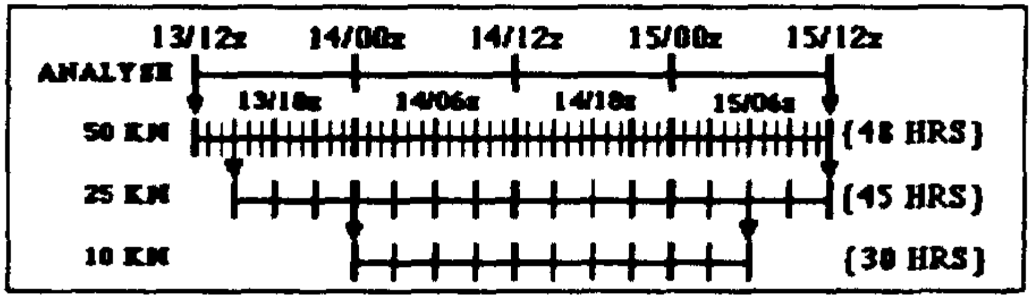

Figure 4: Diagram of the cascade process. Vertical lines indicate the time interval of the pilot file. The arrows show the beginning and the end of the pilot file used for higher-resolution simulations. Numbers bracketed together are the period of integration at this resolution.

However, only results from runs 1, 4, 6, 7, 8, 10, and 11 are presented in this paper. Results from the other simulations were more like experiments.

Note that hydrostaticity runs revealed no real difference between a hydrostatic atmosphere and a nonhydrostatic atmosphere at the resolutions used in this study. Twelve to thirty hours of real time were taken to run simulations of 48 to 30 hours at different resolutions and with different parameters, including hydrostaticity and various SST fields.

RUN	Resolution (KM)	Timestep (SEC)	Hydrostaticity	SST
1	50	600	non-hydrostatic	analyse
2			hydrostatic	↓
3			non-hydrostatic	filt. anal
4	25	300	non-hydrostatic	digitized 25km
5			hydrostatic	↓
6			non-hydrostatic	main eddies(S1)
7			non-hydrostatic	no eddies (S2)
8	10	120	non-hydrostatic	digitized 25km
9			hydrostatic	↓
10			non-hydrostatic	main eddies(S1)
11			non-hydrostatic	no eddies (S2)

Table 1: Table of the simulations carried out. The third column is the timestep used for the different resolutions. The arrows indicate the source for the filtered SST field.

5. VALIDATION

5.1 CMC analysis versus buoy observations

Time-dependent nesting of the lateral boundary conditions, for the MC2 model, were supplied by the CMC analysis (in modeller jargon, this is described as piloting the model). Different fields, such as wind, pressure at sea level, and temperature from the analysis were compared with the real synoptic fields and buoy observations. Canadian buoys report winds as 10 minutes vector averages (Skey et al., 1995).

First, visual comparisons indicated that CMC analysis was a good numerical representation of the real situation. Second, comparisons between buoy observations and data from grid points representing the buoys in the analysis were done at each buoy. Table 2 lists the buoys employed the Figure 5 shows their location in relationship with the detailed 25 km SST field.

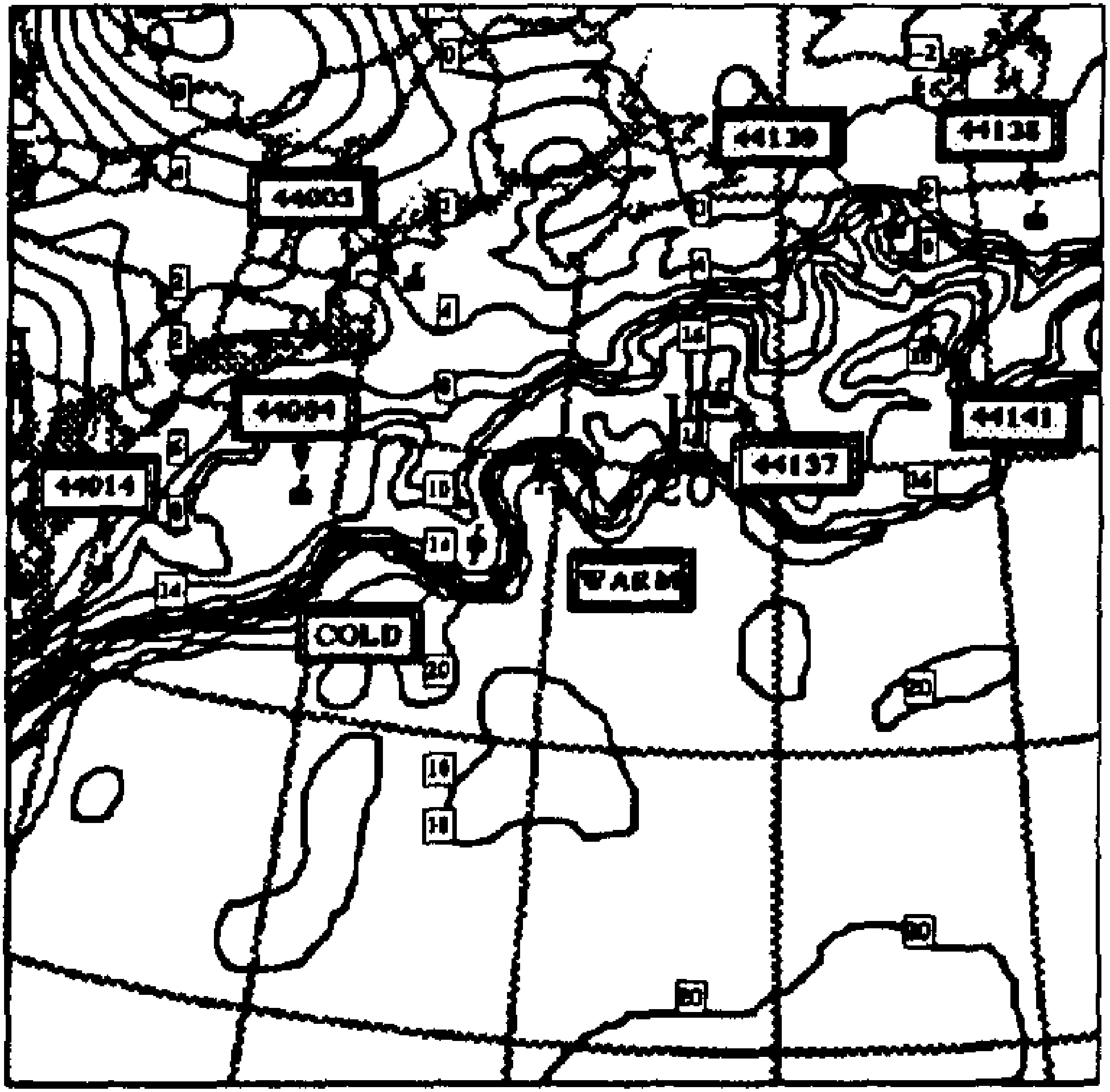

Figure 5: Location of the buoys used for 25km and 10 km resolutions, in relationship to the detailed 25 km SST field.. "Cold" and "warm" indicate the location of the eddies used for the time series in section 7.2. For more details on the SST field, see Figure 3b, legend.

code	name	Location (N lat/W long)	Resolution
41002	S. Cape Hatteras	32.3/75.2	a,50
44004	Hotel	39.5/70.7	a,50,25*
44005	Gulf of Maine	42.6/68.6	50,25
44014	Virginia beach	36.6/74.8	a,50
44137	E. Scotian slope	41.2/61.1	a,50,25,10
44138	SW Grand Banks	44.2/53.6	a,50,25,10**
44139	Banquereau	44.3/57.3	a,50,25,10
44141	Laurentian Fan	42.0/56.1	a,250,25,10

Table 2: Buoys used and their location. The third column indicates at which resolution the observations from the buoy had been used. The ”a” refers to analysis. Single and double asterisks indicate that the buoy was near or in the pilot-buffer zone respectively.

Note that because of the availability of the fields from the analysis, grid point data were taken from different levels. Wind data came from the surface level (sigma 1) while temperature data were extracted at 1000 hPa.

However, the trend of the data analysis was more significant than the magnitude of the values recorded. Comparisons of time series between data from numerical analysis and from observations gave very similar results for each buoy. Figure 6 shows the results for Hotel buoy (44004). It demonstrates that data from the analysis followed the trend of the observations. One can conclude that CMC analysis was a valid numerical representation of the surface observations. It is noteworthy, however, that winds from the analysis at 1200 UTC on March 14 reflected more closely the values of the maximum wind than the mean wind at the Canadian buoys. On the other hand, temperatures from the analysis were a few degrees warmer at the American buoys.

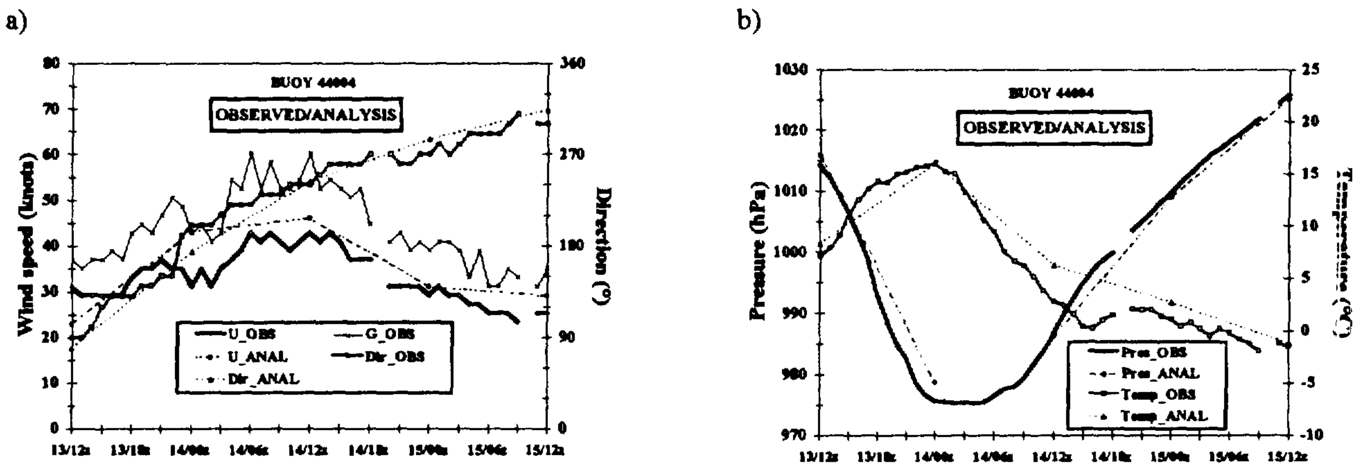

Figure 6: Comparisons between buoy observations and grid point data from analysis of a) wind speed and direction; and b) pressure and temperature. For the definition of lines, see legend in graphs.

5.2 CMC analysis versus prognostics

In general, the evolution of the storm was well forecasted by all numerical models. In this research, the nonhydrostatic MC2 50km output from run 1 was compared with the Regional Finite Element model (hereinafter RFE) output as well as with the CMC analysis. Both models and the analysis agreed closely on the position and the center value of the low and the main isobaric features such as troughs. The main differences occurred after 24 hours of simulation, where the low pressure system from both models slowed down compared to the analysis. This had a direct effect on the timing of the wind shift behind the low pressure system. Isobaric patterns as well as surface wind directions generated by both numerical models were very comparable to those derived from the analysis.

The comparison of the wind fields generated by both numerical models and the analysis showed no major difference. Differences in wind speed were less than 10 knots. Figure 7 shows a comparison between the pressure field at sea level from the analysis (solid thick lines), the RFE 50km (thin dash) and run 1 (thick dash). The 1000 hPa wind field from the analysis (thick) and from run 1 (thin) are presented in windbarbs. As can be seen, the analysis had stronger winds in the southerly low-level jet, while the MC2 developed stronger winds behind the storm However, the difference was only about 5 knots.

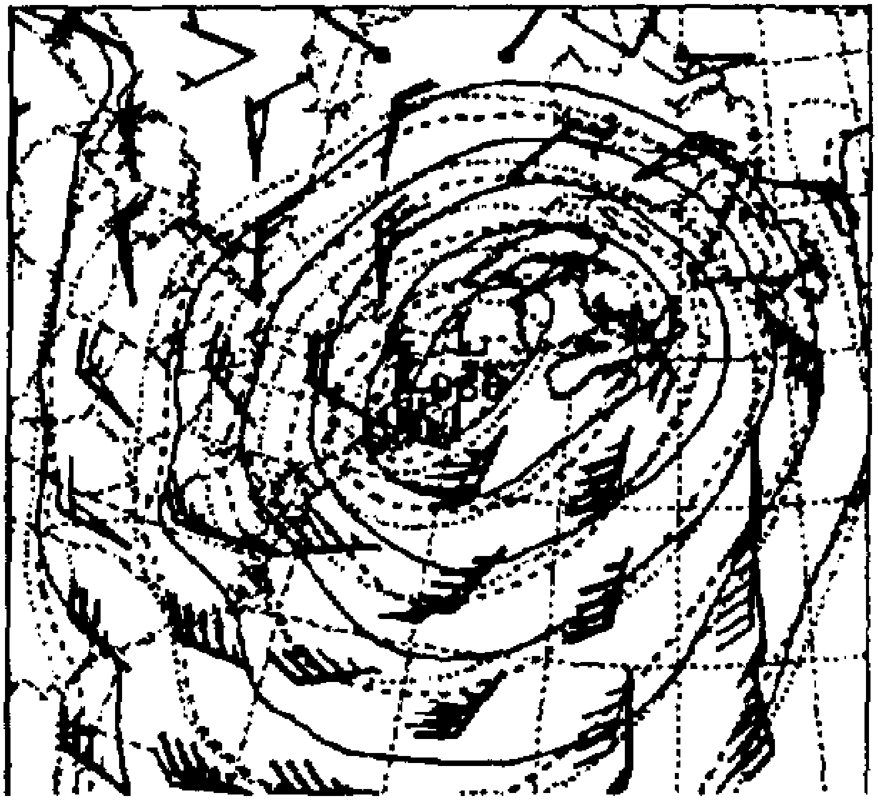

Figure 7: Sea-level pressure field [10 hPa] at 1200 UTC on March 14 from the analysis (solid) compared with those generated by the RFE (thin dash) and by the MC2 (thick dash). Superimposed are 1000 hPa winds from the analysis (thick) and the MC2 (thin). The model outputs are 50km 24HR prog from RFE and run 1. Windbarbs are in knots.

6. HIGHER-RESOLUTION RUNS

A more detailed SST field was introduced in run 4. The subtraction of the 25 km SST field from the 50 km SST field (identical to the analysis field), superimposed over the 25 km SST field, showed that the 50km SST was warmer by 4 to 8 degrees over the cold eddies and was cooler by about 4 degrees over warm meanders and eddies than in reality. A similar comparison was made between the 25 km SST field and its interpolation at 10 km. Subtraction of the two fields showed that the interpolation did not alter the field.

The introduction of a more detailed SST field for run 4 and subsequent ones hid slightly the effect of going to higher resolutions. However, as shown in Figure 8a , the combination of the two parameters did not seem to bring major changes in surface pressure and 10km wind fields. The pressure field at both resolutions (runs 1 and 4) was identical except in the vicinity of the frontal trough. Very minor differences in wind direction were observed, although there were local differences in wind speed.

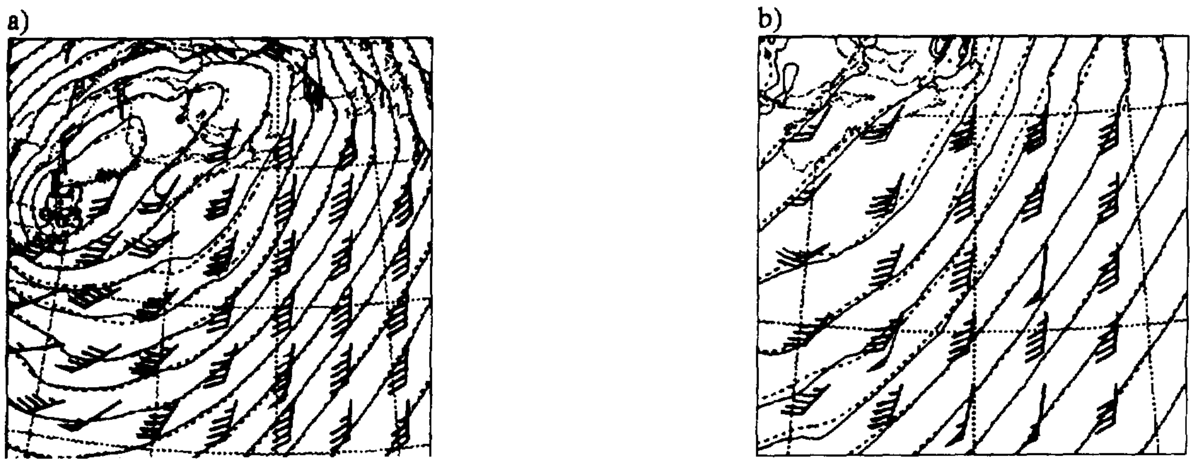

Figure 8: Comparisons between simulations from different resolutions at 1500 UTC on March 14. In a), pressure at sea level [4 hPa] (25km: solid; 50km: dash) and 10m winds (25km: thick; 50 km: thin). In b), same as a), but for 10 and 25 km simulations. The respective model outputs are: a) 27HR prog of run 1 and 25Hr prog of run 4; b) 24HR prog of run 4, and 15HR prog of run 8. Windbarbs are in knots.

Figure 9a shows the difference between the 10m wind speeds from both resolutions (UV50-UV25). The superposition of the detailed SST demonstrated its influence on the surface wind speed. Warm and cold mesoscale eddies or meanders in the SST, especially over the northern wall of the Gulf Stream, increased or decreased locally the wind speed from run 1 by 5 to 15 knots when compared with the wind speed from run 4. The reason for this will be treated in the next section. The elongated band extending from southwest to northeast in Figure 9a was caused by the difference in the speed of the surface trough.

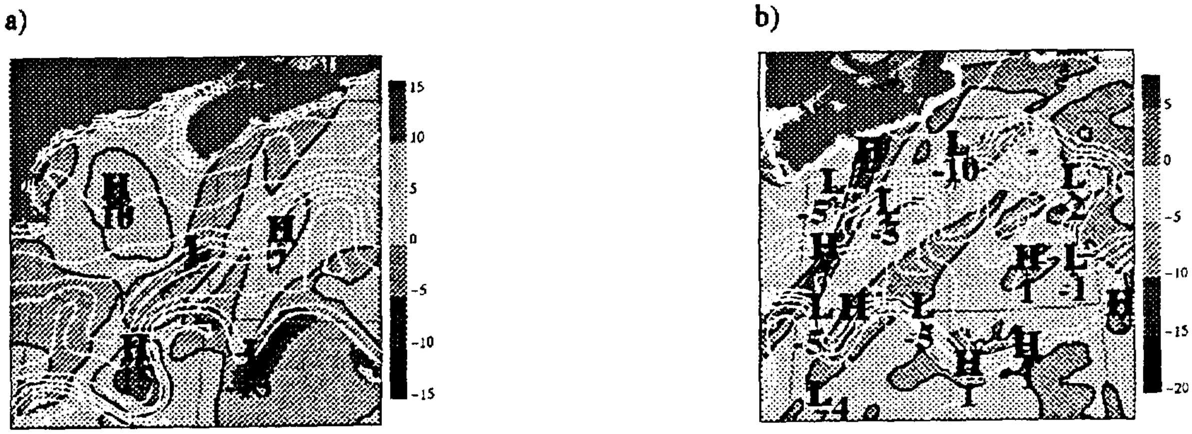

Figure 9: Differences in 10m wind speed [5 knots, black lines] from different resolutions at 1500 UTC on March 14 superimposed over the 25km SST field [2° C, white lines]. In a), UV_{50}–UV_{25}. In b) UV_{25}–UV_{10}. The respective model outputs are: a) 27HR prog of run 1 and 25Hr prog of run 4; b) 24HR prog of run 4, and 15HR prog of run 8.

Runs 8 through 11 were done at 10 km, using an interpolated 25 km SST field. Again, going to higher resolutions did not bring major changes in the surface pressure, as Figure 8b shows. Slight changes in wind direction and wind speed resulted from the difference in the speed of the surface trough rather than from the SST field. Differences in wind speed at 10m (UV25-UV10) were less than or equal to 10 knots (Figure 9b). From Figures 8 and 9 , one can conclude that higher resolutions brought minor differences in the pressure field without causing significant changes in the wind field. Most of the changes were local and were due to a more detailed SST field, resulting in changes in the magnitude of the wind but with little effect on its direction.

7. RESULTS

7.1 Stability factor

Figure 9a has shown that a more detailed SST added or subtracted locally 7 to 15 knots to the 50km wind field. Most of the changes occurred over both cold and warm eddies. In fact, this figure revealed the influence of the meanders of the Gulf Stream on the generation of surface wind. Figure 10 includes two maps of the 10m wind generated by the nonhydrostatic MC2 25 km (run 8) superimposed over the detailed SST.

Figure 10a represents the situation ahead of the cold front. Warm air between 10 to 20 degrees was pushed by the southerlies over cooler sea waters. The magnitude of the wind field was shaped by the meanders of the Gulf Stream. In a general south-southwesterly flow at 45 knots, maximum wind speeds of 50 to 60 knots were found locally over the meanders. No real decrease in wind speed was noticed over the cold eddies, but the fact that these cold eddies were surrounded by warm meanders created a local minimum in the wind speed. The cold front lay ahead of the elongated lighter wind band, west of the meanders.

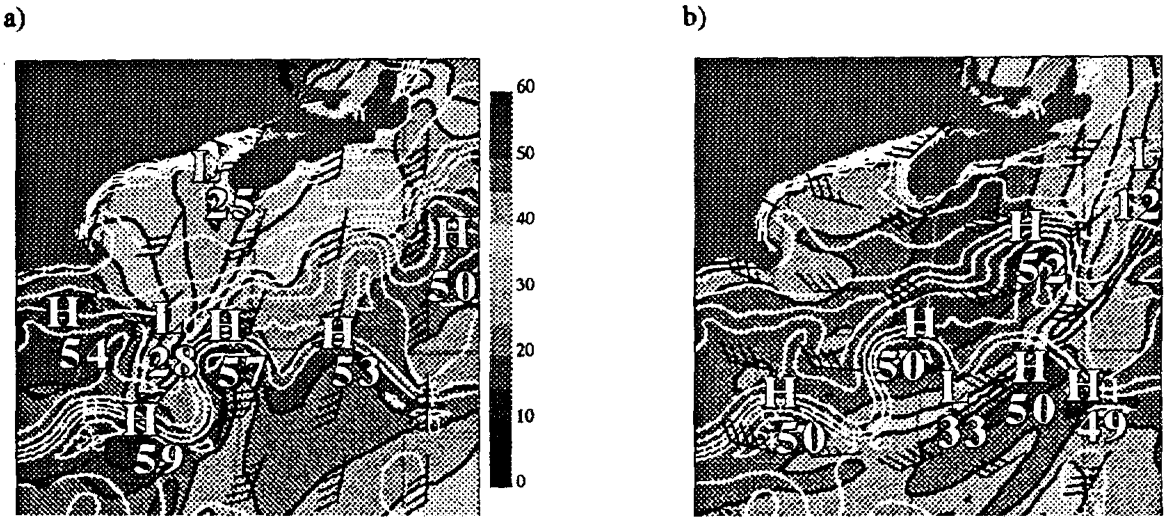

Figure 10: Wind speed at 10m [10 knots, black] from run 4, superimposed over the detail SST field [2°C, white]. Hours represented are a) 1200 UTC on March 14, corresponding to a 21HR prog; and b) 0000 UTC on March 15, corresponding to a 33HR prog. Maxima (H) and minima (L) in wind speed are highlighted in white.

Figure 10b represents the situation <u>behind the cold front</u>, where a cold airmass at a temperature near zero degrees was passing over warmer waters. In a general westerly circulation of 35 to 45 knots, maximum wind speeds of about 50 knots were found again over wan-n eddies. However, the magnitude of the wind field was no longer shaped by the meanders of the Gulf Stream. *The passage of the front changed the stability of the marine boundary layer.*

Figure 11 shows the remainder of the vertical lapse rate of the temperature calculated by (4) in the first 100 meters for the same time frame as in Figure 10 . The detailed SST is superimposed over it. In Figure 11a , <u>ahead of the front</u> the remainder of the vertical lapse rate indicated stable conditions in the lower levels of the atmosphere except over the meanders, where conditions were neutral or unstable. Vertical momentum transfer occurred, enhancing locally the wind speed. On the other hand, over cold eddies, very stable conditions prevailed and cut the vertical momentum transfer. Cold air invasion could already be noticed on the left edge of the figure, where the dark color indicates unstable condition. In Figure 11b , behind the cold front, cold air advection had uniformly destabilized the low levels of the atmosphere over the region. However, maximum destabilization occurred over the warm eddies because the maxima in wind speed were found there (see Figure 10b).

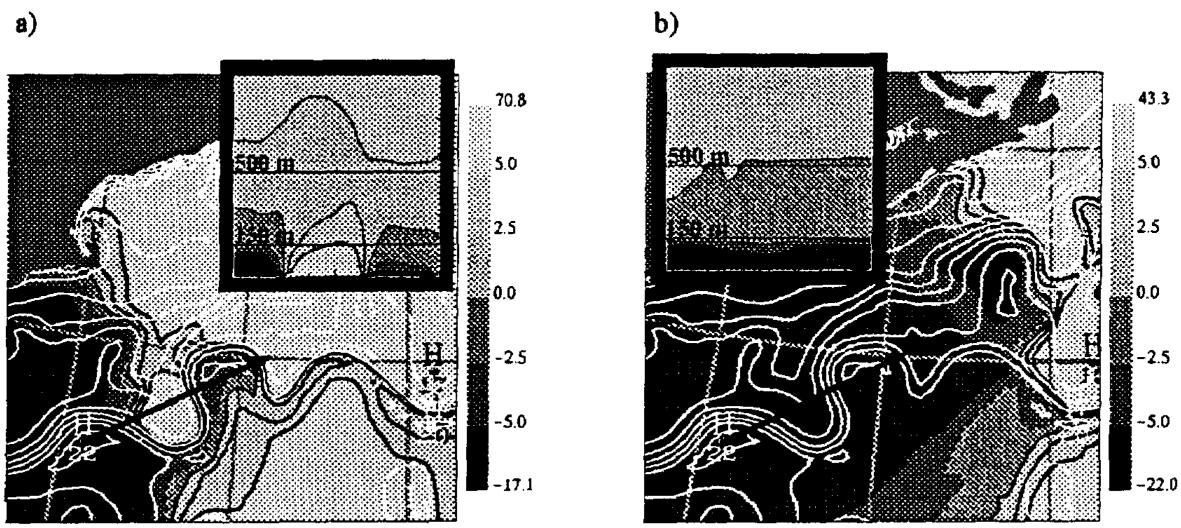

Figure 11: Remainder of the vertical lapse rate of temperature in the first 100m (black) from run 4 superimposed over the SST field [2°C, white]. Hours represented are a) 1200 UTC on March 14, corresponding to a 21HR prog and b) 0000 UTC on March 15, corresponding to a 33HR prog. Inset shows vertical cross section in the first km along the arrow. Color scale goes from light (stable) to dark (unstable).

The insets in Figure 11 are a vertical cross-section of the first km taken along the arrow They show that, ahead of the front (Figure 11a), the boundary layer was locally unstable over warm eddies and locally stable over cold eddies. Behind the front, the cold air destabilized the low-level layers of the atmosphere up to 500 m, allowing vertical momentum trader throughout the region and masking the influence of the Gulf Stream and the sea surface temperature on the wind field.

7.2 The influence of the meanders and the eddies

Results to this point have shown that the Gulf Stream influenced the wind speed. In particular, the meanders of the Gulf Stream seem to increase locally the wind speed by about 10 knots. However, most of the previous results were largely related to the resolution of the model. Using fictitious SST fields, one can see the influence of the real SST field on the generation of surface wind. Runs 10 and 11 used smoother SST fields. The S1 SST field (see Figure 3c) used in run 10 was very similar to the SST from the analysis (see Figure 3a), except the latter did not have the western cold eddy. The S2 SST field (see Figure 3d) used in run 11 simulated a Gulf Stream with practically no meanders and eliminated all eddies north of it. Note however, that the filtering slightly cooled the southern wall of the Gulf Stream and warmed the northern waters. Based on previous results, this cooling and warming will diminish the maxima in wind speed found over warm eddies and slightly decrease the unstable westerlies behind the cold front.

A subtraction of the 10 km S2 SST from the detailed 10 km SST field (hereinafter S0 SST) superimposed over the S0 SST ([S0-S2], not shown here) revealed local differences over cold and warm eddies. A sinusoidal band of 3 degrees of warmer water for the S0 SST followed the meanders of the Gulf Stream while local maxima of 5 degrees for the S0 SST indicated the location of the warmer eddies north of the Gulf Stream. Over cold eddies, the S0 SST was found 3 degrees cooler when compared to the S2 SST. Similar results were found when the S0 SST and the S1 SST fields were compared ([S0-S1], not shown here). The differences were 3 degrees or less and were less concentrated.

Figure 12 shows a superposition of the 10m wind field resulting from runs 8, 10 and 11. <u>Ahead of the front</u> (see Figure 12a), the strongest wind and most detailed field was generated by the S0 SST. Minor differences between the wind fields generated by various runs were noticed. In fact, the main differences were found along the meanders of the Gulf Stream. In a general southerly circulation at 40 to 45 knots, a band of 50 to 57 knots was generated over the meanders by the S0 SST field. This latter field slightly decreased wind speed over the cold eddies when compared to those generated by the S1 and S2 SST fields. <u>Behind the front</u> (see Figure 12b), winds generated by the various runs were again very similar. The smoother SST fields, especially the S2 SST, produced lighter winds behind the front.

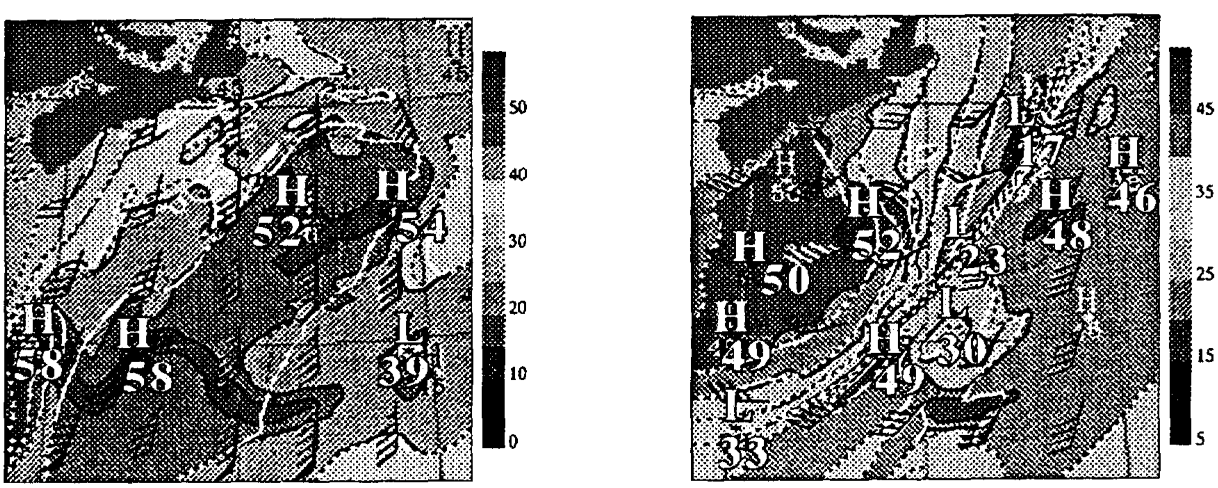

Figure 12: Wind fields at 10m [5 knots] from run 8 (solid black), run 10 (dashed black) and run 11(solid, white). Hours represented are a) 1200 UTC on March 14, corresponding to a 12 HR prog and b) 0000 UTC on March 15, corresponding to a 24 HR prog. Maxima (H) and minima (L) in wind speed are highlighted in white.

In Figure 13 , the S0 SST field has been superimposed over the subtraction of the wind speed at 10m generated by the S2 and S0 SST fields {US0 - US2) behind the front. Enhancement of wind speeds still prevails over the meanders ahead of the cold front. Over the warm eddy where buoy 44137 is located (see Figure 5), a subtraction of the 10 km S2 SST from the detail,M 10 km SST fields (S0-S2) indicated a maximum of 5 degrees for the S0 SST over this eddy. A wind speed 10 knots higher (generated by the S0 SST) was also found when compared to that generated by the S2 SST (see Figure 13). Again, the explanation is related to the stability of the marine boundary layer. A similar comparison (not shown here) was done for the same time frame used in Figure 12a . The meanders of the Gulf Stream generated a ribbon of winds 5 to 8 knots stronger for the S0 SST when compared to those produced by like S2 SST field. It is also noteworthy that the S0 SST field generated 9 knots higher wind speeds when compared to those produced by the S2 SST over the large warm eddy where buoy 44141 is located (see Figure 5). Finally, similar comparisons were made with the S1 SST field, which revealed essentially the same results found previously but to a lesser degree.

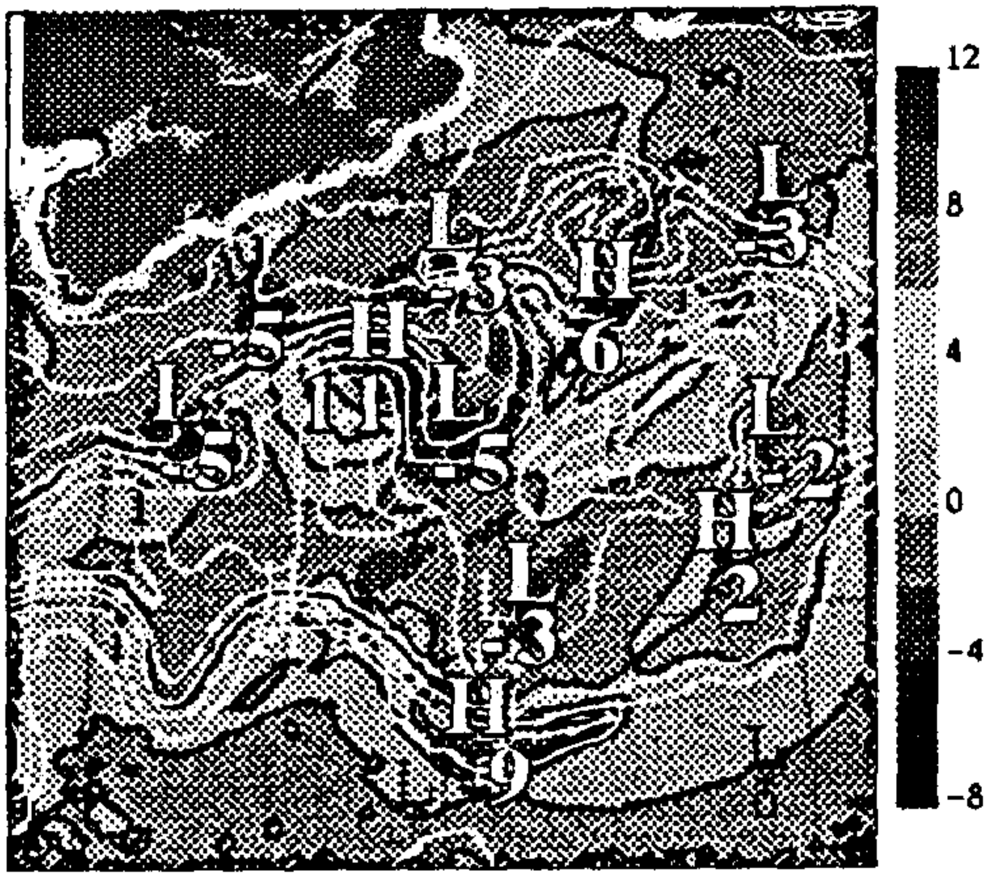

Figure 13: Difference between 10m wind speed at 1500 UTC on March 14 from 24HR prog from run 8 and run 11 $\{U_{s0} - U_{s2}\}$[2 knots, black] superimposed over the 10km SST [2°C, white] field. Maxima (H) and minima (L) in subtraction field are highlighted in white.

Since most of the changes occurred over cold and warm eddies, it will be interesting to see the evolution through time of the wind speed. Figure 14 shows the temporal series from runs 4, 5 and 6 of the 10m wind speed at a grid point located over a warm eddy. The location of the grid point is indicated in Figure 5 . No observations were available since no buoys were located in these eddies. Consequently, the results and conclusions will be drawn from numerical simulations only. However, as will be shown in the next section, model outputs were very similar to the observations. Wind speed series are found at the top of the graph and refer to the left axis. Remainders of the subtraction of the wind speed generated by the real SST field and the smoother SST fields $\{U_{S0} - U_{S1\ or\ S2}\}$ are found in the lower part of the graph and refer to the right axis. The figure shows that smoother SST fields generated lighter winds than the real SST. The biggest differences were found between S2 and the real SST. The real SST field generated winds about 5 knots stronger than the S2 SST field During a period of 6 hours, 6 to 12 knot differences prevailed between the wind speed of the two simulations, This was followed by a rapid decrease in the difference, corresponding to the passage of the cold front. After this period, no real difference was noticed.

The same graph was produced for the situation prevailing over the cold eddy (not shown here; see Figure 5 for its location). It revealed similar results as Figure 14 but kw marked. It is noteworthy, however, that for both warm and cold eddies, the difference in the wind generated by the various SST fields almost disappeared behind the cold front.

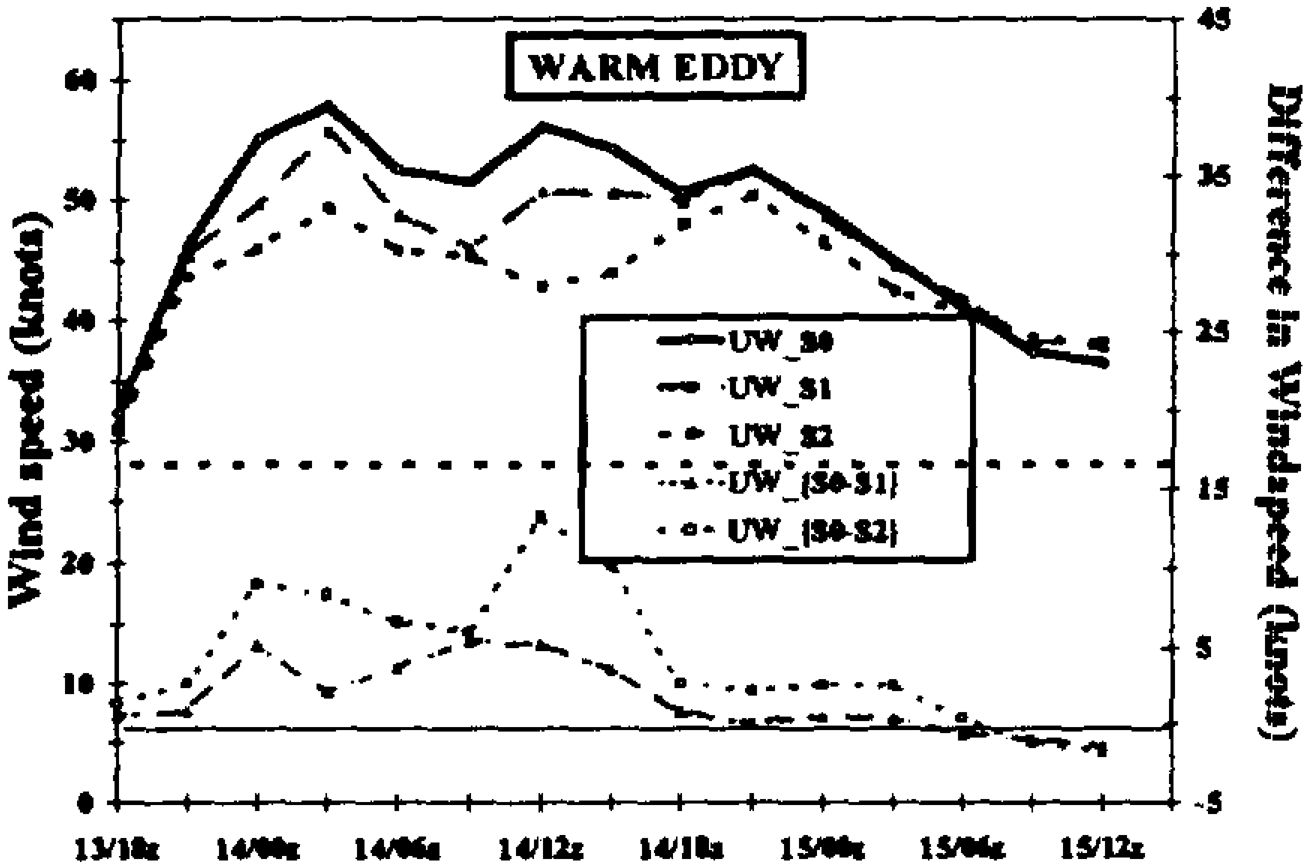

Figure 14: Comparisons of 10m wind speed from run 8, 10, and 11, over a warm eddy (left axis). Separated by a dashed line, at the bottom of the graph, Subtraction of the wind speeds generated by smoother SST fields from that one generated by the real SST (right axis). The thin solid line represents the zero on the right axis. For the definition of lines, see legend in graph

Figure 15 groups together winds over cold and warm eddies and those generated by the different SST fields. The straight lines represent the SST difference between cold and warm eddies for the different SST fields. From this figure, one can conclude that stronger winds of about 10 knots, with occasional peaks of 12 to 15 knots, were found over the warm eddy when compared with those over the cold eddy. The S1 SST field diminished this difference to 4 to 8 knots. Wind generated by the S2 SST field was weaker over the warm eddy because the SST was colder over the warm eddy, as demonstrated in Figure 15 . As anticipated, the S2 SST developed a more uniform wind field over both the cold and warm eddy. However, after the passage of the cold front around 14/15z, for both locations and both smoother fields, the difference in wind speed increased for the next 9 to 12 hours. This rapid increase was more attributable to the synoptic situation, where stronger winds developed in the north (warm eddy), than to the influence of the SST field.

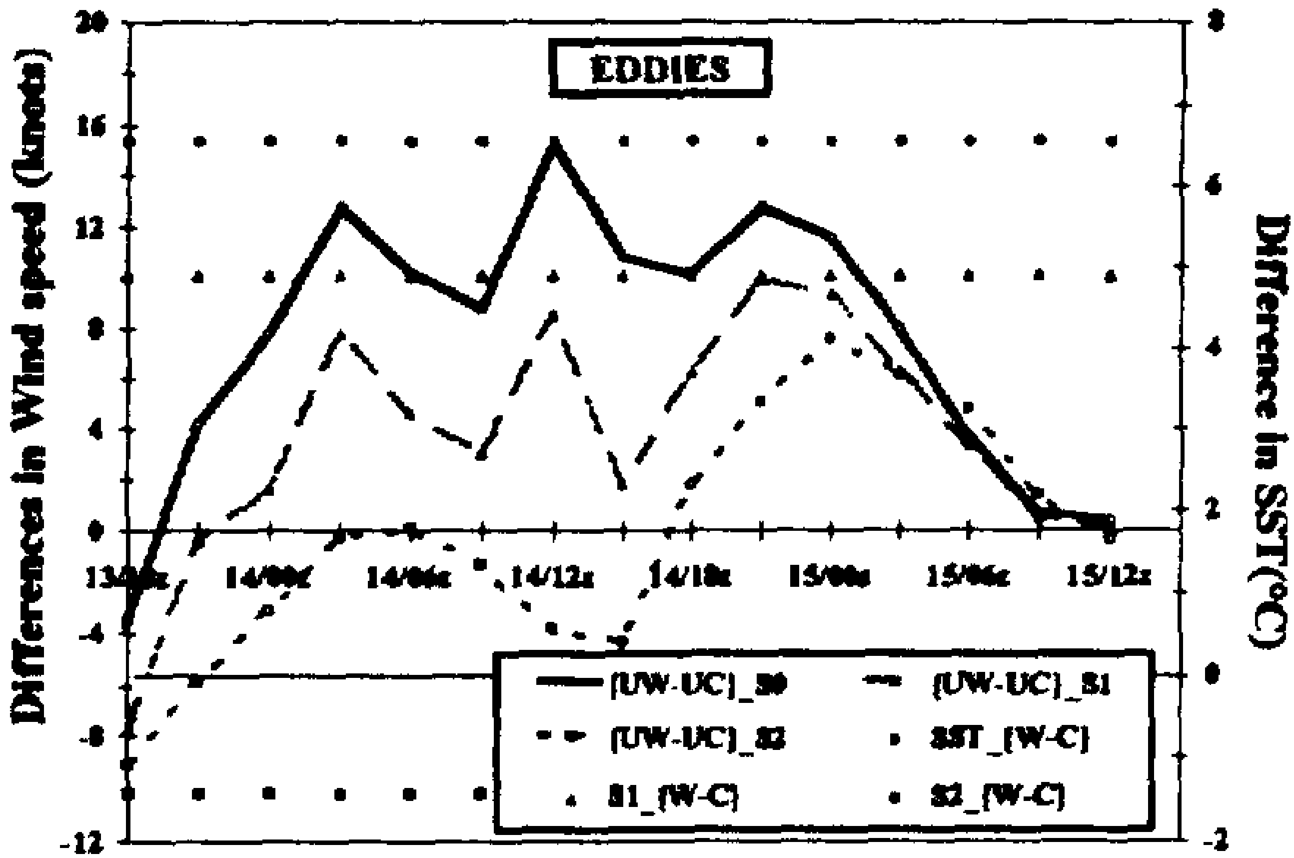

Figure 15: Differences of 10m wind speed from run 8, 10, and 11 between a warm and a cold eddies (left axis). Right axis refers to the SST difference between the cold and warm eddies for the various SST fields. The thin solid line represents the zero on the right axis. For the definition of lines, see legend in graph.

8. GRID POINTS VERSUS BUOY DATA

Up to this point, the results and conclusions an the influence of the Gulf Strewn on the surface wind field were based essentially on model outputs. In this section, the link is made between these model outputs at different resolutions and the buoy observations. Figures 16 and 17 are two sets of graphs, forming a series of eight sets for each buoy used in this study. They represent conditions over warm (Figure 16) and over cold (Figure 17) waters, north of the Gulf Stream. They are also representative of the situation at the other buoys (not shown here) and cover all resolutions (see Table 2). Each set is composed of 4 graphs of time series of wind direction, wind speed, temperature and pressure at sea level. Wind and temperature model output data were taken at 10m. Using the Smith conversion table (Smith, 1981), 5m mind speeds from buoys were converted to a height of 10 m. This conversion added little to real buoy wind speed observations. Finally, no correction was made for temperature and wind direction.

From an examination of the 4 graphs in Figures 16 and 17 , one can conclude that the 50km, 25km and 10km MC2 outputs closely simulated the real situation. Numerical and observed directions of wind were consistent at all buoy sites (see Figures 16a and 17a). The air temperature from the model outputs was, in general, warmer than the observed temperatures especially behind the cold front (see Figure 16c and 17c). This resulted in a less unstable marine layer and generated weaker winds. A delay of about 6 hours in the minimum value of the pressure between observation and numerical simulations (see Figures 16d and 17d) was also present at each buoy site. It indicates that the frontal trough generated by the MC2 was slower than the real one. This delay is reflected as well in the wind speed (see Figures 16b and 17b). The minimum wind speed at the passage of the front occurred 6 hours later in the 50 km simulation. This delay was reduced by 3 hours in the 25 and 10 km simulations, supporting the hypothesis that it was caused by the analysis. Wind speed values from numerical outputs were, in general, more comparable to the maximum observed winds than the average ones, as shown in Figures 16b and 17b . This was true for all Canadian buoys. However, for American buoys, wind speed values from numerical simulations were between the average speed and the maximum wind speed observed, during the first 24 hours. They then adopted a value closer to the maximum observed wind speed at the end of the simulation. This could be caused by the initialisation period of the model.

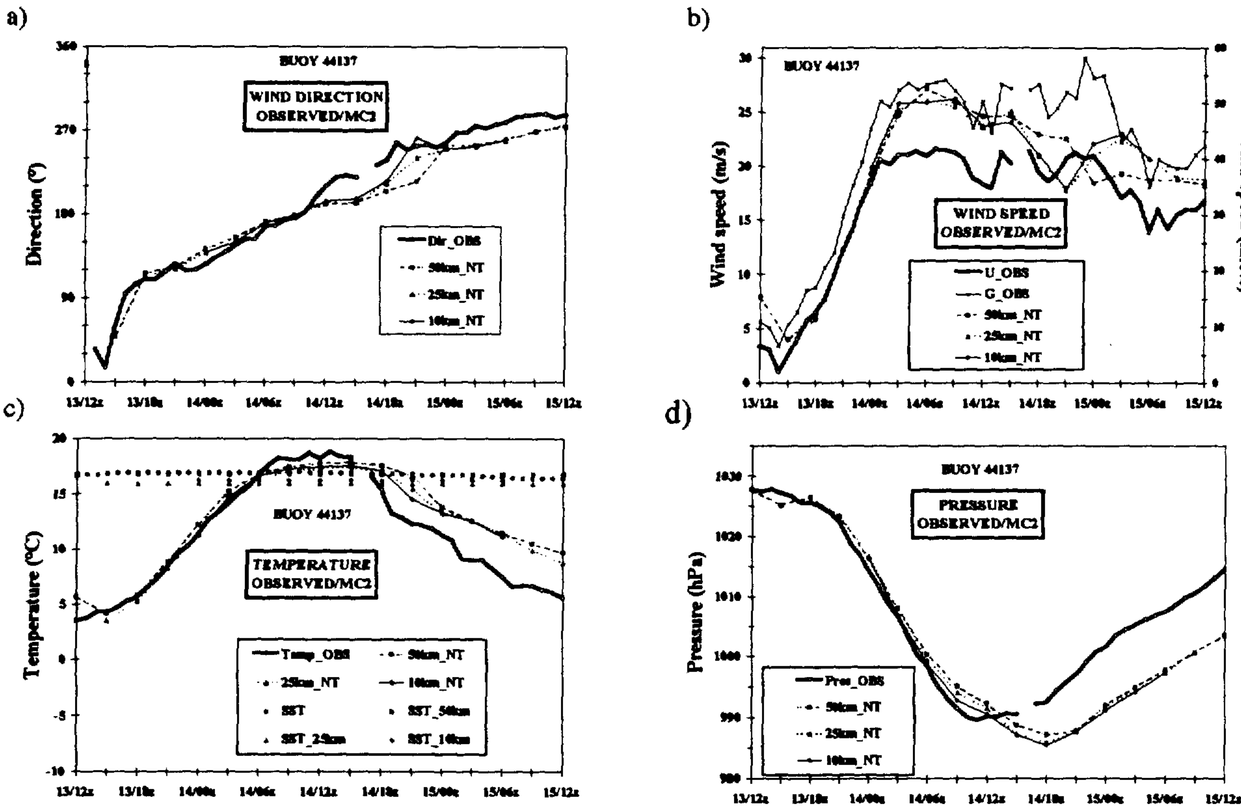

Figure 16: Grid point data at 10 m from runs 1, 4 and 8, representing buoy 44137 compared with the buoy observations. In a) wind direction, in b) wind speed, in c) temperature and sea surface temperature and in d) surface pressure. For the definition of lines, see legend in graph.

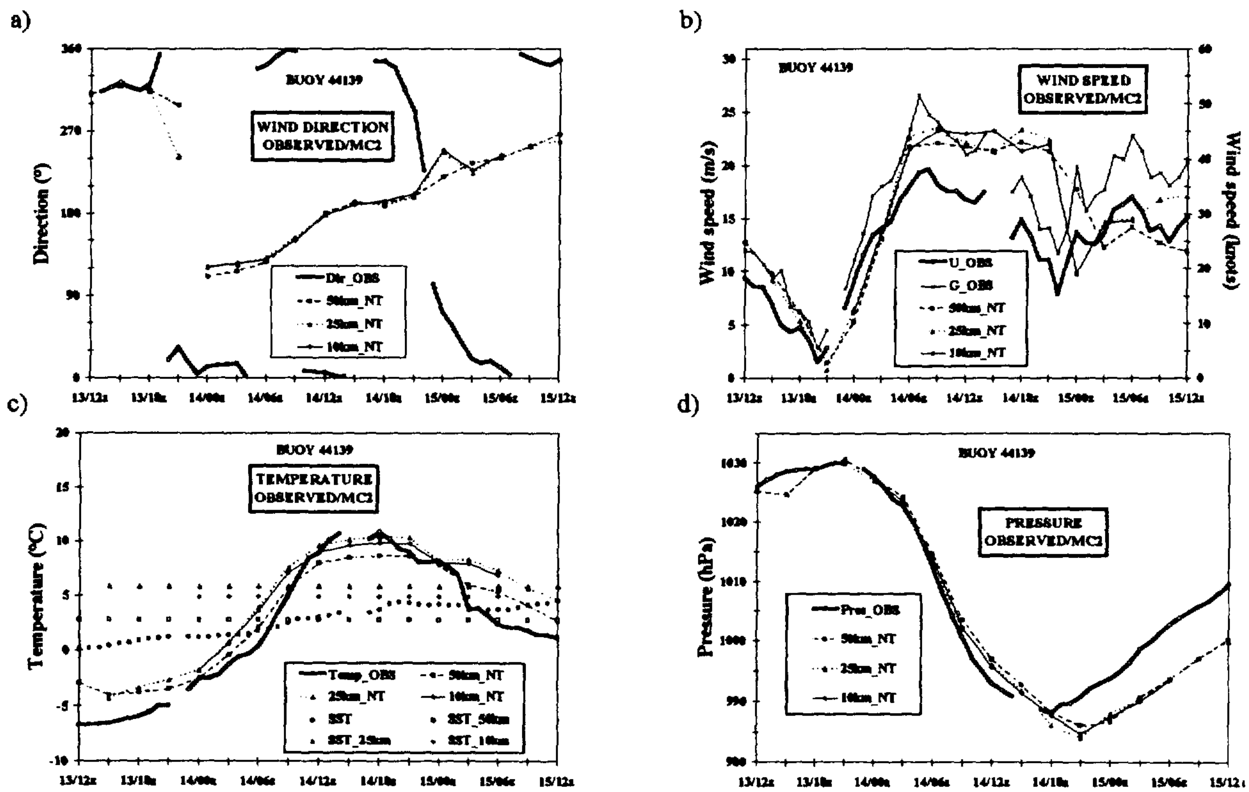

Figure 17: Same as Figure 16 but for buoy 44139.

Now let us look more specifically at the graphs chosen for this section. From Figure 16a and 17a), the passage of the front was marked by an abrupt change in wind direction at both buoys, becoming more pronounced as the resolution of the model increases, This also corresponded to the tune when a minimum was found in the time series of the wind speed (see Figure 16 and 17b) as well as when the temperature began falling (see Figures 16c and 17c). Figure 16c shows that the low level layers of the marine boundary were practically always unstable at buoy 44137, while Figure 17c shows that buoy 44139 had a more stable marine boundary layer during the strongest wind event.

The SST at buoy 44139 rose from zero to 5 degrees during the period (this buoy was located on the eastern edge of a warm eddy of 8 degrees). This could mean that the eddy moved eastward during the period, bringing less stable conditions at the end of the period. It is noteworthy that the SST chosen for the simulations reflected more closely the situation over this warm eddy and as a result created a less stable marine boundary layer than the buoy had through most of the period. This would explain why wind speed values from numerical simulations were the same or higher than the maximum wind speed ahead of the front at buoy 44139.

Finally, behind the front, the air temperature dropped rapidly, changing the stability of the marine boundary layer and allowing the maximum wind speed observed to remain high while the mean winds decreased (see Figures 16b and 17b). However, the air temperature from all simulations dropped less drastically than those observed (see Figures 16 and 17c), implying a less rapid destabilization of the marine boundary layer. This last fact can explain why wind values from numerical simulations which had more or less the value of the maximum wind, ahead of the front, reached a value closer to the mean wind after the passage of the front.

9. DISCUSSION AND CONCLUSION

A study of the influence of the sea surface temperature distribution, particularly in the vicinity of the Gulf Stream's meanders, on the generation of winds was made, using the Storm of the Century (March 13-15, 1993) as a laboratory. All model outputs were generated by the MC2 model piloted at its lateral boundaries by the CMC analysis. Several validation tests were made to insure consistency between numerical representations and the real situation. Comparisons between buoy observations and the analysis showed that the CMC analysis was a valid numerical representation of the real storm. Comparisons between the 50 km RFE prog, the 50 km MC2 prog and the analysis demonstrated that both numerical models closely converged at the analysis. From this point, the 50 km MC2 outputs were considered as a valid and continuous representation of the atmosphere,

In the process of running the MC2 at higher resolutions, a more detailed SST field replaced the SST field from the analysis used for the 50 km run. This replacement hid somewhat the effect of going to higher resolutions. A few tests were done to see the effect of running the MC2 model at higher resolutions then showed no major differences in the isobaric and wind fields. The variation in the speed of the frontal trough produced most of the differences when compelling the numerical outputs from different resolutions. However, the implantation of a more detailed SST showed that wind speeds from the 50 km run were stronger and weaker by about 15 knots over cold and warm eddies, respectively.

A study of the 25 km MC2 nonhydrostatic simulation at two different times, representing the situation ahead of and behind the front, revealed the influence of the Gulf Stream and its meanders on surface wind speeds. It was demonstrated dim the stronger influence was ahead of the front, where the wind speed pattern was shaped by the meanders of the Gulf Stream. Behind the front, the Gulf Stream continued to influence the surface winds, since the maxima in the wind speeds were found over the warmest spots in its meanders, but they no longer shaped the wind field pattern.

A study of the stability of the marine boundary layers demonstrated that unstable conditions prevailed ahead of the front over warm eddies and meanders, allowing vertical momentum transfer which enhanced locally die wind speed. Momentum transfer was cut by stable conditions persisting over cold eddies. Behind the front, cold air above warmer sea waters destabilized the marine boundary layer throughout the region. This generalized destabilization masked the effect of the warm eddies and of the Gulf Stream's meanders on the surface minds. However, the meanders still affected the wind field, but to a lesser degree.

The influence of the SST distribution was tested by making simulations with smoother SST fields. A comparison between winds generated by an SST without meanders and eddies and a real SST field, showed that the warm eddies together with the meanders of the Gulf Stream enhanced the wind speeds by about 10 knots, ahead of the front, while winds weaker by about 5 knots prevailed over cold eddies. Behind the front, the warm eddies, especially those north of the Gulf Stream, increased the instability of the marine boundary layer, enhancing locally the winds by about 10 knots.

Finally, a link between model outputs at various resolutions and buoy observations was made. Time series of different parameters, such as wind direction, wind speed, temperature and pressure, when compared with those observed, demonstrated that model outputs at all resolutions corresponded closely to the observations. The time series confirmed the results and conclusions drawn from the numerical simulations, and allowed them to be extended to the real situation.

Overall, the sea surface temperature distribution particularly in the vicinity of the Gulf Stream, influences the surface winds. The Gulf Stream's meanders create a mesoscale wind field pattern because they destabilize locally the marine boundary layer when synoptic stable conditions prevail. With a synoptic unstable marine boundary layer, the warm eddies, especially those located north of the Gulf Stream, enhance locally the instability, allowing an increase in wind speed.

Although this study revealed that warmer eddies and meanders increased locally wind speeds by approximately 10 knots, it also showed that local wind speed maxima were persistent and stationary. This mesoscale pattern along the meanders of the Gulf Stream ahead of a cold front and these stationary maxima of wind over warm eddies behind the front, definitely have an impact on the generation of ocean waves. One can anticipate that these mesoscale features in the wind field generate a mesoscale pattern in the ocean wave field that can be detected with a fine mesh of wave observations.

10 References

Arya S. Pal, 1988: Introduction to Micrometeorology. First edition. International geophysics Series, Academic Press, New York, 42, 307 pp.

Bergeron Guy, Rene Laprise and Daniel Caya et al., 1994: The numerical formulation of the mesoscale compressible community (MC2) model. CCRM report, UQAM, Montreal, Canada. 165 pp.

Cardone, V. J., R. E. Jensen, D. T. Resio, V. R. Swail and A. T. Cox, 1995: Evaluation of contemporary ocean wave models in rare extreme events: "Halloween Storm" of October, 1991; "Storm of the Century" of March, 1993. (accepted for publication in J. Atmos. Ocean. Technology).

Desgagne, Michel, Robert Benoit and Yves Chartier, 1994: The mesoscale compressible community model (MC2) user's manual. RPN publication. Montreal, Canada.

Garratt, J. R., 1992: The Atmospheric boundary layer First edition. Cambridge atmospheric and space, science series. Cambridge University Press, Cambridge. 316 pp.

Holton, J. R., 1992: An Introduction to dynamics meteorology. third edition. International geophysio Series, Academic Press, New York, 48, 523 pp.

Huo Songhui, Da-Lin Zhang, John Gyakum and A. Staniforth, 1995: A diagnostic analysis of the superstorm of March 1993. Mon. Wea. Rev., 12.3, 1740-1761.

Low-Nam, Simon and Ying-Hwa Kuo, 1991: The mesoscale structure of sea surface temperature and its impact on rapid cyclogenesis. First Symposium of Winter Storm, Jan. 14-18 1991, 426-430.

Mailhot, J., 1994: the Regional Finite-Element (RFE) model scientific description. Part 2: Physics. RPN publication/March 94. Montreal, Canada.

Mailhot, J. and C. Chouinard, 1989: Numerical forecast of explosive winter storms: Sensitivity experiments with a meso-model. Mon. Wea. Rev., 117,1311-1343.

Nuss, Wendell A.: Air-sea interaction influences on the structure and intensification of an idealized marine cyclone. Mon. Wea. Rev., 117, 351-369.

Perkey, Donald J., William M. Lapenta, Franklin R. Robertson and Carl W. Kreitzberg, 1991: The role of the sea surface temperature distribution on numerically simulated cyclogenesis during ERICA IOP-4. First Symposium of Winter Storm, Jan. 14-18 1991, 4 18422.

Skey, S.G.P., Berger-NOrth, and V. R. Swail, 1995. Detailed measurement of winds and waves in high sea states from a moored NOMAD weather buoy. Proc 4th International Workshop on Wave Hindcasting arid Forecasting, October 16-20,1995, Banff, Alta.

Smith, S. D., 198 1: Factor for adjustment of wind speed over water to a 10 metre height. Report Series/BI-R-81-3/March 81. Bedford Institute of Oceanography Bedford, Canada. 29 p.

Shuman, F. G., 1957: Numerical Methods in Weather Prediction: H Smoothing and Filtering. Mon. Wea. Rev., 85,357-361.

Tanguay, M., Andre Robert and Rene Laprise, 1990: A semi-implicit semi-lagrangian fully compressible regional forecast model. Mon. Wea. Rev., 118, 19701980.

Thomas, B, 1995: Use of an interactive graphical analysis system to hindcast the Storm of the Century, March 12-15,1993. Proc. 4th International Workshop on Wave Hindcasting and Forecasting, October 16-20, 1995, Banff, Alta.

Warner, Thomas T., Mercedes N. Lakhtakia, James D Doyle and Robert A. Pearson, 1990: Marine atmospheric boundary layer circulations forced by Gulf Stream sea surface temperature gradients. Mon. Wea Rev., 119, 309-323.

OPERATIONAL WAVE FORECASTING AT FLEET NUMERICAL METEOROLOGY AND OCEANOGRAPHY CENTER

P.A. Wittmann and R.M. Clancy

Ocean Models Division
Fleet Numerical Meteorology and Oceanography Center
Monterey, CA 93943

T. Mettlach

Applied Technology Division
Computer Science Corporation
Stennis Space Center, MS 39529

1. INTRODUCTION

The U.S. Navy's Fleet Numerical Meteorology and Oceanography Center is the Department of Defense central production site for all standard fully-automated real-time meteorological and oceanographic prediction products (Plante, 1995). Fleet Numerical fulfills this role through a suite of sophisticated global and regional meteorological and atmospheric models, extending from the top of the atmosphere to the bottom of the ocean (see Plante and Clancy, 1994). The Third Generation Wave Model (WAM; WAMDI Group, 1988) is an integral and important part of this model suite, providing twice-daily ocean wave forecasts to a variety of customers from both global and regional implementations.

2. GLOBAL WAVE MODEL

The Global WAM (GWAM) became operational in May of 1994, replacing the first-generation Global Spectral Ocean Wave Model (GSOWM), which had been operational at Fleet Numerical since 1985 (see Clancy et al., 1986). The replacement of GSOWM with WAM was part of a larger transition at Fleet Numerical in which an obsolete Cyber 205 computer was replaced by a state-of-the-art Cray Y-MP C90 as the primary production platform at the center (see Plante and Clancy, 1994).

GWAM is forced by surface wind stresses provided by the Navy Operational Global Atmospheric Prediction System (NOGAPS), the Fleet Numerical global numerical weather prediction model (see Hogan and Rosmond, 1991). GWAM runs in a fully automated fashion, making two "ontime" and two "offtime" runs per day keyed to the four-per-day NOGAPS run cycle. The two ontime runs produce wave forecasts to forecast times of 144 hours from 0000 GMT and 1200 GMT The two offtime runs are initialized from the 6-hour forecasts of directional wave energy spectra produced by the previous ontime run and valid at either 0600 GMT or 1800 GMT. The offtime runs integrate the model's energy spectra forward in time 6 hours (to either 1200 GMT or 0000 GMT) using forecast wind stresses front the corresponding NOGAPS offtime run (see Bayler and Lewit, 1992). These spectra become the initial conditions for the following ontime run, thus maintaining continuity.

The GWAM runs on a 1° spherical grid, with directional wave energy spectra resolved into 24 directions and 25 frequencies. A weekly updated northern and southern ice edge is applied to suppress waves under the icc. The input wind stress fields are available at three-hour intervals, but are interpolated to a one-hour wind forcing time step. The wave propagation time step is 20 minutes. Output fields are produced every 6 hours into the forecast, and include significant wave height, maximum wave height, sea height, swell height, mean wave period and direction, peak wave period and direction, sea period and direction, swell period and direction, and white cap probability. Directional wave energy spectra are also output every 12 hours into the forecast and available as a random access data base vt each model grid node to support ship routing and other applications. All GWAM output is managed via the Integrated Stored Information System (ISIS) data base management system (see Copeland and Plante, 1994).

3. REGIONAL WAVE MODELS

WAM was first applied operationally at Fleet Numerical as a regional model for the Mediterranean, becoming operational on the Cyber 205 in July of 1990 (see Clancy and Wittmann, 1990). This initial regional implementation of WAM replaced the first generation Mediterranean Spectral Ocean Wave Model (MSOWM), which had been operational at Fleet Numerical since the early 1970s.

The current regional implementations of WAM run on the Cray Y-MP C90 and are forced by the Navy Operational Regional Atmospheric Prediction System (NORAPS), the Fleet Numerical regional numerical weather prediction model (see Hodur, 1987). All of the regional WAM models run in a fully automated fashion, making two ontime runs per day to conform to the twice-per-day NORAPS run cycle. Thus, continuity is maintained by initiating the models with the 12-hour forecast directional wave energy spectra from the previous (12-hour old) ontime run.

The Mediterranean regional WAM (MEDWAM) and the Indian Ocean regional WAM (IOWAM) have grid resolutions of 0.25° latitude/longitude, while the Korean WAM (KORWAM) has a grid resolution of 0.20°. IOWAM and KORWAM obtain open boundary conditions for directional wave energy spectra from GWAM. All three of the regional WAM implementations run with shallow water physics to include the effects of bottom friction and wave refraction (see WAMDI Group, 1988). In addition, all three output the same fields as GWAM to ISIS at every 6 hours into the forecast.

A summary of the Fleet Numerical WAM implementations is given in Table 1 .

TABLE 1
FLEET NUMERICAL WAM IMPLEMENTATIONS

	GWAM	IOWAM	MEDWAM	KORWAM
Forecast Time	144	48	72	36
Shallow Water	NO	YES	YES	YES
Wind Forcing	NOGAPS	NORAPS	NORAPS	NORAPS
Nesting	N/A	YES	NO	YES
Latitude Range	90S-90N	0-28N	28N-45N	28N-53N
Longitude Range	0-359E	42E-100E	10W-39.75E	110E-143E
Grid Resolution	1.0°	0.25°	0.25°	0.2°
Model Time Step	20 min	15 min	15 min	10 min
Wind Time Step	3 hours	3 hours	3 hours	3 hours
Ontime Forecast	0600(00Z)	0630(00Z)	0530(00Z)	0630(00Z)
Completion Time	1800(12Z)	1830(12Z)	1730(12Z)	1830(12Z)

4. VERIFICATION

Verification of GWAM is done on a routine basis by comparing predicted wave heights, peak periods and wind speeds to those observed by moored buoys. Standard error statistics are computed on a monthly basis and published in the Fleet Numerical Quarterly Performance Summary Report. Figures 1 and 2 , based on verification of 6-hour forecast model fields produced by both ontime and offtime runs against data from buoys in the Gulf of Alaska during January 1995, show typical results.

As indicated by the dashed least-squares line on the scatter plot of Figure 1 , GWAM shows a tendency to <u>overpredict</u> wave heights in the low wave-height range and <u>underpredict</u> wave heights in the high wave-height range. This tendency is likely a result of the fact that GWAM is run in only a one-way coupled implementation with NOGAPS. That is, GWAM is forced by the wind stress predicted by NOGAPS, but the NOGAPS wind stress calculation is unaffected by the surface roughness implied by the wave-height field predicted by GWAM. This is in marked contrast to the two-way coupled implementation of WAM advocated by Janssen (1994).

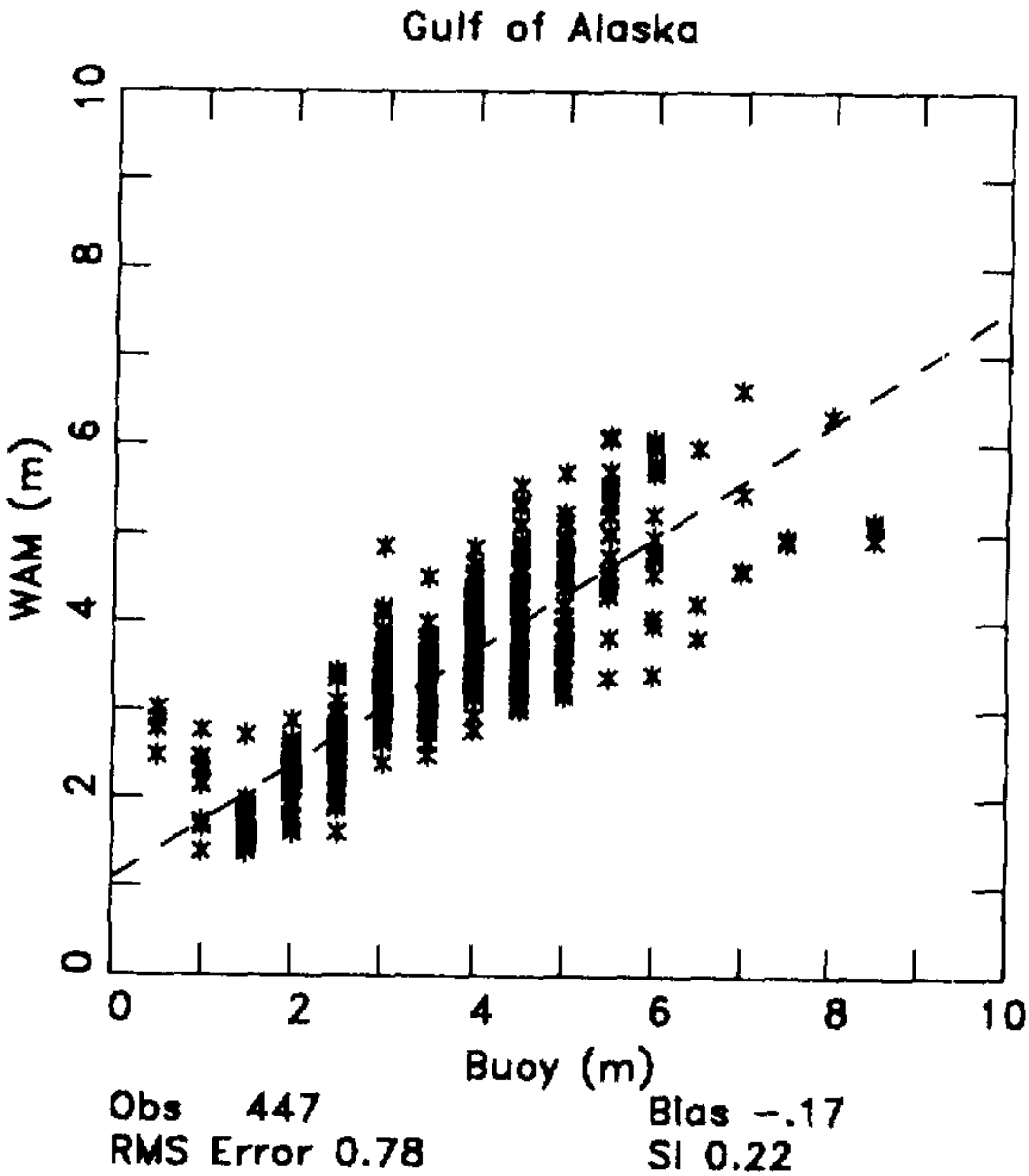

Fig. 1. Scatter plot of significant wave heights predicted by GWAM (6-hour forecasts produced by the ontime and offtime runs and valid at either 0000, 0600, 1200, or 1800 GMT) versus significant wave heights observed at buoys 46001, 46003, 46036 and 46184 in the Gulf of Alaska during January 1995.

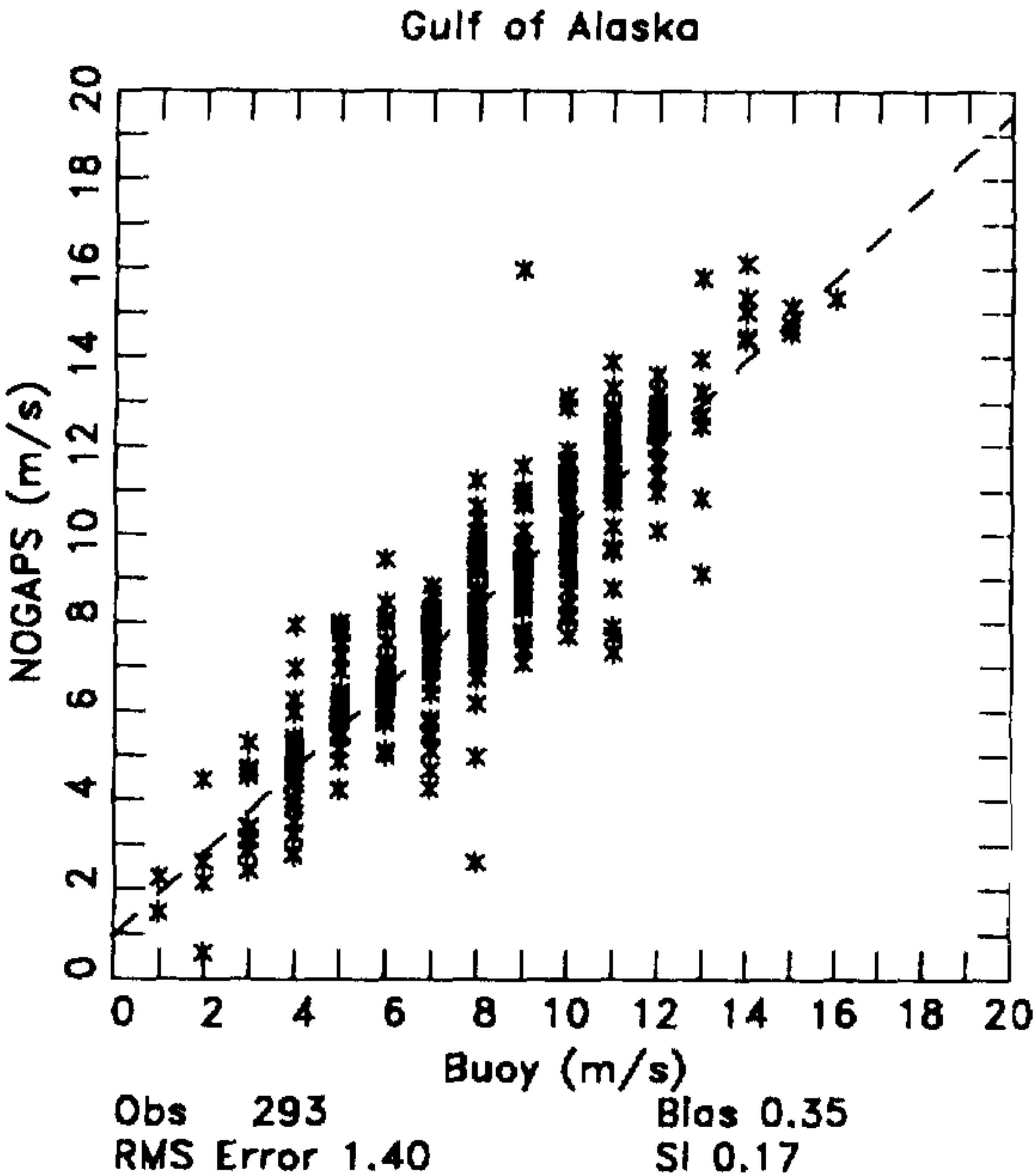

Fig. 2. Same as Fig. 1 but for wind speeds at 10 m height predicted by NOGAPS and wind speeds observed at 10 m height by the buoys.

In any case, the root-mean-square (RMS) wave height error (0.78 m) is quite good for wintertime conditions and substantially better than that reported by Clancy et al. (1986) for GSOMW in this region during January 1985 (i.e., 1.27 m). In addition, the scatter index parameter, defined as the standard deviation of the difference between the predicted and observed fields divided by the mean of the observed field, is also quite good. The GWAM scatter index in the Gulf of Alaska for January 1995 (0.22) is substantially less than the corresponding GSOWM scatter index in the Gulf of Alaska for January 1985 (0.35; see Clancy et al., 1986).

Of course the improvements in wave prediction skill indicated above are due, in part, to improvements in the accuracy of the winds that drive the wave models, As demonstrated by Figure 2 , the NOGAPS 10 m winds were quite good in the Gulf of Alaska during January 1995, showing a low scatter index (0.17) and only a slight tendency to overpredict low wind-speed events and underpredict high wind-speed events.

GWAM has a more marked tendency to underpredict high wave events in swell-dominated regions than in areas dominated by windsea. Figures 3 and 4 show comparisons of wave and wind predictions with buoy observations near the Hawaiian Islands. The NOGAPS winds show only a small negative bias here (-0.23 m S1, while the GWAM wave height shows a negative bias at the upper wave height ranges. A closer look at the wind and wave record at buoy 51001 (Figure 5) indicates an underprediction of swell events, which originate from storms in the north Pacific. This model tendency is consistent with that found by Zambresky (1989). See Wittmann and Clancy (1993) for further verification of Fleet Numerical wind and wave predictions with buoy data.

Monthly trends in the mean and RMS errors for GWAM and NOGAPS can be seen from Figures 6(a) though 6(d) , The monthly RMS errors increase with forecast time for both winds and waves. The RMS errors increase during the northern hemisphere winter, of course, because of increased atmospheric variability. The mean errors for the waves are slightly positive and increase with forecast time, while the mean errors for the winds are sightly negative for a forecast time of zero, and also increase and become positive with forecast time.

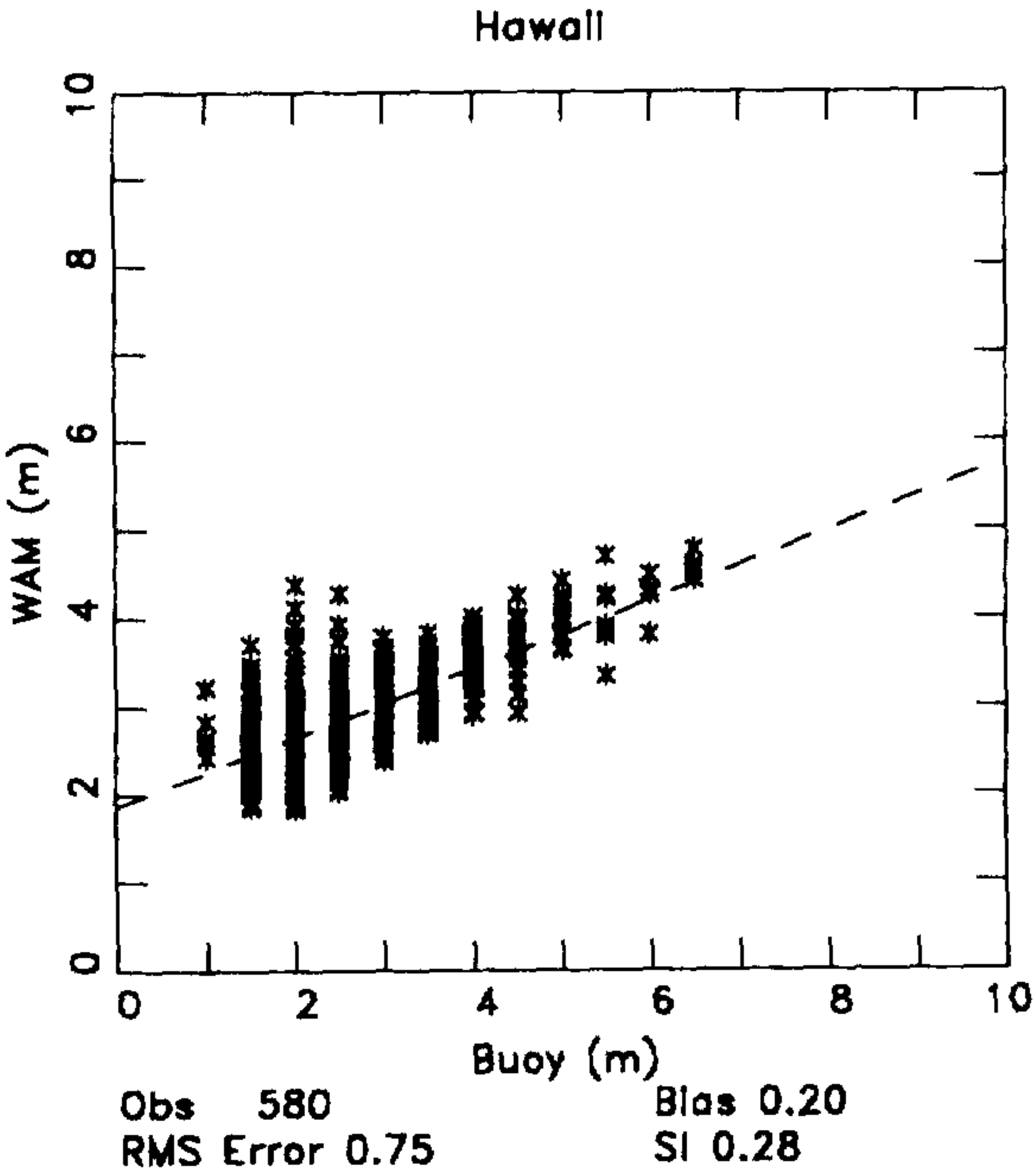

Fig. 3. Scatter plot of significant wave heights predicted by GWAM (6-hour forecasts produced by the ontime and offtime runs and valid at either 0000, 0600, 1200, or 1800 GMT) versus significant wave heights observed at buoys 51001, 51002, 51003, 51004, 51026 and 51027 near Hawaii during January 1995.

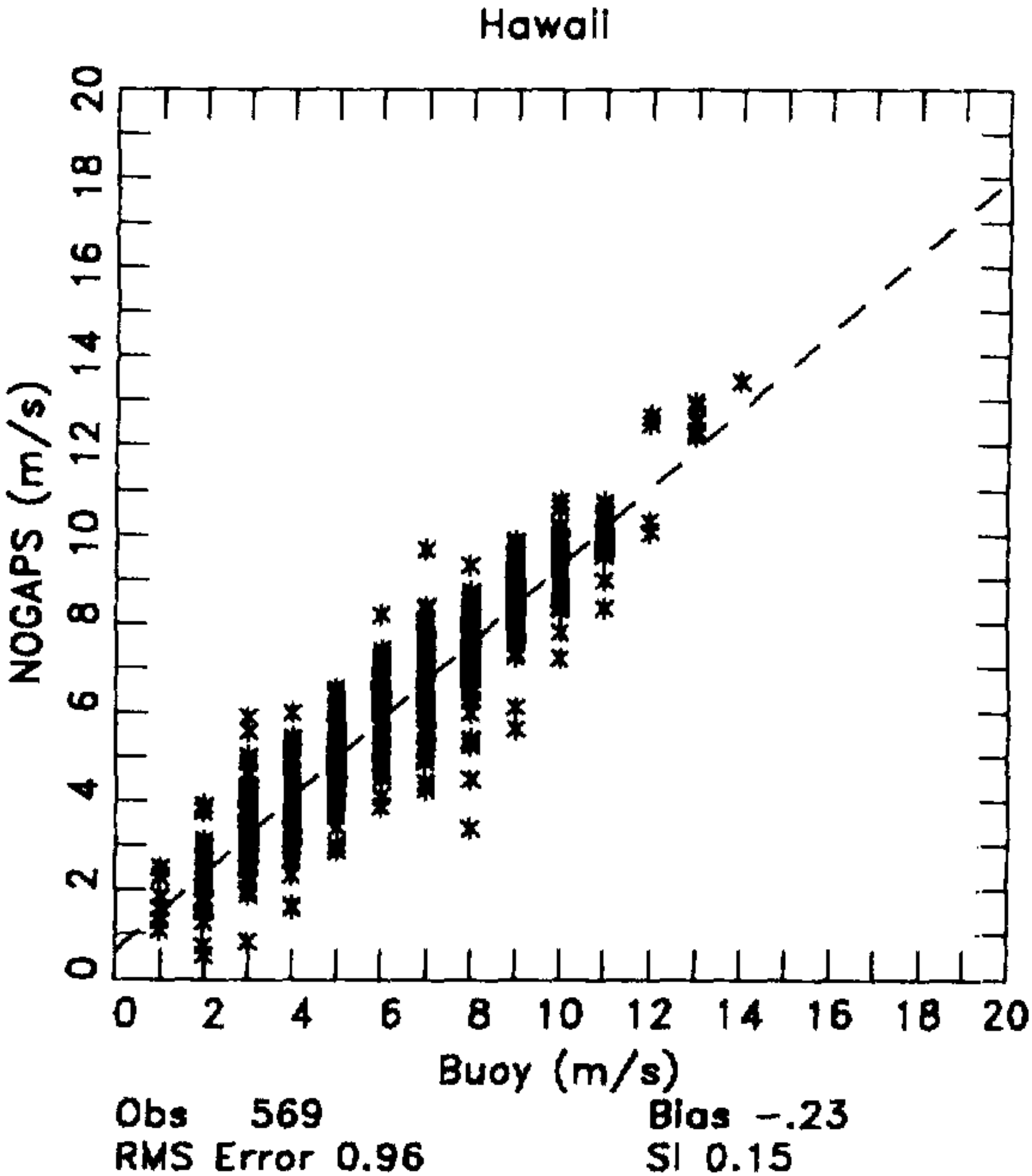

Fig. 4. Same as Fig. 3 but for wind speeds at 10 m height predicted by NOGAPS and wind speeds observed at 10 m height by the buoys.

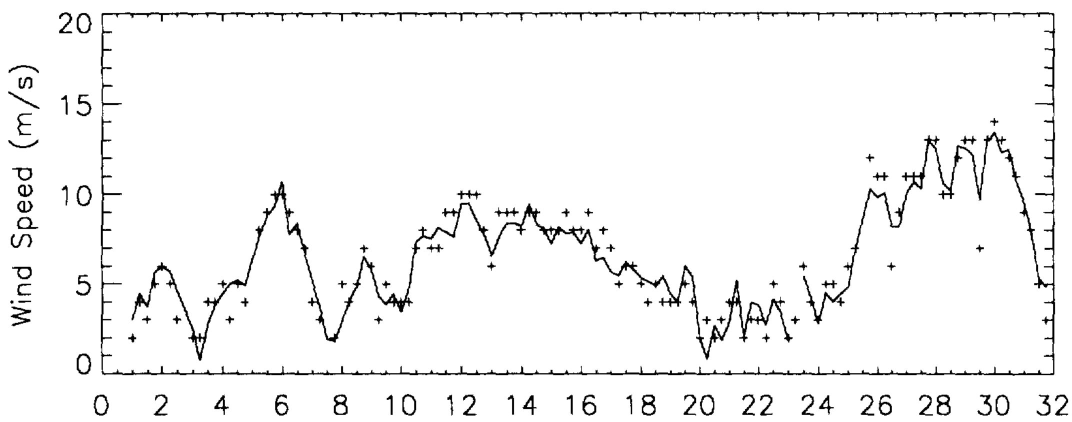

Fig. 5(a). Observed (crosses) and predicted (solid line) wind speed at 10 m height at buoy 51001 near Hawaii during January 1995. Predictions are from the NOGAPS analysis (i.e., for a forecast time of zero hours).

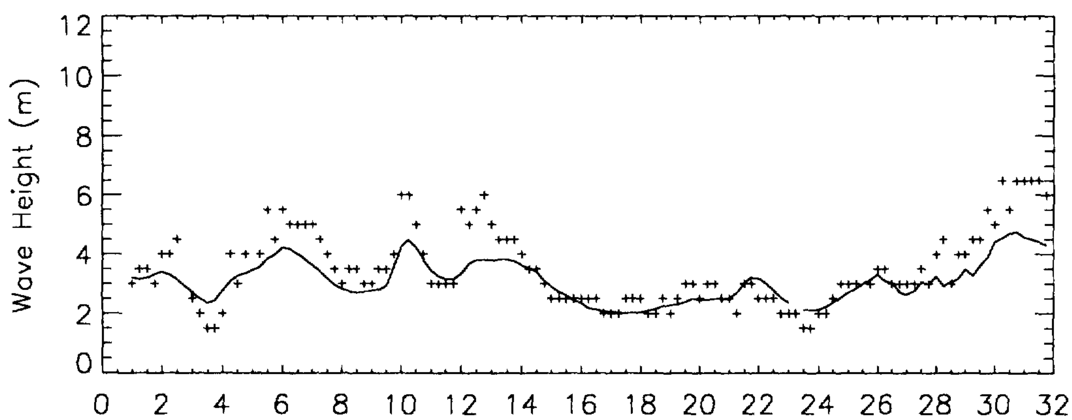

Fig. 5(b). Same as 5(a) but for significant wave height observed by the buoy and predicted by GWAM.

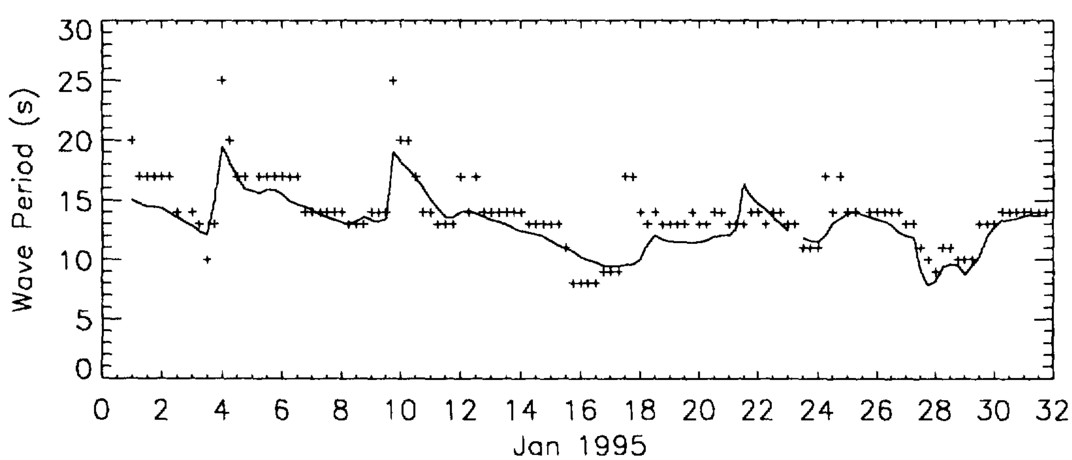

Fig. 5(c). Same as 5(a) but for peak wave period observed by the buoy and predicted by GWAM.

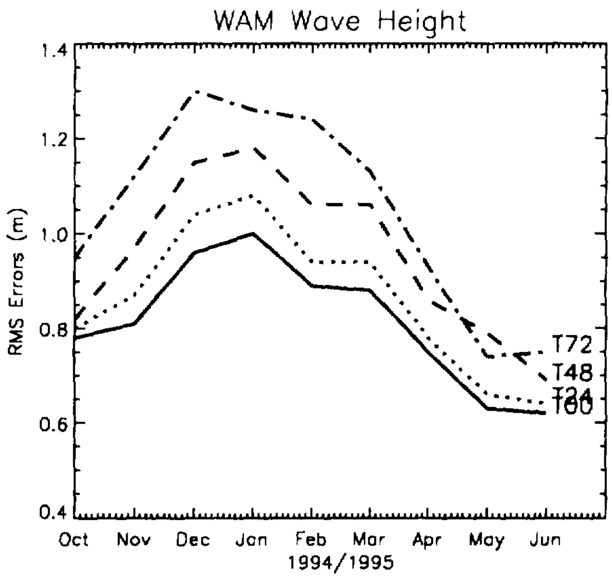

Fig. 6(a). Monthly averaged RMS significant wave height errors for GWAM for forecast times of 0 (solid), 24 (dotted), 48 (dashed) and 72 (dash-dot) hours based on comparison with all available moored buoy data in the North Atlantic and North Pacific from October 1994 through June 1995.

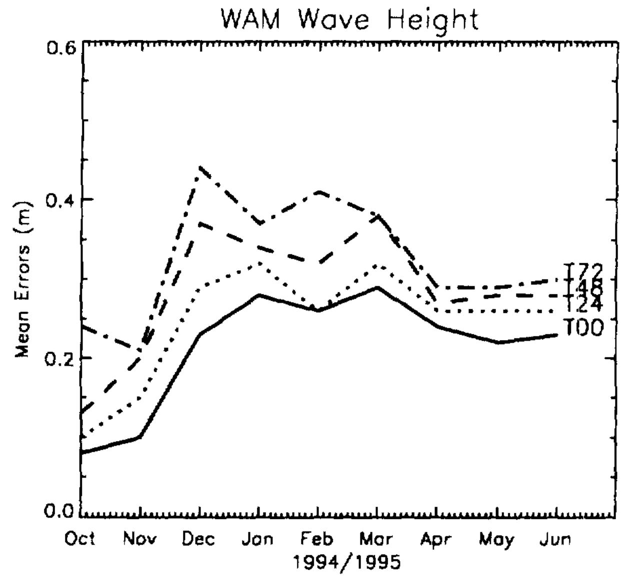

Fig. 6(c). Monthly averaged mean significant wave height errors for GWAM for forecast times of 0 (solid), 24 (dotted), 48 (dashed) and 72 (dash-dot) hours based on comparison with all available moored buoy data in the North Atlantic and North Pacific from October 1994 through June 1995.

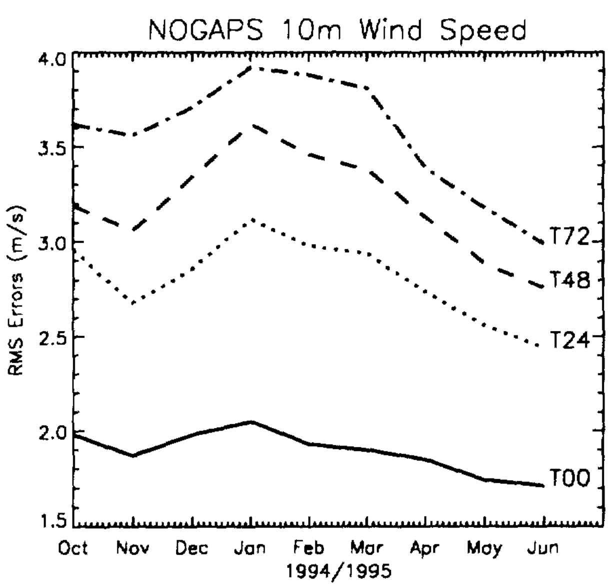

Fig. 6(b). Same as Fig. 6(a) but for wind speed at 10 m height predicted by NOGAPS.

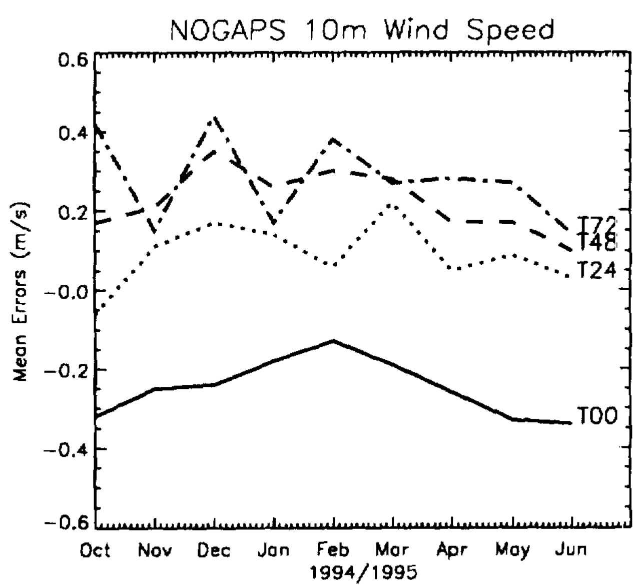

Fig. 6(d). Same as Fig. 6(c) but for wind speed at 10 m height predicted by NOGAPS.

During the spring of 1995, directional wave energy spectra predicted by GWAM were compared with data produced by National Data Buoy Center (NDBC) directional wave buoy 46042, located offshore of Monterey, CA, near 36.75°N, 122.40°W. The water depth at this location is 2103 m and there are no islands to the west which would interfere with swell propagation. The model predicted spectra were simply taken from the GWAM gridpoint closest to the buoy (37.00°N, 123.00°W). Comparisons were made for an 8 day period, from 31 May 95 to 7 June 95, during, which time significant wave heights ranged up to about 2 m.

Figure 7(a) shows the comparison of the GWAM and buoy wave energy spectra for 0000 GMT 1 June 95. The agreement, in terms of spectral shape and peak frequency, is very good. However the total wave energy predicted by GWAM tends to be slightly higher than that observed by the buoy. The directional comparisons are shown in Figure 7(b). The buoy does not measure the full directional spectrum, only the peak direction for each frequency bin. Agreement of the peak directions predicted by GWAM with those observed by the buoy is generally good. Note the presence of low frequency swell from the southwest and higher frequency windsea from the northwest, which is typical of spring conditions off the coast of California.

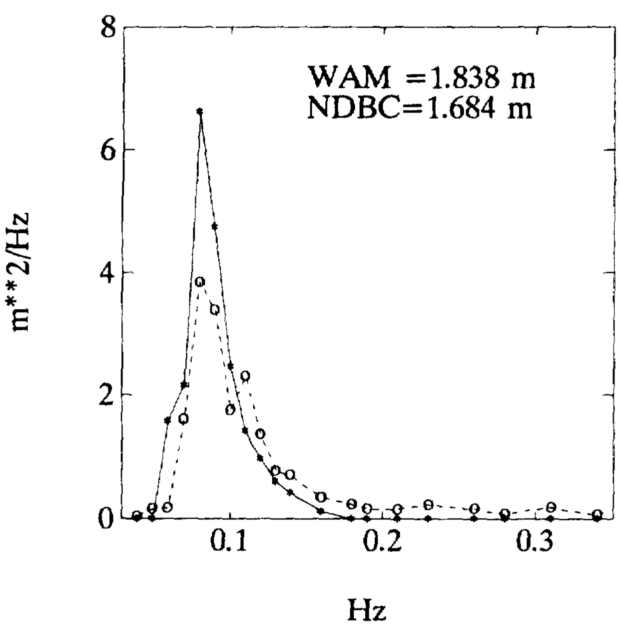

Fig. 7(a). One-dimensional wave energy spectrum observed at buoy 46042 near Monterey, CA, at 0000 GMT 1 June 95 (dashed line and circles) and corresponding 6-hour prediction from GWAM (solid line and asterisks).

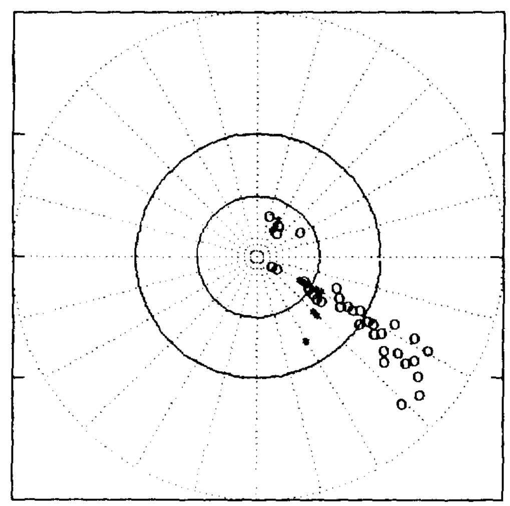

Fig. 7(b). Peak wave energy direction relative to true north for each frequency bin observed by buoy 46042 (circles) and corresponding 6-hour prediction from GWAM (asterisks) for 0000 GMT 1 June 95. Wave frequency increases linearly with radial distance from the center of the polar plot from 0 Hz at the center to 0.4 Hz on the outermost ring. True north is taken as vertically upward on the page, and the convention adopted is to display the directions toward which the wave energy is propagating.

5. SUMMARY AND OUTLOOK

Ocean wave modeling has been an integral part of Fleet Numerical's operation for over 30 years. Through a succession of upgrades to both wave models and the meteorological models that drive them, the accuracy of the wave predictions produced by Fleet Numerical has improved steadily. At present, Fleet Numerical employs the advanced third-generation wave model WAM in both global and regional implementations, with windstress forcing provided by the NOGAPS global and NORAPS regional meteorological models.

To address the problem of underprediction of peak wave-height events, the GWAM will soon be "loosely coupled" with NOGAPS in that the surface roughness predicted by the wave model will be provided to the NOGAPS boundary layer for use in its wind stress calculation (see Clancy and Plante, 1993). Also, a higher order propagation scheme, which reduces numerical dissipation (Bender and Leslie, 1994), will be tested in GWAM.

Other future enhancements in wave modeling at Fleet Numerical are expected to include assimilation of wave height data from satellite altimeters, coupling with surface current models to account for wave/current interactions, and implementation of any improvements to the WAM wave growth, dissipation and propagation algorithms that emerge from R&D. The spatial resolution of GWAM will be increased to 0.75° and, eventually, 0.50° to keep abreast of the increased spatial resolution expected in NOGAPS. Additional fully automated high-resolution regional applications; of WAM may be implemented in response to new

requirements. Finally, WAM, or a similar wave model, will be integrated into the Coupled Ocean/Atmosphere Mesoscale Prediction System (COAMPS) model (see Hodur, 1993). In this way, COAMPS will provide the very high-resolution, two-way interactive and internally self-consistent wind/wave products for the coastal regions of the world on which the Navy is now focused (Clancy and Plante, 1993).

6. REFERENCES

Bayler, G. and H. Lewit, 1992: The Navy Operational Global and Regional Atmospheric Prediction Systems at the Fleet Numerical Oceanography Center. Weather and Forecasting, 7, 273-279.

Bender, L.C. and L.M. Leslie, 1994: Evaluation of a third generation ocean wave model for the Australian region. Bureau of Meteorology Research Centre, BMRC Research Report No. 43, Melbourne, Australia.

Clancy, R.M., J.E. Kaitala and L.F. Zambresky, 1986: The Fleet Numerical Oceanography Center Global Spectral Ocean Wave Model. Bulletin of the American Meteorological Society, 67, 489-512.

Clancy, R.M. and P.A. Wittmann, 1990: FNOC implements advanced wave model, Naval Oceanography Command News, **10(11)**, 1-4.

Clancy, R.M. and R.J. Plante, 1993: Evolution of coupled air-sea models at Fleet Numerical Oceanography Center, Proceedings of the MTS'93 Conference, 22-24 September 1993, Long Beach, California, Marine Technology Society, 1828 L Street NW, Suite 906, Washington, DC 20036, pp. 284-290.

Copeland, J.L. and R.J, Plante, 1994: The development of an integrated environmental data base for Navy operational production computers into the 21 st century. Proceedings, Tenth International Conference on Interactive Information and Processing Systems for Meteorology, Oceanography and Hydrology, American Meteorological Society, 45 Beacon Street, Boston, MA 02108-3693, pp. 278-282,

Hodur, R.M., 1987: Evaluation of a regional model with an update cycle. Monthly Weather Review, **115**, 2707-2718.

Hodur, R.M., 1993: Development and testing of the Coupled Ocean/Atmosphere Mesoscale Prediction System (COAMPS). Technical Report NRL/MR/7533-93-7213, Naval Research Laboratory, Monterey, CA 93943-5502, 81 pp.

Hogan, T.F. and T.E. Rosmond, 1991: The description of the Navy Operational Global Atmospheric System's spectral forecast model. Monthly Weather Review, **119**, 1786-1815.

Janssen, P.A.E.M., 1994: Results with a coupled wind wave model. ECMWF Technical Report No. 71, European Centre for Medium-Range Weather Forecasts, Shinfield Park, Reading, Berkshire, RG2 9AX, England.

Plante R.J. and R.M. Clancy, 1994: An overview of operational prediction capabilities at Fleet Numerical Meteorology and Oceanography Center. Proceedings of the MTS'94 Conference, 7-9 Sep 94, Washington, DC, Marine Technology Society, 1828 L Street, NW, Suite 906, Washington, DC 20036, pp. 352-358.

Plante, R.J., 1995: Operational predictions for expeditionary warfare. Sea Technology, **36**, 23-31.

WAMDI Group, 1988: The WAM model - A third generation ocean wave prediction model. Journal of Physical Oceanography, **18**, 1775-1810.

Wittmann, P. A. and R. M. Clancy, 1993: Implementation and validation of a global third generation wave model at Fleet Numerical Oceanography Center. In Ocean Wave Measurement and Analysis, Proceedings of the Second International Symposium, 25-28 July 1993, New Orleans, O.T. Magoon and J.M. Hemsley, Editors, American Society of Civil Engineers, 345 East 47th Street, New York, NY 10017-2398, pp. 406-419.

Zambresky, L.F., 1989: A verification study of the global WAM, December 1987 - November 1988. ECMWF Technical Report No. 63, European Centre for Medium-Range Weather Forecasts, Shinfield Park, Reading, Berkshire, RG2 9AX, England.

4th International Workshop on Wave Hindcasting & Forecasting

LONG-TERM VARIABILITY AND ITS IMPACT TO THE EXTREME-VALUE PREDICTION FROM TIME SERIES OF SIGNIFICANT WAVE HEIGHT

G.A. Athanassoulis, T.H. Soukissian, Ch.N. Stefanakos

Dept. of Naval Arch. and Marine Engineering, National Technical University of Athens
Athens, GREECE

1. INTRODUCTION

Long-term time series of significant wave height, as well as many other environmental parameters, are non-stationary time series, exhibiting a year-to-year statistical variability and a longer-term climatic variability. However, the traditional approach for calculating return values of extreme values of the above parameters is based on the oversimplified notion of a sequence of independent and identically distributed random variables (i.i.d.-sequence). The restrictive assumptions involved in the i.i.d.sequence are clearly unrealistic and, thus, new techniques overcoming this oversimplifications are highly desirable. One direction for improving extreme-value predictions is to apply the same concept (i.i.d.-sequence) to appropriate data sets, that is to data sets consistent with the underlying assumptions. The Gumbel's (or annual maxima) approach represents a step towards this direction. A different approach aiming to the same goal is to improve the theoretical modeling, replacing the basic assumptions by less restrictive ones, and develop methods for extreme-value calculations in the context of these enhanced stochastic models. In this paper, an attempt towards this second direction is presented.

A new method for calculating return periods of various level values from non-stationary time series data is presented. The key-idea of the method is a new definition of the return period, based on the MEan Number of Upcrossings of the level x* (MENU method). The special case of a Gaussian, periodically-correlated time series is studied in detail. The whole procedure is numerically implemented and applied first to simulated data. Comparisons with results obtained by using several variants of the traditional (Gumbel's) approach are also presented. The numerical results show that the predictions obtained by means of MENU method are in agreement with the traditional predictions corresponding to the best data sets (annual extremes), analyzed by the best statistical techniques (tail-weighted analysis of tail data). Such an analysis is rarely possible in real cases, since it requires a large amount of high quality data. On the other hand. the predictions based on our method are stable and, in contrast to the traditional approach, essentially independent of statistical-estimation details.

2. THE RETURN PERIOD CONCEPT

In this Section. the traditional as well as some improved techniques for return period calculations are briefly reviewed, and some new ideas for the return period concept are introduced. These ideas are mainly based on a more elaborated stochastic modeling of the time series of significant wave height (Soukissian 1995, Athanassoulis & Soukissian 1995), and on a level crossing interpretation of the return period concept.

The concept of return period is traditionally defined by means of a sequence of random variables

$$X_1, X_2, \ldots, X_i, \ldots \tag{1}$$

which are:

A1. independent, and
A2. identically distributed (i.i.d.).

*Definition. The return period associated with a level value x** is defined as the mean value of the index i for which the event

$$x_i > x^* \quad i \geq 1$$

happens for the first time (see, e.g., Borgman 1975). This quantity, is converted to time by assuming (arbitrarily, more or less) that

A3. $\Delta\tau$= time between successive events (e.g., duration of sea states) is constant.

The above definition essentially realizes the simplest means for modeling and calculating the mean first passage time of the level value x^* . It admits of the well known closed-form solution

$$T_R(x^*) = \frac{\Delta\tau}{1 - F(x^*)} \tag{2}$$

where F(x) denotes the (common) cumulative distribution function of X_i, i = 1,2....

In ocean engineering practice, the above described concept is applied to either initial or extreme population data.

2.1 Initial population data

First, let us suppose that the stochastic sequence (1) represents a sequence of significant wave height observations H_s, i.e.

$$\left\{H_{S_n}, n \in N\right\} \equiv \left(H_{S_n}\right) \tag{3}$$

If the sample size is large, the frequency table (histogram) of the sample values can be obtained and the empirical distribution of H_S is estimated. Then the return periods associated with various levels x* is calculated by simply applying equ. (2). The use of an appropriate probability paper (e.g., Weibull probability, paper) permits one to extrapolate and calculate return periods at level values x* greater than the observed values of H_S. See e.g., Ochi (1982).

Examining closely the compatibility of theoretical assumptions A1, A2, A3, on which the return period concept is based, and the specific (statistical) characteristics of the stochastic sequence (3). we cannot disregard that:

- Successive or neighboring H_{Sn} are not independent. See e.g , Athanassoulis & Stefanakos (1995a), This can be partly confronted by considering appropriate modifications of the cumulative distribution function F(x) , so that the dependence structure of the time series is taken into account. See, e.g., Pugh & Vassie (1978,1980), Tawn & Vassie (1989). This technique is based on the concept of extremal index introduced by Loynes (1965) and elaborated by Leadbetter (1974).
- H_{Sn} cannot be considered identically distributed. A decisive reason for this is the seasonal variability, (A modification of the standard approach taking into account the fact that monthly H_S distributions are different is presented by, Carter & Challenor 1981).
- In any case, the exact distribution(s) of H_S is (are) not known. Of course one can always assume an analytical probability law, e.g., log-normal, Weibull or Gamma distribution, and estimate the parameters. See, e.g.. Ochi (1993), Teng et al. (1994). However, such an assumption is more or less arbitrary and its effect on the return period calculations is strong at high level values.
- Finally, it is well known that the time interval between specific events is not constant and its value seriously affects the return period calculations. (A partial solution of this difficulty, is to use as $\Delta\tau$ the mean or the most probable value of the random variable $\Delta\tau$ usually ranging from 3 to 6 hours. See, e.g., Haring & Heideman 1978, Athanassoulis & Soukissian 1991).

2.2 Extreme population data

In this case, the stochastic sequence (1) corresponds to a sequence of successive maximum values of significant wave height corresponding to fixed time intervals (e.g., months, years. etc), This sequence is denoted by

$$\left\{H_{S_{max,n}}, n \in N\right\} \equiv \left\{H_{S_{max,n}}\right\} \tag{4}$$

Predicting return periods and the corresponding design values by using data of maxima is known as the Gumbel's approach. This approach, when based on annual maxima, essentially overcomes all difficulties enumerated above concerning the validity of assumptions A1,A2,A3, as well as the fact that the distribution of the initial population is unknown. For, now A1,A2,A3 are more or less valid and, moreover and most importantly, the distribution of the population of maxima, denoted here by G(x), is "almost" known. Clearly, we are referring to the well known theoretical result that the limiting (as $n \to \infty$) form of G(x) can be only one of the following three (extreme-type) distribution:

- FT-I (Gumbel distribution),
- FT-II (Frechet distribution), or
- FT-III (reversed Weibull distribution).

This result is due to Fisher & Tippet (1928). See also Gnedenko (1943), Galambos (1978).

The estimation of return periods for high levels x* is again based on the formula (2),

$$T_R(x^*) = \frac{\Delta\tau}{1 - G(x^*)} \qquad (5)$$

but now G(x) is used instead of the initial population distribution F(x).

The use of G(x) instead of F(x) in equation (5), is justified by the fact that the two distributions G(x) and F(x) are right-tail equivalent. See, e.g., Resnick (1971). Castillo (1988). In ocean and coastal engineering practice, equation (5) is considered as a milestone for return-period calculations of various wave and wind parameters (Ochi 1982, 1990, Bishop 1984),

Obviously, the application of the above method to the calculation Of return periods goes through the following two steps:

(i) Decide upon the appropriate type of the asymptotic extreme-value distribution G(x), and

(ii) Estimate the parameters of the asymptotic distribution G(x) , selected in step (i).

See. e.g., Castillo & Sarabia (1992), Soukissian (1995). Practically, the most expedient method to accomplish step (i) is to calculate

$G_{emp}(x)$ by means of appropriate plotting formulas. Then, the selection of the type of $G(x)$ should be based on the behaviour of $G_{emp}(x)$ at <u>the right tail only</u>. This task can be processed by adopting a variety of short-cut procedures or by analytical methods either of purely statistical nature or based on a combination of physical observations and statistical arguments. Some serious problems arising during the selection procedure are well referenced in Muir & El Shaarawi (1986), Castillo (1988). Castillo & Sarabia (1992) and Soukissian (1995),

If we focus on physical arguments, the most "reasonable" choice of the type of the asymptotic distribution of H_{Smax} seems to be the FT-III, which is upper limited, as H_{Smax} is expected to be. (Recall that steep waves break). However, working with the FT-111 distribution, one faces the difficult problem of estimating the position parameter λ, which is the cut-off value of H_{Smax}. This estimation is so sensitive to data peculiarities that renders the results unreliable (Muir & El-Shaarawi 1986, Soukissian 1995).

Step (ii) can be performed by a variety of methods, most of them well-known and widely used: the maximum likelihood method (MLM), the method of moments, as well as various types of linear tail-weighted least-squares methods (LSM). An application of these methods is presented analytically in Section 5 . Another method for estimating the parameters of the asymptotic type distributions is the one of the r-largest values introduced by Weissman (1978) (see also Leadbetter et al. 1983) and subsequently used by Smith (1986), Tawn (1988).

In principle, Gumbel's approach forms a complete methodology for predicting long-term extreme values and the corresponding return periods. The most serious, and practically unresolved (up to now), problem of this approach is the lack of sufficiently large extreme population data samples that would permit the type of distribution to be safety selected and its parameters to be reliably estimated.

2.3 <u>The Peak-Over-Threshold method</u>

Apart from the traditional approaches described above, various alternative methods for return period prediction have also been developed. Most of them are primarily developed in the context of stochastic hydrology, in order to overcome the deficiencies of the traditional approach. A common characteristic Of these methods is that they use quite different data from those used by the traditional approach. The most important of them is the so called Peak-Over-Threshold (POT) method, which has been introduced in ocean engineering (although in a simplified manner) the last decade. See e.g., Rosbjerg & Knudsen (1984), van Vledder & Zitman (1992), van Vledder et al. (1994).

In this method, instead of the stochastic sequence (1) the sequence of "extreme events" (e,g., storms with H_S greater than a threshold value) is considered. Special attention should be paid during the sampling procedure in order to avoid clustering. The selection of intensities of the extreme events must be done in a way ensuring their statistical independence. A weak point of this method is that it is entirely based on ad hoc statistical models which cannot be justification theoretically. However, a significant advantage of the POT method is its potentiality to deal, in some way, with seasonality and serial dependence, which are always present in many-year long time series of wave and wind parameters (see. e.g., Smith 1984).

A complete description of the POT method and its interrelation with classical extreme-value theory can be found in Smith (1984). Interesting applications Of it are presented in Rosberg & Knudsen (1984); see also van Vledder & Zitman (1992), van Vledder el al. (1994).

2.4 Approaches based on the stochastic modeling of long-term time series of data

The motivation for developing such kind of methods comes from the fact that long-term time series of wave parameters (as well as of many other environmental parameters) are non-stationary time series, exhibiting a year-to-year statistical variability and longer-term climatic variability. Under these circumstances. it is natural to try to predict extreme values by using an appropriate stochastic modeling of the basic process (see representations (1) and (2) of section 4).

These methods are very recently introduced in ocean engineering applications by Athanassoulis & Soukissian (1995) and Soukissian (1995). Their basic characteristics are:

a) Replace assumptions A1 and A2 by, less restrictive ones,

b) Disregard assumption A3,

c) Model and treat the stochastic character and the dynamic nature of the underlying phenomenon (e.g., the various time scales involved and the correlation structure of the wave parameters),

Return period associated with the level value x* is calculated as the time period in which the **ME**an **N**umber of **U**pcrossings of the level x* becomes equal to unity (**MENU** method). The theoretical background of this method has been developed in the pioneering work by, Rice (1944/45). However, a version of MENU method as a technique for extreme value predictions first appeared in 1986 (Middleton & Thompson

1986, Hamon & Middleton 1989). in the context of sea-level extreme-value prediction. A detailed description of the method along with its complete implementation for the case the underlying process is Gaussian is given here. See also Soukissian (1995), Athanassoulis & Soukissian 1995. The implementation is heavily based on a non-stationary, representation for the stochastic process $H_S(\tau)$ introduced by Athanassoulis & Stefanakos (1995a).

3. RETURN PERIODS FOR NON-STATIONARY CONTINUOUS-TIME STOCHASTIC PROCESSES

In this Section, a new definition of the notion of return period associated with a given level value is introduced, which works well even if the underlying stochastic process is a general non-stationary one. This definition will be based on an appropriate crossing problem, Crossing problems are a major part of stochastic geometry which deals. among others things, with the stochastic description of the number of crossings of a given level by the graph of a (non-stationary) stochastic process, as well as the stochastic description of the time intervals between crossings or until a stochastic process reaches (crosses) a given upper or lower level (barrier). One of the most interesting problems is the so-called "one-sided barrier problem" or "one-sided first passage problem" which can be stated as follows:

> Given that at a time instant τ_0 the stochastic process $X(\tau;\beta)$ has a known value $X(\tau_0;\beta)$, find the stochastic structure of the time interval $T(\tau_0;\beta)$ until the process reaches for the first time the level x* .

A detailed review of the stochastic crossing problems can be found in Blake & Lindsey (1973) and Abrahams (1986). See also Berman (1992).

It is clear that the time interval $T(\tau_0;\beta)$ is, in general, a random variable. Therefore, its complete stochastic characterization requires the knowledge of its cumulative distribution function. The problem, in its greatest generality, remains unsolved except for some very special cases. Significant theoretical progress has been made for stationary and nonstationary Gaussian processes but, in any case, the problem is still in its infancy. Fortunately, however, for the applications we are interested in, it suffices to know only some "gross" statistical characteristics of $T(\tau_0;\beta)$ as the mean value and the variance. In fact, our new definition of the return period (Definition 2 below) is tailored in such a way that the knowledge of the first and second moments of the underlying process to be sufficient for the corresponding calculation.

Let us now state the general definition of return period which is applicable whatever the nature of the underlying process may be.

Definition 1: Assume that $\{X(\tau;\beta), \beta \in B\}$ is a non-stationary stochastic process with mean-square differentiable path functions (β is a choice variable, used for distinguishing different path functions). Let t be a given time instant and x* a given level value. Further, let us denote by $\tau_1(x^*;t;\beta)$ the first passage time of level x* by the path function $X(\tau;\beta)$ occurring after the time instant t. Then, the mean value of the quantity $T_R(x^*;t;\beta) = \tau_1(x^*;t;\beta) - t$, is called *the return period of* $X(\tau;\beta)$ *associated with the level value x* and the starting time t*, and it is denoted by $\overline{T_R}(x^*,t)$:

$$\overline{T_R}(x^*,t) = E^{\beta}\left[T_R(x^*;t;\beta)\right] \qquad (1)$$

This definition is quite general and, clearly, free of any restrictive assumptions as regards the underlying stochastic process $\{X(\tau;\beta), \beta \in B\}$. However, to facilitate the numerical calculations, an alternative definition will now be introduced, which applies equally well to general stochastic processes, but treats the first passage on the basis of the number of upcrossings of the level x*.

Definition 2: Assume that $\{X(\tau;\beta), \beta \in B\}$ is a non-stationary stochastic process with mean-square differentiable path functions. Let $M(x^*;t,t+T)$ be the mean number of upcrossings of the level x* by the process $\{X(\tau;\beta), \beta \in B\}$ in the time interval $(t,t+T)$. When $M(x^*;t,t+T)$ becomes equal to unity, the time lag (interval) T = (t + T) - t will be called *the return period of* $X(\tau;\beta)$ *associated with the level value x* and the starting time t*, and it will be denoted by $T_R(x^*,t)$.

The second definition has been first used by Middleton & Thompson (1986) (see also Hamon & Middleton 1989), in the context of statistical prediction of sea-level extremes. Although it seems likely the above two definitions of return period to be equivalent. this has not yet been established. However, on intuitive basis, one can conjecture that the numerical results obtained by means of these two definitions should be either the same or very near.

Now, in order to implement Definition 2, we have to calculate the mean number of upcrossings of the level x* by the non-stationary process $X(\tau;\beta)$. As it is well known (Rice 1944/1954), an upcrossing of the level x* by the process $X(\tau;\beta)$ occurs when

$$X(\tau;\beta) = x^* \qquad (2a)$$

and

$$\frac{dX(\tau\,;\,\beta)}{d\tau} > 0 \tag{2b}$$

The total number of the upcrossings of the level x* within the time interval (t_1,t_2) is given by the equation

$$C_R^+(x^*;t_1,t_2;\beta) = \frac{1}{2}\int_{\tau_1}^{\tau_2} |x'(\tau;\beta)|\,\delta(X(\tau;\beta)-x^*)d\tau \tag{3}$$

where $\delta(\cdot)$ is the Dirac delta function, Equation (3) was first derived by Rice (1944/1954). Recalling now that, for any, (possibly, generalized) function F(x, y)

$$E^{\beta}[F(X(\tau_1;\beta),Y(\tau_2;\beta))] = \int_{-\infty}^{\infty}\int_{-\infty}^{\infty} F(x,y)f_{\tau_1\tau_2}(x,y)dxdy \tag{4}$$

where $f_{\tau_1,\tau_2}(x,y)$ is the joint probability, density function of the random vector ($X(\tau_1;\beta)$,$y(\tau_2;\beta)$), and applying the ensemble average operator $E^{\beta}[\cdot]$ in both sides of equation (3), we obtain

$$E^{\beta}[C_R^+(x^*;t_1,t_2;\beta)] = \frac{1}{2}\int_{t_1}^{t_2}\int_{-\infty}^{\infty}\int_{-\infty}^{\infty} |x'|\,\delta(x-x^*)\,f_{\tau,\tau}(x^*,x')dxdx'd\tau \tag{5}$$

Integrating equ. (5) with respect to x, and observing that $E^{\beta}[C_R^+(x^*;t_1,t_2;\beta)]$ is not but the quantity $M(x^*;t_1,t_2)$ appearing in Definition 2 above, we easily obtain

$$M(x^*;t_1,t_2) = \frac{1}{2}\int_{t_1}^{t_2}\int_{-\infty}^{\infty} f_{\tau,\tau}(x^*,x')\,|x'|\,dx'd\tau \tag{6}$$

Since $f_{\tau,\tau}(x^*,x')$ is an even function with respect to the second argument x' (see, e.g., Levine 1973, Vol. 1, pp. 201,424), equ. (6) can be written in the following more convenient form

$$M(x^*;t_1,t_2) = \int_{t_1}^{t_2}\int_0^{\infty} x' f_{\tau,\tau}(x^*,x')dx'd\tau \qquad (7)$$

It should be noted that the above relation is totally independent from the specific type of the underlying bivariate distribution considered. Clearly, the deterministic quantity $M(x^*;t_1,t_2)$ has the following analytical properties:

(i) For any $t_1 > t_2$, and any $x^* > 0$, $M(x^*;t_1,t_2) \geq 0$ and $M(x^*;t,t) = 0$

(ii) for constant t_1 and $x^* > 0$, $M(x^*;t_1,t_2)$ is an increasing function of t_2

(iii) for constant $t_1 > t_2$, $M(x^*;t_1,t_2)$is a decreasing function of x^*

It should be emphasized that $M(x^*;t_1,t_2)$ is dependent on both time instants t_1 and t_2, since the underlying process $\{X(\tau;\beta),\beta \in B\}$ may be nonstationary .

In accordance with Definition 2, the return period $T_R(x^*,t)$ associated with the level x* and the starting time t is calculated as the unique value T for which

$$M(x^*;t,t+T) = 1 \qquad (8)$$

Let it be noted that the above definition of return period can be applied for any level value x* (high or low) and any starting time t. Accordingly. seasonal weather windows can be obtained in this manner.

4. AN APPLICATION TO THE CASE OF GAUSSIAN STOCHASTIC PROCESSES

Assume that $X(\tau;\beta)$ is a periodically-correlated stochastic process, admitting of a representation of the form

$$X(\tau;\beta) = \overline{X}(\tau) + \mu(\tau) + \sigma(\tau)W(\tau;\beta) \equiv G(\tau)\sigma(\tau)W(\tau;\beta) \qquad (1)$$

where $\overline{X}(\tau)$, $\mu(\tau)$ and $\sigma(\tau)$ are deterministic time-dependent functions and $W(\tau;\beta)$ is a zero-mean stationary stochastic process, which will be called hereafter the *residual stochastic process*. Representation

(1) has been introduced in wave climate modeling by Athanassoulis & Stefanakos (1995a,b) who applied model (1) to long-term time series of significant wave height,
The complete stochastic characterization of a general stochastic process $X(\tau;\beta)$ is a very complicated task, consisting in finding the sequence of cumulative distribution functions of all orders. In this work, we are interested solely in the first-order joint stochastic characterization of $X(\tau;\beta)$ and $X'(\tau;\beta)$, since for the numerical implementation of the MENU method use is only made of the joint probability density function $f_{\tau,\tau}(x,x')$. From now on the assumption is made that $X(\tau;\beta)$ and $X'(\tau;\beta)$ are jointly, Gaussian.

In order to evaluate the building elements of equation (8) of Section 3 , equation (1) is differentiated with respect to time, obtaining an analytical representation of the process $X'(\tau;\beta)$

$$X'(\tau;\beta) = G'(\tau) + \sigma'(\tau)W(\tau;\beta) + \sigma(\tau)W'(\tau;\beta) \qquad (2)$$

Under the assumption that $X(\tau;\beta)$ and $X'(\tau;\beta)$ are jointly Gaussian, the joint probability density function $f_{\tau,\tau}(x,x')$ is given by the equation

$$f_{\tau,\tau}(x^*,x') = \frac{1}{2\pi\sigma_X(\tau)\sigma_{X'}(\tau)\left(\sqrt{1-\rho^2_{XX'}(\tau)}\right)} \times$$
$$\times \exp\left\{-\frac{1}{2(1-\rho^2_{XX'}(\tau))}\left[\left(\frac{x^*-m_X(\tau)}{\sigma_X(\tau)}\right)^2 - 2\rho_{XX'}(\tau)\left(\frac{x^*-m_X(\tau)}{\sigma_X(\tau)}\right)\left(\frac{x'-m_{X'}(\tau)}{\sigma_{X'}(\tau)}\right) + \right.\right.$$
$$\left.\left. + \left(\frac{x'-m_{X'}(\tau)}{\sigma_{X'}(\tau)}\right)^2\right]\right\}. \qquad (3)$$

where $m_X(\tau)$, $\sigma_X(\tau)$ and $m_{X'}(\tau)$, $\sigma_{X'}(\tau)$ are the mean value and the standard deviation of the processes $X(\tau;\beta)$ and $X'(\tau;\beta)$, respectively, while $\rho_{XX'}(\tau)$ represents the correlation coefficient function of these two processes.

Subsequently, the five time-dependent parameters appearing in the right-hand side of equation (3), will be expressed in terms of the functions $G(\tau)$, $\sigma(\tau)$ and their derivatives, as well as of the zeroth and second-order spectral moments m_0 and m_2 respectively, of the stationary process $W(\tau;\beta)$.

4.1 Calculation of the parameters of $f_{\tau,\tau}(x,x')$

Applying ensemble average operator $E^{\beta}[\cdot]$ to equation (1) we get at once

$$m_X(\tau) = E^{\beta}[(X(\tau;\beta)] = E^{\beta}[G(\tau) + \sigma(\tau)W(\tau;\beta)] = G(\tau) \qquad (4)$$

On the other hand, forming the product $[X(\tau_1;\beta)X(\tau_2;\beta)]$ and taking the corresponding average $E^{\beta}[\cdot]$ we obtain

$$C_{XX}(\tau_1\tau_2) = \sigma(\tau_1)\sigma(\tau_2)C_{WW}(\tau_1-\tau_2) \qquad (5)$$

where $C_{XX}(\tau_1\tau_2)$ and $C_{WW}(\tau_1\tau_2)$ denote the autocovariance functions of $X(\tau;\beta)$ and $W(\tau;\beta)$ respectively. It should be noted that $C_{WW}(\cdot)$ is an even function of one time argument, since $W(\tau;\beta)$ is a stationary process.

For $\tau_1 = \tau_2 = \tau$, equation (5) reduces to:

$$\sigma^2{}_X(\tau) = \sigma^2(\tau)m_0 \qquad (6)$$

since $C_{WW}(0) = m_0$

For calculating the moments of $X'(\tau;\beta)$ we can use standard results of mean-square stochastic calculus, expressing the moments of $X'(\tau;\beta)$ by means of the corresponding moments of $X(\tau;\beta)$ (see, e.g., Levine 1973):

The mean value of the process $X'(\tau;\beta)$ is simply the derivative of $m_X(\tau)$

$$m_{X'}(\tau) = \frac{d}{dt}m_X(\tau) = G'(\tau) \qquad (7)$$

whereas the autocovariance function of $X'(\tau;\beta)$ is given by the well known relation

$$C_{X'X'}(\tau_1,\tau_2) = \frac{\partial^2}{\partial\tau_1\partial\tau_2}C_{XX}(\tau_1,\tau_2) = \frac{\partial}{\partial\tau_1}\left[\frac{\partial}{\partial\tau_2}\sigma(\tau_1)\sigma(\tau_2)R_{WW}(\tau_1-\tau_2)\right] =$$

$$= \sigma'(\tau_1)\sigma'(\tau_2)R_{WW}(\tau_1-\tau_2) + \sigma(\tau_1)\sigma'(\tau_2)R'_{WW}(\tau_1-\tau_2) -$$

$$- \sigma'(\tau_1)\sigma(\tau_2)R'_{WW}(\tau_1-\tau_2) - \sigma(\tau_1)\sigma(\tau_2)R''_{WW}(\tau_1-\tau_2). \qquad (8)$$

where $R_{WW}(\cdot)$ denotes the autocorrelation function of the process $W(\tau;\beta)$. For $\tau_1 = \tau_2 = \tau$ the above relation reduces to

$$\sigma^2{}_{X'}(\tau) = \sigma^2(\tau)m_0 + \sigma^2(\tau)m_2 \tag{9}$$

since $R'_{WW}(0) = 0$ and $R''_{WW}(0) = -m_2$

The cross-covariance function $C_{XX'}(\tau_1\tau_2)$ of $X(\tau;\beta)$ and $X'(\tau;\beta)$ can be calculated by means of the equation

$$C_{XX'}(\tau_1\tau_2) = \frac{\partial}{\partial\tau_2} C_{XX}(\tau_1\tau_2) \tag{10}$$

which, after some algebra, for $\tau_1 = \tau_2 = \tau$ reduces to

$$\sigma_{XX'}(\tau) = \sigma(\tau)\sigma'(\tau)m_0 \tag{11}$$

Finally $\rho_{XX'}(\tau)$ is given by

$$\rho_{XX'}(\tau) = \frac{\sigma_{XX'}(\tau)}{\sigma_X(\tau)\sigma_{X'}(\tau)} \tag{12}$$

4.2 Calculation of $M(x^*, t_1, t_2)$

In order to efficiently calculate the mean number of upcrossings of the level x* in the time interval (t_1, t_2), we shall obtain a more convenient form for $f_{\tau,\tau}(x^*, x')$. To simplify the notation we shall disregard temporarily the time argument from the functions $m_X(\tau), m_{X'}(\tau)$, $\sigma_X(\tau)$ $\sigma_{X'}(\tau), \rho_{XX'}(\tau)$, $G(\tau)$ and $\sigma(\tau)$.

Thus, let us set

$$Q(\tau) = \frac{1}{2\pi\sigma_X\sigma_X(\sqrt{1-\rho^2\chi\chi'})} \tag{13}$$

and denote by $P(x^*, x'; \tau)$ the exponent of the bivariate normal probability density function (3). Using equation (12) we obtain

$$P(x^*, x'; \tau) =$$

$$-\frac{1}{2(\sigma_X^2\sigma_{X'}^2 - \sigma_{XX'}^2)}\left[(x^* - m_X)^2\sigma_X^2 - -2\sigma_{XX'}(x^* - m_X)(x' - m_{X'}) + (x' - m_{X'})^2\sigma_{X'}^2\right]$$

(14a)

To facilitate integration with respect to x' in equation (8) of Section 3 , $P(x^*,x';\tau)$ will be treated as a function of x' , the variables x* and τ being treated as parameters. After some algebra, equation (14a) gives the following, quadratic with respect to x' , form for $P(x^*,x';\tau)$

$$P(x^*,x';\tau) = -C(\tau)x'^2 - D(x^*,\tau)x' - E(x^*,\tau) \tag{14b}$$

where

$$C(\tau) = \frac{\sigma_X^2}{2(\sigma_X^2\sigma_{X'}^2 - \sigma_{XX'}^2)} \tag{15a}$$

$$D(x^*,\tau) = \frac{\sigma_{XX'}G - \sigma_X^2 G' - x^*\sigma_{XX'}}{\sigma_X^2\sigma_{X'}^2 - \sigma_{XX'}^2} \tag{15b}$$

$$E(x^*,\tau) = \frac{(x^*-G)^2\sigma_{X'}^2 + 2x^*\sigma_{XX'}G' - 2\sigma_{XX'}GG' + \sigma_X^2 G'^2}{2(\sigma_X^2\sigma_{X'}^2 - \sigma_{XX'}^2)}$$

(15c)

The probability density function $f_{\tau,\tau}(x^*,x')$ can now be expressed as follows

$$f_{\tau,\tau}(x^*,x') = Q(\tau)\exp\left\{-C(\tau)x'^2 - D(x^*,\tau)x' - E(x^*,\tau)\right\} \tag{16a}$$

or, equivalently,

$$f_{\tau,\tau}(x^*,x') = B(x^*,\tau)\exp\left\{-C(\tau)x'^2 - D(x^*,\tau)x'\right\} \tag{16b}$$

where

$$B(x^*,\tau) = Q(\tau)\exp\left\{-E(x^*,\tau)\right\} \quad (17)$$

Using equation (16b), equation (8) of Section 3 is written as:

$$M(x^*;t_1,t_2) = \int_{t_1}^{t_2}\int_0^{\infty} x'\,B(x^*,\tau)\exp\left\{-C(\tau)x'^2 - D(x^*,\tau)x'\right\}dx'\,d\tau \quad (18)$$

Since C > 0 (see equation (15a)), the integral in the right hand side of (18) is convergent and integration with respect to x′ can be performed analytically by using the formula (see Gradshteyn & Ryzhik 1980, p. 338)

$$\int_0^{\infty} u\exp\left\{-Cu^2 - Du\right\}du = \frac{1}{2C} - \frac{D}{4C}\sqrt{\frac{\pi}{C}}\exp\left\{\frac{D^2}{4C}\right\}\left[1 - \Phi(D/2\sqrt{C})\right] \equiv I(x^*,\tau) \quad (19)$$

where $\Phi(\cdot)$ denotes the standard error function. Using this result, $M(x^*,t_1,t_2)$ is finally written in the form

$$M(x^*,t_1,t_2) = \int_{t_1}^{t_2} B(x^*,\tau)\,I(x^*,\tau)\,d\tau \quad (20)$$

We recall here that $B(x^*,\tau)$ is defined by equation (17), while $I(x^*,\tau)$ is defined by equation (19), the quantities $C = C(\tau)$ and $D = D(x^*,\tau)$ being defined by equations (15a.b).

Now, given a starting time t_1 and a level value x* the corresponding return period $T_R(x^*,t_1)$ is simply calculated by considering $M(x^*,t_1,t_2)$ as a function of t (the upper limit of integration), and determining $T_R(x^*,t_1)$ so that

$$\int_{t_1}^{t_1 + T_R(x^*,t_1)} B(x^*,\tau)I(x^*,\tau)d\tau = 1 \quad (21)$$

5. NUMERICAL RESULTS AND COMPARISON WITH CLASSICAL APPROACHES

In this section, MENU method is applied to the calculation of return period $T_R(x^*, t_1)$ as a function of the level value x*, for the case of a Gaussian and periodically, correlated time series. The emphasis is mainly put on high level values x*, in which the starting time t_1, is of no importance. (in any case t_1 is always taken to be "January 1st"). Note, however, that MENU method applies equally well to low level values, in fact to any level value x*.

Our main concern in this paper is the error-free and efficient numerical implementation of MENU method and a first assessment of it by means of comparisons with analogous results derived from the classical (Gumbel's) approach and some variants of it. Thus, in order that:

(i) The comparisons are free of the uncertainties due to data-structure imperfections, and
(ii) We are able to investigate the effect of various parameters by means of systematic variations,

we decided to use simulated wave data (cf. Goda et al. 1994). The characteristic statistical parameters of simulated time series have been given values which are more or less typical for wave data. (Recall that the time series of the logarithms of significant wave height is approximately a Gaussian periodically correlated time series).

5.1 Simulated data generation and treatment

Several time series have been produced, using numerical stochastic simulation, as realizations of a Gaussian, periodically correlated stochastic process $X(\tau;\beta)$. The data generation procedure is briefly described as follows:

- Produce i.i.d. N(0,1) time series $\varepsilon(\tau_i)$, i=1,2,... (Gaussian white noise).
- Produce AR(2) time series by means of the model

$$W(\tau_i) = a_1 W(\tau_{i-1}) + W(\tau_{i-2}) + \varepsilon(\tau_i) \tag{1}$$

This is an asymptotically stationary, zero-mean, Gaussian time series. A typical form of the spectral density function $S_{WW}(\omega)$ is shown in Fig. 1 .

· Produce a periodically correlated (non-stationary) Gaussian time series using the linear transformation

$$X(\tau) = \overline{X}(\tau) + \mu(\tau) + \sigma(\tau)W(\tau) \qquad (2)$$

The above data generation procedure is very flexible, permitting both the investigation of the robustness of our method (insensitivity, to non-essential factors as, e.g., to the specific realization of the process) and the investigation of its sensitivity, to the essential factors on which it is dependent.

After simulating several 19-year long time series $X(\tau)$, 19 annual and 228(=19xl2) monthly extremes were extracted from each series.

5.2 Extreme-value prediction by means of traditional methods

In order to calculate return periods by means of classical methods, the simulated time series were also subjected to standard extreme value analysis. The estimation of return periods for high levels x* by means of Gumbel's approach is based on the formula (5) of Section 2 .

A first idea for selecting the domain of attraction is based on a short-cut procedure consisting of plotting the maxima on Gumbel probability paper. These plots are shown on Fig. 2(a) for monthly maxima and Fig. 2(b) for annual maxima. The plots are based on the classical plotting position

$$p_i = \frac{i}{n+1} \qquad (3)$$

where i denotes the order of the maximum value in the sample of maxima, and n denotes the sample size. The behavior of the data shown in Fig. 3(a) clearly indicates an FT-I type domain of attraction, while the data plotted in Fig, 3(b) exhibits the same behavior only if we ignore the last point.

The selection of the domain of attraction from a sample of maxima can also be made by means of analytic methods (statistical tests): the curvature method (Castillo & Galambos 1986), and the Pickands III method (Pickands 111, 1975). Applying both methods to extreme data (either monthly or annual) we confirm that the distribution function F(x) lies in the domain of attraction of FT-I (Gumbel distribution). This result is compatible with the theoretical result that the normal distribution belong to the domain of attraction of FT-I for maxima.

The Gumbel distribution for maxima is of the form

$$G(x) = \exp\left\{-\,exp\left[\frac{-(x-\lambda)}{\delta}\right]\right\} \qquad -\infty < x < \infty, \qquad \delta > 0 \qquad (4)$$

where λ and δ are known as the location and scale parameter. respectively. Estimation of the parameters λ and δ can be based either on the maximum likelihood method or on a weighted least-square method (see Castillo 1988, and references cited there in). The distance (error) to be minimized in the latter approach is the relative return-period error:

$$\sum_{i=k}^{n} \frac{\left(\frac{1}{1-p_i} - \frac{1}{1-G(x_i)}\right)^2}{\left(\frac{1}{1\_G(x_i)}\right)^2} = \qquad (5)$$

$$= \sum_{i=k}^{n} \frac{1}{(1-p_i)^2}\left[p_i - G(x_i)\right]^2$$

where p_i, i=1,2, ... , n, is the plotting positions (3). The name of the method comes from the meaning of the terms appearing under the summation symbol: Quantity $(1-p_i)^{-1}$ is an estimate of the return period of the i-th order statistic (i-th maximum), while $(1 - G(x_i))^{-1}$ represents the corresponding return period as calculated by means of the analytic (asymptotic function $G(\cdot)$. Note also that

1. The quantity $(1-p_i)^{-2}$ which acts as a weighting factor to $[p_i - G(x_i)]^2$, increases with i, giving thus more importance to higher values of the sample of maxima,

2. The lower value of index i in the summation (6) is k, which means that the (k-1) lower order statistics in the sample are not used in the estimation of parameters.

For more details see Castillo (1988), Chapter 4.

The estimation procedure has been applied both to tail data and to the whole sample of maxima (the last case is very usual in ocean engineering applications). The resulting values of λ and δ are summarized in Table 1 , for monthly maxima, and Table 2 , for annual maxima.

Having at our disposal parameters λ and δ we can calculate return periods of extreme events by using formula (5) of Section 2 . If $T_R(x^*)$ is expressed in years, then for the case of annual maxima we may assume $\Delta\tau=1$ year, while for the case of monthly maxima $\Delta\tau=1/12$ year. The return period obtained by using formula (5) of Section 2 is systematically compared with the return period predicted by means of MENU method.

TABLE 1: Parameters of FT-I distribution for monthly maxima

	Maximum likelihood	Weighted least-squares
Tail data	λ=8.126	λ=7.9
k≥1	δ=0.88	δ=0.979
All data	λ=6.825	λ=7.316
k=1	δ=2.1048	δ=1.75

TABLE 2: Parameters of FT-I distribution for annual maxima

	Maximum likelihood	Weighted least-squares
Tail data	λ=10.271	λ=10.065
k≥1	δ=0.717	δ=0.9536
All data	λ=10.204	λ=10.171
k=1	δ=0.748	δ=0.8457

5.3 <u>Return period calculations based on MENU method. Comparisons</u>

A very important feature of MENU method is that, to any given time series of data there corresponds essentially, one return-period curve $T_R(x^*)$. This is not the case with the classical approach, the results of which are strongly dependent on

- The chosen population to be analyzed (initial population, monthly extremes, annual extremes),
- The domain of attraction (type of extreme-value distribution) to which the (unknown) population distribution belongs,

- The statistical method used for the estimation of parameters of the asymptotic extreme-value distribution,

Thus, there is a large number of practically, realizable alternatives, which usually lead to very different results. In the present work, we restrict ourselves only to two choices of the population-to-be-studied (monthly and annual extremes) and two different statistical methods of parameters estimation (maximum likelihood and tail weighted linear least squares). Since, however, the estimation procedure is applied either to the whole population or to tail data, we obtain eight different return period curves. Note that the more reliable approaches for high-level return periods (e.g., annual extreme data, tail data in statistical estimation) requires many-year data, which are usually, not available in the case of measured data.

In Fig. 4(a) the return-period function $T_R(x^*)$ calculated by means of MENU method is plotted along with curves obtained by using traditional (Gumbel's) approach based on monthly maxima, while in Fig. 4(b) similar results are shown with the traditional extreme-value prediction being based on annual maxima. Since in applying Gumbel's approach we use two different samples (entire population of maxima and tail data) and two different methods (maximum likelihood method and weighted least-squares method) for estimating parameters δ and λ of FT-I distribution function, we obtained four different curves in each case. In the same figures the return-period function $T_R(x^*)$ obtained by using equation (1) of Section 2 , is also shown. This function is derived by, using initial population data (X population). Thus, we obtain ten (10) profoundly different curves, that all represent the same function, namely, $T_R(x^*)$. The total variability of x* values for a given value of T_R is dramatically large. For example, for T_R=50 years, the value of x* varies from 12.2 to 20.2 m (monthly data) or from 12.8 in to 14 (annual data). In contrast to this situation, MENU method produces a single $T_R(x^*)$ curve, which is essentially independent of the underlying estimation procedure and the specific time-series realization used, Moreover, MENU method results are in very, good agreement with the traditional results obtained by using tail data.
Thus MENU-method predictions for the return period are in agreement with the traditional predictions corresponding to the best data sets (annual extremes) analyzed by the best statistical techniques (tail-weighted analysis of tail data). Moreover, MENU-method predictions are stable and can be obtained by much less data. A thorough analysis in order to find the least amount of data required by MENU method is under way.

ACKNOWLEDGEMENTS

This work has been partly funded by the Commission of the European Communities under contract No. MAS2-CT92-0025 with title *"Probabilistic Methodology for Coastal Site Investigation Based on Stochastic Modelling of Waves and Currents"* (WAVEMOD). Other participants of WAVEMOD project are IST and IH (Portugal), IFRENIER. LHF, STCPMVN, and STNMTE (France), SINTEF and OCEANOR (Norway), MARTEDEC (Greece), PCM (Spain) and DUT (the Netherlands).

REFERENCES

Abrahams, J., 1986: A survey, of recent progress on level crossing problems for random processes. Communications and Networks. A survey of recent advances, I.F. Blake and H.V. Poor (eds.), Springer-Veriag, pp. 6-25.

Athanassoulis, G.A., and T.H. Soukissian, 1991: Return periods of extreme sea states in the Greek Seas. 2nd Environmental Science and Technology Conf. pp. 770-778 (in Greek)

Athanassoulis, G.A.. and T.H. Soukissian, 1995: Return periods of extreme sea-states from long-term time series of Hs. Report TEC-3.301(0), WAVEMOD Project, MAS2-CT920025

Athanassoulis. G.A., and Ch.N. Stefanakos, 1995a: A nonstationary, stochastic model for longterm time series of significant wave height. J Geopkvs. Res., **100**(C8), 16149-16162.

Athanassoulis, G.A., and Ch.N. Stefanakos, 1995b: Non-stationary time series analysis of wave data. in the presence of missing values. Technical Report, National Technical University of Athens (Submitted for publication).

Berman, S.M., 1992: Sojourns and Extremes of Stochastic Processes, Wadsworth & Brooks/Cole Advanced Books & Software Pacific Grove.

Bishop, J.M, 1984: Applied Oceanography. John Willey & Sons.

Blake, I.F., and W.C. Lindsey, 1973: Level-crossing problems for random processes. IEEE Trans. Inform. Theory, **19**(3), 295-315.

Borgman, L.E, 1975: Extremal statistics in ocean engineering. Civil Engineering in the Oceans, **3**, 117-131

Carter, D.J.T., and P.G. Challenor, 1981: Estimating return values of environmental parameters, Quart. J. R. Afet. Soc., **107**, 259-266.

Castillo, E., 1988: Extreme Value Theory in Engineering. Academic Press.

Castillo, E., and J. Galambos, 1986: Determining the domain of attraction of an extreme value distribution. Technical Report. Temple University.

Castillo, E., and J.M. Sarabia, 1991 Engineering analysis of

extreme value data selection of models. J. Waterw. Port Coastal Ocean Engng., **118**(2), 129-147.
Fisher. R.A.. and L.H. Tippet, 1928: Limiting forms of the frequency distributions of the largest or smallest member of a sample. Proc, Camb. Philos. Soc., **24**, 180-190,
Galambos, J., 1978: The Asymptotic Theory of Extreme Order Statistics. John Wiley and Sons.
Gnedenko, B.V., 1943: Sur la distribution limite du terme maximum d'une série aldatoire. Ann. Math.. **44**, 423-453.
Goda, Y., P. Hawkes, E. Mansard, M.J. Martin, M. Mathiesen, E. Peltier, E.F. Thompson. and G. van Vledder, 1994, Intercomparison of extremal wave analysis methods using numerically simulated data. Ocean wave Measurement and Analysis, O.T. Magoon and J.M. Hemsley (eds.), pp. 962-976.
Gradshteyn. I.S., and I.M. Ryzhik, 1980: Table of Integrals, Series, and Products. Academic Press.
Hamon, B.V, and J.F, Middleton, 1989: Return periods of extreme sea levels: The exceedance probability method. Int. Hydrogr. Rev., **66**(2), 165-177.
Haring, R.E.. and J.C. Heideman, 1978: Gulf of Mexico rare wave return periods. 10th OTC pp. 1537-1550,
Leadbetter, M.R., 1974: On extreme values in stationary sequences. Zeitschrift fur Wahrsch Verw., **28**, 289-303.
Leadbetter, M.R.. G. Lindgren, and H. Rootzen. 1983: Extremes and Related Properties of Random Sequences and Series. Springer-Verlag.
Loynes, R.M., 1965: Extreme values in uniformly mixing stationary stochastic processes. Ann. Math. Stat., **36**, 993-999.
Levine, B., 1973: Fondements Théoriques de ia Radiotechnique Statistique. Editions MIR.
Middleton, J.F, and K.R. Thompson, 1986: Return periods of extreme sea levels from short records. J Geophys. Res., **91**, 11707-11716.
Muir, L.R. and A.H. El-Shaarawi, 1986: On the calculation of extreme wave heights: A review. Ocean Engng., **13**(1), 93-118.
Ochi, M. K., 1982: Stochastic analysis and probabilistic of random seas. Adv. Hydrosc., **13**, 217-375.
Ochi, M.K., 199O.- Applied Probability and Stochastic Processes, John Willey & Sons.
Ochi, M.K., 1993: Marine environment and its impact on the design of ships and marine structures, SNAME Trans., **101**, 673-703.
Pickands, J., III. 1975: Statistical inference using extreme order statistics. Ann. Stat., **3**, 119-131.
Pugh, D,T. and J.M. Vassie, 1978.- Extreme sea levels from tide and surge probability. 16th Coastal Engng. Conf., Vol. 1. pp, 911-930
Pugh, D.T. and J.M. Vassie, 1980: Applications of the joint

probability method for extreme sea level computations. Proc. Instn. Civ. Engrs, Part 2, **69**, 959-975.

Resnick, S.I., 1971: Tail equivalence and its applications, J. Appl. Probab., **8**, 136-156.

Rice. S.O., 1944/1945: Mathematical analysis of random noise. Bell System Technical Journal, **23**, 282-332, and **24**, 46-156 (Selected Papers on Noise and Stochastic Processes, N. Wax (ed.), Dover, New York, 1954).

Rosjberg, D. and J. Knudsen, 1984: POT-estimation of extreme sea-states and the benefit of using wind data. Statistical Extremes and Applications, JT. de Oliveira (ed.), NATO Scientific Affairs Division, D. Reidel Publishing Co.

Smith, R.L., 1984: Threshold methods for sample extremes. Statistical Extremes and Applications, J.T. de Oliveira (ed.), NATO Scientific Affairs Division, D. Reidel Publishing Co.

Smith, R.L., 1986, Extreme value theory based on the r largest annual events. J Hydrol., **86**, 27-43,

Soukissian, T.H., 1995: Methods of long-term analysis and prediction of sea wave climate. Ph.D. thesis, Dept. of Naval Architecture & Marine Engineering, National Technical University of Athens (in Greek).

Tawn, J.A., 1988: An extreme value theory model for dependent observations. J. Hydrol., **101**, 227-250.

Tawn, J.A., and J.M. Vassie, 1989: Extreme sea levels: The joint probabilities method revisited and revised. Proc, Instn. Civ. Engrs., Part 2, **78**, 429-442

Teng, C.-C., G.L. Timpe, I.M. Palao, and D.A. Brown, 1994: Design waves and wave spectra for engineering applications. Ocean Wave Measurement and Analysis, O.T. Magoon and J.M. Hemsley (eds.), pp. 992-1006.

van Vledder, G. and T. J. Zitman, 1992: Design waves: Statistics and engineering practice, 2nd ISOPE Conf, Vol. III, pp. 170-178.

van Vledder, G., Y. Goda, P. Hawkes. E. Mansard. M.J, Martin. M. Mathiesen, E. Peltier, and E.F. Thompson, 1994: Case studies of extreme wave analysis - A comparative analysis. Ocean Wave Measurement and Analysis, O.T. Magoon. and J.M. Hemsley (eds.), pp. 977-991.

Weissman, I., 1978: Estimation of parameters and large qunatiles based on the kth largest observations, J Amer. Stat. Assoc., **63**, 812-815.

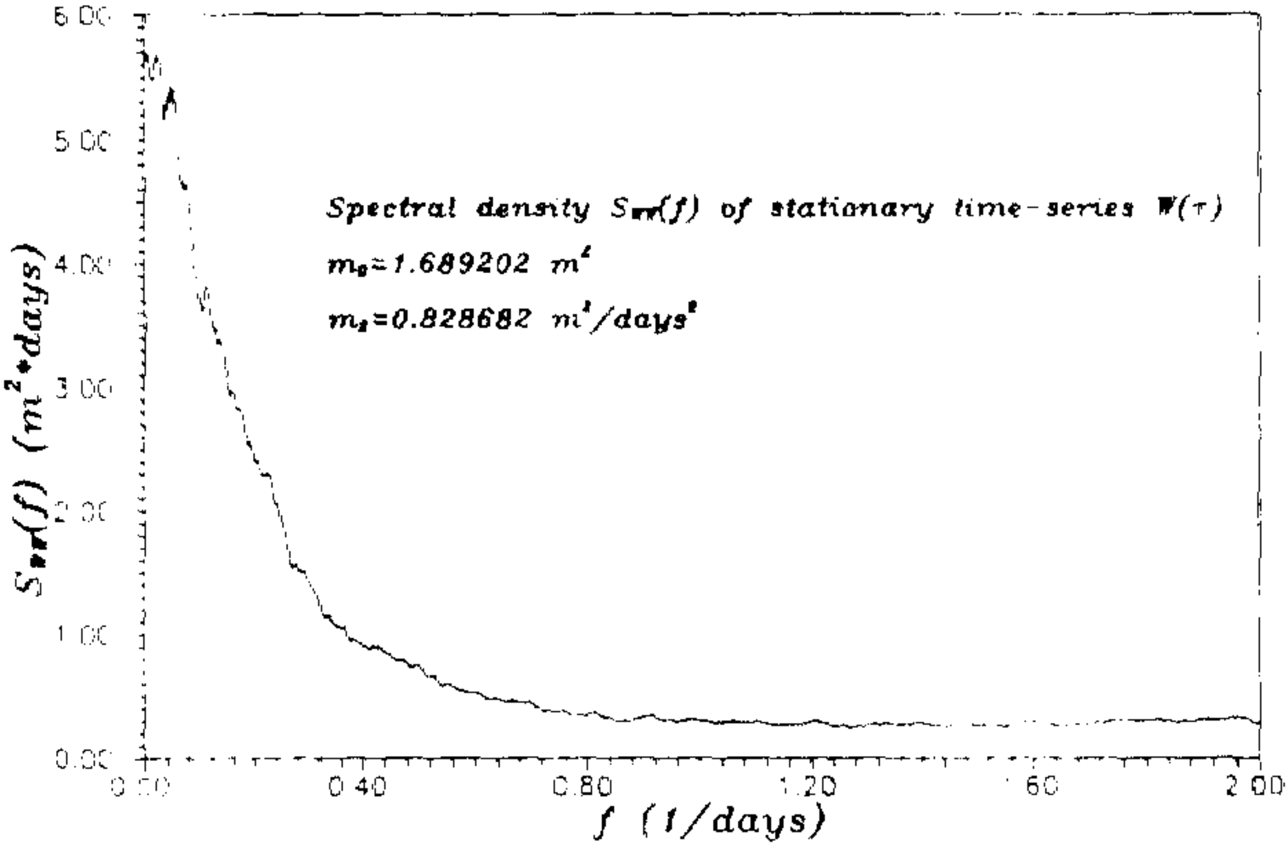

Figure 1: Spectral density function $S_{WW}(f)$ of the simulated time series $W(\tau)$.

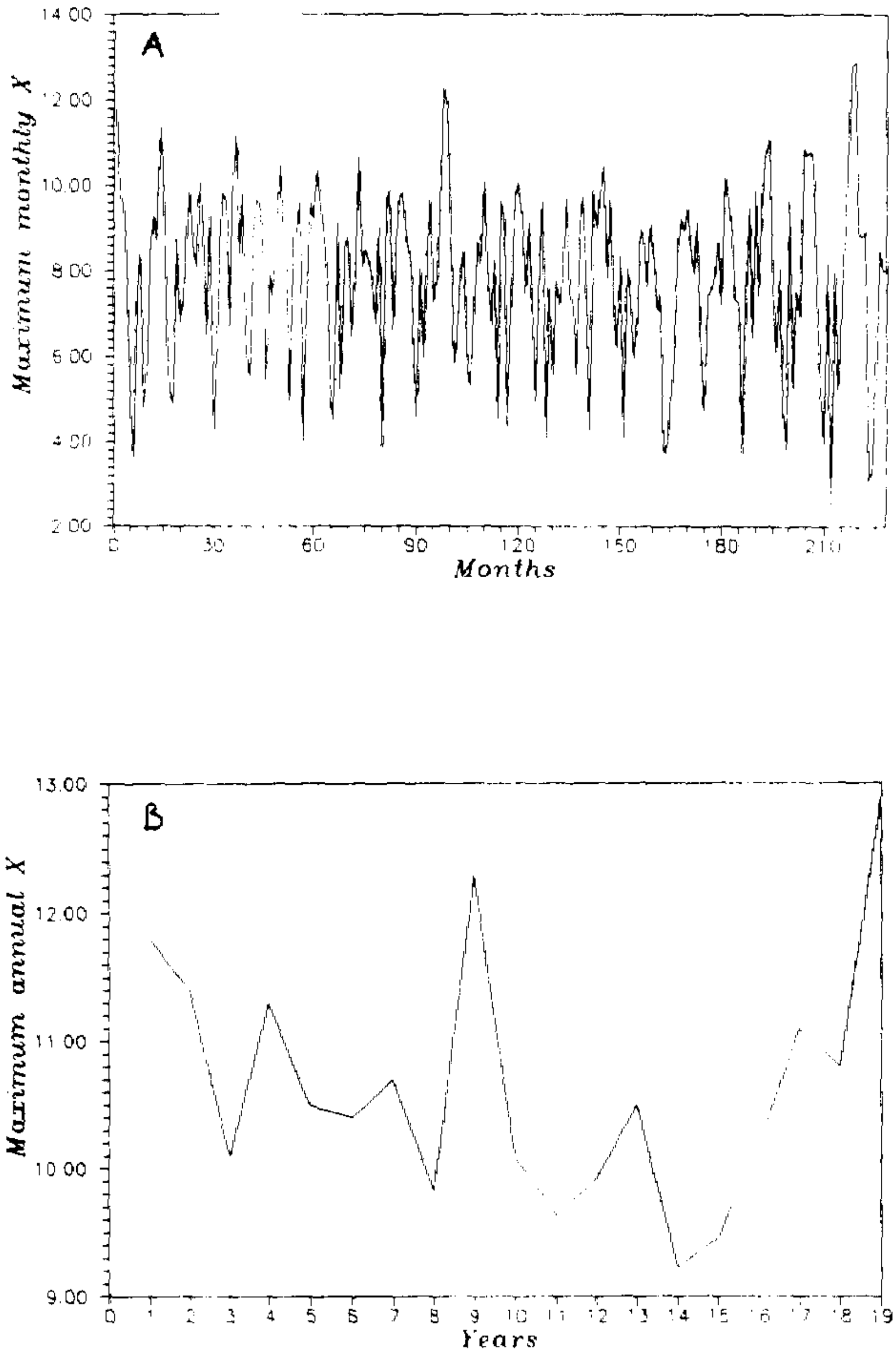

Figure 2: Time series of monthly maxima (A) and annual maxima (B).

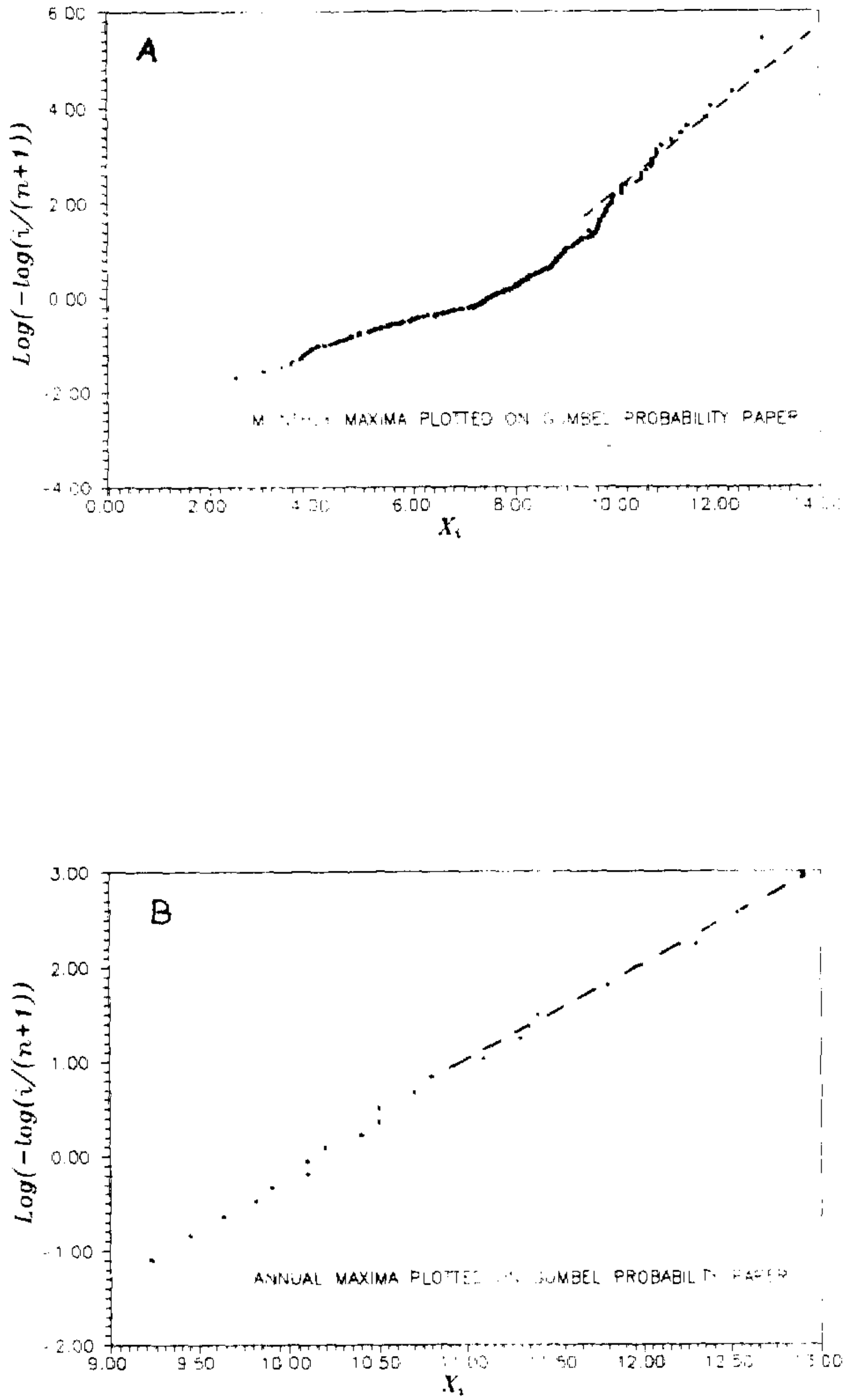

Figure 3: Gumbel probability paper plots of monthly (A) and annual (B) maxima.

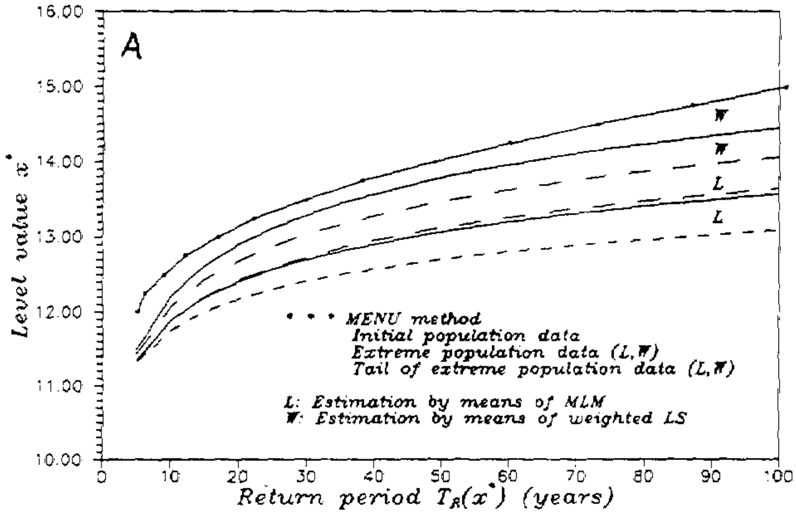

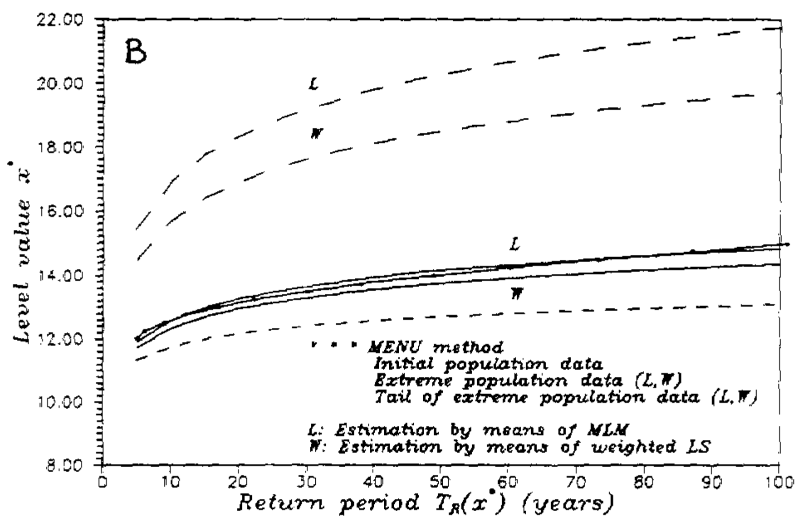

Figure 4: Return period $T_R(x^*)$ of monthly (A) and annual (B) maxima for various level values x^*, estimated by means of MENU method and Gumbel's approach (simulated data).